

High-valent late transition metal complexes for hydrocarbon oxidation



A thesis submitted to the University of Dublin in fulfilment of the
requirements for the degree of Doctor of Philosophy by

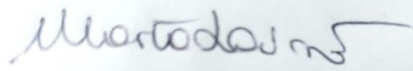
Marta Lovisari

Under the supervision of Prof. A. R. McDonald

School of Chemistry
Trinity College Dublin

January 2022

I declare that this thesis has not been submitted as an exercise for a degree at this or any other university and is my own work. Parts of the work described herein are the product of collaboration and are acknowledged at the beginning of each chapter. I agree to deposit this thesis in the University's open access institutional repository or allow the library to do so on my behalf, subject to Irish Copyright legislation and Trinity College Library conditions of use and acknowledgements.



Marta Lovisari

Marta Lovisari

Summary

Saturated hydrocarbons are the constituents of the main feedstocks for energy production but their oxidation to valuable fine chemicals is still very challenging. Therefore the design and optimization of new catalysts for the functionalization of inert C–H bonds is a compelling goal to access more valuable chemicals through milder and more selective processes. High-valent late transition metal complexes have been widely invoked as powerful oxidants, taking inspiration from the active oxidants found in several enzymatic catalytic cycles in nature. High-valent metal-oxo (O), -hydroxide (OH), -halide (Cl, F, Br, I) and porphyrin π -cation radical complexes are in fact present as biologically relevant species such as Compound 1 in cytochrome P450, the active oxidants in lipoxygenases, halogenases and haloperoxidases, P680 in chlorophyll and P865 in bacteriochlorophyll. A lot of focus has been directed on their synthetic counterparts, both containing first-row late transition metals, such as Ni and Cu, due to the overall dearth of high-valent oxidants containing these metals, and third-row transition metals such as Au, due to the lack of mechanistic insights on this class of oxidants. The main topics reported in the present thesis are therefore the design, characterization and mechanistic studies of high-valent late transition metal (Ni, Cu and Au) oxidants for the oxidative activation of substrates bearing C–H bonds.

As the first step, in Chapters 2 and 3 we investigate the reactivity of two Au^{III} complexes, differing only in the ancillary ligand: [Au(X)(terpy)](ClO₄)₂ (X = Cl, **1**; X = OH, **2**). These complexes were characterized in polar aprotic solvents (DMF, DMSO) by ¹H NMR, electronic absorption spectroscopy, CV and XRD and they showed to oxidise substrates bearing weak C–H bonds (DHA, CHD) and O–H bonds at room temperature. The kinetics of these oxidation reactions were monitored by electronic absorption spectroscopy and EPR showing the formation of stable radicals as a result of a PCET oxidation on the substrates bearing O–H bonds, which were employed as useful probes to gain mechanistic insights. The kinetic analysis showed that both complexes were reacting via a hydrogen atom transfer (HAT) mechanism, but **1** was a more competent oxidant with respect to **2**. In fact the free energy of activation (ΔG^\ddagger) was lower for **1**, showing that a lower barrier for HAT occurs with the chloride as ancillary ligand. We proposed two explanations for this difference: the former is an electronic reason, the latter a thermodynamic one. The first reason, supported by quantum chemical calculations, consisted of the Au–Cl bond showing higher covalency than the Au–OH bond,

with a major contribution of the $\text{Au}^{\text{II}}\text{-Cl}^\cdot$ bond description. The partial radical character on the chlorine therefore could explain the higher reactivity for **1** with respect to **2**. The second argument was the thermodynamic driving force lying in the strength of the bonds of the products formed upon HAT. For **2**, the species formally obtained upon HAT is a $[\text{Au}^{\text{II}}(\text{H}_2\text{O})(\text{terpy})]^{2+}$ complex, for which we have estimated a $\text{BDFE}_{\text{O-H}}$ of 81 ± 3 kcal/mol, whereas for **1**, we were not able to trap the species formed after the HAT event (a putative $[\text{Au}^{\text{II}}(\bullet\bullet\text{HCl})(\text{terpy})]^{2+}$ adduct) therefore we compared the reported value of $\text{BDE}_{\text{H-Cl}}$ (103 kcal/mol). We believe that this striking 22 kcal/mol difference is the main driving force for the higher reactivity of **1** compared to **2**. These results proved for the first time that Au^{III} complexes can be effective HAT oxidants and that Au^{III} -halide adducts can be more effective oxidants than the Au^{III} -oxygen ones.

In Chapter 4 we synthesized and characterized three late-transition metal porphyrin complexes, $[\text{Cu}(\text{T}(\text{OMe})\text{PP})]$ (**1**), $[\text{Ni}(\text{T}(\text{OMe})\text{PP})]$ (**2**) and $[\text{Au}(\text{T}(\text{OMe})\text{PP})]^+$ (**3**), taking inspiration from nature in the attempt to find effective high-valent late transition metal oxidants for hydrocarbon oxidation. Cyclic voltammetry highlighted the presence of two reversible oxidation waves below 0.89V for **1** and **2**, therefore both complexes were successfully oxidised to higher-valent species, **1OX** and **2OX**, by using phenoxythiinyl hexachloroantimonate. The electronic nature of **1OX** and **2OX** was elucidated by electronic absorption spectroscopy, EPR and infra-red spectroscopy to be porphyrin π -cation radicals, respectively $\text{Cu}^{\text{II}\cdot+}$ and $\text{Ni}^{\text{II}\cdot+}$ complexes. After comparing their relative reactivity towards a phenolic substrate, we reacted the more competent **2OX** with hydrocarbon substrates with BDFEs ranging from 73 to 79 kcal/mol at 20 °C in DCM. A kinetic analysis performed by monitoring the reaction via electronic absorption spectroscopy and allowed us to determine that **2OX** was performing hydrocarbon oxidation via a CPET mechanism. The combination of these results and further EPR studies allowed us to propose a mechanism of reaction: the addition of the oxidant yields a Ni^{II} porphyrin π -cation radical (**2OX**), which upon addition of the substrate shifts the equilibrium towards the Ni^{III} tautomer. Then the CPET oxidation occurs within this species, with the nickel ion accepting the electron and the ligand accepting the proton to yield a Ni^{II} isoporphyrin and the oxidised substrate.

In Chapter 5 we proposed the synthesis and characterization of novel tailored ligands to isolate the precursors of putative high-valent late transition metal oxidants in order to hurdle the “Oxo-

wall” by enforcing a trigonal planar geometry around the metal ions. These IMAM (Imino Amido) ligands were designed to bear a strong anionic σ -donor as a deprotonated amide, a neutral iminic donor and tunable bulky substituents on the phenyl rings to ensure a low coordination number. We were able to achieve the desired ligands in a two-step synthesis, with different substituents on the aryl rings (isopropyl = IMAM 1, methyl = IMAM 2) and characterized them by ^1H NMR, ^{15}N NMR, ATR-FTIR and XRD. During the first complexation attempts we observed that the acidity of the α -protons lead to their deprotonation in the presence of a base. Therefore we optimized the ligands by methylating that position, yielding the alkylated IMAM 3 (bearing isopropyl substituents on the phenyl rings). We then attempted the complexation with Co^{II} , Ni^{II} and Cu^{II} where we reported interesting preliminary results: MS, ^1H NMR and EPR suggested in fact the formation of mononuclear low-coordinate complexes with these metal ions.

Acknowledgements

I would like to thank all the people who have inspired, assisted, befriended and supported me during this PhD journey. First and foremost, I would like to thank my supervisor Prof. Aidan McDonald for his endless support, both from a scientific and a human perspective, which helped me to grow and become a more independent scientist. I am wholeheartedly thankful for all the trust he placed in me and for the opportunities he has given me during these four years and a half.

I would like to thank all the technical staff in the School of Chemistry that helped me to put together the experimental pieces that make up this work. Thanks to Dr. John O'Brien for his patience and infinite knowledge on NMR spectroscopy, to Dr. Manuel Ruether for being a jack of all trades capable to solve every issue, to Dr. Brendan Twamley for his patience and priceless support on X-Ray diffraction and for collecting data and solving all the structures reported in this thesis, to Dr. Gary Hessmann for his support on Mass Spectrometry. I am grateful to Prof. Robert Barklie for his extensive training on EPR spectroscopy and his passion for science.

I am really thankful to Dr. John O'Donoghue who allowed me to discover the world of science communication, for his passion in coordinating everything outreach related and for being a real inspiration. Thanks for trusting me and allowing me to improve my communication skills, I will always remember our chats during the journeys for the workshops!

I would like to acknowledge all the past and present members of the McDonald's lab: Adriana, Xin, Ciara, Paolo, Peppe, Robert, Bertrand, Chaka, Duenpen, Lorna, Alex, Daniel, Philipp and Prasenjit. Working with you all has been a great craic! I would like to thank in particular Dr. Robert Gericke for his scientific support, for performing the quantum chemical calculations reported in this thesis and for the chats in front of beer and tacos. Thanks to Lorna for sharing all the fun at the EPR and for our chats about literally everything, I wish you all the best for your PhD! Thanks to my good friend Adriana for our lunches and coffees, I hope you keep up with your well-deserved shiny career. A huge thanks goes to Peppe, an incredible scientist and a true friend, you welcomed me on day 1 and from then we shared so many chats, tears, laughs, discussions, pub nights and questionable music playlists that I have to admit that I really miss you. I wish you all the best in your future endeavours!

I would like to thank all of my friends in Trinity, especially the Italian group (Delva, Chiara, Bruno, Emanuele, Angelica, Matteo, Federico), Nikolina, Natalia and Martha for all the fun memories and for helping me to stay sane until the end of this journey. Thanks to all my friends back home who have visited me in Dublin or kept close through long Skype chats.

A huge thanks to Paolo P. for all the happy memories and for the support during the tough times of these years we have shared in Dublin, I wish you happiness and a great career.

Thanks to Paolo B. for believing in me despite the circumstances and for supporting me during most of the writing of this thesis, you have been a great unexpected surprise and I am curious to see which other adventures will await us.

Last but not the least, I would like to thank my whole family, from my aunt and uncles to my little cousins, who have supported me endlessly during this PhD. Thanks for showing me affection and giving me strength from afar even during the toughest times.

Thanks to Mum and Dad, I really wish we could celebrate this one together and I hope you would be proud of me, you are what made me persist until the end and this goal is just for you.

Abbreviations

Afa	Azafulvene-amine
ATR/FTIR	Attenuated Total Reflection/Fourier Transform Infra-red Spectroscopy
BDE	Bond Dissociation Energy/Enthalpy
BDFE	Bond Dissociation Free Energy
bim	Bis(1-imidazolyl)methane
bipy	2,2'-bipyridine
Buea	tris[(N'-tertbutylureaylato)-N-ethyl]aminato
CAN	Cerium (IV) ammonium nitrate
CHD	1,4-cyclohexadiene
COSY	Correlation Spectroscopy
CPET	Concerted Proton-Electron Transfer
CYP	Cytochrome P450
DEPT	Distortionless Enhancement by Polarization Transfer
DCM	Dichloromethane
DFT	Density Functional Theory
DHA	9,10-dihydroanthracene
DHPE	Dihydrophosphinoethane
DMA	N,N-Dimethylacetamide
DMF	N,N- Dimethylformamide
DMSO	Dimethylsulfoxide
dpaq	2-[bis(pyridin-2-ylmethyl)]amino- N-quinolin-8-yl-acetamidate
DRM	Dry reforming of methane
2,6-DTBP	2,6-di- <i>tert</i> -butylphenol
EPR	Electron Paramagnetic Resonance
ESI	Electrospray Ionisation
ET	Electron Transfer
Et ₂ O	Diethyl Ether
EtOAc	Ethyl Acetate
GC-FID	Gas Chromatography-flame ionisation detector

GooF	Goodness of Fit
H ₃ buea	tris[(N'-tert-butylureaylato)-N-ethylene]aminato
HAA	Hydrogen Atom Abstraction
HAT	Hydrogen Atom Transfer
HSQC	Heteronuclear single quantum coherence spectroscopy
HMBC	Heteronuclear Multiple Bond Correlation
HT	Hydride Transfer
HXO	Hypohalous acid
IMAM ^{Me₂}	N-(2,6-dimethylphenyl)-3-((2,6-dimethylphenyl)imino)butanamide
IMAM ^{iPr₂}	N-(2,6-diisopropylphenyl)-3-((2,6-diisopropylphenyl)imino)butanamide
IR	Infra-red
KIE	Kinetic Isotope Effect
α -KG	α -ketoglutarate
KHMDS	Potassium bis(trimethylsilyl)amide
LTMOs	Late Transition Metal Oxo complexes
<i>m</i> -CPBA	<i>meta</i> -chloroperbenzoic acid
Magic Blue	Tris(4-bromophenyl)ammoniumyl hexachloroantimonate
Magic Green	Tris(2,4-dibromophenyl)ammoniumyl hexachloroantimonate
MeIMAM ^{Me₂}	N-(2,6-dimethylphenyl)-3-((2,6-dimethylphenyl)imino)-2,2-dimethylbutanamide
MeIMAM ^{iPr₂}	N-(2,6-diisopropylphenyl)-3-((2,6-diisopropylphenyl)imino)-2,2-dimethylbutanamide
Me ₂ EBC	4,11-dimethyl-1,4,8,11-tetraazabicyclo[6.6.2]hexadecane
MO	Molecular Orbital
MS	Mass Spectrometry
NacNac	β -diketiminato
NMR	Nuclear Magnetic Resonance
<i>n</i> -BuLi	<i>n</i> -Butyllithium
NEt ₃	Triethylamine
OAc	Acetate
OAT	Oxygen Atom Transfer
OEP	2,3,7,8,12,13,17,18-Octaethylporphyrin
OTf	Trifluoromethansulfonate
PCET	Proton-coupled electron transfer
(Phenox)SbCl ₆	Phenoxythiinylyl hexachloroantimonate

ppy	2-phenylpyridine
PT	Proton Transfer
PTSA	<i>p</i> -toluenesulfonic acid
pyN ₂ ^{iPr2}	<i>N,N'</i> -bis(2,6-diisopropylphenyl)-2,6-pyridine-dicarboxamide
pyN ₂ ^{Me2}	<i>N,N'</i> -bis(2,6-dimethylphenyl)-2,6-pyridine-dicarboxamide
PY5	2,6-bis-(bis(2-pyridyl)methoxymethane)pyridine)
PyPz	tetramethyl-2,3-pyridino porphyrazine
Py ₂ Py-(pi ^{Cy})	2,2',2'-methylbis-pyridyl-6-(2,2',2'-methylbis-5-cyclohexyliminopyrrol)-pyridine
Pytacn	1-(2-pyridylmethyl)-4,7-dimethyl-1,4,7-triazacyclononane
SLO	Soybean lipoxygenase
TAML	Tetraamidomacrocyclic ligand
TEMPOH	1-hydroxy-2,2,6,6-tetramethyl-piperidine
terpy	2,2':6',2''-terpyridine
THF	Tetrahydrofuran
tpa	tris(2-pyridylmethyl)amine
13-TMC	1,4,7,10-tetramethyl-1,4,7,10-tetraazacyclotridecane
TMC	Tetramethylcyclam
TMC-Py	1-(pyridyl-2'-methyl)-4,8,11-trimethyl-1,4,8,11-tetrazacyclotetradecane)
TMG ₂ dien	1,1-bis{2-[N ₂ -(1,1,3,3-tetramethylguanidino)]ethyl}amine
Mes ^{TMP}	<i>meso</i> -Tetramesitylporphyrin
TOF	Time of Flight
TPA	Tris-(2-pyridylmethyl)amine
TPP	5,10,15,20-Tetraphenylporphyrin
T(OMe)PP	5,10,15,20-Tetrakis-(4-methoxyphenyl)porphyrin
TPFPP	5,10,15,20-Tetrakis-(2,3,4,5,6-pentafluorophenyl)porphyrin
Tp ^{Ph2}	hydrotris(3,5-diphenylpyrazol-1-yl)borate
Tren	Tris-(2-aminoethyl)amine
Ttpc	tris(2,4,6-triphenylphenyl) corrole
TTBTD	3,3',5,5'-tetra- <i>tert</i> -butyl-[1,1'-bis(cyclohexane)]-2,2',5,5'-tetraene-4,4'-dione
TQA	Tris-(quinolylmethyl)amine
XAS	X-Ray Absorption Spectroscopy
XRD	X-Ray Diffraction

Contents

Summary	iii
Acknowledgements	vi
Abbreviations	viii
Contents	xi
Introduction	1
1.1 Small molecule activation.....	2
1.1.1 Hydrocarbon oxidation catalysis.....	3
1.1.2 Biological oxidation.....	4
1.1.2.1 High-valent metal-hydroxides in nature	6
1.1.2.2 High-valent metal-halides in nature	7
1.1.3 Reactivity mechanisms	8
1.1.3.1 Proton coupled electron transfer	8
1.1.3.2 Hydrogen atom transfer	9
1.1.3.3 Other mechanisms.....	12
1.1.4 First-row transition metals in oxidation catalysis	13
1.1.4.1 The “Oxo Wall”	14
1.1.4.2 Synthetic mid- and high-valent metal-hydroxides.....	17
1.1.4.2.1 Mid- first row transition metals (Fe and Mn)	17
1.1.4.2.2 Late first-row transition metals (Cu).....	23
1.1.4.3. Synthetic high-valent metal halides	24
1.1.4.3.1. Iron.....	24

1.1.4.3.2. Manganese	28
1.1.4.3.3. Nickel.....	30
1.1.4.3.4. Copper.....	32
1.1.4.4 Second and third row late transition metals in oxidation catalysis.....	36
1.1.4.4.1 Platinum	37
1.1.4.4.2 Palladium	38
1.1.4.4.3 Iridium.....	38
1.1.4.4.4 Rhodium.....	39
1.1.4.4.5 Osmium.....	39
1.1.5 Gold in oxidation catalysis.....	41
1.1.5.1 Heterogeneous gold oxidation catalysis.....	42
1.1.5.2 Homogeneous gold oxidation catalysis	44
1.1.5.2.1 Gold(III)-oxygen adducts.....	46
1.1.5.2.1.1 Gold(III)-hydroxide complexes	46
1.1.5.2.1.2 Gold(III)-bis- μ -oxo complexes	49
1.1.5.2.2 Gold(III)-halide complexes.....	50
1.1.5.2.2.1 Gold(III)-chloride and bromide complexes	51
1.1.5.2.2.1.1 Neutral N-donors	51
1.1.5.2.2.1.2 Anionic donors.....	52
1.1.5.2.2.1.3 Cyclometallating ligands	52
1.1.5.2.2.2 Gold(III)-fluoride complexes.....	57
1.1.6 Aims and methods.....	60
1.1.7 References.....	61
Hydrogen atom transfer reactivity by a gold-hydroxide complex	68
2.1 Introduction	69
2.2 Characterization of $[\text{Au}^{\text{III}}(\text{OH})\text{terpy}](\text{ClO}_4)_2$ and $[\text{Au}^{\text{III}}(\text{OD})\text{terpy}](\text{ClO}_4)_2$ in polar aprotic solvents.....	69

2.3 Reactivity of [Au ^{III} (OH)terpy](ClO ₄) ₂ with C–H bonds.....	73
2.4 Reactivity of [Au ^{III} (OH)terpy](ClO ₄) ₂ with O–H bonds	78
2.5 Mechanistic insights.....	88
2.6 Conclusions	94
2.7 Experimental section.....	95
2.8 References	100
Au^{III}–Cl in oxidative C–H and O–H bond activation	102
3.1 Introduction	103
3.2 Characterization of [Au ^{III} (Cl)terpy](ClO ₄) ₂	103
3.3 Reactivity with O–H bonds	107
3.4 Mechanistic insights.....	114
3.5.1 Driving forces for the reactivity differences: estimation of BDFE _{H–X}	117
3.5.2 Driving forces for the reactivity differences: electronic arguments	123
3.6 Reactivity with C–H bonds	125
3.7 Conclusions	126
3.8 Experimental section.....	127
3.9 References	130
A [Ni^{II}(porphyrin^{•+})] complex for C–H bond activation	132
4.1 Introduction	133
4.2 Synthesis and characterization of [M(T(OMe)PP)] ⁿ⁺ complexes (M = Cu, Ni, Au ; n = 0, 0, 1).....	134
4.3 Reactivity with oxidants.....	139
4.4 Reactivity with X sources (X = Cl [•] , F [•] , I [•] , OH [•]).....	146
4.5 Reactivity with O–H bonds	148
4.6 Reactivity with C–H bonds	150
4.7 Mechanistic insights.....	156
4.8 Conclusions	163

4.9 Experimental section	164
4.10 References	168
IMAM ligands for low-coordinate late transition metal complexes.....	169
5.1 Introduction	170
5.2 Unalkylated IMAM ligands	171
5.2.1 Synthesis.....	171
5.2.2 Characterization.....	172
5.2.3 Complexation.....	177
5.3 Alkylated IMAM ligands	181
5.3.1 Synthesis.....	181
5.3.2 Characterization.....	183
5.3.3 Complexation.....	189
5.3.3.1 Nickel.....	192
5.3.3.2 Cobalt.....	196
5.2.3.3 Copper.....	198
5.4 Conclusions	201
5.5 Experimental section	202
5.6 References	208
Conclusions and future work.....	211
6.1 Summary and conclusions.....	212
6.2 Future work	218
6.3 References	220
Appendix A.....	221
A.1 Chapter 2	221
A.2 Chapter 3	250
A.3 Chapter 4	263
A.4 Chapter 5	272

Chapter 1

Introduction

1.1 Small molecule activation

Small molecules such as O_2 , N_2 , H_2 , CO_2 , H_2O , N_2O and CH_4 play a pivotal role in fundamental biochemical processes (e.g. respiration and photosynthesis), in energy production and environmental issues such as climate change.¹ Most of these molecules are abundant and ubiquitous and given their potential to reversibly store energy in their chemical bonds they constitute the ideal candidates as main feedstock for a more sustainable energy production. This purpose is limited by the inertness of most of these small molecules, whose activation is thermodynamically demanding. For example on an industrial scale, nitrogen conversion to ammonia is achieved through the Haber-Bosch process, which approximately yields yearly 140 million metric tons of ammonia. Despite enabling a fertilizer supply sufficient to sustain global agriculture, this process is not devoid of heavy environmental and energetic implications.² The Haber-Bosch process in fact requires pressures between 150 and 350 atm and temperatures up to 600 °C, accounting for ~ 2% of annual global energy consumption. Furthermore, massive emission of CO_2 , the predominant greenhouse gas, and pollution of aqueous environment upon runoff with major environmental drawbacks are related to this process.²

Another example is given by the transformation of readily available carbon sources such as CO_2 or CH_4 into higher value chemicals. Catalytic CO_2 hydrogenation yields methanol, formic acid, carbon monoxide and other alcohols but requires high pressures (30-300 bars) and large volumes of H_2 .³ When methane is used as a hydrogen source in combination with CO_2 the process is called dry reforming of methane (DRM).^{3,4} DRM relies on CO_2 as a carbon source and on CH_4 activation to yield syngas, a mixture of CO and H_2 which is a building block for other fuels and fine chemicals, such as acetic acid.⁴ This process requires very high temperatures (> 700 °C) and faces catalysts inactivation issues on industrial scale due to carbon deposition. Moreover, further conversion of syngas into fuels and chemicals requires high pressures, making the overall reaction of activation of CO_2 and CH_4 very demanding from an energetic point of view.³ These examples highlight the challenge that contemporary chemists are facing with respect to the activation of small molecules to provide a more sustainable energy feedstock.

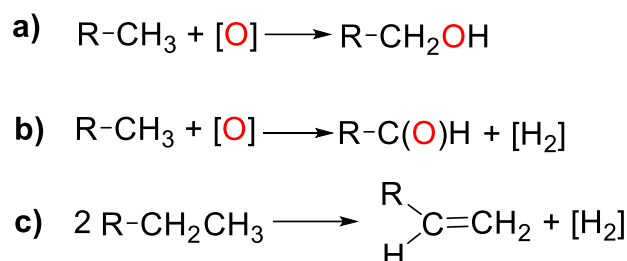
1.1.1 Hydrocarbon oxidation catalysis

Saturated hydrocarbons are the major constituents of crude oil and natural gas but their activation, required for their conversion into higher value fuels and precursors of fine chemicals, is still very challenging.⁵ Notably, alkanes are made up of strong, localized σ -bonds which account for their inertness towards functionalization and in particular towards selective oxidation. The oxidation of alkanes would in fact lead to many derivatives of higher economic and synthetic relevance, such as alcohols, aldehydes, ketones or acids and alkenes (Scheme 1.1) but the existing methods require harsh conditions and lack selectivity.⁶ The case of methane, the main component of natural gas and part of shale gas, coal bed gas and biogas, epitomizes the potential advantages linked to a better conversion of alkanes. The direct oxidation of methane gas to methanol, which is a liquid, would have major economic implications, allowing its facile transportation and storage from the remote locations where natural gas feedstocks are currently located. This would enable the exploitation of natural gas in a more sustainable and efficient way than mere combustion.

Unfortunately, the direct and selective oxidation of methane to methanol presents many challenges: first of all the C–H bond of methane has a bond dissociation enthalpy (BDE) of 105 kcal/mol, the highest among saturated hydrocarbons.⁶ Secondly, the oxidised product would have a weaker C–H bond ($\text{BDE}_{\text{C-H}} \text{CH}_3\text{OH} = 96 \text{ kcal/mol}$) and higher polarity, making it more prone to further react with any oxidation catalyst to yield the corresponding acid. Another issue is given by the nature of the oxidant employed: atmospheric dioxygen would be the ideal candidate but its triplet ground state makes it kinetically inert due to spin restrictions in the reactions with most substrates.⁷ For this reason, metal-based catalysts have shown to be the best to explore the feasibility of the direct oxidation of alkanes, given their possibility to switch among different spin states and thus to allow reactions with atmospheric dioxygen.

Platinum group metals such as Pt⁸, Rh⁹ or Ir¹⁰ have been widely employed by industries in the last decades.¹¹⁻¹³ Despite their effectiveness, solutions based on such expensive metals are not realistically applicable to bulk commodities production. For the above-listed reasons, an efficient and cost-effective way for large scale direct conversion of methane to methanol has yet to be identified. Industry still relies on indirect methods, such as steam reforming of methane, partial oxidation of methane in presence of oxygen or air and reforming of methane with CO₂. All these processes lead to the production of syngas, which needs further energy to

be converted in valuable fuels and chemicals and two of them (steam reforming and DRM) are highly endothermic. The partial oxidation exhibits low selectivity and poor reaction control over the catalyst surface.⁴ These considerations highlight the urge of finding catalysts which are able to allow mild, direct and selective conversion of saturated hydrocarbons into chemical commodities.



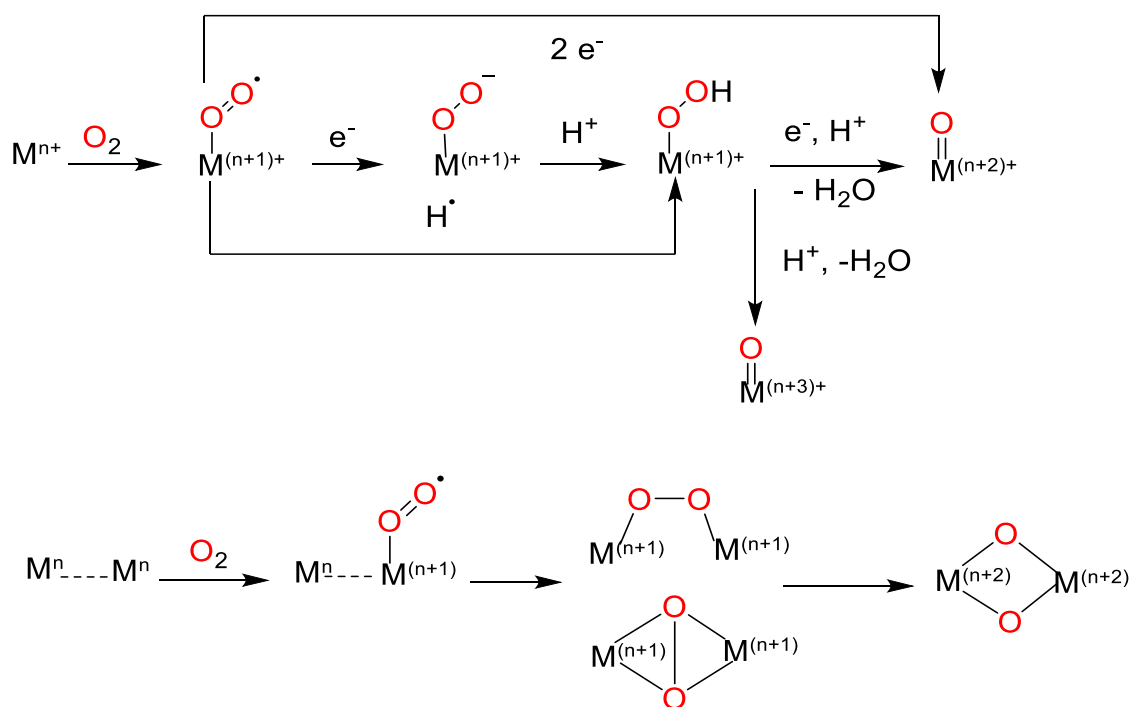
Scheme 1.1. Products of oxidation of alkanes: a) alcohols; b) aldehydes, ketones or acids; c) alkenes.

1.1.2 Biological oxidation

One promising approach to the rational design of oxidation catalysts takes inspiration from biology. A plethora of metalloenzymes are known to perform oxidation of inert substrates in a mild and selective way.¹⁴ These enzymes are in fact capable of introducing oxygen-containing functionalities in C–H bonds, even the one of methane,^{15, 16} with a chemo- and stereoselective approach, at atmospheric pressure and physiological temperature and pH. Furthermore, the active site of several of these enzymes contains mostly iron and copper, two redox-active metals that are cheap and abundant.¹⁷ Eventually the use of dioxygen as oxidant, to insert either one (monooxygenases) or two (dioxygenases) oxygen atoms into the substrate or to act as an electron acceptor (oxidases),⁷ makes these enzymes an ideal target to study in order to design better molecular oxidation catalysts.

Advances in the field of biomimetic catalysis are necessary due to the unfeasible large-scale application of these enzymatic processes and to their often limited substrate scope.¹⁴ The elucidation of the mechanisms of action of these enzymes is thus a compelling topic in order to mimic and improve their functionalities on a synthetic level. Despite the differences among the several metalloenzymes, some common aspects of their functionality have been outlined.¹⁸ All the redox-active metal centres work by reducing dioxygen to superoxide ($\text{O}_2^{\cdot-}$) upon binding, by progressively populating its antibonding orbitals and thus forming species with a lowered O–O bond order. The first reducing equivalent changes the ground state spin multiplicity of dioxygen from 1 to $\frac{1}{2}$ and thus enhances its reactivity. This metal-superoxo

intermediate can then be further reduced, to form a peroxo species which can in turn form a hydroperoxo species upon protonation or by HAA (Hydrogen Atom Abstraction) from a substrate (Scheme 1.2). This metal-hydroperoxo adduct can then undergo homolytic or heterolytic O–O bond scission to form a metal-oxo species. The same mechanism is proposed for dinuclear active sites, where bridged bis- μ -superoxo, end-on or side-on bis- μ -peroxo and bis- μ -oxo species occur (Scheme 1.2). The four reducing equivalents required throughout this oxygen activation process at the active site of metalloenzymes are supplied either by external donors, such as adenine dinucleotides, ascorbate, tetrahydropterin,¹⁹ α -ketoglutarate,²⁰ quinones,²¹ or by the substrate itself, as in the case of Isopenicillin N synthase.²² All the described metal-oxygen adducts can act as highly reactive intermediates and are capable of performing substrate oxidation, nonetheless, the species formed after scission of the O–O bond is most commonly regarded as the active oxidant. These reactive oxygen-based species in metalloenzymes have proved to be effective oxidants towards difficult substrates such as saturated hydrocarbons, thus represent the main inspiration for chemists to design new oxidation catalysts. Another motif common among biological oxidant is a high-valent metalloporphyrin π -cation radical, which is found in several biological oxidants. One notorious example is given by the Compound I found in the catalytic cycle of several enzymes such as cytochrome P450, halogenases and peroxidases.²³ This compound is formally described as a $\text{Fe}^{\text{IV}}=\text{O}$ porphyrin π -cation radical which is capable of abstracting a hydrogen atom from the substrate, a saturated hydrocarbon, yielding a carbon-based radical and a $\text{Fe}^{\text{IV}}-\text{OH}$ species known as Compound II.²⁴ Another relevant example of a powerful oxidant supported by a porphyrinoid ligand is given by P680, the main electron donor in photosystem II, formed by two chlorophyll molecules, which entail a Mg^{2+} ion supported by a chlorin ligand.²⁵ This species is the most powerful oxidant in nature having a redox potential of 1.2 V in its oxidised state (P680^+) and the oxidising equivalents are postulated to be delocalised over the chlorophyll molecules, yielding a formal porphyrinoid π -cation radical.^{25, 26} The corresponding Mg-porphyrin centre found in photosynthetic bacteria, P865, has been demonstrated to show an electronic density distribution indicative of a porphyrin π -cation radical species.²⁷ Therefore porphyrin π -radical cation species are often the active oxidant in the catalytic cycles of enzymes and represent a class of powerful oxidants to look at for inspiration during the design of new synthetic catalysts.



Scheme 1.2. General mechanism for dioxygen activation at mononuclear centres (top) and at dinuclear centres (bottom) in Fe and Cu metalloenzymes.

1.1.2.1 High-valent metal-hydroxides in nature

Despite the metal-oxo species being still regarded as the main oxidants in the catalytic cycles of metalloenzymes, also metal-hydroxide species have been identified as capable C–H bond activators. Lipoyxygenases are a family of non-heme iron enzymes responsible for the conversion of unsaturated fatty acids to hydroperoxides.²⁸⁻³¹ A Fe^{III}–OH species is responsible for the HAT step from a bisallylic position on the fatty acid, then the generated organic radical reacts with dioxygen to yield a hydroperoxide. The iron coordination environment was shown to be pentacoordinate in soybean lipoyxygenase (SLO), with three His residues, one carboxylate and the hydroxide ligand.³¹ The lower coordination number accounts for the higher reactivity of SLO (~ 50-fold enhancement of k_{cat}) when compared to the human one (15-LOX), which presents a hexacoordinate environment, with one more His residue bound to the iron center.²⁹ Spectroscopic evidences showed the existence of a Mn^{III}–OH centre in a manganese lipoyxygenase, which was shown to be responsible for the oxygenation of fatty acids.^{32, 33}

Another example in nature is given by the already mentioned cytochrome P450 (CYP).³⁴ The most widely accepted mechanism for this enzyme entails the generation of the reactive intermediates upon binding of dioxygen: this is progressively reduced to superoxide and peroxide until the heterolytic cleavage of the O–O bond occurs. This would formally generate

a $\text{Fe}^{\text{V}}=\text{O}$, but it is better described as a $\text{Fe}^{\text{IV}}=\text{O}$ -porphyrin π -radical cation³⁵ according to spectroscopic evidences. This electrophilic intermediate is highly reactive and can abstract a hydrogen atom from a substrate, then the organic radical attacks the Compound II, a $\text{Fe}^{\text{IV}}-\text{OH}$, through the so called oxygen rebound mechanism, to form the hydroxylated substrate. In certain cytochromes P450 though this reactivity diverges: the $\text{Fe}^{\text{IV}}-\text{OH}$ in Compound II acts as a hydrogen atom abstractor towards the substrate, yielding a desaturated product instead of a hydroxylated one.^{36, 37} These enzymatic examples have inspired the synthesis of related model complexes which will be reviewed in section 1.1.4.2.

1.1.2.2 High-valent metal-halides in nature

Halogenated alkanes are ubiquitous and play a key role as drugs and agrochemicals. Many synthetic efforts have been made in the last decades to improve the feasibility and the selectivity of hydrocarbon halogenation reactions and much inspiration has been taken from nature.³⁸ A number of enzymes occurring in bacteria and plants in fact have shown the capability to halogenate aliphatic and aromatic C–H bonds: these enzymes are known as halogenases and several classes exist.³⁸ One class is represented by haloperoxidases, which are enzymes that generate hypohalous acid (HXO , $\text{X} = \text{F}, \text{Cl}, \text{Br}, \text{I}$) in the presence of hydrogen peroxide and halide ions. These enzymes have been shown to perform chlorination, bromination and iodination, often by the same enzyme with different rates, but no fluorination by haloperoxidases has been reported to date.³⁸ Among haloperoxidases containing transition metals as cofactors, both heme and non-heme iron variants are found. The catalytic cycle of heme haloperoxidases starts by the binding of peroxide to yield a Fe^{III} -hydroperoxide, which then undergoes heterolytic cleavage to yield a Fe^{IV} -oxo porphyrin π -cation radical, also known as Compound I (Figure 1.6a). This compound is also observed in the catalytic cycle of heme oxidases such as CYP450 or heme peroxidases but the presence of halide anions differentiates the following steps of the cycle of haloperoxidases. In fact the halide is intercepted by Compound I to yield a Fe^{III} -hypohalite species, which can directly functionalize the C–H bonds of substrates or, in a low pH environment, can release HXO which can halogenate substrates remotely from the active site (Figure 1.1a).³⁹ The mechanism of halogenation of substrates susceptible to electrophilic attack by hypohalous acids is not yet clearly understood.³⁸

Another class of halogenases is represented by α -ketoglutarate dependent non-heme iron halogenases.³⁸ These enzymes perform the halogenation of aliphatic carbons and the Fe^{II} in the

active site is coordinate to 2 His residues, a halide ion, generally chloride or bromide, and a α -ketoglutarate (α -KG) molecule (Figure 1.1b).⁴⁰ In the catalytic cycle of these enzymes, binding of dioxygen to the active site yields a Fe^{III}-superoxo species which attacks the ketonic carbon in the α -KG (Figure 1.6b). Heterolytic cleavage of the obtained peroxohemiketal intermediate releases CO₂ and forms a Fe^{IV}-oxo-halide intermediate.⁴⁰ This high-valent species abstracts a hydrogen atom from the C–H bond of the substrate, yielding a Fe^{III}-hydroxide-halide species. The rebound of the carbon-based radical can thus occur either with the hydroxide or with the halide, but for this class of enzymes halogenation is favoured almost completely over hydroxylation (Figure 1.1b). Site-directed mutagenesis studies suggested this selectivity to be directed by the relative proximity of the halogen respect to the substrate.⁴⁰ Chemists have therefore tried to mimic these enzymes to achieve halogenation of saturated hydrocarbons, obtaining several model complexes which will be illustrated in section 1.1.4.3.

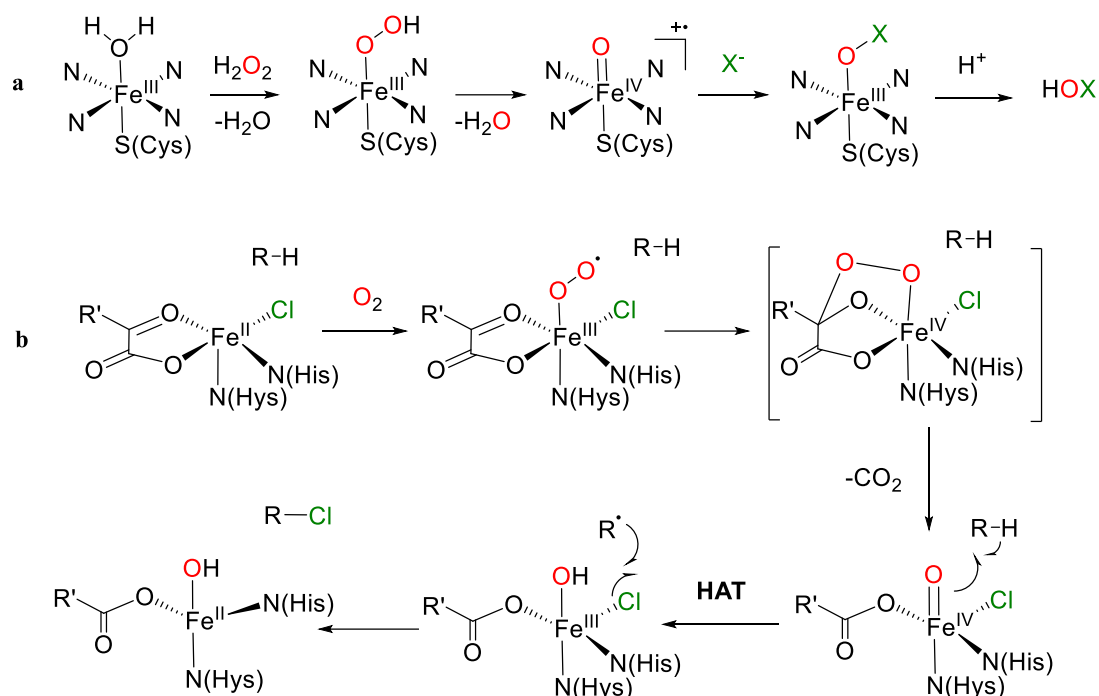


Figure 1.1. Reaction mechanism for haloperoxidases (a) and α -ketoglutarate-dependent non-heme halogenases (b).

1.1.3 Reactivity mechanisms

1.1.3.1 Proton coupled electron transfer

Both natural and synthetic transition-metal based systems have shown their ability to perform a variety of oxidation reactions towards different substrates with diverse mechanisms. One

common feature is that most of these are redox reaction coupled to a proton transfer, a mechanistic step denoted by the term proton coupled electron transfer (PCET) which was first introduced by Meyer and co-workers in 1981.⁴¹ Over time, this became an umbrella term for all the redox reactions in which one or more protons modulate their rate or energetics, even if the eventual transfer of those protons does not occur.⁴² Mayer and co-workers extensively delineated and classified the PCET reactions performed by metal-based oxidants,⁴²⁻⁴⁸ allowing to distinguish between three types of stepwise or concerted mechanisms. When a stepwise mechanism occurs could be either an ET/PT when the electron transfer (ET) occurs first and then is followed by the proton transfer (PT) or a PT/ET where conversely the proton transfer is followed by the electron transfer. When a concerted mechanism occurs, the transfer of the two particles occurs in a single kinetic step and this has been designated as concerted proton-electron transfer (CPET). Furthermore, in a concerted reaction the transfer of the particles can be synchronous or not according to the position of the transition state along the reaction coordinate.⁴⁸ Last, the proton and the electron might be transferred to the same atom or to different sites within the acceptor molecule in a multi-site concerted transfer (MS-CPET), further differentiating the possible mechanism.^{42, 46, 48}

Among the CPET reaction, hydrogen atom transfer (HAT) defines a concerted mechanism in which the proton and the electron are transferred from the same donor to the same acceptor in a single kinetic step.⁴⁶ Different meanings for this definition have arisen in literature, generating confusion in delineating the exact difference between CPET and HAT. Hammes-Schiffer for example theoretically defined as HAT those reactions in which electronically adiabatic proton transfer occurs, conversely to PCET in which the same transfer is non-adiabatic.^{49, 50} For the sake of clarity from now on we will adopt the latest definition of HAT reported by Mayer, indicating any concerted mechanism in which the proton and the electron are transferred from the same donor to the same acceptor molecule in a single kinetic step.⁴⁶

1.1.3.2 Hydrogen atom transfer

One important indication of a HAT mechanism is the linear correlation between the rate of the reaction and the bond strength of the oxidised substrate.⁴⁵ In the 30s, pioneering studies by Bell,⁵¹ Evans and Polanyi⁵² stated that for a family of reactions the difference in activation energy is proportional to the difference of their enthalpy of reaction ($E_a = E_o + \alpha \Delta H^\circ$, where E_a is the activation energy and ΔH the difference in enthalpy). Historically HAT reactions have

been analyzed by taking in account that ΔH is equal to the difference between BDE of the bond broken in the substrate and the BDE of the bond formed in the oxidant (Scheme 1.3).⁴² Mayer though has demonstrated that when the oxidant is a transition metal complex there is a non-negligible entropic contribution due to the rearrangement of the vibrational states upon the change in oxidation state in the metal ion.⁵³ Thus, the assumption that in an HAT reaction $\Delta S^\circ \cong 0$ is valid only for reactions involving organic-based oxidants and therefore the formal treatment of those where a transition metal-based oxidant is present requires the use of bond dissociation free energies (BDFEs) instead of BDEs.^{42, 45, 46, 53} Despite this, often BDEs are more available in literature than BDFEs so have been still often used in relation to HAT reactions involving metal-based complexes even though not being formally correct.

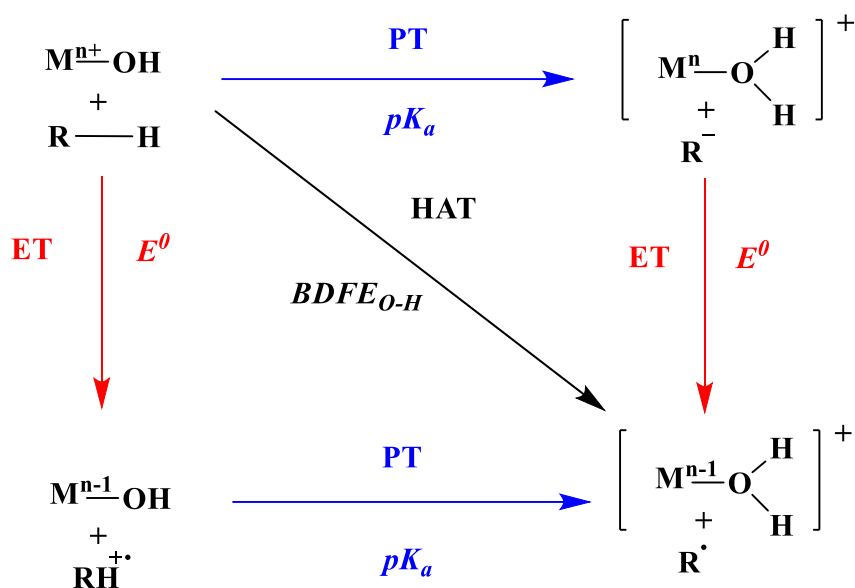
The relationship between the species involved in a HAT mechanism can be described in a thermodynamic square scheme. This approach takes in account that the concerted mechanism can be divided into the ET and PT steps, for which the thermodynamic parameters of reference are respectively the redox potential (E°) and the equilibrium acidity constants in solutions (pK_a) of the species involved in a thermochemical cycle. This relationship was formalized by Bordwell⁵⁴ in the following equation:

$$\text{BDFE}_{\text{X-H}} = 1.37pK_a + 23.06E^\circ + C$$

Where C is a constant relative to the $\text{H}^+/\text{H}^\bullet$ standard reduction potential in a determined solvent.^{42, 54}

Therefore the thermodynamic parameter to evaluate the relative strength of an oxidant performing HAT is the $\text{BDFE}_{\text{X-H}}$ of the species obtained upon the net transfer of a hydrogen atom from the substrate: in case of a metal hydroxide complex, this parameter is the $\text{BDFE}_{\text{O-H}}$ of the reduced aquo complex (Scheme 1.3).

Another fundamental contribution of Mayer and co-workers to the modern theory of HAT is the application of Marcus theory to predict HAT rates.^{43, 44, 47} This theory was in fact originally developed to explain outer-sphere electron transfer reactions but Mayer successfully showed that the rates of HAT reactions follow Marcus cross relation.



Scheme 1.3. Thermodynamic square scheme for proton-coupled electron transfer reactions of a metal-hydroxide complex.

The Marcus equation states that the free-energy barrier of a reaction ΔG^\ddagger is function of the thermodynamic driving force, which for a HAT reaction corresponds with ΔG° , and the intrinsic barrier of the reaction λ .⁴⁷

$$\Delta G^\ddagger = (\lambda + \Delta G^\circ)^2 / 4\lambda$$

The thermodynamic driving force corresponds to the difference in BDFEs between the bonds formed and the bonds broken during the reaction in the case of a HAT mechanism.⁴⁵ According to the Arrhenius-Eyring equation the reaction rate constant is proportional to ΔG^\ddagger :

$$k = A e^{-\Delta G^\ddagger / RT}$$

These equations can be converted into the Marcus cross relation which states that the rate constants of a HAT reaction can be predicted from the driving force estimated from the BDFEs and the λ derived from self-exchange rates for a certain class of reactions.⁴⁴ Thus this model deepens and explains the linear correlation already observed with the Polanyi relationship. This treatment predicts that the slope for a plot of the Eyring barrier versus the thermodynamic driving force, $\Delta G^\ddagger / \Delta G^\circ$ is close to 0.5 for reactions which are not too endo- or exoergonic.⁴⁵ This theory explains also the mechanisms in which either PT or ET are limiting: for instance in cases where ET is rate limiting rate constants will correlate better with E° s than with BDFEs.⁴⁵ The other element of the Marcus cross relation are the intrinsic barriers: these takes in account the self-exchange rates for a certain class of reactions. This explains why reaction rates of the same transition metal-based oxidant are $\sim 10^4$ times faster with O–H bonds than with C–H bonds having similar BDFEs.^{43, 45} The self-exchange rate for H^\cdot from a hydrocarbon

to the corresponding carbon-based radical is in fact $\sim 10^8$ times slower than what predicted for an alcohol having a comparable $\text{BDFE}_{\text{O-H}}$.⁴³

1.1.3.3 Other mechanisms

Beside proton coupled electron transfer there are other mechanisms involved in C–H activation. The key initial step in hydrocarbon oxidation can be often either an electron transfer, a hydrogen atom transfer or a hydride transfer.⁵⁵

Analogously to HAT, hydride transfer (HT) occurs between the same donor and the same acceptor but involving the transfer of a proton and two electrons as a hydride ion (H^-). Many enzymatic cofactors such as pyridine dinucleotide NAD and NADP or flavin nucleotides FAD and FMN are known as reversible hydride acceptors/donors in catalytic enzymatic cycles.⁵⁶ The usual conversion of these cofactors and their synthetic analogues (such as 9,10-dihydroacridine, AcrH_2 , or 1-benzyl-1,4-dihydronicotinamide, BNAH) to their cationic form suggests that the hydride donation is the preferred mechanism of action, but closer examination of their redox potentials and homolytic and heterolytic $\text{BDE}_{\text{C-H}}$ in solution revealed that in certain cases the homolysis, i.e. a HAT mechanism, might be favoured over the heterolysis or equally likely to occur.⁵⁷ Furthermore the formation of the substrate cation is not necessarily indicative of an overall HT mechanism, as can be also obtained by HAT followed by ET.⁵⁵ Mayer and Fukuzumi have shown that both these mechanisms of reaction might compete for a same transition-metal based oxidant^{55, 58-61} One of the indications for a HT mechanism with respect to HAT can be the larger substituent effect on the reaction rates of the oxidant within the same class of substrates.⁵⁸ Nevertheless, the thermodynamic driving forces of each reaction, which for a HT mechanism is given by the hydricity ΔG^\ddagger , must be evaluated case by case to obtain insights on the favoured mechanism.^{55, 58, 62}

Aromatic hydrocarbons normally are difficult to activate via HAT given their very high homolytic bond dissociation free energies (> 110 kcal/mol) and for the instability of the resulting radicals, thus they normally undergo electrophilic aromatic substitution in presence of transition metal-based oxidants.^{63, 64} Other reactions performed by high-valent metal complexes, such as olefin epoxidation or heteroatoms (S, P, N) oxidation, can be identified as oxygen atom transfer reaction (OAT).⁶⁵ This is another concerted mechanism which involves the net transfer of an oxygen atom from the oxidant to the substrate and can be often proved by oxygen labelling experiments. Not all the oxygen transfer reactions though proceed through

a concerted pathway: for example in olefins epoxidation the OAT pathway competes with the ET which generates a radical cation which then further reacts to yield the oxygenated product.⁶⁶

In summary PCET is a common mechanism of C–H bond oxidation among enzymes and biomimetic catalysts. HAT is a type of concerted PCET where the proton and the electron are transferred in a single kinetic step from the same donor to the same acceptor and the thermodynamic key parameter for a HAT oxidant is the $BDFE_{X-H}$ of the species obtained upon transfer of a hydrogen atom from the substrate. Other mechanisms of C–H activation beside PCET are possible, such as hydride transfer, OAT or electrophilic aromatic substitution. Therefore a thorough understanding and evaluation of the mechanism of C–H is required when new high-valent transition metal-based oxidants are assessed and compared.

1.1.4 First-row transition metals in oxidation catalysis

Due to the obstacles in the use of metalloenzymes for producing bulk commodities, a lot of effort has been devoted to the design and synthesis of bioinspired catalysts. First-row transition metal are cheap and abundant, therefore they have gained a lot of attention in the last decades both in homogeneous and heterogeneous oxidative catalysis. One of the fields of increasing interest for complexes of these metals is water oxidation catalysis to yield molecular hydrogen as a clean source of energy. Complexes of Mn, Fe, Cu and Ni, mostly supported by nitrogen-containing pincer ligands, have shown to act as promising catalysts for this transformation.⁶⁷ β -diketiminato ligands have shown to yield stable and versatile complexes with Fe, Mn, Ni, Co and Cu which in some cases have found catalytic applications.⁶⁸ Fe β -diketiminato complexes have been employed as catalysts in lactide polymerization, hydrodefluorination and cross-coupling reactions, while Cu ones have been studied as catalyst in the cyclopropanation of styrenes and in the etherification of cyclohexane.⁶⁸ Catalytic conversion of CO_2 into carboxylic acids, esters, lactones and polymers is another field of growing importance to reduce emissions of this greenhouse gas and to maximise its value by employing it as a chemical synthon.⁶⁹ Ni complexes have shown to promote the coupling of CO_2 to olefins or alkynes or the synthesis of carboxylic acids, whereas Mo and W complexes performed the synthesis of acrylic acid from the same feedstock. Historically in the synthesis of formic acid or formate from CO_2 precious metal-based complexes such as Rh, Ru or Ir have been extensively studied but recently a focus on cheap Fe complexes has been reported for this transformation.⁶⁹

As observed in many proposed enzymatic mechanisms, very often the active oxidant capable of performing PCET oxidation on the substrate is a mid- or late-transition metal-oxo species. Consequently, a lot of synthetic model compounds tried to reproduce the formation of this species, in particular with Fe.

Fe^{III} porphyrin complexes inspired by heme iron enzymes, such as cytochrome P450, have been widely synthesized and then oxidized chemically to obtain a reactive Fe^{IV}=O.⁷⁰⁻⁷³

Diiron complexes behaving as structural and functional models for dinuclear nonheme iron enzymes have been reported since the late 90s.^{74, 75} Model complexes of the postulated active oxidant, a bis- μ -oxo bimetallic species, have been isolated also with Mn and, less extensively, due to their instability at room temperature, with Co, Ni and Cu.⁷⁶ The first crystallographically characterized model of the active oxidant of mononuclear nonheme iron enzymes, a Fe^{IV}=O species supported by the chelating TMC (TMC = tetramethylcyclam) ligand, was reported in 2003,⁷⁷ proving that such a reactive intermediate could be isolated without the support of a porphyrin ligand. Since then, many other terminal Fe=O, together with examples of Mn=O⁷⁸ and Cr=O^{79, 80} complexes, have been isolated using different chelating ligands and chemical oxidants,^{81, 82} showing remarkable reactivity towards hydrocarbons, including ones with relatively strong C-H bonds such cyclohexane (BDE = 99.3 kcal/mol)⁸³ and towards phosphines or sulfides in Oxygen Atom Transfer (OAT) reactions.

1.1.4.1 The “Oxo Wall”

The examples reported in the previous paragraph demonstrate the presence of a profusion of highly reactive synthetic oxo complexes involving Fe. On the other hand, early transition metal oxo adducts such as the vanadyl ion (VO²⁺) are rather unreactive. Considering the increasing electronegativity of the metals along the first transition row, metal-oxo complexes of Co, Ni and Cu are expected to be extremely reactive, also due to the instability of their high oxidation states. These qualitative considerations have been supported by DFT calculations: Cundari for instance has predicted the ability of hydroxylating the strong C-H bond of methane by terminal-oxo species of Fe, Co and Ni supported by diketiminate or dihydrophosphinoethane ligands.⁸⁴ He found it both kinetically and thermodynamically accessible, with the overall HAT and radical rebound pathway becoming more exothermic for Ni species. Also, the lowest activation barrier of 8.1 kcal/mol was predicted for a Ni^{III}=O species supported by a fluorinated diketiminate ligand.⁸⁴ Cramer and co-workers instead performed calculations on the activation

of methane by three different species supported by a β -diketiminato ligand: a $\text{Cu}^{\text{III}}\text{-OH}$, a $\text{Cu}^{\text{III}}\text{-OOH}$ and a $\text{Cu}^{\text{III}}\text{=O}$, showing the lowest reaction enthalpy for the latter.⁸⁵

Despite these theoretical predictions and their postulated involvement as intermediates in oxidation reactions, terminal late-transition metal oxo species (LTMOs) are still elusive and their studying has been hampered by their instability. Electronic arguments can be invoked to account for this aspect, notably by using the molecular orbital model developed in the 60s by Ballhausen and Gray for the vanadyl ion in a tetragonal geometry.⁸⁶ The dianionic oxo ligand interacts with the metal ion leading to the formation of three fully occupied bonding orbitals having mostly s and p character (one with σ symmetry and two with π symmetry) and 5 orbitals having mostly *d* character, being either non-bonding or antibonding (Figure 1.2). For early transition metal ions with a *d* electron count equal to 0, 1 (as VO^{2+}) and 2, these will occupy a non-bonding orbital, leading to a metal-oxygen bond order of 3, which explain their inherent stability. When the *d* electron count increases, antibonding orbitals are progressively populated, reducing the M=O bond order and increasing its polarization and thus destabilizing the metal-oxo interaction. This explains why d^4 $\text{Fe}^{\text{IV}}\text{=O}$ species have been isolated but almost no pure species with $d > 4$ have been reported. This virtual electronic barrier located between groups 8 and 9 in the periodic table is known as “Oxo Wall”. One of the possible strategies to overcome this hurdle is to change the geometry around the metal by tuning the ligand field, hence leading to a different splitting and character of the molecular orbitals. A low-coordination number (e.g. 3 or 4) can lead to a MO scheme that highlights for example the possibility of accommodating up to six *d* electrons by still retaining a bond order of 2, as depicted for a trigonal planar metal-oxo complex with a C_{2v} geometry (Figure 1.2).

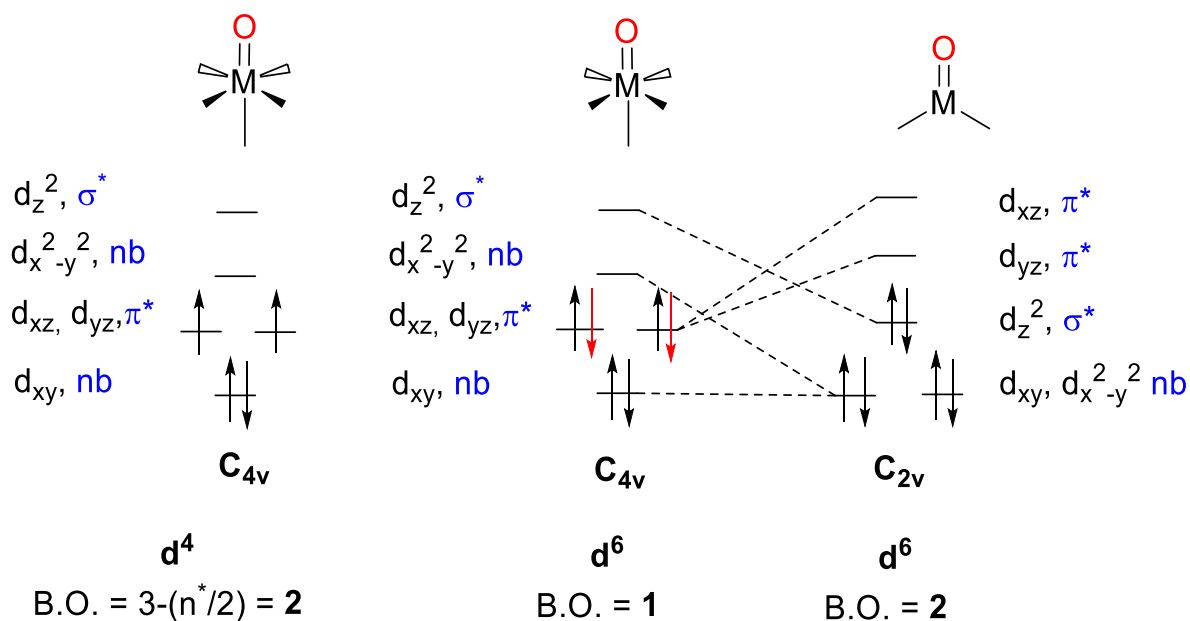


Figure 1.2. Simplified scheme of the d-based MO for a d^4 ion in a tetragonal geometry (C_{4v} symmetry, left) and for a d^6 ion in a tetragonal geometry (centre) and trigonal planar geometry (C_{2v} symmetry, right). Only low spin cases are depicted.

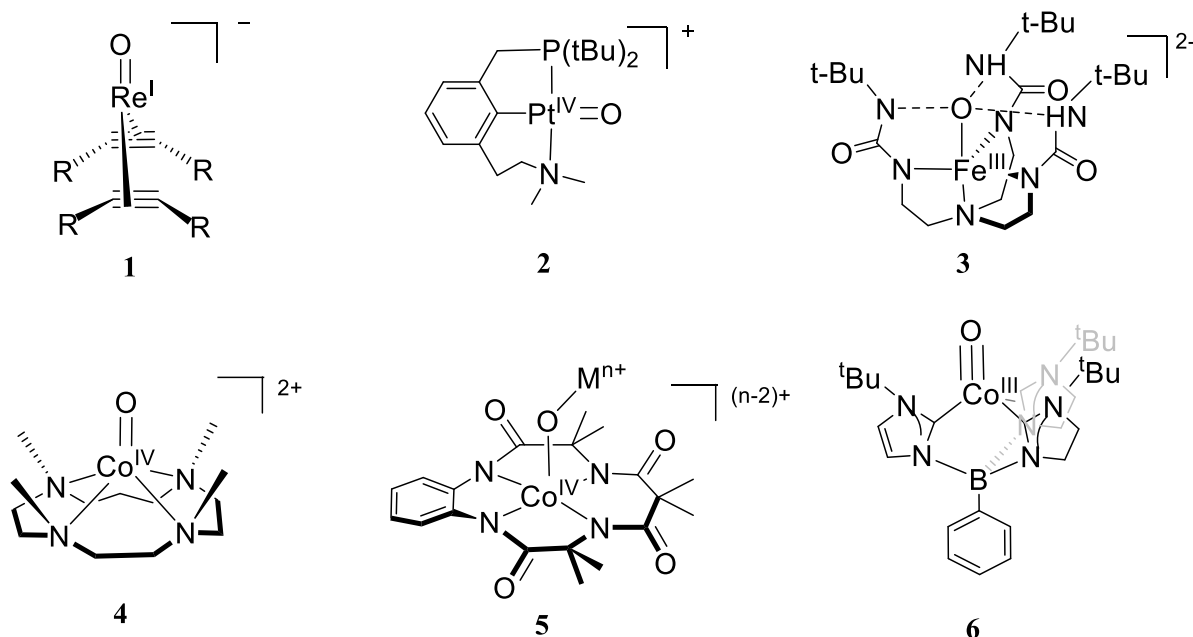


Figure 1.3. Selected examples of metal-oxo complexes with $d > 4$.

This strategy has been used to stabilize the few examples of complexes to date that violate the oxo-wall paradigm (Figure 1.3). Mayer and co-workers reported $Re^I=O$ complexes (**1**) using π -acceptor alkyne ligands: these complexes violate the oxo-wall bearing d^6 ions and having showed some population of antibonding orbitals as an outcome of *ab initio* calculations.⁸⁷ Milstein's square planar $Pt^{IV}=O$ complex (**2**) was isolated using a pincer ligand with no

electron-accepting properties and demonstrated to be able to perform water activation, but did not show reactivity with hydrocarbons.⁸⁸ In Borovik's $[\text{Fe}^{\text{III}}(\text{O})(\text{H}_3\text{buea})]^{2-}$ (**3**) a network of hydrogen bonds stabilize the d^5 Fe-oxo interaction by removing electron density from the latter,⁸⁹ whereas this role is played by redox-inactive Lewis Acids in Nam's $[\text{Co}^{\text{IV}}(\text{O})(\text{M}^{\text{n+}})(\text{TAML})]^{(n-2)+}$ (**4**) (where $\text{M}^{\text{n+}} = \text{oxo-bridged Sc}^{3+}, \text{Ce}^{3+}, \text{Y}^{3+}$ and Zn^{2+})⁹⁰. Nam and coworkers reported a $[\text{Co}^{\text{IV}}(\text{O})(13\text{-TMC})]^{2+}$ complex (**5**) which performed HAT with hydrocarbons up to $\text{BDE}_{\text{C-H}} = 80$ kcal/mol and OAT with styrene and olefins,⁹¹ but an unusual bonding situation allowing the formation of a full Co–O π bond in a tetragonal ligand field accounts for its stabilization, leading to a complex that does not violate the Oxo-Wall and for this reason displays a rather weak hydrocarbon activation capacity. Recently, Anderson and co-workers isolated and characterized spectroscopically and crystallographically a $\text{Co}^{\text{III}}=\text{O}$ supported by a strongly donating tris(imidazol-2-ylidene)borate ligand (**6**).⁹² These examples show the dearth of pure LTMOs examples in the literature, setting a very topical challenge in this field.

We will attempt to isolate these very reactive intermediates by designing tailored ligands capable of enforcing a low-coordinate geometry around the late-transition metal centre in order to hurdle the Oxo Wall. We will design, synthesise and optimise these ligands and we will react them with Co, Ni and Cu to obtain low-valent precursors to reactive oxygen intermediates capable of C–H bond oxidation.

1.1.4.2 Synthetic mid- and high-valent metal-hydroxides

1.1.4.2.1 Mid- first row transition metals (Fe and Mn)

Among synthetic first-row transition metal hydroxide complexes, several iron model complexes of lipoxygenases supported by nitrogen-based ligands have been reported. A manganese lipoxygenase mimic supported by a polypyridyl ligand, $[\text{Mn}^{\text{III}}(\text{OH})(\text{PY5})](\text{OTf})_2$ (**7**, Figure 1.4, Table 1.1), was first synthesized by Stack and coworkers.⁹³ This complex performed hydrocarbon oxidation through a HAT mechanism. **7** was kinetically more competent oxidant compared to its iron-based analogue, $[\text{Fe}^{\text{III}}(\text{OH})(\text{PY5})](\text{OTf})_2$ (**8**, Figure 1.4, Table 1.1).⁹⁴ In fact **7** showed a higher second-order kinetic constant in the oxidation of 9,10-didhydroanthracene (DHA, $\text{BDE}_{\text{C-H}} = 78$ kcal/mol) at 25 °C ($k_2(\mathbf{7}+\text{DHA})/k_2(\mathbf{8}+\text{DHA}) = 3.7$). From a thermodynamic point of view, only **7** was able to oxidise toluene ($\text{BDE}_{\text{C-H}} = 88$ kcal/mol). The analysis of the activation energy parameters for the DHA reaction showed a difference of 10 cal $\text{K}^{-1} \text{mol}^{-1}$ (**7**: $\Delta S^\ddagger = -36$ cal $\text{K}^{-1} \text{mol}^{-1}$, **8**: $\Delta S^\ddagger = -26$ cal $\text{K}^{-1} \text{mol}^{-1}$) which can

be accounted to the greater reorganization energy required for the Mn complex to remove the Jahn-Teller distortion which is present in the reduced species after HAT. This is compensated by the lower enthalpy of activation for **7** respect to **8** (**7**: 9.3 kcal/mol, **8**: 13.2 kcal/mol), allowing an overall lower free energy barrier for HAT for **7**.^{93,94} Furthermore, a comparison of the BDE_{O-H} of the reduced aquo-complexes formed upon HAT showed a 2 kcal/mol difference (BDE_{O-H} (**7H**) = 82 kcal/mol, BDE_{O-H} (**8H**) = 80 kcal/mol). These data confirmed that **7** is a superior oxidant with respect to **8** both kinetically and thermodynamically (Table 1.1).

Masuda and Borovik respectively reported the first examples of crystallographically characterized mimics of lipoxygenases: [Fe^{III}(OH)(tnpa)(PhCOO)](ClO₄)⁹⁵ (**9**, Figure 1.3) and [Fe^{III}(OH)(H₃buea)]^{-96, 97} (**10**, Figure 1.4). The manganese analogue of **10**, [Mn^{III}(OH)(H₃buea)]^{-96, 97} (**11**, Figure 1.4), was structurally characterized too. These complexes benefit from a network of hydrogen bonds in the second coordination sphere which ensure enhanced stability and thus allowed for their structural characterization. Notably the tripodal tris-urea ligand H₃buea employed by Borovik allowed for this reason the isolation of Fe and Mn oxo and hydroxide complexes in different oxidation states thanks to the concomitant presence of strong anionic donors and hydrogen bond donors in the second coordination sphere.^{89, 96, 98-104} Both complexes **10** and **11** were related to their low-valent analogues, [Fe^{II}(OH)(H₃buea)]²⁻ (**12**, Figure 1.4) [Mn^{II}(OH)(H₃buea)]²⁻ (**13**, Figure 1.4) and to the corresponding oxo complexes [Fe^{III}(O)(H₃buea)]²⁻ (**14**, Figure 1.4) and [Mn^{III}(O)(H₃buea)]²⁻ (**15**, Figure 1.4) in a thermodynamic square scheme.⁹⁷ The BDE_{O-H} of **10** and **11** were determined to be 115(4) kcal/mol and 110(4) kcal/mol respectively. None of these hydroxide complexes though exhibited reactivity towards O-H or C-H bonds, only the Mn-oxo complex **15** showed to perform oxidative reactivity towards TEMPOH and DHA.⁹⁷ Complex **11** was chemically oxidized to [Mn^{IV}(OH)(H₃buea)]¹⁰¹ (**16**, Figure 1.4) and the oxidation was monitored by electronic absorption spectroscopy, X-Ray absorption spectroscopy (XAS) and electron paramagnetic resonance (EPR). Interestingly, **16** has been obtained also by protonation of the corresponding oxo complex, [Mn^{IV}(O)(H₃buea)]⁻ (**17**, Figure 1.4) by treatment with [HNEt₃]⁺ at -80 °C and conversely **16** could be deprotonated by *tert*-butoxide (^tBuO⁻) to yield [Mn^{IV}(O)(H₃buea)]⁻. Furthermore, the comproportionation of **16** and **13** yielded **11**: these experiments proved the thermodynamic relationship between the oxo/hydroxo complexes of this ligand and their different redox states.¹⁰¹ To prove the concerted pathway in the thermodynamic square scheme, **16** was cleanly obtained as a product of PCET oxidation of 2,4,6-tri-*tert*-butylphenol by [Mn^V(O)(H₃buea)] (**18**, Figure 1.4).¹⁰¹ Thus the experimental data

proved that the oxo complexes supported by H₃buea can perform PCET oxidation of substrates conversely from their hydroxide counterparts.^{96, 97}

Que and coworkers isolated [Fe^{III}(OH)(TMC-Py)](OTf)₂ (**19**, Figure 1.4, Table 1.1) which was a sluggish oxidant which did not react with 1,4-cyclohexadiene (CHD, BDE_{C-H} = 76 kcal/mol).¹⁰⁵ **19** reacted with 2,2,6,6-tetramethyl-piperidin-1-ol (TEMPOH, BDE_{O-H} = 70.6) at -40 °C with $k_2 = 7.1 \text{ M}^{-1} \text{ s}^{-1}$. When TEMPOD was used, a primary kinetic isotope effect (KIE) of 6 was observed, which is in the classical range (2-7) and indicates that the proton or hydrogen atom transfer is rate-determining. DFT calculations raised evidence for a PCET mechanism of oxidation of TEMPOH by complex **19**.¹⁰⁵ Busch and co-workers reported a manganese dihydroxide complex, [Mn^{IV}(OH)₂(Me₂EBC)](PF₆)₂ (**20**, Figure 1.4, Table 1.1) which performed HAT on hydrocarbons up to fluorene (BDE_{C-H} = 80 kcal/mol). Interestingly, **20** reacted ~ 40 times slower than the corresponding oxo complex, [Mn^{IV}(O)₂(Me₂EBC)], despite having very comparable oxidizing power from a thermodynamic point of view.¹⁰⁶ This difference in reactivity was attributed to the difference in the free energy of activation for the HAT reaction, being 2.4 kcal/mol higher for **20**.¹⁰⁶

Kovacs reported a manganese hydroxide complex supported by a thiolate-containing ligand, [Mn^{III}(OH)(S^{Me}₂N₄(tren))](PF₆)•H₂O (**21**, Figure 1.4, Table 1.1)¹⁰⁷ This complex was able to oxidise TEMPOH with a second-order rate constant $k_2 = 2.1 \times 10^3 \text{ M}^{-1} \text{ s}^{-1}$ at 25 °C in acetonitrile. A KIE = 3.1 was observed and activation energy parameters $\Delta H^\ddagger = 8.2 \text{ kcal/mol}$ and $\Delta S^\ddagger = -25.5 \text{ cal K}^{-1} \text{ mol}^{-1}$ indicated that **21** is oxidising TEMPOH following a concerted mechanism, notably a HAT mechanism.^{107, 108} Jackson isolated [Mn^{III}(OH)(dpaq)](OTf) (**22**, Figure 1.3) from the reaction of [Mn^{II}(dpaq)](OTf) with dioxygen at 25 °C.¹⁰⁹ Among hydrocarbons, **22** reacted slowly only with xanthene (BDE_{C-H} = 74 kcal/mol) at 50 °C, but reacted with TEMPOH and *para*-substituted-2,6-di-*tert*-butylphenols at 25 °C.¹⁰⁹ The kinetics of the reactions of **22** with phenols all showed a saturation behaviour, which was explained by the formation of an intermediate upon an equilibrium prior to the rate determining step of the reaction. The intermediate was postulated to be a hydrogen-bonded complex between **22** and the O-H unit of the phenolic substrate. A linear correlation between the log(k_1) measured for phenolic substrates and the BDFE_{O-H} was observed and this result, together with a KIE = 1.4 for the reaction with phenols, suggest a concerted PCET mechanism occurs during the oxidation of phenols by **22**. In the reaction with TEMPOH, linear kinetics were observed with a rate of reaction four orders of magnitude lower than the one observed for **21** (k_2 (14) = $1.3 \times 10^{-1} \text{ M}^{-1} \text{ s}^{-1}$ at 25 °C in acetonitrile). This is explained by the higher entropy and enthalpy of activation

calculated for **22** ($\Delta H^\ddagger = 9.9$ kcal/mol and $\Delta S^\ddagger = -35$ cal K⁻¹ mol⁻¹) respect to **22**, which accounts for a more ordered transition state which might be explained by the presence of a neutral ligand in **22** with respect to an anionic one in **22**.

Mayer reported that [Fe^{III}(OH)(^{Mes}TMP)] (**23**, Figure 1.4) reacted with TEMPOH to yield TEMPO[•] and H₂O with a $k_2 = 7.6 \times 10^1$ M⁻¹s⁻¹ at 25 °C in toluene.¹¹⁰ Interestingly, both **23** and Fe^{II}(^{Mes}TMP) catalysed the disproportionation of TEMPOH to TEMPO[•] and 2,2,6,6,-tetramethylpiperidine, a reaction which was shown to involve a HAT step.¹¹⁰ Groves reported a cationic complex supported by a porphyrazine ligand, [Fe^{III}(OH)(OH₂)(PyPz)]⁴⁺ (**24**, Figure 1.4), which proved to be a very fast HAT oxidant.¹¹¹ This complex in fact reacted with the benzylic hydrocarbons with BDE_{C-H} up to 82 kcal/mol at 20 °C in water/acetonitrile at pH 2.2 and showed an unusual primary KIE = 20.2 in the reaction with xanthene (Table 1.1). This KIE is beyond the classical range normally observed for Fe or Mn hydroxides and suggests that hydrogen tunneling occurs.

Goldberg isolated a high-valent manganese hydroxide supported by a corrole ligand, [Mn^{IV}(OH)(tppc)] (**25**, Figure 1.4).¹¹² This complex was able to perform HAT oxidation of *para*-substituted-2,6-di-*tert*-butylphenols at 23 °C in benzene. The reaction of **25** with 2,4-di-*tert*-butylphenol gave a second-order rate constant $k_2 = 2.73 \times 10^4$ M⁻¹s⁻¹, three orders of magnitude higher than those measured for the corresponding oxo complex, [Mn^V(O)(tppc)] for the same substrate in the same conditions ($k_2 = 1.74 \times 10^1$ M⁻¹s⁻¹).¹¹² **24** was thus shown to be a more powerful HAT oxidant than its higher-valent oxo counterpart. A comparable complex containing iron, [Fe^{IV}(OH)(tppc)](**26**, Figure 1.4) proved to be a faster HAT oxidant compared to **25**, with second order rate constants two orders of magnitude higher when the same substrate was considered.¹¹³ The calculated BDE_{O-H} of the reduced aquo-complexes obtained upon HAT confirm that **26** is a more powerful oxidant than **25**, since BDE_{O-H}(**25H**) = 85 kcal/mol and BDE_{O-H}(**26H**) = 89 kcal/mol (Table 1.1).¹¹³

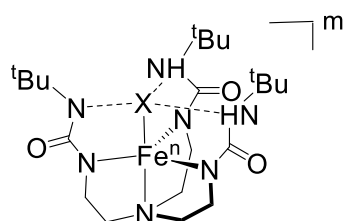
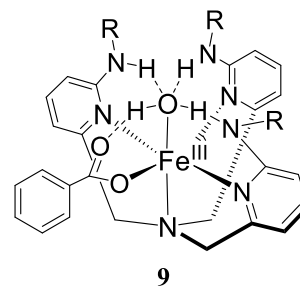
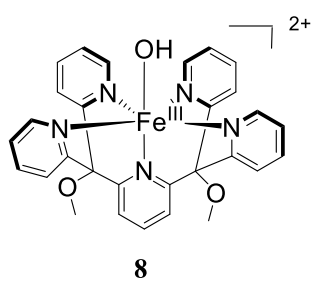
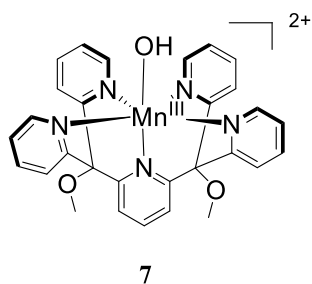
After the formation of a carbon-based radical by HAT oxidation of the substrate, the following step in the CYP catalytic cycles involves a radical rebound between Compound II and the radical, yielding to the eventual hydroxylation of the substrate. This step is present also in many non-heme iron enzymes such as isopenicillin N synthase or α -ketoglutarate dependent halogenases or hydroxylases.¹¹⁴ This reactivity has been object of many recent studies with iron-hydroxide model complexes attempting to mimic the behaviour of the metalloenzymes. **26** was shown to react rapidly at 23 °C in toluene with Gomberg's dimer, the other equilibrium form in which the relatively stable trityl radical is present in solution in organic solvents,

yielding 77% of the hydroxylated product (trityl alcohol).¹¹⁵ The reaction of the isotopically labelled analogue, $[\text{Fe}^{\text{IV}}(^{18}\text{OH})(\text{tppc})]$, yielded a product with 57% incorporation of ^{18}O , confirming the hydroxylation occurs due to radical rebound with the high-valent iron complex. Analysis of the reaction with *para*-substituted trityl radicals gave insights into the rebound mechanism, showing that it follows a concerted pathway compared to a stepwise electron-transfer/"cation"-transfer (ET/CT) pathway.¹¹⁵

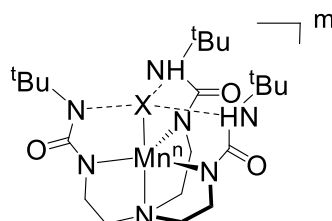
Recently, Goldberg and co-workers isolated $[\text{Fe}^{\text{III}}(\text{OH})(\text{BNPA}^{\text{Ph}_2\text{O}})](\text{OTf})$ (**27**, Figure 1.4),¹¹⁴ which was obtained by reaction with O_2 at 23 °C of a Fe^{II} precursor. This very stable mimic of a non-heme iron complex showed to react at 23 °C in THF with *para*-substituted trityl radicals, which were almost quantitatively (84-87%) hydroxylated in the reaction with **27**.¹¹⁴ ^{18}OH incorporation in the products was quantitative (99%) when the labelled version of **27** was employed.

Similarly, Fout and co-workers reported two stable Fe^{III} -hydroxide complexes, $[\text{Fe}^{\text{III}}(\text{OH})(\text{Py}_2\text{Py}-(\text{afa}^{\text{Cy}})_2)](\text{OTf})_2$ (**28**, Figure 1.5) and $[\text{Fe}^{\text{III}}(\text{OH})(\text{Py}_2\text{Py}-(\text{afa}^{\text{Cy}})(\text{pi}^{\text{Cy}}))](\text{OTf})$ (**29**, Figure 1.4). The two complexes differ for the tautomeric state of the ligands: the pyrrole-imine (pi) is an anionic donor, whereas the azafulvene-amine (afa) is a neutral donor. This strongly affects their reactivity: while **28** reacted with Gombert's dimer to yield quantitatively triphenylmethanol, **29** did not perform this reaction in absence of water. When water was added to **29**, the reaction occurred to completion in 1h, compared to 10 s observed for **28**.¹¹⁶

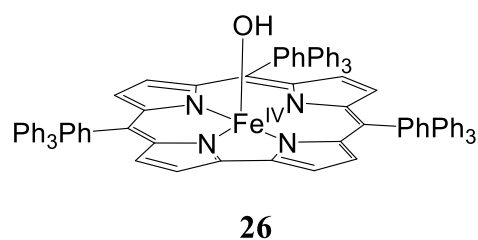
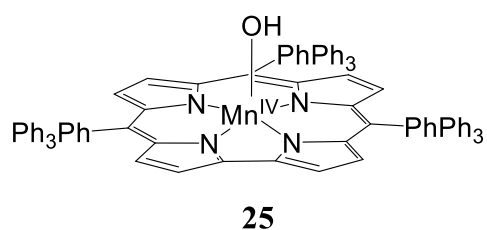
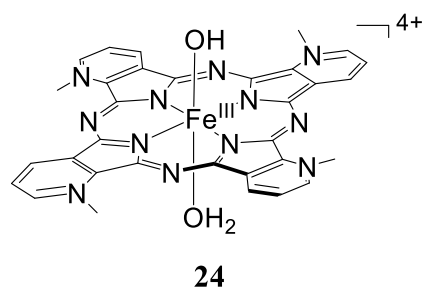
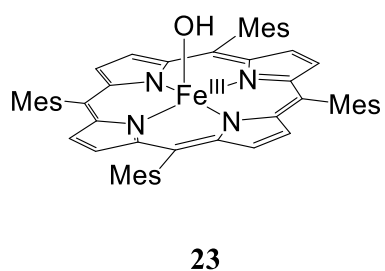
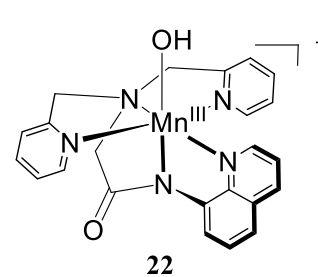
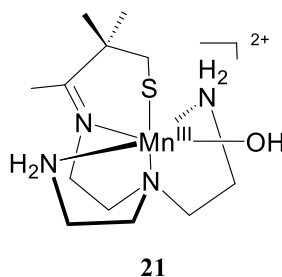
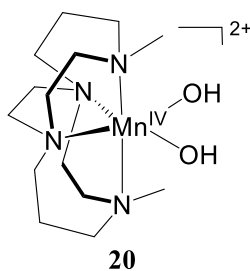
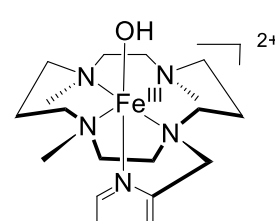
In summary several examples of high-valent Fe and Mn hydroxide complexes have been reported in literature and their reactivity towards C–H and O–H bonds oxidation has been extensively investigated, showing that they predominantly react by HAT. Some recent reactivity studies with these model complexes focused on probing the radical rebound step observed in metalloenzymes.



m=1-, n=3, X=OH **10**
 m=2-, n=2, X=OH **13**
 m=2-, n=3, X=O **14**



m=1-, n=3, X=OH **11**
 m=2-, n=2, X=OH **13**
 m=2-, n=3, X=O **15**
 m=0, n=4, X=OH **16**
 m=1-, n=4, X=O **17**
 m=0, n=5, X=O **18**



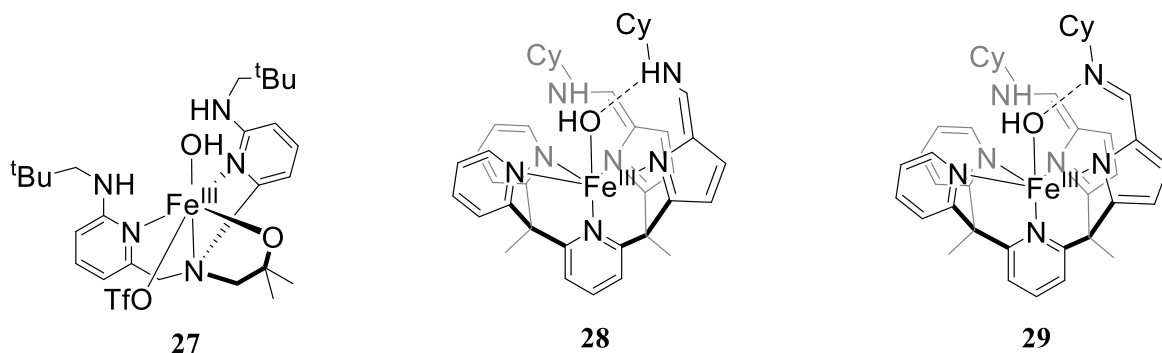


Figure 1.4. Synthetic high-valent Fe and Mn hydroxide complexes.

1.1.4.2.2 Late first-row transition metals (Cu)

To date, no high-valent nickel or cobalt hydroxide has been isolated or extensively spectroscopically characterized. Tolman reported the high-valent copper hydroxide $[\text{Cu}^{\text{III}}(\text{OH})(\text{pyN}_2^{\text{iPr}_2})]$ (**30**, Figure 1.5) which to date remains one of the most-reactive synthetic HAT oxidants.¹¹⁷ Complex **30** was trapped and spectroscopically characterized at $-80\text{ }^\circ\text{C}$ and was shown to react with DHA faster than most of other iron and manganese complexes in the same conditions. Interestingly **30** showed an unusually very high KIE of 44 in the reaction with DHA at $-70\text{ }^\circ\text{C}$ and activation energy parameters comparable to other high-valent metal hydroxide performing HAT ($\Delta H^\ddagger = 5.4\text{ kcal/mol}$ and $\Delta S^\ddagger = -30\text{ cal K}^{-1}\text{ mol}^{-1}$, Table 1.1).¹⁴ Complex **30** reacted with hydrocarbon substrates with $\text{BDE}_{\text{C-H}} = 92\text{ kcal/mol}$ (THF) and $\text{BDE}_{\text{C-H}} = 99\text{ kcal/mol}$ (cyclohexane). Furthermore, the $\text{BDE}_{\text{O-H}}$ for the reduced aquo complex obtained upon HAT, $[\text{Cu}^{\text{II}}(\text{OH}_2)(\text{pyN}_2^{\text{iPr}_2})]$ (**30H**), was calculated to be 90 kcal/mol , a value higher than those for most other metal oxo/hydroxo complexes.¹¹⁸ Starting from a modified, macrocyclic version of the pyridinedicarboxamidate ligand, Tolman isolated and crystallographically characterized a dinuclear complex containing a Cu^{II} and a Na^{I} bridged by an hydroxylated THF molecule.¹¹⁹ This suggested that hydroxylation of the solvent occurred after the formation of a transient Cu^{III} entity.¹¹⁹ Other modifications of the pyridinedicarboxamidate ligand affected the reactivity of the copper hydroxide unit: the complex $[\text{Cu}^{\text{III}}(\text{OH})(\text{pipN}_2^{\text{iPr}_2})]$ (**31**, Figure 1.5, Table 1.1), supported by a more electron-donating ligand, and the complex $[\text{Cu}^{\text{III}}(\text{OH})(\text{NO}_2\text{pyN}_2^{\text{iPr}_2})]$ (**32**, Figure 1.5, Table 1.1), which features a more electron-withdrawing ligand than **30**.¹²⁰ These structural variations were reflected in the rate of oxidation of C–H bonds by the complexes, with second order rate constants following the order **32** > **30** > **31** and with a similar trend for the $\text{BDE}_{\text{O-H}}$ for the reduced aquo complexes obtained upon HAT ($\text{BDE}_{\text{O-H}}$ (**31H**): 88 kcal/mol , $\text{BDE}_{\text{O-H}}$ (**32H**): 91

kcal/mol). All these complexes presented KIE values > 25 at -40 °C and interestingly showed a temperature dependence for the KIE values. This result, together with the differences in activation energy parameters in the complexes series, indicate that the difference in electronic properties of the ligand influence deeply the HAT mechanism.^{118, 120, 121} Reactivity of **30** and **32** with *para*-substituted phenols at -80 °C was explored, showing a concerted proton-electron transfer mechanism (CPET) for all substrates except for the most acidic two, 4-nitrophenol and 4-trifluoromethylphenol. With these substrates a further contribution from a sequential PT/ET mechanism seemed more plausible based on the kinetic data.¹²²

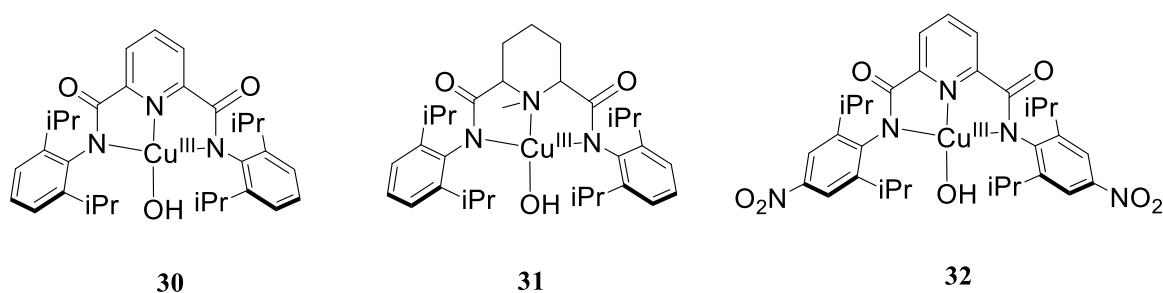


Figure 1.5. Synthetic high-valent Cu hydroxide complexes.

1.1.4.3. Synthetic high-valent metal halides

1.1.4.3.1. Iron

Among synthetic high-valent first row transition metal complexes containing a bound-halide, iron-containing examples are the most prominent, attempting to mimic the active site of haloperoxidases and halogenases. Que and co-workers exchanged the labile acetonitrile ligand in $[\text{Fe}^{\text{IV}}(\text{O})(\text{TPA})(\text{NCMe})]^{2+}$ with Cl^- and Br^- at -40 °C to yield respectively $[\text{Fe}^{\text{IV}}(\text{O})(\text{TPA})(\text{Cl})]^+$ (**33**, Figure 1.6) and $[\text{Fe}^{\text{IV}}(\text{O})(\text{TPA})(\text{Br})]^+$ (**34**, Figure 1.6).¹²³ The half-lives of these complexes appeared reduced with respect to their precursor, stable for hours at -40 °C: **33** has a $t_{1/2} = 4$ hrs whereas **34** showed $t_{1/2} = 2$ hrs.¹²³ These metastable species were characterized by electronic absorption spectroscopy, XAS, Mössbauer spectroscopy and showed that the complexes retain an $S = 1$ spin state despite the substitution of the cis ligand. The same ligand exchange approach applied to a Fe^{IV} -oxo complex supported by the TMG_2dien ligand yielded the $S = 2$ $[\text{Fe}^{\text{IV}}(\text{O})(\text{TMG}_2\text{dien})(\text{Cl})]^+$ (**35**, Figure 1.6).¹²⁴ As observed for the TPA-bearing analogues, **35** showed a drastically reduced half-life respect to the parent compound, being $t_{1/2} = 2$ mins at -30 °C.

Switching to the quinolyl-based supporting ligand TQA, Que and co-workers managed to obtain $S = 2$ complexes $[\text{Fe}^{\text{IV}}(\text{O})(\text{TQA})(\text{Cl})]^+$ (**36**, Figure 1.6, Table 1.1) and $[\text{Fe}^{\text{IV}}(\text{O})(\text{TQA})(\text{Br})]^+$ (**37**, Figure 1.6, Table 1.1).¹²⁵ These complexes showed $t_{1/2} \sim 5$ mins at -40 °C, three-fold faster than the parent oxo complex bearing a labile acetonitrile ligand.¹²⁵ Complexes **36** and **37** were reacted with cyclohexane ($\text{BDE}_{\text{C-H}} = 99$ kcal/mol) at -40 °C in inert atmosphere yielding a mixture of halocyclohexanes (**36** = 35%, **37** = 41%), cyclohexanol (**36** = 7%, **37** = 3%) and cyclohexanone (**36** = 3%, **37** = 4%) as observed by $^1\text{H-NMR}$ spectroscopy. Both complexes showed a preference for halogenation over oxidation of the hydrocarbon substrate with cyclohexane, whereas comparable percentages of benzyl halides and oxygenated products were observed for both complexes when reacted with toluene ($\text{BDE}_{\text{C-H}} = 88$ kcal/mol). Interestingly, the reactions rates of **36** and **37** with toluene were 10-fold slower than those of the parent oxo complex with the same substrate. A KIE = 20 was obtained for the bromination of toluene- H_8/D_8 (Table 1.1), suggesting a tunneling contribution in the HAT oxidation mechanism and closely matching with the one reported for native substrate halogenation by SyrB2, an enzyme belonging to the class of α -KG-dependent non-heme halogenases.¹²⁵ Furthermore, no halogenated products were observed when the reactions were repeated in aerobic atmosphere, giving weight to the mechanistic hypothesis of a competing radical rebound with the halogen or the hydroxide. This step might compete with further oxidation of the organic radical in presence of dioxygen. Interestingly, when the reaction with cyclohexane was repeated under inert conditions at 25 °C using the $S = 1$ complexes **33** and **34** a lower yield of halogenated products was obtained compared to **36** and **37** (respectively **33** = 11% and **34** = 13%) but halogenation was still favoured with respect to oxygation.¹²⁵ The higher temperature required accounts for the lower reactivity of **33** and **34**. These results suggests that the spin state of the Fe^{IV} -oxo complex can affect its capability to act as a more competent halogenation agent.

Costas and co-workers reported the $S = 1$ complexes $[\text{Fe}^{\text{IV}}(\text{O})(\text{Pytacn})(\text{Cl})]^+$ (**38**, Figure 1.6, Table 1.1) and $[\text{Fe}^{\text{IV}}(\text{O})(\text{Pytacn})(\text{Br})]^+$ (**39**, Figure 1.6, Table 1.1).¹²⁶ These oxo complexes presented $t_{1/2} \sim 3$ hrs (**38**) and $t_{1/2} = 2.45$ hrs (**39**) at -30 °C and performed OAT reactivity towards thioanisole and HAT oxidation of hydrocarbon in a range of $\text{BDE}_{\text{C-H}}$ from 75 to 84 kcal/mol at -30 °C. In both cases, **38** appeared to be a faster OAT and HAT reagent compared to **39** and both complexes reacted faster than their precursor bearing an acetonitrile labile ligand.¹²⁶ This is in contrast to what observed with the $S = 2$ complexes **36** and **37** in their

reaction with toluene. No halogenated products though were observed in the reaction with hydrocarbons. This was further tested by reacting **38** with triphenylmethane: this yielded exclusively triphenylmethanol and 90% of incorporation of ^{18}O was observed by mass spectrometry when using labelled **38**.¹²⁶ Therefore for these complexes radical rebound with the hydroxide was favoured over the rebound with the halogen.

Comba reported catalytic and stoichiometric halogenation and oxygenation of cyclohexane when reacted with complex $[\text{Fe}^{\text{II}}(\text{bispa})(\text{Cl})_2]$ in presence of different oxidants (*tert*-butylhydroperoxide (TBHP), H_2O_2 or PhIO).¹²⁷ Conclusive characterization for this complex was not reported, suggesting that the formulation of the active oxidant could either be $[\text{Fe}^{\text{IV}}(\text{O})(\text{bispa})(\text{Cl})]^+$ or $[\text{Fe}^{\text{V}}(\text{O})(\text{bispa})(\text{Cl})]^{2+}$ (**40**, Figure 1.6, Table 1.1), with the second one being more likely when an excess of oxidant was used. The yields of halogenated products varied according to the oxidant used to obtain **40**: a higher yield for the stoichiometric reaction was observed with TBHP (44.3%) with respect to H_2O_2 (19.2%) or PhIO (6.9%), but also a lower selectivity for halogenation with respect to oxygenation ($\text{yield}_\text{X}/\text{yield}_\text{O}$ (TBHP) = 0.80, $\text{yield}_\text{X}/\text{yield}_\text{O}$ (H_2O_2) = 8, $\text{yield}_\text{X}/\text{yield}_\text{O}$ (PhIO) = 17.2).¹²⁷ The yield of halogenated product increased significantly when an excess of oxidant was used (10 equiv. PhIO = 17% after 35 mins and almost 40% after 24 hrs).

Paine reported the reactivity of a $[\text{Fe}^{\text{II}}(\text{Tp}^{\text{Ph}_2})(\text{benzilate})]$ complex in presence of molecular oxygen, pyridinium perchlorate (PyNHClO_4) and tetrabutyl ammonium chloride (TBACl) with different hydrocarbons.¹²⁸ The putative $[\text{Fe}^{\text{IV}}(\text{O})(\text{Tp}^{\text{Ph}_2})(\text{Cl})]$ (**41**, Figure 1.6, Table 1.1) yielded both chlorinated and oxygenated products in the reaction with adamantane ($\text{yield}_\text{X}/\text{yield}_\text{O} = 0.27$), toluene ($\text{yield}_\text{X}/\text{yield}_\text{O} = 0.51$), cyclohexene ($\text{yield}_\text{X}/\text{yield}_\text{O} = 0.5$) and CHD ($\text{yield}_\text{X}/\text{yield}_\text{O} = 0.48$). Only oxygenated products were observed in the reaction with cyclohexene.¹²⁸ When tetrabutylammonium bromide was used, brominated products were detected although in lower yields than the chlorinated ones. Maiti and co-workers reported a new halogenation strategy by combining a $[\text{Fe}^{\text{IV}}(\text{O})(2\text{PyN}2\text{Q})]^{2+}$ complex with a low valent $[\text{Fe}^{\text{II}}(\text{X})(2\text{PyN}2\text{Q})](\text{Y})$ ($\text{X} = \text{Cl}, \text{Br}, \text{Y} = \text{Cl}, \text{Br}, \text{ClO}_4$) to direct the rebound step toward halogenation respect to hydroxylation.¹²⁹ The putative active species are $[\text{Fe}^{\text{III}}(\text{Cl})(2\text{PyN}2\text{Q})]^{2+}$ (**42**, Figure 1.7) or $[\text{Fe}^{\text{III}}(\text{Br})(2\text{PyN}2\text{Q})]^{2+}$ (**43**, Figure 1.6, Table 1.1) which have not been trapped, but insights about the oxidation state of the iron have been obtained by EPR studies. With **43**, a 90% selectivity towards bromination in the reaction with cyclohexane at 25 °C under

inert atmosphere was reported. Bromination of toluene showed 97% selectivity in the same conditions whereas lower ones (46-65%) were reported with other aliphatic substrates.¹²⁹ In presence of **42**, chlorination reactions showed a lower selectivity respect to hydroxylation, e.g. 5:1 in the reaction with cyclohexane.

Recently Goldberg reported that the non-heme iron complexes $[\text{Fe}^{\text{III}}(\text{OH})(\text{BNPA}^{\text{Ph}_2\text{O}})(\text{Cl})]$ (**44**, Figure 1.7) and $[\text{Fe}^{\text{III}}(\text{OH})(\text{BNPA}^{\text{Ph}_2\text{O}})(\text{Br})]$ (**45**, Figure 1.6, Table 1.1), obtained by exposure to O_2 of the corresponding Fe^{II} -halide complexes.¹³⁰ These complexes were reacted with *para*-substituted trityl radicals yielding in all cases the corresponding alcohols in yields > 90%. The selectivity for the hydroxide rebound respect to the halide rebound was confirmed by ^{18}O labelling studies. The same reactivity study was performed with $[\text{Fe}^{\text{III}}(\text{Cl})_2(\text{BNPA}^{\text{Ph}_2\text{O}})]$ (**46**, Figure 1.6) and yielded the halogen rebound products in high-yields (75-84%).¹³⁰ Thus with **44** and **45** where the two competing processes are possible, hydroxylation is favoured over halogenation: this contrasts with what observed with most of the Fe^{IV} -oxo/halide models of halogenase enzymes.

In summary, the majority of high-valent Fe complexes capable of C–H oxidation and halogenation are Fe^{IV} -oxo/halide complexes. Often these complexes are kinetically more competent oxidants than Fe^{IV} -oxo species bearing neutral ancillary ligands, suggesting that the presence of halide ligands can influence their oxidative reactivity and in many cases allows the halogenation of saturated hydrocarbons.

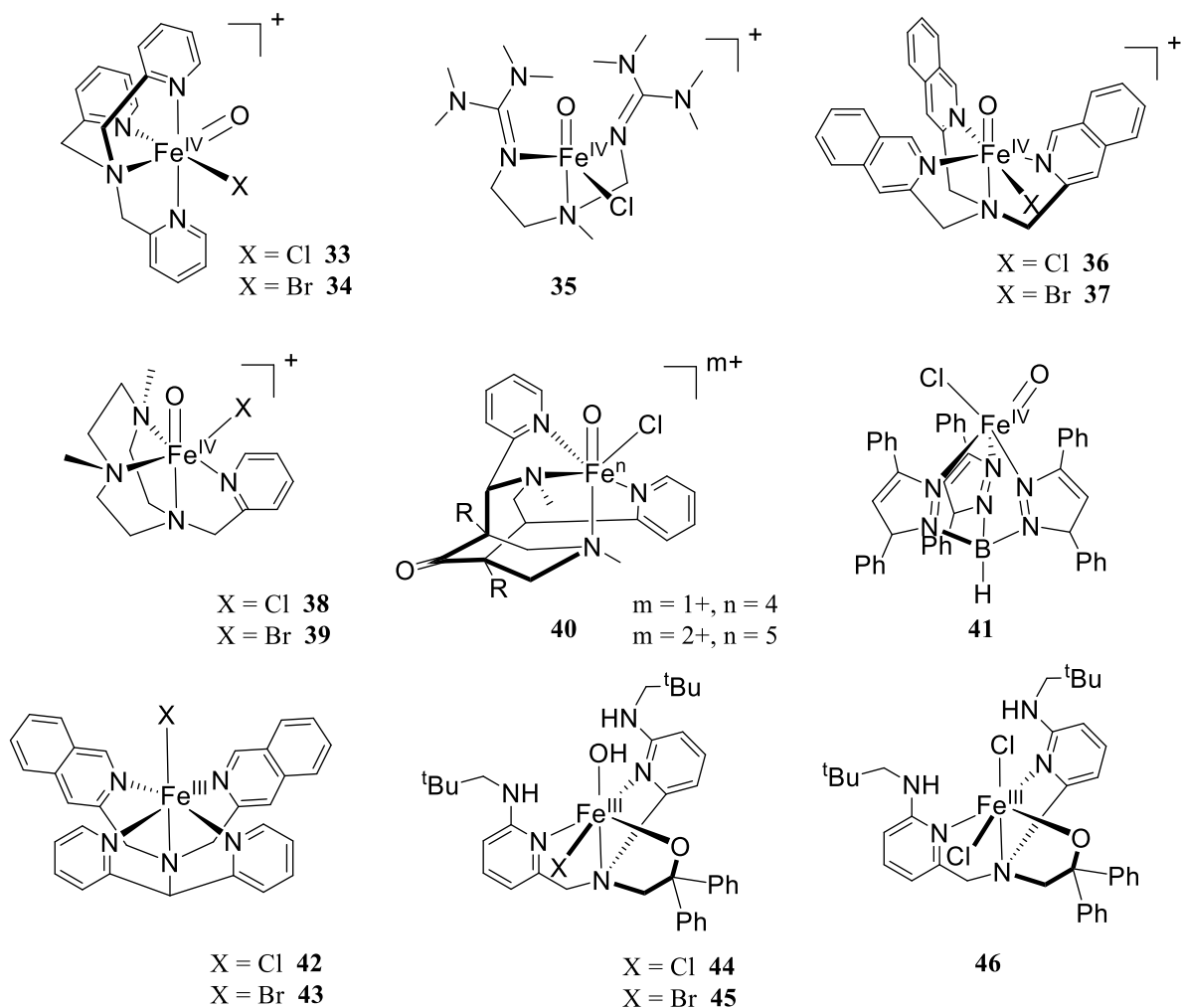


Figure 1.6. Synthetic high-valent Fe-X (X = Cl, Br) complexes.

1.1.4.3.2. Manganese

Groves and co-workers showed multiple examples of effective hydrocarbon halogenation with manganese-porphyrin complexes. Complex $[\text{Mn}^{\text{III}}(\text{Cl})(\text{TPP})]$ (**47**, Figure 1.7) in presence of NaOCl was shown to convert a series of alkanes up to cyclohexane into the corresponding chlorinated products, with selectivities ranging from 38 to 74%.^{131, 132} For substrates with stronger C–H bonds such as neopentane ($\text{BDE}_{\text{C-H}} = 100 \text{ kcal/mol}$), complex $[\text{Mn}^{\text{III}}(\text{Cl})(\text{TMP})]$ (**48**, Figure 1.7) was effective at catalysing the formation of 31% of chlorinated product. Bromination was achieved by exchanging NaOCl with NaOBr.¹³¹ A regioselectivity test with *trans*-decalin showed that 76% selectivity for 1-chlorodecalin was achieved when the more bulky **48** was employed with respect to **47**.¹³¹ The mechanism proposed for this system is that the hypochlorite ion oxidises **47** and **48** to yield Mn^{V} -dioxo intermediates. These are powerful

electrophiles which perform HAT on the substrates yielding a carbon-based radical and a Mn^{IV} -hydroxo complex. This would subsequently react with hypochlorite to yield a Mn^{IV} -hypochlorite complex with which the radical rebound occurs.^{131, 132} In a similar approach, **48** was used in presence of PhIO, AgF and tetrabutylammonium fluoride (TBAF) to achieve fluorination of hydrocarbons.¹³³ Monofluorinated cycloalkanes were obtained in $\sim 50\%$ yield, together with below 20% yield of oxygenated products. Those became the only product when no AgF was employed.¹³³ High stereoselectivity towards the methylenic position was observed in the fluorination of *trans*-decalin, analogous to what was observed in the chlorination reaction. Furthermore, selective fluorination of more complex bioactive molecules, such as steroids, was achieved in yields of $\sim 50\%$.

The proposed mechanism of reaction involves ligand exchange to yield $[\text{Mn}^{\text{III}}(\text{F})(\text{TMP})]$ (**49**, Figure 1.7) which is oxidised by PhIO to $[\text{Mn}^{\text{V}}(\text{O})(\text{F})(\text{TMP})]$ which is supposed to perform the HAT step. Then fluorination is supposed to occur by radical rebound to either a $[\text{Mn}^{\text{IV}}(\text{OH})(\text{F})(\text{TMP})]$ species or a *trans*- $[\text{Mn}^{\text{IV}}(\text{F})_2(\text{TMP})]$ (**50**, Figure 1.7) formed upon ligand exchange with AgF.¹³³ **50** was in fact isolated by treating the corresponding chloride with AgF and structurally characterized. This complex was shown to be able to replace AgF as a fluoride donor in the reaction of **48** and PhIO with cyclooctane, yielding 43% of cyclooctyl fluoride. This suggested that this complex is able to intercept carbon-based radical to yield fluorinated products.¹³³ Complex **48** was also used to yield ^{18}F -labelled compounds for imaging in the presence of oxidant and labelled-fluoride source starting from substrates bearing carboxylic acids functionalities (decarboxylative fluorination).¹³⁴ A more electron-deficient ligand, bearing perfluorinated aryl groups, was used to yield $[\text{Mn}^{\text{III}}(\text{Cl})(\text{TPFPP})]$ (**51**, Figure 1.7).¹³⁵ This complex catalyzed the highly regio- and stereoselective chlorination of hindered and electron-deficient cycloalkanes and lactones in the presence of NaOCl. Fluorination was achieved with the same catalyst in the presence of PhIO, AgF and TBAF under inert atmosphere.

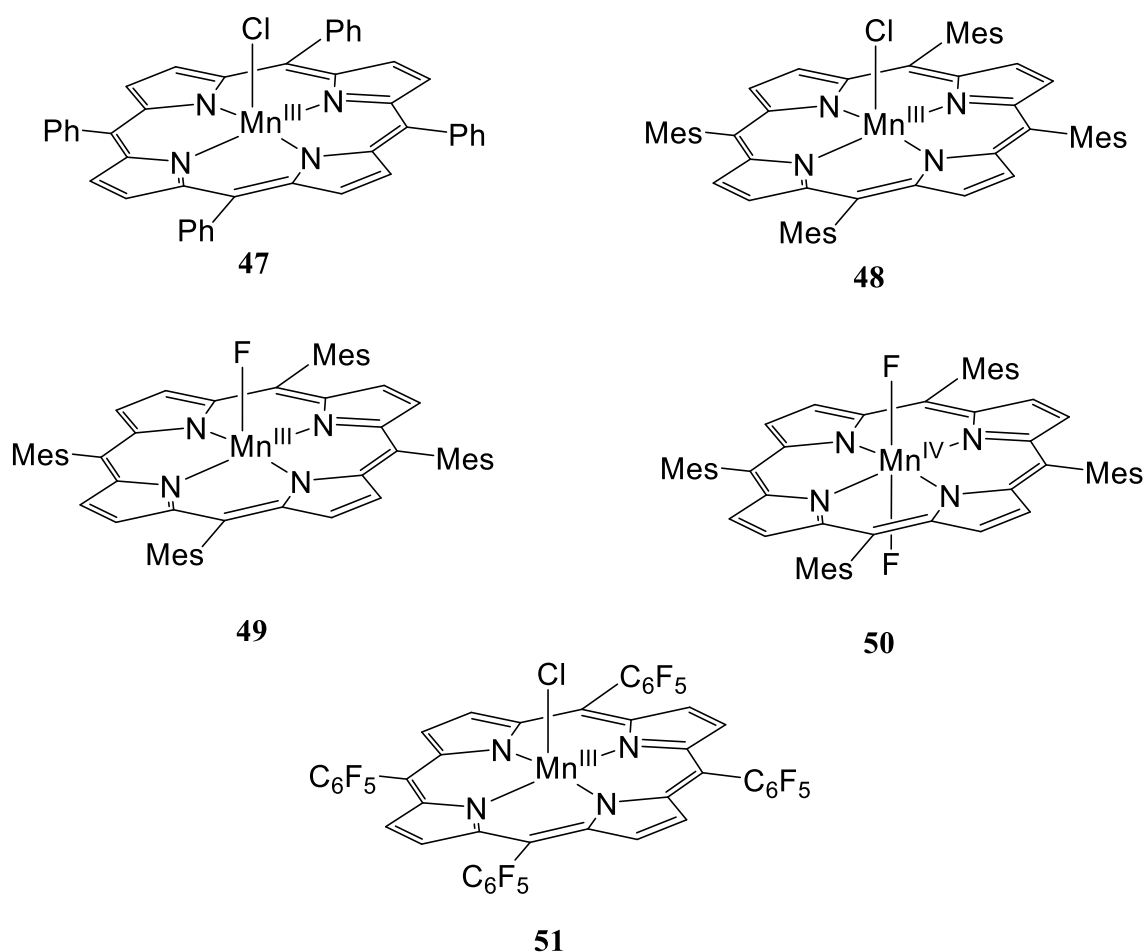


Figure 1.7. Synthetic high-valent Mn–X (X = Cl, F) complexes.

1.1.4.3.3. Nickel

Costas and Browne reported that the low valent Ni-complex $[\text{Ni}^{\text{II}}(\text{Me,HPyTACN})(\text{CH}_3\text{CN})_2](\text{OTf})_2$ in the presence of NaOCl was able to convert alkanes to alkyl chlorides at rt.¹³⁶ In these conditions the yields of chlorinated products were moderate (4.1-16.8%) but when acetic acid was added yields increased (10.7-37.3%). KIE value for the reaction with cyclohexane- $\text{H}_{12}/\text{D}_{12}$ was determined to be 2, too low to suggest the involvement of a high-valent metal-oxo species. MS evidence led to postulate the formulation of active chlorinating species as $[\text{Ni}^{\text{II}}(\text{OCl})(\text{Me,HPyTACN})]^+$ (**52**, Figure 1.8, Table 1.1) whereas EPR and Raman suggested it being either $[\text{Ni}^{\text{III}}(\text{OH})(\text{Me,HPyTACN})]^{2+}$ or $[\text{Ni}^{\text{III}}(\text{OAc})(\text{Me,HPyTACN})]^{2+}$ (**52**) when acetic acid was used, suggesting that chlorine radical formation might be responsible for halogenation.¹³⁶

Company and co-workers reported that the complex $[\text{Ni}^{\text{II}}(\text{damc})](\text{OTf})_2$ in the presence of NaOCl and AcOH was observed to yield a mixture of chlorinated and oxygenated alkanes

under catalytic conditions.¹³⁷ The active species was postulated to be formally a $[\text{Ni}^{\text{IV}}(\text{OCl})(\text{damc})]^+$ (**53**, Figure 1.8, Table 1.1) complex based on spectroscopic and computational studies. This oxidant was able to perform the oxidation of strong C–H bonds such as that of cyclohexane, for which 83% selectivity towards chlorinated products formation was achieved in optimized conditions (-30 °C, substrate excess, equimolar NaOCl/AcOH). The second order rate constants determined for the stoichiometric reactions with a series of hydrocarbons substrates correlated linearly with their $\text{BDE}_{\text{C-H}}$, suggesting a HAT mechanism of oxidation, with a pretty low KIE of 1.5 calculated for the reaction with DHA-H₄/D₄.¹³⁷

Our group reported a spectroscopically characterized $[\text{Ni}^{\text{III}}(\text{Cl})(\text{pyN}_2^{\text{Me}_2})]$ (**54**, Figure 1.8, Table 1.1) with $t_{1/2} \sim 6\text{h}$ at -40 °C which performed HAT oxidation of *para*-substituted-2,6-di-*tert*-butylphenols and hydrocarbons.¹³⁸ The complex was obtained by one-electron oxidation of the low-valent $[\text{Ni}^{\text{II}}(\text{Cl})(\text{pyN}_2^{\text{Me}_2})]^-$ precursor with either ceric ammonium nitrate (CAN) or *tris*-(4-bromophenyl)ammoniumyl hexachloroantimonate (Magic Blue). The retention of the chloride ancillary ligand in **54** was proved by the four-lines hyperfine splitting observed in the EPR spectrum ($I_{\text{Cl}} = 3/2$).¹³⁸ The complex reacted slowly with weak C–H bonds (CHD, xanthene) whereas a linear correlation was observed between the rate constants in the reaction with *para*-substituted-2,6-di-*tert*-butylphenols and their $\text{BDE}_{\text{O-H}}$. A KIE of 2.4 was observed in the reaction with 2,6-DTBP whereas one of 4.5 was determined in the reaction with DHA-H₄/D₄: these values are in the classical range, in agreement with the involvement of a M–OX species instead of a M=O.¹³⁹ The mechanism of reaction was determined to be HAT oxidation and interestingly no chlorinated products were observed. This discovery showed that a high-valent M–X species can be an efficient HAT oxidant without requiring the involvement of a M=O species. The postulated driving force for the HAT reaction is the formation of H–Cl, which has a $\text{BDE} = 103\text{ kcal/mol}$.¹³⁸

The same approach was pursued in the synthesis of $[\text{Ni}^{\text{III}}(\text{F})(\text{pyN}_2^{\text{Me}_2})]$ (**55**, Figure 1.8, Table 1.1) by one-electron oxidation of the low-valent precursor using N-chloromethyl-N-fluorotriethylenediammonium bis(tetrafluoroborate) (Selectfluor).¹⁴⁰ Also in this case EPR confirmed the presence of the fluoride ligand in **55** by showing a two-lines hyperfine splitting on the z component ($I_{\text{Cl}} = 1/2$). Since H–F has a $\text{BDE} = 136\text{ kcal/mol}$, **55** was expected to be a superior oxidant compared to **54**. This was observed in the reactivity of **55** with hydrocarbons at -40 °C: a 4300-fold rate enhancement was observed in the reaction with xanthene and a 2200-

fold in the reaction with CHD with respect to what observed with **54**. Complex **55** reacted with a range of hydrocarbon substrates from xanthene to toluene to yield oxidised product via a HAT mechanism. The KIE was reported to be 110 in the reaction with xanthene-H₂/D₂ and 79 in the reaction with DHA-H₄/D₄ (Table 1.1). These values appeared unusually high for a M–X type of complex and considerably higher than the one determined for **54**, suggesting a contribution from hydrogen tunneling. Oxygenated products only were detected in the reaction with hydrocarbons, but when **55** was reacted with ethylbenzene in presence of excess Selectfluor, TBAF and AgF fluorinated products were detected in the reaction mixture by ¹⁹F-NMR. Furthermore, complex **55** showed to be able to perform halide transfer to PPh₃.¹⁴⁰

1.1.4.3.4. Copper

Very recently, Zhang and co-workers reported the synthesis of [Cu^{III}(F)(pyN₂^{iPr2})] (**56**, Figure 1.8, Table 1.1), [Cu^{III}(Cl)(pyN₂^{iPr2})] (**57**, Figure 1.8, Table 1.1) and [Cu^{III}(Br)(pyN₂^{iPr2})] (**58**, Figure 1.8, Table 1.1).¹⁴¹ These complexes were obtained by one-electron oxidation by magic blue at -80 °C in CH₂Cl₂. While **57** and **58** exhibited stability at 20 °C, **56** decayed at temperatures higher than -20 °C. All complexes were structurally characterized, showing shorter Cu–N_{axial} and Cu–X bond distances respect to their low-valent precursors. XAS and DFT studies supported the formulation of the Cu centre as *d*⁸ Cu^{III} in all three complexes. **56** showed to react with DHA at -30 °C 200-fold faster than **57** and **58**. This is surprising based on the lower *E*^o of the Cu^{II/III} couple for **56** (*E*^o = 0.465 V for **56** vs *E*^o = 0.525 V for **57** and **58**), suggesting that the high basicity of the fluoride ligand plays a role in the exceptional reactivity of **56** respect to **57** and **58**. Carbon radicals capture experiments with azobisisobutyronitrile (AIBN) and trityl radical showed the formation of the corresponding halogenated products in moderate to good yields (45-86%).¹⁴¹ Interestingly, while the reaction of **57** and **58** with trityl radical seemed to occur via a stepwise electron transfer – halide transfer (ET-HT) whereas that of **56** occurred via a concerted mechanism. Furthermore, **56** demonstrated to be able to yield selectively mono-fluorinated products at rt when reacting with THF (69% yield), 1,4-dioxane (45%) and 18-crown-6 (35%), whereas yields were moderate (8-42%) with allylic and benzylic substrates.

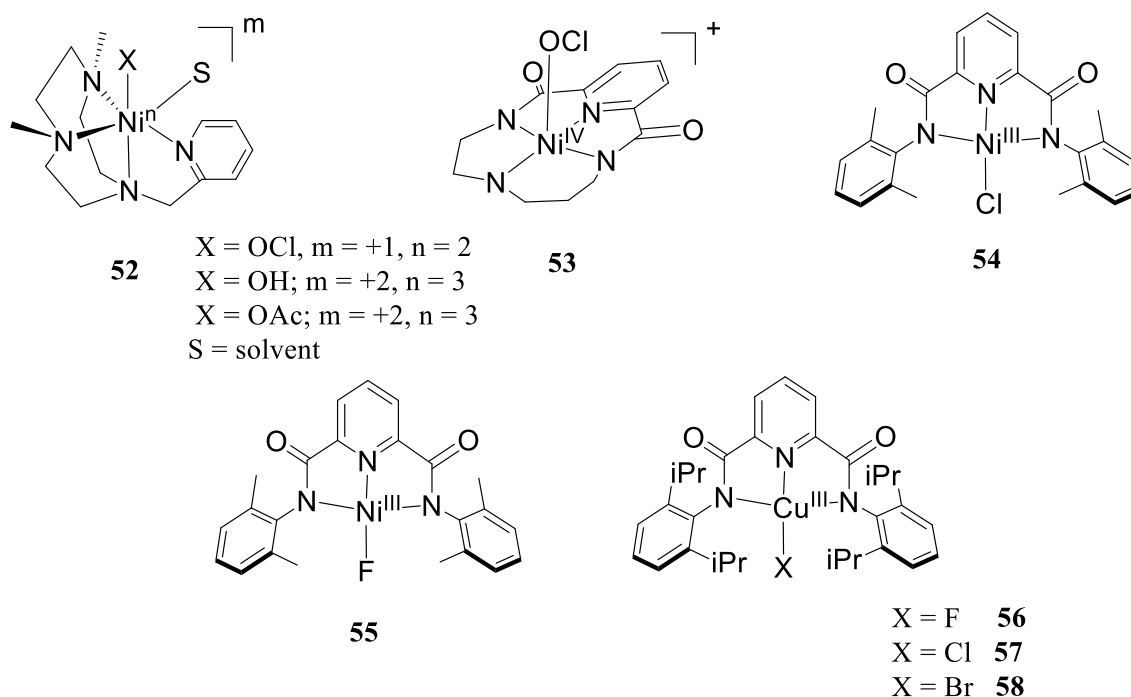


Figure 1.8. Synthetic high valent Ni–X and Cu–X (X = Cl, F, OCl) complexes.

These examples illustrated the growing interest towards high-valent metal halides complexes containing mid- (Fe, Mn) and late (Ni, Cu) first-row transition metals for their role as fast and effective catalysts for C–H bond oxidation. Most of these complexes were demonstrated to follow a HAT mechanism and in certain cases to promote halogenation of the hydrocarbon substrates along with their oxidation. In comparison, similar halide complexes bearing third-row transition metals such as Au have not been investigated for their oxidative reactivity towards C–H bonds so we will explore them in our work, aiming to compare their mechanistic features to those reported for these first-row transition metal examples.

Table 1.1. Kinetic and thermodynamic parameters for M–X (M = Fe, Mn, Ni, Cu; X = OH, Cl, Br, F) complexes that have been examined in the oxidation of O–H and C–H bonds.

Compound	$k_2 / \text{M}^{-1} \text{s}^{-1} (\text{T} / ^\circ\text{C})$ (substrate)	ΔH^\ddagger / kcal/ mol	ΔS^\ddagger / cal/ K mol	KIE (T / $^\circ\text{C}$) (substrate)	BDE _{O–H} kcal/m ol ^[a]	E^0 / V (vs Fc/Fc ⁺) ^[b]	$\Delta G^\ddagger / \Delta(\text{BDE})$ slope ^[c]	Reference
7	1.6 x 10 ⁻³ (25) (DHA)	9.3	-36	2.4 (25) (DHA)	82	0.810	0.07	93
8	4.3 x 10 ⁻⁴ (25) (DHA)	13.2	-26	6.3 (25) (DHA)	80	0.555	0.26	94
10	-	-	-	-	115	0.19	-	97
11	-	-	-	-	110	0.38	-	97
19	7.1 (-40) (TEMPOH)			6 (-40) (TEMPOH)				105
20	4.39 x 10 ⁻⁵ (23.8) (DHA)	13.1	-35	3.27 (23.8) (DHA)	83	0.756	-	106
21	2.1 x 10 ³ (25) (TEMPOH)	8.2	- 25.5	3.1 (25)	70.1	-0.02	-	107
22	1.3 x 10 ⁻¹ (25) (TEMPOH)	9.9	-35	1.8 (25) (TEMPOH)	-	-0.02	0.08	109
23	76 (25)(TEMP OH)	-	-	-	67	-0.83		110
24	2216 (20) (xanthene)	6.8	- 27.2	20.2 (20) (xanthene)	84	1.09	-	111
25	2.73 x 10 ⁴ (23)(2,4- DTBP)	-	-	1.40 (23) (2,4- DTBP)	85	-	-	112, 113
26	1.21 x 10 ⁴ (23) (4- CH ₃ O-2,6- DTBP)	-	-	2.9 (23) (4- CH ₃ O-2,6- DTBP)	89	-	-	113

30	1.9 x 10 ² (25) (DHA)	5.1	-31	29 (-40)	90	0.566	0.37	118, 120
31	5.0 (25) (DHA)	3.8	-38	25(-40)	88	0.380	-	120
32	2.0 x 10 ³ (25) (DHA)	4.9	-27	26(-40)	91	0.764	-	120
36	5.0 x 10 ⁻² (- 40) (toluene)	-	-	-	-	-	-	125
37	7.0 x 10 ⁻² (- 40) (toluene)	-	-	20(-40) (toluene)	-	-	-	125
38	2.22 x 10 ⁻³ (- 30) (DHA)	-	-	25 (-30) (DHA)	-	-	-	126
39	1.89 x 10 ⁻³ (- 30) (DHA)	-	-	25 (-30) (DHA)	-	-	-	126
40	-	-	-	14 [PhIO] 9 [TBHP] 3 [H ₂ O ₂] ^[d] (25) (cyclohexane)	-			127
43	2.42 x 10 ^{- 2} (25) (toluene)			13.5 (25) (toluene)[bromin ation] 9.4 (25) (toluene) [oxidation] ^[e]		0.93		129
52				2 (25) (cyclohexane)		0.72		136
53	8.5 (-30) (DHA)			1.5 (-30) (DHA)		-		137

54	5.5 x 10 ⁻⁴ (-40) (CHD) 1.76 x 10 ⁻¹ (-40) (2,6-DTBP)	8.5	-	2.4 (-40)(2,6-DTBP)	-	0.42	0.66	138, 140
55	1.19 (-40)(CHD) 29.21 (0) (DHA)	6.15	-	79 (-40)(DHA)	-	0.35	0.41	140
56	6.68 x 10 ⁻¹ (-30)(DHA)	3.8	-43	-	-	-	0.46 5	141
57	2.25 x 10 ⁻³ (-30)(DHA)	-	-	-	-	-	0.52 5	141
58	2.95 x 10 ⁻³ (-30)(DHA)	-	-	-	-	-	0.52 5	141

[a] BDE of the X–H bond formed upon HAT. [b] Data are reported vs SHE and corrected when necessary considering SCE = 0.24 V, AgCl = 0.23 V. [c] Bell-Evans-Polanyi slopes calculated from the reported kinetic data by using the Eyring equation where not available. [d] The different oxidants required to obtain the active species are reported in square brackets. [e] The different reaction outcome obtained is reported in square brackets.

1.1.4.4 Second and third row late transition metals in oxidation catalysis

In 1969 Shilov discovered that a mixture of Pt^{II} and Pt^{IV} salts was capable of catalysing the oxidation of inert hydrocarbons to their corresponding alcohols in solution, among which the reportedly difficult transformation of methane to methanol.^{142, 143} This was the first report of a homogeneous saturated C–H bond activation reaction and since then second and third row transition metals have been widely explored for this purpose. Second and third-row transition metals are less abundant and more expensive than those belonging to the first transition row but they present several advantages. In fact they often show remarkable stability and resistance to corrosion, they also display unique selectivity, high affinity for π -bond activation and their complexes are often diamagnetic so easily characterized by ¹H NMR.¹⁴⁴ These metals are

excellent candidates for dioxygen activation in mild conditions, generating oxygen adducts which can be often characterized more easily than their first row metal-base counterparts, allowing for a better understanding of their involvement in hydrocarbon oxidation.¹⁴⁴

1.1.4.4.1 Platinum

Since the development of Shilov system, several similar studies involving platinum salts of complexes as homogeneous hydrocarbon activation catalysts have been reported. Periana observed the selective oxidation of methane to methyl esters in the presence of concentrated H₂SO₄ and Pt^{II} complexes at high temperatures (> 150 °C).¹⁴⁵ The proposed mechanism involves the activation and coordination of methane by a 14-electron Pt^{II} complex which then undergoes oxidative addition to yield a Pt^{IV} intermediate and reductive elimination to yield methyl ester and Pt^{II}.¹⁴⁵ Platinum has shown to be a good candidate for dioxygen activation, thus many efforts been made in trapping Pt-oxygen adducts potentially relevant to C–H bonds functionalization. Sharp has reported the isolation of a platinaoxoethane from the reaction of a trinuclear bridging Pt-dioxo complex and ethylene, highlighting the role of platinum in olefin oxidation.¹⁴⁶ Hambley reported the facile aerial oxidation of Pt^{II} complexes supported by a triazacyclononane ligand to yield a peroxo-bridged Pt^{IV} dimer (**59**, Figure 1.9)¹⁴⁷ Milstein reported a metastable Pt^{IV}=O species, [Pt^{IV}(O)(PCN)]⁺ (**2**), formed by reaction of a low-valent precursor with dioxirane.⁸⁸ Complex **2** showed a diverse reactivity: inter- and intramolecular OAT with CO or phosphines or with the phosphorus donor in the ligand, hydride attack to yield the corresponding Pt^{II}–OH complex and water splitting to yield a Pt^{IV}–(OH)₂ complex.⁸⁸ Britovsek reported the reaction of dioxygen at rt and in ambient light with [Pt^{II}(CH₃)(^{(NH₂)₂terpy)]⁺ to yield [Pt^{II}(OOCH₃)(^{(NH₂)₂terpy)]⁺ (**60**, Figure 1.9).¹⁴⁸ Complex **60** was stable for days at -20 °C in the absence of light, whereas further exposure to ambient light yielded the corresponding Pt^{II}–OH and formaldehyde.¹⁴⁸ The postulated mechanism of self-decay involves the formation of a transient Pt^{IV}=O(OMe) after heterolytic scission of a side-on alkylperoxo intermediate.¹⁴⁸}}

Goldberg reported a similar ambient light-promoted dioxygen insertion reaction with the complex [Pt^{IV}(H)(CH₃)₂(Tp^{Me₂})] to yield [Pt^{IV}(OOH)(CH₃)₂(Tp^{Me₂})] (**61**, Figure 1.9) which then yields the corresponding Pt^{IV}–OH upon thermolysis or OAT to phosphines.¹⁴⁹ The addition of radical initiators increased the yield of **61** in the dark, suggesting a radical pathway via formation of a transient Pt^{IV}–superoxo adduct which then performs HAT on another equivalent

of starting complex to yield **61**.¹⁴⁹ A similar Pt^{III}-superoxo intermediate was postulated by Puddephatt and co-workers in the light-driven dioxygen insertion into a Pt^{IV}-allyl complex yielding a peroxide-bridged Pt^{IV}dimer, [Pt(μ -O₂)(Br)(^{Me}Ph)₂(bipy)]₂ (**62**).¹⁵⁰ Recently, Connick reported the synthesis and full spectroscopic characterization of two [Pt^{IV}(X)₃(terpy)]⁺ (X = Cl, Br) (**63**, **64**, Figure 1.9) complexes by oxidative addition of molecular halides to the low-valent precursors, although their reactivity was not explored.¹⁵⁰

1.1.4.4.2 Palladium

Palladium has been widely employed in cross-coupling reactions for the formation of novel C–C bonds, but its role in hydrocarbon oxidation through metal-centred dioxygen activation is expanding. In 1991 Sen reported the oxidation of methane in the presence of Pd^{II} complexes and peroxytrifluoroacetic acid at 90 °C to yield a methyl ester.¹⁵¹ Van Koten reported the reaction of a low-valent cyclopalladated complex with TBHP to yield the mono- and di-oxygen insertion products, postulating the involvement of a transient Pd^{IV}=O intermediate.^{152, 153} A similar oxygen insertion reaction has been observed by Bandyopadhyay for a Pd^{II} complex supported by a CNS pincer ligand.¹⁵⁴ When PhIO together with a Fe^{III}-porphyrin complex was used as the oxidant, selective oxidation of the thioether functionalization in the ligand was achieved, whereas when TBHP or PhIO only were used insertion into the Pd–C bond was observed, yielding a Pd^{II}-phenolate complex.¹⁵⁴

Goldberg reported dioxygen insertion into a Pd^{II}-CH₃ bond to yield [Pd^{II}(OOCH₃)(CH₃)(bipy)] (**65**, Figure 1.9) at rt.¹⁵⁵ Presence of light or a radical initiator such as AIBN increased the yield of **65**. This observation and more extensive mechanistic studies led the authors to formulate the hypothesis of formation of a five-coordinate Pd^{III} intermediate and the generation of methyl radicals by homolysis.¹⁵⁵ In a later work the same group reported the first dioxygen insertion into a Pd^{II}-H bond to yield the structurally characterized [Pd^{II}(OOH)(PCP)] (**66**) and [Pd^{II}(OH)(PCP)].¹⁵⁶ Stahl reported the reaction of a NHC-Pd⁰ complex with dioxygen at -78 °C and, more slowly, at rt, to yield a side-on Pd^{II}-peroxo complex (**67**) and, upon protonation by acetic acid, a Pd^{II}-hydroperoxo complex.¹⁵⁷

1.1.4.4.3 Iridium

In 1983 Graham reported that cyclopentadienyl (Cp) or pentamethylcyclopentadienyl (Cp^{*}) iridium-carbonyl complexes were able to activate methane by yielding Ir-(H)(CH₃) complexes.

¹⁵⁸ Wilkinson reported the synthesis and structural characterization of a $[\text{Ir}^{\text{V}}(\text{O})(\text{Mes})_3]$ complex (**68**, Figure 1.10),¹⁵⁹ which showed only OAT reactivity with arylphosphines and arsines.¹⁶⁰ In 2010, Crabtree reported that $[\text{Ir}^{\text{III}}(\text{Cl})(\text{Cp}^*)(\text{NC})]$ was shown to hydroxylate alkanes in the presence of CAN and water as a source of oxygen. The postulate oxidant was $[\text{Ir}^{\text{V}}(\text{O})(\text{Cp}^*)(\text{NC})]^+$ and most of the hydroxylations occurred with retention of stereochemistry.¹⁶¹ Complex $[\text{Ir}^{\text{III}}(\text{Cl})(\text{Cp}^*)(\text{NC})]$ and similar $\text{Ir}^{\text{III}}\text{-Cp}^*$ complexes have shown to catalyze water oxidation in presence of CAN as an external oxidant.¹⁶² Recently, a terminal d^6 oxo complex, $[\text{Ir}^{\text{III}}(\text{O})(\text{PNP})]$ (**69**, Figure 1.9) was reported.¹⁶³ This complex could be synthesized both by deprotonation of the corresponding hydroxide or by HAT from the $[\text{Ir}^{\text{II}}(\text{OH})(\text{PNP})]$ with tris-*tert*-butylphenol.¹⁶³ Computational studies supported the hypothesis of a $S = 1$ ground state for complex **69**, which showed OAT reactivity towards phosphines and CO and nucleophilic reactivity towards CO_2 .¹⁶³

1.1.4.4.4 Rhodium

Caulton reported a $[\text{Rh}^{\text{III}}(\text{H})(\text{PNP}^*)]$ complex which reacted with N_2O to yield equimolar $[\text{Rh}^{\text{III}}(\text{OH})(\text{PNP}^*)]$, which is the product of intermolecular HAT performed by an intermediate on a methyl group of the ligand, and $[\text{Rh}^{\text{III}}(\text{N}_2)(\text{PNP}^*)]$.¹⁶⁴ The intermediate was postulated to be $[\text{Rh}^{\text{III}}(\text{O})(\text{PNP}^*)]$ (**70**, Figure 1.9), which was characterized by NMR at -60°C and was predicted by DFT to have an oxyl radical character, explaining its capability in performing HAT.¹⁶⁴ A few stable side-on $\text{Rh}^{\text{III}}\text{-(O)}_2$ complexes have been reported, mostly supported by NHC carbenes and obtained by exposure to oxygen of Rh^{I} precursors.¹⁶⁵ Shul'pin reported a hexanuclear Rh cluster that was capable of catalysing benzene hydroxylation in presence of H_2O_2 with up to 17% total yield of phenol.¹⁶⁶ A mechanism involving the formation of a Rh-hydroperoxide species was proposed for this reaction.¹⁶⁶ Recently, the photochemical generation of $\text{Rh}^{\text{III}}\text{-superoxide}$ complexes was reported: starting from a solution of $[\text{Rh}^{\text{III}}(\text{NH}_3)_5(\text{NO}_2)]^{2+}$ irradiation caused a colour change to intense blue which was attributed to the formation of the binuclear $[\text{Rh}_2^{\text{III}}(\text{O}_2)(\text{NH}_3)_9(\text{NO}_2)]^{4+}$, as determined by EPR and UV-Vis analysis.¹⁶⁷

1.1.4.4.5 Osmium

OsO_4 has been employed as oxidant in various classes of reactions, one of the most known being Sharpless asymmetric dihydroxylation of alkenes.¹⁶⁸

OsO₄ was capable of oxidising methane to yield a small amount of methanol at 50 °C in aqueous solution in the presence of NaIO₄. Neither OsO₄ nor NaIO₄ alone yielded the same result thus the authors proposed that the active oxidant is achieved by combination of the two species.¹⁶⁹ The nitridoosmate anion [Os^{VIII}(N)(O₃)]⁻ was able to perform stoichiometric and catalytic oxidation of alkanes at room temperature upon activation by FeCl₃.¹⁷⁰ This system allowed cyclohexane to be oxidised to cyclohexanol, cyclohexanone and chlorocyclohexane with a ratio of 0.7:0.2:0.06 respectively. The active oxidants were proposed to be osmium oxo species forming adducts with Lewis acidic Fe^{III}, which should increase their electrophilic character.¹⁷⁰

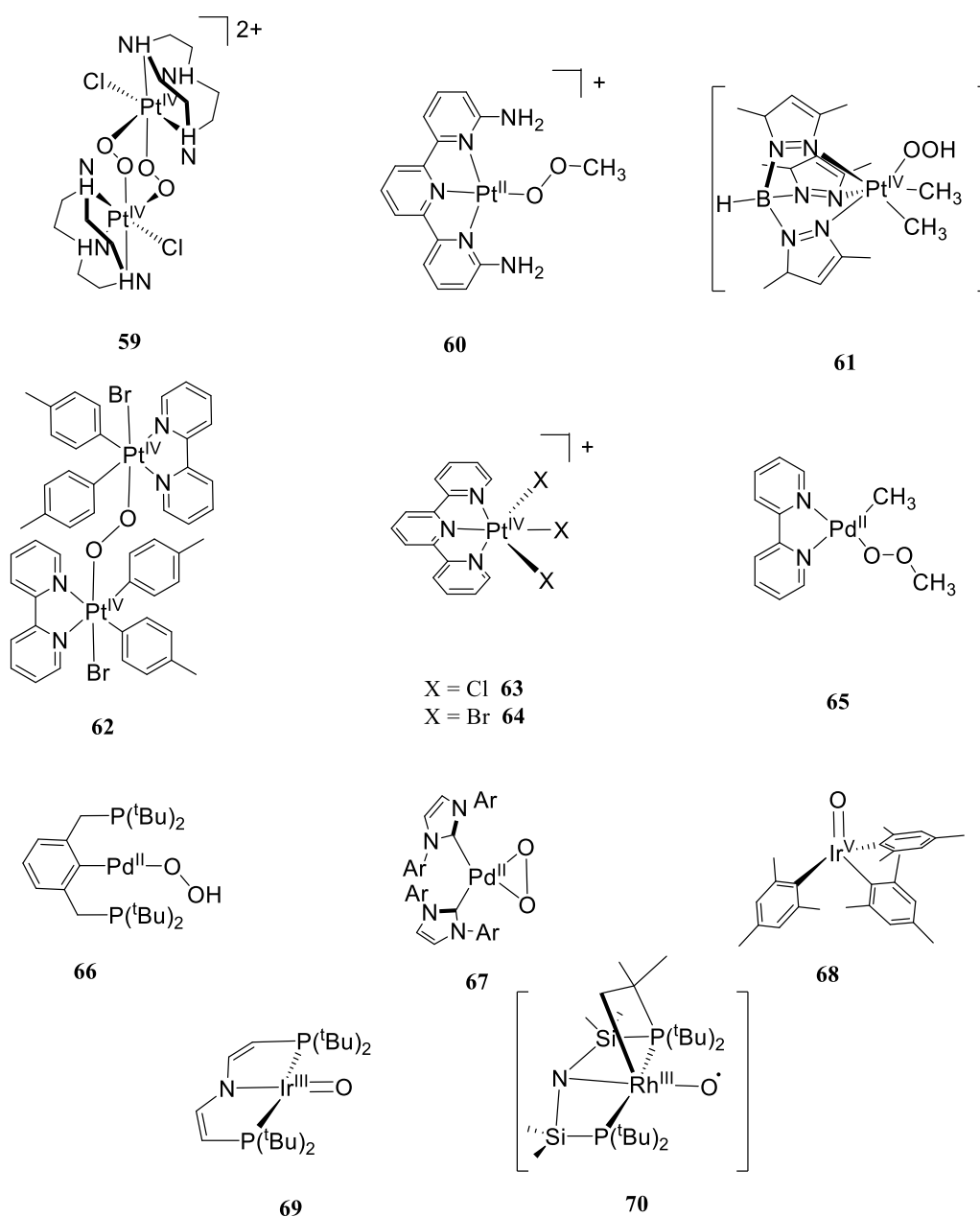


Figure 1.9. Selected synthetic complexes or intermediates relevant to dioxygen and hydrocarbons activation by Pt, Pd, Rh and Ir.

1.1.5 Gold in oxidation catalysis

For decades, gold was considered an inert metal with no catalytic activity (in old literature was referred to as “catalytically dead”).¹⁷¹ Gold is a unique metal due to its exceptional resistance to corrosion and oxidation, therefore has gained its fame as a noble metal and has been employed in coinage and jewelry for centuries.¹⁷² Gold has the highest electronegativity among the *d* block (2.4), in fact the auride ion exists as CsAu, a feature not observed for any other transition metal. Gold only dissolves in aqua regia and does not form oxides or sulfides as most other transition metals.¹⁷²

In 1973 the efficient hydrogenation of alkenes over supported gold catalysts was reported by Bond and co-workers, opening a new horizon of possibilities for gold as a catalyst.¹⁷³ In the 80s, Haruta reported that nanoparticles of gold deposited on semiconducting transition metal oxides were capable of oxidising CO even at low temperature and, almost simultaneously, Hutchings reported that the Au³⁺ cation catalysed the hydrochlorination of acetylene.¹⁷⁴ These two key discoveries opened the perspective of gold as a key player both in heterogeneous and homogeneous catalysis.

Further support to this hypothesis was added in the following years in which Au^I complexes were discovered to catalyse asymmetric aldol condensation,¹⁷⁵ then both Au^{III}¹⁷⁶ and Au^I species¹⁷⁷ catalysed the addition of alcohols to alkynes. Further historical breakthroughs in gold oxidation catalysis were the regioselective oxidation of alcohols with molecular oxygen¹⁷⁸ and the addition of alcohols and arenes to alkenes.¹⁷⁹ In 2002 Hutchings and co-workers reported the direct synthesis of hydrogen peroxide from molecular hydrogen and oxygen at 2 °C over gold supported on alumina.¹⁸⁰ The same group reported that a system based on 1% nanocrystalline Au supported on carbon effectively oxidised cyclohexene and *cis*-cyclooctene using atmospheric oxygen.¹⁸¹ These discoveries turned on the growing attention for research on gold oxidative catalysis, which became a hot topic since the early years 2000 and still focus much attention in current times, both in the heterogeneous and homogeneous fields.¹⁸²

1.1.5.1 Heterogeneous gold oxidation catalysis

The predominant field for gold oxidation catalysis is heterogeneous catalysis, while the homogeneous one is still growing.¹⁷¹ The employed heterogeneous gold catalysts normally consist of gold nanoparticles supported on a metal oxide substrate. Despite the well-established catalytic role of gold in these reactions, the nature of the active species is still debated.¹⁸³

Two key reactions for which gold is a very effective heterogeneous catalyst are low temperature CO oxidation and alcohol oxidation to acids.^{183, 184} Au oxidised CO to CO₂ in presence of dioxygen at temperatures low as 203 K, interestingly showing a rate dependence only from the gold particle size and not from the partial pressures of CO or O₂. This reaction has been investigated both in the gas phase and condensed phase, showing similar rates of reactivity in both phases over Au nanoparticles. In gas phase, the presence of water vapour increased the turnover frequency (TOF) of one order of magnitude, whereas in condensed phase the addition of base to increase of the water pH to 13 showed a 5-fold reaction rate increase compared to the neutral solution.¹⁸⁴ This observation lead to the hypothesis of the presence of hydroxyl groups on the gold surface and their role in enhancing the oxidation reaction. Kung and co-workers proposed a mechanism in which hydroxyl groups are present on the surface of cationic gold particles so they could perform nucleophilic addition on CO molecules adsorbed on the gold atom in close proximity (Figure 1.10).¹⁸⁵ This leads to the formation of an hydroxycarbonyl group on the gold surface, which in aerobic atmosphere is oxidised to a bicarbonate, which then decomposes to CO₂ and Au–OH species, restoring the postulated active species.¹⁸⁶ The nature of the active hydroxide species and the oxidation state of the gold have been supported by both *in situ* XAS studies and isotopic labelling experiments.

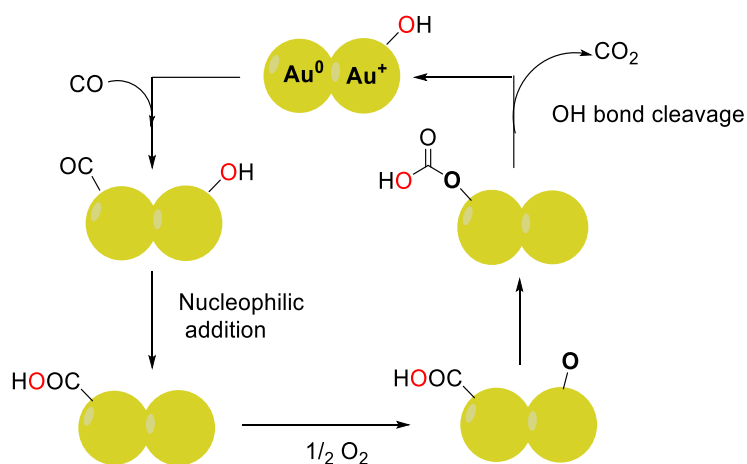


Figure 1.10. Proposed reaction mechanism for CO oxidation over heterogeneous cationic gold species.

Another oxidative reaction in which the role of Au–OH species has been postulated to be crucial is the oxidation of alcohols to acids in the condensed phase. Gold nanoparticles supported on carbon or alumina were excellent catalysts for this reaction at temperatures < 373 K under basic conditions, whereas their activity was almost zero in neutral or acidic conditions.¹⁸⁷ The most widely accepted mechanism entails the attack of the hydroxide on the alcohol adsorbed on the gold surface to yield a metal hydride which is proposed to reduce the atmospheric oxygen (Figure 1.11).^{187, 188} This step yields a hydroperoxide species which then furtherly oxidise the tetrahedral intermediate obtained from the alcohol to yield a carboxylic acid and hydrogen peroxide as by-product (Figure 1.11).^{187, 188} Therefore adsorbed hydroxyl groups on gold surface seem to play a key role in both these key catalytic transformations.¹⁸⁴

Another transformation for which heterogeneous gold catalysts are effective is the aerobic oxidation of propene.¹⁸⁹ This is a crucial process at industrial level since it gives access to propene oxide which is a building block for the synthesis of polyols, polyurethane and propene glycol. Selectivity is an issue for this reaction since multiple products can be obtained: acrolein, acetone, ethanal, propanal and propene oxide. The highest selectivity for this process (> 90% for propene oxide) has been observed for gold particles supported on TiO₂ or TiO₂/SiO₂, with the active oxidant species proposed to be hydrogen peroxide-like but evidences for this and a proposed reaction mechanism are still lacking.¹⁸⁹ Due to the localized surface plasmon resonance effects, gold nanoparticles can also be used as photocatalysts, with application in several catalytic transformations.¹⁹⁰

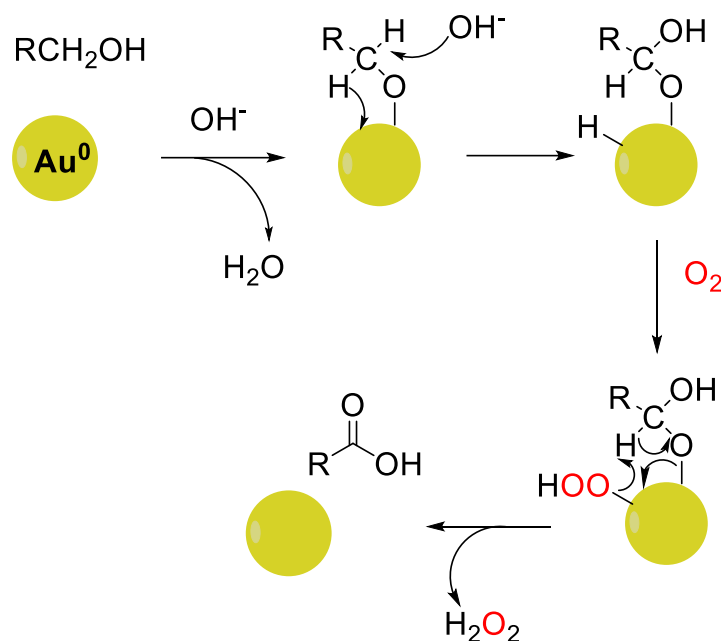


Figure 1.11. Proposed mechanism for the liquid phase oxidation of alcohols over heterogeneous gold catalysts in basic conditions.

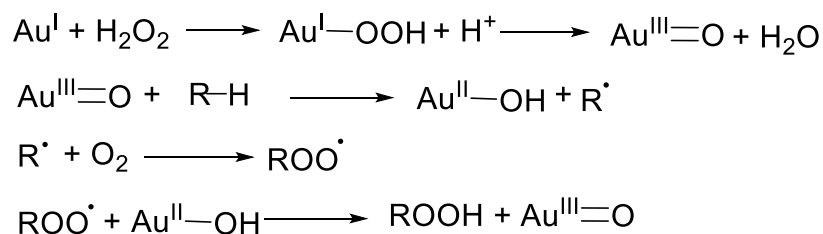
1.1.5.2 Homogeneous gold oxidation catalysis

Compared to heterogeneous catalysis, homogeneous catalysis by gold is still an emerging field. This is partly related to the fact that many metal catalysed transformations rely on the oxidative addition/reductive elimination cycle, and this is difficult to do due to the high redox potential of the $\text{Au}^{\text{I}}/\text{Au}^{\text{III}}$ couple ($E^\circ = 1.41 \text{ V}$).¹⁹¹ In 1935, both AuCl and AuCl_3 were reported to catalyse the chlorination of naphthalene in presence of chlorine gas.¹⁷¹ Since the 80s gold salts and complexes have been explored for a plethora of oxidation reactions, such as the selective oxidation of thioethers to sulfoxides, the synthesis of isoxazoles from alkynes, the oxidative carbonylation of amines, oxidation of ketones, alkanes and new C–C bond formation.¹⁷¹

Generally speaking, Au^{I} is a soft cation particularly suitable for activation of C–C π bonds in alkenes, alkynes and allenes, its complexes are stabilized by ligands bearing S, C or P-donors and are often used as a starting catalysts in gold-catalyzed homocouplings and cross-couplings.¹⁹⁰ On the other hand, Au^{III} is a hard Lewis acid which shows preference for oxygen and nitrogen donors, but for these complexes less applications have been investigated due to their easy reduction to nanoparticles and the strong oxidative conditions required for their synthesis.¹⁹⁰

So far all the homogeneous gold catalysts, either gold salts or discrete complexes, that have been reported were proposed to react via multi-step mechanisms with no clear identification of the intermediates involved in the single steps.¹⁹² In 2001 Shilov reported that Au^I and Au^{III} complexes, notably NaAuCl₄ and Au(Cl)(PPh₃) catalysed the oxidation of alkanes by hydrogen peroxide in acetonitrile solution at 75 °C.¹⁹³ The alkanes explored were heptane, 3-methylhexane, 2,4,4-trimethylpentane and methylcyclohexane and multiple products of oxidation (hydroperoxides, hydroxides and ketones) were obtained in all cases, but with much higher selectivities with respect to those observed for the reaction initiated by OH[•].¹⁹³

The mechanism proposed for this reaction thus involves the formation of a terminal Au^{III}=O species, which is still elusive, via heterolytic bond scission of a Au^I-OOH species (Scheme 1.4). Then the electrophilic Au^{III}=O abstracts a hydrogen atom from the alkane molecule to yield a carbon-based radical and Au^{II}-OH. The carbon-based radical can then react furtherly with dioxygen to yield a hydroperoxyl radical which is either capable of abstracting a hydrogen atom from the substrate, restoring the active high-valent oxidant and closing the cycle (Scheme 1.4), or to undergo radical rebound with the gold-hydroxide species or lead to other oxygenated products via decay of the alkyl hydroperoxide product.¹⁹³ These result and this proposed mechanism, despite its lack of experimental evidence, shed a light on the role of metal-oxygen intermediates in gold catalysis, which will be further explored in the next paragraphs.



Scheme 1.4. Mechanism proposed by Shilov et al. for the oxidation of alkanes in solution in presence of Au^I/Au^{III} catalysts.¹⁹³

Corma and co-workers showed that a Au^{III} complex supported by a chiral oxazoline ligand performed oxidation of alkenes in the presence of PhIO or NaOCl both in aerobic and anaerobic conditions, with a dramatic rate enhancement in the presence of oxygen.¹⁹⁴ Terminal Au^{III}=O or Au^{III}(OH)(OO[•]) species were proposed as postulated active oxidants but with no proof for their formation.¹⁹⁴

Another interesting example of gold-mediated hydrocarbon activation from Shilov and co-workers showed that a goldphilic bacterium, *Micrococcus luteus*, known to accumulate gold from the environment, activated methane oxidation in solution in aerobic conditions, yielding

to ~50% of methanol among the products.¹⁹⁵ Gold demonstrated to be essential for this transformation to occur, in fact when the protein was incubated without Au no change in the methane concentration was observed by chromatography.¹⁹⁵ No mechanistic proofs were reported for this system.

1.1.5.2.1 Gold(III)-oxygen adducts

1.1.5.2.1.1 Gold(III)-hydroxide complexes

In the strive to understand the involvement and the mechanism of oxygen activation by gold, terminal Au^{III}=O species, which are often regarded as the key oxidant species in the proposed mechanisms,^{193, 194, 196, 197} still remain elusive, precluding any insight into their reactivity. Given the expected high basicity of such a reactive intermediate, its protonation might be favoured to yield Au^{III}-OH species. Nevertheless, there are still few examples of stable discrete Au^{III}-OH complexes in literature.

Pitteri reported in 1999 the first crystal structure of a mononuclear gold hydroxide complex, [Au^{III}(OH)(terpy)](ClO₄)₂ (**71**, Figure 1.12).¹⁹⁸ The complex was obtained by treatment of the chloride precursor, [Au^{III}(Cl)(terpy)](ClO₄)₂, with AgClO₄ in hot water. The authors proposed that removal of the chloride ligand as AgCl leads to the formation of a Au^{III}-(H₂O) complex, which is unstable due to the high charge of the metal centre thus behaves as a strong acid ($K_a \geq 0.8$ M) to yield **71**. An analysis of the crystal packing showed that, conversely to what observed for square planar *d*⁸ complexes containing Pd^{II} or Pt^{II} which form metal-metal interacting dimers or chains, complex **71** crystallizes as monomers with two counterions in the secondary coordination sphere.

In 2014 Dutton reported the synthesis of the same complex with triflate counterions, [Au^{III}(OH)(terpy)](OTf)₂ (**72**, Figure 1.12), obtained starting from the tricationic [Au^{III}(^{CN}pyr)₂(^{Me2N}pyr)₂](OTf)₃.¹⁹⁹ This highly reactive precursor was reacted with terpyridine to yield the isolable [Au^{III}(terpy)(^{Me2N}pyr)](OTf)₃, which was then stirred in acetonitrile spiked with H₂O to yield **72**. This suggested that the supporting pyridine ancillary ligand is easily displaced by water and then the acidic Au^{III}-(H₂O) complex dissociates to yield **72**. When the same reaction was performed starting from [Au^{III}(^{Me2N}pyr)₂(pyr)₂]³⁺, an oxo-bridged dimer was isolated, which was postulated to derive from the condensation of two mononuclear hydroxide complexes.¹⁹⁹

Nevado recently reported the synthesis of the cyclometallated $[\text{Au}^{\text{III}}(\text{OH})(^t\text{BuMeNCC})]$ (**73**, Figure 1.12) from the corresponding chloride complex by addition of KOH in a mixture of THF/H₂O at 25 °C.²⁰⁰ The complex was used as starting material to attempt the isolation of a gold-carboxylate by CO insertion without success. This was achieved by starting from a more reactive $[\text{Au}^{\text{III}}(\text{OTMS})(^t\text{BuMeNCC})]$ to yield a carboxylate-bridged dimer, which was then subsequently treated with BnMe₃NOH to afford a mixture of **73** and the terminal carboxylate complex $[\text{Au}^{\text{III}}(\text{COOH})(^t\text{BuMeNCC})]$ at -30 °C.²⁰⁰ A bis- μ -hydroxide complex bearing carbon donors, $[\text{Au}_2^{\text{III}}(\text{OH})_2(\text{NO}_2\text{Ph})_4]$ (**74**, Figure 1.12) was obtained serendipitously by reaction of $[\text{Au}^{\text{III}}(\text{OPh})_2(\text{NO}_2\text{Ph})_2]$ with adventitious water and crystallographically characterized.²⁰¹ No reactivity was explored for this species.

In 2012 Bochmann reported that the stable cyclometallated complex $[\text{Au}^{\text{III}}(\text{OH})(^t\text{BuCNC})]$ (**75**, Figure 1.12) was a versatile synthon to access complexes with different ancillary ligands²⁰² and trapping normally fleeting intermediates such as gold hydroperoxides or peroxides.¹⁹⁷ **75** was obtained directly by reaction of $[\text{Au}^{\text{III}}(\text{Cl})(^t\text{BuCNC})]$ with CsOH in a mixture of THF/toluene and H₂O or indirectly from the reaction with KOH with a $[\text{Au}^{\text{III}}(\text{OTf})(^t\text{BuCNC})]$ intermediate.²⁰² XRD showed that **75** adopts a square planar geometry in the solid state and crystallizes as a monomer, as observed for **71**. The complex reacted as a base yielding acetylide, amido, aryl, heteroaryl and alkyl complexes in mild conditions. In a subsequent work **75** was reacted with TBHP to yield the peroxide complex $[\text{Au}^{\text{III}}(\text{OO}^t\text{Bu})(^t\text{BuCNC})]$, whereas when reacted with hydrogen peroxide yielded the hydroperoxo complex $[\text{Au}^{\text{III}}(\text{OOH})(^t\text{BuCNC})]$, which over time transformed into the corresponding bridging μ -peroxo dimer. This transformation was shown to be reversible by adding water. **75** showed a similar condensation reaction over time to give a μ -oxo dimer, which was reversed to yield **75** upon exposure to moisture. All these complexes have been structurally and spectroscopically characterized and performed OAT reactivity with $\text{P}(\text{MePh})_3$: quantitative formation of $\text{O}=\text{P}(\text{MePh})_3$ was observed by ³¹P-NMR. Unexpectedly, not only this reactivity was observed also with **75** but in that case the major gold product (95%) was a rare $[\text{Au}^{\text{III}}(\text{H})(^t\text{BuCNC})]$. A KIE = 1.45 was measured by performing the OAT reaction with $[\text{Au}^{\text{III}}(\text{OD})(^t\text{BuCNC})]$ (**75D**). The reaction rate was not influenced by the presence of radicals, whereas Hammett analysis showed a negative ρ (-1.05), suggesting that positive charge is built on the reaction centre.

Cinellu and co-workers reported the synthesis of gold hydroxide and dihydroxide complexes, either supported by bipyridine ligands such as $[\text{Au}^{\text{III}}(\text{OH})_2(\text{bipy})]^+$ (**76**, Figure 1.12) or $[\text{Au}^{\text{III}}(\text{OH})(\text{Cl})(\text{bipy})]^+$ (**77**, Figure 1.12),²⁰³ either by a cyclometallated derivative $[\text{Au}^{\text{III}}(\text{OH})(\text{bipy}^{\text{C-H}})]$ (**78**, Figure 1.12).²⁰⁴ These complexes weren't structurally characterized but their electronic absorption spectra showed to be pH independent in aqueous solution, suggesting that Au-hydroxo species are predominant due to the acidity of the metal center.²⁰⁴ The chemical reactivity of complexes **76-78** was not investigated but **76** and **78** were cytotoxic *in vitro* towards cancer cell lines.²⁰⁴

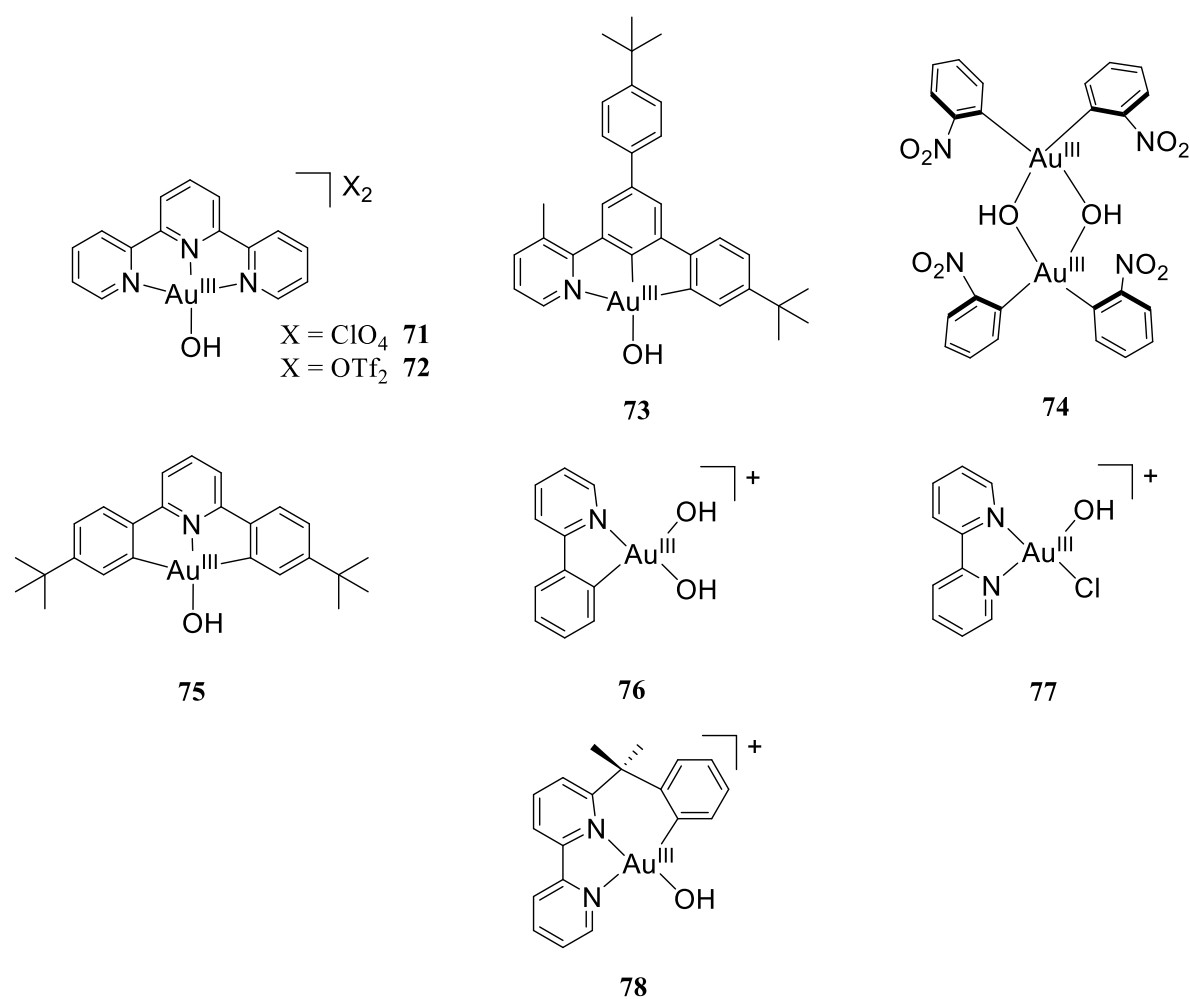


Figure 1.12. Au^{III} -hydroxide complexes.

1.1.5.2.1.2 Gold(III)-bis- μ -oxo complexes

Despite the lack of terminal $\text{Au}^{\text{III}}=\text{O}$ complexes in literature, few examples of Au_2^{III} -bis- μ -oxo complexes have been reported and characterized, even though with limited insights in their oxidative reactivity.

In 2005 Cinellu reported the oxidation of olefins by complexes $[\text{Au}_2^{\text{III}}(\mu\text{-O})_2(\text{bipy}^{\text{R}})_2](\text{PF}_6)_2$ ($\text{R} = \text{Me}, \text{CHMe}_2, \text{CH}_2\text{CMe}_3, 2,6\text{-Me}_2\text{Ph}$, **79-82**, Figure 1.13).¹⁹⁶ When the reaction was performed in presence of strained cyclic alkenes such as norbornene and 2,5-norbornadiene, an unprecedentedly reported auroxetane could be isolated and structurally characterized. This product was observed together with the Au^{I} -alkene complexes and the epoxidised or dihydroxylated organic products. The postulated pathway of formation of the auroxetane from an equivalent of **79-82** involves the formation of two equivalents of a mononuclear $\text{Au}^{\text{III}}=\text{O}$ -alkene adduct, which subsequently attacks the olefin to yield the metallaoxetane or, in presence of moisture, yields an $\text{Au}^{\text{III}}\text{-OH}$ intermediate bound to the hydroxylated alkane. This second species can interconvert in the oxetane by water removal. The addition of another equivalent of alkene to both intermediates is postulated to yield, respectively, the epoxide and the diol products.¹⁹⁶ The mononuclear oxo and hydroxo intermediates in this mechanism are only postulated, no experimental evidence has been observed for their formation. The same group reported the synthesis of the same complex with an unsubstituted pyridine ligand, $[\text{Au}_2^{\text{III}}(\mu\text{-O})_2(\text{bipy})_2](\text{PF}_6)_2$ (**83**, Figure 1.13)²⁰⁵ and another one supported by a substituted phenantroline ligand, $[\text{Au}_2^{\text{III}}(\mu\text{-O})_2(\text{phen}^{\text{Me}_2})_2](\text{PF}_6)_2$ (**84**, Figure 1.13).²⁰⁴ The latter had cytotoxic and antiproliferative activity.²⁰⁴

Lee reported the synthesis of $[\text{Au}_2^{\text{III}}(\mu\text{-O})_2(6^{\text{Me}}\text{bipy})_2](\text{ClO}_4)_2$ (**85**, Figure 1.13) from a hot aqueous solution of the chloride precursor in presence of NaClO_4 .²⁰⁶ This complex was explored as homogeneous catalyst for the intramolecular alkyne hydroamination reaction, together with complexes **79**, **83** and **84** and other mononuclear $\text{Au}^{\text{III}}\text{-Cl}$ complexes and simple gold salts. The bis- μ -oxo complexes enabled higher yields of the desired cyclized products (55-70%) compared to the other catalysts.²⁰⁶ This suggests that Au_2^{III} -bis- μ -oxo complexes might be precursors for unexplored active species in homogeneous catalysis.

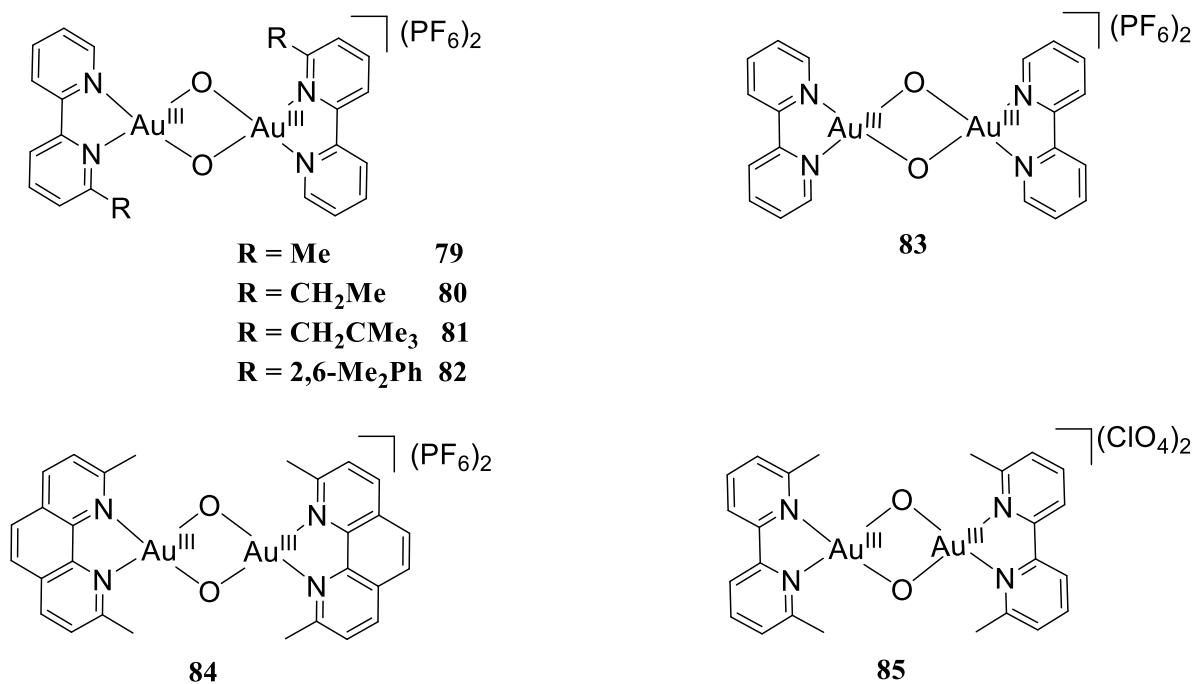


Figure 1.13. Au^{III}-bis-μ-oxo complexes.

1.1.5.2.2 Gold(III)-halide complexes

In 1989 Schwerdtfeger performed some theoretical calculations which proved that the high thermodynamic stability of [Au^{III}-X₄]⁻ (X = Cl, Br, F, I) compared to Au^I-halide complexes has to be ascribed to relativistic effects.²⁰⁷ Au^{III} has a tendency to form tetracoordinate adducts and, in case of halide complexes, the formation of halogen-bridged dimers or oligomers is common.²⁰⁷ Au₂Cl₆ is one among the most known Au^{III} salts, dissolved in HCl provides the [AuCl₄]⁻ anion which is a convenient starting point for the synthesis of many gold complexes.²⁰⁸ By treatment with fluorine gas or BrF₃, AuF₃ can be obtained, which behaves as a strong fluorinating agent.²⁰⁸

Au^{III}-Cl complexes are often employed as starting synthons to prepare high-valent gold complexes bearing different ancillary ligands: chloride removal is often achieved by halide exchange with silver salts.^{198, 202}

In medicinal chemistry, Au^{III}-Cl complexes are often evaluated as drugs for their antiproliferative and cytotoxic properties and one important parameter to evaluate is their stability in physiological conditions since they are prone to hydrolysis to yield the corresponding hydroxides in water solution at pH > 2.²⁰⁹ Several strategies have been

investigated to improve Au^{III}-Cl complexes stability towards both hydrolysis and reduction to Au^I or Au⁰, from using pincer ligands to cyclometallated ligands. The latter have proved to greatly enhance the stability of complexes towards reduction but not towards hydrolysis of the labile chloride ligands.²⁰⁹ Discrete Au^{III}-F complexes, supported either by pincer or cyclometallated ligands, are still quite rare but their chemistry has recently gained more interest due to their possible application in the synthesis of fluorinated organic compounds.²¹⁰

1.1.5.2.2.1 Gold(III)-chloride and bromide complexes

Among Au^{III}-Cl complexes, a distinction should be made between those supported by pincer ligands containing N-donors, those supported by anionic ligands and those supported by cyclometallating ligands.

1.1.5.2.2.1.1 Neutral N-donors

Lippard reported in 1982 the synthesis and crystallographic characterization of the square planar complex [Au^{III}(Cl)(terpy)](Cl)₂·3H₂O (**87**, Figure 1.14) from the reaction of HAuCl₄ with 2,2',2''-terpyridine (terpy) in aqueous solution.²¹¹ Control of the pH demonstrated to be crucial to achieve the desired product: the best yield of **87** was obtained with a pH between 3 and 5, whereas insoluble tetrachloroaurate salts were obtained with pH < 2.5 and metallic gold was the sole product when pH > 6.²¹¹ The same structural unit was reported with different counterions, as [Au^{III}(Cl)(terpy)](ClO₄)₂ (**88**, Figure 1.14)¹⁹⁸ and [Au^{III}(Cl)(terpy)](PF₆)₂ (**89**, Figure 1.14),²¹² but only the latter has been structurally characterized. In presence of silver perchlorate in aqueous solution complex **88** yielded the corresponding hydroxide **71** (discussed in section 1.1.5.2.1.1). Au^{III}-Cl complexes supported by phenantroline ligands with different counterions, [Au^{III}(Cl)₂(phen^R)](X) (X = Cl, ClO₄, PF₆, AuCl₂ and R = H, Me, **90-94**, Figure 1.14) were first reported in the 50s (**90**)²¹³ but structurally and biologically characterized only recently.^{204, 214-216} Similarly, [Au^{III}(Cl)(dien)]²⁺ (**95**, Figure 1.14) was crystallized in 1980²¹⁷ but its physiological stability and anticancer activity was first investigated in 2000.²¹⁵ The synthesis of the dipeptide-supported complex [Au^{III}(Cl)(gly-Lhis)]⁺ (**96**, Figure 1.14) and its crystal structure has been reported in 1992, but its cytotoxic and DNA binding properties were explored only in 2000.²¹⁸

1.1.5.2.2.1.2 Anionic donors

Complex **96** is unusual due to the presence of a pincer ligand containing an anionic donor, a feature that has been less explored in combination with Au^{III} respect to other transition metal cations.²¹⁹ Hashmi reported three dichlorido complexes supported by picolate ligands, [Au^{III}(Cl)₂(^{N,O}pic^R)] (R = H, 4-COOH, 3-OH, **97-99**, Figure 1.14) which showed to be better catalysts for the synthesis of phenols than the widely used AuCl₃.²²⁰ Toste reported the synthesis and characterization of gold-halide complexes supported by N, O and S anionic donors: [Au^{III}(Cl)(pyO₂)] (**100**, Figure 1.14), [Au^{III}(Cl)(^RpyN₂)] (R = iPr, Mes; **101-102**, Figure 1.14) and [Au^{III}(X)(^{N2}pyS₂)] (X = Cl, Br; **103-104**, Figure 1.14).²¹⁹ Complex **100** was prepared in low-yield (9%) from the reaction of 2,6-pyridindicarboxylic acid with KAuCl₄ in presence of Ag₂CO₃, whereas **101-104** were synthesized from the reaction of the potassium salts of the ligands with KAuCl₄ or KAuBr₄.²¹⁹ Electrochemical measurements showed that anionic N or S donors stabilized more the Au^{III} cation with respect to anionic O donors.²¹⁹ Complexes **100-104** showed no reactivity with electrophiles or acids.²¹⁹

Another class of complexes that has been widely investigated for medicinal purposes is the one of Au^{III}-dithiocarbamate complexes, such as the halide-containing [Au^{III}(Cl)₂(DMDT)] (**105**, Figure 1.14) and [Au^{III}(Br)₂(DMDT)] (**106**, Figure 1.14).²²¹ Electrochemical studies on these complexes showed three irreversible reduction waves, which the authors ascribed respectively to the Au^{III}/Au^{II}, the formation of a mixed valent Au^{II}-Au^I species and the full reduction to Au^I. Given the known instability of Au^{II} monomers, the authors postulated the formation of a halide-bridging Au^{II} dimer.²²¹

1.1.5.2.2.1.3 Cyclometallating ligands

The most investigated class of Au^{III} complexes to date is the one of cycloaurated complexes. Several mono or bi-cyclometallating ligand platforms have been used to prepare Au^{III}-X complexes and intermediates, due to the stability towards reduction inferred by these ligands. Given the wealth of examples of this class of Au^{III}-X complexes, just some representatives examples for each class will be reported.²²²

Among C^N gold complexes, the (2-((dimethylamino)methyl)phenyl) ligand was employed to prepare [Au^{III}(Cl)₂(dmamp)] (**107**, Figure 1.15) and [Au^{III}(Br)₂(dmamp)] (**108**, Figure 1.15), which have antiproliferative activity.²²³ Several variants of this ligand could be made, such as

replacing the N-donor with an oxazoline to yield $[\text{Au}^{\text{III}}(\text{Cl})_2(\text{oxap})]$ (**109**, Figure 1.15) and $[\text{Au}^{\text{III}}(\text{Br})_2(\text{oxap})]$ (**110**, Figure 1.15), and most of the complexes reported were obtained by transmetallation of the corresponding organomercury complex with an XAuCl_4 salt.²²³ Casini and co-workers reported the synthesis of biologically active complexes containing 2-benzylpyridine, starting from the precursor $[\text{Au}^{\text{III}}(\text{Cl})_2(\text{py}^{\text{b}}-\text{H})]$ (**111**, Figure 1.15)²²⁴ and substituting one of the chloride ligands with 1,3,5-triazaphosphaadamantane or thioglucose.²²⁵

The more rigid 2-phenylpyridine ligand was used to prepare complexes with different substituents starting from the precursor $[\text{Au}^{\text{III}}(\text{Cl})_2(\text{ppy})]$ (**112**, Figure 1.15).²²⁶ This complex was a good catalyst for the activation of alkynes in presence of amines and aldehydes to yield propargylamines with high stereoselectivities (99:1) when starting from chiral precursors.²²⁷ You and co-workers have employed complexes $[\text{Au}^{\text{III}}(\text{Cl})_2(\text{Meppy})]$ (**113**, Figure 1.15) and $[\text{Au}^{\text{III}}(\text{Br})_2(\text{Meppy})]$ (**114**, Figure 1.15) as catalyst for the oxidative cross-coupling between arenes and arylboronic acids.²²⁸ The independent isolation of the transmetallation intermediate $[\text{Au}^{\text{III}}(\text{Br})(\text{Ph})(\text{Meppy})]$ allowed the possibility to gain insights on the mechanism of the cross-coupling reaction, which is thought to proceed through gold-mediated C–H activation, transmetallation and reductive elimination. This example shows the potential interesting applications of cyclometallated $\text{Au}^{\text{III}}-\text{X}$ complexes in oxidative catalysis.

Another example of this class of compounds is supported by iminophosphorane ligands, first reported by Contel, such as $[\text{Au}^{\text{III}}(\text{Cl})_2(\text{PPh}_2\text{NPh})]$ (**115**, Figure 1.15), which have shown to undergo easily chloride displacement to yield other thiolate or phosphine-bound derivatives.²²⁹

The most investigated ligand motif for cycloaurated compounds is the C[^]N[^]C one.²²² 2,6-diphenylpyridine was adopted by Che to yield the precursor complex $[\text{Au}^{\text{III}}(\text{Cl})(\text{C}^{\wedge}\text{N}^{\wedge}\text{C})]$ (**116**, Figure 1.15) by transmetallation of the mercury complex. These complexes are highly stable and synthetically versatile, allow easy displacement of the chloride to yield N, S, P and alkynyl donors-containing complexes.²³⁰ Nevado pioneered the introduction of the N[^]C[^]C ligand class, synthesizing derivatives of $[\text{Au}^{\text{III}}(\text{Cl})(\text{R}^{\text{N}^{\wedge}\text{C}^{\wedge}\text{C}})]$ (**117**, Figure 1.15) by a facile two-step Au coordination and microwave-assisted cyclometallation.²³¹ Reaction of **117** and derivatives with AgF yielded the corresponding fluoride complexes by easy halide exchange at rt.²³¹ Among the cyclometallating ligands, N[^]C[^]N motifs have been less explored in combination with Au^{III} due to their difficult synthesis. For these complexes the most accessible synthetic method available requires the transmetallation with the organomercury complex of the chosen ligand.²²² Examples of complexes bearing ligands belonging to this class are $[\text{Au}^{\text{III}}(\text{Cl})(\text{Npy}^{\text{Me}}\text{p})]$ (**118**,

Figure 1.15), $[\text{Au}^{\text{III}}(\text{Cl})(^{\text{N}}\text{pyp})]$ (**119**, Figure 1.15)²³² and $[\text{Au}^{\text{III}}(\text{Cl})(^{\text{Hex}}\text{bim})]^+$ (**120**, Figure 1.15).²³³ For **119** removal of the chloride ancillary ligand was not achieved even in presence of silver salts, which instead allowed it with **118**.²³² Complexes containing C[^]C ligands are still rare but Mohr reported the preparation of $[\text{Au}^{\text{III}}(\text{Cl})(^{\text{tBu}}\text{bip})(\text{py})]$ (**121**, Figure 1.15) and derivatives by transmetallation with the organotin derivative and addition of a fourth ligand such as pyridine, carbene, selenourea or carbanions.²³⁴ Toste reported in 2015 the synthesis of the stable complex $[\text{Au}^{\text{III}}(\text{Cl})(\text{iPr})(\text{bip})]$ (**122**, Figure 1.15) by facile oxidative addition of biphenylene to $[\text{Au}^{\text{I}}(\text{iPr})(\text{Cl})]$.²³⁵ **122** was isolated and cristallographically characterized by ligand exchange with the reactive $\text{Au}^{\text{III}}\text{-H}_2\text{O}$ intermediate and exhibited catalytic activity in a range of conjugate additions of dienes and cycloadditions.²³⁵ The same complex and its derivatives showed to enable the enantioconvergent cycloisomerization and kinetic resolution of 1,5-enynes and in the migratory insertion of carbenes into Au–C bonds in a subsequent work.²³⁶ The last class is the one of C[^]N[^]N ligands, of which representatives examples are given by complexes $[\text{Au}^{\text{III}}(\text{Cl})(\text{dpp})]$ (**123**, Figure 1.15)²³⁷ and $[\text{Au}^{\text{III}}(\text{Cl})(\text{bipy}^{\text{C-H}})]$ (**124**, Figure 1.15)²²⁴. Chloride abstraction was achieved for **124** in presence of silver salts but not with phosphines, which coordinated to the gold cation replacing one of the ligand arms.²²⁴

In summary despite the abundance of $\text{Au}^{\text{III}}\text{-X}$ ($\text{X} = \text{Cl}, \text{Br}$) complexes in literature, these species have only been investigated for their biological relevance or as synthetic precursors to other gold complexes, whereas no investigation of their role in hydrocarbon oxidation has been reported so far. This is surprising given the rising interest observed in this field for similar high valent M-X complexes ($\text{M} = \text{Fe}, \text{Mn}, \text{Ni}, \text{Cu}, \text{X} = \text{Cl}, \text{Br}$, see 1.1.4.3), which demonstrated their thermodynamic and kinetic competency in yielding oxidised and halogenated products when reacted with inter hydrocarbon substrates. Given the promising results obtained in the solution studies performed by Shilov with salts like NaAuCl_4 ,¹⁹³ we believe that $\text{Au}^{\text{III}}\text{-X}$ could be promising hydrocarbon oxidants and we are interested in studying their reactivity mechanism and comparing it to those of the reported first-row transition metal M-X complexes.

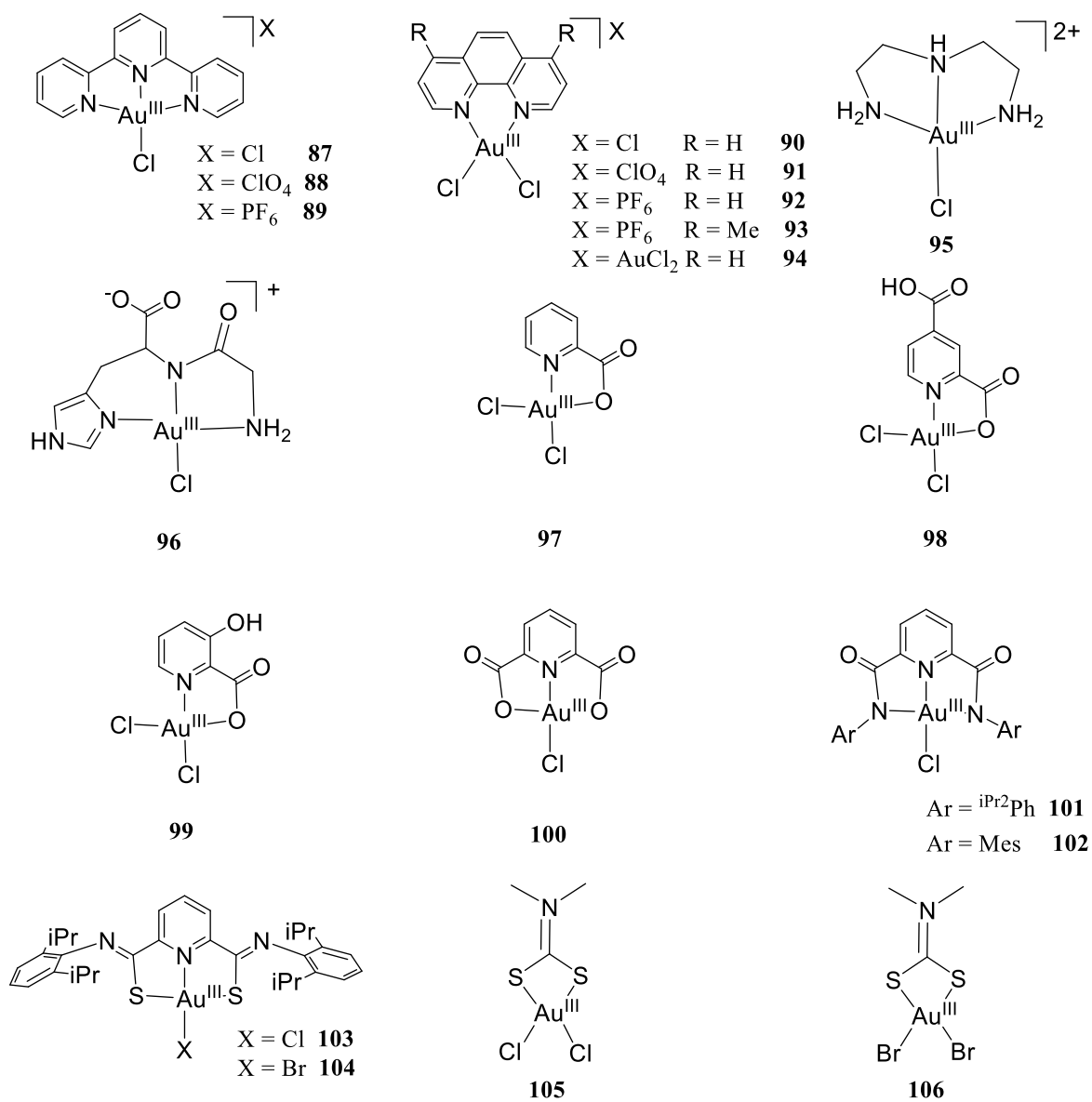


Figure 1.14. Representative $\text{Au}^{\text{III}}\text{-Cl}$ and $\text{Au}^{\text{III}}\text{-Br}$ complexes supported by neutral and anionic pincer ligands.

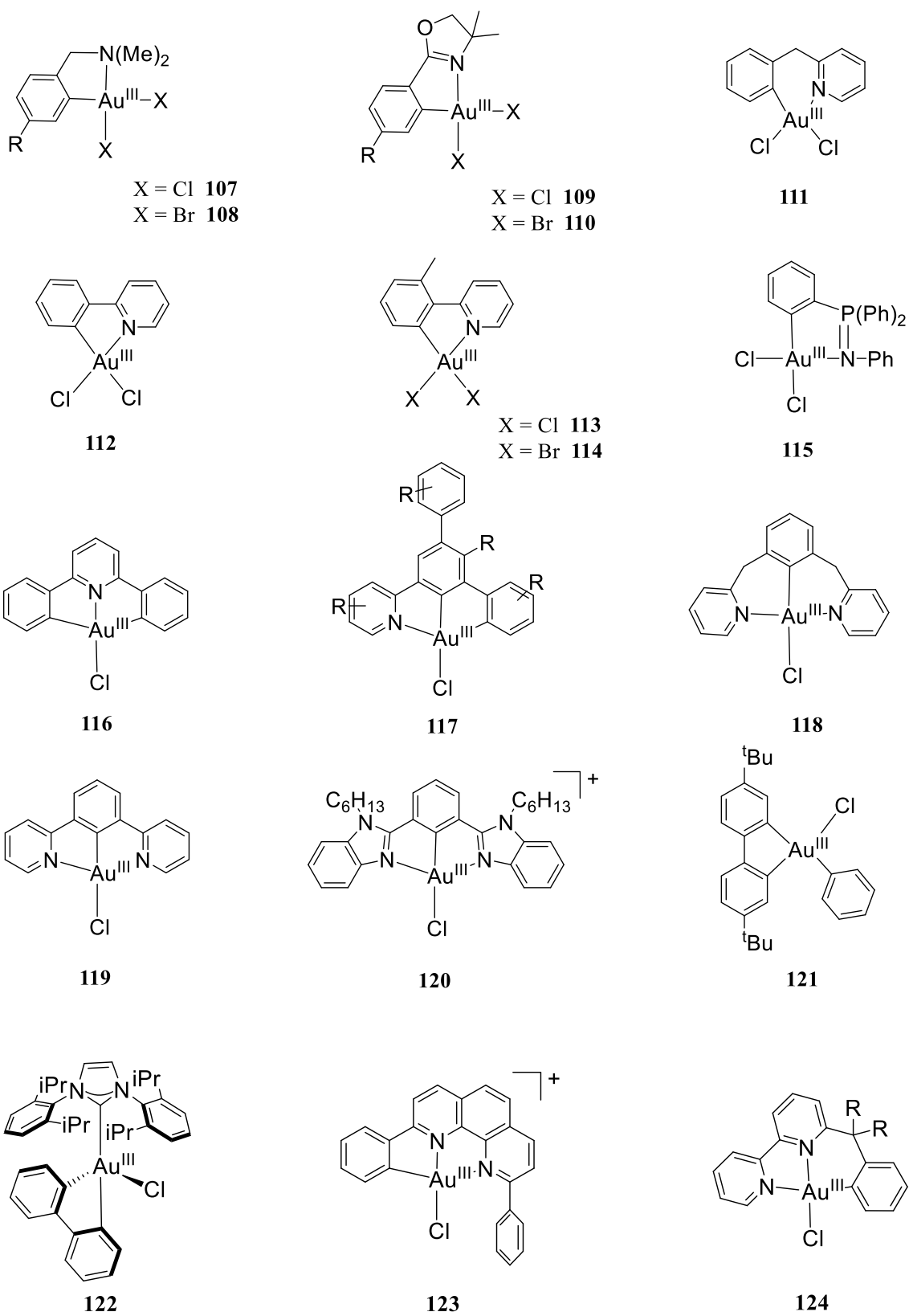


Figure 1.15. Representative $\text{Au}^{\text{III}}\text{-Cl}$ and $\text{Au}^{\text{III}}\text{-Br}$ complexes supported by cyclometalating ligands.

1.1.5.2.2.2 Gold(III)-fluoride complexes

Gold-fluorine chemistry is of increasing interest due to the possibility to generate fluorinated organic molecules which are widespread among pharmaceuticals and agrochemicals, but to date discrete Au^{III}-F organometallic and pincer complexes are still rare.²¹⁰ The groups of Nevado and Toste pioneered the isolation of discrete Au^{III}-F complexes which were first investigated as postulated intermediates in the Au-catalyzed cross-coupling with arylboronic acids.^{231, 238-240}

Toste reported the synthesis of the first isolable organometallic Au^{III}-F complexes [Au^{III}(F)₂(NHC)(Me)] (NHC = SiPr, iPr **125,126**, Figure 1.16) and the dimer [Au₂^{III}(F)₂(NHC)₂(R)₂]²⁺ (R = Me, ^tBu; **127, 128**, Figure 1.16) from the reaction of Au^I precursors with XeF₂.²³⁹ The monomeric and dimeric species coexisted in solution, as shown by the presence of two different ¹⁹F-NMR signals, respectively at $\delta = -201$ ppm and $\delta = -232$ ppm for **125** and at $\delta = -253$ ppm for **127**, whereas only the monomeric species **126** and only dimeric species **128** were observed with modified supporting ligands. Only the dimeric species could be characterized by XRD, whereas the monomer **126** reacted with a range of arylboronic acids to yield new C-C coupled products in moderate to good yields (30-68%).²³⁹ Using different carbanionic ligands, Toste investigated the C(sp³)-F reductive elimination from complexes of the type [Au^{III}(F)₂(NHC)(R)] to obtain fluorinated organic molecules.²⁴¹ This process competed with β -hydride elimination where possible. In a later work, the same group synthesized two series of organometallic Au^{III}-X complexes, [Au^{III}(X)(CF₃)(4-MePh)(PPh₃)] (X = I, Br, Cl, F; **129-132**, Figure 1.16) and [Au^{III}(X)(CF₃)(Cy₃P)(4-FPh)] (**133-136**, Figure 1.16) and explore their propensity to undergo reductive elimination.²⁴⁰ They observed that throughout the series, C(sp³)-X reductive elimination competes with rare C(sp³)-CF₃ bond formation, with selectivity towards the latter increasing according to the halide in the order I < Br < Cl < F, with complete selectivity for the fluoride complexes.²⁴⁰ This reactivity difference was ascribed to the strength of the Au-X bond increasing accordingly to the series, and the higher ionic character of the Au^{III}-F bond allowed it to activate toluene-*h₈/d₈*.²⁴⁰ This work suggested that a stable Au^{III}-F species could potentially behave as an electrophile and activate strong C-H bonds.

Nevado and co-workers reported the synthesis of stable [Au^{III}(F)(^RN[^]C[^]C)] complexes (**137**, Figure 1.16) by halide metathesis of the corresponding chlorides with AgF at 25 °C.²³¹ This

was the first synthesis of Au^{III}-F complexes in which oxidative conditions were not necessary. Complexes **137** showed ¹⁹F-NMR resonances in the $\delta = - (230-225)$ ppm range, confirming the presence of a metal-bound fluoride, and reacted readily with terminal alkynes to give emissive alkynyl complexes.²³¹ In a subsequent work, they isolated stable [Au^{III}(F)(R)(C[^]N)] (R = Alk, Ar, **138**, Figure 1.16) and [Au^{III}(F)₂(C[^]N)] (**139**) complexes by halide metathesis with AgF and explored their ability to undergo transmetalation with arylboronic acids.²³⁸ Complexes **138** showed to undergo direct transmetalation with the coupling partners to yield isolable [Au^{III}(R)(Ar)(C[^]N)] and reductive elimination yielded C-C coupling products in good yields.²³⁸ Dutton reacted cationic Au^I complexes supported by pyridyl or imidazolyl ligands with XeF₂ to obtain stable [Au^{III}(F)₂(py)]⁺ (**140**, Figure 1.16) and [Au^{III}(F)₂(im)]⁺ (**141**, Figure 1.16) which were crystallographically characterized.²¹⁰ Starting from tricationic Au^{III} precursors [Au^{III}(⁴CNpy)₂(py)₂]³⁺ and [Au^{III}(⁴CNpy)₂(im)₂]³⁺ a milder synthetic route towards **137** and **138** was possible, involving ligand exchange with KF in presence of 18-C-6 in acetonitrile. Recently, **140** showed to act as a nucleophile yielding PhIF₂ in the reaction with [PhI(py)₂]²⁺.²⁴² These complexes are one of the two examples to date of *trans*-difluoride complexes, together with the anionic [Au^{III}(F)₂(CF₃)₂]⁻ (**142**, Figure 1.16) reported almost simultaneously by Menjón and co-workers by oxidative fluorination with XeF₂.²⁴³ Riedel and co-workers reported the synthesis of an unusually stable gold trifluoride complex [Au^{III}(F)₃(SIMes)] (**143**, Figure 1.16) supported by an NHC ligand, obtained by reaction of [AuF₄]⁻ with SIMes at -30 °C.²⁴⁴ This complex formed the corresponding cationic difluoride by reaction of the weaker bound *trans* fluorine ligand of **143** with the solvent.²⁴⁴

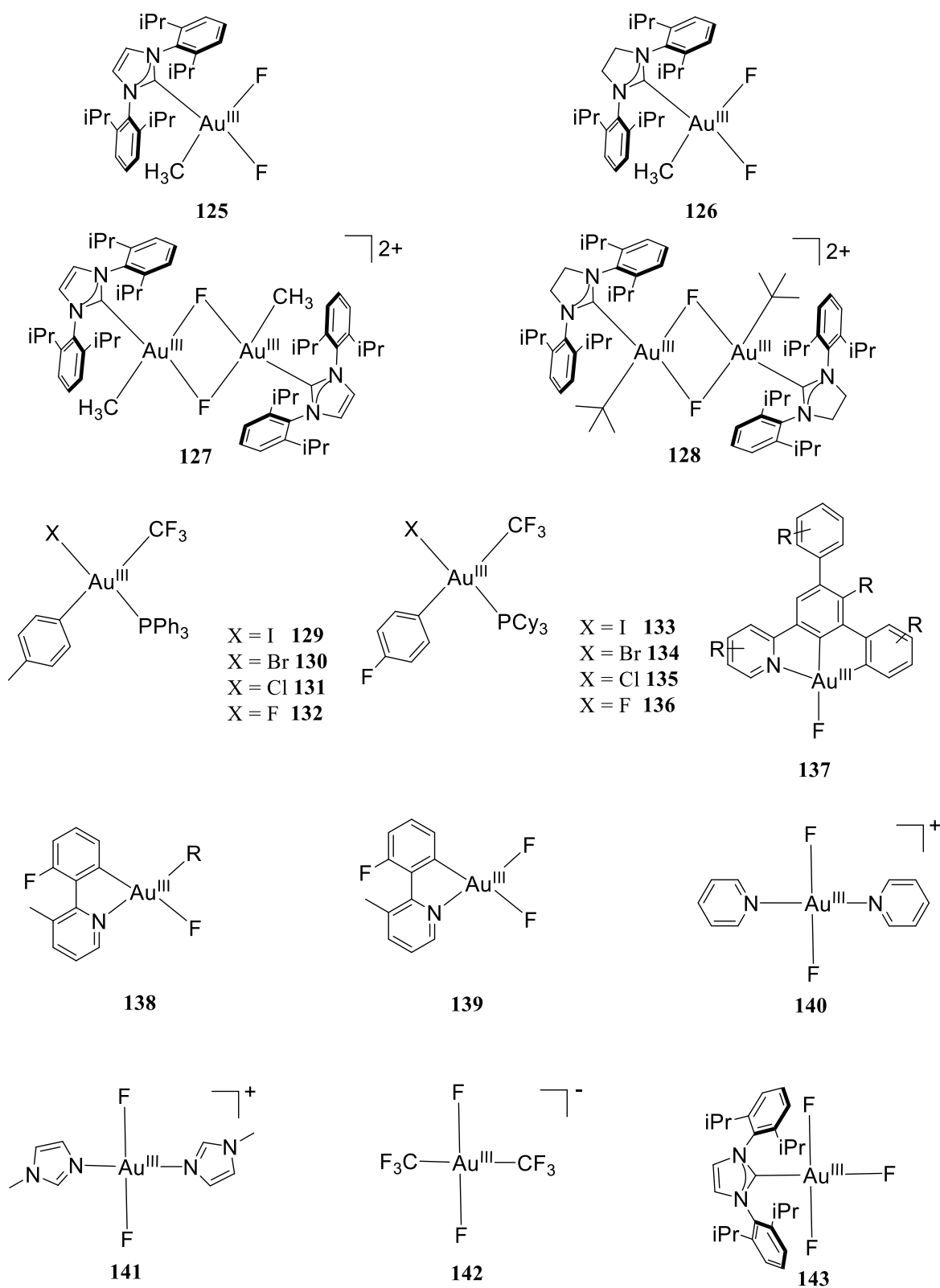


Figure 1.16. Discrete Au^{III}-F complexes.

1.1.6 Aims and methods

The comprehensive aim of our research is the isolation and the mechanistic elucidation of reactive high-valent M–X (X = O, OH, halides) species capable of oxidative activation of saturated C–H bonds. The focus has been directed towards both first and third-row late transition metals for two different reasons. For first row late transition metal the formation of more reactive high-valent oxo intermediates is expected, but due to the Oxo Wall paradigm their isolation and characterization has been elusive so far. Our strategy for this specific scope revolved on designing a tailored ligand to enforce a lower coordination number around the central metal, allowing the formation of precursors that upon oxidation would violate the Oxo Wall paradigm. We therefore designed novel bidentate ligands bearing a localized anionic amidate donor and a neutral iminic N donor which should enforce a tricoordinate environment with first-row transition metals such as Co, Ni and Cu. The ligands synthetic protocols will be outlined and optimized and they will be characterized with spectroscopic techniques (XRD, NMR and vibrationals spectroscopies). Their complexation to Co, Ni and Cu will be studied through ordinary coordination chemistry techniques, ultimately yielding low-coordinate precursors to very reactive high-valent oxidants capable to perform C–H activation. Another motif present among high-valent oxidant in nature is a metalloporphyrin π -cation radical, which is typical of some of the most oxidising species in biology. Therefore we were interested in the synthesis and the reactivity studies of mimics of these species containing first row late-transition metals such as Ni and Cu, to investigate whether they can form strong oxidants capable to activate hydrocarbon substrate. We therefore plan to characterize these high-valent species through NMR, EPR, IR and electronic absorption spectroscopy and monitor their reactivity with extensive kinetic studies.

The second focus of this project is to investigate the reactivity of high-valent third-row late transition M–X complexes, notably with M = Au, since little insights are available to date about their active species and mechanism in hydrocarbon oxidation catalysis. In fact, despite Au^{III}–OH species having been proposed as catalytically active intermediates in homogeneous oxidation catalysis, their intermediacy is still questioned. Similarly, Au^{III}–Cl complexes are often used as precursor in synthesis or as prodrugs in inorganic medicinal chemistry, but very little investigation on their reactivity has been made to date. To understand this, we first chose to investigate the reactivity of a known Au^{III}–OH complex supported by a terpyridine ligand towards substrates containing C–H and O–H bonds to investigate its capability as an oxidant

and to gain information on the reaction mechanism. The pincer ligand of choice allows the straightforward synthesis of a platform which enables us to compare complexes by tuning the ancillary ligand, allowing us to promptly evaluate reactivity trends. An important focus of this project will be in fact on the structure/activity relationships among the same class of high-valent oxidants. We therefore intend to confront the effect of an hydroxide vs. a halide ancillary ligand on the same complex platform $[\text{Au}^{\text{III}}(\text{X})(\text{terpy})]^{2+}$, thus the second step of this focus area will involve the synthesis and characterization of $\text{Au}^{\text{III}}\text{-X}$ (X = halide) complexes and a comparative analysis of their oxidative reactivity. The reactivity will be assessed by monitoring the changes in the spectroscopic (UV-Vis, NMR and vibrational spectroscopies) features of the complexes, measuring reaction kinetics and by examining and quantifying the products of substrate oxidation by NMR spectroscopy and chromatographic techniques. Metastable intermediates could be trapped and studied by low-temperature spectroscopic techniques and, where short-living species will be present, indirect insights on their nature and role will be gained from the reactivity kinetics and products. The results obtained in this field of investigation will bring a crucial understanding of the role of such intermediates in gold oxidation catalysis, eventually contributing to the improvement and design of catalysts for C–H bond oxidation.

1.1.7 References

1. F. Meyer and W. B. Tolman, *Inorg. Chem.*, 2015, **54**, 5039-5039.
2. N. Lehnert and J. C. Peters, *Inorg. Chem.*, 2015, **54**, 9229-9233.
3. L. Wang, Y. Yi, C. Wu, H. Guo and X. Tu, *Angew. Chem. Int. Ed.*, 2017, **56**, 13679-13683.
4. M. Usman, W. M. A. Wan Daud and H. F. Abbas, *Renew. Sustain. Energy Rev.*, 2015, **45**, 710-744.
5. J. A. Labinger and J. E. Bercaw, *Nature*, 2002, **417**, 507.
6. K. I. Goldberg and A. S. Goldman, *Acc. Chem. Res.*, 2017, **50**, 620-626.
7. B. G. Malmstrom, *Annu. Rev. Biochem.*, 1982, **51**, 21-59.
8. A. E. Shilov and A. A. Shteinman, *Coord. Chem. Rev.*, 1977, **24**, 97-143.
9. B. B. Wayland, S. Ba and A. E. Sherry, *J. Am. Chem. Soc.*, 1991, **113**, 5305-5311.
10. C. M. Jensen, *Chem. Commun.*, 1999, 2443-2449.
11. J. T. Kummer, *J. Phys. Chem.*, 1986, **90**, 4747-4752.
12. N. Tsubaki, S. Sun and K. Fujimoto, *J. Catal.*, 2001, **199**, 236-246.
13. D. Pakhare and J. Spivey, *Chem. Soc. Rev.*, 2014, **43**, 7813-7837.
14. L. Que Jr and W. B. Tolman, *Nature*, 2008, **455**, 333.
15. J. D. Lipscomb, *Annu. Rev. Microbiol.*, 1994, **48**, 371-399.
16. R. L. Lieberman and A. C. Rosenzweig, *Crit. Rev. Biochem. Mol. Biol.*, 2004, **39**, 147-164.
17. E. Frieden, *Trends Biochem. Sci.*, 1976, **1**, 273-274.
18. K. Ray, F. F. Pfaff, B. Wang and W. Nam, *J. Am. Chem. Soc.*, 2014, **136**, 13942-13958.
19. E. I. Solomon, T. C. Brunold, M. I. Davis, J. N. Kemsley, S.-K. Lee, N. Lehnert, F. Neese, A. J. Skulan, Y.-S. Yang and J. Zhou, *Chem. Rev.*, 2000, **100**, 235-350.
20. M. Costas, M. P. Mehn, M. P. Jensen and L. Que, *Chem. Rev.*, 2004, **104**, 939-986.
21. E. I. Solomon, P. Chen, M. Metz, S.-K. Lee and A. E. Palmer, *Angew. Chem. Int. Ed.*, 2001, **40**, 4570-4590.
22. P. L. Roach, I. J. Clifton, C. M. H. Hensgens, N. Shibata, C. J. Schofield, J. Hajdu and J. E. Baldwin, *Nature*, 1997, **387**, 827.

23. M. H. Glickman and J. P. Klinman, *Biochemistry*, 1996, **35**, 12882-12892.
24. C. M. McGinley and W. A. van der Donk, *Chem. Commun.*, 2003, 2843-2846.
25. Y. Zheng and A. R. Brash, *J. Biol. Chem.*, 2010, **285**, 39876-39887.
26. Y. Zhang, Q.-F. Gan, E. G. Pavel, E. Sigal and E. I. Solomon, *J. Am. Chem. Soc.*, 1995, **117**, 7422-7427.
27. A. Wennman, E. H. Oliw, S. Karkehabadi and Y. Chen, *J. Biol. Chem.* 2016, **15**, 291, 8130-8139
28. C. Su and E. H. Oliw, *J. Biol. Chem.*, 1998, **273**, 13072-13079.
29. B. Meunier, S. P. de Visser and S. Shaik, *Chem. Rev.*, 2004, **104**, 3947-3980.
30. M. Wirstam, M. R. A. Blomberg and P. E. M. Siegbahn, *J. Am. Chem. Soc.*, 1999, **121**, 10178-10185.
31. A. E. Rettie, P. R. Sheffels, K. R. Korzekwa, F. J. Gonzalez, R. M. Philpot and T. A. Baillie, *Biochemistry*, 1995, **34**, 7889-7895.
32. A. Rettie, A. Rettenmeier, W. Howald and T. Baillie, *Science*, 1987, **235**, 890-893.
33. J. Latham, E. Brandenburger, S. A. Shepherd, B. R. K. Menon and J. Micklefield, *Chem. Rev.*, 2018, **118**, 232-269.
34. C. S. Neumann, D. G. Fujimori and C. T. Walsh, *Chem. Biol.*, 2008, **15**, 99-109.
35. S. Martinez and R. P. Hausinger, *J Biol Chem.*, 2015, **290**, 20702-20711.
36. R. A. Binstead, B. A. Moyer, G. J. Samuels and T. J. Meyer, *J. Am. Chem. Soc.*, 1981, **103**, 2897-2899.
37. J. J. Warren, T. A. Tronic and J. M. Mayer, *Chem. Rev.*, 2010, **110**, 6961-7001.
38. J. M. Mayer, *Annu. Rev. Phys. Chem.*, 2004, **55**, 363-390.
39. J. M. Mayer, *J. Phys. Chem. Lett.*, 2011, **2**, 1481-1489.
40. J. M. Mayer, *Acc. Chem. Res.*, 2011, **44**, 36-46.
41. J. W. Darcy, B. Koronkiewicz, G. A. Parada and J. M. Mayer, *Acc. Chem. Res.*, 2018, **51**, 2391-2399.
42. J. P. Roth, J. C. Yoder, T.-J. Won and J. M. Mayer, *Science*, 2001, **294**, 2524-2526.
43. W. D. Morris and J. M. Mayer, *J. Am. Chem. Soc.*, 2017, **139**, 10312-10319.
44. A. Sirjoosingh and S. Hammes-Schiffer, *J. Phys. Chem. A*, 2011, **115**, 2367-2377.
45. S. Hammes-Schiffer, *J. Am. Chem. Soc.*, 2015, **137**, 8860-8871.
46. R. P. Bell and C. N. Hinshelwood, *Proc. R. Soc. Lond. A* , 1936, **154**, 414-429.
47. M. G. Evans and M. Polanyi, *Trans. Faraday Soc.*, 1938, **34**, 11-24.
48. E. A. Mader, E. R. Davidson and J. M. Mayer, *J. Am. Chem. Soc.*, 2007, **129**, 5153-5166.
49. F. G. Bordwell, J. P. Cheng and J. A. Harrelson, *J. Am. Chem. Soc.*, 1988, **110**, 1229-1231.
50. T. Matsuo and J. M. Mayer, *Inorg. Chem.*, 2005, **44**, 2150-2158.
51. K.-S. You and N. J. Oppenheimer, *Crit. Rev. Biochem.*, 1985, **17**, 313-451.
52. X.-Q. Zhu, H.-R. Li, Q. Li, T. Ai, J.-Y. Lu, Y. Yang and J.-P. Cheng, *Chem. Eur. J.*, 2003, **9**, 871-880.
53. A. S. Larsen, K. Wang, M. A. Lockwood, G. L. Rice, T.-J. Won, S. Lovell, M. Sadílek, F. Tureček and J. M. Mayer, *J. Am. Chem. Soc.*, 2002, **124**, 10112-10123.
54. K. Gardner and J. Mayer, *Science*, 1995, **269**, 1849-1851.
55. J. Yuasa and S. Fukuzumi, *J. Am. Chem. Soc.*, 2006, **128**, 14281-14292.
56. Y. J. Jeong, Y. Kang, A.-R. Han, Y.-M. Lee, H. Kotani, S. Fukuzumi and W. Nam, *Angew. Chem. Int. Ed.*, 2008, **47**, 7321-7324.
57. J. Zhang, J.-D. Yang and J.-P. Cheng, *Chem. Sci.*, 2020, **11**, 3672-3679.
58. A. Ansari, A. Kaushik and G. Rajaraman, *J. Am. Chem. Soc.*, 2013, **135**, 4235-4249.
59. M.-J. Kang, W. J. Song, A.-R. Han, Y. S. Choi, H. G. Jang and W. Nam, *J. Org. Chem.*, 2007, **72**, 6301-6304.
60. R. H. Holm, *Chem. Rev.*, 1987, **87**, 1401-1449.
61. K. K. Singh, M. k. Tiwari, B. B. Dhar, K. Vanka and S. Sen Gupta, *Inorg. Chem.*, 2015, **54**, 6112-6121.
62. A. Singh and L. Spiccia, *Coord. Chem. Rev.*, 2013, **257**, 2607-2622.
63. R. L. Webster, *Dalton Trans.*, 2017, **46**, 4483-4498.
64. M. Cokoja, C. Bruckmeier, B. Rieger, W. A. Herrmann and F. E. Kühn, *Angew. Chem. Int. Ed.*, 2011, **50**, 8510-8537.
65. S. R. Bell and J. T. Groves, *J. Am. Chem. Soc.*, 2009, **131**, 9640-9641.
66. J. T. Groves, Z. Gross and M. K. Stern, *Inorg. Chem.*, 1994, **33**, 5065-5072.
67. V. P. Shedbalkar, S. Modi and S. Mitra, *J. Chem. Soc., Chem. Commun.*, 1988, 1238-1239.
68. G. Yin, *Coord. Chem. Rev.*, 2010, **254**, 1826-1842.
69. J. L. Que, *J. Chem. Soc., Dalton Trans.*, 1997, DOI: 10.1039/A703345A, 3933-3940.
70. D. Lee and S. J. Lippard, *J. Am. Chem. Soc.*, 1998, **120**, 12153-12154.
71. J. L. Que and T. W. B., *Angew. Chem. Int. Ed.*, 2002, **41**, 1114-1137.
72. J.-U. Rohde, J.-H. In, M. H. Lim, W. W. Brennessel, M. R. Bukowski, A. Stubna, E. Münck, W. Nam and L. Que, *Science*, 2003, **299**, 1037-1039.
73. A. S. Borovik, *Chem. Soc. Rev.*, 2011, **40**, 1870-1874.
74. J. Cho, J. Woo, J. Eun Han, M. Kubo, T. Ogura and W. Nam, *Chem. Sci.*, 2011, **2**, 2057-2062.

75. S. Liu, K. Mase, C. Bougher, S. D. Hicks, M. M. Abu-Omar and S. Fukuzumi, *Inorg. Chem.*, 2014, **53**, 7780-7788.
76. A. R. McDonald and L. Que, *Coord. Chem. Rev.*, 2013, **257**, 414-428.
77. W. Nam, *Acc. Chem. Res.*, 2007, **40**, 522-531.
78. M. S. Seo, N. H. Kim, K.-B. Cho, J. E. So, S. K. Park, M. Clemancey, R. Garcia-Serres, J.-M. Latour, S. Shaik and W. Nam, *Chem. Sci.*, 2011, **2**, 1039-1045.
79. A. W. Pierpont and T. R. Cundari, *Inorg. Chem.*, 2010, **49**, 2038-2046.
80. B. F. Gherman, W. B. Tolman and C. J. Cramer, *J. Comput. Chem.*, 2006, **27**, 1950-1961.
81. J. R. Winkler and H. B. Gray, *Struct. Bonding* 2012, **142**, 17-28.
82. T. R. Cundari, R. R. Conry, E. Spaltenstein, S. C. Critchlow, K. A. Hall, S. K. Tahmassebi and J. M. Mayer, *Organometallics*, 1994, **13**, 322-331.
83. E. Poverenov, I. Efremenko, A. I. Frenkel, Y. Ben-David, L. J. W. Shimon, G. Leitun, L. Konstantinovskii, J. M. L. Martin and D. Milstein, *Nature*, 2008, **455**, 1093.
84. C. E. MacBeth, A. P. Golombek, V. G. Young, C. Yang, K. Kuczera, M. P. Hendrich and A. S. Borovik, *Science*, 2000, **289**, 938-941.
85. H. Seungwoo, P. F. F., K. Eunji, W. Yong, S. Mi-Sook, B. Eckhard, R. Kallol and N. Wonwoo, *Angew. Chem. Int. Ed.*, 2014, **53**, 10403-10407.
86. C. J. Burgey, K. A. Robinson and T. A. Lyle, *J. Med. Chem.*, 2003, **46**, 461.
87. M. K. Goetz, E. A. Hill, A. S. Filatov and J. S. Anderson, *J. Am. Chem. Soc.*, 2018, **140**, 13176-13180.
88. C. R. Goldsmith, A. P. Cole and T. D. P. Stack, *J. Am. Chem. Soc.*, 2005, **127**, 9904-9912.
89. C. R. Goldsmith and T. D. P. Stack, *Inorg. Chem.*, 2006, **45**, 6048-6055.
90. S. Ogo, S. Wada, Y. Watanabe, M. Iwase, A. Wada, M. Harata, K. Jitsukawa, H. Masuda and H. Einaga, *Angew. Chem. Int. Ed.*, 1998, **37**, 2102-2104.
91. C. E. MacBeth, R. Gupta, K. R. Mitchell-Koch, V. G. Young, G. H. Lushington, W. H. Thompson, M. P. Hendrich and A. S. Borovik, *J. Am. Chem. Soc.*, 2004, **126**, 2556-2567.
92. R. Gupta and A. S. Borovik, *J. Am. Chem. Soc.*, 2003, **125**, 13234-13242.
93. R. Gupta, T. Taguchi, A. S. Borovik and M. P. Hendrich, *Inorg. Chem.*, 2013, **52**, 12568-12575.
94. C. E. MacBeth, B. S. Hammes, V. G. Young and A. S. Borovik, *Inorg. Chem.*, 2001, **40**, 4733-4741.
95. D. C. Lacy, R. Gupta, K. L. Stone, J. Greaves, J. W. Ziller, M. P. Hendrich and A. S. Borovik, *J. Am. Chem. Soc.*, 2010, **132**, 12188-12190.
96. T. Taguchi, K. L. Stone, R. Gupta, B. Kaiser-Lassalle, J. Yano, M. P. Hendrich and A. S. Borovik, *Chem. Sci.*, 2014, **5**, 3064-3071.
97. A. C. Weitz, E. A. Hill, V. F. Oswald, E. L. Bominaar, A. S. Borovik, M. P. Hendrich and Y. Guo, *Angew. Chem. Int. Ed.*, 2018, **57**, 16010-16014.
98. E. A. Hill, A. C. Weitz, E. Onderko, A. Romero-Rivera, Y. Guo, M. Swart, E. L. Bominaar, M. T. Green, M. P. Hendrich, D. C. Lacy and A. S. Borovik, *J. Am. Chem. Soc.*, 2016, **138**, 13143-13146.
99. J. Mukherjee, R. L. Lucas, M. K. Zart, D. R. Powell, V. W. Day and A. S. Borovik, *Inorg. Chem.*, 2008, **47**, 5780-5786.
100. W.-M. Ching, A. Zhou, J. E. M. N. Klein, R. Fan, G. Knizia, C. J. Cramer, Y. Guo and L. Que, *Inorg. Chem.*, 2017, **56**, 11129-11140.
101. G. Yin, A. M. Danby, D. Kitko, J. D. Carter, W. M. Scheper and D. H. Busch, *J. Am. Chem. Soc.*, 2008, **130**, 16245-16253.
102. L. M. Brines, M. K. Coggins, P. C. Y. Poon, S. Toledo, W. Kaminsky, M. L. Kirk and J. A. Kovacs, *J. Am. Chem. Soc.*, 2015, **137**, 2253-2264.
103. M. K. Coggins, L. M. Brines and J. A. Kovacs, *Inorg. Chem.*, 2013, **52**, 12383-12393.
104. G. B. Wijeratne, B. Corzine, V. W. Day and T. A. Jackson, *Inorg. Chem.*, 2014, **53**, 7622-7634.
105. T. R. Porter and J. M. Mayer, *Chem. Sci.*, 2014, **5**, 372-380.
106. H. Gao and J. T. Groves, *J. Am. Chem. Soc.*, 2017, **139**, 3938-3941.
107. J. P. T. Zaragoza, M. A. Siegler and D. P. Goldberg, *J. Am. Chem. Soc.*, 2018, **140**, 4380-4390.
108. J. P. T. Zaragoza, D. C. Cummins, M. Q. E. Mubarak, M. A. Siegler, S. P. de Visser and D. P. Goldberg, *Inorg. Chem.*, 2019, **58**, 16761-16770.
109. V. Yadav, J. B. Gordon, M. A. Siegler and D. P. Goldberg, *J. Am. Chem. Soc.*, 2019, **141**, 10148-10153.
110. J. P. T. Zaragoza, T. H. Yosca, M. A. Siegler, P. Moënne-Loccoz, M. T. Green and D. P. Goldberg, *J. Am. Chem. Soc.*, 2017, **139**, 13640-13643.
111. M. J. Drummond, C. L. Ford, D. L. Gray, C. V. Popescu and A. R. Fout, *J. Am. Chem. Soc.*, 2019, **141**, 6639-6650.
112. P. J. Donoghue, J. Tehranchi, C. J. Cramer, R. Sarangi, E. I. Solomon and W. B. Tolman, *J. Am. Chem. Soc.*, 2011, **133**, 17602-17605.
113. D. Dhar and W. B. Tolman, *J. Am. Chem. Soc.*, 2015, **137**, 1322-1329.
114. M. R. Halvagar and W. B. Tolman, *Inorg. Chem.*, 2013, **52**, 8306-8308.

115. D. Dhar, G. M. Yee, A. D. Spaeth, D. W. Boyce, H. Zhang, B. Dereli, C. J. Cramer and W. B. Tolman, *J. Am. Chem. Soc.*, 2016, **138**, 356-368.
116. N. Gagnon and W. B. Tolman, *Acc. Chem. Res.*, 2015, **48**, 2126-2131.
117. D. Dhar, G. M. Yee, T. F. Markle, J. M. Mayer and W. B. Tolman, *Chem. Sci.*, 2017, **8**, 1075-1085.
118. J.-U. Rohde, A. Stubna, E. L. Bominaar, E. Münck, W. Nam and L. Que, *Inorg. Chem.*, 2006, **45**, 6435-6445.
119. J. England, Y. Guo, K. M. Van Heuvelen, M. A. Cranswick, G. T. Rohde, E. L. Bominaar, E. Münck and L. Que, *J. Am. Chem. Soc.*, 2011, **133**, 11880-11883.
120. M. Puri, A. N. Biswas, R. Fan, Y. Guo and L. Que, *J. Am. Chem. Soc.*, 2016, **138**, 2484-2487.
121. O. Planas, M. Clémancey, J.-M. Latour, A. Company and M. Costas, *Chem. Commun.*, 2014, **50**, 10887-10890.
122. P. Comba and S. Wunderlich, *Chem. Eur. J.*, 2010, **16**, 7293-7299.
123. S. Chatterjee and T. K. Paine, *Angew. Chem. Int. Ed.*, 2016, **55**, 7717-7722.
124. S. Rana, J. P. Biswas, A. Sen, M. Clémancey, G. Blondin, J.-M. Latour, G. Rajaraman and D. Maiti, *Chem. Sci.*, 2018, **9**, 7843-7858.
125. V. Yadav, R. J. Rodriguez, M. A. Siegler and D. P. Goldberg, *J. Am. Chem. Soc.*, 2020, DOI: 10.1021/jacs.0c00493.
126. W. Liu and J. T. Groves, *J. Am. Chem. Soc.*, 2010, **132**, 12847-12849.
127. W. Liu and J. T. Groves, *Acc. Chem. Res.*, 2015, **48**, 1727-1735.
128. W. Liu, X. Huang, M.-J. Cheng, R. J. Nielsen, W. A. Goddard and J. T. Groves, *Science*, 2012, **337**, 1322-1325.
129. X. Huang, W. Liu, J. M. Hooker and J. T. Groves, *Angew. Chem. Int. Ed.*, 2015, **54**, 5241-5245.
130. G. Li, A. K. Dilger, P. T. Cheng, W. R. Ewing and J. T. Groves, *Angew. Chem. Int. Ed.*, 2018, **57**, 1251-1255.
131. A. Draksharapu, Z. Codolà, L. Gómez, J. Lloret-Fillol, W. R. Browne and M. Costas, *Inorg. Chem.*, 2015, **54**, 10656-10666.
132. T. Corona, A. Draksharapu, S. K. Padamati, I. Gamba, V. Martin-Diaconescu, F. Acuna-Pares, W. R. Browne and A. Company, *J. Am. Chem. Soc.*, 2016, **138**, 12987-12996.
133. P. Mondal, P. Pirovano, A. Das, E. R. Farquhar and A. R. McDonald, *J. Am. Chem. Soc.*, 2018, **140**, 1834-1841.
134. P. Pirovano and A. R. McDonald, *Eur. J. Inorg. Chem.*, 2018, **2018**, 547-560.
135. P. Mondal, M. Lovisari, B. Twamley and A. R. McDonald, *Angew. Chem. Int. Ed.*, n/a.
136. J. K. Bower, A. D. Cypcar, B. Henriquez, S. C. E. Stieber and S. Zhang, *J. Am. Chem. Soc.*, 2020, **142**, 18, 8514-8521.
137. E. S. Aleksandr and B. S. p. Georgiy, *Russ. Chem. Rev.*, 1987, **56**, 442.
138. A. E. Shilov and G. B. Shul'pin, *Chem. Rev.*, 1997, **97**, 2879-2932.
139. J. R. Ludwig and C. S. Schindler, *Chem*, 2017, **2**, 313-316.
140. R. A. Periana, D. J. Taube, S. Gamble, H. Taube, T. Satoh and H. Fujii, *Science*, 1998, **280**, 560-564.
141. E. Szuromi, H. Shan and P. R. Sharp, *J. Am. Chem. Soc.*, 2003, **125**, 10522-10523.
142. M. S. Davies and T. W. Hambley, *Inorg. Chem.*, 1998, **37**, 5408-5409.
143. R. A. Taylor, D. J. Law, G. J. Sunley, A. J. P. White and G. J. P. Britovsek, *Angew. Chem. Int. Ed.*, 2009, **48**, 5900-5903.
144. D. D. Wick and K. I. Goldberg, *J. Am. Chem. Soc.*, 1999, **121**, 11900-11901.
145. S. J. Hoseini, R. H. Fath, M. A. Fard, A. Behnia and R. J. Puddephatt, *Inorg. Chem.*, 2018, **57**, 8951-8955.
146. L. C. Kao, A. C. Hutson and A. Sen, *J. Am. Chem. Soc.*, 1991, **113**, 700-701.
147. P. L. Alsters, H. T. Teunissen, J. Boersma, A. L. Spek and G. van Koten, *Organometallics*, 1993, **12**, 4691-4696.
148. M. Zhou and R. H. Crabtree, *Chem. Soc. Rev.*, 2011, **40**, 1875-1884.
149. K. Kamaraj and D. Bandyopadhyay, *Organometallics*, 1999, **18**, 438-446.
150. L. Boisvert, M. C. Denney, S. K. Hanson and K. I. Goldberg, *J. Am. Chem. Soc.*, 2009, **131**, 15802-15814.
151. M. C. Denney, N. A. Smythe, K. L. Cetto, R. A. Kemp and K. I. Goldberg, *J. Am. Chem. Soc.*, 2006, **128**, 2508-2509.
152. M. M. Konnick, I. A. Guzei and S. S. Stahl, *J. Am. Chem. Soc.*, 2004, **126**, 10212-10213.
153. J. K. Hoyano, A. D. McMaster and W. A. G. Graham, *J. Am. Chem. Soc.*, 1983, **105**, 7190-7191.
154. R. S. Hay-Motherwell, G. Wilkinson, B. Hussain-Bates and M. B. Hursthouse, *Polyhedron*, 1993, **12**, 2009-2012.
155. B. G. Jacobi, D. S. Laitar, L. Pu, M. F. Wargocki, A. G. DiPasquale, K. C. Fortner, S. M. Schuck and S. N. Brown, *Inorg. Chem.*, 2002, **41**, 4815-4823.

156. M. Zhou, N. D. Schley and R. H. Crabtree, *J. Am. Chem. Soc.*, 2010, **132**, 12550-12551.
157. J. F. Hull, D. Balcells, J. D. Blakemore, C. D. Incarvito, O. Eisenstein, G. W. Brudvig and R. H. Crabtree, *J. Am. Chem. Soc.*, 2009, **131**, 8730-8731.
158. D. Delony, M. Kinauer, M. Diefenbach, S. Demeshko, C. Würtele, M. C. Holthausen and S. Schneider, *Angew. Chem. Int. Ed.*, 2019, **58**, 10971-10974.
159. A. Y. Verat, H. Fan, M. Pink, Y.-S. Chen and K. G. Caulton, *Chemistry – A European Journal*, 2008, **14**, 7680-7686.
160. X.-Y. Yu, B. O. Patrick and B. R. James, *Organometallics*, 2006, **25**, 4870-4877.
161. G. B. Shul'pin, D. V. Muratov, L. S. Shul'pina, A. R. Kudinov, T. V. Strelkova and P. V. Petrovskiy, *Applied Organometallic Chemistry*, 2008, **22**, 684-688.
162. V. Nadolinsky, A. Belyaev, A. Komarovskikh, S. Tkachev and I. Yushina, *New J. Chem.*, 2018, **42**, 15231-15236.
163. K. B. Sharpless, W. Amberg, Y. L. Bennani, G. A. Crispino, J. Hartung, K. S. Jeong, H. L. Kwong, K. Morikawa and Z. M. Wang, *J. Org. Chem.*, 1992, **57**, 2768-2771.
164. T. Osako, E. J. Watson, A. Dehestani, B. C. Bales and J. M. Mayer, *Angew. Chem. Int. Ed.*, 2006, **45**, 7433-7436.
165. S.-M. Yiu, Z.-B. Wu, C.-K. Mak and T.-C. Lau, *J. Am. Chem. Soc.*, 2004, **126**, 14921-14929.
166. A. Stephen and K. Hashmi, *Gold Bulletin*, 2004, **37**, 51-65.
167. G. C. Bond and D. T. Thompson, *Catal. Rev.*, 1999, **41**, 319-388.
168. G. C. Bond, P. A. Sermon, G. Webb, D. A. Buchanan and P. B. Wells, *J. Chem. Soc., Chem. Commun.*, 1973, 444-445.
169. M. Haruta, *Nature*, 2005, **437**, 1098-1099.
170. Y. Ito, M. Sawamura and T. Hayashi, *J. Am. Chem. Soc.*, 1986, **108**, 6405-6406.
171. Y. Fukuda and K. Utimoto, *J. Org. Chem.*, 1991, **56**, 3729-3731.
172. J. H. Teles, S. Brode and M. Chabanas, *Angew. Chem. Int. Ed.*, 1998, **37**, 1415-1418.
173. L. Prati and M. Rossi, *J. Catal.*, 1998, **176**, 552-560.
174. A. S. K. Hashmi, L. Schwarz, J.-H. Choi and T. M. Frost, *Angew. Chem. Int. Ed.*, 2000, **39**, 2285-2288.
175. P. Landon, P. J. Collier, A. J. Papworth, C. J. Kiely and G. J. Hutchings, *Chem. Commun.*, 2002, 2058-2059.
176. M. D. Hughes, Y.-J. Xu, P. Jenkins, P. McMorn, P. Landon, D. I. Enache, A. F. Carley, G. A. Attard, G. J. Hutchings, F. King, E. H. Stitt, P. Johnston, K. Griffin and C. J. Kiely, *Nature*, 2005, **437**, 1132-1135.
177. A. S. K. Hashmi and G. J. Hutchings, *Angew. Chem. Int. Ed.*, 2006, **45**, 7896-7936.
178. G. J. Hutchings, *ACS Cent. Sci.*, 2018, **4**, 1095-1101.
179. M. S. Ide and R. J. Davis, *Acc. Chem. Res.*, 2014, **47**, 825-833.
180. M. C. Kung, R. J. Davis and H. H. Kung, *J. Phys. Chem. C*, 2007, **111**, 11767-11775.
181. H. Arakawa, M. Aresta, J. N. Armor, M. A. Barteau, E. J. Beckman, A. T. Bell, J. E. Bercaw, C. Creutz, E. Dinjus, D. A. Dixon, K. Domen, D. L. DuBois, J. Eckert, E. Fujita, D. H. Gibson, W. A. Goddard, D. W. Goodman, J. Keller, G. J. Kubas, H. H. Kung, J. E. Lyons, L. E. Manzer, T. J. Marks, K. Morokuma, K. M. Nicholas, R. Periana, L. Que, J. Rostrup-Nielson, W. M. H. Sachtler, L. D. Schmidt, A. Sen, G. A. Somorjai, P. C. Stair, B. R. Stults and W. Tumas, *Chem. Rev.*, 2001, **101**, 953-996.
182. A. Villa, N. Dimitratos, C. E. Chan-Thaw, C. Hammond, L. Prati and G. J. Hutchings, *Acc. Chem. Res.*, 2015, **48**, 1403-1412.
183. D. Wang, A. Villa, D. Su, L. Prati and R. Schlögl, *ChemCatChem*, 2013, **5**, 2717-2723.
184. B. K. Min and C. M. Friend, *Chem. Rev.*, 2007, **107**, 2709-2724.
185. A. Nijamudheen and A. Datta, *Chem. Eur. J.*, 2020, **26**, 1442-1487.
186. V. Gauchot and A.-L. Lee, *Chem. Commun.*, 2016, **52**, 10163-10166.
187. A. S. K. Hashmi, *Angew. Chem. Int. Ed.*, 2010, **49**, 5232-5241.
188. G. B. Shul'pin, A. E. Shilov and G. Süß-Fink, *Tetrahedron Lett.*, 2001, **42**, 7253-7256.
189. A. Corma, I. Domínguez, A. Doménech, V. Fornés, C. J. Gómez-García, T. Ródenas and M. J. Sabater, *J. Catal.*, 2009, **265**, 238-244.
190. L. A. Levchenko, A. P. Sadkov, N. V. Lariontseva, E. M. Koldasheva, A. K. Shilova and A. E. Shilov, *J. Inorg. Biochem.*, 2002, **88**, 251-253.
191. M. A. Cinellu, G. Minghetti, F. Cocco, S. Stoccoro, A. Zucca and M. Manassero, *Angew. Chem. Int. Ed.*, 2005, **44**, 6892-6895.
192. D.-A. Roşca, J. A. Wright, D. L. Hughes and M. Bochmann, *Nat. Commun.*, 2013, **4**, 2167.
193. B. Pitteri, G. Marangoni, F. Visentin, T. Bobbo, V. Bertolasi and P. Gilli, *J. Chem. Soc., Dalton Trans.*, 1999, 677-682.
194. R. Corbo, T. P. Pell, B. D. Stringer, C. F. Hogan, D. J. D. Wilson, P. J. Barnard and J. L. Dutton, *J. Am. Chem. Soc.*, 2014, **136**, 12415-12421.
195. H. Beucher, E. Merino, A. Genoux, T. Fox and C. Nevado, *Angew. Chem. Int. Ed.*, 2019, **58**, 9064-9067.

196. J. Vicente, M. D. Bermúdez, F. J. Carrión and P. G. Jones, *J. Organomet. Chem.*, 1996, **508**, 53-57.
197. D.-A. Roşca, D. A. Smith and M. Bochmann, *Chem. Commun.*, 2012, **48**, 7247-7249.
198. G. Sanna, M. I. Pilo, G. Minghetti, M. A. Cinellu, N. Spano and R. Seeber, *Inorg. Chim. Acta*, 2000, **310**, 34-40.
199. G. Marcon, S. Carotti, M. Coronello, L. Messori, E. Mini, P. Orioli, T. Mazzei, M. A. Cinellu and G. Minghetti, *J. Med. Chem.* 2002, **45**, 1672-1677.
200. M. A. Cinellu, G. Minghetti, M. V. Pinna, S. Stoccoro, A. Zucca and M. Manassero, *J. Chem. Soc., Dalton Trans.*, 2000, 1261-1265.
201. J. A. T. O'Neill, G. M. Rosair and A.-L. Lee, *Catal. Sci. Technol.*, 2012, **2**, 1818-1821.
202. P. Schwerdtfeger, *J. Am. Chem. Soc.*, 1989, **111**, 7261-7262.
203. *Chemistry of the Elements (Second Edition)*, eds. N. N. Greenwood and A. Earnshaw, Butterworth-Heinemann, Oxford, 1997, pp. 1173-1200.
204. B. Bertrand, M. R. M. Williams and M. Bochmann, *Chem. Eur. J.*, 2018, **24**, 11840-11851.
205. M. Albayer, R. Corbo and J. L. Dutton, *Chem. Commun.*, 2018, **54**, 6832-6834.
206. L. S. Hollis and S. J. Lippard, *J. Am. Chem. Soc.*, 1983, **105**, 4293-4299.
207. K. Czerwińska, M. Golec, M. Skonieczna, J. Palion-Gazda, D. Zygadło, A. Szlapa-Kula, S. Krompiec, B. Machura and A. Szurko, *Dalton Trans.*, 2017, **46**, 3381-3392.
208. B. P. Block and J. C. Bailar, *J. Am. Chem. Soc.*, 1951, **73**, 4722-4725.
209. R. T. Mertens, J. H. Kim, W. C. Jennings, S. Parkin and S. G. Awuah, *Dalton Trans.*, 2019, **48**, 2093-2099.
210. L. Messori, F. Abbate, G. Marcon, P. Orioli, M. Fontani, E. Mini, T. Mazzei, S. Carotti, T. O'Connell and P. Zanello, *J. Med. Chem.*, 2000, **43**, 3541-3548.
211. C. Gabbiani, A. Casini and L. Messori, *Gold Bulletin*, 2007, **40**, 73-81.
212. G. Nardin, L. Randaccio, G. Annibale, G. Natile and B. Pitteri, *J. Chem. Soc., Dalton Trans.*, 1980, DOI: 10.1039/DT9800000220, 220-223.
213. S. Carotti, G. Marcon, M. Marussich, T. Mazzei, L. Messori, E. Mini and P. Orioli, *Chem. Biol. Interact.*, 2000, **125**, 29-38.
214. M. W. Johnson, A. G. DiPasquale, R. G. Bergman and F. D. Toste, *Organometallics*, 2014, **33**, 4169-4172.
215. A. S. K. Hashmi, J. P. Weyrauch, M. Rudolph and E. Kurpejović, *Angew. Chem. Int. Ed.*, 2004, **43**, 6545-6547.
216. L. Ronconi, L. Giovagnini, C. Marzano, F. Bettò, R. Graziani, G. Pilloni and D. Fregona, *Inorg. Chem.*, 2005, **44**, 1867-1881.
217. R. Kumar and C. Nevado, *Angew. Chem. Int. Ed.*, 2017, **56**, 1994-2015.
218. P. A. Bonnardel, R. V. Parish and R. G. Pritchard, *J. Chem. Soc., Dalton Trans.*, 1996, 3185-3193.
219. M. A. Cinellu, A. Zucca, S. Stoccoro, G. Minghetti, M. Manassero and M. Sansoni, *J. Chem. Soc., Dalton Trans.*, 1996, 4217-4225.
220. B. Bertrand, S. Spreckelmeyer, E. Bodio, F. Cocco, M. Picquet, P. Richard, P. Le Gendre, C. Orvig, M. A. Cinellu and A. Casini, *Dalton Trans.*, 2015, **44**, 11911-11918.
221. E. C. Constable and T. A. Leese, *Journal of Organometallic Chemistry*, 1989, **363**, 419-424.
222. V. K.-Y. Lo, K. K.-Y. Kung, M.-K. Wong and C.-M. Che, *J. Organomet. Chem.*, 2009, **694**, 583-591.
223. Q. Wu, C. Du, Y. Huang, X. Liu, Z. Long, F. Song and J. You, *Chem. Sci.*, 2015, **6**, 288-293.
224. N. Shaik, A. Martínez, I. Augustin, H. Giovinazzo, A. Varela-Ramírez, M. Sanaú, R. J. Aguilera and M. Contel, *Inorg. Chem.*, 2009, **48**, 1577-1587.
225. K.-H. Wong, K.-K. Cheung, M. C.-W. Chan and C.-M. Che, *Organometallics*, 1998, **17**, 3505-3511.
226. R. Kumar, A. Linden and C. Nevado, *Angew. Chem. Int. Ed.*, 2015, **54**, 14287-14290.
227. G. Alesso, M. A. Cinellu, S. Stoccoro, A. Zucca, G. Minghetti, C. Manassero, S. Rizzato, O. Swang and M. K. Ghosh, *Dalton Trans.*, 2010, **39**, 10293-10304.
228. A. Herbst, C. Bronner, P. Dechambenoit and O. S. Wenger, *Organometallics*, 2013, **32**, 1807-1814.
229. B. David, U. Monkowius, J. Rust, C. W. Lehmann, L. Hyzak and F. Mohr, *Dalton Trans.*, 2014, **43**, 11059-11066.
230. C.-Y. Wu, T. Horibe, C. B. Jacobsen and F. D. Toste, *Nature*, 2015, **517**, 449.
231. P. T. Bohan and F. D. Toste, *J. Am. Chem. Soc.*, 2017, **139**, 11016-11019.
232. C.-W. Chan, W.-T. Wong and C.-M. Che, *Inorg. Chem.*, 1994, **33**, 1266-1272.
233. R. Kumar, A. Linden and C. Nevado, *J. Am. Chem. Soc.*, 2016, **138**, 13790-13793.
234. N. P. Mankad and F. D. Toste, *J. Am. Chem. Soc.*, 2010, **132**, 12859-12861.
235. M. S. Winston, W. J. Wolf and F. D. Toste, *J. Am. Chem. Soc.*, 2015, **137**, 7921-7928.
236. N. P. Mankad and F. D. Toste, *Chem. Sci.*, 2012, **3**, 72-76.
237. M. Albayer, L. Sharp-Bucknall, N. Withanage, G. Armendariz-Vidales, C. F. Hogan and J. L. Dutton, *Inorg. Chem.*, 2020, **59**, 2765-2770.

238. A. Pérez-Bitrián, M. Baya, J. M. Casas, A. Martín, B. Menjón and J. Orduna, *Angew. Chem. Int. Ed.*, 2018, **57**, 6517-6521.
239. M. A. Ellwanger, S. Steinhauer, P. Golz, T. Braun and S. Riedel, *Angew. Chem. Int. Ed.*, 2018, **57**, 7210-7214.

Chapter 2

Hydrogen atom transfer reactivity by a gold-hydroxide complex

The work described in this chapter has been published in an article in *Inorganic Chemistry*.¹ The ¹H NMR kinetics were performed by Dr. John O'Brien. The XRD data collection and refinement was performed by Dr. Brendan Twamley.

Reproduced in part with permission from: Lovisari, M.; McDonald, A.R., *Inorg. Chem.*, **2020**, *59*, 6, 3659-3665.

2.1 Introduction

Both in homogeneous and heterogeneous catalysis, cationic Au species have proved to be relevant electrophilic oxidants. Au^{III} complexes have proven to be excellent catalysts for various classes of oxidation reactions, such as alkane oxygenation,² olefin epoxidation,^{3,4} oxidative cross-couplings,^{5,6} and alkyne hydroamination.⁷ Au^{III}-OH species have been proposed as the active species in the oxidation of carbon monoxide (CO) by Au supported on metal oxides,^{8,9} while in other cases the active oxidant has been postulated to be a terminal Au^{III}-oxo (Au^{III}=O) species, both in homogeneous⁴ and heterogeneous oxidations.^{8,10,11} A terminal Au^{III}=O complex remains elusive precluding insight into its reactivity properties. Given the expected high basicity of a terminal Au^{III}=O, its protonation might be favored to yield Au^{III}-OH as the active oxidant. Bis- μ -oxo-Au^{III}₂ species have been shown to be adequate oxidants in olefin hydroxylation and epoxidation.^{4,12,13} Bochmann and coworkers have shown how a Au^{III}-OH complex, supported by a cyclometallated CNC ligand, allowed the isolation of Au^{III}-peroxide and -hydroperoxide complexes and showed OAT reactivity towards phosphines.¹⁴ Despite the existence of stable Au^{III}-OH complexes,¹⁴⁻¹⁷ little attention has been dedicated to their capability to perform oxidation chemistry. We believed that the reported complex [Au(OH)(terpy)](ClO₄)₂¹⁸ (terpy = 2,2':6',2'-terpyridine) (**1**) was the ideal candidate to allow us to explore the oxidation reactivity of this class of compounds in order to gain mechanistic insights relevant to putative intermediates in Au oxidation catalysis. In this chapter we describe the characterization in polar aprotic solvents of [Au(OH)(terpy)](ClO₄)₂ and its reactivity towards substrates bearing C-H and O-H bonds.

2.2 Characterization of [Au^{III}(OH)terpy)](ClO₄)₂ and [Au^{III}(OD)terpy)](ClO₄)₂ in polar aprotic solvents

Complex **1** was synthesized as reported.¹⁸ The identity and purity of **1** was confirmed by ¹H nuclear magnetic resonance (NMR) spectroscopy, attenuated total reflectance Fourier transform infrared (ATR-FTIR) spectroscopy, and mass spectrometry. The ¹H NMR spectra of **1** in DMSO-D₆ (Figure 2.1) and DMF-D₇ (Figure 2.2) displayed comparable resonances, in agreement with those reported for similar complexes.¹⁹ The integrity of the hydroxide ligand in these solvents was confirmed by the presence of a signal at $\delta = 6.35$ ppm in DMSO-D₆ (Figure 2.1) and $\delta = 6.65$ ppm in DMF-D₇

(Figure 2.2). This signal disappeared upon addition of a drop of D₂O and when the analogous [Au(OD)(terpy)](ClO₄)₂ (**2**) was independently synthesized (Figures A1, A2).

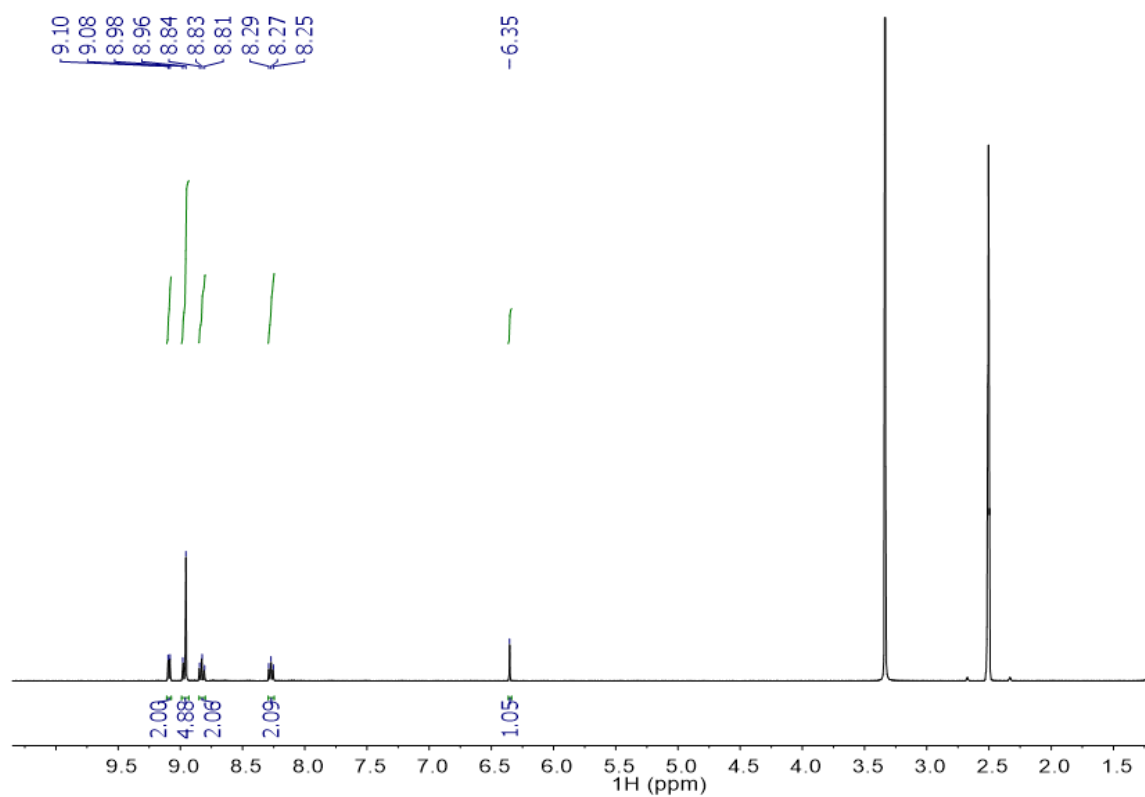


Figure 2.1. ¹H NMR spectrum of **1** in DMSO-D₆. The signal at 6.35 ppm is assigned to the hydroxide proton.

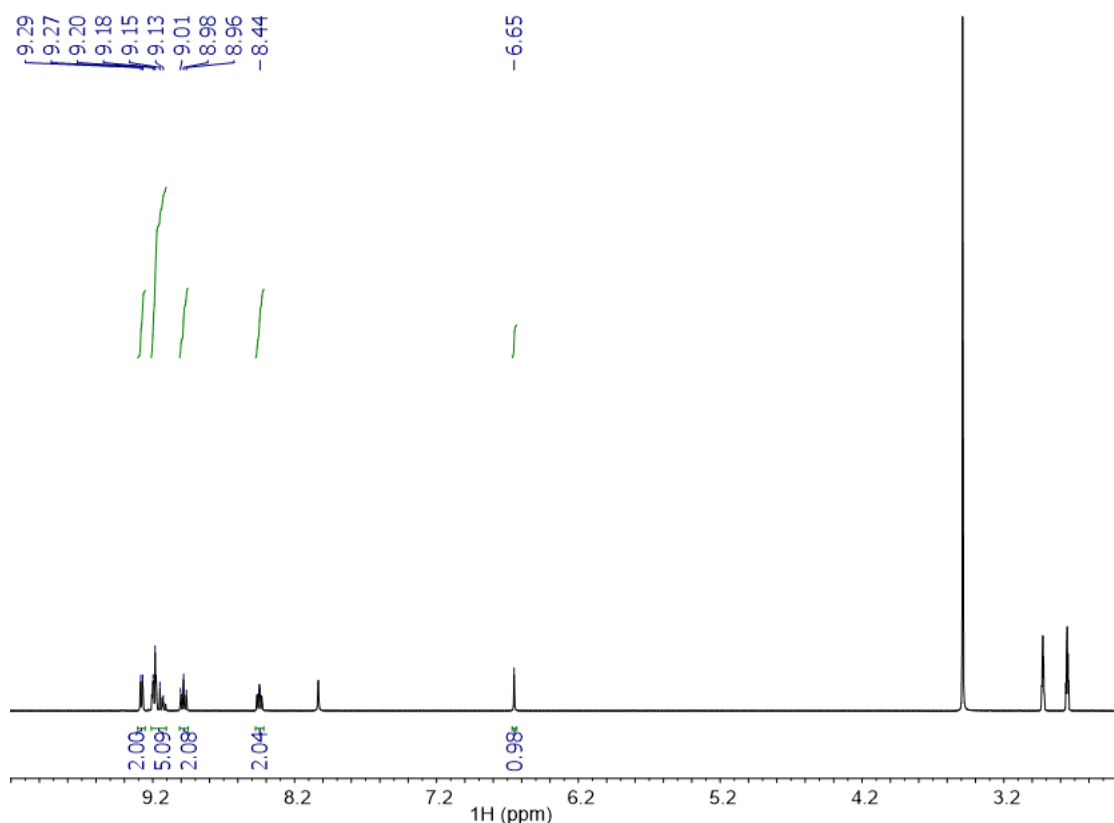


Figure 2.2. ¹H NMR spectrum of **1** in DMF-D₇. The signal at 6.65 ppm is assigned to the hydroxide proton.

Complex **2** was synthesized analogously to complex **1** but using D₂O instead of H₂O as a solvent. The NMR of this complex appeared analogous to the one of **1** apart from the resonance at 6.35 ppm (Figure A4). This enabled us to confirm the assignment of this peak to the O–H proton. The ATR-FTIR spectrum of **2** (Figure 2.3) showed a peak at $\nu = 2430 \text{ cm}^{-1}$ which is consistent with an O–D stretching. In fact, considering the O–H stretching in complex **1** falls at $\nu = 3425 \text{ cm}^{-1}$, the analogous O–D stretching this is expected to be shifted 862 cm^{-1} lower. The observed experimental shift of $\Delta\nu = 995 \text{ cm}^{-1}$ is in agreement with the calculated one, within the experimental error.

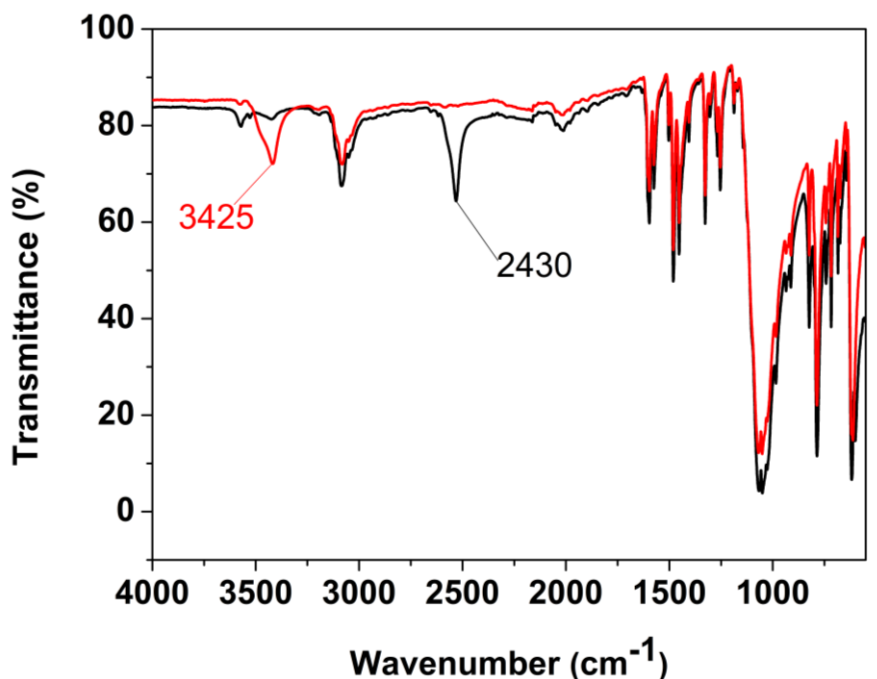


Figure 2.3. ATR-FTIR spectra of **1** (red trace) and **2** (black trace).

Mass Spectrometry confirmed the molecular structure of the complex (Figure A3). **1** displayed a yellow color in the solid state but yielded pink solutions once dissolved in polar aprotic solvents such as DMF ($\lambda_{\text{max}} = 545 \text{ nm}$) and DMSO ($\lambda_{\text{max}} = 537 \text{ nm}$, Figure 2.4). Similar solvatochromism has been observed in analogous d^8 complexes containing polypyridyl ligands.¹⁹⁻²¹ We ascribed this behaviour to a perturbation of the solvation sphere of the hydroxide ancillary ligand, which might be affected by the change in the hydrogen bonding network. The low energy transition in electronic absorption spectra of similar Au^{III} complexes has in fact been assigned as a charge transfer band resulting from LMCT (ligand-to-metal charge transfer) and ILCT (intra-ligand charge transfer) contributions.^{19,20,22} The cyclic voltammogram of **1** showed one irreversible reduction peak $E_{\text{red}} = -0.13 \text{ V}$ versus the ferrocene/ferrocenium (Fc/Fc^+) standard (Figure A5). Most commonly, Au^{III} complexes supported by non-cyclometallating ligands present two reduction peaks: one relative to the reduction of Au^{III} to Au^{I} and another one at more negative potential relative to the reduction of Au^{I} to Au^0 .^{16,23,24} Similarly to **1** though, other complexes such as $[\text{Au}(\text{OH})_2(\text{bipy})][\text{PF}_6]$ (bipy = 2,2'-bipyridine) reported only one irreversible reduction peak relative to the Au^{III} to Au^0 reduction.²³ **1** was thus a weak oxidant which maintained its hydroxide ligand in a variety of polar aprotic solvents.

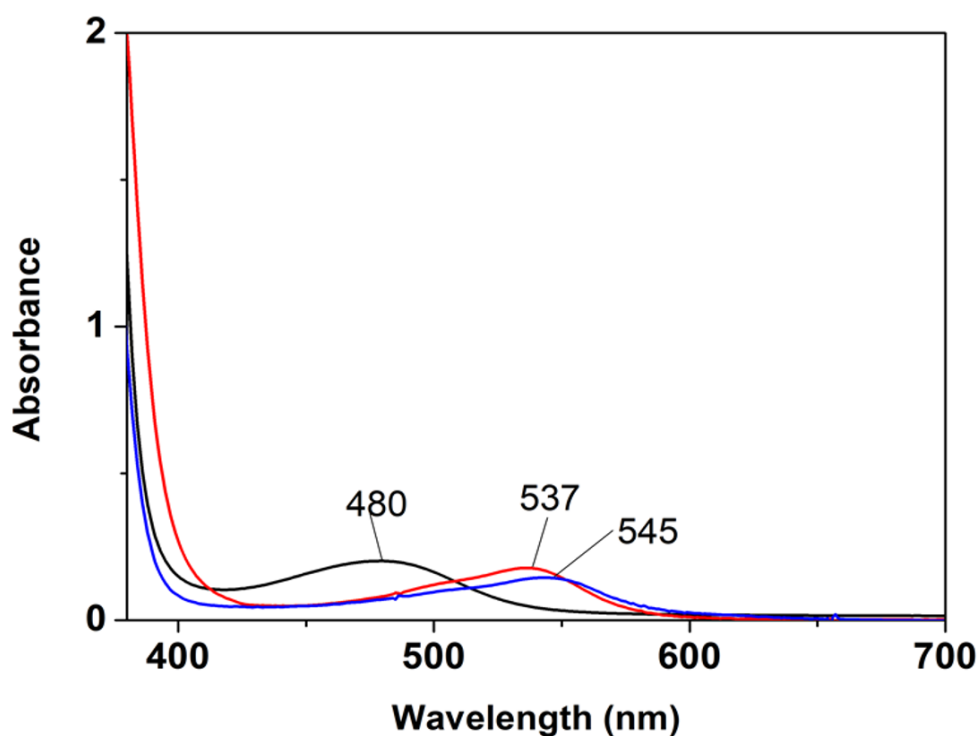


Figure 2.4. Electronic absorption spectrum of **1** in water (black trace), DMSO (red trace) and DMF (blue trace).

2.3 Reactivity of $[\text{Au}^{\text{III}}(\text{OH})\text{terpy}](\text{ClO}_4)_2$ with C–H bonds

We started exploring the reactivity of **1** with substrates bearing C–H bonds by monitoring changes by electronic absorption spectroscopy at 25°C in DMF. **1** (0.55 mM) was reacted with 1,4-cyclohexadiene (CHD, 1000 equiv.), resulting in a change in its electronic absorption spectrum (Figure 2.5). An initial growth of features at $\lambda = 545, 630$ nm was observed within 300 s, followed by a slower growth in the region between $\lambda = 400\text{--}1000$ nm over 2000 s, together with a drop in the intensity of the bands at $\lambda < 380$ nm. During the latter process a dark purple precipitate was observed, which we attribute to colloidal Au formation.^{22, 23, 25} We postulated that the initial reaction was the oxidation of CHD by **1** to yield a reduced form of **1** and benzene (Scheme 3.1 a).

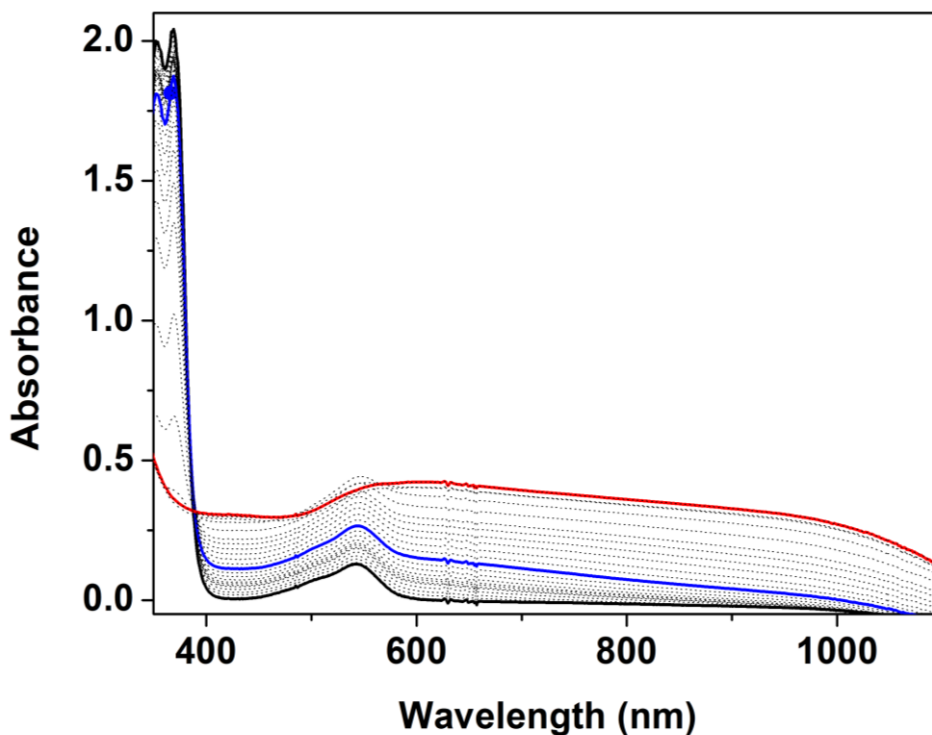
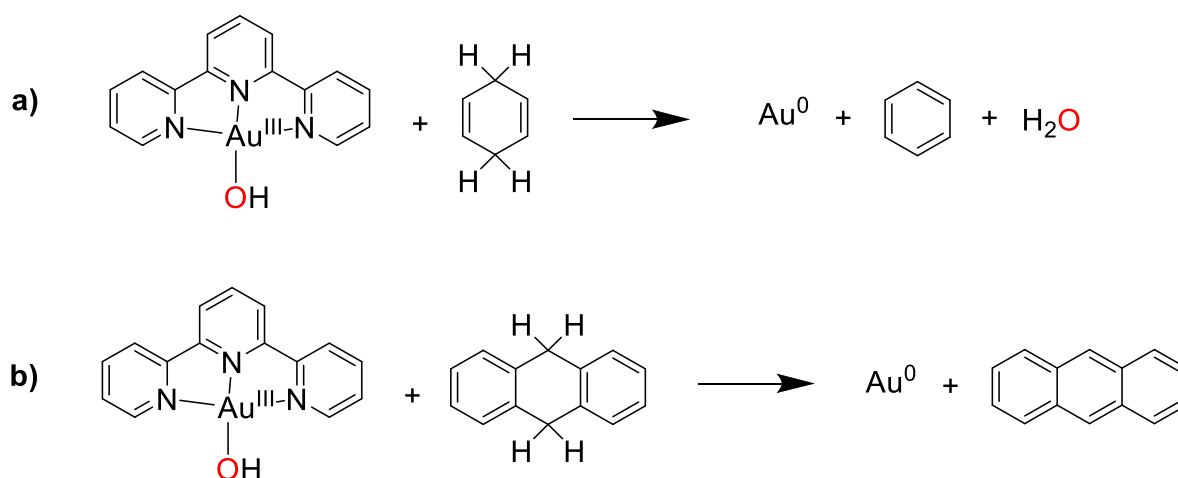


Figure 2.5. Electronic absorption spectra of the reaction between **1** (DMF, 25 °C, 0.55 mM) and CHD (1000 equiv.). black trace = 0 s; blue trace = 300 s; red trace = 2000 s.



Scheme 2.1. a) Reaction of **1** with CHD with the final identified products; b) Reaction of **1** with DHA with the final identified products.

To monitor the reaction by ^1H NMR, the same reaction was performed in $\text{DMSO-}d_6$ (25 equiv. CHD, Figure 2.6). We observed the growth in intensity of a signal at $\delta = 7.36$ ppm over 24 h from the mixing of the reagents, which was assigned to the C–H resonances of benzene.²⁶ A change of the resonances of the complex between 8 and 9.5 ppm and its complete conversion into a new species was also observed (Figure 2.6). The ^1H NMR spectra also showed a significant shift and

broadening of the residual signal attributed to H₂O ($\delta = 3.32$ ppm to $\delta = 3.73$ ppm). Previous reports showed that increased water content can shift H₂O resonances downfield,²⁷ and notably a progressive peak shift is evident in DMSO-D₆ mixtures with variable water content.²⁸

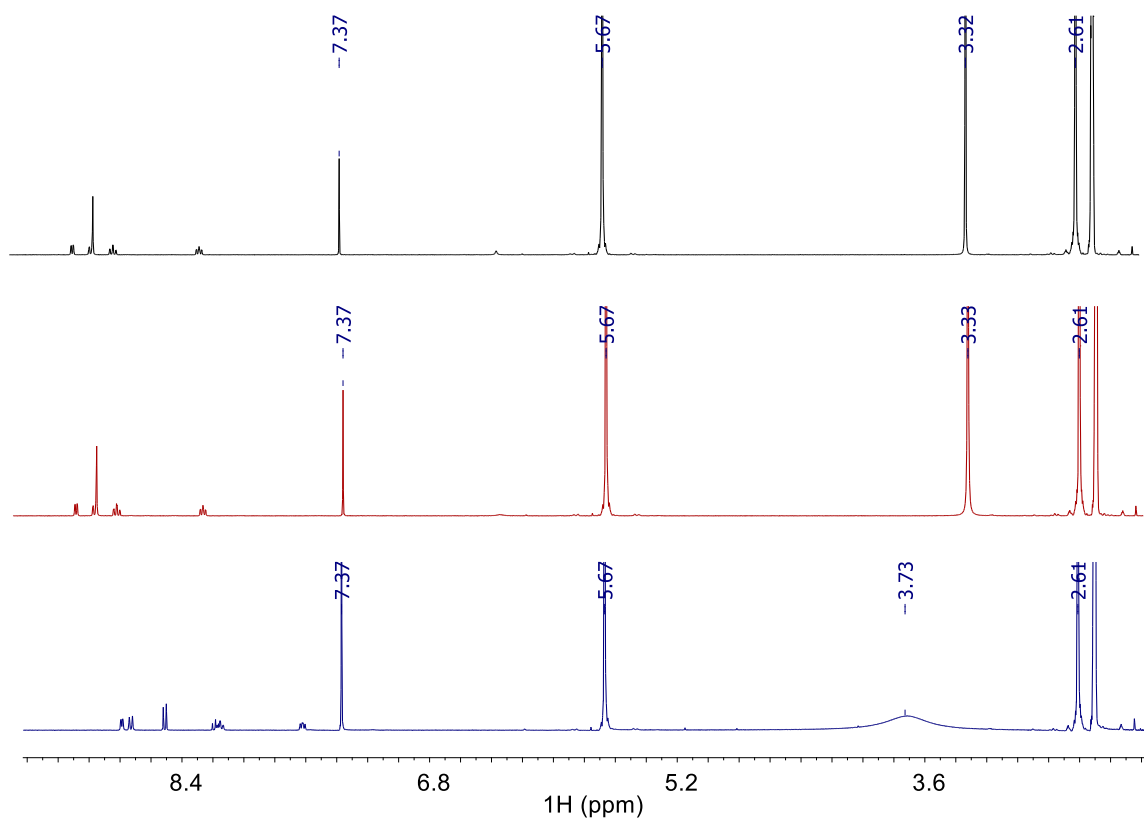


Figure 2.6. ¹H NMR spectra (400 MHz, DMSO-D₆) of the reaction between complex **1** and 25 equiv. of CHD. Black trace = 0 s, red trace = 600 s, blue trace = 24 h.

This observation confirmed that the water content during the reaction between **1** and CHD increased significantly. The experiment was repeated by electronic absorption spectroscopy and ¹H NMR on a different scale (100 equiv. CHD, Figure A6) to allow a quantification of the product and a monitoring of the benzene formation over time by ¹H NMR. A *pseudo*-first order constant (k_{obs}) for the rate of benzene formation was determined from the ¹H NMR data to be $1.2 \times 10^{-3} \text{ s}^{-1}$ in DMSO-D₆. The yield of benzene was determined to be $90 \pm 15\%$ with respect to **1** if each molecule of complex was responsible for one H-atom transfer (Table 2.1). In fact, the oxidation of CHD to benzene requires that two H-atoms are removed. The calculation above takes this into account. Given the observation of colloidal gold at the end of the reaction, we cannot exclude that 1, 2, or 3 electrons and protons might be theoretically transferred to each equivalent of **1** which could lower the estimated yield of benzene with respect to **1**. Combined with the electronic absorption analysis,

these results show that **1** was capable of oxidizing CHD to yield benzene, presumably through a proton-coupled electron transfer (PCET) oxidation.

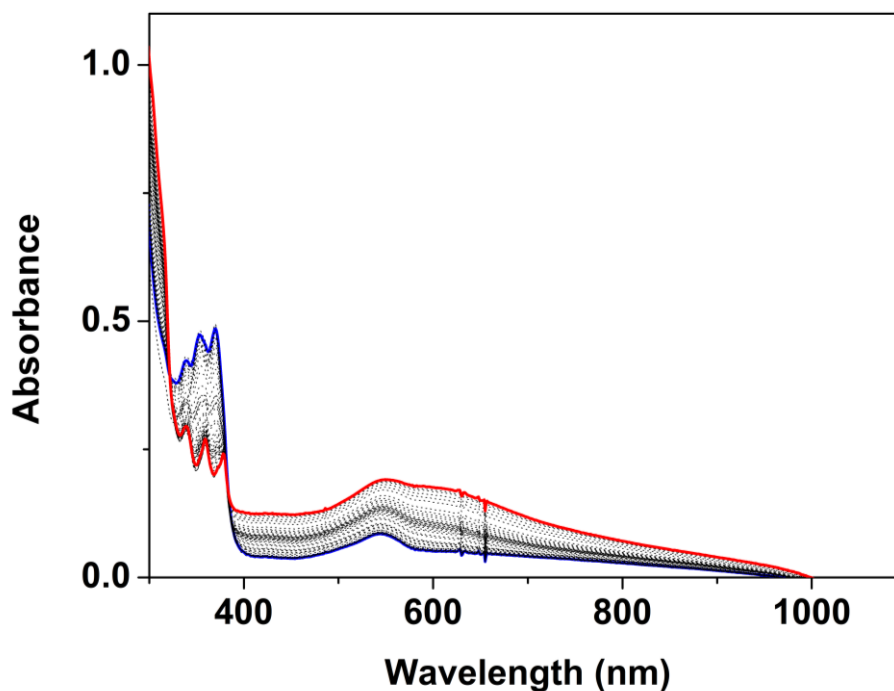


Figure 2.7. Electronic absorption spectra of the reaction between complex **1** (0.15 mM, DMF, 25 °C) and DHA (500 equiv.). blue trace = 0 s; red trace = 2800 s.

Complex **1** (DMF, 25 °C, 0.15 mM) also reacted with 9,10-dihydroanthracene (DHA, > 200 equiv.). As for the reaction with CHD, the electronic absorption spectra showed a slow increase of the bands at $\lambda = 545, 630$ nm, followed by indications of colloidal Au formation (Figure 2.7). At the end of the reaction, which appeared to be very slow, the characteristic absorption bands of anthracene were observed ($\lambda = 341, 360$ and 379 nm in DMF). Anthracene formation was confirmed by gas chromatography (GC) with a measured yield of $65 \pm 25\%$ with respect to **1** (Table 2.1). Note that no oxygen-containing organic products (e.g. anthraquinone, anthrone) were identified by gas chromatography. This confirmed that **1** was reacting with DHA to yield anthracene (Scheme 2.1 b), presumably as a result of PCET oxidation.

The rate of the reaction with DHA was measured by monitoring the decay of the band at $\lambda = 369$ nm, assigned to complex **1**. *Pseudo*-first order rate constants (k_{obs}) were obtained by exponential fitting of the plot of absorbance vs time up to 2800 s (Figure 2.7, Figure A7). A second-order rate constant (k_2) was determined from the slope of the plot of k_{obs} versus [DHA] to be $0.020 \text{ M}^{-1}\text{s}^{-1}$ (Figure 2.8). The same reaction was repeated with $[D]_4$ -DHA, showing $k_2 = 0.006 \text{ M}^{-1}\text{s}^{-1}$, yielding

a primary kinetic isotope effect (KIE) of 3.3 (Figure 2.8). This result suggested that the cleavage of the C–H bond is involved in the rate-determining step.

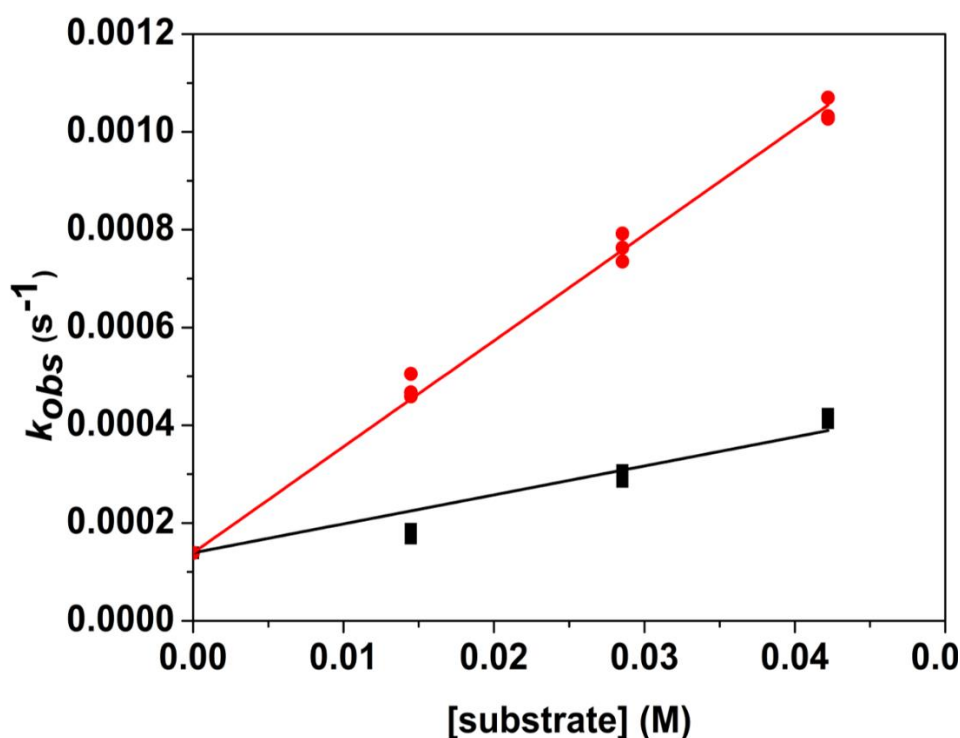


Figure 2.8. Plot of k_{obs} versus [substrate] determined for the reaction between complex **1** and $[D]_4$ -DHA (black trace) and $[H]_4$ -DHA (red trace).

This KIE value lies in the classical range (2-7) and in agreement for what observed for other high-valent metal-oxygen adducts (M–O–X), including hydroxides, in contrast to high-valent metal-oxo (M=O) oxidants. For M=O large KIEs (>10) have been reported, which have been explained to stem from tunneling effects.²⁹ The KIE value suggests that the rate-limiting step is proton or H-atom transfer.

For both hydrocarbon substrates we can obtain little mechanistic insight into the initial PCET reaction because the products that we can identify represent two-electron, two-proton PCET oxidised products, meaning exploration of the mechanism of the PCET is not possible. It is therefore also not possible to explore if Au^{III} as present in complex **1** was solely responsible for all PCET oxidation steps or if the reduced derivatives of **1** (Au^{II}, Au^I) also contributed to the oxidation of CHD and DHA. Therefore, to obtain more insights in the mechanism of reaction of **1**, we explored its reaction with substrates bearing O–H bonds.

2.4 Reactivity of $[\text{Au}^{\text{III}}(\text{OHterpy})](\text{ClO}_4)_2$ with O–H bonds

When 4-methoxy-2,6-di-*tert*-butylphenol (4- CH_3O -2,6-DTBP, 100 equiv.) was added to **1** (0.4 mM, DMF, 25 °C) an immediate reaction was observed. The electronic absorption spectrum displayed a sharp band at $\lambda = 407$ nm, alongside the growth of features at $\lambda = 545, 630$ nm (Figure 2.9). The band at $\lambda = 407$ nm reached a maximum after 160 s and subsequently slowly decayed. After 1000 s a dark purple precipitate was observed to form in the reaction mixture, as observed for the latter stages of CHD and DHA oxidations.

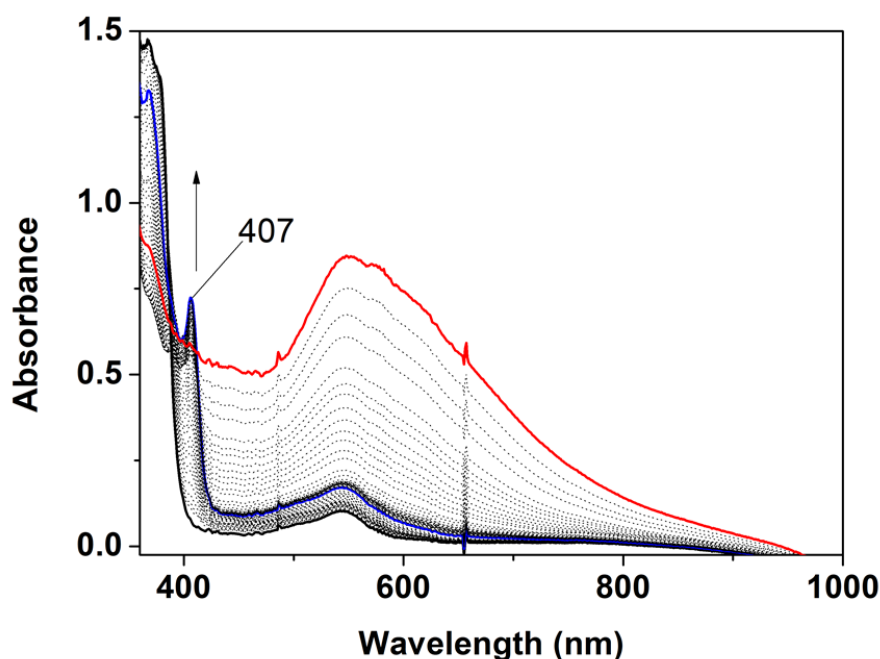


Figure 2.9. Electronic absorption spectra of the reaction of **1** (black trace) with 4- CH_3O -2,6-DTBP (100 equiv.) at 25 °C. blue trace = 160 s; red trace = 1000 s.

An X-band EPR spectrum of the reaction mixture prepared at 160 s (initial phase of the reaction) showed an isotropic signal at $g = 2.00$ typical of an organic radical (Figure 2.10 left). We postulated it to be the 4-methoxy-2,6-di-*tert*-butylphenoxyl radical, which was confirmed by independent synthesis of this compound and comparison of its EPR spectra to that measured for the reaction mixture (Figure 2.10 right).³⁰ Likewise, the electronic absorption spectrum of the independently synthesized radical displayed a feature at $\lambda = 407$ nm (Figures A8-11). The yield of 4-methoxy-2,6-di-*tert*-butylphenoxyl radical was determined to be 80 ± 15 % by EPR and 85 ± 15 % by electronic absorption spectroscopy (Table 2.1, Figure A13) when a one-electron reaction is considered. Thus, the initial product of the reaction between **1** and 4- CH_3O -2,6-DTBP was 4-methoxy-2,6-di-*tert*-butylphenoxyl radical, presumably formed through PCET oxidation.

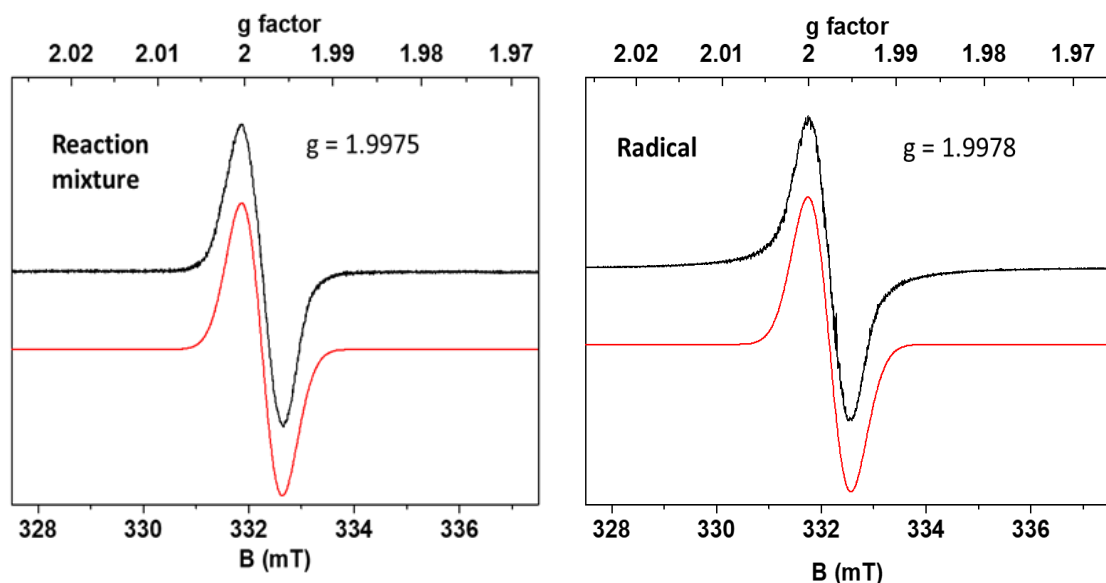


Figure 2.10. X-Band EPR spectra of the reaction mixture of **1** with 4-CH₃O-2,6-DTBP (left) and the independently synthesized phenoxyl radical (right). Black = experimental spectra, red = simulated spectra. The spectra were acquired from a frozen DMF solution and measured at 77 K with a 0.2 mW microwave power and a 0.2 mT modulation amplitude.

A plot of the absorbance at $\lambda_{\max} = 407$ nm versus time showed an initial phase (160 s, coinciding with the maximum yield of radical) with an exponential growth and a second phase showing its decay up to 400 s (Figure A12). *Pseudo*-first order rate constants (k_{obs}) were obtained by exponential fitting of the plot of absorbance vs time up to 160 s. The rate of this initial phase was shown to be dependent on [substrate] and the plot of the k_{obs} versus [substrate] exhibited a non-linear correlation (Figure 2.11 left). This was consistent with a saturation kinetic model, thus we employed the following kinetic equation to fit the obtained results: $k_{\text{obs}} = k_1[\text{substrate}]/(K + [\text{substrate}])$. A linearization of the data (Figure 2.11 right) was performed to determine k_1 (0.0305 s^{-1}), the maximum rate of the reaction, and K (0.016 M), the [substrate] at which half of the maximum rate was reached (Table 2.2).

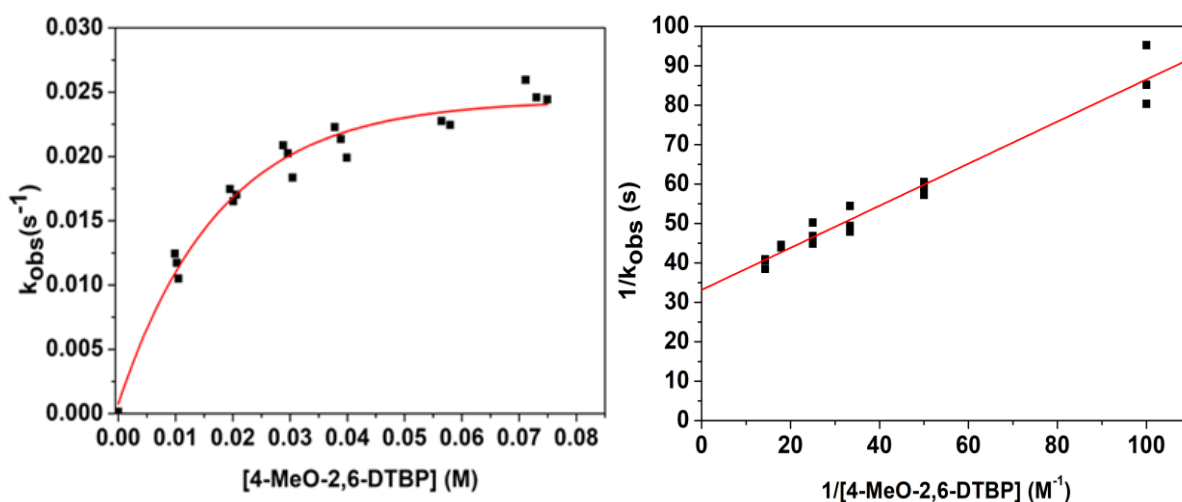


Figure 2.11. Left: Plot of k_{obs} against [4-CH₃O-2,6-DTBP] determined for the reaction between **1** and 4-CH₃O-2,6-DTBP. Right: Plot of $1/k_{obs}$ against $1/[4\text{-CH}_3\text{O-2,6-DTBP}]$.

The k_{obs} of the reaction of 4-CH₃O-2,6-DTBP with different concentrations of **1** was measured in saturating conditions (350 equiv. of substrate) in order to ensure a maximum rate was achieved in the saturating region. The linear correlation observed between k_{obs} and **1** suggested that the oxidation was first order in **1** in the range of concentrations explored (Figure A15).

The fate of the 4-methoxy-2,6-di-*tert*-butylphenoxy radical, after it reached its maximum yield, was explored by ¹H NMR in DMSO-D₆. A ¹H NMR of 4-CH₃O-2,6-DTBP showed resonances at $\delta = 6.52$ (O-H), 6.62 (ArCH), 3.66 (OCH₃), and 1.36 ppm (C(CH₃)₃) (Figure 2.12, Figure A16). Upon reaction of 15 equiv. of 4-CH₃O-2,6-DTBP with **1** in DMSO-D₆, these resonances disappeared together with the growth of new features at $\delta = 6.50$, 3.16, and 1.23 ppm. It should be noted that we were unable to identify the 4-methoxy-2,6-di-*tert*-butylphenoxy radical product by ¹H NMR, and thus focus on the yield of the 2-electron oxidized, two-proton lost product by ¹H NMR. The signals at $\delta = 6.50$ and 1.23 ppm have been attributed to 2,6-di-*tert*-butylquinone (2,6-DTBQ) and that at $\delta = 3.16$ ppm has been attributed to CH₃OH (Figure 2.12, Figure A17).²⁶

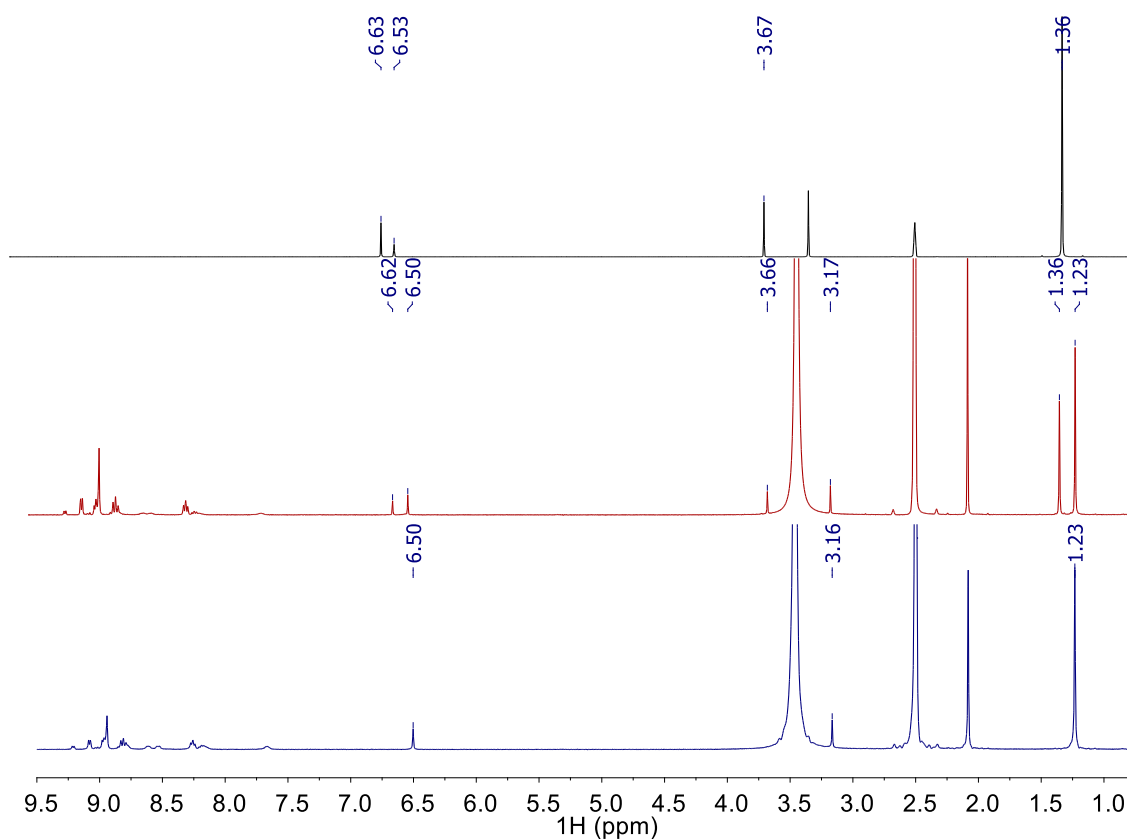


Figure 2.12. ^1H NMR in DMSO-D_6 of 4- CH_3O -2,6-DTBP (black) and of **1** in the presence of 4- CH_3O -2,6-DTBP (15 equiv.). Red = ~ 300 s, blue = ~ 600 s from the mixing of reagents (blue trace). H_2O : $\delta = 3.32\text{-}3.46$ ppm.

Finally, as for CHD, we observed a shift and broadening in the H_2O residual peak ($\delta = 3.33$ ppm to $\delta = 3.46$ ppm). We used time-monitored ^1H NMR to explore the rate of formation of 2,6-DTBQ (Figure 2.13). When 25 equiv. of 4- CH_3O -2,6-DTBP were added to **1**, the same disappearance of the peaks relative to the substrate was observed, together with the growth of the resonances of the quinone product and the peak relative to methanol. (Figure 2.13) The observed shift in the water peak was more pronounced in these conditions ($\delta = 3.33$ ppm to $\delta = 3.90$ ppm, Figure 2.12). The k_{obs} for the rate of formation of 2,6-DTBQ measured with this kinetic experiment was 0.0034 s^{-1} , one order of magnitude lower than the k_1 calculated for the formation of the radical (Table 2.1, Figure A18). The yield of 2,6-DTBQ was quantified by GC as $80 \pm 12\%$ when a 2-electron oxidation was considered (Table 2.1). These observations were consistent with the formation of the radical occurring first followed by its further decay to 2,6-DTBQ and CH_3OH , supporting a mechanism that has been previously proposed in literature for the oxidation of 4- CH_3O -2,6-DTBP (Scheme 2.2).³¹

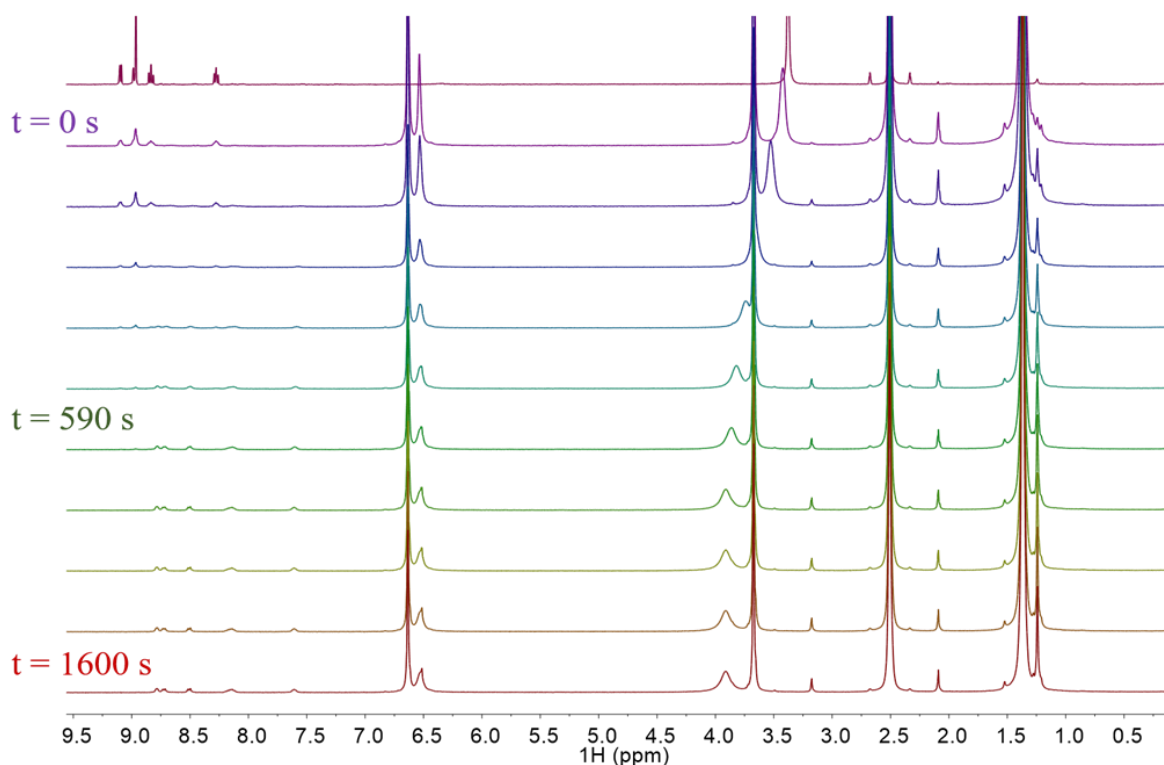
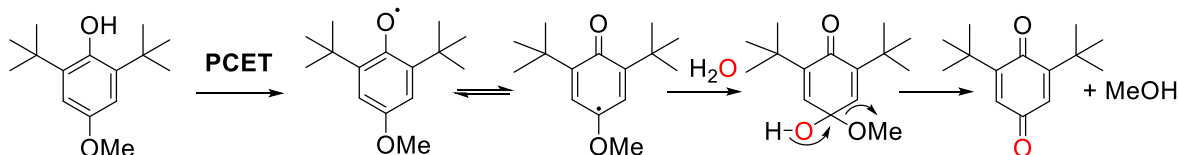


Figure 2.13. Selected $^1\text{H-NMR}$ spectra in DMSO-D_6 for the reaction between **1** and 4- $\text{CH}_3\text{O-2,6-DTBP}$ (25 equiv.) monitored for 1600 s.



Scheme 2.2. Proposed mechanism of formation of DTBQ by PCET oxidation of 4- $\text{CH}_3\text{O-2,6-DTBP}$.

We observed no difference in the k_I for the 4-methoxy-2,6-di-*tert*-butylphenoxy radical formation in the reaction between **1** and 4- $\text{CH}_3\text{O-2,6-DTBP}$ in an aerobic versus an anaerobic atmosphere (0.0318 s^{-1} vs 0.0305 s^{-1} , respectively, Table 2.2, Figures A19-22). This showed that O_2 played no significant role in the oxidation of phenols by complex **1**. For the reaction of **1** with deuterated 4- $\text{CH}_3\text{O-2,6-DTBP}$ (Figure A23) a $k_I = 0.0106 \text{ s}^{-1}$ was determined, yielding a KIE of 2.9 (Figure 2.14), which suggests that proton or H-atom transfer was rate-limiting in the oxidation of phenols by the complex. This value lies in the classical range (2-7), analogously to the one observed for the reaction of **1** with hydrocarbons (KIE = 3.3). This observation is in agreement with the data reported for other high-valent metal-hydroxides²⁹ and suggests that the cleavage of the O–H and C–H bonds of the substrates are involved in the rate-determining step of the oxidation reaction.

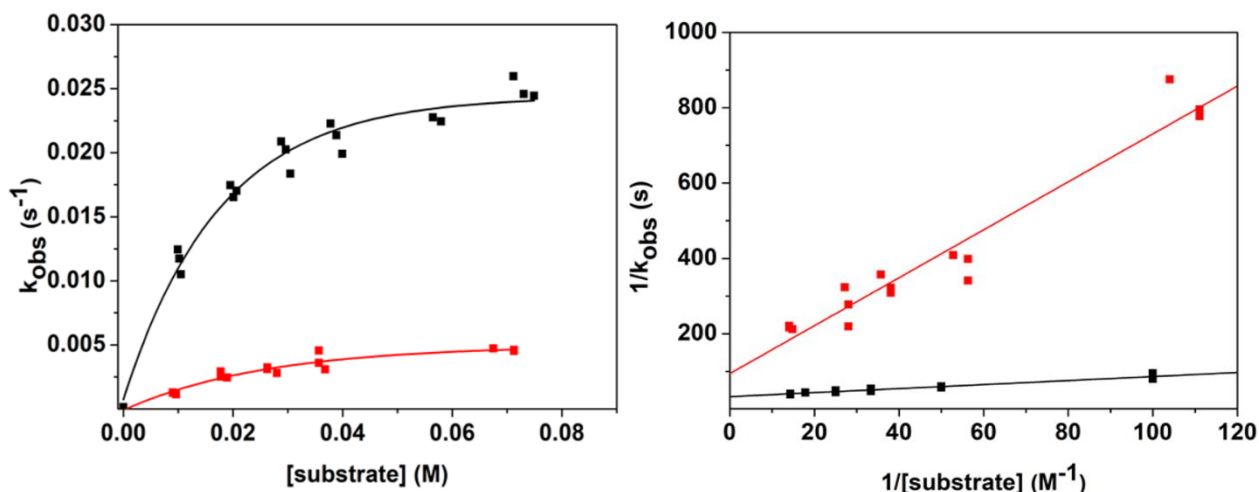


Figure 2.14. Left: plot of k_{obs} versus [substrate] determined for the reaction between complex **1** and 4-proto-CH₃O-2,6-DTBP (black trace) and 4-deutero-CH₃O-2,6-DTBP (red trace). Right: plot of $1/k_{\text{obs}}$ against $1/[\text{substrate}]$ determined for the reaction between complex **1** and 4-proto-CH₃O-2,6-DTBP (black trace) and 4-deutero-CH₃O-2,6-DTBP (red trace).

1 was then reacted with 2,4,6-tri-*tert*-butylphenol (2,4,6-TTBP, DMF, 25 °C, 0.4 mM), where the electronic absorption spectrum showed the formation of a band at $\lambda = 402$ nm (maximum yield at 1500 s), together with the slower growth of features at $\lambda = 545, 630$ nm (Figure 2.15). An X-band EPR spectrum after 1500 s showed a signal at $g = 2.00$ (Figure 2.16, left). The 2,4,6-tri-*tert*-butylphenoxy radical was synthesized independently (Figure 2.16, right),³² and was found to display the same EPR g -values and electronic absorption features, confirming that the 2,4,6-tri-*tert*-butylphenoxy radical was the product (Figures A24-27). The yield of radical was determined to be $88 \pm 15\%$ by EPR and $85 \pm 20\%$ by electronic absorption spectroscopy, when a 1-electron reaction was considered (Table 2.1). k_1 for this reaction was determined to be 0.0014 s^{-1} (Figure A28-31, Table 2.2). The final product of this reaction was found to be 2,6-DTBQ and its yield was calculated by GC to be $120 \pm 60\%$ for a net 2-electron reaction (Table 2.1). Complex **1** also reacted with 2,6-di-*tert*-butylphenol (2,6-DTBP, > 10 equiv.) showing the growth of a band at $\lambda = 426$ nm and the features at $\lambda = 545, 630$ nm (Figure 2.17). ESI-MS analysis of the post-reaction mixture showed the presence of 3,3',5,5'-tetra-*tert*-butyl-[1,1'-bis(cyclohexane)]-2,2',5,5'-tetraene-4,4'-dione (TTBTD, Figure A32). This product was presumably formed by the coupling of two 2,6-di-*tert*-butylphenoxy radicals formed by PCET oxidation of 2,6-DTBP (Scheme 2.3).³³

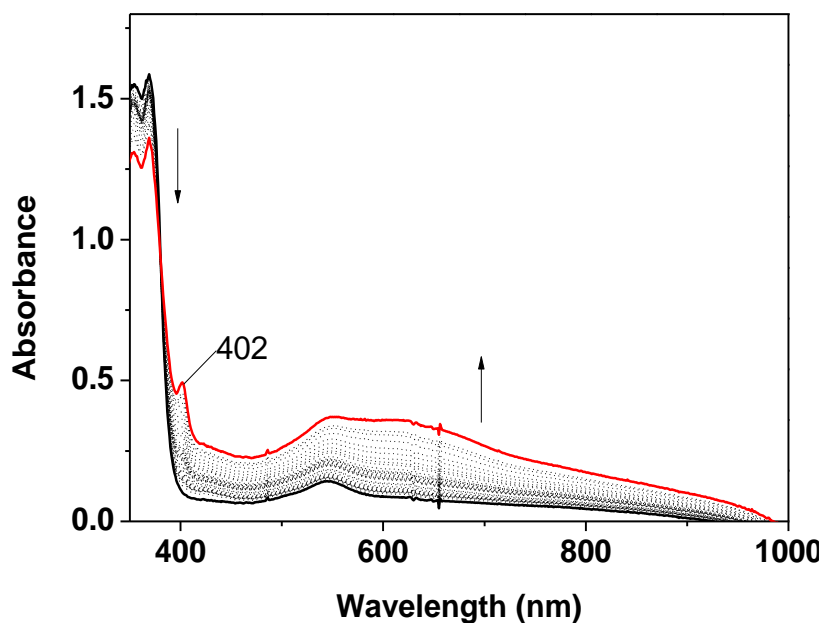


Figure 2.15. Electronic absorption spectra of the reaction of **1** (DMF, 25°C, 0.4 mM) with 2,4,6-TTBP (500 equiv.) monitored for 2000 s. black trace = 0s, red trace = 2000 s.

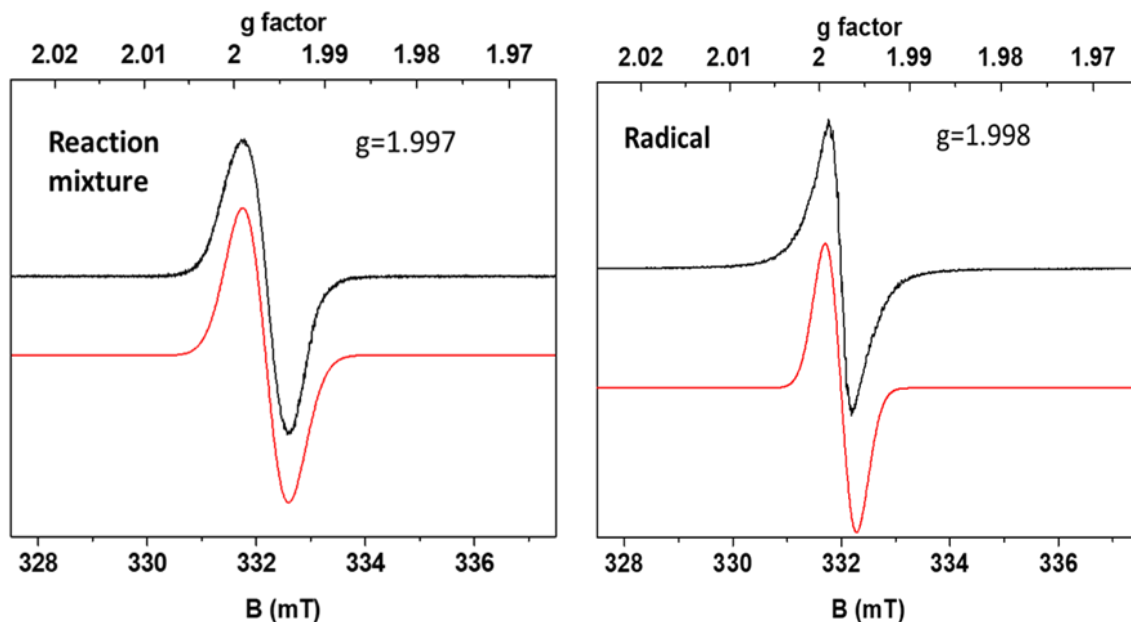


Figure 2.16. X-Band EPR spectra of the reaction mixture of **1** with 2,4,6-TTBP (left) and the independently synthesized 2,4,6-tris-*tert*-butylphenoxy radical (right). Black: experimental spectra, Red: simulated spectra. The spectra were acquired from a frozen DMF solution and measured at 77 K with a 0.2 mW microwave power and 0.2 mT modulation amplitude.

An electronic absorption spectrum of pure TTBDT demonstrated that the feature at $\lambda = 426$ nm belonged to TTBDT. ^1H NMR spectroscopy confirmed the formation of TTBDT (10% yield for a

2-electron reaction, Table 2.2, Figure A33-39) and 2,6-DTBQ (10% yield for a 2-electron reaction, Table 2.2, Scheme 2.3). Given the sigmoidal trend observed by following the absorbance at $\lambda = 426$ nm over time, we deemed the kinetics of the formation of TTBDT not related to the initial PCET by **1**. These data could not be compared with the formation of the radicals for the previous substrates, since it would not provide insight into the initial PCET reaction. Formation of TTBDT was observed when **1** was reacted with 4-X-2,6-DTBP (X = Br, NO₂), thus for the same reason we excluded these substrates from our kinetic analysis.

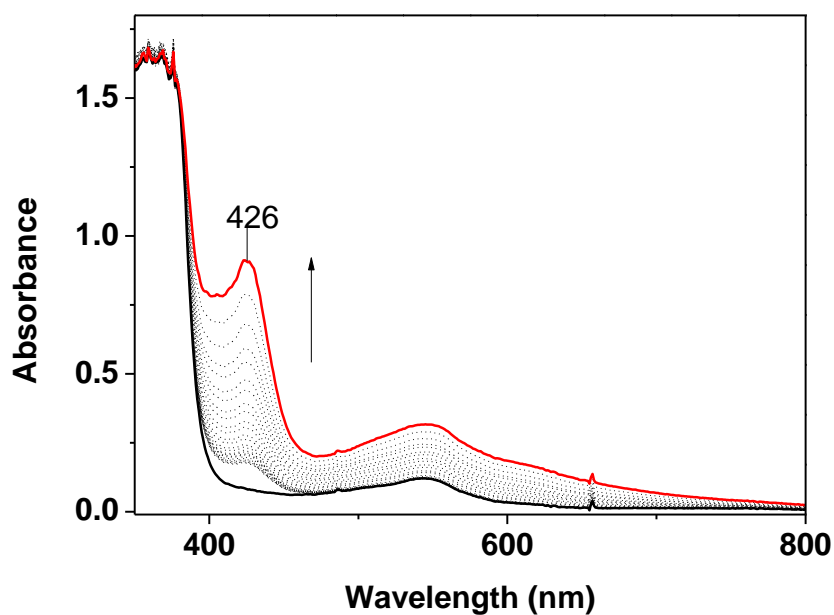
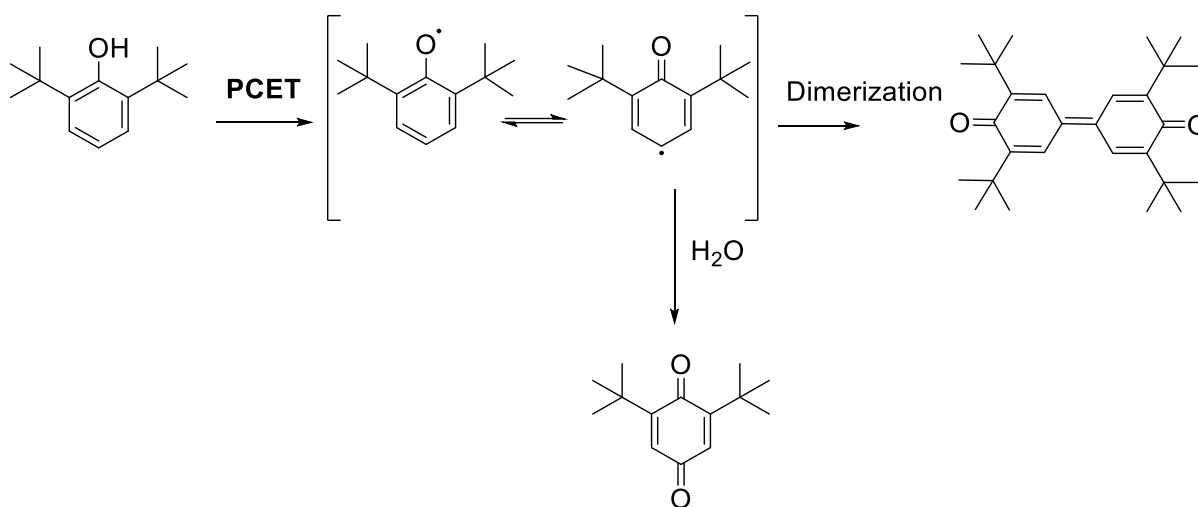


Figure 2.17. Electronic absorption spectra of the reaction between **1** (DMF, 25 °C, 0.45 mM) and 2,6-DTBP (300 equiv.), monitored for 1800 s.



Scheme 2.3. Proposed mechanism of formation of products TTBDT and 2,6-DTBQ by oxidation of 2,6-DTBP.

Complex **1** reacted with 4-X-1-hydroxy-2,2,6,6-tetramethyl-piperidines (4-X-TEMPOH, X = H, CH₃O, O). Upon reaction with 4-X-TEMPOH (>10 equiv.), the electronic absorption spectrum of **1** showed a drop of the feature at $\lambda = 369$ nm that was complete within 150 s (for TEMPOH), together with the increase in absorbance of the features at $\lambda = 545, 630$ nm over 1000 s, that was common for all substrates (Figure 2.18, Figure A40).

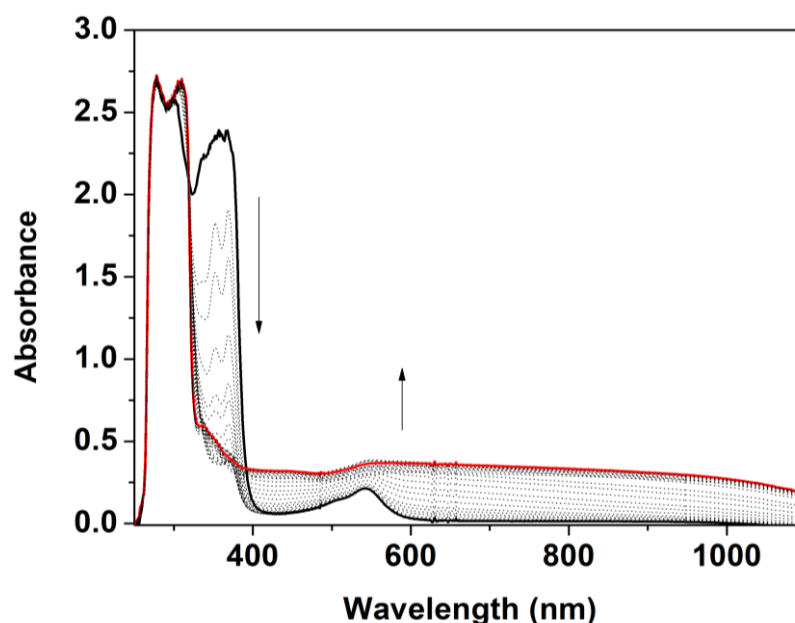


Figure 2.18. Electronic absorption spectra of the reaction of **1** (0.7 mM in DMF) with 4-H-TEMPOH (50 equiv.), monitored for 1000 s.

For 4-H-TEMPOH, an X-Band EPR spectrum of a frozen sample of the reaction mixture after 150 s showed a rhombic signal with $g_{av} = 2.00$ which was consistent with previously reported spectra of (2,2,6,6-tetramethyl-piperidin-1-yl)oxyl (TEMPO) (Figure 2.19).³⁴

The reactions with 4-CH₃O-TEMPOH and 4-oxo-TEMPOH gave comparable radical signals in similar time frames (Appendix). The yield of 4-X-TEMPO radicals was calculated to be $80 \pm 10\%$ for TEMPOH, $77 \pm 15\%$ for 4-CH₃O-TEMPOH, and $75 \pm 15\%$ for 4-oxo-TEMPOH by EPR, all considering a one-electron oxidation (Table 2.1).

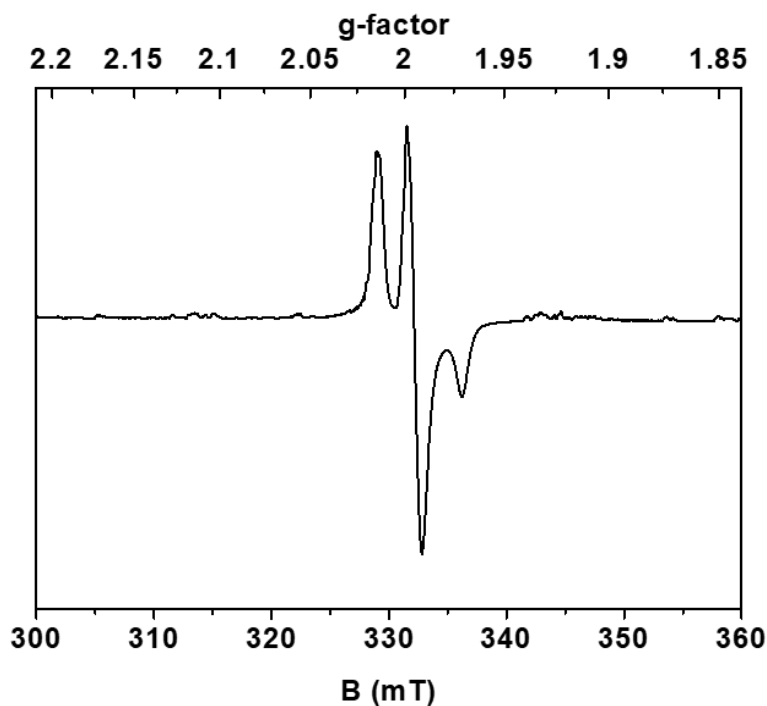


Figure 2.19. X-Band EPR spectrum of the reaction mixture of **1** with 4-H-TEMPOH (200 equiv.) after 150 s. The spectrum was acquired from a frozen DMF solution and measured at 77 K with a 2.02 mW microwave power and a 0.3 mT modulation amplitude.

We monitored the change at $\lambda = 369$ nm and obtained *pseudo*-first order rate constants (k_{obs}). As for the phenolic substrates, saturation kinetic behavior was observed. k_1 was calculated to be 0.808 s^{-1} for TEMPOH (Figures A41-42), 1.2 s^{-1} for 4-CH₃O-TEMPOH (Figures A43-46) and 0.49 s^{-1} for 4-oxo-TEMPOH (Figures A47-51), all approximately one order of magnitude higher than that observed for 4-CH₃O-2,6-DTBP (Table 2.2). In summary, as with 4-CH₃O-2,6-DTBP and 2,4,6-TTBP, the 4-X-TEMPOH family of substrates reacted with **1** yielding oxygen-based radical products in high yields (>75 %, calculated considering a one-electron oxidation with respect to the starting complex) and displaying *pseudo*-first order rates of reaction, indicating PCET oxidation by **1**.

Table 2.1. Yield of products identified from the reactions of substrates with **1**.

Substrate	Product	Stoichiometry	Yield (%)	Method		
4-CH ₃ O-2,6-DTBP	phenoxy radical	1-electron	82 ± 15	EPR		
			85 ± 15	UV-Vis		
2,4,6-TTBP	2,6-DTBQ	2-electrons	80 ± 12	GC-FID		
			phenoxy radical	1-electron	88 ± 15	EPR
				85 ± 20	UV-Vis	
2,6-DTBP	2,6-DTBQ	2-electrons	120 ± 60	GC-FID		
2,6-DTBP	TTBTD	2-electrons	10 ± 2	UV-Vis		
TEMPOH	TEMPO	1-electron	80 ± 10	EPR		
4-CH ₃ O-TEMPOH	4-CH ₃ O-TEMPO	1-electron	77 ± 15	EPR		
4-oxo-TEMPOH	4-oxo-TEMPO	1-electron	75 ± 15	EPR		
DHA	Anthracene	2-electrons	65 ± 25	GC-FID		
CHD	Benzene	2-electrons	90 ± 15	¹ H NMR		

2.5 Mechanistic insights

The kinetic analysis allowed us to determine values of k_1 for five different substrates bearing O–H bonds (Table 2.2). Plotting the k_1 values against the bond dissociation enthalpies (BDEs) of the O–H bonds in the substrates (BDE_{O-H}) in acetonitrile (given the absence in literature of values in DMF)³⁵, a linear correlation was observed (Figure A53). This is an indication of a concerted mechanism, such as hydrogen atom transfer (HAT) respect to non-concerted mechanism in which proton-transfer (PT) and electron-transfer (ET) are occurring stepwise. Gibbs energies of activation were derived from the measured k_1 values to determine a ΔG^\ddagger and plot against the change in O–H bond dissociation energy ($BDFE_{O-H}$) yielding a slope = 0.30

(Figure 2.19), which is close to the ideal value for hydrogen atom transfer (HAT) of 0.5 predicted by Marcus theory.^{36,37} This value falls in the range of $\Delta G^\ddagger/\Delta(\text{BDFE})$ slopes ascribed to HAT mechanisms (0.15 - 0.7) and indicates that HAT is the mechanism by which **1** oxidized these substrates.^{35,38} A much higher slope (0.99) has been reported for a non-concerted PCET mechanism.³⁹ It must be noted that BDFEs are not always available for all substrates in certain solvent environments, notably in this case the BDFEs in DMF weren't available in literature so we compared those in acetonitrile. The relative trend between substrates should be the same in different solvents, as observable by the values reported by Mayer and coworkers.³⁵ The BDFE value for 4-CH₃O-2,6-DTBP wasn't available in acetonitrile, thus it was estimated based on the values in DMSO and benzene (Table 2.2).³⁵ Furthermore, there is no correlation between k_1 and the pK_a of the substrates: the pK_a of TEMPO-H is reported to be 41 in acetonitrile³⁵, whereas that of 4-CH₃O-2,6-DTBP and 2,4,6-TTBP is reported to be 14.82 in the same solvent.⁴⁰ Also the correlation between k_1 and the redox potentials of the substrates is poor, since TEMPO-H is much more difficult to oxidize to its radical-cation ($E_{\text{ox}} = 0.71$ V vs Fc/Fc⁺ in CH₃CN)³⁵ than 4-CH₃O-2,6-DTBP ($E_{\text{ox}} = 0.53$ V vs Fc/Fc⁺ in CH₃CN).³¹ This strongly suggests that a concerted mechanism such as HAT is involved in the first step of the oxidation of these substrates by **1**.

Table 2.2. Kinetic parameters for radical formation from the reaction between **1** and O–H bonds.^{35,40} The value in italics is estimated.

Substrate	k_1 (s ⁻¹)	K (M ⁻¹)	BDFE_{O-H} (kcal/mol)
4-CH ₃ O-TEMPOH	1.2	-	65.0
4-oxo-TEMPOH	0.49	1.5	65.6
TEMPOH	0.808	0.016	66.5
[<i>H</i>]-4-CH ₃ O-2,6-DTBP	0.0305	0.016	74
[<i>D</i>]-4-CH ₃ O-2,6-DTBP	0.0106	0.067	-
2,4,6-TTBP	0.0014	0.025	77.1

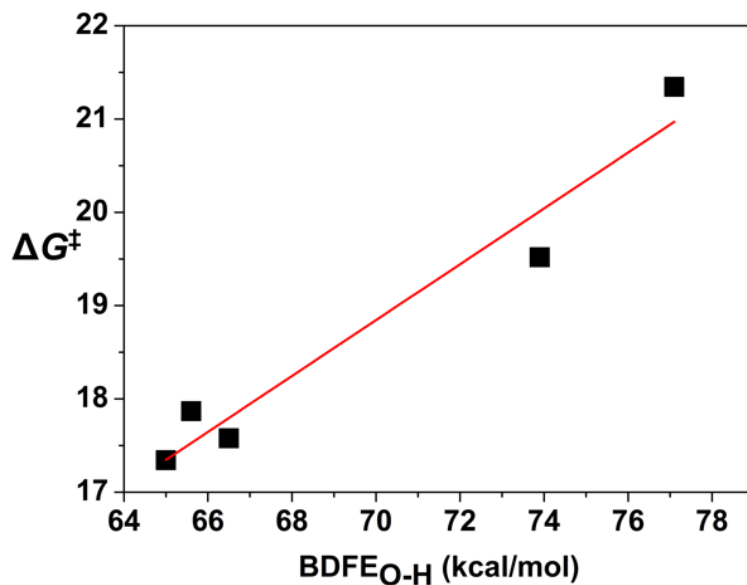


Figure 2.20. Plot of ΔG^\ddagger against the $\text{BDFE}_{\text{O-H}}$ of the substrates. The values of ΔG^\ddagger was determined from the calculated first-order constants k_1 via the Eyring equation (slope = 0.30).

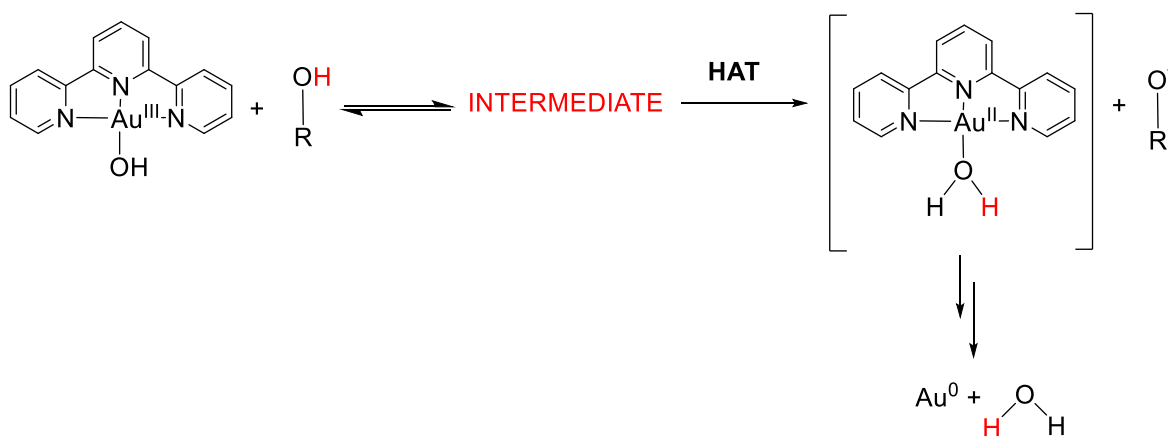
From the first order kinetics constants calculated for the reaction of **1** with 4- CH_3O -2,6-DTBP we have determined activation energy parameters from the reaction of complex **1** with 4- CH_3O -2,6-DTBP (Figure 2.20, Figure A54). The activation enthalpy was determined to be $\Delta H^\ddagger = 9.9(4)$ kcal/mol, whereas the activation entropy value was determined to be $\Delta S^\ddagger = -33(3)$ cal $\text{mol}^{-1}\text{K}^{-1}$. This value is close to those reported for metal-based oxidants performing HAT.^{41, 42} Furthermore, these values are also similar to those reported for other metal-hydroxide complexes which have been determined to perform a HAT oxidation (it must be noted these values were calculated from second order kinetic constants, Table 2.3). All these hydroxide complexes based on mid- or high-valent first-row transition metals (Mn, Fe, Cu) in fact show a relatively large and negative entropic contribution for a bimolecular reaction within the same order of magnitude of that experimentally identified for **1**. The entropic variation in fact is normally small when a HAT oxidation involves organic radicals, whereas when metal-based oxidants are considered large variations are observed and this has been ascribed to the rearrangement in the vibrational states occurring during the reaction.⁴¹ This corroborates the mechanistic hypothesis of HAT for **1** in the reaction with O–H bonds. The primary KIE values calculated for the reaction of complex **1** with O–H (2.9) and C–H bonds (3.3) further supports this mechanistic hypothesis. These results confirm that a $\text{Au}^{\text{III}}\text{-OH}$ entity is a capable oxidant of hydrocarbons and a plausible intermediate in Au oxidation catalysis.

Table 2.3. Activation energy parameters for metal hydroxide complexes in HAT oxidation.

Complex	ΔH^\ddagger (kcal/mol)	ΔS^\ddagger (cal/mol.K)
1	9.9(4)	-33(3)
$[\text{Mn}^{\text{III}}(\text{OH})(\text{S}^{\text{Me}_2}\text{N}_4(\text{tren}))]^{43}$	8.2	-25.5
$[\text{Mn}^{\text{III}}(\text{OH})(\text{dpaq})]^{34}$	9.9(9)	-35(3)
$[\text{Mn}^{\text{III}}(\text{OH})(\text{PY5})]^{44}$	9.3(5)	-36(5)
$[\text{Fe}^{\text{III}}(\text{OH})(\text{PY5})]^{45}$	13.2(5)	-26(5)
$[\text{Cu}^{\text{III}}(\text{OH})(\text{L})]^{46}$	5.1(1)	-31(3)
$[\text{Cu}^{\text{III}}(\text{OH})(\text{pipMeL})]^{46}$	3.8(2)	-38(3)
$[\text{Cu}^{\text{III}}(\text{OH})(\text{NO}_2\text{L})]^{54}$	4.9(1)	-27(1)

L= 2,6-X-diphenylpyridine-dicarboxamidate; dpaq = 2-[bis(pyridin-2-ylmethyl)]amino-N-quinolin-8-yl-acetamidate; PY5 = 2,6-bis-(bis(2-pyridyl)methoxymethane)pyridine; $\text{S}^{\text{Me}_2}\text{N}_4(\text{tren})$ = dimethylmercapto-tris(2-aminoethyl)amine)

We postulate that the $\text{Au}^{\text{III}}\text{-OH}$ complex **1** abstracted a H-atom from hydrocarbons and alcohols formally resulting in the formation of a transient $\text{Au}^{\text{II}}\text{-OH}_2$ adduct and a C- or O-based radical (Scheme 2.4).

**Scheme 2.4.** Mechanism of the HAT oxidation of alcohols by complex **1**.

The increased water content in all reactions from the transformation of the ancillary hydroxide ligand of **1** into an aquo ligand after HAT (Scheme 2.4) adds support to this postulate. We postulate that the product of the HAT step ($[\text{Au}^{\text{II}}(\text{H}_2\text{O})(\text{terpy})]^{2+}$) decays to yield Au nanoparticles either by oxidizing substrate or via other routes. We weren't able to independently synthesize

$[\text{Au}^{\text{II}}(\text{H}_2\text{O})(\text{terpy})]^{2+}$. To the best of our knowledge, only one mononuclear Au^{II} complex has been isolated,⁴⁷ suggesting such species are unstable. The instability of Au^{II} has been shown theoretically to be influenced by multiple factors such as solvation energy, the ancillary ligand dissociation mechanism, the charge of the intermediate, the nature of the solvent and of the ancillary ligands.^{25, 48-51} The exact nature of the decay of Au-products *after* HAT oxidation is therefore very complex and needs further investigation. We conclude from the experimental evidence available at this time that **1** facilitates HAT which was subsequently followed by decay of the $[\text{Au}^{\text{II}}(\text{H}_2\text{O})(\text{terpy})]^{2+}$ product to H_2O and Au^0 .

Saturation kinetics best described the relationship between k_{obs} and [substrate], which would suggest an oxidant/substrate interaction prior to irreversible HAT (Scheme 2.4). Such saturation behavior has been observed for $\text{Mn}^{\text{III}}\text{-OH}^{34}$ and $\text{Cu}^{\text{III}}\text{-OH}$ complexes,⁵² where both hydrogen-bonding interactions and coordination of substrate were implicated. The former is supported for **1** by $K = 0.016$ M for proto-4- CH_3O -2,6-DTBP and $K = 0.067$ M for deuterio-4- CH_3O -2,6-DTBP. This difference suggests that the initial interaction step was perturbed by substituting a hydrogen with a deuterium atom and is thus plausibly a form of hydrogen bonding. Substrate coordination at Au^{III} was eliminated as a plausible option, because Au^{III} -phenol species would be expected to display diagnostic resonances which were not observed in the ^1H NMR and EPR spectra of the reaction with phenols. Furthermore, when an excess of pyridine, a known coordinating ligand for Au^{III} ,¹⁶ was added to **1**, its ^1H NMR features were unchanged and a shift of the pyridine resonances was not observed. Similarly, when an excess of phenol ($\text{C}_6\text{H}_5\text{OH}$) was added to **1** the ^1H NMR resonances of both the phenol and the complex did not show a shift (Figures A55-56). We thus concluded that the saturation behavior displayed by **1** was most likely as a result of substrate hydrogen bonding interactions with the $\text{Au}^{\text{III}}\text{-OH}$ entity prior to HAT.

Many Au-based homogeneous oxidation catalysts have been queried as to whether the true oxidant was a discreet Au cation or Au nanoparticles formed upon reduction of the former.^{25, 53} Au nanoparticles have demonstrated the ability to reduce atmospheric dioxygen to superoxide, which in turn was postulated to act as the oxidant.²⁵ In the HAT oxidation by **1** we observed that the electronic absorption features associated with Au^0 appeared *after* the features associated with the HAT reaction products - thus Au nanoparticles formed *after* initial HAT by the Au^{III} complex, possibly as a result of the decay of a $\text{Au}^{\text{II}}\text{-OH}_2$ product. Furthermore, no characteristic superoxide resonances were observed in the EPR spectra of the reaction mixtures prepared during the first phase of the reaction. Finally, k_1 for the reaction of complex **1** with 4- CH_3O -2,6-DTBP did not differ significantly when performed in aerobic or anaerobic conditions (Table 2.2). These combined results

show that in this instance the active oxidant in HAT was the discreet $\text{Au}^{\text{III}}\text{-OH}$ complex, demonstrating that such an entity is a plausible oxidant in Au-mediated oxidation catalysis.

The formation of colloidal gold would suggest that the final ligand is recovered at the end of the reaction due to the decomplexation of the reduced metal cation. A decrease in the electronic absorption bands below 380 nm, assigned to the $\pi\rightarrow\pi^*$ transitions of the terpyridine ligand bound to the metal ion,²⁰ was observed to different extents in all the reactions explored. The $\pi\rightarrow\pi^*$ intraligand transitions of the free terpyridine ligand in fact give rise to absorption band below 320 nm, as confirmed by its electronic absorption spectrum in DMF. We therefore associated the decay of these bands below 380 nm to the loss of the chelating ligand on the gold upon reduction of the cation. Nevertheless, the ^1H NMR spectra of the reactions of **1** with 4-MeO-2,6-DTBP, 2,6-DTBP and CHD showed a similar pattern of the resonances in the terpyridine region which was not matching with the one of free terpyridine, but appeared to be similar to the one of doubly protonated terpyridine, $[\text{H}_2\text{terpy}]^{2+}$ (Figure 2.21).

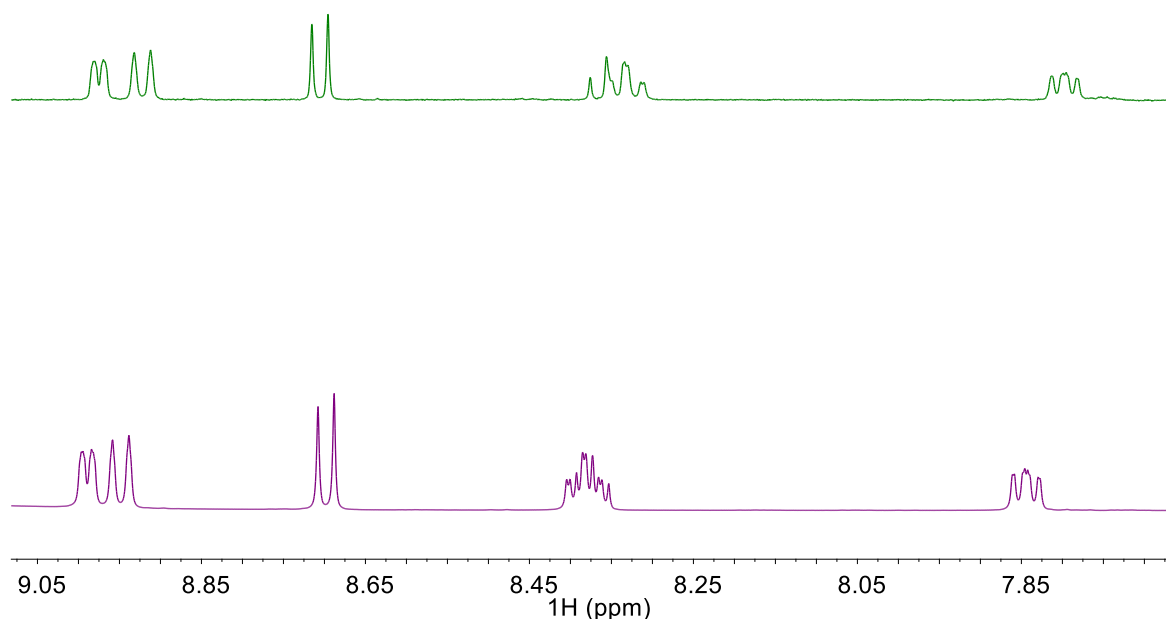


Figure 2.21. ^1H NMR spectra (400 MHz, DMSO-D_6) of the terpyridine region (7.5-9.05 ppm) of the reaction mixture between **1** and 100 equiv. CHD (green trace) and of 2,2':6',2'-terpyridine with 2 equiv. of trifluoroacetic acid (purple trace).

The crystallization of the reaction mixture between **1** and CHD from $\text{DMF/Et}_2\text{O}$ confirmed this hypothesis by yielding elemental gold and colourless crystals of protonated terpyridine with two perchlorate counterions, $[\text{H}_2\text{terpy}](\text{ClO}_4)_2$ (Figure 3.22). We thought that the ligand protonation

might occur due to the formation of acidic $\text{Au}^x\text{-(H}_2\text{O)}$ species in the decay of the postulated $[\text{Au}(\text{H}_2\text{O})(\text{terpy})]^{2+}$ formed upon HAT. Notably, $\text{Au}^{\text{III}}\text{-OH}_2$ complexes are known to be very acidic and thus have only been postulated as precursors in the synthesis of $\text{Au}^{\text{III}}\text{-OH}$ complexes.^{16, 18, 24} The decay of the postulated $\text{Au}^{\text{II}}\text{-OH}_2$ product might therefore involve disproportionation of the metal centre and partial proton release from putative $\text{Au}^{\text{III}}\text{-OH}_2$ species, yielding an acidic environment which leads to the formation of $[\text{H}_2\text{terpy}](\text{ClO})_2$.

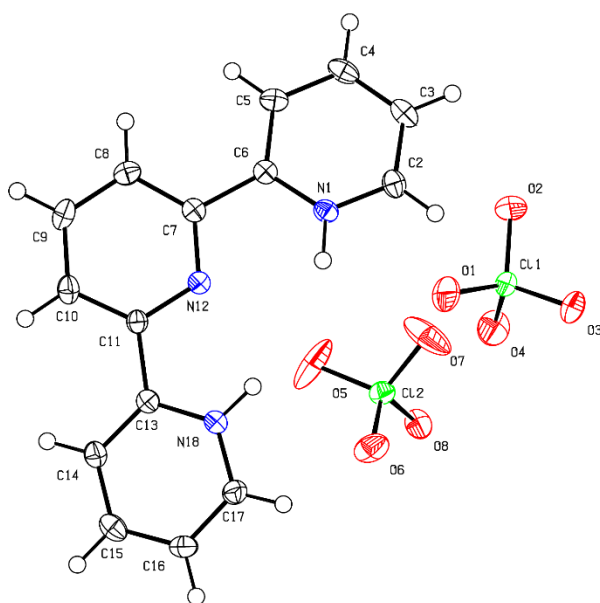


Figure 2.22 Ellipsoids plot (at 50% probability) of the crystallographic structure of the reaction product between complex **1** and CHD in DMF, $[\text{H}_2\text{terpy}](\text{ClO})_2$.

2.6 Conclusions

In conclusion, the $\text{Au}^{\text{III}}\text{-OH}$ complex **1** performed the oxidative activation of C–H and O–H bonds through a HAT mechanism. Stable O-based radicals were detected as the product of almost quantitative HAT of alcohols by **1** suggesting a form of PCET oxidation had occurred. Kinetic analysis confirmed the oxidation followed a HAT mechanism where proton and electron were transferred in a concerted manner from the substrate to the $\text{Au}^{\text{III}}\text{-OH}$ entity. These findings provide new insights in the potential involvement of $\text{Au}^{\text{III}}\text{-OH}$ species in gold oxidation catalysis and demonstrate that soft and heavy transition metal-oxygen adducts can also effect PCET oxidation.

2.7 Experimental section

Physical Methods

^1H and ^{13}C nuclear magnetic resonance (NMR) analyses were performed on an Agilent MR400 instrument (400.13 MHz for ^1H NMR, 100.61 MHz for ^{13}C NMR). Electronic absorption spectra were recorded on a Hewlett Packard (Agilent) 8453 diode array spectrophotometer. Gas chromatography experiments have been performed using a ThermoFisher TRACE™ 1300 Gas Chromatograph equipped with a Flame Ionisation Detector. Hydrogen was provided by a Parker Hydrogen Gas Generator 20H-MD. Air was provided by Parker Zero Air Generator UHP-10ZA-S. The column used was a ThermoFisher TraceGOLD TG-1MS GC column. Electrospray ionization (ESI) mass spectra were acquired using a Micromass time of flight spectrometer (TOF), interfaced to a Waters 2690 HPLC. Attenuated total reflectance infra-red (ATR-FTIR) spectra were recorded on a Perkin-Elmer Spectrum 100 Fourier transform infrared spectrometer. Cyclic voltammetry (CV) experiments were conducted with a CH Instruments 600E electrochemical analyzer, using a glassy carbon working electrode, a platinum wire counter electrode and an Ag/AgNO₃ 0.01 M reference electrode.

Materials

All solvents and reagents were purchased from commercial sources and used as received, unless otherwise stated. Complex **1** was synthesised as reported.¹⁸ Either KAuCl₄ or HAuCl₄ were used as starting materials for the synthesis of complex **1**, they were purchased from Sigma Aldrich or Fisher Scientific and used as received. *p*-X-2,6-di-*tert*-butylphenols were recrystallized from hexane or ethanol/water prior to use. For reactions performed in the absence of oxygen, solvents (N,N-dimethylformamide, tetrahydrofuran, diethyl ether) were freeze-pump-thawed three times and stored in a nitrogen atmosphere glovebox. TEMPOH (1-hydroxy-2,2,6,6-tetramethyl-piperidine) and 4-CH₃O-TEMPOH (4-methoxy-1-hydroxy-2,2,6,6-tetramethyl-piperidine) were synthesized according to reported procedures.^{56,3} 4-oxo-TEMPOH (4-oxo-1-hydroxy-2,2,6,6-tetramethyl-piperidine) was synthesized by adapting a reported procedure for 4-CH₃O-TEMPOH.⁵⁷ 4-CH₃O-[*D*]-2,6-DTBP was synthesized according to a reported procedure.³¹ [*D*]₄-9,10-dihydroanthracene ([*D*]₄-DHA) was synthesized according to a reported procedure (deuteration degree = 97% by ^1H NMR).⁵⁸

EPR analysis

Electron paramagnetic resonance (EPR) spectra of frozen solutions were acquired on a Bruker EMX X-band EPR, equipped with an Oxford Instruments CE 5396, ESR9 Continuous Flow Cryostat, a precision Temperature Controller and an Oxford Instruments TTL20.0/13 Transfer Tube. EPR samples were prepared by freezing the EPR tubes containing the analyte solutions, previously prepared at the UV-Vis spectrophotometer, in liquid nitrogen. EPR spectra of the phenoxy radicals were recorded at 77 K, 9.2 GHz, 0.2 mW microwave power, with a 10 mT field sweep in 84 s, and 0.2 mT field modulation amplitude. EPR spectra of 4-X-TEMPO were recorded at 77 K, 9.2 GHz, 2.02 mW microwave power, with a 60 mT field sweep in 84 s, and 0.3 mT field modulation amplitude. Integration, simulation, and fitting were performed with Matlab and the easySpin computational package.⁵⁹ The simulation for the phenoxy radicals spectra was modelled as an $S = \frac{1}{2}$ electron spin with an isotropic g tensor. The oxidation yield of the samples was calculated by quantification of the concentration of spin in the samples. This was obtained by comparison of the double integral of the signals to that of a frozen reference 3 mM solution of (2,2,6,6-tetramethyl-piperidin-1-yl)oxyl (TEMPO), measured under the same conditions.

Electrochemistry

Cyclic voltammetry experiments were conducted on a 1.0 mM solution of **1** in DMF at room temperature, with a 0.05 V s^{-1} . The supporting electrolyte was 0.1 M $^n\text{Bu}_4\text{NPF}_6$ was used as the supporting electrolyte. Potentials were referenced against the Fc^+/Fc couple (Fc = ferrocene). The voltammograms of Fc were acquired under the same conditions.

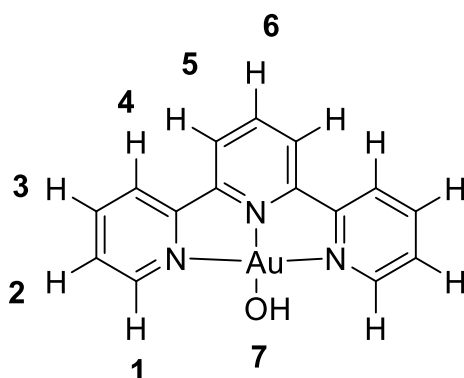
Gas chromatography-Flame Ionisation Detector (GC-FID) analysis

Post-reaction solutions from the reaction of **1** with different substrates were prepared at 25 °C. Different amounts of substrate (4-CH₃O-2,6-DTBP, 2,4,6-TTBP, 2,6-DTBP, DHA) were added as DMF solutions under continuous stirring until completion of the reaction, after which the mixture was analysed by GC-FID. A reference standard solution was prepared by adding the same amount of equivalents of substrate to 2 mL of pure DMF. The instrument method for anthracene was based on a temperature ramp (2 min at 175 °C, 10 °C/min to 250 °C, 2 min at 250 °C) with splitless injections of 1 µL each. Under these conditions, the retention time for anthracene was between 6.3-6.4 min. The instrument method for 2,6-di-*tert*-butylquinone was based on a temperature ramp (2 min at 75 °C, 10°C/min to 200 °C, 2 min at 200 °C) with

splitless injections of 1 μL each. Under these conditions, the retention time for 2,6-di-*tert*-butylquinone was between 12.3-12.4 min. The quantitative analysis of the analytes was based on a calibration curve. Yields were calculated as an average of four different solutions containing the same number of equivalents of substrate and repeating it for 2-3 different substrates concentrations.

Characterization of $[\text{Au}^{\text{III}}(\text{OH})(\text{terpy})](\text{ClO}_4)_2$ [1]

^1H NMR peaks have been assigned based on data obtained for the related complex $[\text{Au}(\text{Cl})(\text{terpy})]^{2+}$ in $\text{DMSO}-\text{D}_6$.¹⁹



δ_{H} (ppm) (400 MHz, $\text{DMSO}-\text{D}_6$): 9.09 (dd, $J = 5.8, 1.1$ Hz, 2H, **1**), 8.98 (m, 1H, **6**), 8.96 (m, 4H, **4,5**), 8.83 (td, $J = 7.9, 1.3$ Hz, 2H, **3**), 8.27 (ddd, $J = 7.5, 5.8, 1.4$ Hz, 2H, **2**), 6.35 (s, 1H, **7**).

δ_{H} (ppm) (400 MHz, $\text{DMF}-\text{D}_7$): 9.28 (dd, $J = 5.8, 1.3$ Hz, 2H, **1**), 9.16 (m, 4H, **4,5**), 9.13 (m, 1H, **6**), 8.98 (td, $J = 7.9, 1.3$ Hz, 2H, **3**), 8.44 (ddd, $J = 7.5, 5.8, 1.3$ Hz, 2H, **2**), 6.65 (s, 1H, **7**).

ν_{max} (FT-IR)/ cm^{-1} : 3425 (O–H), 3082, 3049, 3034 (terpy C–H stretch), 1605, 1597 (terpy C–H bend), 1574, 1503, 1481, 1453, 1443, 1406, 1327, 1303, 1297, 1268, 1254, 1188, 1171, 1071, 1052 (ClO_4), 1026, 984, 935, 912, 823, 787, 743, 718, 685, 675, 642, 620, 613, 552

Synthesis and characterization of $[\text{Au}(\text{OD})(\text{terpy})](\text{ClO}_4)_2$ [2]

Complex **2** was synthesized starting from $[\text{Au}(\text{Cl})(\text{terpy})](\text{ClO}_4)_2$ by following the same procedure used to synthesize **[14]**¹⁸ but using D_2O instead of H_2O as solvent.

δ_{H} (ppm) (400 MHz, $\text{DMSO}-\text{D}_6$): 9.10 (dd, $J = 5.8, 1.1$, 2H, **1**), 8.98 (m, 1H, **6**), 8.96 (m, 4H, **4**), 8.83 (td, $J = 7.9, 1.3$ Hz, 2H, **3**), 8.28 (ddd, $J = 7.5, 5.8, 1.3$, 2H, **2**).

ν_{max} (FT-IR)/ cm^{-1} : 3082, 3049, 3034 (terpy C–H stretch), 2531 (O–D stretch), 1605, 1597 (terpy C–H bend), 1574, 1503, 1481, 1453, 1443, 1406, 1327, 1303, 1297, 1268, 1254, 1188,

1171, 1071, 1052 (ClO₄), 1026, 984, 935, 912, 823, 787, 743, 718, 685, 675, 642, 620, 613, 552

Synthesis of 4-methoxy-2,6-di-*tert*-butylphenoxy radical

4-methoxy-2,6-di-*tert*-butylphenoxy radical was synthesized by following a reported procedure.³⁰ The purple oil obtained was washed three times with deoxygenated diethyl ether (Et₂O), then the solvent was removed and the oil dried under vacuum for one hour. Then it was stored in a nitrogen atmosphere glovebox where the solutions for the calculation of the extinction coefficient in DMF were prepared by using freshly deoxygenated DMF. Path length = 1 cm.

$$\epsilon_{535 \text{ nm}} = 365 \pm 20 \text{ M}^{-1}\text{cm}^{-1}$$

$$\epsilon_{407 \text{ nm}} = 2090 \pm 100 \text{ M}^{-1}\text{cm}^{-1}$$

$$\epsilon_{390 \text{ nm}} = 1574 \pm 210 \text{ M}^{-1}\text{cm}^{-1}$$

Synthesis of 2,4,6-tris-*tert*-butylphenoxy radical

2,4,6-tris-*tert*-butylphenoxy radical was synthesized according to the reported procedure.⁶⁰ The compound was then stored in a nitrogen atmosphere glovebox where the solutions for the calculation of the extinction coefficient in DMF were prepared by using freshly freeze-pumped-thawed DMF. Path length $b = 1$ cm. The calculated molar extinction coefficients are ~15% lower than those reported in acetonitrile, suggesting a lower stability of the radical in DMF.

$$\epsilon_{631 \text{ nm}} = 341 \pm 15 \text{ M}^{-1}\text{cm}^{-1}$$

$$\epsilon_{402 \text{ nm}} = 1830 \pm 200 \text{ M}^{-1}\text{cm}^{-1}$$

$$\epsilon_{384 \text{ nm}} = 1574 \pm 210 \text{ M}^{-1}\text{cm}^{-1}$$

4-oxo-1-hydroxy-2,2,6,6-tetramethyl-piperidine (4-oxo-TEMPOH)

4-oxo-TEMPOH was synthesized by adapting a reported procedure for 4-CH₃O-TEMPOH.⁵⁷ A suspension of 4-oxo-TEMPO[•] (1.00 g, 5.9 mmol) and Na₂S₂O₄ (2.15 g, 12.3 mmol) in acetone/water (1:1, 15 ml each) was stirred for one hour at room temperature under inert atmosphere. During this time the bright yellow colour of the solution disappeared giving a colourless mixture. The solvent was then partially evacuated under vacuum to remove acetone. The residual aqueous

layer was extracted with dry Et₂O (3x15 mL) and the solvent was evaporated to give a white solid (890 mg, 88%).

δ_{H} (ppm) (400 MHz, DMSO-D₆): 7.60 (s, 1H, -OH, disappears by adding a drop of D₂O), 2.34 (s, 4H, -CH₂), 1.07 (s, 12H, -CH₃).

δ_{C} (ppm) (100 MHz, DMSO-D₆): 207.67 (C=O), 60.93 (C2), 52.89 (C3), 26.53 (CH₃).

Reactivity studies protocol

Solutions of **1** were prepared at 25 °C and stored at 4 °C wrapped in aluminium foil up to 2 days after the preparation. The changes in the electronic absorption spectra were monitored at 25 °C. Substrates were added neat or as concentrated DMF solutions under continuous stirring. The formation of products was monitored using electronic absorption spectroscopy, by observing the decay of the band at $\lambda = 369$ nm (for reactions with 4-X-TEMPOH) or the growth of specific absorption bands of the oxidised products. The post-reaction mixtures were used as obtained for GC analysis. For rate constant determinations a minimum of 12.5 equivalents of substrate (with respect to **1**) were used to ensure *pseudo*-first order conditions. Values for k_{obs} were obtained by fitting the decay of the band at $\lambda = 369$ nm for TEMPOH and its derivatives or the growth of the absorbance band of the phenoxyl radical products (see Table 1) as an exponential. Each set of experiments was repeated three times and these data were fitted following a saturation kinetic model.^{34, 52}



$$k_{\text{obs}} = k_1 \frac{[\text{S}]}{(\text{K} + [\text{S}])}$$

C = complex **1**; S = substrate; P = products

The plot was linearized by using the following equation and from this plot the k_1 and the K were determined:

$$\frac{1}{k_{\text{obs}}} = \frac{\text{K}}{k_1} \frac{1}{[\text{S}]} + \frac{1}{k_1}$$

2.8 References

1. M. Lovisari and A. R. McDonald, *Inorg. Chem.*, 2020, **59**, 6, 3659-3665.
2. G. B. Shul'pin, A. E. Shilov and G. Süß-Fink, *Tetrahedron Lett.*, 2001, **42**, 7253-7256.
3. A. Corma, I. Domínguez, A. Doménech, V. Fornés, C. J. Gómez-García, T. Ródenas and M. J. Sabater, *Journal of Catalysis*, 2009, **265**, 238-244.
4. M. A. Cinellu, G. Minghetti, F. Cocco, S. Stoccoro, A. Zucca and M. Manassero, *Angew. Chem. Int. Ed.*, 2005, **44**, 6892-6895.
5. G. Zhang, L. Cui, Y. Wang and L. Zhang, *J. Am. Chem. Soc.*, 2010, **132**, 1474-1475.
6. T. de Haro and C. Nevado, *Angew. Chem. Int. Ed.*, 2011, **50**, 906-910.
7. J. A. T. O'Neill, G. M. Rosair and A.-L. Lee, *Catal. Sci. Technol.*, 2012, **2**, 1818-1821.
8. G. C. Bond and D. T. Thompson, *Gold Bulletin*, 2000, **33**, 41-50.
9. M. A. Sanchez-Castillo, C. Couto, W. B. Kim and J. A. Dumesic, *Angewandte Chemie*, 2004, **116**, 1160-1162.
10. M. S. Ide and R. J. Davis, *Acc. Chem. Res.*, 2014, **47**, 825-833.
11. J. Guzman and B. C. Gates, *J. Am. Chem. Soc.*, 2004, **126**, 2672-2673.
12. M. Agostina Cinellu, G. Minghetti, M. Vittoria Pinna, S. Stoccoro, A. Zucca, M. Manassero and M. Sansoni, *J. Chem. Soc., Dalton Trans.*, 1998, **11**, 1735-1742.
13. M. Agostina Cinellu, G. Minghetti, M. Vittoria Pinna, S. Stoccoro, A. Zucca and M. Manassero, *Chem. Commun.*, 1998, DOI: 10.1039/A805672B, 2397-2398.
14. D.-A. Roşca, J. A. Wright, D. L. Hughes and M. Bochmann, *Nature Communications*, 2013, **4**, 2167.
15. B. Pitteri, G. Marangoni, F. Visentin, T. Bobbo, V. Bertolasi and P. Gilli, *J. Chem. Soc., Dalton Trans.*, 1999, **5**, 677-682.
16. R. Corbo, T. P. Pell, B. D. Stringer, C. F. Hogan, D. J. D. Wilson, P. J. Barnard and J. L. Dutton, *J. Am. Chem. Soc.*, 2014, **136**, 12415-12421.
17. H. Beucher, E. Merino, A. Genoux, T. Fox and C. Nevado, *Angew. Chem. Int. Ed.*, 2019, **58**, 9064-9067.
18. B. Pitteri, G. Marangoni, F. Visentin, T. Bobbo, V. Bertolasi and P. Gilli, *J. Chem. Soc., Dalton Trans.*, 1999, 677-682.
19. K. Czerwińska, M. Golec, M. Skonieczna, J. Palion-Gazda, D. Zygadło, A. Szlapa-Kula, S. Krompiec, B. Machura and A. Szurko, *Dalton Trans.*, 2017, **46**, 3381-3392.
20. M. A. Mansour, R. J. Lachicotte, H. J. Gysling and R. Eisenberg, *Inorg. Chem.*, 1998, **37**, 4625-4632.
21. F. Camerel, R. Ziesel, B. Donnio, C. Bourgogne, D. Guillon, M. Schmutz, C. Iacovita and J.-P. Bucher, *Angew. Chem. Int. Ed.*, 2007, **46**, 2659-2662.
22. A. Maroń, K. Czerwińska, B. Machura, L. Raposo, C. Roma-Rodrigues, A. R. Fernandes, J. G. Małecki, A. Szlapa-Kula, S. Kula and S. Krompiec, *Dalton Trans.*, 2018, **47**, 6444-6463.
23. G. Sanna, M. I. Pilo, G. Minghetti, M. A. Cinellu, N. Spano and R. Seeber, *Inorg. Chim. Acta*, 2000, **310**, 34-40.
24. M. Bortoluzzi, E. De Faveri, S. Daniele and B. Pitteri, *Eur. J. Inorg. Chem.*, 2006, **2006**, 3393-3399.
25. A. Corma and H. Garcia, *Chem. Soc. Rev.*, 2008, **37**, 2096-2126.
26. H. E. Gottlieb, V. Kotlyar and A. Nudelman, *J. Org. Chem.*, 1997, **62**, 7512-7515.
27. E. Kang, H. R. Park, J. Yoon, H.-Y. Yu, S.-K. Chang, B. Kim, K. Choi and S. Ahn, *Microchem. J.*, 2018, **138**, 395-400.
28. K. Mizuno, S. Imafuji, T. Ochi, T. Ohta and S. Maeda, *J. Phys. Chem. B*, 2000, **104**, 11001-11005.
29. P. Pirovano and A. R. McDonald, *Eur. J. Inorg. Chem.*, 2018, **2018**, 547-560.
30. J. M. Wittman, R. Hayoun, W. Kaminsky, M. K. Coggins and J. M. Mayer, *J. Am. Chem. Soc.*, 2013, **135**, 12956-12959.
31. J. Y. Lee, R. L. Peterson, K. Ohkubo, I. Garcia-Bosch, R. A. Himes, J. Woertink, C. D. Moore, E. I. Solomon, S. Fukuzumi and K. D. Karlin, *J. Am. Chem. Soc.*, 2014, **136**, 9925-9937.
32. V. W. Manner, T. F. Markle, J. H. Freudenthal, J. P. Roth and J. M. Mayer, *Chem. Commun.*, 2008, **2**, 256-258.
33. S. A. Bedell and A. E. Martell, *J. Am. Chem. Soc.*, 1985, **107**, 7909-7913.
34. G. B. Wijeratne, B. Corzine, V. W. Day and T. A. Jackson, *Inorg. Chem.*, 2014, **53**, 7622-7634.
35. J. J. Warren, T. A. Tronic and J. M. Mayer, *Chem. Rev.*, 2010, **110**, 6961-7001.
36. J. P. Roth, S. Lovell and J. M. Mayer, *J. Am. Chem. Soc.*, 2000, **122**, 5486-5498.
37. J. M. Mayer, *Acc. Chem. Res.*, 2011, **44**, 36-46.
38. S. Hammes-Schiffer, *Chem. Rev.*, 2010, **110**, 6937-6938.
39. C. McManus, P. Mondal, M. Lovisari, B. Twamley and A. R. McDonald, *Inorg. Chem.*, 2019, **58**, 4515-4523.

40. S. Kundu, P. Chernev, X. Engelmann, C. S. Chung, H. Dau, E. Bill, J. England, W. Nam and K. Ray, *Dalton Trans.*, 2016, **45**, 14538-14543.
41. E. A. Mader, E. R. Davidson and J. M. Mayer, *J. Am. Chem. Soc.*, 2007, **129**, 5153-5166.
42. E. A. Mader, V. W. Manner, T. F. Markle, A. Wu, J. A. Franz and J. M. Mayer, *J. Am. Chem. Soc.*, 2009, **131**, 4335-4345.
43. M. K. Coggins, L. M. Brines and J. A. Kovacs, *Inorg. Chem.*, 2013, **52**, 12383-12393.
44. C. R. Goldsmith, A. P. Cole and T. D. P. Stack, *J. Am. Chem. Soc.*, 2005, **127**, 9904-9912.
45. C. R. Goldsmith and T. D. P. Stack, *Inorg. Chem.*, 2006, **45**, 6048-6055.
46. D. Dhar, G. M. Yee, A. D. Spaeth, D. W. Boyce, H. Zhang, B. Dereli, C. J. Cramer and W. B. Tolman, *J. Am. Chem. Soc.*, 2016, **138**, 356-368.
47. S. Preiß, C. Förster, S. Otto, M. Bauer, P. Müller, D. Hinderberger, H. Hashemi Haeri, L. Carella and K. Heinze, *Nat. Chem.*, 2017, **9**, 1249.
48. K. A. Barakat, T. R. Cundari, H. Rabaâ and M. A. Omary, *J. Phys. Chem. B*, 2006, **110**, 14645-14651.
49. K. Dang Nguyen VÔ, C. Kowandy, L. Dupont and X. Coqueret, *Chem. Commun.*, 2015, **51**, 4017-4020.
50. S. Eustis, H.-Y. Hsu and M. A. El-Sayed, *The Journal of Physical Chemistry B*, 2005, **109**, 4811-4815.
51. T. Dann, D.-A. Roşca, J. A. Wright, G. G. Wildgoose and M. Bochmann, *Chem. Commun.*, 2013, **49**, 10169-10171.
52. D. Dhar and W. B. Tolman, *J. Am. Chem. Soc.*, 2015, **137**, 1322-1329.
53. C. D. Pina, E. Falletta and M. Rossi, *Chem. Soc. Rev.*, 2012, **41**, 350-369.
54. P. S. Braterman, J. I. Song and R. D. Peacock, *Inorg. Chem.*, 1992, **31**, 555-559.
55. R. Shunmugam, G. J. Gabriel, K. A. Aamer and G. N. Tew, *Macromolecular Rapid Communications*, 2010, **31**, 784-793.
56. K. S. Chan, X. Z. Li, W. I. Dzik and B. de Bruin, *J. Am. Chem. Soc.*, 2008, **130**, 2051-2061.
57. A. Wu, E. A. Mader, A. Datta, D. A. Hrovat, W. T. Borden and J. M. Mayer, *J. Am. Chem. Soc.*, 2009, **131**, 11985-11997.
58. C. Arunkumar, Y.-M. Lee, J. Y. Lee, S. Fukuzumi and W. Nam, *Chem. Eur. J.*, 2009, **15**, 11482-11489.
59. S. Stoll and A. Schweiger, *J. Mag. Res.*, 2006, **178**, 42-55.
60. V. W. Manner, T. F. Markle, J. H. Freudenthal, J. P. Roth and J. M. Mayer, *Chem. Commun.*, 2008, 256-258.

Chapter 3

Au^{III}-Cl in oxidative C-H and O-H bond activation

The work described in this chapter has been submitted for publication to Inorganic Chemistry at the time of submission of this thesis. The XRD data collection and refinement were performed by Dr. Brendan Twamley. The quantum chemical calculations were performed by Dr. Robert Gericke.

3.1 Introduction

High-valent late transition metal halides have recently shown their exceptional ability to activate C–H bonds via a HAT mechanism, showing to be fast and powerful oxidants able to yield both oxygenated and halogenated products when reacted with hydrocarbons.¹⁻³ A Ni^{III}–F entity² showed rate constants 4300-fold enhanced respect to its Ni^{III}–Cl counterpart¹, a difference ascribed to the higher driving force ascribed by the stronger bond formed in the product (HF, 136 kcal/mol vs HCl, 103 kcal/mol). In their pioneering work, Doyle and co-workers have shown that Ni^{II}–Cl complexes can photocatalytically promote the formation of new C(sp³)–H bonds: in this case the postulated active species is a Ni^{III}–Cl that it is believed to release Cl[•], which can perform HAT.⁴⁻⁷

The intermediacy of Au–oxygen adducts has been widely postulated in gold oxidation catalysis.⁸⁻¹¹ On the other hand, Au-halide, in particular Au^{III}–Cl complexes have been mostly reported as precursors to other functionalities or as biologically relevant mediators, without insights on their reactivity. Interestingly, Shilov reported the oxidation of linear and branched hydrocarbons in solution with salts like NaAuCl₄ and Au(PPh₃)Cl in presence of H₂O₂.¹² Despite the active oxidant was postulated to be the elusive Au^{III}=O, we believe that also Au^{III}–Cl species could be effective in this perspective. Since we explored the reactivity of [Au(OH)(terpy)](ClO₄)₂¹³ (terpy = 2,2':6',2'-terpyridine) (**2**) in Chapter 2, we are interested in drawing a reactivity comparison by changing the ancillary ligand from OH to Cl. Thus, in this chapter we will describe the characterization in polar aprotic solvents of [Au(Cl)(terpy)](ClO₄)₂ and its reactivity towards substrates bearing C–H and O–H bonds, in comparison with the data obtained for [Au(OH)(terpy)](ClO₄)₂.¹⁴ With this study we aim to gain insights into the comparison between traditional oxygen-based high-valent oxidants and halide-based ones towards hydrocarbons and enhance our knowledge into their mechanism of reaction.

3.2 Characterization of [Au^{III}(Cl)terpy)](ClO₄)₂

[Au^{III}(Cl)(terpy)](ClO₄)₂ **1** was synthesized as reported.¹³ The identity and purity of **1** was confirmed by ¹H NMR and mass spectrometry. The ¹H NMR spectra of **1** in DMSO-D₆ showed an overall downfield shift of the resonances in the terpyridine region respect to **2** and the absence of the OH resonance at δ = 6.35 ppm (Figure 3.1).

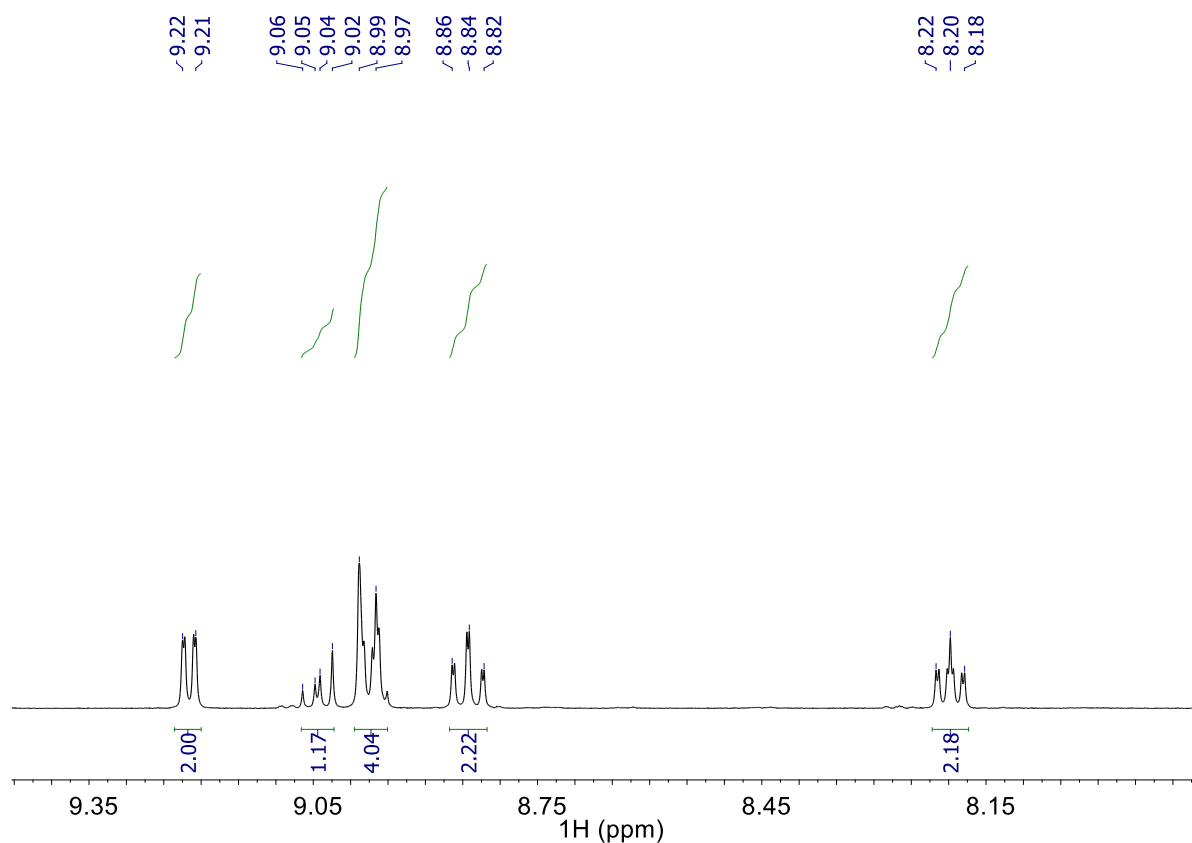


Figure 3.1. ^1H NMR spectrum (400 MHz, DMSO-D_6) of **1**.

To perform a reactivity comparison with **2**, the stability of complex **1** in DMF was assessed. Crystals suitable for XRD were grown over two days from a DMF/ Et_2O mixture, enabling the structural characterization of the complex (Figure 3.2, Table A1). The structure consisted of $[\text{Au}^{\text{III}}(\text{Cl})(\text{terpy})]^{2+}$ cation and perchlorate counterions in 1:2 ratio, with the gold atom displaying a slightly distorted square planar coordination. The Au1–Cl1 distance of 2.2544(13) Å appeared comparable to those reported for similar gold complexes bearing a chloride ancillary ligand and a substituted terpyridine as pincer ligand (Table 3.1). The distance between Au1 and the axial terpyridine nitrogen N1 at 1.944(5) Å was also comparable with other $[\text{Au}^{\text{III}}(\text{Cl})(^{\text{R}}\text{terpy})]^{2+}$ complexes (Table 3.1). The angles around the metal centre were in good agreement with those reported for similar complexes, highlighting the slight distortion from a perfect square planar geometry (Table 3.1). This result showed that the chloride ligand is retained in dry DMF at rt and no ligand substitution occurs within two days, allowing the reactivity of **1** to be explored in such conditions.

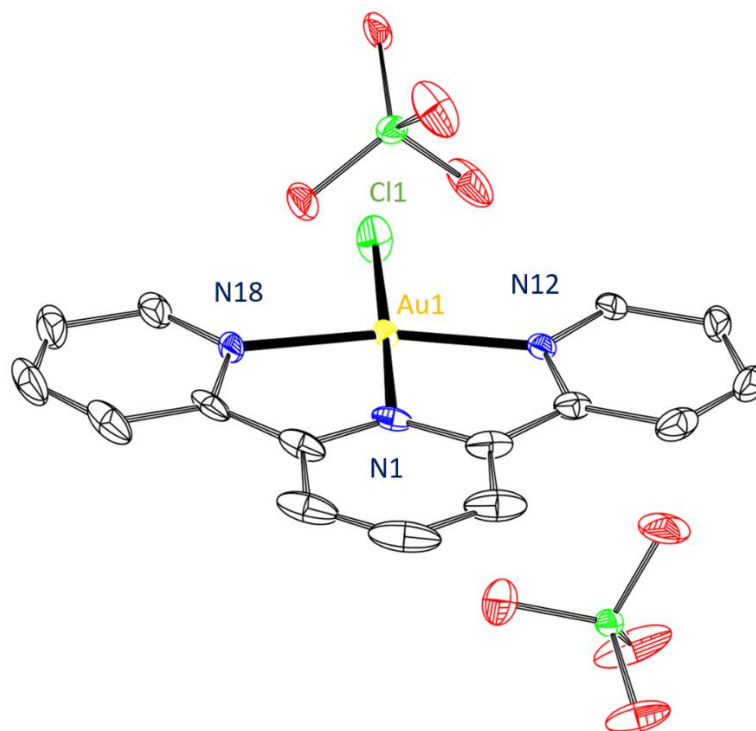


Figure 3.2. Crystal structure of **1**. Thermal ellipsoids are represented at 50% probability. Hydrogen atoms and disorder in the perchlorate counterions are not depicted for clarity.

Table 3.1. Selected bond distances for Au^{III}–Cl complexes supported by terpyridine ligands.

Complex	Au(1)–Cl(1) (Å)	N _{ax} –Au(1) (Å)	N _{eq} –Au(1)– Cl(1) (°)	N _{eq} –Au(1)– N _{ax} (°)	Reference
1	2.2544(13)	1.944(5)	99.23(14) 97.54(18)	81.8(2) 81.37(15)	-
[Au ^{III} (Cl)(terpy)]Cl ₂	2.269(2)	1.931(7)	98.7(2) 98.5(2)	81.4(3) 81.4(3)	15
[Au ^{III} (Cl)(4-MeOPh- terpy)](PF ₆) ₂	2.2559(24)	1.924(6)	-	80.1(3) 82.5(3)	16
[Au ^{III} (Cl)(4-2Py- terpy)](PF ₆) ₂	2.257(3)	1.938(8)	98.5(2) 98.6(3)	81.6(3) 81.3(3)	17
[Au ^{III} (Cl)(4-3Py- terpy)](PF ₆) ₂	2.257(3)	1.971(7)	99.6(2) 98.5(3)	79.8(3) 82.1(3)	17

Once the structural characterization was performed, the crystals of **1** were employed to record its electronic absorption spectra in DMF at 25 °C and determine the extinction coefficient in

the same conditions. The electronic absorption spectra of **1** in DMF showed a structured absorption band in the near-UV region with peaks at 375 and 357 nm and a shoulder at 338 nm (Figure 3.3). These absorption features are typical of complexes supported by substituted terpyridine ligands and can be assigned to the $\pi \rightarrow \pi^*$ and $n \rightarrow \pi^*$ intraligand transitions, perturbed by complexation to the Au^{III} cation.¹⁷ A lower energy feature at $\lambda = 530$ nm was present in the spectrum of **1**, similar to the one at $\lambda = 545$ nm observed in the electronic absorption spectrum of **2**, which in electronic absorption spectra of similar Au^{III} complexes has in fact been assigned as a charge transfer band resulting from LMCT (ligand-to-metal charge transfer) and ILCT (intra-ligand charge transfer) contributions.¹⁷⁻¹⁹ The extinction coefficients for the absorption maxima of **1** in DMF at 25 °C were calculated to be $\epsilon_{375} = 7700 \pm 200 \text{ M}^{-1} \text{ cm}^{-1}$ and $\epsilon_{357} = 10500 \pm 400 \text{ M}^{-1} \text{ cm}^{-1}$ (Figures A57-58)

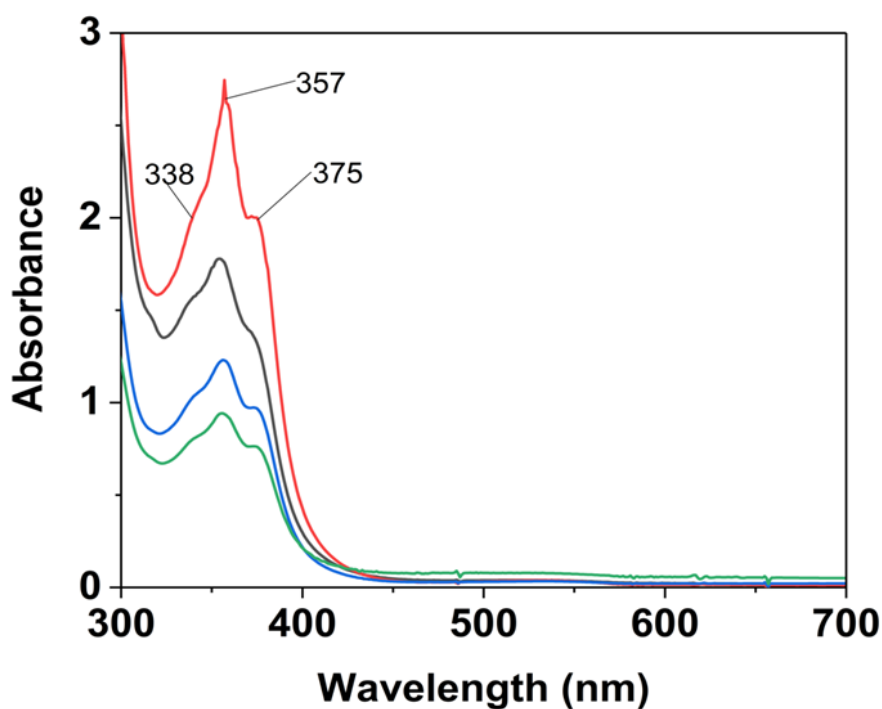


Figure 3.3. Electronic absorption spectra (0.035, 0.07, 0.125 and 0.25 mM, DMF, 25 °C) of **1**.

Cyclic voltammetry of **1** in DMF showed an irreversible reduction peak at $E_{\text{red}} = 0.18$ V versus the ferrocene/ferrocenium (Fc/Fc^+) standard and an irreversible oxidation wave at high potential, $E_{\text{ox}} = 0.74$ V (Figure 3.4). The peak at 0.18 V was assigned to the full reduction from Au^{III} to Au^0 , falling at a higher potential than the one observed for **2** (-0.13 V).^{14, 20, 21} Therefore **1** appeared to be less easily reduced compared to **2**.

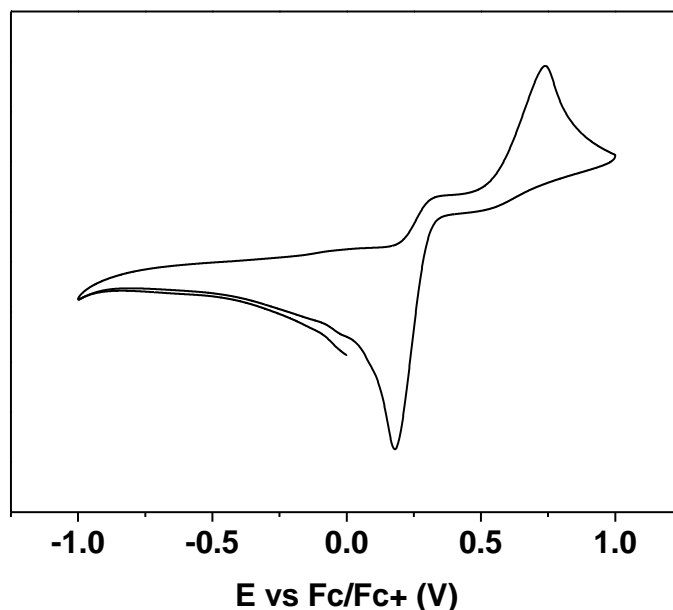


Figure 3.4. Cyclic voltammetry of complexes **1** (DMF, rt, *left*) versus Fc/Fc⁺.

3.3 Reactivity with O–H bonds

Once the characterization of **1** was performed, its reactivity towards substrates bearing O–H bonds was explored to gain more insights about its reactivity.

When complex **1** (0.15 mM, DMF, 25 °C) was reacted with an excess of **2** was reacted with 2,4,6-tri-*tert*-butylphenol (2,4,6-TTBP, > 150 equiv.), the electronic absorption spectrum showed first the formation of a band at $\lambda = 402$ nm (maximum yield at 2000 s) and the decay of the bands at $\lambda = 357$ nm and $\lambda = 375$ nm (Figure 3.5). A slower growth of features between $\lambda = 500$ and $\lambda = 1000$ nm over 3000 s was observed in a second phase of the reaction. A dark purple solution was observed at the end of the reaction, which we attribute to the formation of colloidal gold, in analogy to what was previously observed for **2**.¹⁴ The sharp feature at $\lambda = 402$ nm was assigned to the 2,4,6-tri-*tert*-butylphenoxy radical,¹⁴ the yield of which was determined to be $80 \pm 12\%$ by UV-Vis spectroscopy. An X-band EPR spectrum was taken after 2000 s (maximum yield of $\lambda = 402$ nm), showing a signal at $g = 2.00$ (Figure 3.5, inset). This spectrum displayed the same EPR g -value of the independently synthesized 2,4,6-tri-*tert*-butylphenoxy radical, confirming the identity of the product (see Chapter 2). The yield of radical was determined to be $75 \pm 20\%$ by EPR (Table 3.2) with respect to the concentration of **1**. We conclude that the radical was formed as a result of a formal one proton, one-electron oxidation of 2,4,6-TTBP by **1**.

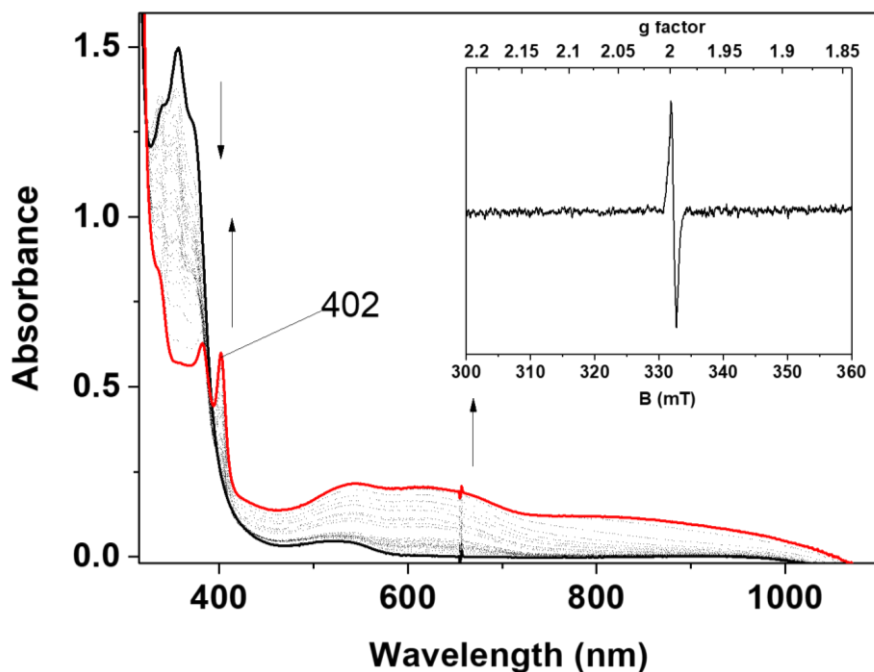


Figure 3.5. Electronic absorption spectra of the reaction of **1** (DMF, 25 °C, 0.20 mM) with 2,4,6-TTBP (600 equiv.). black trace = 0_s, red trace = 3000 s. Inset: X-Band EPR spectrum of the reaction mixture at $t = 3000$ s. The EPR spectra was acquired from a frozen DMF solution and measured at 77 K with a 0.2 mW microwave power and 0.2 mT modulation amplitude.

The reaction kinetics were followed by monitoring the decay of the complex band at $\lambda = 375$ nm over time. *Pseudo*-first order rate constants (k_{obs}) were obtained by exponential fitting of the plot of absorbance vs time (Figure AX). The plot of k_{obs} versus [2,4,6-TTBP] exhibited a linear correlation (Figure 3.6), and the second-order reaction rate constant, k_2 , was determined from the slope of the plot to be $0.056 \text{ M}^{-1}\text{s}^{-1}$ (Table 3.3). The *end-product* of the reaction between **1** and 2,4,6-TTBP was found to be 2,6-di-*tert*-butylquinone (2,6-DTBQ) and its yield was calculated by GC to be $71 \pm 6\%$, where for every Au in **1** a 2-electron reaction occurred (2,6-DTBQ is a 2-electron, 2-proton oxidation product of 2,4,6-TTBP).¹⁴ **1** was thus capable of proton coupled electron transfer (PCET) oxidative activation of phenolic O–H bonds.

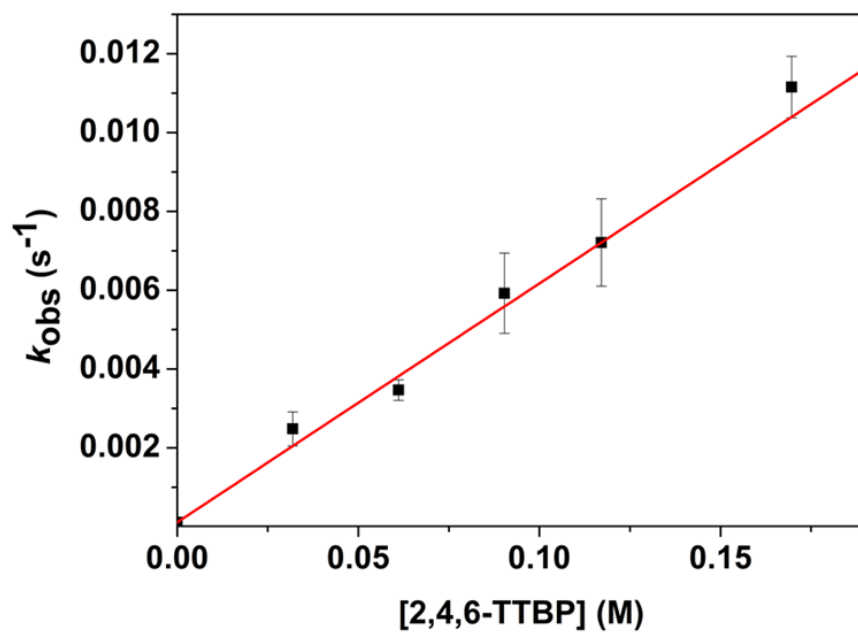


Figure 3.6. Plot of k_{obs} against [2,4,6-TTBP] determined for the reaction between **1** and 2,4,6-TTBP.

Table 3.2. Yield of oxidation products for complex **1** with different substrates.

Substrate	Product	Stoichiometry	Yield (%)	Method
4-CH ₃ O-2,6-DTBP	phenoxy radical	1-electron	-	EPR
			-	UV-Vis
2,4,6-TTBP	2,6-DTBQ	2-electrons	96±7	GC-FID
			75±20	EPR
2,6-DTBP	TTBTD	2-electrons	80±12	UV-Vis
			71±6	GC-FID
TEMPOH	TEMPO	1-electron	10 ± 1	UV-Vis
4-CH ₃ O-TEMPOH	4-CH ₃ O-TEMPO	1-electron	77±20	EPR
4-oxo-TEMPOH	4-oxo-TEMPO	1-electron	82±20	EPR
CHD	benzene	2-electrons	105±10	¹ H-NMR
DHA	anthracene	2-electrons	80±5	GC-FID

In order to gain mechanistic insight, **1** was reacted with a scope of substrates bearing O–H bonds: 4-methoxy-2,6-di-*tert*-butylphenol (4-CH₃O-2,6-DTBP), 4-methyl-2,6-di-*tert*-butylphenol (4-CH₃-2,6-DTBP), 4-X-1-hydroxy-2,2,6,6-tetramethyl-piperidines (4-X-TEMPOH, X = H, O, CH₃O). In presence of all the substrates the electronic absorption spectra displayed the decay of the complex features at $\lambda = 357$ nm and $\lambda = 375$ nm to obtain k_{obs} and k_2 values from the plots of k_{obs} versus [substrate] (Figures A59-66, Table 3.3). X-band EPR measurements of the reaction mixtures for the family of 4-X-TEMPOH substrates gave a rhombic signal with $g_{\text{av}} = 2.00$, typical of 4-X-TEMPO[•] species (Figure 3.7, Figure AX).^{14, 22} The oxyl radicals were obtained in ~80% yields (Table 3.2).

Table 3.3. Kinetic parameters for the reactions between **1** and substrates bearing O–H bonds.^{23, 24}

Substrate	k_2 ($M^{-1} s^{-1}$)	BDFE _{O-H} (kcal/mol) ^a
4-oxo-TEMPOH	93.28	65.6
TEMPOH	200.02	66.5
4-CH ₃ O-TEMPOH	142.15	65.0
[<i>H</i>]-4-CH ₃ O-2,6-DTBP	4.48	74
[<i>D</i>]-4-CH ₃ O-2,6-DTBP	2.34	-
4-CH ₃ -2,6-DTBP	0.053	77
2,4,6-TTBP	0.056	77.1

^a The values in italics are estimated based on those reported in other solvents.

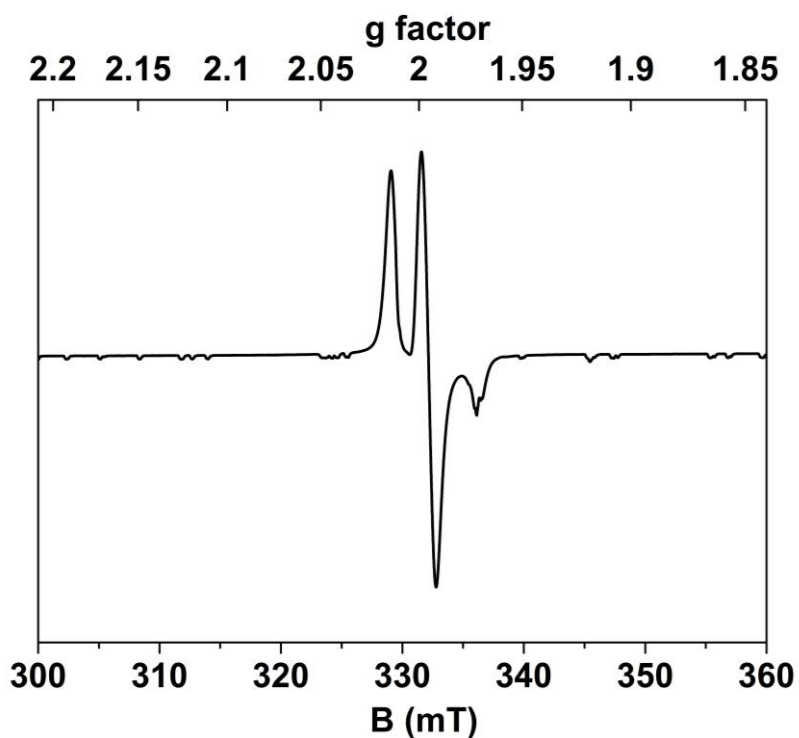


Figure 3.7. X-Band EPR spectrum of the spectrum of the reaction mixture of **1** with 4-oxo-TEMPOH (50 equiv.) after 100 s. The spectrum was acquired from a frozen DMF solution and measured at 77 K with a 1.98 mW microwave power and a 0.3 mT modulation amplitude.

In the reaction of **1** with 4-CH₃O-2,6-DTBP no electronic absorption or EPR signals indicating accumulation of a radical species were observed, conversely to what observed in the same reaction with **2** (Figure 3.8).¹⁴ This suggested that the 4-methoxy-2,6-di-*tert*-butylphenoxy radical likely decayed too quickly to lead to its accumulation and observation. ¹H NMR analysis of this reaction showed the formation of new features at $\delta = 6.50$ and 1.23 ppm, that were attributed to 2,6-DTBQ (yield = $96 \pm 7\%$ by GC-FID),¹⁴ and one at $\delta = 3.17$ ppm attributed to CH₃OH (Figure 3.9).^{25, 26} These compounds are the apparent final products of the reaction between **1** and 4-CH₃O-2,6-DTBP, analogously to what observed in the reaction of **2** with this substrate, confirming that they are the result of PCET oxidation of 4-CH₃O-2,6-DTBP by **1**. Overall, substrates bearing weak O–H bonds reacted initially with **1** to yield stable O-based radical species indicating that a PCET oxidation by **1** had occurred.

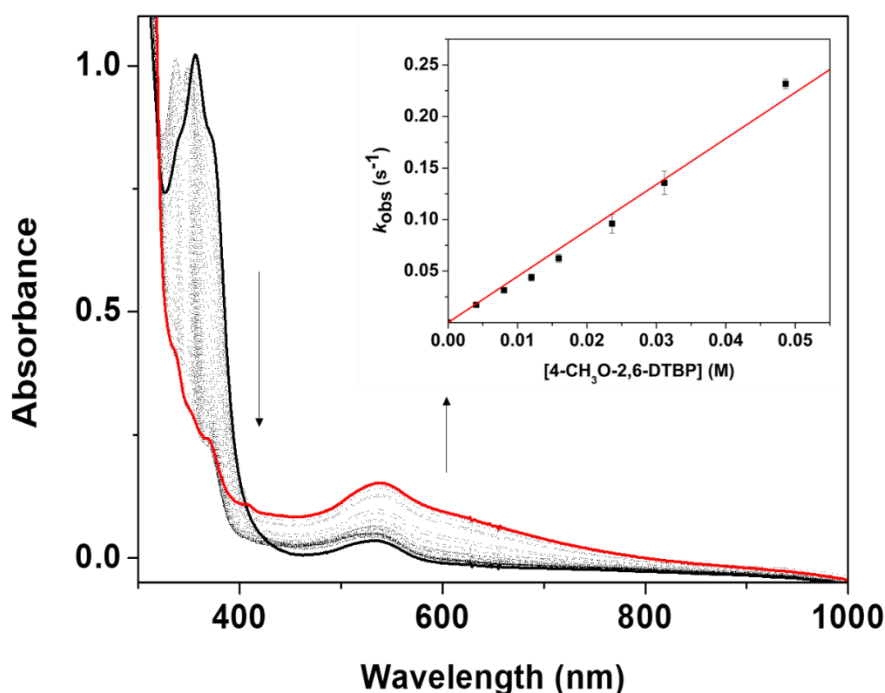


Figure 3.8. Electronic absorption spectra of the reaction of **1** (0.1 mM, 25 °C, DMF) with 4-CH₃O-2,6-DTBP (100 equiv.). Black trace = 0 s, red trace = 1000 s. Inset: plot of k_{obs} against [4-CH₃O-2,6-DTBP] determined for the reaction between **1** and 4-CH₃O-2,6-DTBP.

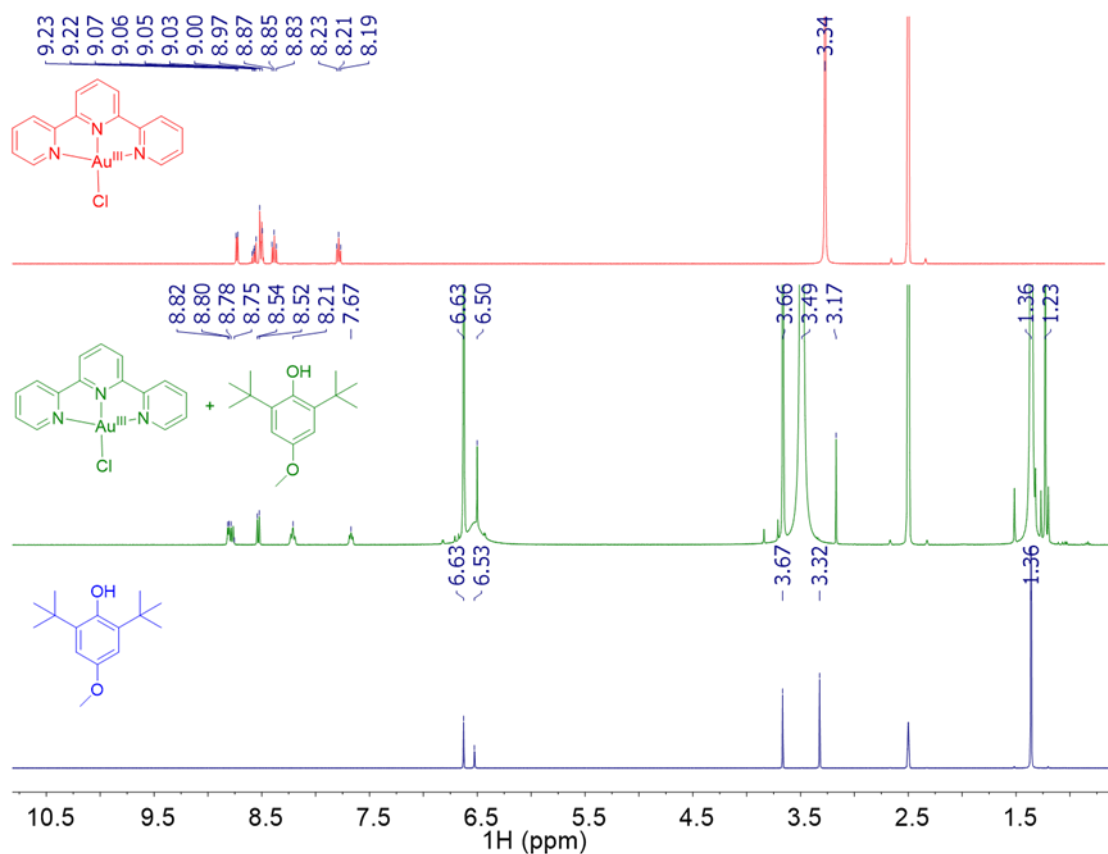


Figure 3.9. ^1H NMR (400 MHz, DMSO-D_6) of the reaction between **1** and 25 equiv. 4- CH_3O -2,6-DTBP. Red = complex **1**, Blue = 4- CH_3O -2,6-DTBP, Green = complex **1** in presence of 25 equiv. 4- CH_3O -2,6-DTBP after $\sim 4'$ from the mixing of the reagents.

For the reaction of **1** with deuterated (OD) 4- CH_3O -2,6-DTBP a $k_2 = 2.34 \text{ M}^{-1}\text{s}^{-1}$ was determined, yielding a primary kinetic isotope effect (KIE) of 1.9 (Table 3.3, Figure 3.10). This indicates that proton or H-atom transfer were involved in the rate-limiting step. This value is in the classical KIE range (2-7) and indicates no tunneling was involved in these reactions. The KIE is in the range typical of high-valent metal-halides and M-OX PCET oxidants.^{1, 22, 27-30}

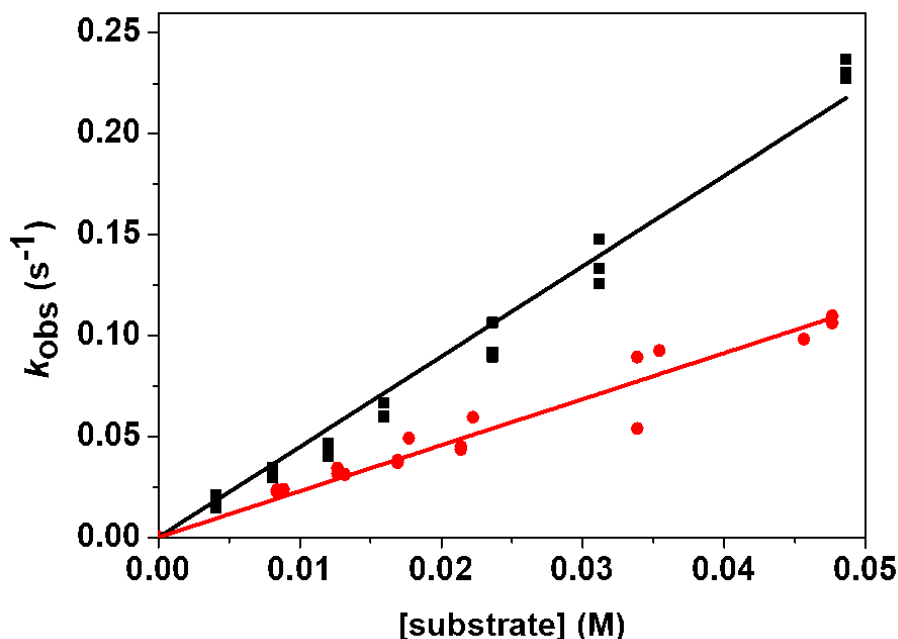


Figure 3.10. Plot of k_{obs} versus [substrate] determined for the reaction between complex **1** and 4-proto-CH₃O-2,6-DTBP (black trace) and 4-deutero-CH₃O-2,6-DTBP (red trace).

3.4 Mechanistic insights

The reactions of **1** with 4-X-TEMPOH substrates showed relatively fast rates whereas those with phenols showed relatively slower rates. The entity of the variations of the k_2 can be rationalized by plotting Gibbs free energies of activation (ΔG^\ddagger , derived from k_2) against BDFE_{O-H} (Bell-Evans-Polanyi plot, Figure 2). A slope = 0.39 was obtained from linear fitting of the data, which is close to the ideal value (0.5) reported for a concerted proton and electron transfer (CPET) or hydrogen atom transfer (HAT) mechanism as predicted by Marcus theory.^{31, 32} This value also falls in the range of $\Delta G^\ddagger/\Delta(\text{BDFE})$ slopes ascribed to HAT mechanisms for transition-metal-based oxidants (0.15–0.7),^{2, 31-34} and is also close to the value of 0.30 reported for **2** (Figure 3.11).¹⁴ Activation energy parameters were determined via an Eyring analysis for the reaction of **1** with 4-CH₃O-2,6-DTBP (Figure 3.12). The activation enthalpy was determined to be $\Delta H^\ddagger = 12.5 \text{ kcal mol}^{-1}$, and the activation entropy value was determined to be $\Delta S^\ddagger = -18 \text{ cal mol}^{-1}\text{K}^{-1}$. The large, negative entropy is consistent with a metal-based oxidant, because the metal centre gets reduced during a HAT reaction the vibrational entropy contribution is much higher compared to reactions involving organic radicals.^{35, 36} The enthalpy of activation for **2** was 2.6 kcal/mol lower than the one measured for **1**, a small difference which we do not expect to have a dramatic impact on the final Gibbs free energy of activation. However, the value of $-18 \text{ cal mol}^{-1}\text{K}^{-1}$ measured for **1** is markedly smaller than measured for **2** ($\Delta S^\ddagger = -33 \text{ cal mol}^{-1}\text{K}^{-1}$)¹⁴ (Table 3.4). The activation parameters are consistent with a metal-

mediated HAT oxidation reaction by **1**, with parameters that indicating that free Cl-atom mediated HAT oxidation of the substrate (expected $\Delta S^\ddagger = < 5 \text{ cal mol}^{-1}\text{K}^{-1}$) is unlikely.

It must be highlighted that between **1** and **2** the profile of the kinetics of reaction were different: in fact **1** showed saturation kinetics whereas **2** showed linear kinetics even at high substrate concentrations. For **2** we attributed the saturation behaviour to the presence of an intermediate during a pre-equilibrium phase prior to the HAT step, where a substrate was hydrogen bonding to the hydroxide ligand prior to the HAT oxidation by **2**,³⁷ as postulated for other high-valent metal hydroxides showing similar kinetic profiles.²² For **1** the presence of such an intermediate does not occur, presumably because the Cl ligand in **1** is less prone to form hydrogen bonds with exogenous donors relative to the hydroxide ligand in **2**.³⁸ This behaviour was observed for two $\text{Mn}^{\text{III}}\text{-OH}$ and $\text{Mn}^{\text{III}}\text{-Cl}$ complexes supported by the same polypyridyl ligand, where a larger reorganization energy is observed for the former due to its tendency to form a hydrogen bonding network with water molecules in the second coordination sphere.³⁹

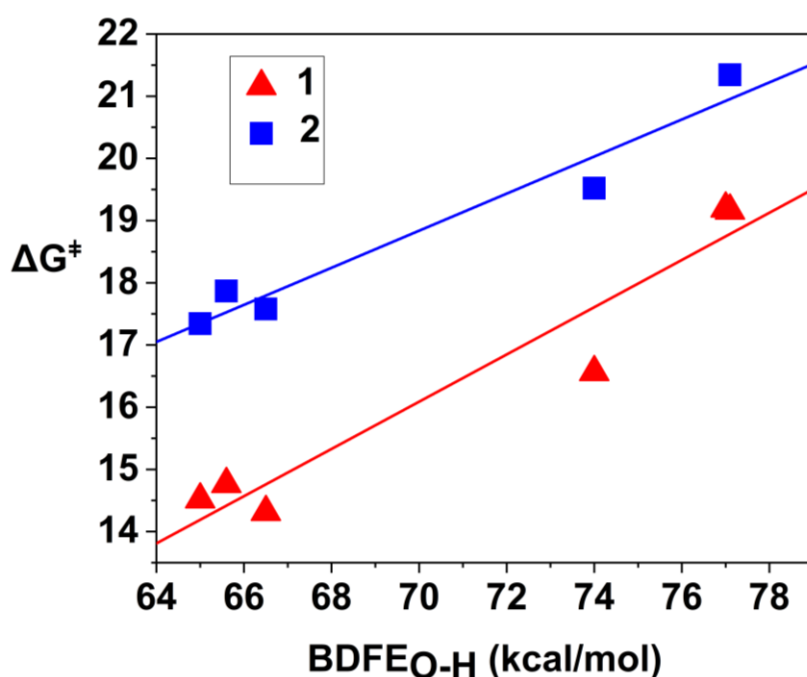


Figure 3.11. Plot of ΔG^\ddagger against the $\text{BDFE}_{\text{O-H}}$ of the substrates for **1** (red triangles) and **2** (blue squares).¹⁴ The values of ΔG^\ddagger were determined from the calculated k_2 constants via the Eyring equation (**1**: slope = 0.39, **2**: slope = 0.30). $\text{BDFE}_{\text{O-H}}$ values are not available for these substrates in DMF; hence, we have plotted $\text{BDFE}_{\text{O-H}}$ values for CH_3CN .²³

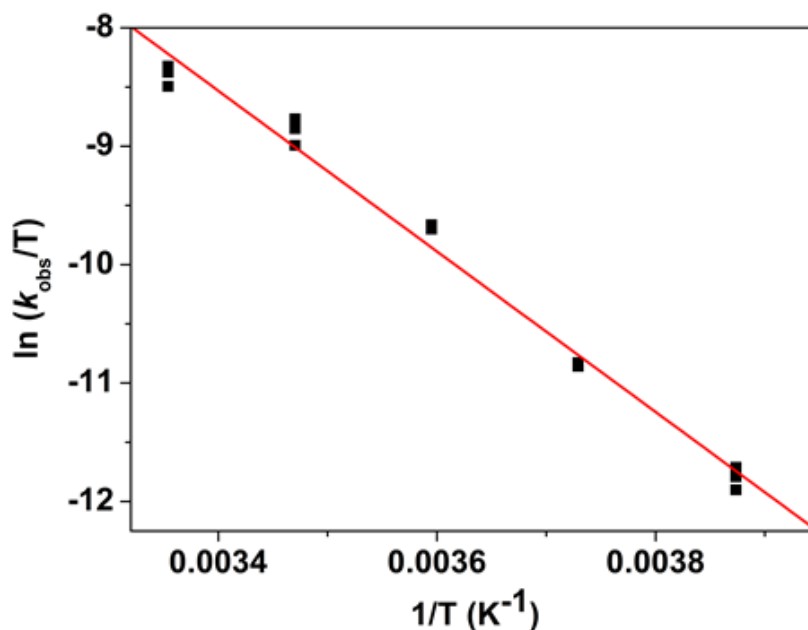


Figure 3.12. Plot of $\ln(k_{\text{obs}}/T)$ versus $1/T$ for **1** in its reaction with 4-CH₃O-2,6-DTBP.

We therefore observed that **1** outperformed **2** consistently for all substrates (Figure 3.11), with the activation barrier on average 2-3 kcal/mol lower for all substrates explored. The Gibbs free energy of activation (ΔG^\ddagger) for the reaction of both complexes with 4-CH₃O-2,6-DTBP was calculated *both* from the Eyring plot (Figure 3.12) and the Bell-Evans-Polanyi plot (Figure 3.11, Table 3.3): for **2** values of 19.7 kcal/mol and 19.5 kcal/mol were obtained, respectively; whereas for **1** values of 17.8 kcal/mol and 16.5 kcal/mol, respectively, were found. Thus, with both methods, **1** showed a lower free energy of activation for the HAT oxidation of a substrate compared to **2**.

Table 3.4. Thermodynamic and kinetic parameters for the reaction of **1** and **2** with 4-CH₃O-2,6-DTBP.

Complex	ΔH^\ddagger (kcal/mol)	ΔS^\ddagger (cal/mol K)	ΔG^\ddagger	ΔG^\ddagger	$\Delta G^\ddagger/\Delta(\text{BDFE})$	KIE ^a
			(Eyring plot)	(Polanyi plot)		
			(kcal/mol) ^a			
1	12.5	-18	17.8	16.5	0.39	1.9
2	9.9	-33	19.7	19.5	0.30	2.9

3.5.1 Driving forces for the reactivity differences: estimation of $BDFE_{H-X}$

After noticing the differences in reactivity between the two complexes, we questioned ourselves about the driving force responsible for the higher competency of **1** with respect to **2**. For HAT oxidants, the thermodynamic parameter to investigate is the $BDFE_{H-Cl/O}$ of the reduced conjugate acids obtained after HAT (*i.e.* $[Au^{II}(\bullet\bullet HCl)(terpy)]^{2+}$ for **1** and $[Au^{II}(H_2O)(terpy)]^{2+}$ for **2**).³² The synthesis of these complexes was not possible because of the tendency of Au^{II} to undergo disproportionation to yield colloidal gold.^{14, 21, 40-42} Nevertheless, $BDFE$ values for both complexes could be estimated using the Bordwell equation: $BDFE_{H-X} = 1.37 (pK_a) + 23.06 (E_{1/2}^{II/III}) + C_G$.²³ We therefore attempted to determine pK_a and redox potential values for the Au^{III} H-X adducts of **1** and **2** ($[Au^{III}(\bullet\bullet HCl)(terpy)]^{3+}$ (**1H⁺**) and $[Au^{III}(H_2O)(terpy)]^{3+}$ (**2H⁺**)), which would allow us to estimate $BDFE_{H-X}$ values in $[Au^{II}(\bullet\bullet HCl)(terpy)]^{2+}$ and $[Au^{II}(H_2O)(terpy)]^{2+}$.

To understand the nature of the $[Au^{II}(\bullet\bullet HCl)(terpy)]^{2+}$ product, we reacted **1** with several carboxylic acids with different pK_a s, observing only very small changes in the ultraviolet region of the electronic absorption spectra (Figures A67-68, Table 3.5). We could not isolate the product of this reaction. We explored by 1H NMR the reaction between **1** and 20 equivalents of trifluoroacetic acid, which showed a marked shift of the water residual peak from $\delta = 3.4$ to $\delta = 10.2$ ppm and showed new resonances in the terpyridine region (8.0-9.5 ppm, Figure 3.13). The shift in the water residual signal is consistent with the formation of protonated water by the acidic species, but the formation of the new set of resonances was indicative that a reaction with the complex had occurred.

To investigate the site of protonation within the complex, we reacted *free* terpyridine with trifluoroacetic acid, which yielded a new set of resonances for the protonated terpyridine that were markedly different to those obtained when trifluoroacetic acid was added to **1** (Figures A69-70). We concluded that the most likely site for protonation was the Cl^- ligand of **1** to yield HCl, therefore surmise that free HCl acts as the thermodynamic driver for HAT by **1**. To the best of our knowledge, a metal-HCl coordination compound has not been reported to date.

Table 3.5. Acids screened for reaction with **1** in DMF at 25 °C. The reported pK_a values are in H₂O.

Acid	pK_a in H ₂ O	Reaction?
HCl	-5.9	Yes, apparent decomplexation
<i>p</i> -toluenesulfonic acid	-2.8	Yes
Trifluoroacetic acid	0.52	Yes
Nitrobenzoic acid	3.41	Yes
Formic acid	3.75	Yes
Benzoic acid	4.19	Yes
Acetic acid	4.75	Yes
Pyridinium triflate	5.21	No
Dimethylformamidium triflate	6.1	No

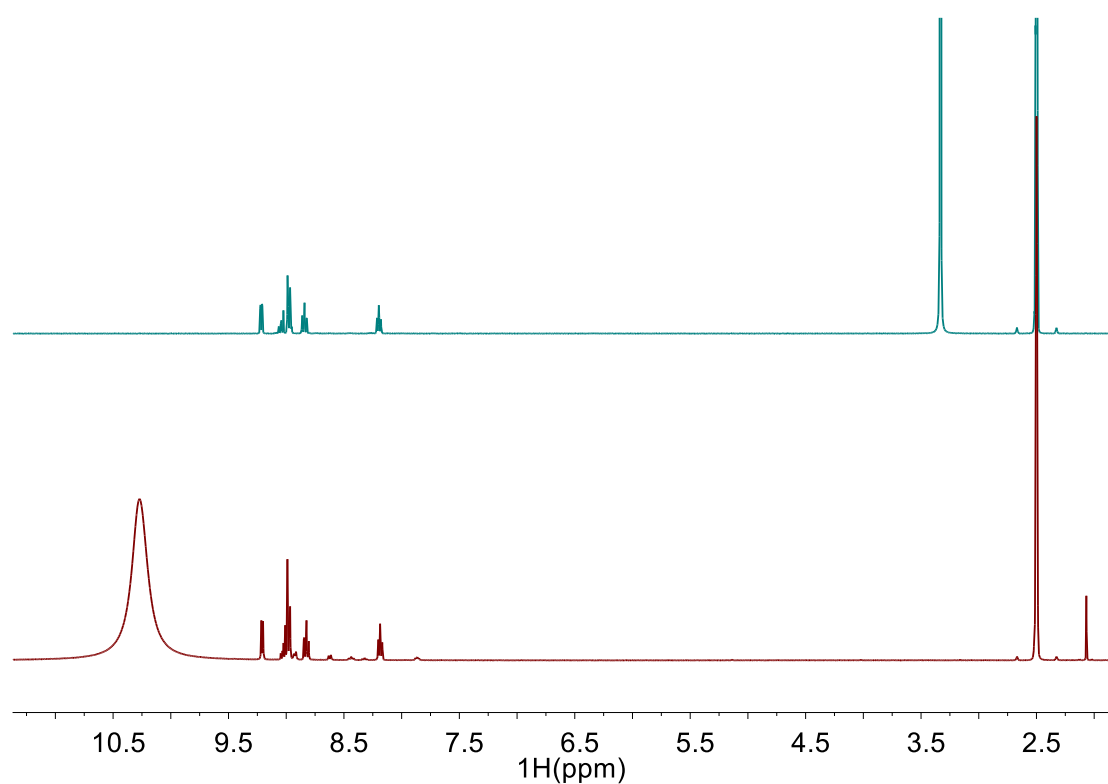


Figure 3.13. ¹H-NMR spectra (400 MHz, DMSO-D₆) of **1** before (green trace) and after (red trace) the addition of 20 equiv. of trifluoroacetic acid.

Then we reacted several H⁺ donors with **2** in an attempt to measure the pK_a of [Au^{III}(H₂O)(terpy)]³⁺ (**2H**⁺) (Figure 3.14, Table 3.6). A blueshift of the bands below $\lambda = 400$ nm and a change in the feature at $\lambda = 545$ nm was observed upon addition of acids with pK_a below 6.1, therefore we postulated that the addition of these acids yielded a new species, **2H**⁺ (Figure A71, Figure 3.14). We observed that formation of this species was reversible by electronic absorption spectroscopy through addition of 2,6-lutidine (Figure 3.15, Figure A72).

We investigated these changes by ^1H NMR and observed that the addition of pyridinium triflate (PyHOTf, 5 equiv.) to **2** resulted in the disappearance of the resonance at $\delta = 6.35$ ppm, assigned to the hydroxide ligand.¹⁴ We subsequently added 5 equiv. of 2,6-lutidine and observed the reappearance of the resonance at $\delta = 6.35$ ppm, indicating the restoring of the hydroxide ligand (Figure 3.15). We therefore concluded that this acid/base reaction was consistent with the interconversion between $[\text{Au}^{\text{III}}(\text{OH})(\text{terpy})]^{2+}$ (**2**) and $[\text{Au}^{\text{III}}(\text{H}_2\text{O})(\text{terpy})]^{3+}$ (**2H⁺**).

Table 3.6. Acids screened for the protonation of complex **2** to yield **2H⁺** in DMF at 25 °C.

Acid	$\text{p}K_{\text{a}}$ in H_2O	Reaction to give 2H⁺ ?
HCl	-5.9	No, apparent decomplexation
<i>p</i> -toluenesulfonic acid	-2.8	Yes
2,6-dimethylbenzoic acid	3.36	Yes
Nitrobenzoic acid	3.41	Yes
Formic acid	3.75	Yes
Toluic acids	3.91	Yes
Benzoic acid	4.19	Yes
Phenylacetic acid	4.31	Yes
Acetic acid	4.75	Yes
Pyridinium triflate	5.21	Yes
Dimethylformamidium triflate	6.1	Yes
Lutidinium perchlorate	6.72	No
Boric acid	9.2	No
Phenol	10	No
Ethanol	16	No

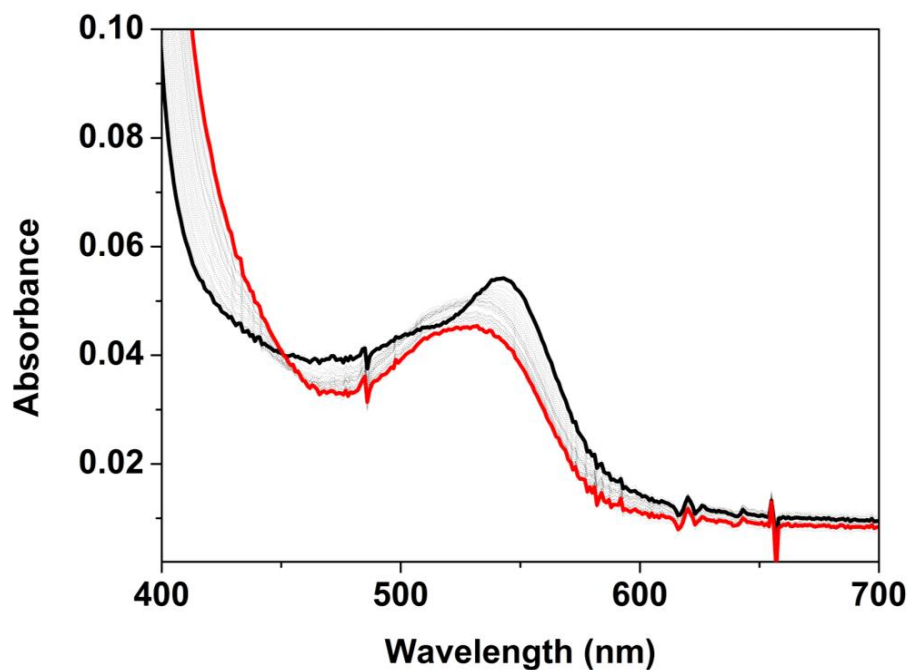


Figure 3.14. Change in the region between 400 and 700 nm of the electronic absorption spectra of **2** (black trace) upon the progressive addition of 1 equiv. of pyridinium triflate to yield **2H⁺** (red trace, 15 equiv. pyridinium triflate).

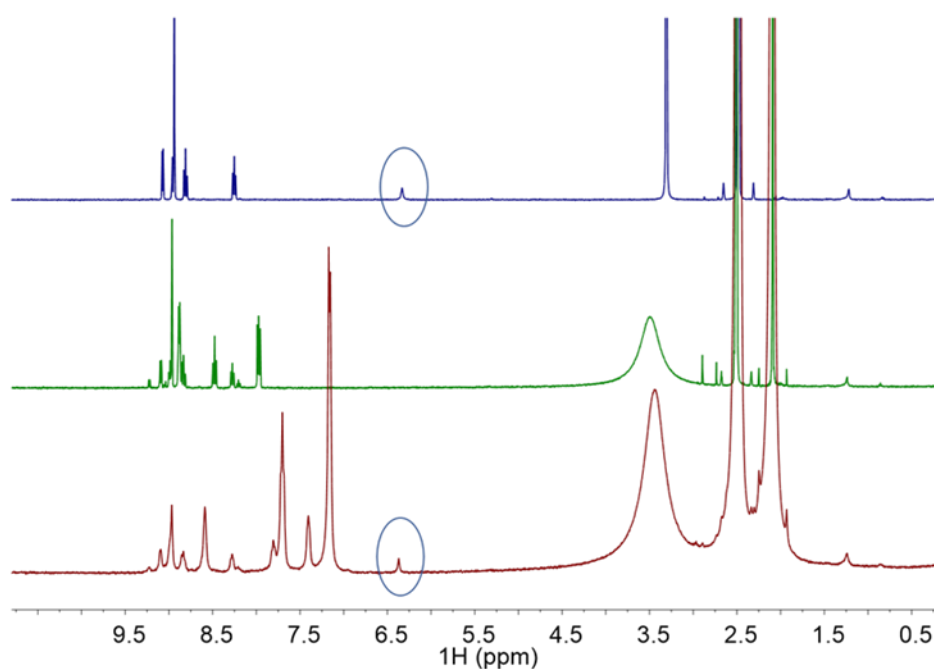


Figure 3.15. ¹H NMR spectra (400 MHz, DMSO-D₆) of **2** (blue trace, 2.6 mM), of **2** upon addition of 5 equiv. of PyHOTf (**2H⁺**, green trace) and of **2H⁺** upon addition of 5 equiv. of 2,6-lutidine (red trace).

We proceeded to measure the equilibrium constant (K_a) for the reaction $\mathbf{2} + \text{PyHOTf} \rightarrow \mathbf{2H}^+ + \text{Py}$ in order to determine $\text{p}K_a$ for $\mathbf{2H}^+$. We adopted a method reported by Mayer and co-workers to determine K_a .⁴³ We monitored the absorptivity changes upon addition of sub-stoichiometric equivalents of PyHOTf to $\mathbf{2}$. For the plot of $[\mathbf{2H}^+][\text{Py}]/[\mathbf{2}]$ against $[\text{PyHOTf}]$, $[\mathbf{2H}^+][\text{Py}]/[\mathbf{2}]$ was calculated as follows: $(A - A_0\mathbf{2})/(A_0\mathbf{2H}^+ - A)$ where A = absorbance intensity at $\lambda = 369$ nm, $A_0\mathbf{2}$ = absorbance intensity at $\lambda = 840$ nm at 100% of $\mathbf{2}$; $A_0\mathbf{2H}^+$ = absorbance intensity at $\lambda = 840$ nm at 100% of $\mathbf{2H}^+$; $[\text{Py}] = (A - A_0\mathbf{2H}^+)/ (A_0\mathbf{2H}^+ - A_0\mathbf{2})$; $[\text{PyHOTf}] = \text{total } [\text{PyHOTf}] \text{ added} - [\text{Py}]$.

The plot of $[\mathbf{2H}^+][\text{Py}]/[\mathbf{2}]$ against $[\text{PyHOTf}]$ showed a linear trend considering the absorbance data taken at $\lambda = 369$ nm, with a slope = 0.11 which is equal to the equilibrium constant for the protonation of $\mathbf{2}$ (K_{eq}). (Figure 3.16). The same result (slope = 0.10) was obtained by plotting the data taken at $\lambda = 545$ nm (Figure A73). A final $\text{p}K_a$ of $\mathbf{2H}^+$ was calculated to be 4.54. Cyclic voltammetry measurements on $\mathbf{2H}^+$ showed the presence of a reversible redox wave at $E_{1/2} = 0.22$ V vs Fc/Fc⁺ (Figure 3.17, Figure A74). This redox wave was assigned to the reversible reduction of Au^{III} to Au^{II}, which occurs at higher potential for $\mathbf{2H}^+$ compared to $\mathbf{2}$ ($E_{\text{red}} = -0.13$ V). Considering the Bordwell equation, we could estimate a BDFE_{O-H} of 81 ± 3 kcal/mol for the aquo-ligand in $[\text{Au}^{\text{II}}(\text{H}_2\text{O})(\text{terpy})]^{2+}$. This result is consistent with the range of the BDFE_{O-H} of the substrates that reacted with $\mathbf{2}$ (65-82 kcal/mol).^{14, 23}

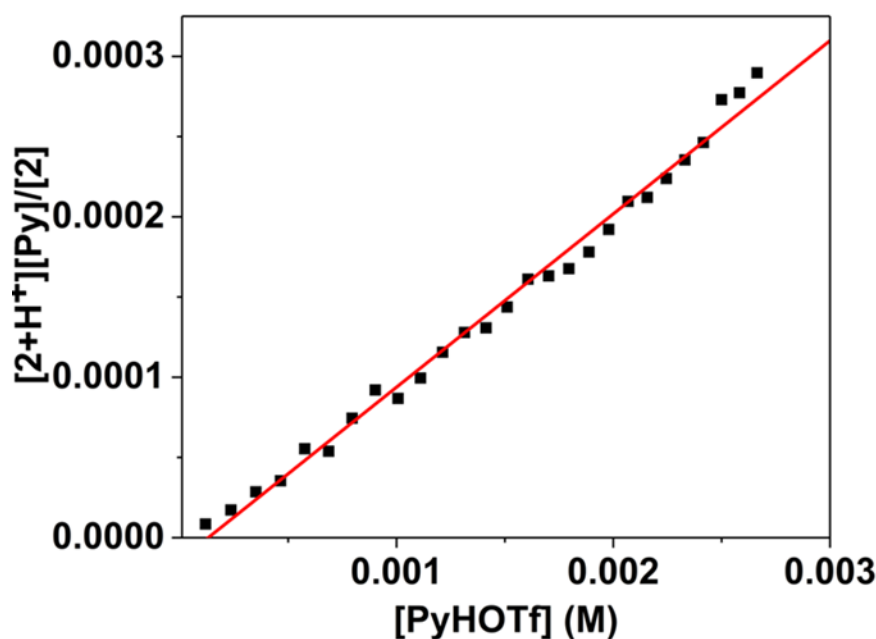


Figure 3.16. Plot of $[\text{PyHOTf}]$ vs $[\mathbf{2H}^+][\text{Py}]/[\mathbf{2}]$. Slope = 0.11

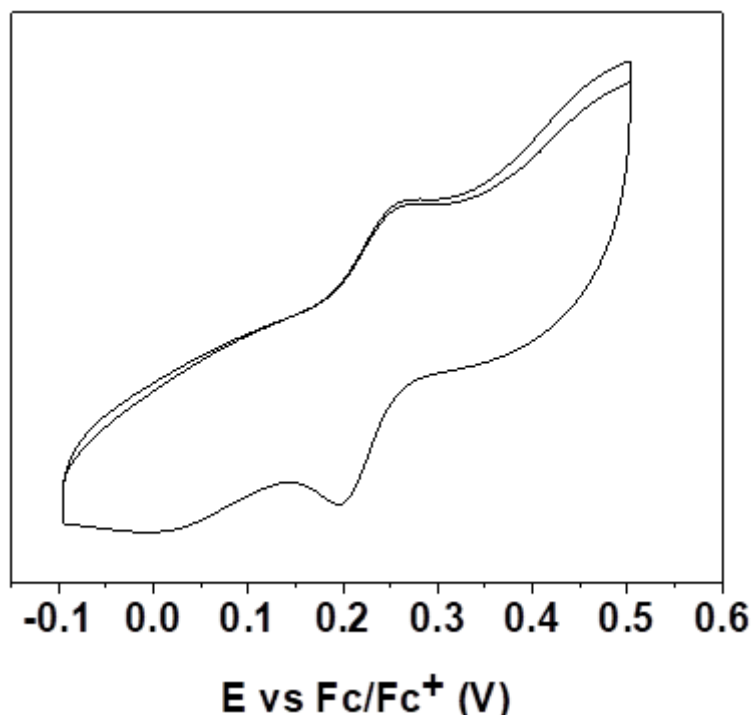


Figure 3.17. Cyclic voltammetry of 2H^+ obtained by adding 1 equiv. of PyHOTf to **2** (DMF, 1 mM), with a focus on the redox wave at $E_{1/2} = 0.22$ V.

The reactivity differences between **1** and **2** can thus be compared with the differences in $\text{BDFE}_{\text{H-X}}$ in the products. For free HCl, $\text{BDFE}_{\text{H-Cl}}$ is only available in the gas phase and equals to 103 kcal/mol,⁴⁴ while for the H_2O ligand in $[\text{Au}^{\text{II}}(\text{H}_2\text{O})(\text{terpy})]^{2+}$ we have estimated a value of 81 kcal/mol. This results in a 22 kcal/mol difference in the BDFE values of the products formed upon HAT by the two complexes. It must be noted that we don't have an estimate for $\text{BDFE}_{\text{H-Cl}}$ in DMF. **1** and **2** displayed similar slope values in the plots that related the $\text{BDFE}_{\text{C-H}}$ and ΔG^\ddagger (0.39 and 0.30, respectively), which indicated that both complexes react through a comparable HAT mechanism. A direct comparison can thus be made between the ratio of the $\text{BDFE}_{\text{H-X}}$ in the products ($\text{BDFE}_{\text{H-Cl}}/\text{BDFE}_{\text{H-O}}$), which represents the thermodynamic driving force, and the ratio of the activation free energies for both oxidants ($\Delta G^\ddagger_2/\Delta G^\ddagger_1$).

This comparison would allow us to assess if the increased value of $\text{BDFE}_{\text{H-Cl}}$ results in a comparable and predictable reduction in activation energy for HAT for the metal-halide adduct compared to the metal-oxygen adduct. In this case $\text{BDFE}_{\text{H-Cl}}/\text{BDFE}_{\text{H-O}} = 1.27$, while $\Delta G^\ddagger_2/\Delta G^\ddagger_1 = 1.10$ or 1.18 depending whether ΔG^\ddagger was calculated through the Eyring or the Polanyi plot (Table 3.4). Given the errors related to these kind of measurements, the similarities in these ratios are striking. A 22 kcal/mol difference in product BDFE value, has resulted in a 2-3 kcal/mol difference in activation energy for HAT.

We conclude that replacing the hydroxide ancillary ligand with the chloride, the stronger HCl bond formed imbues **1** with superior reaction rates, indicating that metal-chloride oxidants would generally yield kinetically more competent oxidants than analogous hydroxides.

3.5.2 Driving forces for the reactivity differences: electronic arguments

The enhanced reactivity of **1** could alternatively be explained considering that the Au–Cl bond displayed greater radical character on the Cl atom. Indeed, **1** showed a higher activation enthalpy and a smaller ΔS^\ddagger than **2**. The ΔS^\ddagger for **1** might suggest that for this complex the reorganization of the vibrational levels after the HAT event was less influenced by the metal centre and possibly more by the Cl ligand, given that it is the only variable in the system. Mader and co-workers observed large negative values of ΔS^\ddagger during a HAT reaction when Fe^{II} complexes bearing different ligands were involved, but very small values when organic radicals were employed for the same type of oxidative mechanism.³⁶ Zhang and co-workers partially ascribed the HAT reactivity of three Cu^{III}–X complexes (X = F, Cl, Br) to the partial radical character on the halogen atoms, as shown by quantum chemical calculations.⁴⁵ Notably, the Cu^{III}–F complex showed a 200-fold higher reactivity with DHA compared to the other two and this was as well attributed to the higher contribution from a Cu^{II}–F[•] bonding situation, despite still reporting a very large and negative ΔS^\ddagger (–43 cal mol^{–1} K^{–1}).⁴⁵ Therefore we investigated the electronic structure of **1** and **2** to have more insight on their possible role on the reactivity of the complexes.

Starting from the respective single crystal X-ray structures of **1** (Figure 3.2) and **2**⁴⁶ the geometry was optimized via DFT calculations using unrestricted BP86/def2-TZVPP (C, H, N, O, Cl)/SARC-ZORA-TZVPP (Au) with 0th order regular approximation and COMSO(DMF) level of theory (Figures A75-76, Tables A2-3). The obtained geometries were in good agreement with the X-ray structures (Figures S34-S35, Tables S7-S8). *Ab initio* CASSCF(8,5) calculations were conducted to shed light on the ligand field differences between **1** and **2** (Figure 3.18). For **1**, the *d* orbitals followed this order energetically: *d*(z²), E=0.00 eV; *d*(xz), E=0.48 eV; *d*(xy), E=0.70 eV; *d*(yz), E=0.71 eV; *d*(x²-y²), E=5.61 eV. Interestingly, the same orbitals for **2** presented markedly different energies and a different order: *d*(z²), E=0.00 eV; *d*(xz), E=0.33 eV; *d*(yz), E=0.38 eV; *d*(xy), E=1.02 eV; *d*(x²-y²), E=5.98 eV. Therefore the *d*(yz) and the *d*(xy) orbitals were inverted in the energy order for **1** with respect

to **2** and the lifting of the d(yz) orbital was indicative of a stronger π -back bonding of Au toward Cl over the Au-OH bond along the yz-plane.

From this analysis, the Racah parameter B could be obtained in order to quantify the interelectronic repulsion.⁴⁷ A decrease of magnitude of B with respect to the free Au^{III} ion (B_0) showed a correlation, known as the nephelauxetic effect. The ratio $\beta = B/B_0$ gives an indication of charge transfer from the metal center towards the ligand: the smaller β , the higher charge transfer and therefore more covalency is present in the metal-ligand bond.⁴⁸ The parameter β is lower for **1** (0.49) than **2** (0.64), which is in alignment with a decrease in magnitude of the Mulliken atomic charges going from **2** (Au: 1.43, O: -0.77) to **1** (Au: 1.28, Cl: -0.46). This suggests a higher contribution of Au^{II}-Cl' together with the dominant Au^{III}-Cl bond description for **1**.⁴⁷

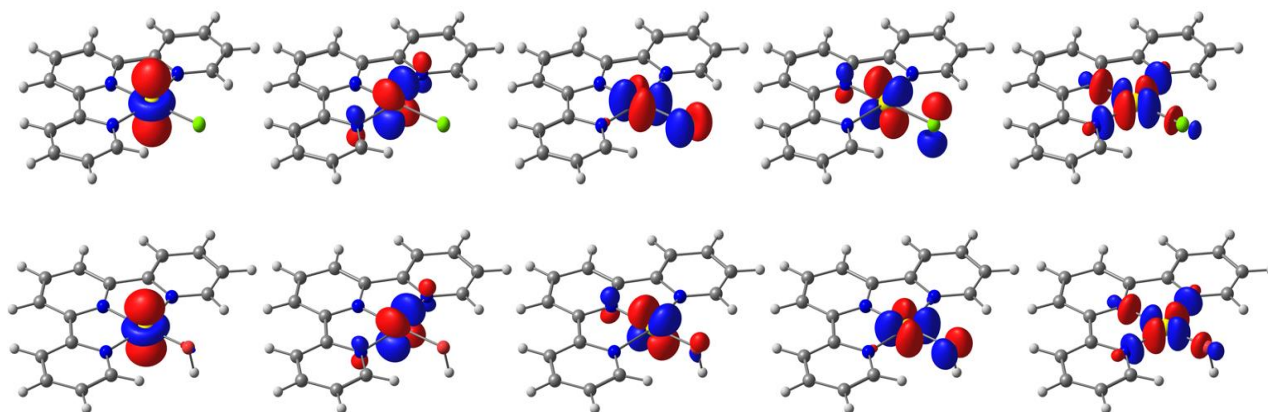


Figure 3.18. AILFT CASSCF(8,5) orbitals of **1** (top) and **2** (bottom) at 0.08 au isosurface value.

The Electron Localised Function (ELF) showed a minimum along the bond path between the Au cation and the oxygen of the hydroxide ligand in **2** (ELF at bond critical point: 0.23), whereas a higher likelihood of localisation was observed along the bond path between Au and Cl in **1** (ELF at bond critical point: 0.29; Figure S36). This result also indicates that the Cl ligand has more radical character due to a shift in electron density of the Au-Cl bond from a purely ionic interaction (Au^{III}••Cl) towards covalent contributions (Au^{II}-Cl'). These calculations suggest that the Cl atom in **1** may display marginally greater radical character than the O-atom in **2**, potentially lowering the barrier to HAT in reactions with phenols.

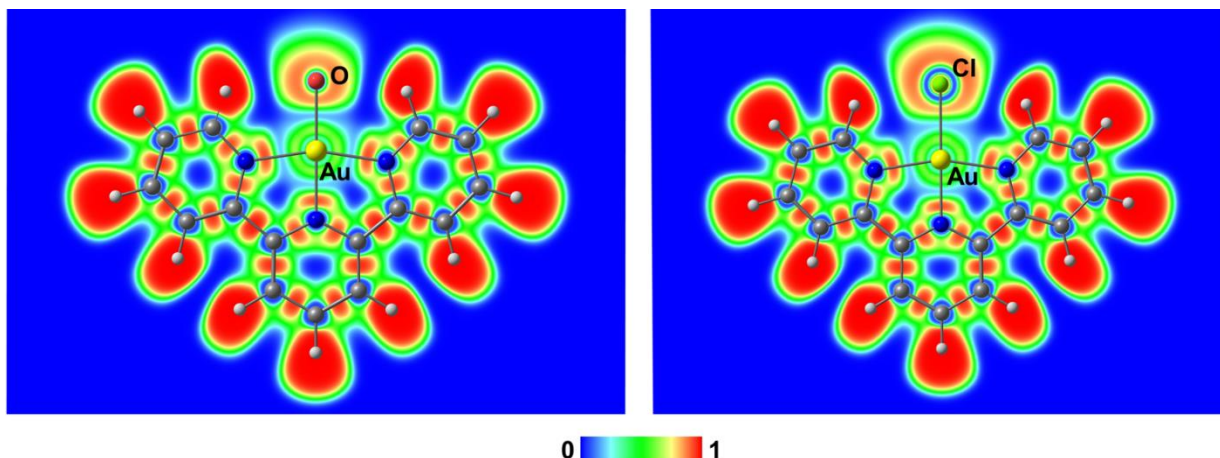


Figure 3.19. ELF plots for **2** (left) and **1** (right). The scale in the center refers to the probability of finding electron density along the depicted plane in the range 0-1, from the lowest (0, blue) to the highest (1, red).

We could not exclude that a synergic effect of the lowered barrier for HAT due to the formation of the stronger HCl bond and the greater radical character on the Cl atom could be responsible for the higher competency of **1** respect to **2**. Nevertheless, we currently favour the thermodynamic driving force argument because of the stronger experimental support for this postulate.

3.6 Reactivity with C–H bonds

Analogously to what observed for **2**, **1** also reacted with the hydrocarbons 1,4-cyclohexadiene (CHD) and 9,10-dihydroanthracene (DHA). For CHD, benzene was identified as the only product (yield = $105 \pm 10\%$ for a 2-electron oxidation by **1** monitored by ^1H NMR, Table 3.2, Figures A77-78). The ^1H NMR spectra from this reaction also showed a shift and broadening of the residual signal attributed to H_2O ($\delta = 3.34$ ppm to $\delta = 3.72$ ppm), suggesting the increase in the water content upon reaction with CHD which could be attributed to the change in pH occurring in the solution (Figure AX).¹⁴ The reaction with DHA (500 equiv., DMF, 25 °C, Figure A79) showed a change in the electronic absorption spectrum together with the formation of the absorption bands typical of anthracene ($\lambda = 341, 360,$ and 379 nm), a 2 protons, 2 electrons PCET oxidised product. The plot of k_{obs} versus [DHA] showed a linear correlation with $k_2 = 0.046 \text{ M}^{-1}\text{s}^{-1}$, which is slightly higher compared to that measured for **2** ($0.020 \text{ M}^{-1}\text{s}^{-1}$).¹⁴ The reaction was repeated using DHA- D_4 ($k_2 = 0.018 \text{ M}^{-1}\text{s}^{-1}$), yielding a primary kinetic isotope effect of 2.5 (Figure 3.20). The yield of anthracene was determined by GC-FID to be

$80 \pm 5\%$, when a 2-electron reaction was considered (Table 3.2). We therefore concluded that **1** was a capable hydrocarbon oxidant at room temperature and reacted more rapidly than **2**. Interestingly, these observations for the activation of substrates bearing C–H bonds are consistent with the kinetic and mechanistic analysis performed using substrates containing O–H bonds.

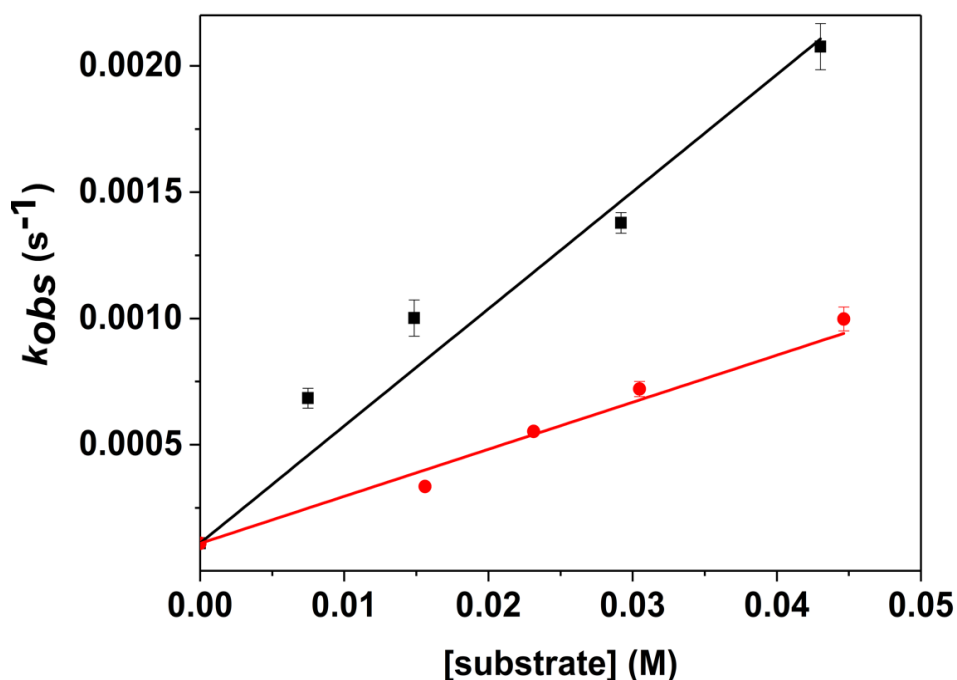


Figure 3.20. Plot of k_{obs} versus [substrate] determined for the reaction between complex **1** and DHA-[H]₄ (black trace) and DHA-[D]₄ (red trace).

3.7 Conclusions

In conclusion, we compared the reactivity of two high-valent oxidants differing only by their ancillary ligand, Cl⁻ (**1**) vs OH⁻ (**2**). The two complexes were reacted under the exact same conditions (DMF, 25 °C). Both oxidants followed a HAT mechanism of C–H and O–H bond activation. The Au^{III}–Cl complex reacted at superior rates with all substrates compared to the Au^{III}–OH complex. We ascribed this to a greater thermodynamic driving force provided by the HCl product of HAT oxidation by **1** compared to [Au^{II}(H₂O)(terpy)]²⁺, which is the product of HAT oxidation by **2** for which we estimated a 22 kcal/mol lower BDFE_{H-X}. We therefore compared the free energy of activation of the two complexes, finding it to be 2-3 kcal/mol lower for **1** respect to **2**, according to the method used for the calculation. We discovered that there is a correlation between the ratio of the thermodynamic driving forces, BDFE_{H-Cl}/BDFE_{H-O}, and the ratio of the free energies of activation, $\Delta G^{\ddagger}_2 / \Delta G^{\ddagger}_1$, which were very close within the experimental error. Therefore we concluded that the replacement of the ancillary

ligand can tune the properties and the reactivity of a HAT oxidant and that metal-halide oxidants can yield lower activation barriers towards activation of C–H and O–H bond than their corresponding metal-oxygen adducts.

3.8 Experimental section

Materials

All solvents and reagents were purchased from commercial sources and used as received, unless otherwise stated. Complex **1** was synthesized as reported.⁴⁶ Either KAuCl₄ or HAuCl₄ were used as starting materials for the synthesis of **1**, they were purchased from Sigma Aldrich or Fisher Scientific and used as received. p-X-2,6-di-*tert*-butylphenols were recrystallized from hexane or ethanol/water prior to use. For reactions performed in the absence of oxygen, solvents (N,N-dimethylformamide, tetrahydrofuran, diethyl ether) were freeze-pump-thawed three times and stored in a nitrogen atmosphere glovebox. TEMPOH (1-hydroxy-2,2,6,6-tetramethyl-piperidine), 4-CH₃O-TEMPOH (4-methoxy-1-hydroxy-2,2,6,6-tetramethyl-piperidine) and 4-oxo-TEMPOH (4-oxo-1-hydroxy-2,2,6,6-tetramethyl-piperidine) were synthesized according to reported procedures.⁴⁹ 4-CH₃O-[*D*]-2,6-DTBP was synthesized according to a reported procedure.⁵⁰ [*D*]₄-9,10-dihydroanthracene ([*D*]₄-DHA) was synthesized according to a reported procedure (deuteration degree = 97% by ¹H-NMR).⁵¹

Physical Methods

¹H and ¹³C{¹H} nuclear magnetic resonance (NMR) analyses were performed on an Agilent MR400 instrument (400.13 MHz for ¹H NMR, 100.61 MHz for ¹³C{¹H} NMR). The signals were internally referenced to tetramethylsilane. Electronic absorption spectra were recorded on a Hewlett Packard (Agilent) 8453 diode array spectrophotometer. Electrospray ionization (ESI) mass spectra were acquired using a Micromass time of flight spectrometer (TOF), interfaced to a Waters 2690 HPLC. Attenuated total reflectance infra-red (ATR-FTIR) spectra were recorded on a Perkin-Elmer Spectrum 100 Fourier transform infrared spectrometer.

Crystallographic analysis

Crystals suitable for single crystal X-ray diffraction measurements were grown over two days from a N,N-dimethylformamide (DMF)/ diethyl ether (Et₂O) mixture. Data were measured ($\lambda = 0.71073 \text{ \AA}$) at 100(2)K on a Bruker D8 Quest Eco with an Oxford Cryostream low temperature device using a MiTeGen micromount. Bruker APEX⁵² software was used to

collect the data and correct for Lorentz and polarization effects. Data were integrated with SAINT⁵³ and corrected for absorption effects using the Multi-Scan method, SADABS.⁵⁴ The structure was solved with the XT⁵⁵ structure solution program using Intrinsic Phasing and refined with the XL⁵⁶ refinement package using Least Squares minimization with Olex2,⁵⁷ using the space group P2₁, with Z = 2. This confirms the desired structure with formula unit, C₁₅H₁₁AuCl₃N₃O₈, with slightly different cell parameters with respect to those already reported⁵⁸.^[6] The structure was refined as an inversion twin, with a refined Flack parameter of 0.011(6). One perchlorate displays disorder in one oxygen site which was modelled in two orientations with the majority population 0.58(4) using geometric (SADI) and displacement (ISOR, SIMU) restraints. The growth of such crystals over two days showed that was **1** stable in dry DMF, allowing its reactivity to be explored in such conditions. Crystallographic data for this paper have been deposited with the Cambridge Crystallographic Data Centre as supplementary publication no. 2079645. Copies of the data can be obtained, free of charge, on application to CCDC, 12 Union Road, Cambridge CB2 1EZ, UK, (fax: +44-(0)1223-336033 or e-mail:deposit@ccdc.cam.ac.uk).

EPR analysis

Electron paramagnetic resonance (EPR) spectra of frozen solutions were acquired on a Bruker EMX X-band EPR, equipped with an Oxford Instruments CE 5396, ESR9 Continuous Flow Cryostat, a precision Temperature Controller and an Oxford Instruments TTL20.0/13 Transfer Tube. EPR samples were prepared by freezing the EPR tubes containing the analyte solutions, previously prepared at the UV-Vis spectrophotometer, in liquid nitrogen. EPR spectra of the 2,4,6-tris-*tert*-butylphenoxy radical were recorded at 77 K, 9.2 GHz, 0.2 mW microwave power, with a 10 mT field sweep in 84 s, and 0.2 mT field modulation amplitude. EPR spectra of 4-X-TEMPO were recorded at 77 K, 9.2 GHz, 2.02 mW microwave power, with a 60 mT field sweep in 84 s, and 0.3 mT field modulation amplitude. Integration, simulation, and fitting were performed with Matlab and the easySpin computational package.⁵⁹ The simulation for the phenoxy radicals spectra was modelled as an $S = \frac{1}{2}$ electron spin with an isotropic g tensor. The oxidation yield of the samples was calculated by quantification of the concentration of spin in the samples. This was obtained by comparison of the double integral of the signals to that of a frozen reference 3 mM solution of (2,2,6,6-tetramethyl-piperidin-1-yl)oxyl (TEMPO), measured under the same conditions.

Electrochemistry

Cyclic voltammetry (CV) experiments were conducted with a CH Instruments 600E electrochemical analyzer, using a glassy carbon working electrode, a platinum wire counter electrode and an Ag/AgNO₃ 0.01 M reference electrode. Cyclic voltammetry experiments were conducted on a 1.0 mM solution of **1** in DMF and on a 1.0 mM solution of **2H**⁺ in DMF at room temperature, with a 0.05, 0.1 and 0.2 V s⁻¹ under an argon atmosphere. In both experiments 0.1 M ⁿBu₄NPF₆ was used as the supporting electrolyte. Potentials were referenced against the Fc⁺/Fc couple (Fc = ferrocene). The voltammograms of Fc were acquired under the same conditions.

Gas chromatography-Flame Ionisation Detector (GC-FID) analysis

Gas chromatography experiments have been performed using a ThermoFisher TRACE™ 1300 Gas Chromatograph equipped with a Flame Ionisation Detector. Hydrogen was provided by a Parker Hydrogen Gas Generator 20H-MD. Air was provided by Parker Zero Air Generator UHP-10ZA-S. The column used was a ThermoFisher Trace GOLD TG-1MS GC column. Post-reaction solutions from the reaction of **1** with different substrates were prepared at 25 °C. Different amounts of substrate (4-CH₃O-2,6-DTBP, 2,4,6-TTBP, 2,6-DTBP, DHA) were added as DMF solutions under continuous stirring until completion of the reaction, after which the mixture was analysed by GC-FID. A reference standard solution was prepared by adding the same amount of equivalents of substrate to 2 mL of pure DMF. The instrument method for anthracene was based on a temperature ramp (2 min at 175 °C, 10 °C/min to 250 °C, 2 min at 250 °C) with splitless injections of 1 µL each. Under these conditions, the retention time for anthracene was between 6.3-6.4 min. The instrument method for 2,6-di-*tert*-butylquinone was based on a temperature ramp (2 min at 75 °C, 10°C/min to 200 °C, 2 min at 200 °C) with splitless injections of 1 µL each. Under these conditions, the retention time for 2,6-di-*tert*-butylquinone was between 12.3-12.4 min. The quantitative analysis of the analytes was based on a calibration curve. Yields were calculated as an average of four different solutions containing the same number of equivalents of substrate and repeating it for 2-3 different substrates concentrations.

Quantum chemical calculations

The geometry optimizations of **1** and **2** were carried out with ORCA 4.1.2 using DFT unrestricted BP86 functional, def2-TZVPP basis set for C, H, N, O, Cl and SARC-ZORA-TZVPP for Au atoms and atom pairwise dispersion correction with Becke-Johnson damping scheme (D3BJ). Calculations were started from the molecular structures of **1** and **2** obtained by single crystal X-ray diffraction. From the DFT obtained geometries, the CASSCF(8,5) orbitals were pre-converged using a much smaller basis set SV for C, H, N, O, Cl and SARC-ZORA-TZVPP for Au only in singlet state (n roots = 15) without COSMO(DMF). *Ab initio* ligand field analysis were performed at stage-average CASSCF(8,5) level of theory using the def2-TZVPP basis set for C, H, N, O, Cl and SARC-ZORA-TZVPP for Au in singlet (nroots 15) and triplet (nroots 10) states including COSMO(DMF). Mulliken atomic charges and ELF calculations were performed on the final CASSCF(8,5) wavefunction using MultiWFN.⁶⁰ Graphics were generated using ChemCraft.⁶¹

3.9 References

1. P. Mondal, P. Pirovano, A. Das, E. R. Farquhar and A. R. McDonald, *J. Am. Chem. Soc.*, 2018, **140**, 1834-1841.
2. P. Mondal, M. Lovisari, B. Twamley and A. R. McDonald, *Angew. Chem. Int. Ed.*, 2020, **59**, 13044-13050.
3. J. K. Bower, A. D. Cypcar, B. Henriquez, S. C. E. Stieber and S. Zhang, *J. Am. Chem. Soc.*, 2020, **142**, 8514-8521.
4. B. J. Shields and A. G. Doyle, *J. Am. Chem. Soc.*, 2016, **138**, 12719-12722.
5. M. K. Nielsen, B. J. Shields, J. Liu, M. J. Williams, M. J. Zacuto and A. G. Doyle, *Angew. Chem. Int. Ed.*, 2017, **56**, 7191-7194.
6. B. J. Shields, B. Kudisch, G. D. Scholes and A. G. Doyle, *J. Am. Chem. Soc.*, 2018, **140**, 3035-3039.
7. S. I. Ting, S. Garakyaraghi, C. M. Taliaferro, B. J. Shields, G. D. Scholes, F. N. Castellano and A. G. Doyle, *J. Am. Chem. Soc.*, 2020, **142**, 5800-5810.
8. A. Corma and H. Garcia, *Chem. Soc. Rev.*, 2008, **37**, 2096-2126.
9. R. Ciriminna, E. Falletta, C. Della Pina, J. H. Teles and M. Pagliaro, *Angew. Chem. Int. Ed.*, 2016, **55**, 14210-14217.
10. C. D. Pina, E. Falletta and M. Rossi, *Chem. Soc. Rev.*, 2012, **41**, 350-369.
11. M. A. Cinellu, G. Minghetti, F. Cocco, S. Stoccoro, A. Zucca and M. Manassero, *Angew. Chem. Int. Ed.*, 2005, **44**, 6892-6895.
12. G. B. Shul'pin, A. E. Shilov and G. Süß-Fink, *Tetrahedron Lett.*, 2001, **42**, 7253-7256.
13. B. Pitteri, G. Marangoni, F. Visentin, T. Bobbo, V. Bertolasi and P. Gilli, *J. Chem. Soc., Dalton Trans.*, 1999, DOI: 10.1039/A806098C, 677-682.
14. M. Lovisari and A. R. McDonald, *Inorg. Chem.*, 2020, **59**, 3659-3665.
15. L. S. Hollis and S. J. Lippard, *J. Am. Chem. Soc.*, 1983, **105**, 4293-4299.
16. H.-Q. Liu, T.-C. Cheung, S.-M. Peng and C.-M. Che, *J. Chem. Soc., Chem. Commun.*, 1995, DOI: 10.1039/C39950001787, 1787-1788.
17. K. Czerwińska, M. Golec, M. Skonieczna, J. Palion-Gazda, D. Zygadło, A. Szlapa-Kula, S. Krompiec, B. Machura and A. Szurko, *Dalton Trans.*, 2017, **46**, 3381-3392.
18. A. Maroń, K. Czerwińska, B. Machura, L. Raposo, C. Roma-Rodrigues, A. R. Fernandes, J. G. Małecki, A. Szlapa-Kula, S. Kula and S. Krompiec, *Dalton Trans.*, 2018, **47**, 6444-6463.
19. M. A. Mansour, R. J. Lachicotte, H. J. Gysling and R. Eisenberg, *Inorg. Chem.*, 1998, **37**, 4625-4632.

20. G. Sanna, M. I. Pilo, G. Minghetti, M. A. Cinellu, N. Spano and R. Seeber, *Inorg. Chim. Acta*, 2000, **310**, 34-40.
21. T. Dann, D.-A. Roşca, J. A. Wright, G. G. Wildgoose and M. Bochmann, *Chem. Commun.*, 2013, **49**, 10169-10171.
22. G. B. Wijeratne, B. Corzine, V. W. Day and T. A. Jackson, *Inorg. Chem.*, 2014, **53**, 7622-7634.
23. J. J. Warren, T. A. Tronic and J. M. Mayer, *Chem. Rev.*, 2010, **110**, 6961-7001.
24. S. Kundu, P. Chernev, X. Engelmann, C. S. Chung, H. Dau, E. Bill, J. England, W. Nam and K. Ray, *Dalton Trans.*, 2016, **45**, 14538-14543.
25. H. E. Gottlieb, V. Kotlyar and A. Nudelman, *J. Org. Chem.*, 1997, **62**, 7512-7515.
26. G. R. Fulmer, A. J. M. Miller, N. H. Sherden, H. E. Gottlieb, A. Nudelman, B. M. Stoltz, J. E. Bercaw and K. I. Goldberg, *Organometallics*, 2010, **29**, 2176-2179.
27. P. Pirovano, E. R. Farquhar, M. Swart and A. R. McDonald, *J. Am. Chem. Soc.*, 2016, **138**, 14362-14370.
28. T. Corona, A. Draksharapu, S. K. Padamati, I. Gamba, V. Martin-Diaconescu, F. Acuna-Pares, W. R. Browne and A. Company, *J. Am. Chem. Soc.*, 2016, **138**, 12987-12996.
29. M. K. Goetz and J. S. Anderson, *J. Am. Chem. Soc.*, 2019, **141**, 4051-4062.
30. G. Spedalotto, R. Gericke, M. Lovisari, E. Farquhar, B. Twamley and A. R. McDonald, *Chem. Eur. J.*, **25**, 11983-11990.
31. J. M. Mayer, *Annu. Rev. Phys. Chem.*, 2004, **55**, 363-390.
32. J. M. Mayer, *Acc. Chem. Res.*, 2011, **44**, 36-46.
33. R. Gericke, L. M. Doyle, E. R. Farquhar and A. R. McDonald, *Inorg. Chem.*, 2020, **59**, 13952-13961.
34. P. Pirovano and A. R. McDonald, *Eur. J. Inorg. Chem.*, 2018, **2018**, 547-560.
35. E. A. Mader, E. R. Davidson and J. M. Mayer, *J. Am. Chem. Soc.*, 2007, **129**, 5153-5166.
36. E. A. Mader, V. W. Manner, T. F. Markle, A. Wu, J. A. Franz and J. M. Mayer, *J. Am. Chem. Soc.*, 2009, **131**, 4335-4345.
37. M. Lovisari and A. R. McDonald, *Inorg. Chem.*, 2020, **59**, 6, 3659-3665.
38. C. Costentin, M. Robert and J.-M. Savéant, *J. Am. Chem. Soc.*, 2007, **129**, 5870-5879.
39. S. E. Ghachtouli, R. Guillot, A. Aukauloo, P. Dorlet, E. Anxolabéhère-Mallart and C. Costentin, *Inorg. Chem.*, 2012, **51**, 3603-3612.
40. S. A. C. Carabineiro, L. M. D. R. S. Martins, M. Avalos-Borja, J. G. Buijnsters, A. J. L. Pombeiro and J. L. Figueiredo, *Appl. Catal. A*, 2013, **467**, 279-290.
41. K. Dang Nguyen VÕ, C. Kowandy, L. Dupont and X. Coqueret, *Chem. Commun.*, 2015, **51**, 4017-4020.
42. S. Preiß, C. Förster, S. Otto, M. Bauer, P. Müller, D. Hinderberger, H. Hashemi Haeri, L. Carella and K. Heinze, *Nat. Chem.*, 2017, **9**, 1249.
43. A. Wu, J. Masland, R. D. Swartz, W. Kaminsky and J. M. Mayer, *Inorg. Chem.*, 2007, **46**, 11190-11201.
44. J. Berkowitz, G. B. Ellison and D. Gutman, *J. Phys. Chem.*, 1994, **98**, 2744-2765.
45. J. K. Bower, A. D. Cypcar, B. Henriquez, S. C. E. Stieber and S. Zhang, *J. Am. Chem. Soc.*, 2020, **143**, 1, 46-52.
46. B. Pitteri, G. Marangoni, F. Visentin, T. Bobbo, V. Bertolasi and P. Gilli, *J. Chem. Soc., Dalton Trans.*, 1999, **5**, 677-682.
47. S. K. Singh, J. Eng, M. Atanasov and F. Neese, *Coord. Chem. Rev.*, 2017, **344**, 2-25.
48. H. Lueken, *Magnetochemie – Eine Einführung in Theorie und Anwendung*, Teubner Studienbücher Chemie, 1999.
49. K. S. Chan, X. Z. Li, W. I. Dzik and B. de Bruin, *J. Am. Chem. Soc.*, 2008, **130**, 2051-2061.
50. J. Y. Lee, R. L. Peterson, K. Ohkubo, I. Garcia-Bosch, R. A. Himes, J. Woertink, C. D. Moore, E. I. Solomon, S. Fukuzumi and K. D. Karlin, *J. Am. Chem. Soc.*, 2014, **136**, 9925-9937.
51. C. Arunkumar, Y.-M. Lee, J. Y. Lee, S. Fukuzumi and W. Nam, *Chem. Eur. J.*, 2009, **15**, 11482-11489.
52. B. A. I. APEX3 v2017.3-0, Madison, WI, USA.
53. SAINT v8.38A, Bruker AXS Inc., Madison, WI, USA.
54. L. Krause, R. Herbst-Irmer, G. M. Sheldrick and D. Stalke, *J. Appl. Cryst.*, 2015, **48**, 3-10.
55. G. Sheldrick, *Acta Cryst.*, 2015, **71**, 3-8.
56. G. Sheldrick, *Acta Cryst.*, 2015, **71**, 3-8.
57. O. V. Dolomanov, L. J. Bourhis, R. J. Gildea, J. A. K. Howard and H. Puschmann, *J. Appl. Cryst.*, 2009, **42**, 339-341.
58. M. D. Đurović, Ž. D. Bugarčić, F. W. Heinemann and R. van Eldik, *Dalton Trans.*, 2014, **43**, 3911-3921.
59. S. Stoll and A. Schweiger, *J. Mag. Res.*, 2006, **178**, 42-55.
60. T. Lu and F. Chen, *J. Comput. Chem.*, 2012, **33**, 580-592.
61. Chemcraft ver. 1.8 (build 164).

Chapter 4

A [Ni^{II}(porphyrin^{•+})] complex for C–H bond activation

4.1 Introduction

Heme-based oxidant species take part in many enzymatic catalytic cycles. One example is given by the Compound I found in the catalytic cycle of several enzymes such as cytochrome P450, halogenases and peroxidases.¹ Another relevant example of a powerful oxidant supported by a porphyrinoid ligand is given by P680, the main electron donor in photosystem II,² which is known as the most powerful oxidant in nature having a redox potential of 1.2 V in its oxidised state (P680⁺) with the oxidising equivalents delocalised over the chlorophyll molecules, yielding a formal porphyrinoid π -radical cation.^{2, 3} A similar structure has been postulated for the corresponding center found in photosynthetic bacteria, P865.⁴ Therefore porphyrin π -radical cation species are often the active oxidant in the catalytic cycles of enzymes and represent a class of powerful oxidants to look at for inspiration during the design of new synthetic catalysts. Spectroscopic studies on oxidised metalloporphyrins showed that valence tautomerism is possible between the π -radical cation, where the oxidation is borne on the porphyrin ligand, and a species where the oxidation is borne on the metal: the most favourable tautomer is influenced by the temperature, the solvent and the presence of ancillary ligands.^{5, 6} The introduction of a fifth or sixth ligand in particular can switch the equilibrium towards the metal-oxidised species, yielding a potential oxidant with different physical and chemical features.⁷

To this respect, many examples of powerful metal-based oxidants supported by porphyrin and porphyrinoid ligands have been reported. Goldberg reported a [Mn^{IV}(OH)(tppc)] (tppc = tris-(2,4,6-triphenylphenyl)corrole) and a [Fe^{IV}(OH)(tppc)] which were powerful HAT oxidants towards phenolic substrates at room temperature.^{8, 9} Groves reported a [Mn^{III}(F)(TMP)] (TMP = tetramesitylporphyrin) complex which is oxidised by PhIO to [Mn^V(O)(F)(TMP)], a powerful oxidant capable of abstracting a hydrogen atom from a hydrocarbon substrate to yield a carbon based radical.¹⁰ Then the rebound of the radical to either a [Mn^{IV}(OH)(F)(TMP)] species or a *trans*-[Mn^{IV}(F)₂(TMP)], formed upon ligand exchange with AgF, yields the fluorinated alkane product.¹⁰ Recently, our group reported a *meso*-chloro isoporphyrin complex, [Fe^{III}(Cl)₂(T(OMe)PP-Cl)] (T(OMe)PP = *meso*-tetra(4-methoxyphenyl)porphyrin), capable of oxidation of hydrocarbons at 20 °C, which followed a HAT mechanism of oxidation.¹¹ Many of these examples show how reactive species of mid-transition metals

supported by porphyrin ligands acted as competent oxidants towards substrates containing C–H bonds.

On the other hand, to the best of our knowledge no investigation has been done on the oxidative reactivity of high-valent late transition (Ni, Cu) porphyrin complexes. We believe that the π -radical cation of these complexes would be more reactive due to the presence of metals with higher d electron count which are purportedly more reactive when oxidised.

Furthermore, we are interested in exploring the addition of ancillary ligands ($X = F^-$, Cl^- , I^- , OH^-) to the oxidised species to investigate the effect on the valence tautomerism of the oxidised species and possibly on their reactivity, notably towards hydrocarbon substrates. We are in fact inspired by the strong oxidative potential of porphyrin π -radical cations in nature and we believe that these synthetic mimics containing late-transition metal could be powerful candidates towards the mild oxidation of saturated hydrocarbons.

4.2 Synthesis and characterization of $[M(T(OMe)PP)]^{n+}$ complexes ($M = Cu, Ni, Au$; $n = 0, 0, 1$)

The electron-rich porphyrin ligand $H_2T(OMe)PP$ was synthesized according to literature procedures.¹² The synthesis of the copper complex, $[Cu(T(OMe)PP)]$ (**1**) was achieved by refluxing the ligand in DMF for 4 hours in the presence of an excess of $Cu(OAc)_2$, in a modification of a literature procedure for a similar complex.¹² The achievement of the complexation was ascertained by the shift and the reduction in number of the Q bands typical of the ligands in the electronic absorption spectrum in DCM at 20 °C (Figure 4.1, left). The extinction coefficients of the Q absorption bands of $[Cu(T(OMe)PP)]$ were calculated from solutions of the recrystallized complex in DCM to yield the following values: $\epsilon_{541} = 14640 \pm 500 \text{ M}^{-1} \text{ cm}^{-1}$, $\epsilon_{578} = 3420 \pm 80 \text{ M}^{-1} \text{ cm}^{-1}$ and $\epsilon_{618} = 2430 \pm 50 \text{ M}^{-1} \text{ cm}^{-1}$.

Mass Spectrometry showed the presence of the peak relative to the complex (Figure A80), confirming the successful complexation. X-Band EPR spectroscopy, where a spectrum typical of a rhombic $S = 1/2$ system was observed. The analysis of the spectral features suggested the presence of an unpaired spin coupling with a Cu nucleus on the g_x component ($I = 3/2$) and four nitrogen atoms from the porphyrin ligand, giving a nine lines superhyperfine splitting on the g_y and g_z component ($2nI+1$, $n = 4$, $I = 1$) (Figure 4.1, right).

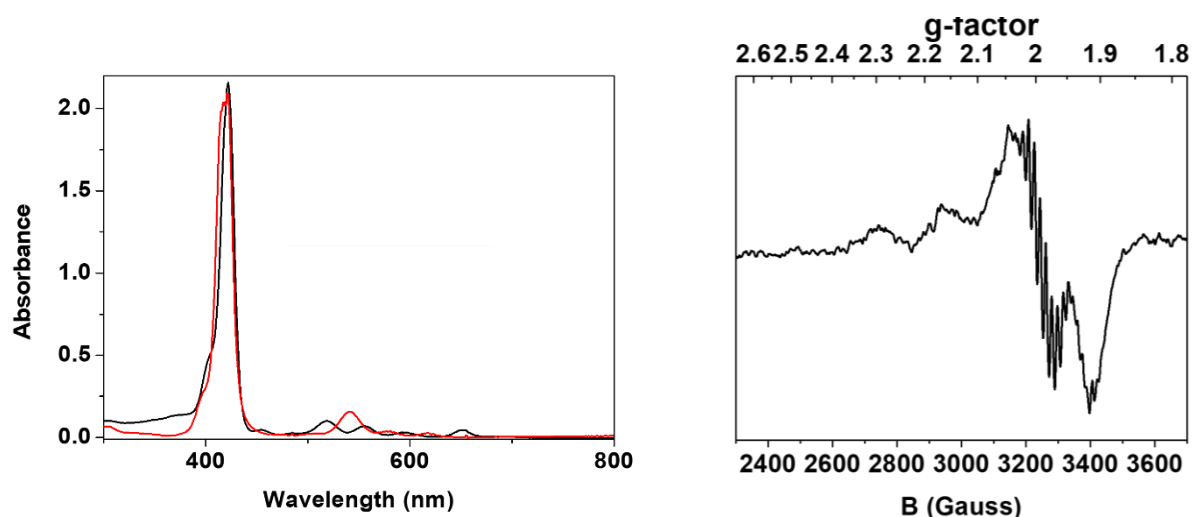


Figure 4.1. *Left:* Electronic absorption spectra (DCM, 20°C) of the ligand H₂T(OMe)PP (black trace) and of **1** (red trace). *Right:* X-Band EPR spectrum of **1** acquired from a frozen DCM solution, T = 77 K, 1.95 mW microwave power, 0.5 mT modulation amplitude.

The synthesis of the nickel complex, [Ni(T(OMe)PP)] (**2**) was performed with two alternative procedures. First, a literature procedure was employed by reacting Ni(COD)₂ with the free base porphyrin at room temperature in toluene.¹³ In this reaction, the oxidative insertion of the nucleophilic metal salt is supposed to yield the desired Ni^{II} complex. The product obtained though required purification through two subsequent column chromatography processes (first: 20:1 DCM, MeOH, second: 100% DCM) to respectively get rid of paramagnetic Ni^I impurities and excess free ligand. The second procedure entailed the refluxing of the free base porphyrin with an excess (3 equiv.) of NiCl₂·6H₂O in DMF for 3 hours and yielded a product that was possible to obtain pure after one column chromatography (100% DCM). Therefore, given the cheaper Ni salt employed and the easier purification process, we adopted the second procedure for all the subsequent syntheses of **2**.

The ¹H NMR spectrum of **2** in CD₂Cl₂ showed the disappearance of the signal relative to the β-pyrrolic hydrogens which was present in the ligand at δ = -2.81 ppm, confirming that the complexation had occurred. The other resonances in the spectrum showed an upfield shift with respect to the free ligand which was consistent with the complexation (Figure 4.2). Other indications of complexation were given by Mass Spectrometry (Figure A81) and electronic absorption spectroscopy where, similarly to what was observed with Cu, the number of the Q bands was reduced with respect to the ligand, yielding only one absorption band at λ = 530 nm beside the Soret band (Figure 4.3). The extinction coefficient of the Q absorption band of

[Ni(T(OMe)PP)] was calculated from solutions of the recrystallized complex in DCM to yield a value of $\epsilon_{530} = 18400 \pm 400 \text{ M}^{-1} \text{ cm}^{-1}$.

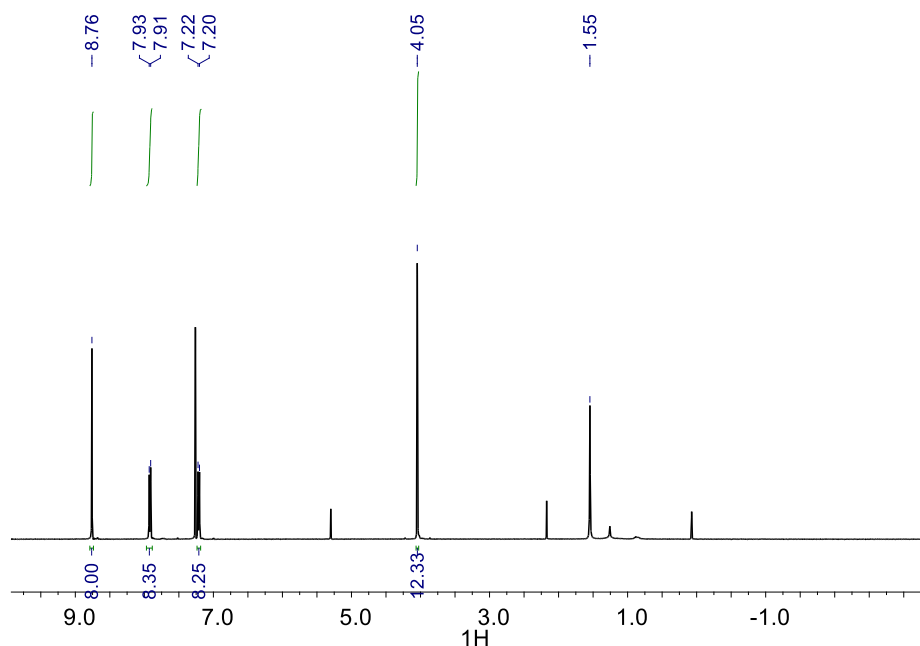


Figure 4.2. ^1H NMR (400 MHz, CD_2Cl_2) of **2**.

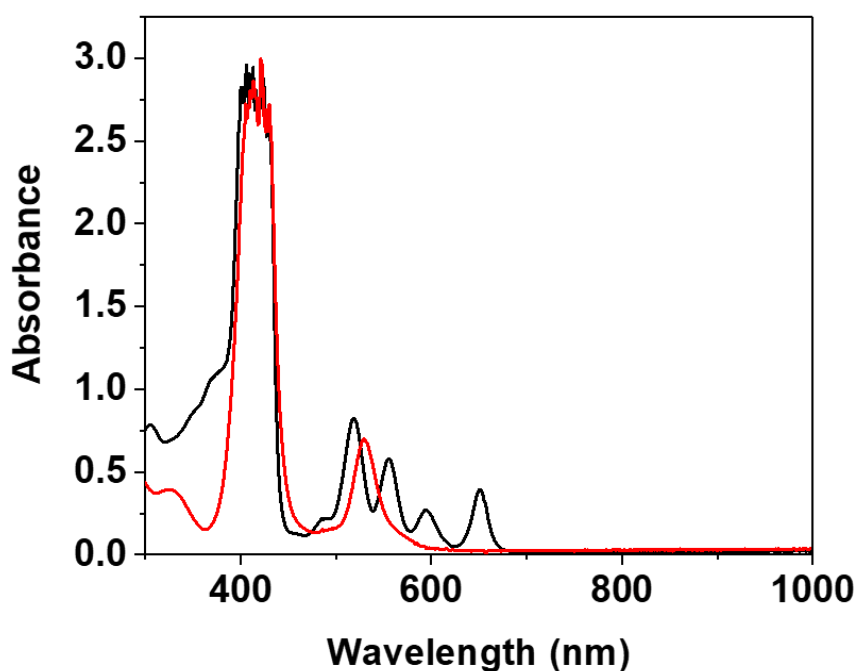


Figure 4.3. Electronic absorption spectra (DCM, 20 °C) of the ligand $\text{H}_2\text{T(OMe)PP}$ (black trace) and of **2** (red trace).

The synthesis of the gold complex, $[\text{Au(T(OMe)PP)]Cl}$ (**3**), was performed by adapting a literature procedure used for a similar complex, $[\text{Au(TPP)}]^+$ (TPP = 5,10,15,20-tetraphenylporphyrin).¹⁴ The free base ligand was refluxed in the presence of a slight excess of KAuCl_4 in an acetic acid/sodium acetate buffer. The complex obtained was purified through

column chromatography (20:1 DCM/methanol) and the exchange of the AuCl_4^- counterion was performed by stirring the complex in a biphasic solution of DCM/water in the presence of an excess LiCl for 72 h. The complexation was confirmed by ^1H NMR with the disappearance of the upfield resonance typical of the β -pyrrolic protons at $\delta = -2.81$ ppm (Figure 4.4). The other resonances were shifted downfield in comparison with the free ligand (Figure 4.4). Mass spectrometry showed the presence of the $[\text{Au}(\text{T}(\text{OMe})\text{PP})^+]$ cation, confirming that the desired product was obtained (Figure A82). The electronic absorption spectrum showed one Q band with a shoulder compared to the four observable in the spectrum of the free ligand, in analogy to what was observed for **1** and **2** (Figure 4.5).

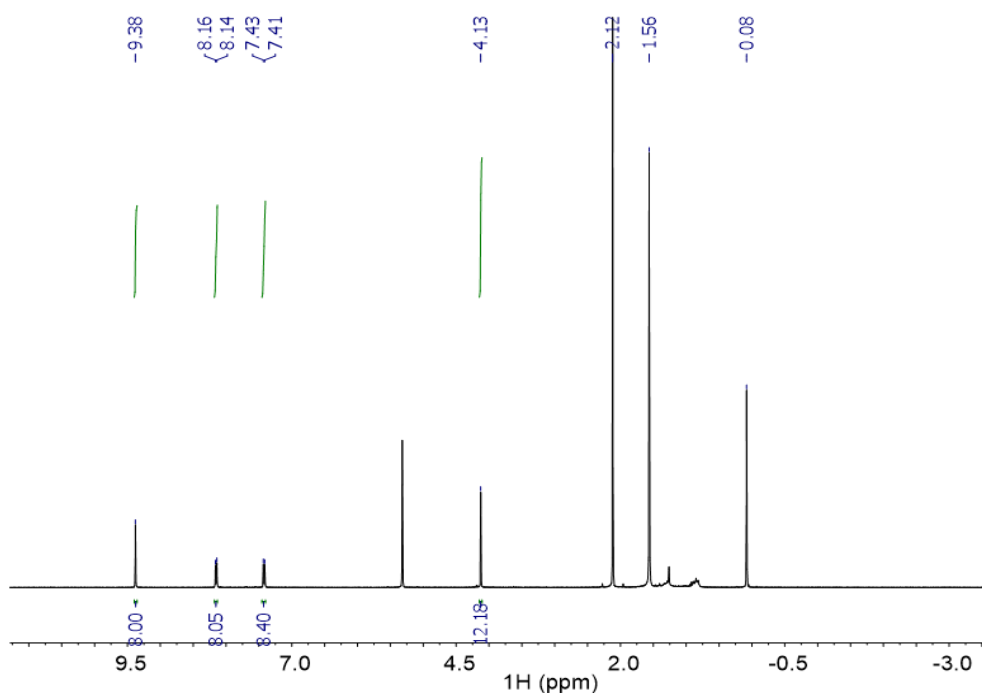


Figure 4.4. ^1H NMR (400 MHz, CD_2Cl_2) of **3**.

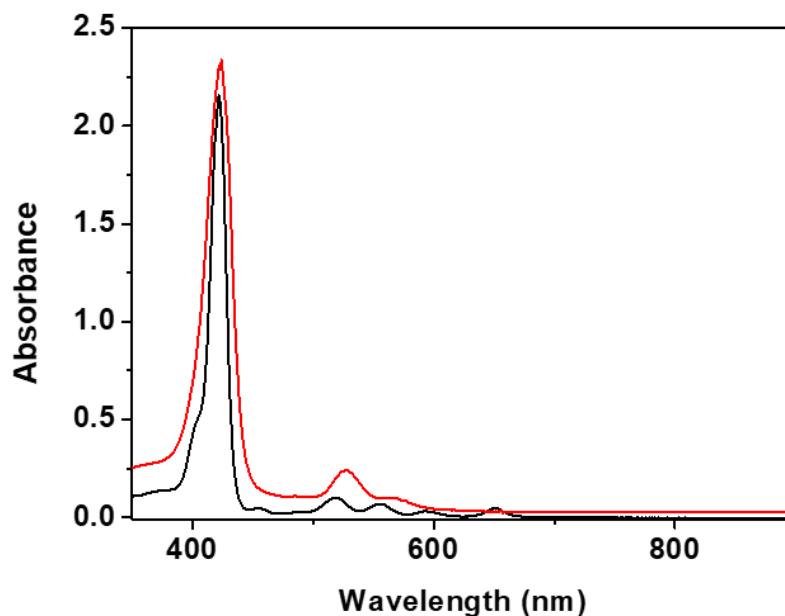


Figure 4.5. Electronic absorption spectra (DCM, 20 °C) of the ligand and of **3** (red trace).

Cyclic voltammetry measurements were performed on the three complexes (1 mM in DCM, 20 °C, 0.1 M $n\text{Bu}_4\text{NPF}_6$ supporting electrolyte, 0.1 V/s scan rate) showing a similar redox behaviour for **1** and **2** (Figures A83-84). The Cu complex **1** in fact showed two reversible oxidation waves respectively at $E_{1/2}^{\text{I}} = 0.44$ V, which was assigned to the redox couple $\text{Cu}^{\text{II}}/\text{Cu}^{\text{III}}$ and $E_{1/2}^{\text{II}} = 0.89$ V against Fc/Fc^+ , which we assigned to the formal $\text{Cu}^{\text{III}}/\text{Cu}^{\text{IV}}$ oxidation (Figure 4.6). Given the possibility of localization of the oxidising equivalents either on the ligand or on the metal, the two redox events might be identified as well as $\text{Cu}^{\text{II}}/\text{Cu}^{\text{II}\cdot+}$ and $\text{Cu}^{\text{II}\cdot+}/\text{Cu}^{\text{III}\cdot+}$, since these redox states are impossible to distinguish by voltammetry. Other Cu^{II} -porphyrin such as $[\text{Cu}(\text{TPP})]$ showed a similar voltammogram with two reversible waves respectively at 1.05 and 1.29 V vs Ag/AgCl and EPR measurements confirmed that the oxidations were centred on the porphyrin ligand.¹⁵

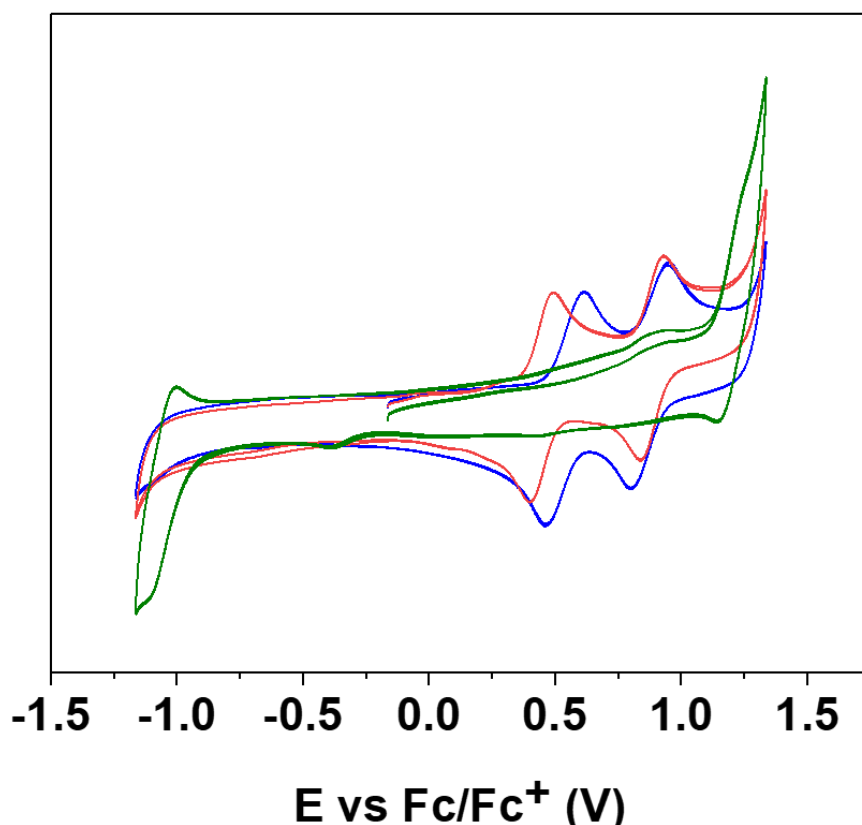


Figure 4.6. Cyclic voltammograms of **1** (red trace), **2** (blue trace) and **3** (green trace) in DCM, 1 mM, scan rate: 0.1 V/s.

A similar behaviour was observed for **2**, with two reversible redox waves observed respectively at $E_{1/2}^I = 0.54$ V, which was assigned to the redox couple $\text{Ni}^{\text{II}}/\text{Ni}^{\text{III}}$ or $\text{Ni}^{\text{II}}/\text{Ni}^{\text{II}\cdot+}$ and $E_{1/2}^{\text{II}} = 0.85$ V against Fc/Fc^+ , which we assigned to the $\text{Ni}^{\text{III}}/\text{Ni}^{\text{IV}}$ oxidation which could also be formalised as $\text{Ni}^{\text{II}\cdot+}/\text{Ni}^{\text{III}\cdot+}$. **3** instead showed only one irreversible reduction wave at low potential (-1.15 V), as expected for a stable Au^{III} complex, and an irreversible oxidation wave at $E = 1.16$ V, which is likely related to the oxidation of the ligand (Figure 4.6).

4.3 Reactivity with oxidants

We investigated the reactivity of **1** and **2** with one or two-electron oxidants. Instead, when excess tris (4-bromophenylammoniumyl) hexachloroantimonate (magic blue), tris (2,4-dibromophenylammoniumyl) hexachloroantimonate (magic green), WCl_6 or phenoxathiinyl hexachloroantimonate ($(\text{Phenox})\text{SbCl}_6$) were added to a solution of **1**, the formation of a new species was observed by electronic absorption spectroscopy (Figure 4.7, Figures A85-86). These oxidants were chosen since their oxidation potential is comparable or higher with respect to the potential of $E_{1/2}^{\text{II}}$ for both **1** and **2**: $(\text{Phenox})\text{SbCl}_6$ has a potential comparable with the

thianthrene (0.86 V in acetonitrile, WCl_6 has a formal oxidation potential of 1.1 V in DCM whereas magic blue and magic green have respectively a potential of 0.7 and 0.9 V in dichloromethane vs Fc/Fc^+ .¹⁶ The new species showed a dramatic change in the Q-bands region of the electronic absorption spectrum of **1**, with new absorption maxima at $\lambda = 506$, $\lambda = 614$ and $\lambda = 790$ nm. These features were obtained with all the oxidants listed above, suggesting that the same oxidised species, that we will indicate as **1OX**, was reached in different conditions. The different nature of the species was also indicated by a dramatic colour change in the solution, from pink (for **1**) to intense green. Given that the addition of $(\text{Phenox})\text{SbCl}_6$ yielded the cleanest reaction, we decided to optimize the conditions of the reaction to obtain **1OX** with this oxidant. The new species presented a relatively short lifetime at 20 °C (~ 100 s), therefore the oxidation was performed at low temperature (-20 °C) to yield a tenfold increase of the lifetime of **1OX**.

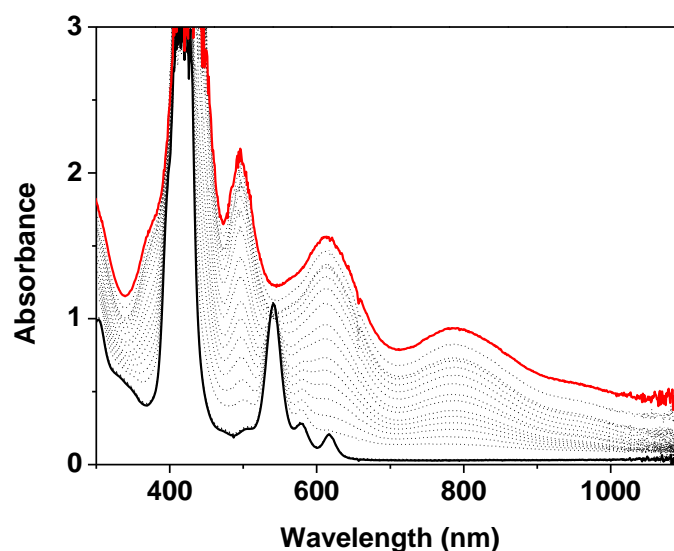


Figure 4.7. Electronic absorption spectra of **1** before (0.085 mM, DCM, -20 °C, black trace) and after the addition of 1.5 equiv. of $(\text{Phenox})\text{SbCl}_6$ to yield a new species (red trace).

A titration with different equivalents of oxidant $(\text{Phenox})\text{SbCl}_6$ was performed by monitoring the absorbance both at $\lambda = 790$ nm and at $\lambda = 614$ nm and it was observed that the maximum yield of **1OX** was reached when 1.5 equivalents of oxidant were employed (Figure 4.8). We then concluded that a new oxidised species **1OX** was obtained in the conditions explored. The features observed for this oxidised species match with the optical absorption features of Cu porphyrin π -cation radical reported in literature. $[\text{Cu}(\text{TPP})]^{+\cdot}$ derivatives normally show two intense absorption bands, one between $\lambda = 500$ nm and $\lambda = 600$ nm and one beyond $\lambda = 600$ nm,¹⁵ notably at $\lambda = 592$ nm and $\lambda = 656$ nm for $[\text{Cu}(\text{TPP})]^{+\cdot}$.¹⁵ $[\text{Cu}(\text{OETPP})]^{+\cdot}$ showed an

intense oxidation band at $\lambda = 625$ nm and a weak shoulder around $\lambda = 800$ nm.¹⁷ The allowed transition and their intensity might vary according to the degree of structural distortion of the oxidised species due to the effect of the substituents on the porphyrin ring.^{17, 18} **10X** showed three bands in the regions expected for a Cu porphyrin π -cation radical species, notably at $\lambda = 506$, $\lambda = 614$ and $\lambda = 790$ nm, with a decreasing relative intensity going towards the less energetic transition. The near-IR transitions are often typical of more flexible complexes, whose oxidised species show a higher degree of distortion from planarity.¹⁹ Therefore we could postulate the electronic nature of **10X** as $[\text{Cu}^{\text{II}}((\text{OMe})\text{TPP})]^{+\cdot}$.

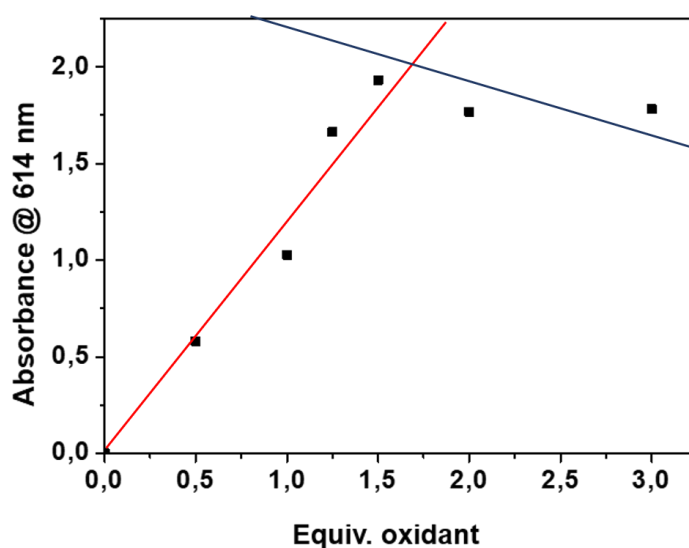


Figure 4.8. Titration of the equivalents of $(\text{Phenox})\text{SbCl}_6$ needed to obtain the maximum yield of oxidised species **10X** (-20°C , DCM) by monitoring the absorbance at $\lambda = 614$ nm.

We then investigated the nature of the oxidised species **10X** by EPR. An X-band EPR spectrum of **10X** showed an isotropic signal at $g = 2.00$ which is typical of a $S = 1/2$ organic species (Figure 4.9). This spectrum was strikingly different from the one observed for **1** (Figure 4.1, right) which showed a pattern typical of a $S = 1/2$ Cu^{II} species. The absence of any residual signal typical of a Cu^{II} species confirmed the complete oxidation of **1** to a different species in the explored conditions. As mentioned previously, the one-electron oxidation of **1** could be borne either on the metal, yielding a formal Cu^{III} species, which would be EPR silent, or on the ligand, yielding a π -radical cation ($\text{Cu}^{\text{II}\cdot+}$). In this case the signal relative to the unpaired electron on the ligand ($S = 1/2$) would likely be ferromagnetically ($S = 1$) or antiferromagnetically ($S = 0$) coupled to the unpaired spin on the metal (Cu^{II} , d^9 , $S = 1/2$), therefore in both cases no signal would be detected by perpendicular mode X-band EPR.^{17, 18}

Nevertheless, in rare cases non-interacting $S = \frac{1}{2}$, $S = \frac{1}{2}$ spin states have been detected for some copper porphyrin π -radical cations, due to their distortion from planarity and to their aggregation state in solution.¹⁸ In this case though we postulated that the oxidation of Cu^{II} to $\text{Cu}^{\text{II}\cdot+}$ occurs and that the excess oxidant ((Phenox)SbCl₆) is responsible for the signal at $g = 2.00$. ((Phenox)SbCl₆) is in fact EPR active being an organic radical. Therefore we concluded that also the EPR confirmed the complete oxidation of **1** to **1OX**. We attempted to acquire a ¹H-NMR and a FTIR spectrum but due to the short lifetime of **1OX** at room temperature we could not obtain satisfying data.

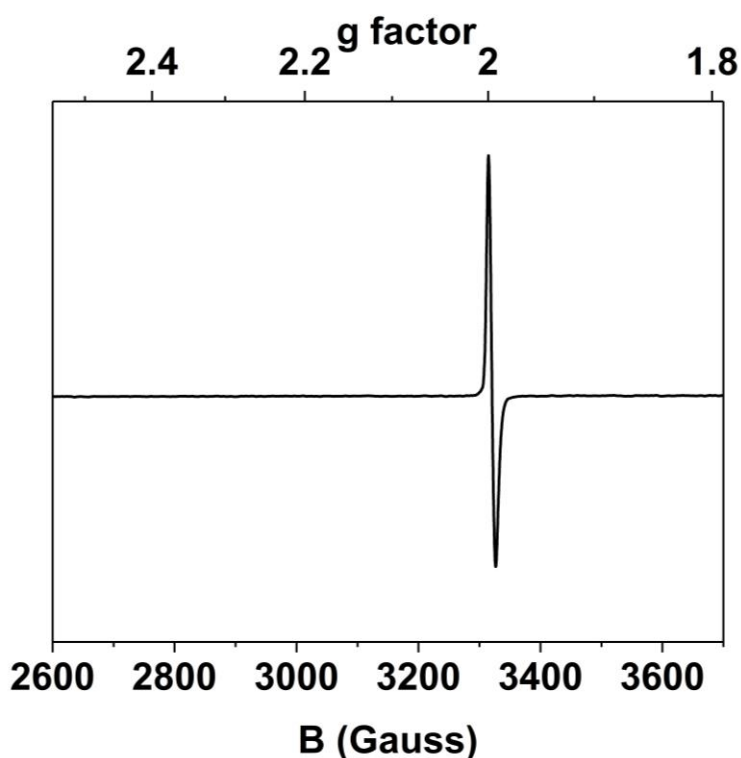


Figure 4.9. X-Band EPR spectrum of **1OX** acquired from a frozen DCM solution, 77 K, 1.95 mW microwave power, 0.5 mT field modulation amplitude.

In a similar fashion to what was observed for **1**, we attempted the oxidation of the Ni^{II} complex **2**. **2** was reacted both at 20 °C at -20 °C with an excess of the same oxidants tested for the formation of **1OX**: phenoxathiinyl hexachloroantimoniate, WCl₆, magic blue and magic green (0.86 – 1.36 V, Figures A87-88).¹⁶ By adding all the above-mentioned oxidants we observed the formation of a new species by electronic absorption spectroscopy (Figure 4.11). This new species showed a dramatic change in the Q-bands region of the electronic absorption spectrum of **2**, with new absorption maxima at $\lambda = 657$ and $\lambda = 900$ nm. These features are red-shifted with respect to the ones observed for **1OX** but are in similar regions to those reported for Ni^{II}

π -cation radical species.²⁰ In fact broad absorptions between $\lambda = 600$ and $\lambda = 700$ nm have been attributed to the formation of $[\text{Ni}^{\text{II}}(\text{porph})]^{\cdot+}$ species, whereas a less intense shift in the Q bands yielding a sharp peak around $\lambda = 570$ nm has been attributed to $[\text{Ni}^{\text{III}}(\text{porph})]$ species.²⁰ Often a valence tautomerism is observed, such as in the case of $[\text{Ni}(\text{TPP})]$ where the one-electron oxidation at room temperature yields a green solution with a sharp EPR signal near $g = 2.00$, indicative of oxidation to $[\text{Ni}^{\text{II}}(\text{TPP})]^{\cdot+}$, but when frozen at 77 K the solution turns from green to orange and yields an anisotropic EPR signal indicative of an isomerization to $[\text{Ni}^{\text{III}}(\text{TPP})]$.⁵ The presence and the intensity of the near-IR features is normally dependent on the degree of distortion of the geometry of the oxidised species: for example these are absent for $[\text{Ni}^{\text{II}}(\text{TPP})]^{\cdot+}$ but present for the more flexible $[\text{Ni}^{\text{II}}(\text{OEP})]^{\cdot+}$, which shows an absorption band at $\lambda = 911$ nm.¹⁹

As observed in the transition from **1** to **1OX**, the starting red solution of **2** turned into a deep green one upon addition of all the above-listed oxidants. Given the presence of features typical of those attributed in literature to porphyrin π -radical cation species, we postulated that **2OX** could be described as a $[\text{Ni}^{\text{II}}((\text{OMe})\text{TPP})]^{\cdot+}$ species. The cleanest reaction was observed with $(\text{Phenox})\text{SbCl}_6$, therefore we optimized the conditions of synthesis of **2OX** in presence of this oxidant. A spectroscopically-monitored titration with different equivalents of oxidant $(\text{Phenox})\text{SbCl}_6$ was performed, checking the absorbance at $\lambda = 657$ nm and at $\lambda = 900$ nm. This experiment showed that the maximum yield of **2OX** was reached when 2.0 equivalents of oxidant were employed (Figure 4.11).

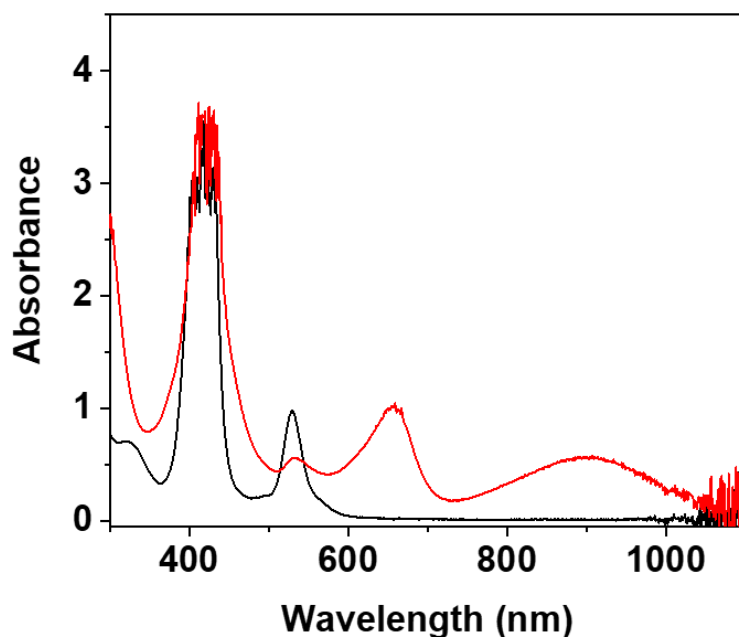


Figure 4.10. Electronic absorption spectra of **2** before (0.085 mM, DCM, -20 °C, black trace) and after the addition of 2.0 equiv. of (Phenox)SbCl₆ to yield a new species (red trace).

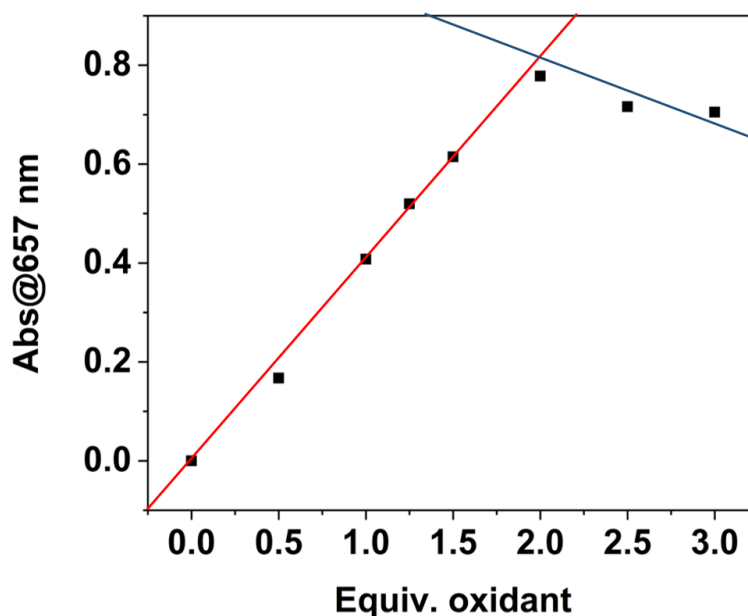


Figure 4.11. Titration of the equivalents of (Phenox)SbCl₆ needed to obtain the maximum yield of oxidised species **2OX** (-20°C, DCM) by monitoring the absorbance at $\lambda = 657$ nm.

To obtain more evidences of the oxidation of **2** we recorded an ATR-FTIR spectrum of **2OX** (Figure 4.12). This technique is useful since a sharp infra-red band in the region between $\nu = 1250$ and 1295 cm^{-1} is diagnostic of a porphyrin-based oxidation for metalloporphyrins, yielding a $[\text{M}(\text{porph})]^{+\cdot}$ species.²¹ The ATR-FTIR of **2OX** showed an intense and sharp new feature at $\nu = 1263$ cm^{-1} which was not present in the spectrum of the low-valent complex **2**

(Figure 4.12). This band is ascribed to a ring vibrational mode typical of π -radical cations of [M(TPP)] complexes.²¹ Therefore this result corroborated our assignment of **2OX** as [Ni^{II}((OMe)TPP)]^{•+}.

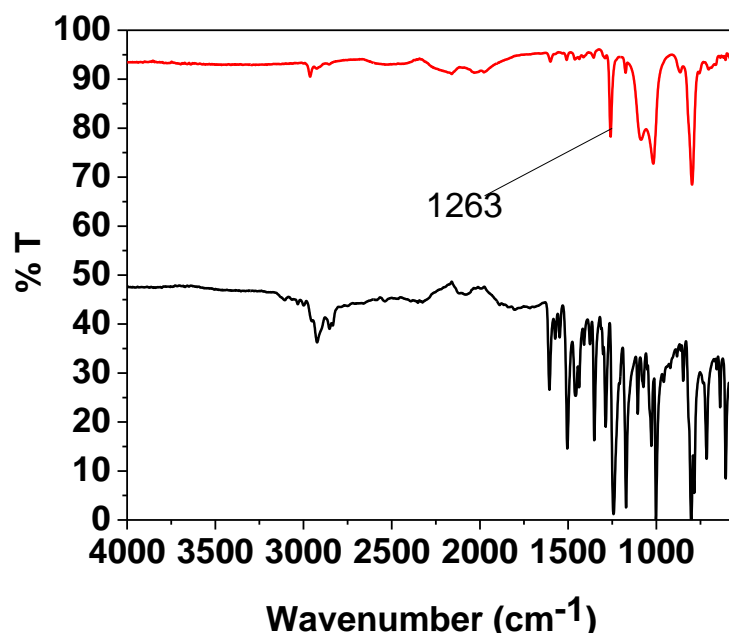


Figure 4.12. ATR-FTIR spectra of **2** (black) and **2OX** (red). The peak at $\nu = 1263 \text{ cm}^{-1}$ is indicative of a porphyrin π -radical cation.

An X-band EPR spectrum of **2OX** showed an isotropic signal at $g = 2.00$, indicative of a $S = \frac{1}{2}$ organic radical species (Figure 4.13). The X-Band EPR spectrum of the starting material **2** appeared to be silent, as expected for a low-spin Ni^{II} complex ($S = 0$). We therefore ascribed the observed signal for **2OX** to a one-electron oxidised species, where the oxidation is borne on the ligand to yield a porphyrin π -radical cation species Ni^{II•+}. This was also confirmed when changing the oxidant to WCl₆ to exclude the attribution of the signal to the excess equivalent of (Phenox)SbCl₆. WCl₆ is EPR silent since the metal cation has a d^0 electronic configuration, and when reduced to W(V) upon involvement in an oxidation reaction it forms an antiferromagnetically coupled dimer, W₂Cl₁₀, which is still EPR silent.²² When we added 2.0 equiv. of WCl₆ to **2** in order to obtain **2OX**, an isotropic signal at $g = 2.00$ was observed by X-Band EPR, confirming the formation of a porphyrin π -radical cation (Figure A89). We also questioned ourselves on the possibility of having performed a 2-electron oxidation of **2** given the two equivalents of oxidant added. A Ni^{IV} or Ni^{III•+} species would give a silent EPR spectrum in perpendicular mode ($S = 1$ or $S = 0$) and given that no excess oxidant that would yield an isotropic signal would be employed in that case, we excluded this possibility. This hypothesis

was also excluded due to the fact that no change in the spectroscopic features of **2OX** is observed in presence of increasing equivalents of oxidants, starting from one equivalent. Therefore we assigned the signal observed by EPR to a $\text{Ni}^{\text{II}\cdot+}$ species.

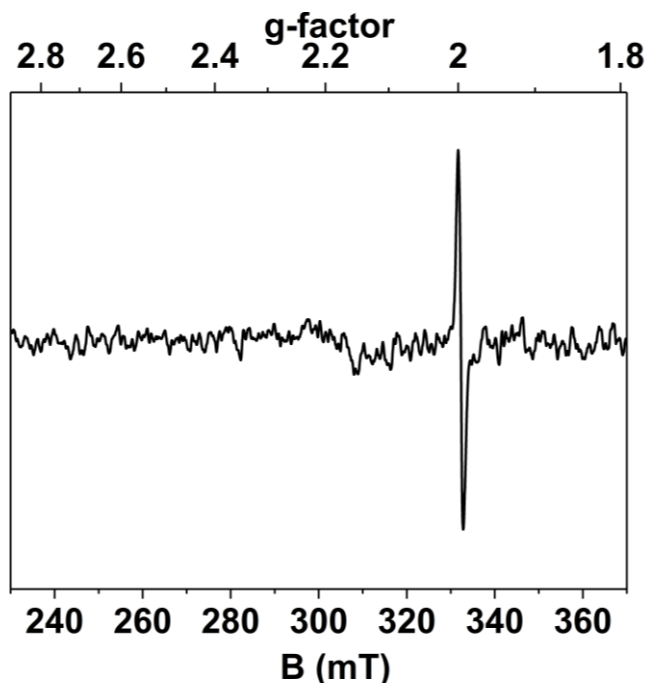


Figure 4.13. X-Band EPR spectrum of **2OX** acquired from a frozen DCM solution, 77 K, 1.95 mW microwave power, 0.5 mT field modulation amplitude.

4.4 Reactivity with X sources (X = Cl⁻, F⁻, I⁻, OH⁻)

To evaluate the effect of potential extra ligands X on the valence tautomerism of the oxidised porphyrin π -radical cations **1OX** and **2OX** and on their potential as oxidants, we reacted them with sources of X (X = Cl⁻, F⁻, I⁻, OH⁻). We were as well interested in isolating high-valent halide or hydroxide species to possibly study their reactivity, as we have done in Chapters 2 and 3. The reaction of **1** with an excess of Et₄NCl, ⁿBu₄NF, Et₄NOH and ⁿBu₄NI (20 °C and -20 °C in DCM) did not yield any significant spectroscopic change. On the other hand, the reaction of **1OX** with the same salts lead to some interesting changes (Figure 4.14, left). When up to 10 equiv. of Et₄NCl were added to **1OX**, an immediate decay of the spectroscopic features characteristic of the oxidised species was observed, to yield an electronic absorption trace containing both features of the starting compound **1** as well as of another species showing absorption feature sin the near-IR region. The near-IR features at $\lambda = 812$ nm and $\lambda = 918$ nm and a split Soret band are matching closely with the spectroscopic features reported for metal

isoporphyrin species.^{11, 23} Conversely, the addition of up to 10 equiv. of ⁿBu₄NF (Figure 4.10, right) did not lead to the same spectroscopic changes observed for Et₄NCl, but gave an immediate drop of the absorption features of **1OX** to give a mixture of **1** and of a species bearing low-intensity features at $\lambda = 680$ nm and $\lambda = 850$ nm. The addition of Et₄NOH and ⁿBu₄NI did not yield new spectroscopic features but simply caused the decay of **1OX** back to **1** (Figure A90). We therefore examined more closely the optical absorption features formed in the reaction of **1OX** with Et₄NCl, notably those in the near-IR at $\lambda = 812$ nm and $\lambda = 918$ nm (Figure 4.14 left). Isoporphyrins present a quaternary *meso*-carbon and are generally obtained by nucleophilic attack on a higher oxidised species (2 oxidising equivalents above the resting state compound), which is highly electrophilic.²³ In this case we postulated that a disproportionation between two molecules of **1OX** is occurring, which in presence of the nucleophilic Cl⁻ would lead to a mixture of **1** and of the isoporphyrin, explaining the coexistence of the spectroscopic features of both species. These results showed that the addition of nucleophiles mainly caused the decay of the oxidised species, apart from what was observed with Cl⁻ which lead to the disproportionation to **1** and an isoporphyrin.

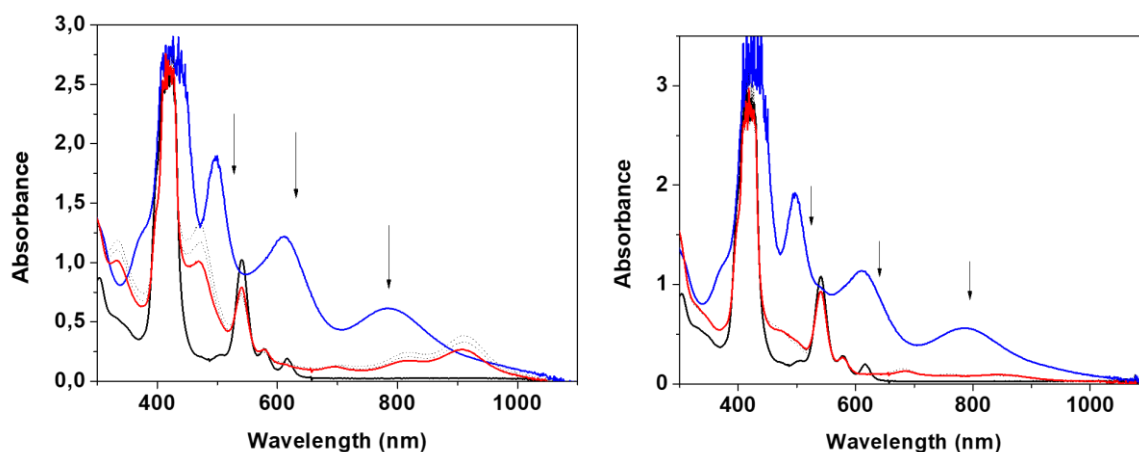


Figure 4.14. *Left:* Electronic absorption spectra of **1** (0.08 mM, DCM, - 20 °C, black trace), of **1OX** (blue trace) and after the addition of 1 equiv. Et₄NCl to **1OX** (red trace). *Right:* Electronic absorption spectra of **1** (0.08 mM, DCM, - 20 °C, black trace), of **1OX** (blue trace) and after the addition of 1 equiv. ⁿBu₄NF to **1OX** (red trace).

Similarly to what was done for **1**, **2** was reacted with the same sources of X (X = Cl⁻, F⁻, I⁻, OH⁻), showing a similar outcome. In fact the addition of up to 10 equiv. of Et₄NCl, ⁿBu₄NF, Et₄NOH and ⁿBu₄NI to a solution of **2** did not yield to any significant spectroscopic change (Figure A91). On the other hand, the addition of the same salts to **2OX** yielded to the immediate decay of the oxidised specie in all cases, with a full restoration of **2** for all the salts with exception of Et₄NCl (Figure 4.15). In this case, analogously to what observed for **1**, both

features of **2** and of a different species were observed at the end of the reaction with a chloride ion source (Figure 4.15 left). In fact the electronic absorption spectrum at the end of the reaction showed a splitted Soret band and two near-IR feature at $\lambda = 805$ nm and at $\lambda = 910$ nm, similar to the ones detected at the end of the same reaction with **1OX**. We therefore postulated that a similar mechanism to the one hypothesized for **1OX** occurs in presence of Cl^- , where two molecules of **2OX** disproportionate to yield **2** and an isoporphyrin species. We therefore concluded that the addition of sources of X did not yield any high-valent halide or hydroxide species, nor to an effect on the valence tautomerism on the porphyrin π -cation radicals, except for the formation of an isoporphyrin species upon addition of excess Cl^- to both **1OX** and **2OX**.

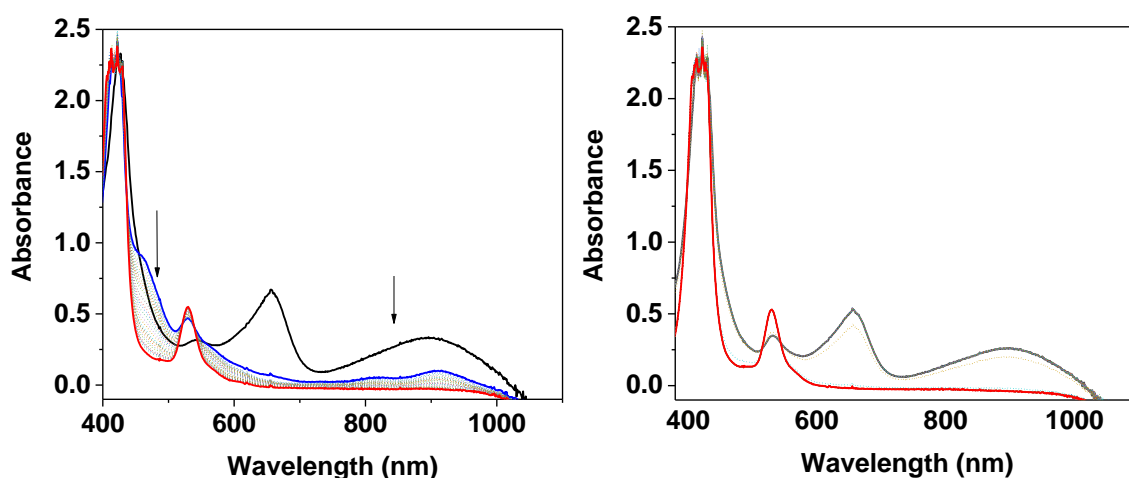


Figure 4.15. *Left:* Electronic absorption spectra of **2** (0.038 mM, DCM, -20 °C, red trace), of **2OX** (black trace) and after the addition of 1 equiv. Et_4NCl to **2OX** (blue trace). *Right:* Electronic absorption spectra of **2OX** (black trace) and after the addition of 1 equiv. $^t\text{Bu}_4\text{NF}$ to **2OX** (red trace).

4.5 Reactivity with O–H bonds

Once we were able to optimize the synthesis of the two oxidised species **1OX** and **2OX** and established them to be metalloporphyrin π radical-cations, we proceeded to investigate their reactivity. We reacted both **1OX** and **2OX** with substrates bearing O–H bonds to probe their potential as oxidants. Both complexes were therefore reacted with an excess (> 10 equiv.) of 4-methoxy-2,6-di-tert-butylphenol (4- CH_3O -2,6-DTBP) at -20 °C in DCM and the reactions were monitored by electronic absorption spectroscopy. When **1OX** was reacted with 4- CH_3O -2,6-DTBP, a rather slow decay of the features typical of the oxidised species at $\lambda = 614$ and $\lambda = 790$ nm was observed and monitored through time. *Pseudo*-first order rate constants (k_{obs}) were obtained by exponential fitting of the plot of absorbance measured at $\lambda = 614$ vs time (Figure 4.16 left). The plot of k_{obs} versus [4- CH_3O -2,6-DTBP] exhibited a saturation kinetics

and the first-order reaction rate constant, k_1 , was determined from the fitting of the plot to be 0.064 s^{-1} (Figure 4.17 left).

The same approach was then adopted for the evaluation of the oxidative capabilities of **2OX**. The complex reacted more readily with an excess of 4-CH₃O-2,6-DTBP compared to **1OX** in the same experimental conditions (-20 °C, DCM), as demonstrated by the faster decay of the bands typical of **2OX** at $\lambda = 657 \text{ nm}$ and at $\lambda = 900 \text{ nm}$ (Figure 4.16 right). Analogously to **1OX**, the exponential fitting of the plot of absorbance measured at $\lambda = 657$ vs time yielded *pseudo*-first order rate constants (k_{obs}) (Figure 4.17 right). The plot of k_{obs} versus [4-CH₃O-2,6-DTBP] exhibited a saturation kinetics and the first-order reaction rate constant, k_1 , was determined from the fitting of the plot to be 0.957 s^{-1} (Figure 4.17 right). The saturation in fact is evidently reached at higher substrate concentration than those explored experimentally, but already at 0.0037 M the decay of **2OX** was too fast to be monitored in the experimental and instrumental conditions employed (Figure 4.16 right).

The saturation kinetics are generally indicative of an equilibrium leading to an intermediate prior to the rate-determining step of a reaction.²⁴ In this case, with both **1OX** and **2OX** saturation kinetics are observed in presence of 4-CH₃O-2,6-DTBP. We postulated that this type of substrate might interact with the π -radical cation forming an adduct prior to the reaction to occur, the equilibrium leading to the adduct would be affected by the concentration of substrate, as confirmed by the type of kinetics observed experimentally. The interaction of external ancillary ligands with metalloporphyrin π -radical cations is known to yield adducts that can modify the valence tautomerism of the oxidised species. Therefore we postulate that the formation of an adduct with the substrate is responsible for the saturation kinetics.

When comparing the two oxidants **1OX** and **2OX** we observed that the reaction with **2OX** was one order of magnitude faster than the one of **1OX** with the same substrate in the same conditions (DCM, - 20 °C). We also observed some differences in the electronic absorption traces found at the end of the reaction of the two complexes with 4-CH₃O-2,6-DTBP. For **1OX** the features of the low-valent species **1** were found, together with some residual features ascribed to the π -radical cation. For **2OX** instead, the features typical of the low-valent species **2** were found (notably at $\lambda = 530 \text{ nm}$), together with some very weak features in the near-IR. These broad features between $\lambda = 800$ and $\lambda = 1000 \text{ nm}$ are reminiscent of those observed for the isoporphyrins (paragraph 4.4), even though the intensity is too low to attribute these features to such a species with certainty. Therefore we cannot exclude that the higher reactivity of **2OX** might be ascribed to a different mechanism of reaction with respect to **1OX**.

Therefore we observed that **2OX** was a much more competent oxidant towards a phenolic substrate already at low temperatures (-20 °C) compared to **1OX**. For this reason we decided to test **2OX** for hydrocarbon oxidation, given the promising result obtained in these conditions.

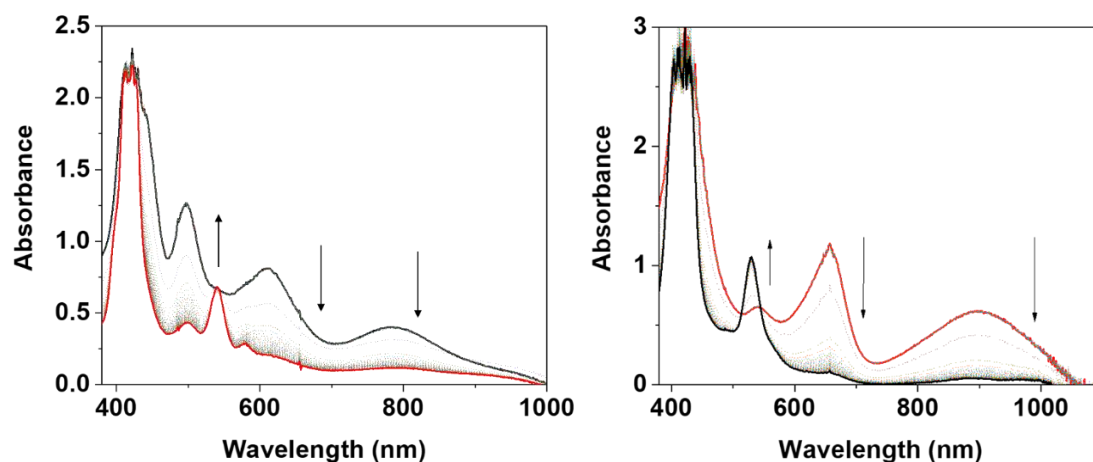


Figure 4.16. *Left:* Reaction of **1OX** (black trace) with 400 equiv. of 4-CH₃O-2,6-DTBP monitored via electronic absorption spectroscopy (-20 °C, DCM). *Right:* Reaction of **2OX** (red trace) with 50 equiv. of 4-CH₃O-2,6-DTBP monitored via electronic absorption spectroscopy (-20 °C, DCM).

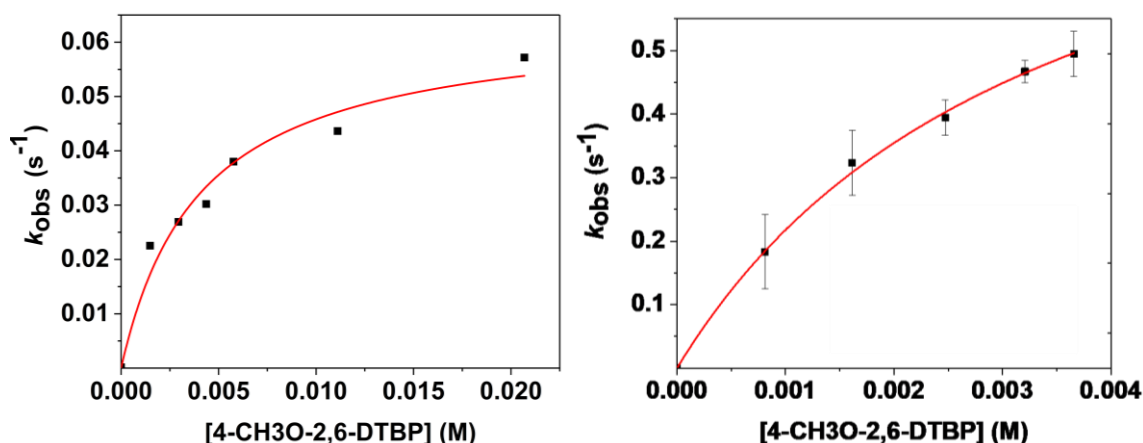


Figure 4.17. *Left:* Plot of k_{obs} versus [4-CH₃O-2,6-DTBP] determined for the reaction between complex **1OX** and 4-CH₃O-2,6-DTBP. *Right:* Plot of k_{obs} versus [4-CH₃O-2,6-DTBP] determined for the reaction between complex **2OX** and 4-CH₃O-2,6-DTBP.

4.6 Reactivity with C–H bonds

In order to test the reactivity of **2OX** with hydrocarbon substrates, the stability of the oxidised species was monitored at 20 °C in DCM. The half-life of **2OX** in these conditions was determined to be ~ 3.5 hours, making the oxidised species long-lasting enough to perform the reactivity studies with hydrocarbons in these conditions.

Then **2OX** was reacted with an excess of xanthene in *pseudo*-first order conditions, showing a relatively fast decay of the bands at $\lambda = 657$ nm and at $\lambda = 900$ nm by electronic absorption spectroscopy (Figure 4.17 left). In particular, in the presence of xanthene the band at $\lambda = 657$ nm decayed completely over 1000 s, showing a first-order exponential decay (Figure 4.18 right). The decay of the feature at $\lambda = 657$ nm was fitted exponentially to obtain *pseudo*-first order rate constants which were plotted against [xanthene] (Figure 4.18). A linear trend was observed and from the slope of the plot we could obtain a second-order rate constant, $k_2 = 0.29$ $\text{M}^{-1} \text{s}^{-1}$ (Figure 4.18, Table 4.1). At the end of the reaction we observed the full decay of the features typical of **2OX**, showing the restoration of the optical absorption trace of **2** (Figure 4.18 left). Interestingly, the linear kinetics was different than the saturation one observed for the phenolic substrate. This suggests that an equilibrium does not occur prior to the rate determining step of the reaction and whether an adduct with this substrate is formed, that does not happen in a separate kinetic step. Encouraged by this result which showed us that **2OX** reacted readily at room temperature with a substrate bearing a C–H bond, we proceeded to extend the substrate scope to other hydrocarbons.

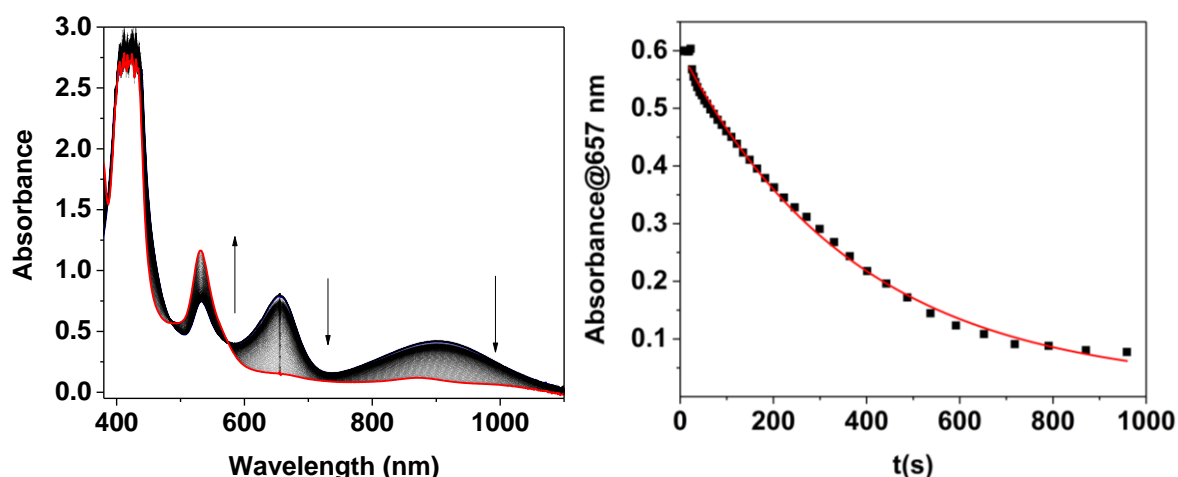


Figure 4.18. *Left:* Electronic absorption spectra of the reaction between **2OX** (blue trace) and 50 equiv. of xanthene (20 °C, DCM). *Right:* Plot of the decay of the absorbance measured at $\lambda = 657$ nm over time for the reaction of **2OX** with 50 equiv. of xanthene.

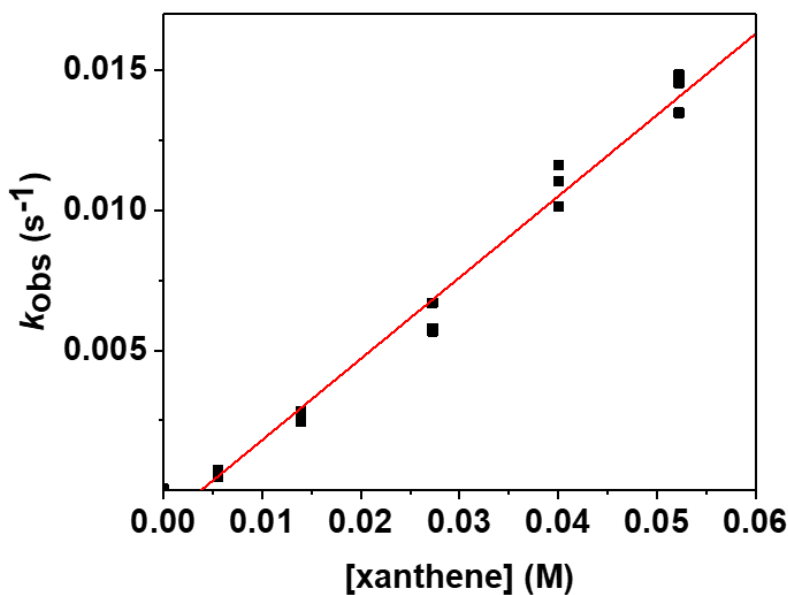


Figure 4.19. Plot of k_{obs} versus [xanthene] determined for the reaction between complex **2OX** and xanthene.

2OX was reacted with an excess of 1,4-cyclohexadiene (CHD), showing a slower decay of the features at $\lambda = 657$ nm and at $\lambda = 900$ nm by electronic absorption spectroscopy (Figure 4.20). With the same approach adopted for the reaction with xanthene, we plotted the pseudo-first order kinetic rate constants obtained by fitting the exponential decay of the feature at $\lambda = 657$ nm against [CHD] and from the slope a $k_2 = 0.026 \text{ M}^{-1}\text{s}^{-1}$ was obtained (Figure 4.20 right, Table 4.1). This value was therefore an order of magnitude lower than the one obtained for the reaction of **2OX** with xanthene.

An analysis of the optical absorption trace obtained at the end of the reaction of **2OX** with CHD, new features could be observed (Figure 4.20 left). A split of the Soret band and the appearance of two absorption in the near-IR region, notably at $\lambda = 860$ nm and $\lambda = 980$ nm. These features looked like those typical of an isoporphyrin complex, being similar to the ones reported²³ and observed in the reaction of **2OX** and excess Cl^- (see Section 4.4). Thus the inorganic product obtained at the end of the reaction of **2OX** with CHD looked like an isoporphyrin complex. No evidence of loss of the metallic ion were observed by ^1H NMR. A ^1H NMR analysis of the post-reaction mixture showed the formation of benzene, a formally 2-proton, 2-electron oxidation product of CHD, was formed in $72 \pm 8\%$ yield. It must be noted that the yield of this product has been calculated considering a formal one-electron reduction of **2OX** to **2** and a 2-electron oxidation of CHD to benzene. We therefore concluded that **2OX** was capable of performing the oxidation of CHD at room temperature.

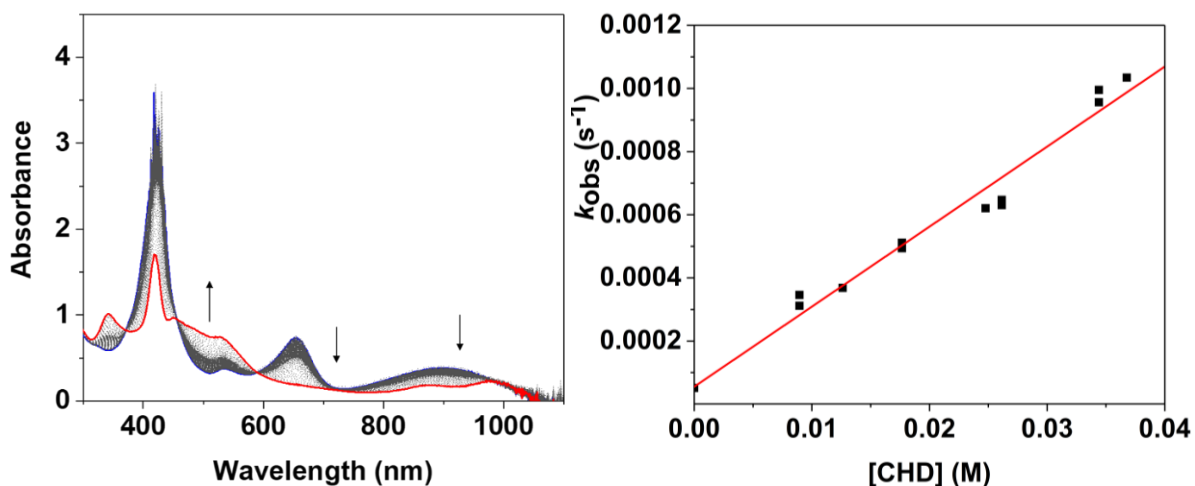


Figure 4.20. *Left:* Electronic absorption spectra of the reaction between **2OX** and CHD (250 equiv., 20 °C, DCM). *Right:* Plot of k_{obs} versus [CHD] determined for the reaction between complex **2OX** and CHD.

We then explored the reactivity of **2OX** with 9,10-dihydroanthracene (DHA, Figure 4.21 left). In the same fashion adopted for the reactions with xanthene and CHD, we monitored the decay of the band at $\lambda = 657$ nm. The k_2 was determined to have a value of $0.019 \text{ M}^{-1}\text{s}^{-1}$, slightly lower to the one observed for CHD (Figure 4.22 right, Table 4.1).

We observed that upon completion of the decay of the features of **2OX**, an optical absorption trace with a split Soret band and absorptions at $\lambda = 860$ nm and $\lambda = 980$ nm was present. The features looked the same to those observed at the end of the reaction with CHD (Figure 4.21 left). We therefore postulated that a Ni-isoporphyrin species was formed in the reaction with this substrate as well. An analysis by ^1H NMR of the reaction of **2OX** with 25 equiv. of DHA showed a different spectrum compared to the one of the starting complex **2** (Figure A92). In fact we observed an upfield shift of the resonances in the aromatic region, together with a splitting of the singlet of the $-\text{OCH}_3$ group, which appeared to be shifted and split into three signals at $\delta = 4.02$, $\delta = 4.07$ and $\delta = 4.09$ ppm after the reaction with DHA. This is indicative of an acquired chemical inequivalence for the protons in the $-\text{OCH}_3$ group on the aromatic substituents, which would be observed with the formation of a quaternary carbon typical of an isoporphyrin.

This result corroborated the hypothesis of the formation of an isoporphyrin at the end of this reaction.

A GC analysis of the post-reaction mixture showed a high yield ($152 \pm 16\%$) of the 2-electron, 2-proton oxidised product anthracene even when taking in account the effect of the excess oxidant (1 equiv.) in the blank measurements (Table 4.2). When the quantification was repeated by performing the reaction in inert atmosphere (glove box), the yield decreased to 65%, showing that the substrate could undergo autooxidation in presence of an aerobic atmosphere.

This result was nevertheless important since it showed a very high yield of oxidised product by **2OX** was achieved in very mild conditions. The formation of anthracene as oxidation product was confirmed by optical spectroscopy, by the increase of the absorption bands typical of this organic molecule ($\lambda = 341, 360$ and 379 nm, Figure 4.21 left).

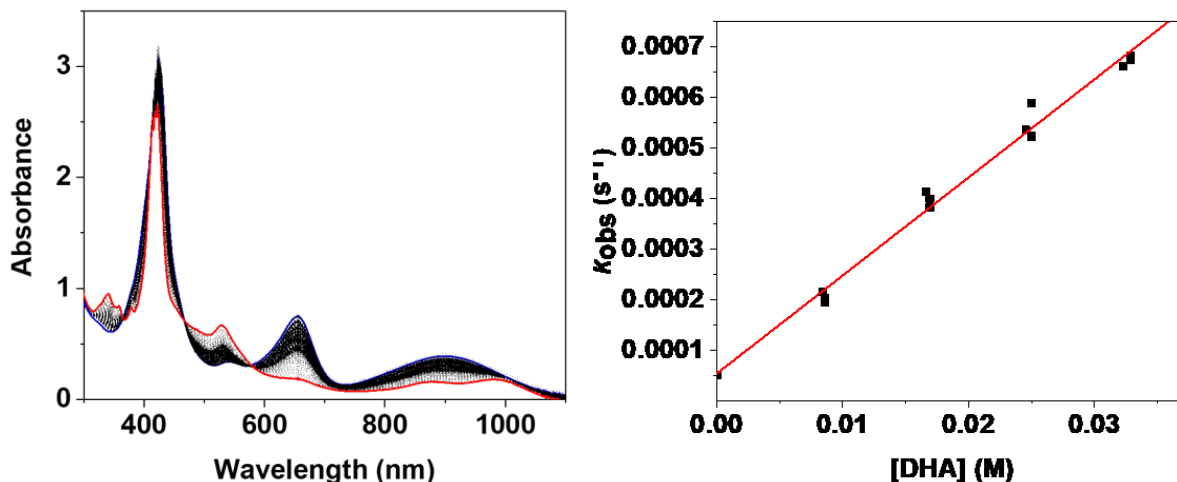


Figure 4.21. *Left:* Electronic absorption spectra of the reaction between **2OX** (blue trace) and DHA (250 equiv., 20 °C, DCM). *Right:* Plot of k_{obs} versus [DHA] determined for the reaction between complex **2OX** and DHA.

Then the substrate scope was extended to hydrocarbons with stronger C–H bonds, in particular fluorene and triphenylmethane (Table 4.1). For these substrates, which bear a higher BDFE for their C–H bonds (respectively 77.4 and 78.8 kcal/mol), the monitoring of the reactions showed a very slow decay of the features of **2OX**, yielding values of k_2 respectively equal to 0.0086 and $0.0073 \text{ M}^{-1} \text{ s}^{-1}$, the lowest values among all the substrates (Figure 4.22 Table 4.1). For both substrates, upon decay of the features of **2OX**, the appearance of the features ascribed to the isoporphyrin species were observed (Figures A93-94). For the reaction with fluorene, we managed to identify by GC-FID the main oxidation product, 9-fluorenone, a formally 4-protons, 4-electron oxidised product which was formed in $92 \pm 6\%$ yield (Table 4.2, yield calculated by taking in account a formal 1-electron reduction from **2OX** to **2**).

In summary we observed that **2OX** was reacting with a pool of hydrocarbon substrates, with BDFEs ranging from 73 to 79 kcal/mol, at room temperature, yielding a Ni-isoporphyrin complex while performing the oxidation of the organic substrates.

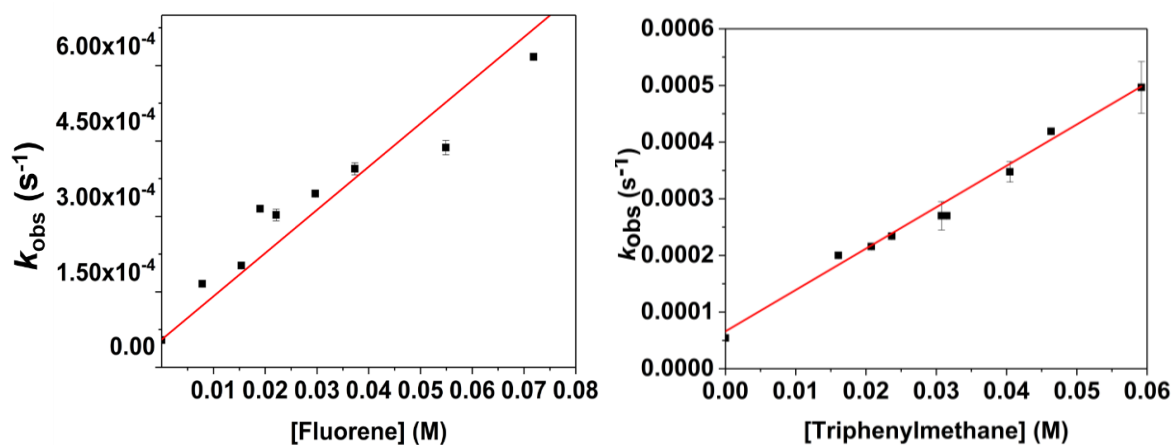


Figure 4.22. *Left:* Plot of k_{obs} versus [Fluorene] determined for the reaction between complex **2OX** and fluorene. *Right:* Plot of k_{obs} versus [Triphenylmethane] determined for the reaction between complex **2OX** and triphenylmethane.

Table 4.1. Second-order rate constants for the reactions of hydrocarbons substrates with different BDFEs (the BDFEs are reported for DMSO since they were not available in DCM).¹¹

Substrate	BDFE (kcal/mol)	k_2 ($\text{M}^{-1} \cdot \text{s}^{-1}$)
Xanthene	73.3	0.29
DHA	76.1	0.019
CHD	75.8	0.026
Fluorene	77.4	0.0086
Triphenylmethane	78.8	0.0073

The values in italics were not available in DMSO so were estimated on the basis of those reported for other substrates.

Table 4.2. Yields of oxidation products formed during the reaction of **2OX** with different hydrocarbon substrates (DCM, 20 °C). All the yields have been calculated by taking in account a formal 1-electron reduction of **2OX** to **2**, the stoichiometry for the substrate oxidation is indicated in the table.

Substrate	Product	Conditions	Yield	Stoichiometry
DHA	Anthracene	GC-FID	152 ± 16%	2-electron
DHA	Anthracene	GC-FID (inert atmosphere)	65 ± 5%	2-electron
Fluorene	9-fluorenone	GC-FID	92 ± 6%	4-electron
CHD	Benzene	¹ H NMR	72 ± 8%	2-electron

4.7 Mechanistic insights

The kinetic analysis performed allowed us to determine values of k_2 for the five substrates bearing C–H bonds (Table 4.1). The conversion of the k_2 values into the Gibbs free energies of activation was performed by using the Eyring equation. The plot of the ΔG^\ddagger values against the bond dissociation free energies (BDFEs) of the C–H bonds of the substrates, also known as Polanyi plot, showed a linear correlation, which is suggestive of a PCET mechanism, with a slope = 0.40 (Figure 4.23). This value within the range reported for oxidants following concerted mechanisms, such as HAT (0.15-0.7)²⁵⁻²⁷. We then evaluated the Marcus plot, where the oxidation potential of the substrate is plotted against the logarithm of the rate constants (Figure 4.24 left), which gave a value of -0.22. These plot have been employed to gain understanding of the mechanism of PCET oxidation: a slope closer to 0.00 has been ascribed to a concerted PCET mechanism, one close to -0.50 suggests that electron-transfer (ET) is rate

limiting, whereas a slope close to -1.00 indicates rate-limiting proton transfer (PT).²⁸ Therefore from the value obtained, which is closer to 0.00 within the error related to these measurements, the hypothesis of a concerted PCET mechanism is supported. Moreover, a plot of the pK_a of the substrates against the $\log(k_2)$ showed no correlation, which is generally observed in asynchronous mechanisms where the proton transfer is rate-limiting (Figure 4.24 right).²⁹ A HAT mechanism would imply the synchronous transfer of the proton and the electron to the same site in the acceptor molecule. In this case though, we have observed from the spectroscopic results that the electron is more likely accepted by the Ni ion, whereas the proton migrates to the ligand to yield an isoporphyrin. Therefore this is more likely an example of CPET (Concerted Proton electron Transfer).³⁰

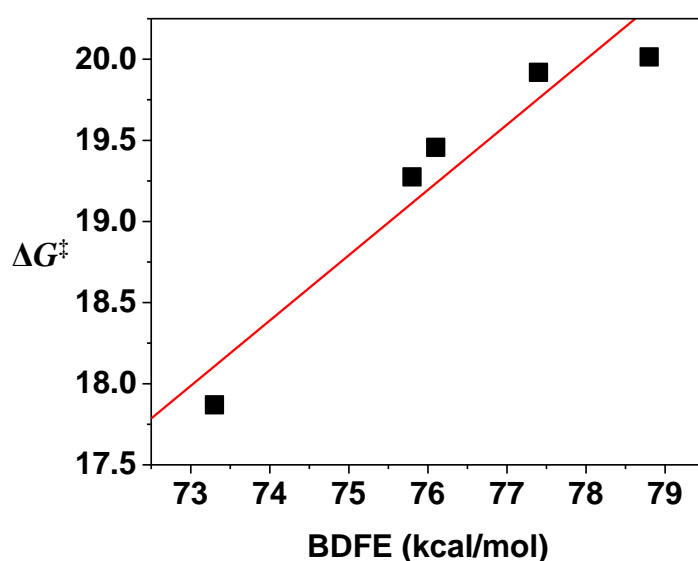


Figure 4.23. Plot of ΔG^\ddagger against the $BDFE_{C-H}$ of the substrates. The values of ΔG^\ddagger was determined from the calculated second-order rate constants k_2 via the Eyring equation (slope = 0.40).

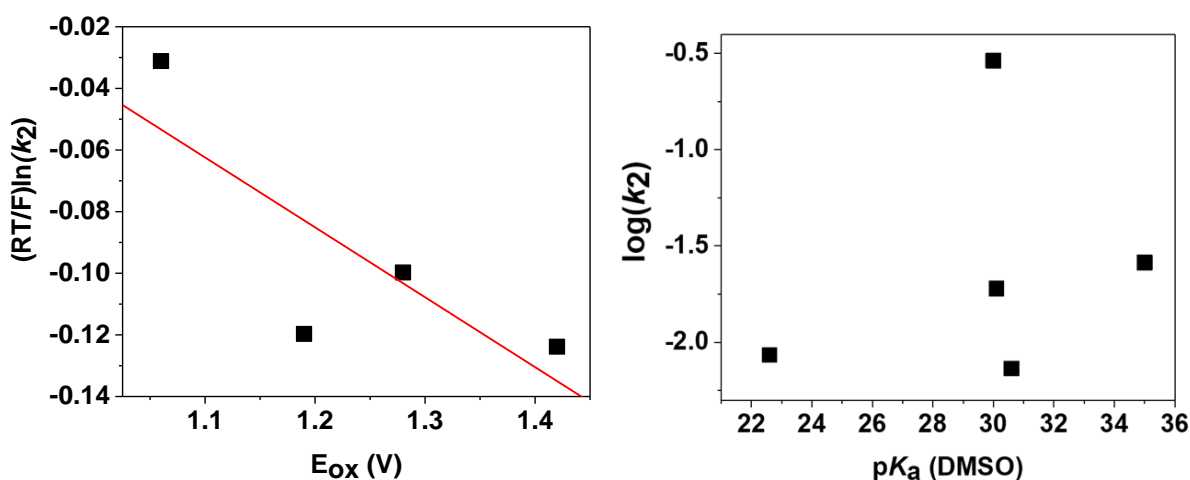


Figure 4.24. *Left:* Plot of $(RT/F) \ln(k_2)$ against the oxidation potential (E_{ox}) of hydrocarbon substrates for the reactions of **2OX** with hydrocarbon substrates in DCM. *Right:* Plot of $\log(k_2)$ against the pK_a of the hydrocarbon substrates in DMSO.

Activation energy parameters were determined via Eyring analysis for the reaction of **2OX** with xanthene (Figure 4.25). The activation enthalpy was determined to be $\Delta H^\ddagger = 8.7 \text{ kcal mol}^{-1}$, and the activation entropy value was determined to be $\Delta S^\ddagger = -37.5 \text{ cal mol}^{-1}\text{K}^{-1}$. The large, negative entropy is consistent with a metal-based oxidant performing a concerted PCET oxidation, due to the higher contribution from vibrational entropy during the reduction of the metal center compared to the reactions involving organic radicals.^{31, 32} The entropic value is therefore suggestive of a metal-centred CPET oxidation, which might appear in contrast with the formulation of **2OX** as a π cation-radical species formally described as $\text{Ni}^{\text{II}\cdot+}$.

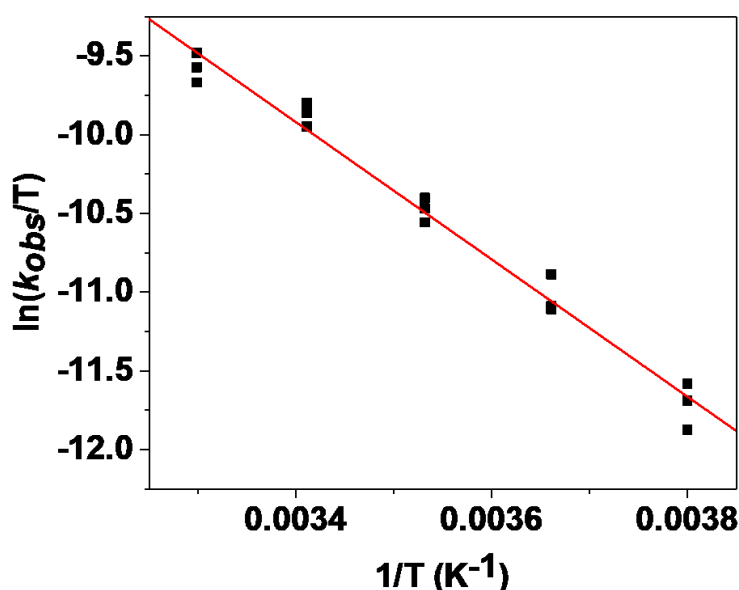


Figure 4.25. Plot of $\ln(k_{\text{obs}}/T)$ versus $1/T$ for **2OX** in its reaction with xanthene.

To gain more insights on the electronic state of **2OX** during the reaction we performed an EPR analysis. We then monitored the reaction of DHA (1500 equiv.) with **2OX** by X-Band EPR (Figure 4.26): in the absence of substrate the signal observed was centred at $g = 2.00$ (Figure 4.26 green trace), as already seen for **2OX** (Figure 4.13).

Upon addition of the DHA substrate a spectrum was recorded, showing the appearance of an additional $S = 1/2$ rhombic signal with $g_x = 2.3$, $g_y = 2.23$ and $g_z = 2.07$ (Figure 4.26, red trace). The average g value $g_{\text{av}} = 2.2$ suggested the localisation of the unpaired spin on the metal center, yielding a formal Ni^{III} species. In this case the $g = 2.00$ was still present.

This result was similar to what reported for the addition of imidazole or pyridine to $[\text{Ni}^{\text{II}}(\text{OEP})]^{+\cdot}$, for which both the signal at $g = 2.00$ typical of the radical cation and an axial signal with $g_{\text{av}} = 2.13$ typical of a Ni^{III} species.⁶ In fact, as mentioned in section 4.3, a valence

tautomerism exists for Ni^{II} π -cation radical species to Ni^{III} and is influenced by several factors such as solvent, temperature and complexation with an external ligand.^{6, 17, 33} Sometimes the coexistence of both the Ni^{II} π -cation radical and the Ni^{III} tautomer in solution is possible.⁶ Therefore we postulated that the addition of an excess of substrate to **2OX** shifts the valence tautomerism of $\text{Ni}^{\text{II}+}$ and Ni^{III} in a similar fashion, yielding a complexed radical formally described as a *d* orbital-centered species as observable from the red trace in Figure 4.26. After 3600 s from the beginning of the reaction with **2OX**, a lowering of the intensity of the Ni^{III} species was observed (blue trace, Figure 4.27), suggesting that consumption of the complexed radical occurred over time. After 4500 s the reaction appears to be completed with a colour change of the solution to brown-red: the X-band EPR spectrum taken at this point of time suggested the complete consumption of the oxidised species, yielding a silent trace compatible with a formal low-spin Ni^{II} species (black trace, Figure 4.27).

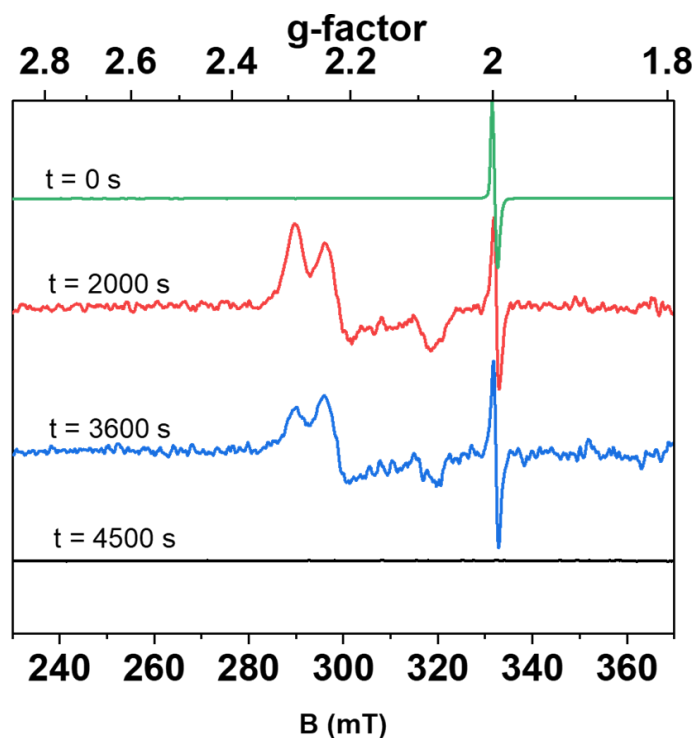


Figure 4.26. X-Band EPR spectra of the reaction of **2OX** (green trace) in the presence of 1500 equiv. of DHA after 2000 s (red trace) from the addition of the substrate, after 3600 s (blue trace) and after 4500 s (black trace). The spectra were acquired from a frozen DCM solution, 1.95 mW microwave power, 0.5 mT field modulation amplitude.

We therefore believe that an excess of substrate could form an adduct with the π -cation radical and change its electronic nature and geometry. To corroborate this assumption, we recorded an X-band EPR spectra of **2OX** in the presence of an excess of the oxidized product (anthracene,

Figure A95). We observed only the $g = 2.00$ signal, suggesting that the complexed radical species is formed only prior to the oxidation event in presence of the substrate prior to its oxidation.

We then wanted to test if these signals could arise from an auto-oxidation process, thus we added a solution of **2** to **2OX** and then recorded an X-Band EPR signal, which showed only a signal at $g = 2.00$ (Figure A96). Therefore we excluded the attribution of the coexisting Ni^{III} and $\text{Ni}^{\text{II}\cdot+}$ signal to an autooxidation of **2**.

To assess the possible role of the oxidant in the generation of these coexisting Ni^{III} and $\text{Ni}^{\text{II}\cdot+}$ species, we performed the reaction in presence of a different oxidant. We generated **2OX** by using WCl_6 , which is EPR silent as mentioned earlier in the text (see section 4.3). The addition of 2 equiv. of WCl_6 yielded a green species with a signal at $g = 2.00$ which we identified as **2OX**. Then we added 500 equiv. of DHA to **2OX** and we recorded an EPR spectra: this showed two coexisting signals, an isotropic one with $g = 2.00$ and a rhombic one with $g_x = 2.3$, $g_y = 2.23$ and $g_z = 2.07$ ($g_{\text{av}} = 2.2$, Figure 4.27). These signals are the same observed when DHA was added to a solution of **2OX** obtained with 2 equiv. of $(\text{Phenox})\text{SbCl}_6$. This result supports the conclusion that an equilibrium between the two tautomers Ni^{III} and $\text{Ni}^{\text{II}\cdot+}$ is induced when the substrate is added to **2OX**, no matter what oxidant is used to obtain this oxidizing species.

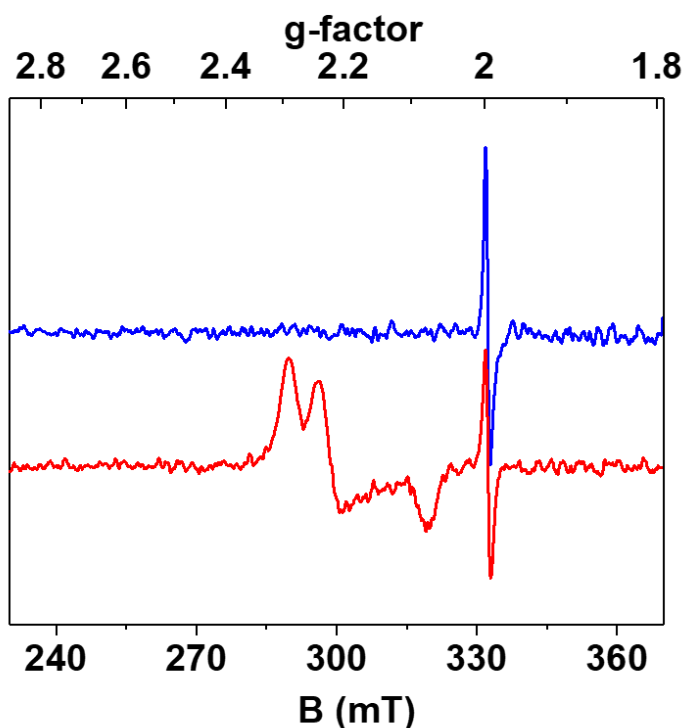


Figure 4.27. X-Band EPR spectra of the reaction of **2OX** (blue trace) formed by adding 2 equiv. of WCl_6 in presence of 500 equiv. of DHA after 2000 s (red trace). The spectra were acquired from a frozen DCM solution, $T = 77 \text{ K}$, 2.02 mW microwave power, 0.5 mT modulation amplitude

Then we proceeded with the mechanistic analysis by investigating the role of atmospheric dioxygen in the reaction of **2OX** with DHA. We repeated the reaction of **2OX** with DHA in anoxic conditions by preparing the solutions of both complex and substrates in the glove box and monitoring it by electronic absorption spectroscopy in DCM at $20 \text{ }^\circ\text{C}$: interestingly, the rate constant $k_2 = 0.011 \text{ M}^{-1} \text{ s}^{-1}$ was comparable with the one obtained in aerobic conditions within the experimental error intrinsic to these measurements ($k_2 = 0.019 \text{ M}^{-1} \text{ s}^{-1}$, Table 4.1). This result suggested that dioxygen does not affect the kinetics of reaction of **2OX** with the substrate, excluding the formation of transient Ni-O adducts.

We evaluated the presence of a kinetic isotope effect (KIE) by reacting **2OX** with D_2 -xanthene. The plot of k_{obs} versus the concentration of substrate yielded a $k_2 = 0.189 \text{ M}^{-1} \text{ s}^{-1}$ which, in comparison to the one obtained during the reaction with H_2 -xanthene, yielded a $\text{KIE} = 1.5$ (Figure 4.29). This value is quite low to be indicative of a primary kinetic isotope effect when compared to the reported values in the classical range (2-7): these are normally indicative of a mechanism in which proton or hydrogen atom transfer are rate-determining.^{25, 26, 28, 34, 35} This is unusual for a HAT mechanism, which normally shows a primary KIE in the classical range.

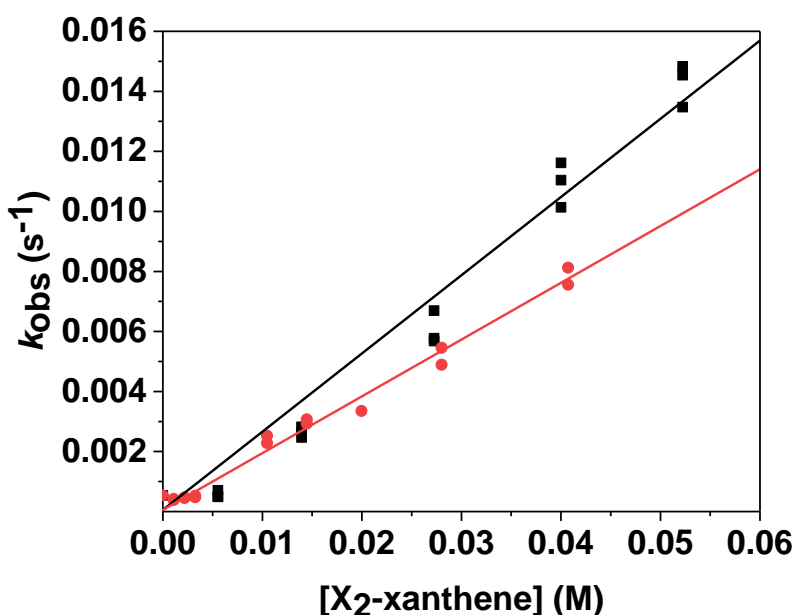
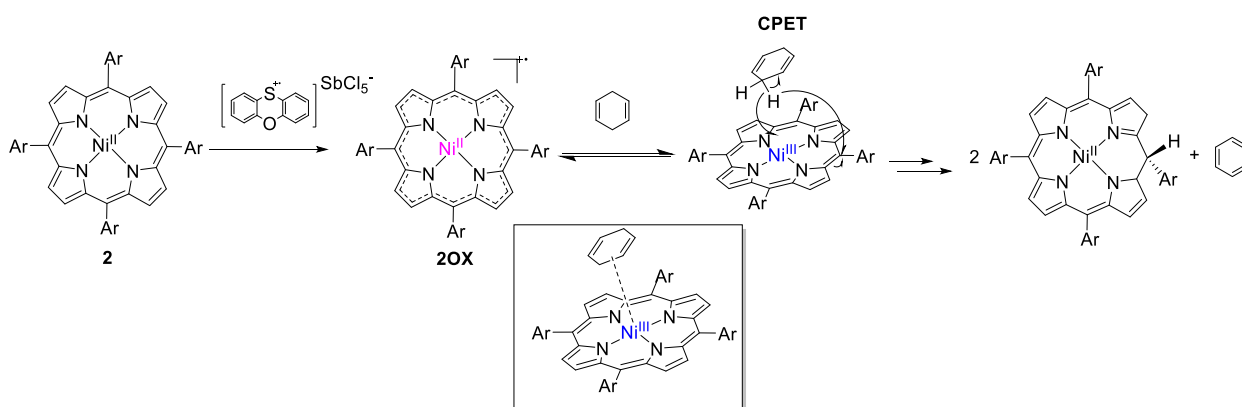


Figure 4.28. Plot of k_{obs} versus [substrate] determined for the reaction between **2OX** and H₂-xanthene (black trace) and D₂-xanthene (red trace).

With the elements collected so far, we tried to propose a reaction mechanism (Scheme 4.1): complex **2** is oxidised in the presence of (Phenox)SbCl₆ to yield the π -cation radical **2OX**. Then this species is reacted with a substrate (as exemplified with CHD in scheme 4.1) which affects the valence tautomerism of **2OX**, as often reported for oxidised metalloporphyrins.^{6, 17} This yields an adduct which can be formalized as Ni^{III} as observed by EPR, which accounts for the different geometry and electronic state induced by the introduction of an extra ligand (Figures 4.26 and 4.27). The mechanistic analysis suggests that the oxidation occurs with a CPET mechanism, yielding the oxidised substrate and a new inorganic species. The spectroscopic features of this species suggested it to be a Ni^{II} isoporphyrin species (Scheme 4.1).



Scheme 4.1. Postulated mechanism of oxidation of hydrocarbons by **2OX**, with a highlight on the adduct formed between substrate and complex.

In the case of the substrate with the weakest C–H bond, notably xanthene, we postulated that the oxidant might act as an external proton acceptor, yielding to the restoration of the initial complex **2** as observed by electronic absorption spectroscopy. It is also possible that the isoporphyrin is formed but is not stable and the equilibrium is driven back to the initial Ni^{II} complex or that the isoporphyrin is a minor product compared to **2**.

To prove this hypothesis, we tried to reoxidise **2** to **2OX** after its reaction with xanthene, to assess the possible regeneration of the oxidising species. We assessed this possibility by monitoring the absorbances at $\lambda = 530$ nm (diagnostic of **2**) and at $\lambda = 657$ nm and $\lambda = 900$ nm (diagnostic of **2OX**, Figure 4.29) over time. Upon depletion of **2OX** in presence of xanthene over ~ 600 s, addition of 2 equiv. of (Phenox)SbCl₆ yielded **2OX** again, as shown by an increase of the features at $\lambda = 657$ nm and $\lambda = 900$ nm (Figure 4.29). The newly formed **2OX** then reacted with the excess of xanthene again to yield the restoration of **2**. After ~ 1600 s, 2 more equiv. of oxidant were added, showing that **2OX** could be regenerated again (Figure 4.29). This observation is interesting since it could open new avenues for catalytic applications of **2OX** with substrates bearing weak C–H bonds.

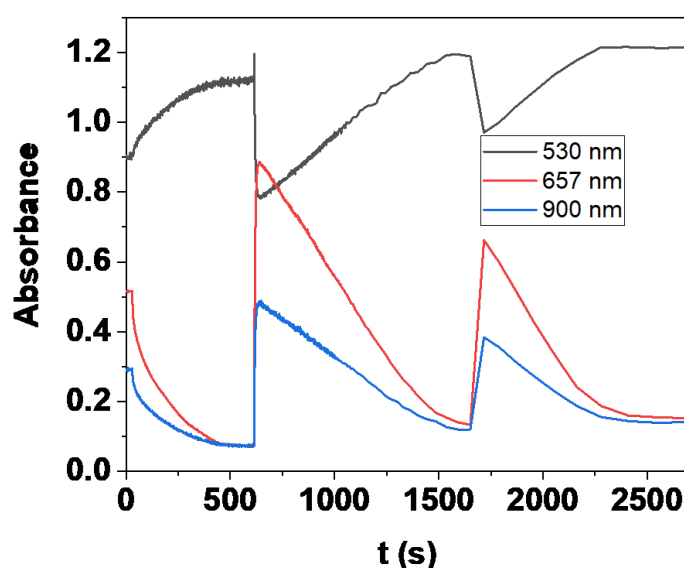


Figure 4.29. Time trace of the reaction of **2OX** with 500 equiv. of xanthene monitored via electronic absorption spectroscopy (black trace $\lambda = 530$ nm, red trace $\lambda = 657$ nm, blue trace $\lambda = 900$ nm).

4.8 Conclusions

While interested in exploring the potential reactivity of π -cation radicals of late transition metals, we explored the properties of Cu and Ni electron-rich porphyrin complexes. Once the complexes were synthesized and characterized, we observed that both Cu(T(OMe)PP) (**1**) and

Ni(T(OMe)PP) (**2**) showed two reversible redox waves at close value of potentials. The oxidised species, **1OX** and **2OX**, were obtained by chemical oxidation and their relative reactivity was assessed by reacting them with 4-CH₃O-2,6-DTBP at -20 °C, when we observed that **2OX** presented a k_1 one order of magnitude higher than the one observed for **1OX**. We then decided to focus our efforts on exploring the reactivity of the more promising **2OX** with hydrocarbons, which are more interesting substrates for oxidation both from a synthetic and an economic perspective. We then observed that **2OX** reacted with hydrocarbon substrates with BDFEs ranging from 73 to 79 kcal/mol at room temperature, yielding oxidised products and in most cases a new species which we ascribed to a Ni^{II} isoporphyrin due to its spectroscopic features. We then performed a kinetic analysis to gain more insights on the mechanism of oxidation of substrates by **2OX** and we postulated that the π -cation radical species oxidises substrates via a CPET mechanism. We believe that these insights are important because they highlight the potential role and mechanistic features of late transition metal porphyrin π -cation radicals as hydrocarbon activators. Given that the most oxidising species in biology, P680, is a Mg²⁺ porphyrinoid π -cation radical, we believe that this class of late-transition metal porphyrin π -cation radicals could act as interesting mimics of these species which are present in nature and react as powerful oxidants.

4.9 Experimental section

Materials

All solvents and reagents were purchased from commercial sources and used as received, unless otherwise stated. Complex **1** was synthesized with a modification of a reported procedure, where the reaction time was extended to 6 h instead of 3.¹² Complex **2** was synthesized both according to a reported¹³ and a novel procedure, entailing the reflux of 3 equiv. of NiCl₂*6H₂O with H₂(T(OMe)PP) in DMF for 3 hours. Complex **3** was synthesized by adapting a reported procedure for the synthesis of [Au(TPP)]⁺ to the compound.¹⁴ The oxidized complex **1OX** was obtained by adding 1.5 equiv. of (Phenox)SbCl₆ to a solution of **1** at -20 °C. **2OX** was obtained by adding 2 equiv. of (Phenox)SbCl₆ to a solution of **2** at 20 °C. 4-CH₃O 2,6-di-*tert*-butylphenol was recrystallized from hexane or ethanol/water prior to use. For reactions performed in the absence of oxygen, solvents (DCM) were freeze-pump-thawed three times and stored in a nitrogen atmosphere glovebox. The phenoxythiinyll hexafluorophosphate and the N-methylacridane were synthesized according to reported

procedures.¹¹ D₂-xanthene was synthesized according to a reported procedure (deuteration degree = 97% by ¹H-NMR).³⁶

Synthesis of [Cu((OMe)TPP)] (1)

Complex **1** was synthesized with a modification of a reported procedure, where the reaction time was extended to 6 h instead of 3.¹²

ESI-MS: found: $m/z = 796.2105$ (M+H)⁺, C₄₈H₃₇CuN₄O₄ requires 791.2105

UV-Vis (DCM, 20 °C, nm): $\lambda = 423$ (Soret), 541, 581, 618

Synthesis of [Ni((OMe)TPP)] (2)

H₂OMeTPP (240 mg) was refluxed in 50 mL of DMF for 30'. Then, NiCl₂·6H₂O (1.50 g) was added to the mixture and refluxed for 3 more hours. Then the reaction was allowed to cool down to 70 °C and 50 mL of water were added, then the purple solid was filtered and dried at 130 °C for 1 hour. Purification was achieved by flash column chromatography over silica gel using 100% DCM as eluent.

δ^1_H (400 MHz, CD₂Cl₂): 4.05 (12H, s, -OCH₃), 7.21 (8H, d, 2,6 -CH on Ph), 7.92 (8H, d, 3,5 -CH on Ph), 8.76 (8H, d, -CH on Py).

ESI-MS: found: $m/z = 791.2172$ (M+H)⁺, C₄₈H₃₇NiN₄O₄ requires 791.2163

UV-Vis (DCM, 20 °C, nm): $\lambda = 428$ (Soret), 530

Synthesis of [Au((OMe)TPP)]Cl (3)

H₂OMeTPP (50 mg) and KAuCl₄ (128 mg) were refluxed in 18 mL of glacial acetic acid in presence of 300 mg of sodium acetate for 20 hours. The mixture was allowed to cool down, then after addition of 100 mL of DCM was extracted twice with water and a saturated solution of Na₂CO₃. The red solution was dried over MgSO₄, filtered and the solvent removed in vacuo. The mixture was purified through flash column chromatography over silica gel using 20:1 DCM : MeOH as eluent. Then the product was dissolved in 50 mL of DCM and 50 mL of water, an excess (1.5 g) of LiCl were added and the biphasic solution was stirred for 72 hours. The product was then extracted twice with water, dried over MgSO₄, filtered and the solvent removed in vacuo.

δ^1_H (400 MHz, CD₂Cl₂): 4.13 (12H, s, -OCH₃), 7.42 (8H, d, 2,6 -CH on Ph), 8.15 (8H, d, 3,5 -CH on Ph), 9.38 (8H, d, -CH on Py).

ESI-MS: found: $m/z = 929.2388$ (M)⁺, C₄₈H₃₆AuN₄O₄ requires 929.2397

UV-Vis (DCM, 20 °C, nm): $\lambda = 425$ (Soret), 536, 570

Physical Methods

^1H and $^{13}\text{C}\{^1\text{H}\}$ nuclear magnetic resonance (NMR) analyses were performed on an Agilent MR400 instrument (400.13 MHz for ^1H NMR, 100.61 MHz for $^{13}\text{C}\{^1\text{H}\}$ NMR). The signals were internally referenced to tetramethylsilane. Electronic absorption spectra were recorded on a Hewlett Packard (Agilent) 8453 diode array spectrophotometer. Electrospray ionization (ESI) mass spectra were acquired using a Micromass time of flight spectrometer (TOF), interfaced to a Waters 2690 HPLC. Attenuated total reflectance infra-red (ATR-FTIR) spectra were recorded on a Perkin-Elmer Spectrum 100 Fourier transform infrared spectrometer.

EPR analysis

Electron paramagnetic resonance (EPR) spectra of frozen solutions were acquired on a Bruker EMX X-band EPR, equipped with an Oxford Instruments CE 5396, ESR9 Continuous Flow Cryostat, a precision Temperature Controller and an Oxford Instruments TTL20.0/13 Transfer Tube. EPR samples were prepared by freezing the EPR tubes containing the analyte solutions, previously prepared at the UV-Vis spectrophotometer, in liquid nitrogen. EPR spectra of **1**, **2**, **10X** and **20X** were recorded at 77 K, 9.2 GHz, 1.95 mW microwave power, with a 140 mT field sweep in 84 s, and 0.5 mT field modulation amplitude. EPR spectra of the reaction mixtures with DHA were recorded at 77 K, 9.2 GHz, 2.02 mW microwave power, with a 140 mT field sweep in 84 s, and 0.5 mT field modulation amplitude.

Electrochemistry

Cyclic voltammetry (CV) experiments were conducted with a CH Instruments 600E electrochemical analyzer, using a glassy carbon working electrode, a platinum wire counter electrode and an Ag/AgNO₃ 0.01 M reference electrode. Cyclic voltammetry experiments were conducted on a 1.0 mM solution of **1**, **2** and **3** in DCM at room temperature, with a 0.05, 0.1 and 0.2 V s⁻¹ scan rate, with 0.1 M ⁿBu₄NPF₆ as the supporting electrolyte. Potentials were referenced against the Fc⁺/Fc couple (Fc = ferrocene). The voltammograms of Fc were acquired under the same conditions.

Gas chromatography-Flame Ionisation Detector (GC-FID) analysis

Gas chromatography experiments have been performed using a ThermoFisher TRACE™ 1300 Gas Chromatograph equipped with a Flame Ionisation Detector. Hydrogen was provided by a Parker Hydrogen Gas Generator 20H-MD. Air was provided by Parker Zero Air Generator UHP-10ZA-S. The column used was a ThermoFisher Trace GOLD TG-1MS GC column. Post-reaction solutions from the reaction of **1** with different substrates were prepared at 20 °C. Different amounts of substrate (DHA, fluorene) were added as DCM solutions under continuous stirring until completion of the reaction, after which the mixture was analysed by GC-FID. A reference standard solution was prepared by adding the same amount of equivalents of substrate to 2 mL of pure DCM. The instrument method for anthracene was based on a temperature ramp (2 min at 175 °C, 10 °C/min to 250 °C, 2 min at 250 °C) with splitless injections of 1 µL each. Under these conditions, the retention time for anthracene was between 6.3-6.4 min. The instrument method for 9-fluorenone was based on a temperature ramp (1 min at 60 °C, 10°C/min to 160 °C, 1 min at 160 °C) with splitless injections of 1 µL each. Under these conditions, the retention time for 9-fluorenone was 5.7 min. The quantitative analysis of the analytes was based on a calibration curve. Yields were calculated as an average of four different solutions containing the same number of equivalents of substrate and repeating it for 2-3 different substrates concentrations.

Reactivity studies protocols

Solutions of **1** and **2** were prepared at room temperature and used immediately. Solutions of **1OX** were prepared by adding 1.5 equiv. of phenoxythiinyll hexachloroantimonate at - 20°C and reacted immediately with substrates. Solutions of **2OX** were prepared at 20 °C upon addition of 2 equiv. of phenoxathiinyll hexachloroantimonate and reacted immediately with substrates. Substrates were added as concentrated DCM solutions under continuous stirring. The reactions were monitored using electronic absorption spectroscopy, by observing the decay of the bands at $\lambda = 657$ nm for **2OX** and the decay of the band at $\lambda = 614$ nm for **1OX**. For rate constant determinations a minimum of 12.5 equivalents of substrate (with respect to **1OX** or **2OX**) were used to ensure *pseudo*-first order conditions. Each set of experiments was repeated three times and these data were fitted following a linear kinetic model.

4.10 References

1. R. Silaghi-Dumitrescu, *J. Biol. Inorg. Chem.*, 2004, **9**, 471-476.
2. J. Barber, *Bioelectrochemistry*, 2002, **55**, 135-138.
3. J. Barber and M. D. Archer, *J. Photochem. Photobiol. A*, 2001, **142**, 97-106.
4. B. Robotham and P. J. O'Malley, *Biochemistry*, 2008, **47**, 13261-13266.
5. J. Seth, V. Palaniappan and D. F. Bocian, *Inorg. Chem.*, 1995, **34**, 2201-2206.
6. M. W. Renner, K. M. Barkigia, D. Melamed, J.-P. Gisselbrecht, N. Y. Nelson, K. M. Smith and J. Fajer, *Res. Chem. Intermed.*, 2002, **28**, 741-759.
7. A. Ghosh, T. Wondimagegn, E. Gonzalez and I. Halvorsen, *J. Inorg. Biochem.*, 2000, **78**, 79-82.
8. J. P. T. Zaragoza, M. A. Siegler and D. P. Goldberg, *J. Am. Chem. Soc.*, 2018, **140**, 4380-4390.
9. J. P. T. Zaragoza, D. C. Cummins, M. Q. E. Mubarak, M. A. Siegler, S. P. de Visser and D. P. Goldberg, *Inorg. Chem.*, 2019, **58**, 16761-16770.
10. W. Liu, X. Huang, M.-J. Cheng, R. J. Nielsen, W. A. Goddard and J. T. Groves, *Science*, 2012, **337**, 1322-1325.
11. R. Gericke, L. M. Doyle, E. R. Farquhar and A. R. McDonald, *Inorg. Chem.*, 2020, **59**, 13952-13961.
12. Z.-Y. Wu and S.-Y. Yang, *J. Mol. Struct.*, 2019, **1188**, 244-254.
13. M. K. Peters and R. Herges, *Inorg. Chem.*, 2018, **57**, 3177-3182.
14. S. Preiß, J. Melomedov, A. Wünsche von Leupoldt and K. Heinze, *Chem. Sci.*, 2016, **7**, 596-610.
15. A. Wahab, M. Bhattacharya, S. Ghosh, A. G. Samuelson and P. K. Das, *J. Phys. Chem. B*, 2008, **112**, 2842-2847.
16. N. G. Connelly and W. E. Geiger, *Chem. Rev.*, 1996, **96**, 877-910.
17. M. W. Renner, K. M. Barkigia, Y. Zhang, C. J. Medforth, K. M. Smith and J. Fajer, *J. Am. Chem. Soc.*, 1994, **116**, 8582-8592.
18. W. F. Scholz, C. A. Reed, Y. J. Lee, W. R. Scheidt and G. Lang, *J. Am. Chem. Soc.*, 1982, **104**, 6791-6793.
19. K. E. Brancato-Buentello, S.-J. Kang and W. R. Scheidt, *J. Am. Chem. Soc.*, 1997, **119**, 2839-2846.
20. G. S. Nahor, P. Neta, P. Hambright and L. R. Robinson, *J. Phys. Chem.*, 1991, **95**, 4415-4418.
21. E. T. Shimomura, M. A. Phillippi, H. M. Goff, W. F. Scholz and C. A. Reed, *J. Am. Chem. Soc.*, 1981, **103**, 6778-6780.
22. V. N. Pak and D. V. Korol'kov, *Theor. Exp. Chem.*, 1973, **6**, 315-317.
23. D. Dolphin, R. H. Felton, D. C. Borg and J. Fajer, *J. Am. Chem. Soc.*, 1970, **92**, 743-745.
24. G. B. Wijeratne, B. Corzine, V. W. Day and T. A. Jackson, *Inorg. Chem.*, 2014, **53**, 7622-7634.
25. P. Pirovano and A. R. McDonald, *Eur. J. Inorg. Chem.*, 2018, **2018**, 547-560.
26. J. J. Warren, T. A. Tronic and J. M. Mayer, *Chem. Rev.*, 2010, **110**, 6961-7001.
27. S. Hammes-Schiffer, *J. Am. Chem. Soc.*, 2015, **137**, 8860-8871.
28. P. Mondal, P. Pirovano, A. Das, E. R. Farquhar and A. R. McDonald, *J. Am. Chem. Soc.*, 2018, **140**, 1834-1841.
29. M. K. Goetz and J. S. Anderson, *J. Am. Chem. Soc.*, 2019, **141**, 4051-4062.
30. W. D. Morris and J. M. Mayer, *J. Am. Chem. Soc.*, 2017, **139**, 10312-10319.
31. E. A. Mader, E. R. Davidson and J. M. Mayer, *J. Am. Chem. Soc.*, 2007, **129**, 5153-5166.
32. E. A. Mader, V. W. Manner, T. F. Markle, A. Wu, J. A. Franz and J. M. Mayer, *J. Am. Chem. Soc.*, 2009, **131**, 4335-4345.
33. K. M. Barkigia, M. W. Renner and J. Fajer, *J. Phys. Chem. B*, 1997, **101**, 8398-8401.
34. P. Mondal, M. Lovisari, B. Twamley and A. R. McDonald, *Angew. Chem. Int. Ed.*, 2020, **59**, 13044-13050.
35. D. Dhar, G. M. Yee, A. D. Spaeth, D. W. Boyce, H. Zhang, B. Dereli, C. J. Cramer and W. B. Tolman, *J. Am. Chem. Soc.*, 2016, **138**, 356-368.
36. C. Arunkumar, Y.-M. Lee, J. Y. Lee, S. Fukuzumi and W. Nam, *Chem. Eur. J.*, 2009, **15**, 11482-11489.

Chapter 5

IMAM ligands for low-coordinate late transition metal complexes

The XRD data collection and refinement was performed by Dr. Brendan Twamley.

5.1 Introduction

The aim of this project is to synthesize a family of tailored ligands to obtain tri-coordinate precursors for putative late transition metal-oxo complexes (LTMOs). This should be theoretically enabled by the trigonal planar geometry of the precursors, which would lead to the potential stabilization of metal-oxo species with a high d electron count, beyond the so-called “oxo-wall”. To enforce this particular coordination geometry, tailored ligands are required. This led us to the synthesis of novel N-(2,6-R-phenyl)-3-((2,6-R-phenyl)imino)butanamide ligands, abbreviated to IMAM (IMino AMido) ligands (Figure 5.1), bearing a strong σ donor in the form of a deprotonated amide which is aimed to confer higher oxidative robustness to its framework and better stabilization capacity towards high-valent species. β -diketiminates ligands have in fact been successfully employed to isolate low-coordinate complexes of Fe, Co, Ni and Cu,¹⁻⁵ but no LTMOs have been so far isolated with these ligands. Two variants of IMAM ligands, alkylated and unalkylated, have been synthesized, once the susceptibility of the α -hydrogens to deprotonation was observed. This chapter describes the synthesis of IMAM ligands and their complexation studies.

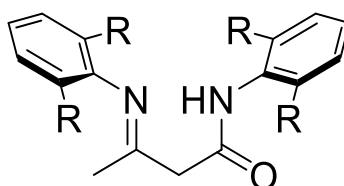
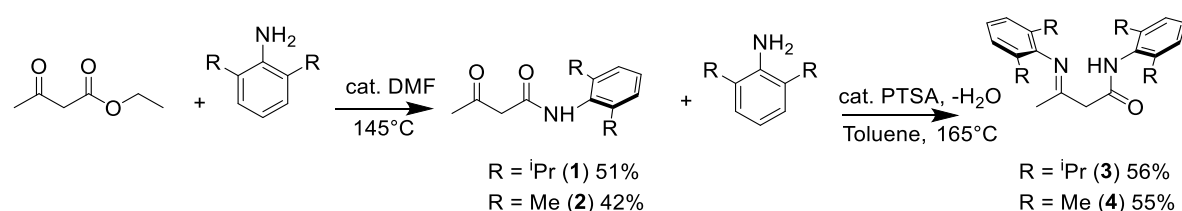


Figure 5.1. Structure of the target N-(2,6-R-phenyl)-3-((2,6-R-phenyl)imino)butanamide (IMAM) ligands.

5.2 Unalkylated IMAM ligands

5.2.1 Synthesis

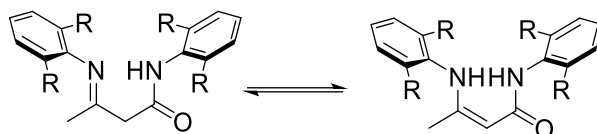
The synthetic pathway for IMAM ligands was designed with the aim of starting from a cheap, non-toxic precursor, notably the ethyl acetoacetate. The first step is a neat amidation reaction adapted from a reported procedure (Scheme 5.1),⁶ performed by using a slight excess of 2,6-substituted aniline with respect to the ester (1.1 equiv.) and heating the mixture in an inert atmosphere overnight at 145°C in presence of ~ 0.1 eq. of DMF. The postulated role of DMF is to perform nucleophilic addition on the ester carbonyl, increasing its electrophilicity and favouring the nucleophilic acyl substitution by aniline. The desired product, an acetoacetamide, was obtained in 51% starting from the 2,6-diisopropylaniline (**1**) and 42% yield starting from the 2,6-dimethylaniline (**2**) (Scheme 5.1). The second step is an acid-catalyzed Schiff base formation, achieved by adding one equivalent of the corresponding aniline to the acetoacetamide and refluxing overnight in toluene. Increase in the electrophilic character of the amidic carbon is achieved by protonation by the acid catalyst, in this case *p*-toluenesulfonic acid (PTSA). Then the aniline performs a nucleophilic addition to yield a hemiaminal, followed by elimination of water to yield the target imine product. Water was removed by using a Dean-Stark apparatus. The final product, a β -iminoamide, was obtained pure either through recrystallization for the N-(2,6-diisopropylphenyl)-3-((2,6-diisopropylphenyl)imino)butanamide (**3**) or flash column chromatography for the N-(2,6-dimethylphenyl)-3-((2,6-diisopropylphenyl)imino)butanamide (**4**). The overall yields for the final products were 29% (**3**) and 23% (**4**).



Scheme 5.1 Two-step synthetic pathway for IMAM ligands.

5.2.2 Characterization

Due to the presence of an iminic functional group and of an α -methylene group, **3** and **4** could exist either as iminic or enaminic tautomer (Scheme 5.2). One of the aims of the characterization was then to discover which of these tautomeric forms was prevalent both in solution and in the solid state to plan rationally the conditions required for the complexation.



Scheme 5.2 Structure of the iminic (left) and the enaminic tautomers (right) of the IMAM ligands.

The IMAM ligands were characterized by ^1H NMR, ^{13}C NMR, selected 2D NMR experiments (^1H - ^1H COSY, ^1H - ^{13}C HSQC, ^1H - ^{13}C HMBC, ^1H - ^{15}N HSQC), FTIR spectroscopy, XRD and ESI-MS. The ^1H - ^{15}N HSQC is a heteronuclear 2D NMR experiment which is helpful to investigate the coupling between protons directly bound to nitrogen atoms, notably in amide groups (Figure 5.1). The chemical shift of both amide nitrogen and proton is highly sensitive to subtle changes in the local chemical environment (for example, the presence of a bound ligand or changes in backbone conformation).⁸ For **3**, we observed a correlation peak at $\delta^1\text{H} = 10.5$ ppm and $\delta^{15}\text{N} = 97$ ppm and another one at $\delta^1\text{H} = 8.6$ ppm and $\delta^{15}\text{N} = 113$ ppm (Figure 5.1). Similarly, the ^1H - ^{15}N HSQC spectrum for **4** presented two correlation peaks, one at $\delta^1\text{H} = 10.3$ ppm and $\delta^{15}\text{N} = 102$ ppm and another one at $\delta^1\text{H} = 8.6$ ppm and $\delta^{15}\text{N} = 117$ ppm (Figure 5.1). The presence of two correlation peaks suggested the presence of two N–H groups in both **3** and **4**.

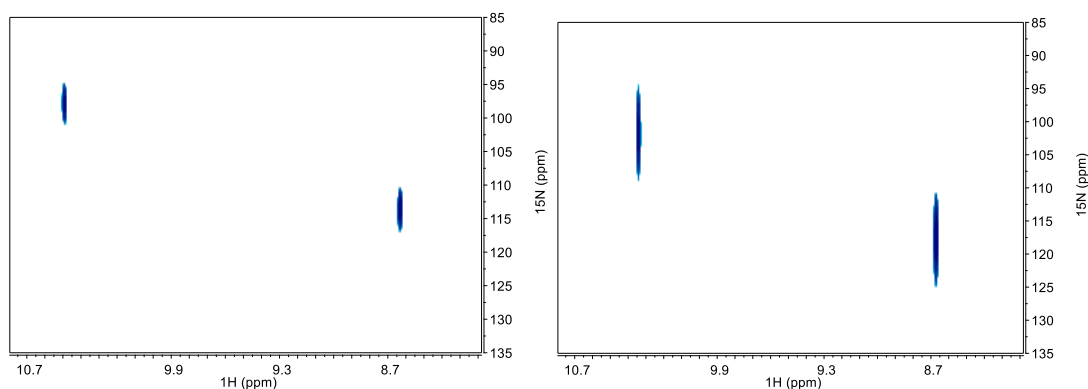


Figure 5.1. ^1H - ^{15}N HSQC spectra of **3** (left) and **4** (right) in DMSO- D_6 .

Further insights were given by the ^1H -NMR spectra of **3** and **4** in DMSO- D_6 (Figure 5.2). In the ^1H -NMR spectrum of **3**, the most deshielded peak was a singlet observed at $\delta^1_{\text{H}} = 10.47$ ppm (integrating roughly to one proton, 1H), then another singlet was observed at $\delta^1_{\text{H}} = 8.62$ ppm (1H), two triplets respectively at $\delta^1_{\text{H}} = 7.25$ ppm (1H) and $\delta^1_{\text{H}} = 7.21$ ppm (1H), two doublets respectively at $\delta^1_{\text{H}} = 7.17$ ppm (2H) and $\delta^1_{\text{H}} = 7.12$ ppm (2H), a singlet at $\delta^1_{\text{H}} = 4.95$ ppm (1H), two septets respectively at $\delta^1_{\text{H}} = 3.15$ ppm (2H) and $\delta^1_{\text{H}} = 3.11$ ppm (2H), a singlet at $\delta^1_{\text{H}} = 1.54$ ppm (3H) and three sets of doublets, respectively at $\delta^1_{\text{H}} = 1.20$ ppm (6H), $\delta^1_{\text{H}} = 1.14$ ppm (12H) and $\delta^1_{\text{H}} = 1.03$ ppm (6H), (Figure 5.2). The total number of proton accounting for the integration was 40. The three most shielded doublets integrating to overall 24 protons were assigned to the methyl groups in the four isopropyl substituents on the aryl rings in **3**. These resonate as three doublets instead of four because two signals are merged into one at $\delta^1_{\text{H}} = 1.14$ ppm, given the integration to 12 protons instead of 6: this happens for isopropyl groups which are free to rotate at room temperature thus merging of resonances occurs. The septets at $\delta^1_{\text{H}} = 3.15$ ppm and $\delta^1_{\text{H}} = 3.11$ ppm were assigned to the corresponding four $-\text{CH}$ groups of the isopropyl substituents. The singlet at $\delta^1_{\text{H}} = 1.54$ ppm integrating to three protons was assigned to the methyl group in the backbone of the ligand. The two doublets at $\delta^1_{\text{H}} = 7.17$ ppm and 7.12 ppm were assigned to the *meta* protons of the aromatic substituents, whereas those in *para* position gave rise to the triplets at $\delta^1_{\text{H}} = 7.25$ ppm and 7.21 ppm. The singlet at $\delta^1_{\text{H}} = 4.95$ ppm appeared to be typical of a vinylic proton, integrating to one. The two signals at $\delta^1_{\text{H}} = 10.47$ and 8.62 ppm were then assigned to two N–H protons on the basis of the results of the ^1H - ^{15}N HSQC (Figure 5.1). These results suggested that **3** existed in solution as the enaminic tautomer. The same observations were done in relation to **4**. The ^1H NMR spectrum of **4** in DMSO- D_6 presented two singlets at $\delta^1_{\text{H}} = 10.31$ ppm (1H) and $\delta^1_{\text{H}} = 8.63$ ppm (1H) integrating to one proton each, then two singlets at $\delta^1_{\text{H}} = 7.09$ ppm (3H) and $\delta^1_{\text{H}} = 7.02$ ppm (3H), a singlet at $\delta^1_{\text{H}} = 4.90$ ppm (1H), a singlet at $\delta^1_{\text{H}} = 2.16$ ppm (12 H) and a singlet at $\delta^1_{\text{H}} = 1.53$ ppm (3H). The total number of proton accounting for the integration was 24. The signal at $\delta^1_{\text{H}} = 2.16$ ppm was assigned to the methyl substituents on the aryl rings, whereas the one at $\delta^1_{\text{H}} = 1.53$ ppm was assigned to the methyl group in the backbone. The other aromatic protons in *meta* and *para* positions on the aryl rings resonated as the two singlets at $\delta^1_{\text{H}} = 7.09$ and 7.02 ppm. The singlet at $\delta^1_{\text{H}} = 4.90$ was assigned to a vinylic $-\text{CH}$ in the ligand backbone, whereas the two most deshielded peaks at $\delta^1_{\text{H}} = 10.31$ and 8.63 ppm to two N–H resonances

based on the ^1H - ^{15}N HSQC (Figure 5.1), analogously to what observed for **3**. This suggested that also **4** existed as an enamine in solution.

Further support to this hypothesis was given by the ^{13}C - $\{^1\text{H}\}$ NMR signals coupling to the resonance at $\delta^1_{\text{H}} = 4.95$ ppm for **3** and $\delta^1_{\text{H}} = 4.90$ ppm in **4**, which showed to be in phase in a DEPT 135 experiment. This excluded the possibility for these resonances to be attributed to a methylenic group.

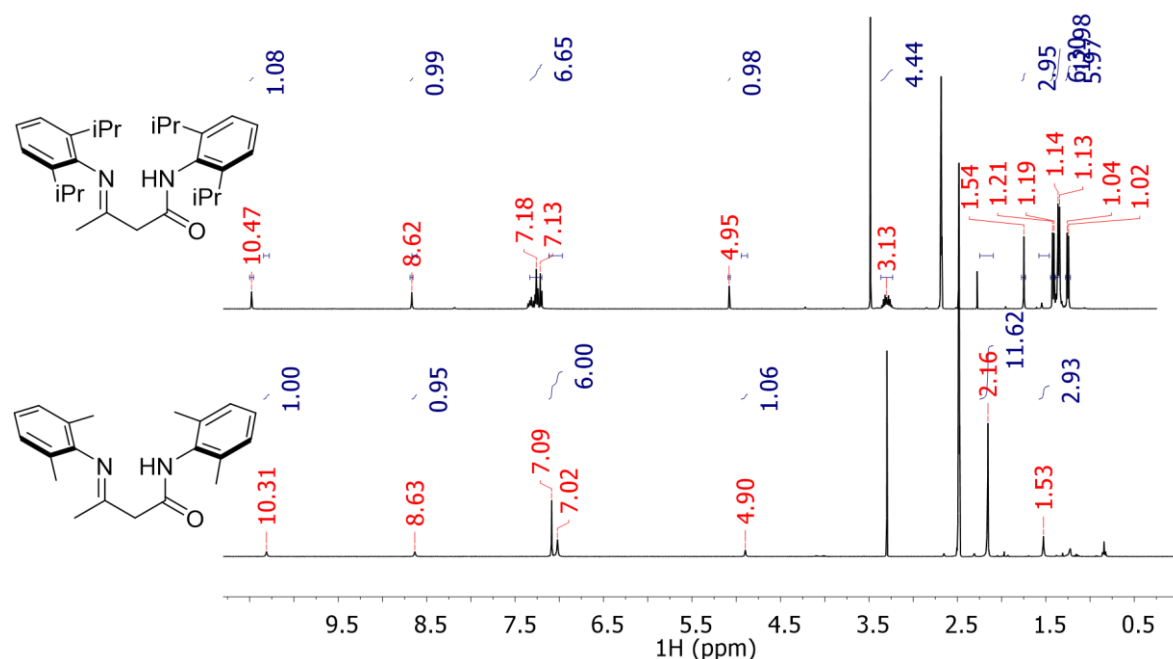


Figure 5.2. ^1H -NMR spectra of **3** (top) and **4** (bottom) in $\text{DMSO-}d_6$. Peaks at 2.5 ppm and 3.30 ppm are residual solvent and water peaks respectively (present in the solvent).

Moreover, the fact that for **4** the aromatic protons are resonating as two singlets suggested that the lower steric hindrance of the methyl substituents compared to the isopropyl ones in **3** allows for free rotation of the aryl rings.

ESI-MS measurements confirmed the identity of the desired molecules, showing peaks matching with the expected mass of each ligand (Figures A97-98). These experiments enabled the predominance of the enaminic tautomer in solution to be determined but were not decisive in understanding the behaviour of the ligands in the solid state.

Crystals suitable for XRD were obtained by recrystallization from Et_2O for both **3** and **4** (Figure 5.3, Tables A4-5).

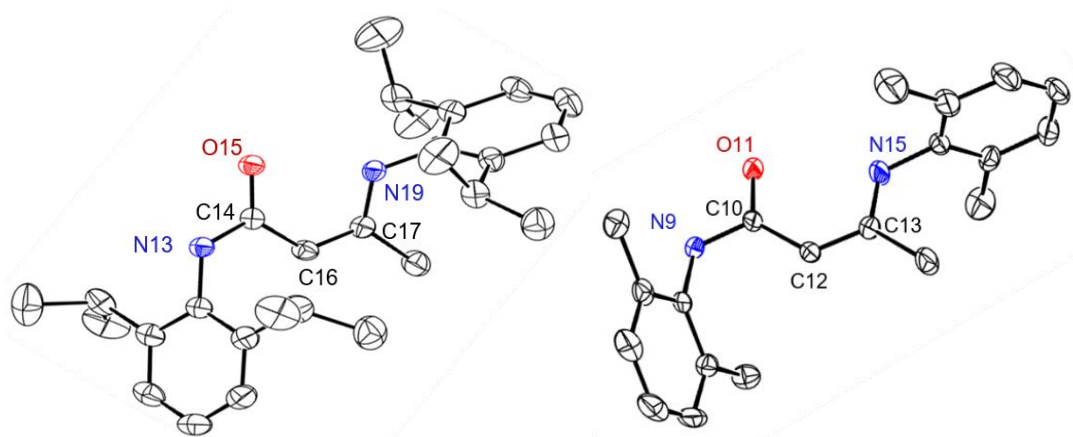


Figure 5.3. Ellipsoids plots at 50% probability of **3** (left) and **4** (right) with selected labelled atoms. Hydrogen atoms and solvents molecules have been omitted for clarity.

The crystal structures confirmed the achievement of the synthesis of the desired ligands. Crystals of **3** showed two molecules per asymmetric unit plus a diethyl ether solvate molecule, whereas **4** presented an asymmetric unit containing four molecules of ligand and a disordered diethyl ether molecule. The bond distance for the imine group was respectively of 1.358(2) Å for **3** (C17-N19) and 1.349(4) Å for **4** (C13-N15, Table 5.1), whereas those for the adjacent carbon-carbon bond in the backbone was respectively 1.362(2) Å for **3** (C16-C17) and 1.364(4) Å for **4** (C12-C13, Table 6.1). The latter are considerably shortened than the other carbon-carbon bond in the backbone: in fact C14-C16 = 1.436(2) Å in **3** and C10-C12 = 1.440(4) Å in **4**. This suggested that this C–C bond had more a single bond character, whereas the one closer to the imine moiety had more a double bond character. The fact that the adjacent C–C and iminic C–N bonds had comparable bond distances in both ligands suggested the presence of a delocalization of the π electrons along the backbone of the ligands to create a more stable conjugated system. This is achieved when the ligands are in their enaminic forms.

Table 5.1. Selected bond distances for the unalkylated IMAM ligands.

3		4			
Atom 1	Atom 2	Distance (Å)	Distance (Å)		
C14	O15	1.263(2)	C10	O11	1.265(3)
C14	C16	1.436(2)	C10	C12	1.440(4)
N13	C14	1.358(2)	N9	C10	1.346(4)
C16	C17	1.362(2)	C12	C13	1.364(4)
C17	N19	1.352(2)	C13	N15	1.349(4)

The bond distances observed for both ligands appeared to be comparable with those reported for other β -diketiminato ligands (Figure 5.4, Table 5.2). For diaryl-substituted β -diketiminato ligands such as Dipp₂nacnacH (**5**)⁹ distances were comparable with those observed for **3** and **4**, showing that these ligands adopt the enaminic tautomer in solid state. Even when the aryl substituent presented a chiral arm, such as in bis-N,N'-(2-phenylethyl)-2,4-diiminopentane (**6**),¹⁰ or when a heteroatom-containing pendant was added, such as in Me₂nacnac^{iPr,SPh} (**7**),¹¹ the imine-enamine form appeared to be still favoured in the solid state compared to the diamine one. This was also observed when bulkier substituents were present on one of the N-aryl groups, such as in ^{TbtPh}nacnacH (**8**).¹² The presence of a sterically encumbered 2,4,6-tris[bis(trimethylsilyl)methyl]phenyl (Tbt) group does not affect the relative stability of the tautomers and favours again the enaminic one, which appears to be predominant in all cases in which aryl substituents are present.

On the other hand, bond distances for N,N'-chelating ligands bearing different substituents in the β positions in the backbone appear to be different from the above-mentioned examples. One example is given by PhN(nacnac)H (**9**) and DippN(nacnac)H (**10**),¹³ in which the C1-N1 distance is considerably shorter and the C1-C2 one longer than those reported for compounds **3-8** (Table 5.2). This phenomenon was also observed in a β -diketiminato ligands bearing electron-donating ethoxy substituents in the backbone (**11**)¹⁴ and in another one presenting electron-withdrawing trifluoromethyl groups in the same position (**12**).¹⁵

In all these systems bond distances suggest that the backbone is not planar and the ligands adopt preferentially the diimine form in the crystalline state. The IMAM ligands **3** and **4** thus appear to behave as ligands **3-8** by adopting the enaminic tautomer in the crystalline state, compared to ligands **9-12** that adopt the iminic one.

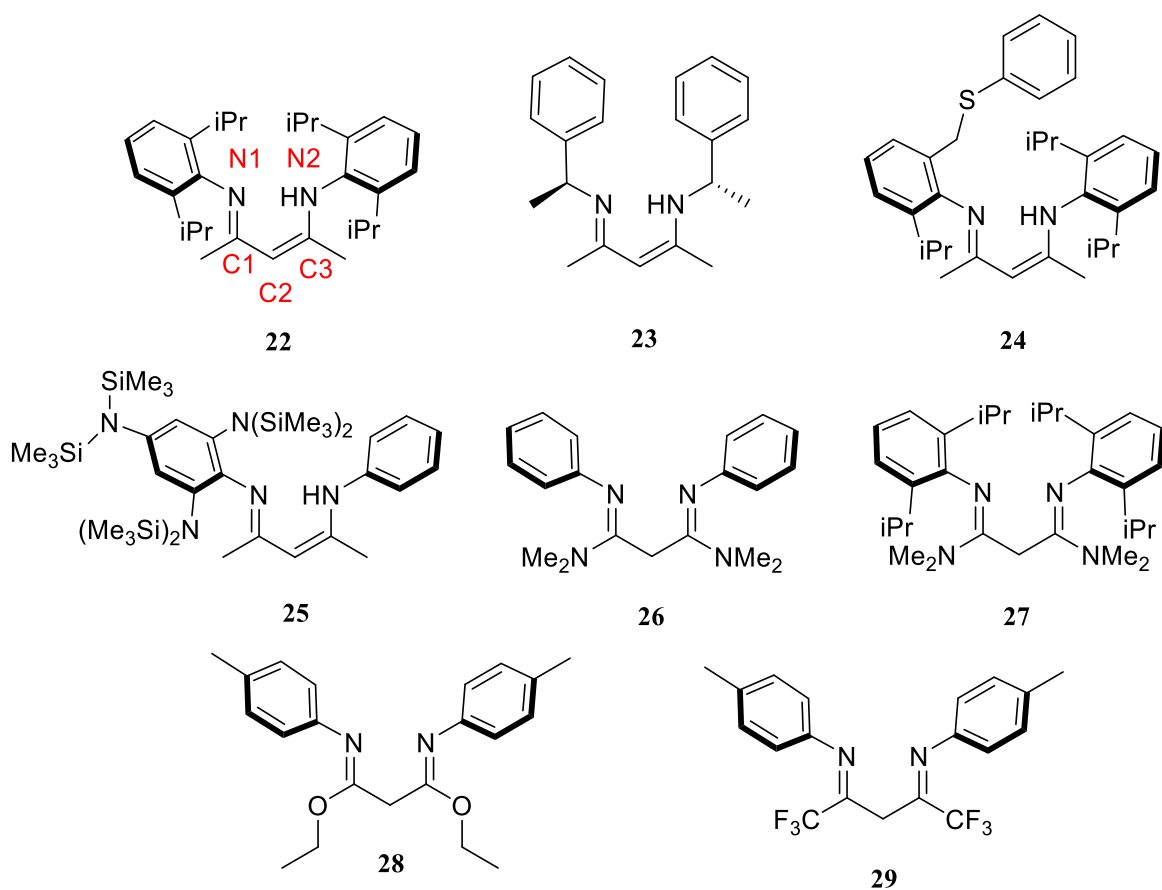


Figure 5.4. Selected examples of β -diketiminato ligands and numbering scheme for atoms in the backbone.

Table 5.2. Selected bond distances for selected β -diketiminato ligands.

Ligand	C1-N1 (Å)	C1-C2 (Å)	C2-C3 (Å)	C3-N2 (Å)
5	1.318(3)	1.418(4)	1.386(4)	1.341(3)
6	1.312(4)	1.415(4)	1.393(4)	1.335(3)
7	1.310(3)	1.417(3)	1.384(3)	1.331(3)
8	1.318(3)	1.426(3)	1.366(3)	1.354(3)
9	1.292(1)	1.527(2)	1.524(2)	1.288(1)
10	1.287(2)	1.512(2)	1.529(2)	1.286(2)
11	1.2643(15)	1.5078(16)	1.5110(16)	1.2614(15)
12	1.287(3)	1.528(2)	1.524(3)	1.292(2)

5.2.3 Complexation

Once the ligands were obtained and characterized, complexation trials with late first-row transition metals were performed. First base-free complexations were tried, in order to assess

the coordination capability of the ligand and to investigate whether this occurred either through nitrogen or oxygen donor atoms. Several metal salts (MX_2 , where $\text{X} = \text{Cl}$, acetate (OAc), trifluoromethanesulfonate (OTf) and $\text{M} = \text{Fe}$, Co , Ni , Cu) were used and THF was employed as solvent. When a slight excess (1.1 equiv.) of $\text{Cu}(\text{OTf})_2$ was added to both ligands, an immediate colour change of the solution, turning from colourless to intense green, was observed. Crystals suitable for XRD were obtained from the outcome of these reactions (Figure 5.5). With **3**, a 1:1 complex containing two molecules of solvent, N,N-dimethylacetamide (DMA) was obtained, $[(\text{DMA})_2(\text{IMAM}^{\text{iPr}_2})(\text{OTf})\text{Cu}^{\text{II}}]\text{OTf}$ (**13**, Table A6). Instead, **4** afforded a 2:1 $[(\text{IMAM}^{\text{Me}_2})_2(\text{OTf})\text{Cu}^{\text{II}}]\text{OTf}$ complex (**14**). Unfortunately for the latter the quality of diffraction was too low to be able to refine the data without a large error, thus it was not possible to calculate bond distances.

Both complexes appeared to be pentacoordinate and cationic, with a bound triflate and another triflate as a counterion. The adopted geometry was distorted square pyramidal for both complexes, as confirmed by the structural parameter¹⁶ τ_5 for **13**. This parameter¹⁶ is normally calculated for a pentacoordinate compound starting from two angles around the central metal, in this case $\text{O}(45)\text{--Cu}(1)\text{--N}(19)$ with a value of $155.85(8)^\circ$ and $\text{O}(15)\text{--Cu}(1)\text{--O}(39)$ with a value of $166.73(7)^\circ$. The τ_5 parameter is equal to 0 when a perfect square pyramidal geometry is adopted whereas is equal to 1 for a perfect trigonal bipyramid. For **13**, a τ_5 value of 0.18 was calculated, indicating that the complex adopts a distorted square pyramidal geometry. Considering the donor atoms coordinated to the Cu^{II} ion at the base of the pyramid, we observed that both IMAM ligands coordinated to the metal through the amidic oxygen and through the iminic nitrogen. This was coherent with the expected outcome of a base-free reaction with these ligands, considering that amides normally require relatively strong bases in order to be deprotonated and complex to a metal ion.¹⁷ The coordination number of 5 could also be related to the presence of the neutral ligands, since the shielding effect on the metal coordination sphere should be exerted by the aryl groups when the ligand is coordinating through the amidic nitrogen. Given this, considerations about the role of the N-aryl substituents could be made: in fact, the bulkier **3** gave a 1:1 complex with the metal, with only two solvent (DMA) molecules coordinated, whereas **4** gave a 2:1 complex. These structures confirmed nevertheless that IMAM ligands are effective chelators even in their neutral form and can easily form pentacoordinate complexes with Cu^{II} .

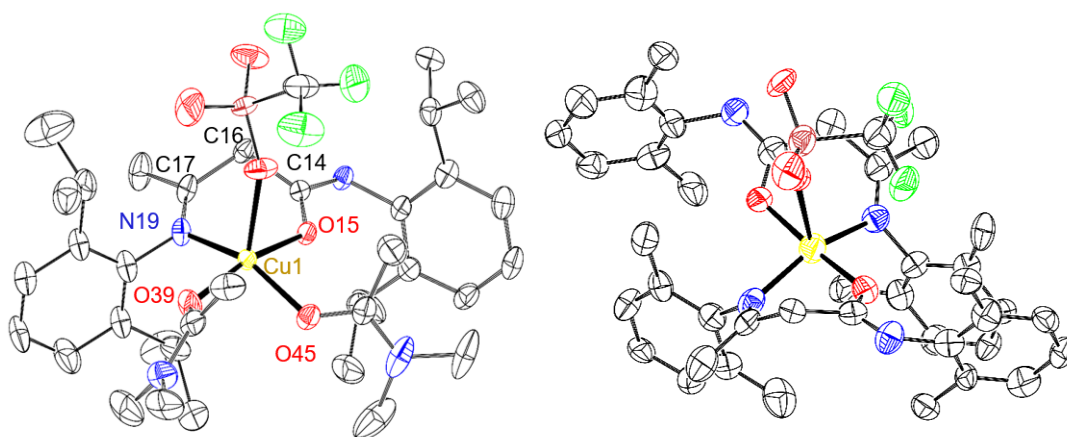


Figure 5.5 Ellipsoids plots (at 50% probability) of **13** (left) and **14** (right) with selected labelled atoms. Hydrogen atoms and triflate counterions are omitted for clarity.

A base was then added to achieve the desired coordination in the complexation of first-row transition metals. Several bases were assessed: triethylamine (Et_3N) and sodium ethoxide (EtONa) were not strong enough to deprotonate the amide, whereas stronger bases like potassium *tert*-butoxide (tBuOK), potassium hexamethyldisilazide (KHMDS), potassium hydride (KH) and *n*-butyllithium (nBuLi) appeared to be effective. A ^1H NMR comparison of the effect of the addition of 2 equiv. of these bases (Figure 5.6) to a solution of **3** in $\text{DMSO-}D_6$ was performed. All the spectra showed that both resonance peaks at $\delta^1_{\text{H}} = 8.62$ and 10.47 ppm assigned to the N–H disappeared from the spectrum, but also the signal assigned to the α -C–H at $\delta^1_{\text{H}} = 4.95$ ppm was no longer present. Given that the imine/enamine tautomerism can be still present in solution, we believe that the acidity of the methylenic alpha protons in the imine tautomer might make them susceptible to deprotonation in the first instance. The pK_a of these proton has not been determined but examples from the literature suggest that methylenic protons in alpha position to β -diketones, β -ketoesters (~ 9 - 13)¹⁸, β -ketoamides or β -diamides¹⁹ (~ 6 - 10) and β -diketimate²⁰ present a non-negligible acidity. We therefore postulated that the addition of bases favours the shift to the diiminic tautomer in solution and affects the alpha hydrogens first, being more acidic than the amidic proton. These observations suggested that the ligand is thus susceptible to strong bases and eventually is destroyed during the deprotonation attempts. A detailed examination of the ^1H NMR spectra (Figure 6.6) revealed that also the signal relative to the methyl group in the backbone (at $\delta^1_{\text{H}} = 1.54$ ppm) disappeared when KHMDS was added. This was a further indication of the instability of the ligand respect to bases. To prove this, we investigated the addition of a weak acid, notably H_2O ($\text{pK}_a = 14$ at 25°C) to the ligand in presence of bases to assess whether the acid was able to

reverse the deprotonation of the alpha position and restore the initial ligand **3**. Addition of an excess (20 equiv.) of water was performed (Figure 6.7) and in all cases the initial ^1H NMR spectrum of **3** was not observed. This result indicated that the ligand was irreversibly affected by the addition of bases. Such an outcome also accounted for the failure of all the previously attempted complexation trials.

All these results suggested that structural modification of the ligand to avoid tautomerism was essential to achieve the desired fashion of complexation. The most straightforward modification appeared to be the dialkylation of the α -carbon. This modification should in fact block the imine/enamine tautomerism in solution and prevent the deprotonation of the methylenic α -protons.

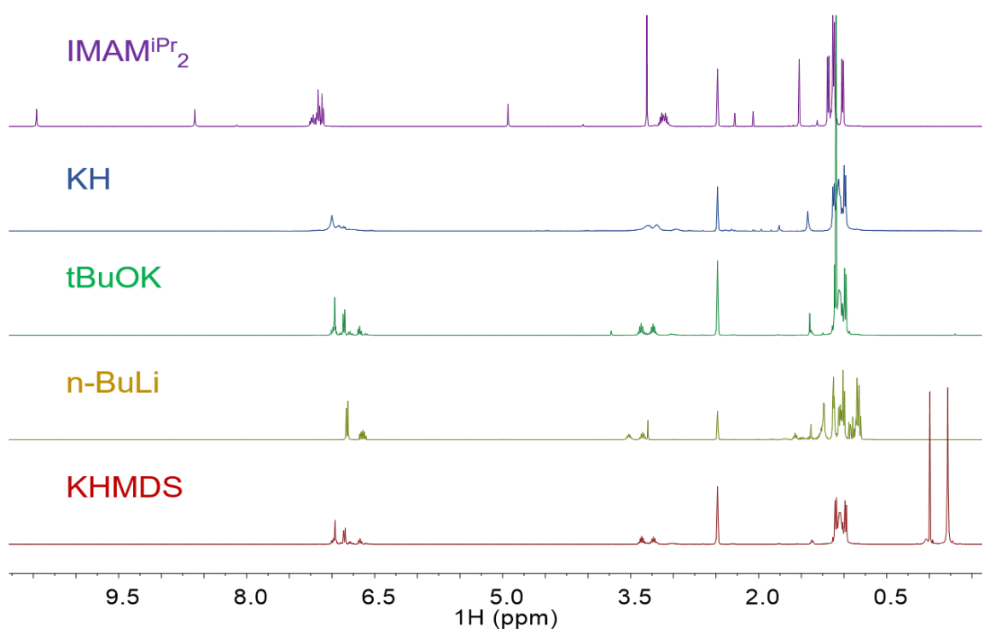


Figure 6.6. Stacked ^1H NMR spectra (DMSO- D_6 , 400 MHz) of **20** (purple) before and after the addition of 2 equiv. of different bases: KH (blue), tBuOK (green), n-BuLi (yellow) and KHMDS (red).

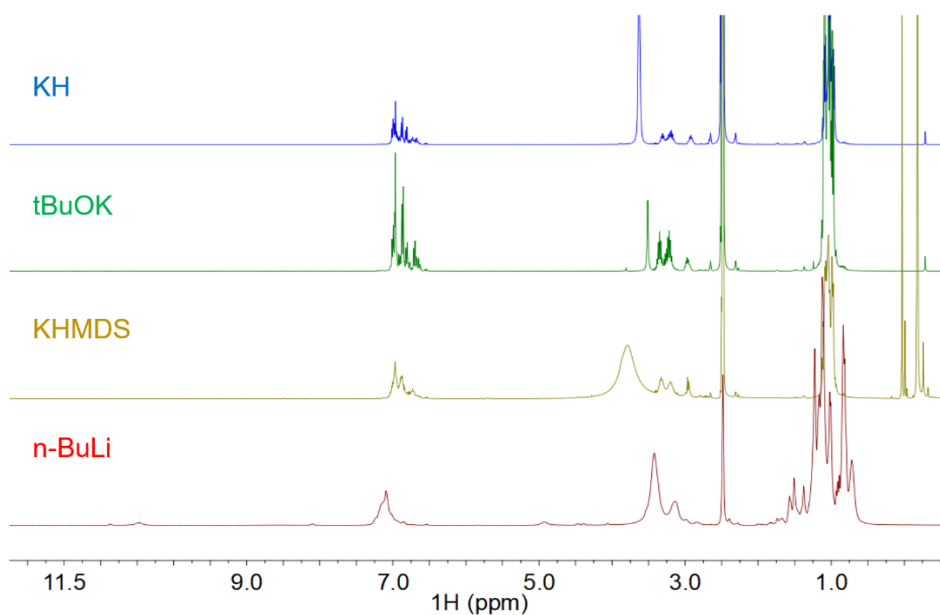


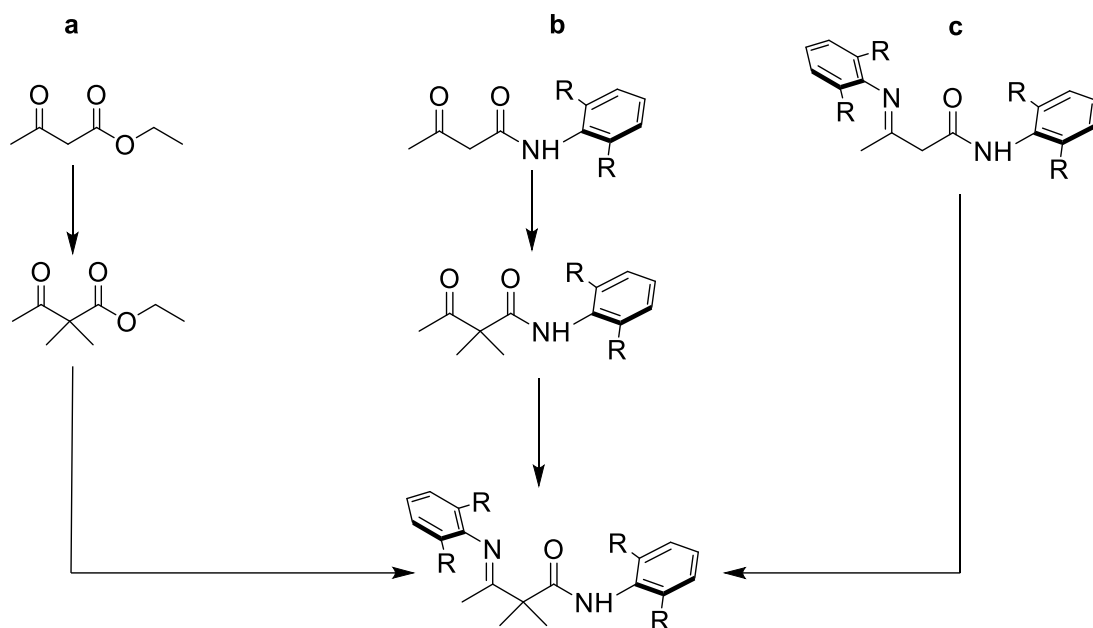
Figure 5.7 Stacked ^1H NMR spectra (DMSO- D_6 , 400 MHz) of **3** in presence of different bases after the addition of 20 equiv. of H_2O . The bases used in the experiment are KH (blue), tBuOK (green), KHMDS (yellow) and n-BuLi (red).

5.3 Alkylated IMAM ligands

5.3.1 Synthesis

Once the necessity to alkylate the acidic site on the α -carbon in the backbone of the IMAM ligands was established, three different synthetic strategies were pursued to reach this goal (Scheme 5.3). The first one (**a**) entailed the dimethylation of the starting material, ethyl acetoacetate, by adapting a reported procedure,²¹ and then the subsequent hydrolysis of the ester to obtain the corresponding carboxylic acid, an amidation of the acid and eventually the Schiff base formation (4 overall steps). The second strategy (**b**) involved the dimethylation of the acetoacetamide intermediate according to a reported procedure²² and the subsequent imine bond formation (3 overall steps), whereas the third one (**c**) involved the direct alkylation of the IMAM ligands (3 overall steps). Both strategies **a** and **b** were found to be unsuccessful, despite obtaining the desired alkylated synthons. In fact, in strategy **a** the alkylated product obtained was a mixture of mono- and dialkylated ethyl acetoacetate, which was difficult to purify and affected negatively the following steps of the synthesis.

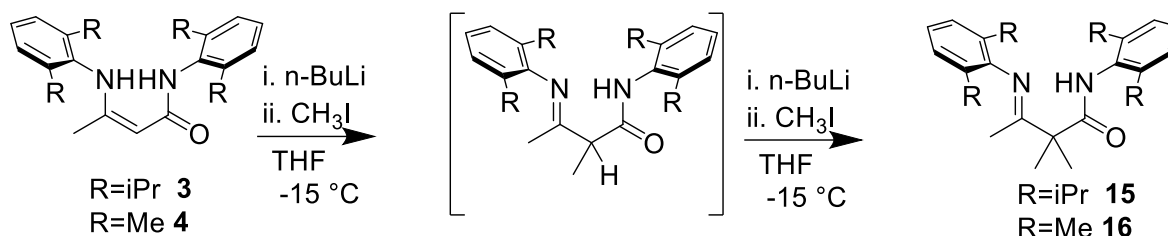
In strategy **b** the formation of the Schiff base was found to be difficult, likely because of the hindrance of the new neopentyl centre, affording extremely low yields of the desired product together with prevalent unreacted starting material. This issue has been reported previously in the attempt of obtaining dialkylated β -diimines.²⁰



Scheme 5.3. Different strategies pursued for the alkylation of IMAM ligands.

Eventually, strategy **c** proved to be effective. A screening of bases showed that strong bases, such as *n*-BuLi or KHMDS, were required to perform the alkylation of the IMAM ligands, since carbonates or alkoxides proved to be ineffective (Scheme 5.4). The electrophile of choice was iodomethane. The reaction was first performed by adding two equivalents of base followed by two equivalents of the electrophile at 0°C and then leaving the mixture to stir at room temperature overnight. This protocol led us to find the mass of *N*-(2,6-diisopropylphenyl)-3-((2,6-diisopropylphenyl)imino)-2,2-dimethylbutanamide (**15**) and *N*-(2,6-dimethylphenyl)-3-((2,6-dimethylphenyl)imino)-2,2-dimethylbutanamide (**16**) by ESI-MS (Figures A99-100). Nevertheless, a ¹H-NMR spectrum suggested that multiple alkylated products were present. In fact, there are five potential alkylated products: two monomethylated products (either on the α -carbon or on the amidic nitrogen), two dimethylated products (both methyl groups on the α -carbon or one on the amidic nitrogen) and the permethylated product. The presence of these competing outcomes triggered the optimization of the synthetic protocol to get selectivity toward the product of interest (Scheme 5.4). A two-step procedure proved to be crucial to obtain the desired MeIMAM ligands, in analogy to a similar procedure reported for the alkylation of β -enamineimines²⁰: first an equivalent of *n*-BuLi was added to the ligand in solution at low temperature, then after 15 minutes an equivalent of electrophile was added dropwise. After an hour of stirring while thawing, the procedure was repeated and then the solution was stirred overnight at room temperature.

Also, the reaction temperature was screened in order to improve the selectivity towards the desired product, finding that using a NaCl and ice cooling mixture (-15 °C) gave the best result. The final product was obtained in good yields (70%) as a yellow sticky oil.



Scheme 5.4. Synthetic protocol for the 2,2-dimethylation of IMAM ligands

5.3.2 Characterization

Ligand **15** was characterized by ^1H -NMR, ^{13}C - $\{^1\text{H}\}$ NMR, selected 2-D NMR experiments (^1H - ^1H COSY, ^1H - ^{13}C HSQC, ^1H - ^{13}C HMBC, ^1H - ^{15}N HSQC), IR Spectroscopy, XRD and ESI-MS. In the ^1H - ^{15}N HSQC spectrum of **15** we observed only one correlation peak at $\delta^1_{\text{H}} = 9.10$ ppm and $\delta^{15}_{\text{N}} = 120$ ppm (Figure 5.8). This suggested that only one N–H is present in **15**.

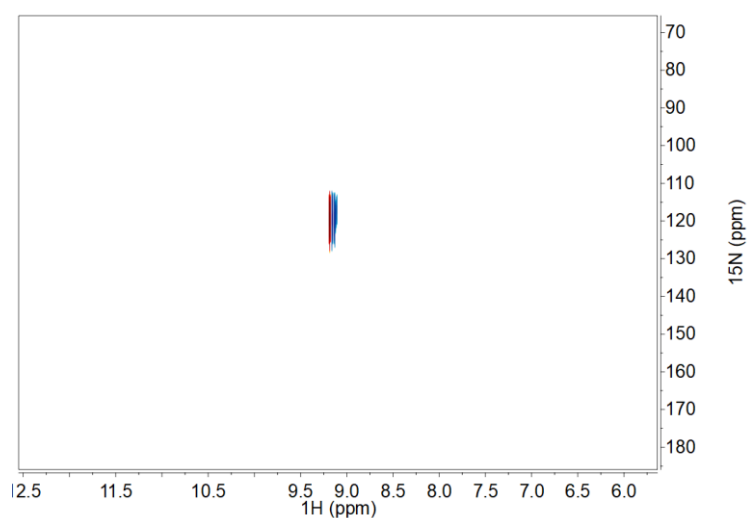


Figure 5.8. ^1H - ^{15}N HSQC spectrum of **15** in DMSO- D_6 .

Further insights were given by the ^1H NMR spectra of **15** in DMSO- D_6 (Figure 5.9). The most downfield peak in the spectrum appeared to be a singlet at $\delta^1_{\text{H}} = 9.08$ ppm (1H) integrating to one proton, then a triplet:doublet:doublet:triplet resonance pattern, respectively at $\delta^1_{\text{H}} = 7.27$ ppm (1H), $\delta^1_{\text{H}} = 7.17$ ppm (2H), $\delta^1_{\text{H}} = 7.07$ ppm (2H) and $\delta^1_{\text{H}} = 6.97$ ppm (1H). Two septets integrating to two protons each resonated respectively at $\delta^1_{\text{H}} = 2.77$ ppm (2H) and 3.10 ppm (2H). Then a singlet at $\delta^1_{\text{H}} = 1.66$ ppm (3H), another one at $\delta^1_{\text{H}} = 1.61$ ppm (6H) and three

doublets respectively at $\delta^1_{\text{H}} = 1.17$ ppm (6H), $\delta^1_{\text{H}} = 1.08$ ppm (12H) and $\delta^1_{\text{H}} = 1.04$ ppm (6H) completed the spectrum. The total number of proton accounting for the integration was 44. The three most shielded doublets integrating to overall 24 protons were assigned to the methyl groups in the four isopropyl substituents on the aryl rings in **15**. As observed for the ^1H NMR spectrum of **3**, there is overlap among the expected resonances likely due to free tumbling of the substituents: thus instead of four doublets, two sharp and distinct doublets ($\delta^1_{\text{H}} = 1.08$ and 1.04 ppm) and a broad one ($\delta^1_{\text{H}} = 1.17$ ppm) are observed for **32**. The septets at $\delta^1_{\text{H}} = 2.77$ ppm and $\delta^1_{\text{H}} = 3.10$ ppm were assigned to the corresponding four $-\text{CH}$ groups of the isopropyl substituents. The singlet at $\delta^1_{\text{H}} = 1.66$ ppm was assigned to the methyl group in the backbone of the ligand and the one at $\delta^1_{\text{H}} = 1.61$ ppm integrating to 6 protons was assigned to the two methyl groups on the α -carbon. The two doublets at $\delta^1_{\text{H}} = 7.17$ ppm and 7.07 ppm were assigned to the *meta* protons of the aromatic substituents, whereas those in *para* position gave rise to the triplets at $\delta^1_{\text{H}} = 7.27$ ppm and 6.97 ppm. The signal at $\delta^1_{\text{H}} = 9.08$ ppm was then assigned to the N–H proton on the basis of the results of the ^1H - ^{15}N HSQC (Figure 5.8). The presence of the singlet at $\delta^1_{\text{H}} = 1.61$ ppm in the ^1H -NMR spectrum of **15**, the disappearance of the resonance of the vinylic proton that was present in the spectrum of **3** ($\delta^1_{\text{H}} = 4.95$ ppm) and the evidence for only one N–H proton in the spectra of **15** confirmed the successful alkylation of the α -carbon. Compared to **3**, we observe a downfield shift of the resonance relative to the methyl group in the backbone (1.66 ppm in **15** respect to 1.54 ppm in **3**) which suggests a change in the electronic environment for this group. We also observed a change for the resonance pattern of the protons on the N-aryl substituents: for **15** a t:d:d:t pattern occurs, whereas for **3** a d:d:t:t one was observed. These data might be explained considering the loss of the conjugation throughout the molecule in **15**: the overall spin system has changed, with the transition from enamine to imine allowing less rotational freedom for the corresponding N-aryl substituent. These spectral data highlighted the achievement of the target alkylated ligand and its existence in solution as an imino-amide.

A clean ^1H NMR spectrum of **16** was not obtained, likely due to the lower solubility of the starting ligand in most of the organic solvents.

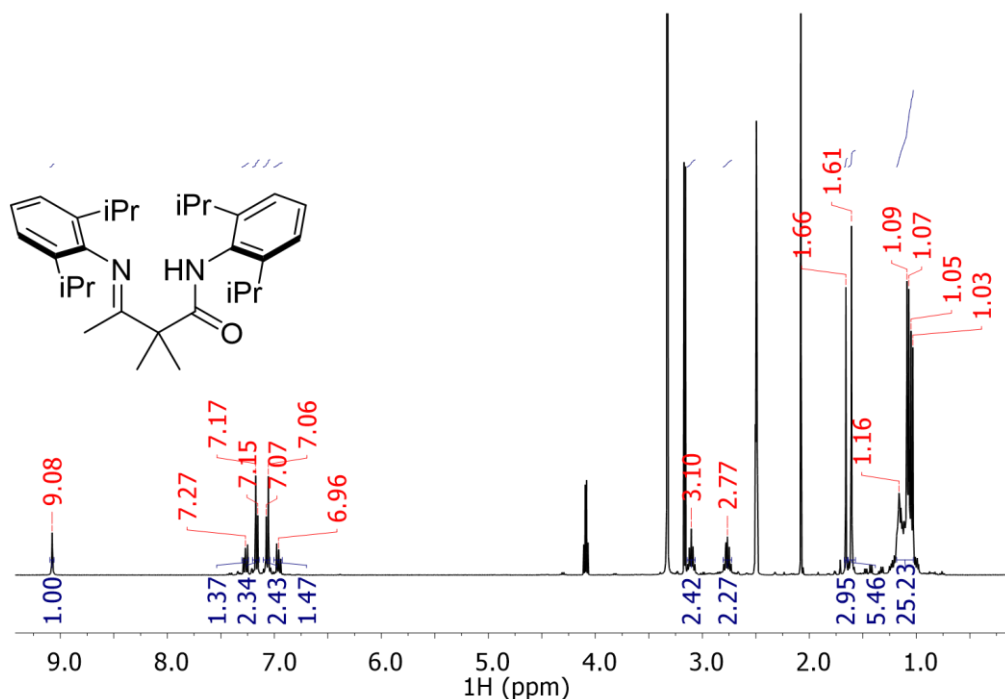


Figure 5.9. ^1H NMR spectrum (400 MHz, DMSO-D_6) of **15**.

The ATR-FTIR spectra (Figure 5.10) showed for both ligands an isolated peak around $\nu = 3300 \text{ cm}^{-1}$ which can be ascribed to the amidic N–H stretching mode. A similar behaviour is observed in other amide-containing ligands, such as pyridine carboxamides.^{23,24} An intense band was observed for both compounds around $\nu = 1650 \text{ cm}^{-1}$: this, being more intense, could be tentatively ascribed to the amidic C=O stretching, whereas the signal at 1590 cm^{-1} could be ascribed to the imine C=N stretch which is reduced in intensity with respect to the precursor due to the loss of conjugation. Both ligands contain features between 2860 and 2970 cm^{-1} , which are due to the stretching of the C–H bonds present in the backbone of the ligands. Furthermore, the absence of a broad O–H stretching peak around 3500 cm^{-1} confirmed the absence of H_2O .

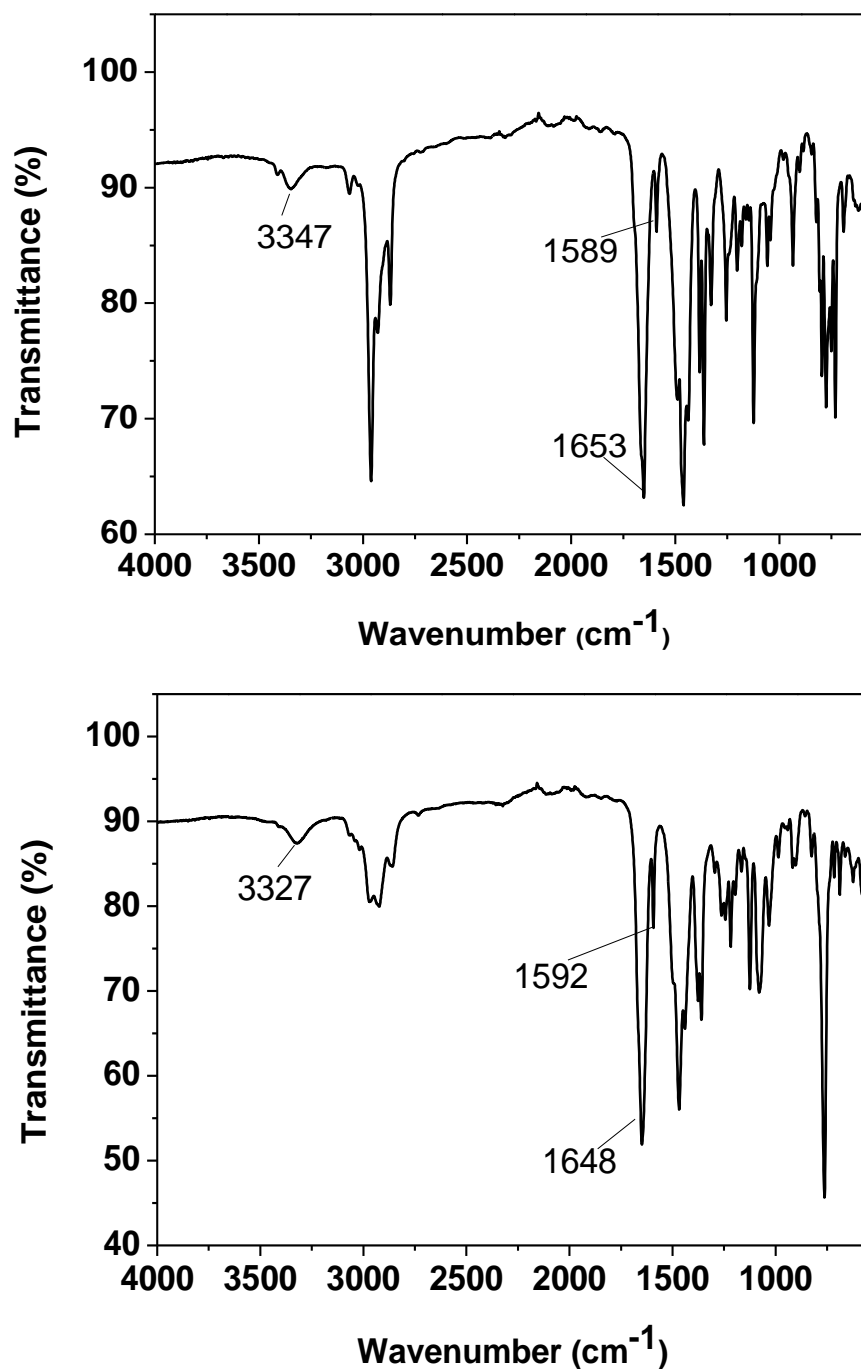


Figure 5.10. ATR-FTIR Spectra of **15** (top) and **16** (bottom).

Crystals of **15** in DMSO- D_6 spontaneously formed in an NMR tube (Figure 5.11). XRD analysis showed two molecules per asymmetric unit plus a DMSO- D_6 molecule. The bond distance for the imine group was of 1.263(6) Å (C14-N13), whereas the one for the adjacent carbon-carbon bonds in the backbone were 1.534(6) Å (C14-C16) and 1.535(6) Å (C16-C19). The amide C19-N21 bond had a distance of 1.346(6) (Table 6.3). The imine bond appear to be shorter than the ones reported for **3** (1.358(2) Å, Table 5.1), whereas the carbon-carbon bonds in the backbone appear to be longer for **15**. This confirms that there is no electronic

delocalization in the ligand upon alkylation and **15** exists as one only possible tautomer bearing an imine moiety. Furthermore the bond distances observed for **15** are closely matching those observed for β -diketiminates which crystallize as diimines (Table 6.2),¹³⁻¹⁵ confirming the expected lack of conjugation for this ligand.

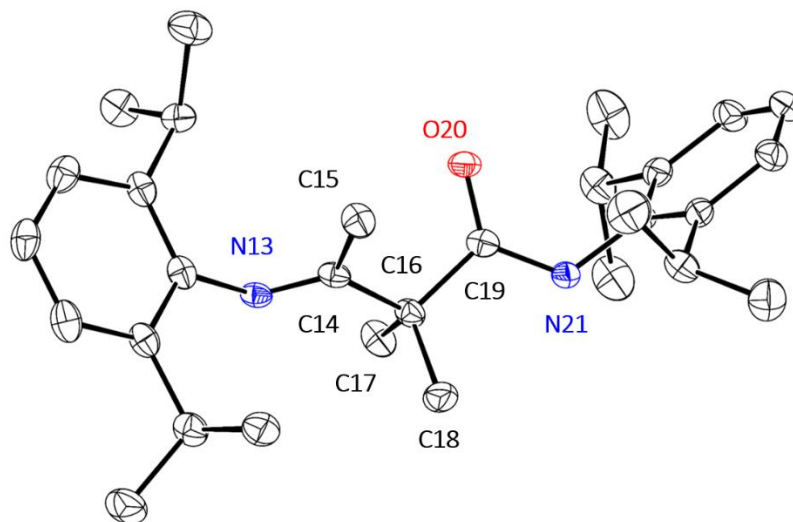


Figure 5.11. Ellipsoids plot at 50% probability of **15**. A molecule of DMSO-D₆ has been omitted for clarity.

Ultimately, the crystallization of a complexation reaction trial gave a single crystal of a potassium salt of MeIMAM^{iPr}₂, (**17**) (Figure 5.12, Table A7). In the asymmetric unit two molecules of the alkylated ligand were present, with the carbonyl oxygens interacting with two K⁺ ions and in presence of two THF molecules (omitted here for clarity). Considering that potassium hydride was used in the reaction and that the two cations require the charge to be balanced by the ligand since no counterions are present, this suggested that the amide must have been deprotonated. A closer look at the bond lengths of **17** showed that the amide bond C14-N13 had a distance of 1.299(4) Å, shorter than the one reported in the crystal of **15** (Table 5.3). Furthermore, the C=O distance for **17** appeared to be longer, at 1.283(4) Å (C14-O15) versus 1.221(5) Å for **15** (Table 5.3). This confirmed that the amide was deprotonated and the bond lengths suggested that it was present as the resonance form in which the negative charge is localized on the oxygen and the C–N bond has a double bond character (Scheme 5.5). In fact the latter has a distance which is intermediate between a pure imine and an amide (Table 5.3), thus suggesting a rearrangement in the electron density of the amide upon protonation has occurred. Furthermore, the close spatial interaction of the potassium cation with the amide oxygen corroborates the hypothesis of an anionic character on the latter (Scheme 5.5). These data confirmed the lack of conjugation upon alkylation in **15** and its effective deprotonation in presence of a strong base to yield **17**.

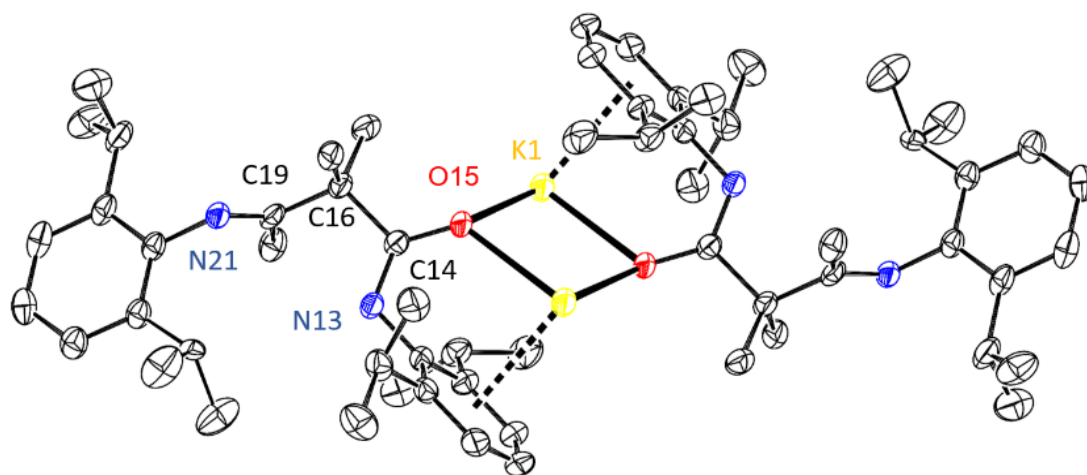
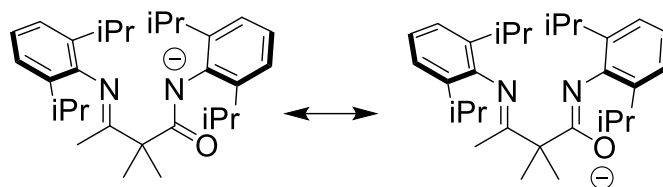


Figure 5.12 Crystal structure of $\text{K}(\text{MeIMAM}^{\text{iPr}_2})$ **17**. Thermal ellipsoids are represented at 50% probability. THF molecules present in the asymmetric unit are not depicted for clarity.

Also, the amidic C–N distance appeared to be shorter than the ones observed in the two IMAM ligands, giving strength to the assumption of deprotonation of the amide.

Table 5.3. Selected bond distances for **15** and **17**.

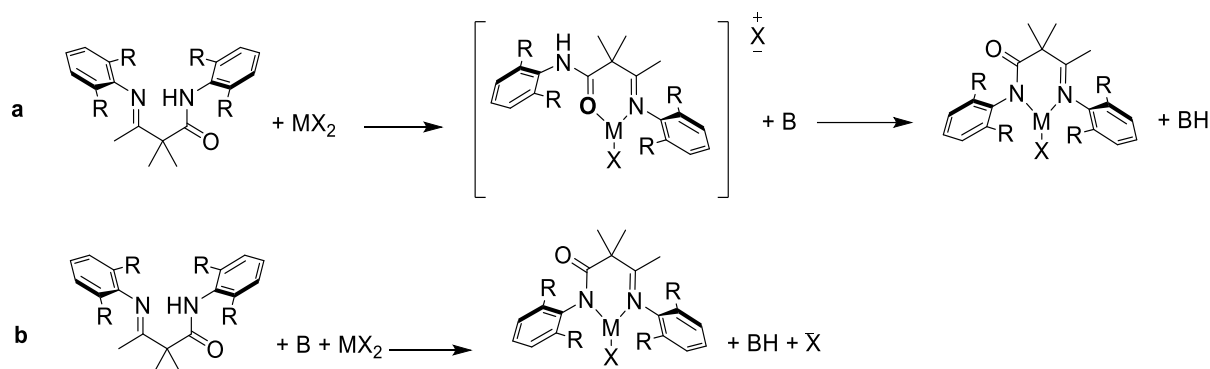
15			17		
Atom 1	Atom 2	Distance (Å)	Atom 1	Atom 2	Distance (Å)
C19	O20	1.221(5)	C14	O15	1.283(4)
C19	N21	1.346(6)	C14	N13	1.299(4)
C14	C16	1.534(6)	C14	C16	1.547(4)
C16	C19	1.535(6)	C16	C19	1.518(5)
C14	N13	1.263(6)	C19	N21	1.277(4)



Scheme 5.5. Possible resonance forms of the deprotonated **15**.

5.3.3 Complexation

Once the modified ligands were obtained, complexation trials were performed following two main strategies (Scheme 5.6). The first one (**a**) involved the base-free complexation of **3** to a metal and then the subsequent deprotonation of the amide to obtain the desired coordination mode, whereas the second one (**b**) required the deprotonation of the ligands with a strong base and then the addition of a metal salt.



Scheme 5.6. Strategies for complexation reactions using **15** (B = base, M = Co, Ni, Cu, X = OAc, OTf).

Strategy **a** (Scheme 5.6) was pursued mainly with copper, since **15**, analogous to what observed for **3** and **4**, reacted readily with $\text{Cu}(\text{OTf})_2$ in THF forming an intensely green species. For the complex $[(\text{MeIMAM}^{\text{iPr}_2})(\text{THF})(\text{CH}_3\text{CN})(\text{OTf})\text{Cu}^{\text{II}}]\text{OTf}$ (**18**), crystals suitable for XRD were obtained (Table A8). The complex (Figure 5.13) appeared to be pentacoordinate with a distorted square pyramidal geometry, bearing a triflate anion bound to the copper and a triflate counterion. The alkylated isopropyl-substituted ligand favoured a 1:1 cationic complex with copper, leaving space only for two more molecules of solvent (THF and CH_3CN) and a triflate anion. This is similar to what observed for **13**, obtained in similar conditions with the corresponding unalkylated ligand. The effect of the ligand dimethylation was evident especially on the change of the τ_5 parameter compared to **13**: this in fact lowered to 0.07, indicating an almost perfect square pyramidal geometry. This is ascribed to the diminishment of the bite angle (N13-Cu1-O20), which was of $88.38(15)^\circ$ for **18** instead of $90.18(7)^\circ$ for **13**, which is reflected into the geometry of the complex.

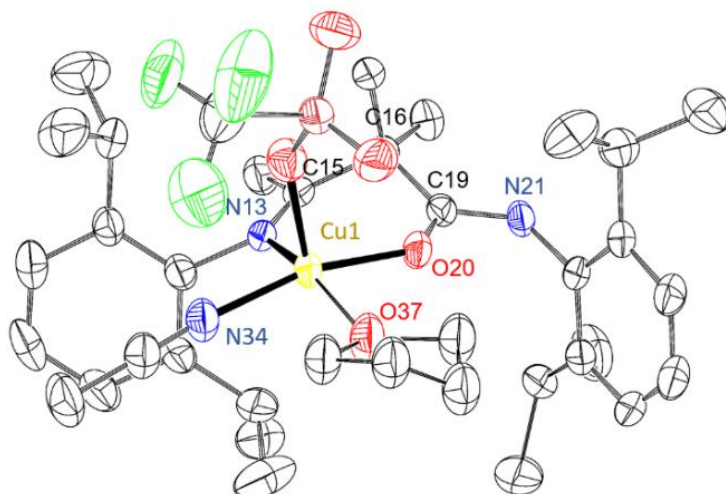


Figure 5.13 Ellipsoids plot at 50% probability of [(MeMAM^{iPr₂})(THF)(CH₃CN)(OTf)Cu^{II}](OTf) (**18**). Triflate counterion, diethyl ether and acetonitrile solvent molecules are omitted for clarity.

We observed again the chelation of copper through the iminic nitrogen and the amidic oxygen, leaving a free amidic N–H whose stretching mode was evident in the FTIR Spectrum (Figure 5.14, top). In fact, a sharp feature at $\nu = 3295 \text{ cm}^{-1}$ was observed in the FTIR spectrum of **18**, shifted towards lower wavenumbers with respect to the free ligand (Figure 5.10). This sharp feature could be ascribed to the free amidic N-H stretching. The three features between $\nu = 2342 \text{ cm}^{-1}$ and 2244 cm^{-1} were ascribed to the C≡N stretching modes of a bound acetonitrile molecule.^{25,26} The binding of acetonitrile to the metal caused a blueshift of the bands with respect to those reported for the a free acetonitrile molecule,²⁷ together with a change of symmetry and thus the appearance of a third band in its vibrational spectrum. The overall vibrational pattern in the region of C=N and C=O bonds stretching appeared different, with a reduction of the intensity of the band at $\nu = 1660 \text{ cm}^{-1}$ which was assigned to the amidic C=O stretching and the appearance of a more intense band at $\nu = 1519 \text{ cm}^{-1}$. Instead the previously remarkable feature around $\nu = 1590 \text{ cm}^{-1}$ observed for **15**, which was assigned to the imine C=N stretching, appears greatly reduced in intensity. This observation confirmed that the coordination to the metal cation in **18** occurs through the oxygen and the iminic nitrogen.

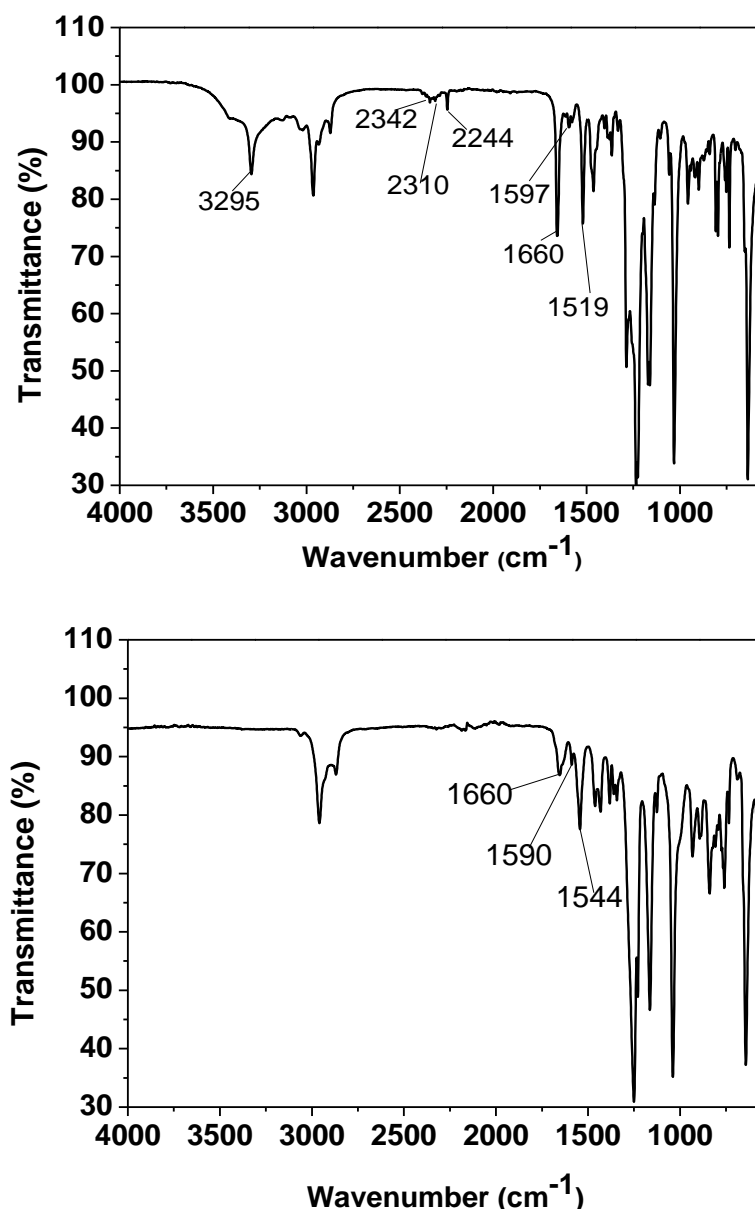


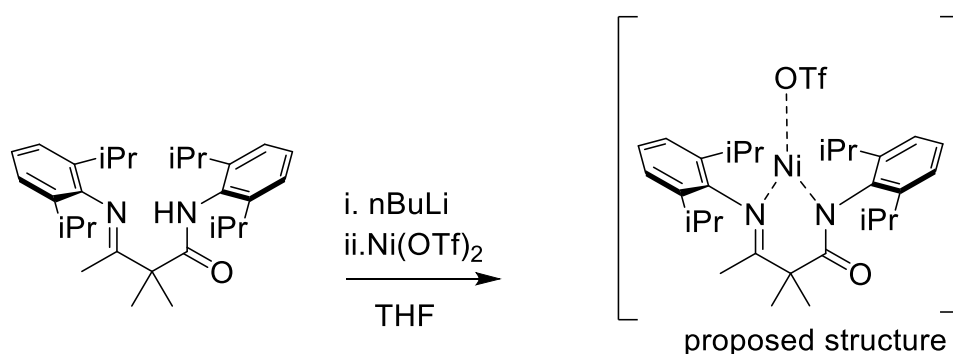
Figure 5.14. ATR-FTIR spectra of complex **17** before (top) and after the addition of 1.2 equivalents of KHMDS (bottom).

Several bases (Et_3N , EtONa , tBuOK and KHMDS) were then added to **17** to target the change in coordination mode: with KHMDS the colour of the solution changed immediately from green to brown. Also the FTIR spectrum witnessed a change when compared to that of complex **17** (Figure 5.14, bottom). The most noticeable variation is the disappearance of the N–H stretching band, confirming the deprotonation of the amide has occurred. Furthermore, a change in the frequencies and in the relative intensity of the peaks in the region between Also the FTIR spectrum witnessed a change when compared to that of complex **17** (Figure 5.14, bottom). The most noticeable variation is the disappearance of the N–H stretching band,

confirming the deprotonation of the amide has occurred. Furthermore, a change in the frequencies and in the relative intensity of the peaks in the region between $\nu = 1660$ and 1544 cm^{-1} suggested a variation in the coordination mode of **15**. Further evidence for a structural change was not successfully collected.

Strategy **b** (Scheme 6.6) was pursued using *n*BuLi to deprotonate the ligand in THF. This was established after a screening of several bases and in analogy to reported protocols for the deprotonation of β -diketiminates and similar ligands.^{52, 28, 84 29} In all reactions a slight excess (1.2 equiv.) of base was used and then the metal salts were added. In all cases upon addition of *n*BuLi to a solution of **15** an intense colour change to yellow confirmed the *in situ* preparation of the Li salt of **15**.

5.3.3.1 Nickel



Scheme 5.7 Complexation reactions of **15** with $\text{Ni}(\text{OTf})_2$ to yield **19**.

Upon addition of $\text{Ni}(\text{OTf})_2$ to the *in situ* prepared lithium salt of **15** (Scheme 5.7), the solution turned immediately brown-red. The ATR/FTIR spectra showed clearly the disappearance of the band at $\nu=3347 \text{ cm}^{-1}$ (Figure 5.15, top). $[(\text{MeIMAM}^{\text{iPr}_2})\text{Ni}^{\text{II}}(\text{OTf})]$ (**19**) showed a reduction in intensity of the bands ascribed to the amidic C=O and iminic C=N stretching and the appearance of bands in the region from $\nu = 1289$ to 636 cm^{-1} . These new features can be ascribed to the stretching and bending vibrations within a triflate anion.^{30,31} Notably, the band at $\nu=1289 \text{ cm}^{-1}$ could be ascribed to the CF_3 group asymmetric stretching, whereas the band at $\nu=1251 \text{ cm}^{-1}$ is related to the symmetric one. The bands at $\nu=1164 \text{ cm}^{-1}$ and $\nu=1043 \text{ cm}^{-1}$ are respectively assigned to the asymmetric and symmetric stretching of the SO_3 group. The proposed structure of this compound was also confirmed by ESI-MS, which, in positive mode, showed a peak at $m/z=655.2413$ corresponding to $[\text{M}+\text{H}]^+$ ($\text{C}_{31}\text{H}_{44}\text{F}_3\text{N}_2\text{NiO}_4\text{S}^+$ requires 655.2322). As observable in Figure 5.15 (bottom), the calculated isotopic pattern for this ion matched with the experimental one within the limit of experimental error.

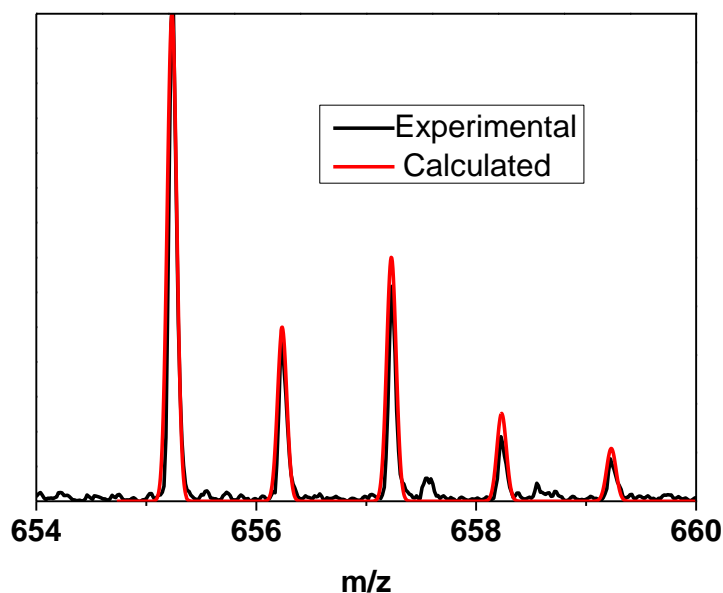
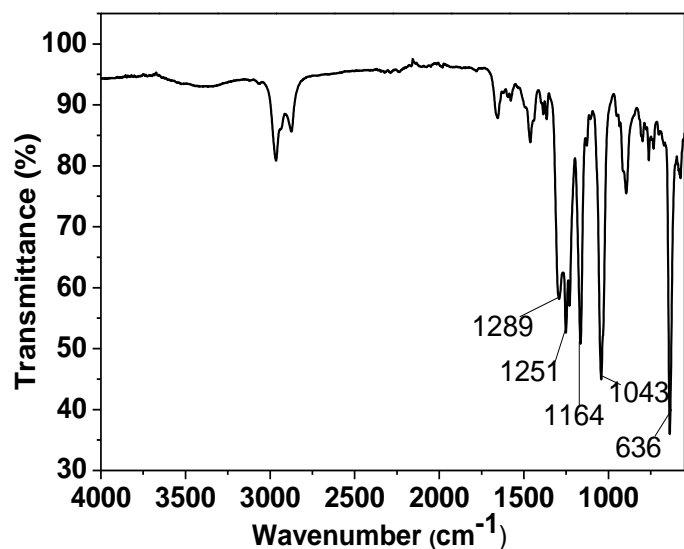


Figure 5.15. ATR/FTIR spectrum of complex **19** (top) and isotopic pattern of the ion [**19** + H⁺] (black) compared with the calculated isotopic pattern (red, bottom).

The ¹H NMR in THF-D₈ (Figure 5.16) clearly showed the presence of five broadened and paramagnetically shifted peaks in a range between 35 and -25 ppm. The peaks were enough sharp and well resolved. The presence of paramagnetically shifted peaks suggests that complex **19** is in a high-spin configuration. Normally Ni^{II} complexes might display ¹H NMR spectra indicative of diamagnetic, low-spin complexes when the metal center is tetracoordinate in a square planar geometry, whereas a high-spin configuration is adopted when complexes are in a tetrahedral geometry or five or six-coordinate. In these cases, Ni^{II} complexes show very short longitudinal relaxation times (T₁) causing the broadening and the shift of the resonance peaks, which makes their assignment often difficult, especially in the case of monomeric complexes.

³² On the other hand, very few examples of three-coordinate Ni^{II} complexes have been reported to date (Figure 5.17). Holland and co-workers synthesized a three-coordinate Ni^{II} complex bearing a chloride ancillary ligand and supported by a bulky β -diketiminato ligand, [Ni^{II}(Cl)(^tBu₂nacnacⁱPr)] (**20**, Figure 5.17) which showed paramagnetically shifted peaks in its ¹H-NMR spectrum in CD₂Cl₂.¹ Six peaks occurred in the range between +30 and -15 ppm, with only the backbone resonance appearing upfield at -123.5 ppm. Unambiguous assignment of the peaks was hampered by the short relaxation times (10-20 ms) but DFQ-COSY experiments helped to assign two of the peaks and suggest the assignment for the others. Magnetic moment measurements for complex **20** were consistent with an S = 1 ground state and XRD measurements on the crystals showed a distorted trigonal planar geometry around the metal centre.¹ Another example of a three-coordinate Ni^{II} complex was reported by the same group bearing a less bulky β -diketiminato ligand and a bis-(trimethylsilyl)amido ligand, [Ni^{II}(N(SiMe₃)₂(^{Me}nacnacⁱPr))] (**21**).² This complex showed paramagnetically shifted ¹H NMR resonances in C₆D₆ in a range between +49 and -66 ppm, whereas XRD analysis on crystals grown at -35°C showed a trigonal planar geometry around the metal centre.²

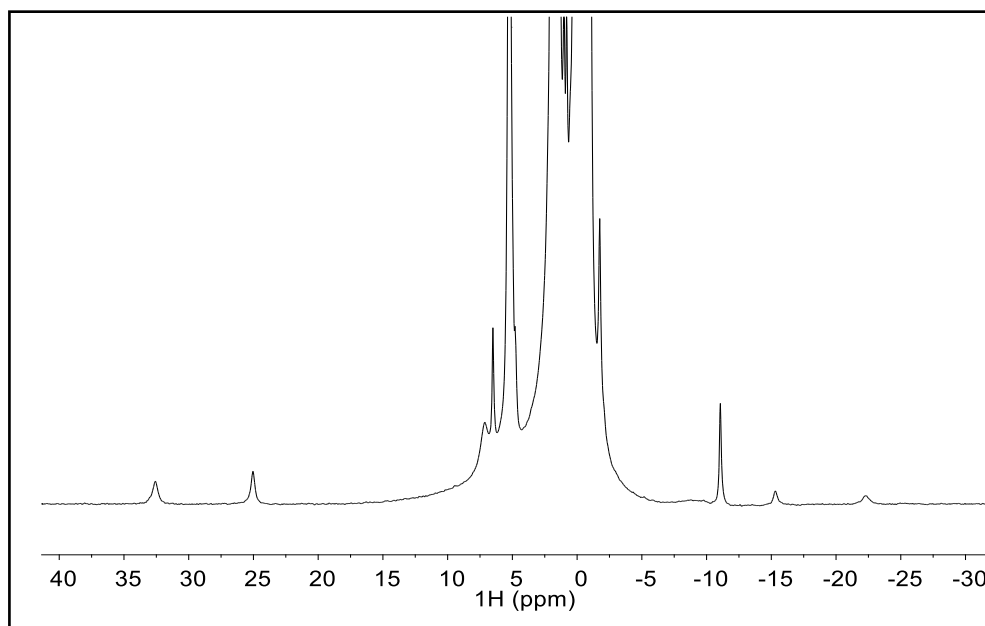


Figure 5.16 ¹H NMR (400 MHz, THF-D₈) of complex **19**.

Hillhouse and co-workers isolated a Ni^{II}-imido and a Ni^{II}-carbene complexes supported by a 1,2-bis(di-*tert*-butylphosphino)ethane ligand (dtbpe): [Ni^{II}(N(2,6-(CHMe₂)₂C₆H₃)(dtbpe)] (**22**)³³ and [Ni^{II}(CPh₂)(dtbpe)] (**23**, Figure 5.17).³⁴ Both complexes were crystallographically characterized and showed a C_{2v} symmetry, but no paramagnetically shifted peaks were observed in their ¹H-NMR spectra. This can be ascribed to a low-spin configuration enforced by the

more electron-donating phosphorus-containing ligand dtbpe respect to β -diketiminato. Limberg reported two three-coordinate complexes bearing a thiolate ligand, $[\text{Ni}^{\text{II}}(\text{SPh})(^{\text{tBu}}\text{nacnac}^{\text{iPr}})]$ (**24**)⁷ and $[\text{Ni}^{\text{II}}(\text{SEt})(^{\text{tBu}}\text{nacnac}^{\text{iPr}})]$ (**25**, Figure 5.17).³⁵ In both cases they appeared to be in a distorted trigonal planar geometry in the solid state, with different bending of the ancillary ligand in the plane. Their ¹H NMR spectra showed paramagnetically shifted peaks, in the range between +40 and -200 ppm for **24**⁷ and +48 and -201 ppm for **25**.³⁵ Similarly, Hayton reported two complexes bearing a bulkier sulphide, $[\text{Ni}^{\text{II}}(\text{SCPh}_3)(^{\text{Me}}\text{nacnac}^{\text{iPr}})]$ (**26**) and $[\text{Ni}^{\text{II}}(\text{SCPh}_3)(^{\text{tBu}}\text{nacnac}^{\text{iPr}})]$ (**27**, Figure 5.17).³⁶ These complexes showed similar ¹H NMR spectra to **24** and **25**, with paramagnetically shifted resonances extending from +29 to -137 ppm for **26** and from +14 to -39 ppm in the case of **27**. This striking difference in the spectral width even though the complexes differs only for the substituents in the β -diketiminato backbone highlighted the influence on the electronic properties of the ligand on the chemical shift of the protons in proximity to the metal centre. Both complexes showed a magnetic moment consistent with an $S = 1$ state. These data suggested that complex **19** is a high-spin Ni^{II} complex given the similarity of its ¹H NMR spectrum to those reported for high-spin three-coordinate Ni^{II} complexes supported by β -diketiminato ligands (**20-21**, **24-27**).

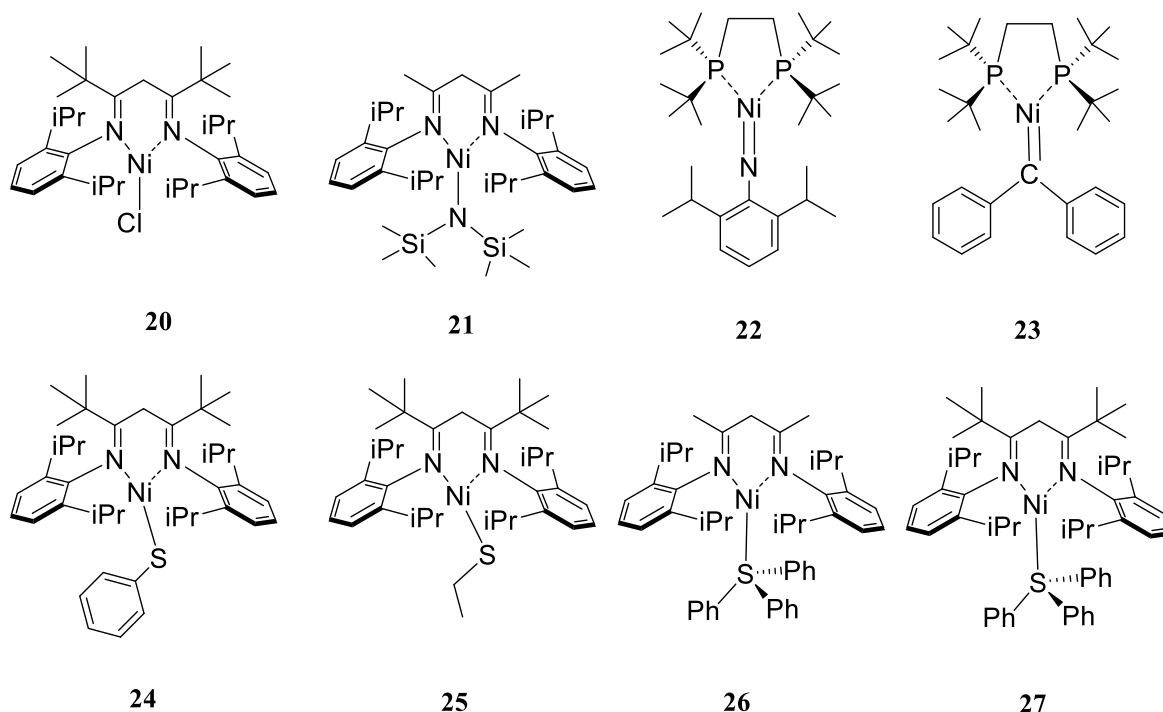
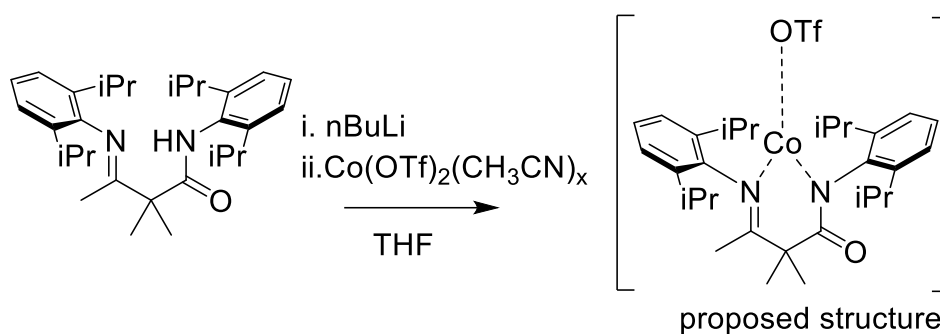


Figure 5.17. Spectroscopically characterized three-coordinate Ni^{II} complexes.

5.3.3.2 Cobalt



Scheme 5.8. Complexation reactions of **15** with $\text{Co}(\text{OTf})_2$ to yield **28**.

Upon addition of $\text{Co}(\text{OTf})_2$ to the lithium salt solution of **15** obtained *in situ* (Scheme 5.8), the solution turned immediately an intense dark blue. The ATR/FTIR spectra showed clearly the disappearance of the band at $\nu = 3347 \text{ cm}^{-1}$ (Figure 5.18, top). $[(\text{MeIMAM}^{\text{iPr}})_2\text{Co}^{\text{II}}(\text{OTf})]$ (**28**) showed a very similar spectrum to **19**, with the diagnostic triflate bands in the region from $\nu = 1290$ to $\nu = 631 \text{ cm}^{-1}$ and a reduction in intensity of the bands ascribed to the amidic $\text{C}=\text{O}$ and iminic $\text{C}=\text{N}$ stretching. Also two bands were observed respectively at $\nu=2288$ and $\nu=2195 \text{ cm}^{-1}$, which can be related to the nitrile stretching of free acetonitrile molecules,²⁷ which were present in the coordination sphere of the initial $\text{Co}(\text{OTf})_2$ salt. The supposed structure of this compound was also confirmed by ESI-MS (Figure 5.18, bottom), which, in positive mode, showed the main peak at $m/z = 656.2334$ corresponding to $[\text{M}+\text{H}]^+$ ($\text{C}_{31}\text{H}_{44}\text{CoF}_3\text{N}_2\text{O}_4\text{S}^+$ requires 656.2300). As observable in Figure 5.18, the calculated isotopic pattern for this ion matched with the experimental one within the limit of experimental error. The ^1H NMR in $\text{DMSO-}d_6$ of **28** (Figure 5.19) showed the presence of paramagnetically shifted and broadened peaks in a spectral window ranging from +50 to -30 ppm. Co^{II} complexes have 7 *d*-electrons thus are expected to give rise to paramagnetically shifted peaks in their ^1H -NMR spectra both in low and high-spin configuration. Three-coordinate Co^{II} complexes bearing β -diketiminone ligands have been reported by Holland, such as $[\text{Co}^{\text{II}}(\text{Cl})(^{\text{tBu}}\text{nacnac}^{\text{iPr}})]$ (**29**) and $[\text{Co}^{\text{II}}(\text{CH}_3)(^{\text{tBu}}\text{nacnac}^{\text{iPr}})]$ (**30**, Figure 5.20).¹ These complexes presented paramagnetically shifted resonances in their ^1H NMR spectra, these features ranged from +61 to -91 ppm for **29** and from +78 to -118 for **30**. Magnetic moment measurements yielded values compatible with a $S=3/2$, thus suggesting the complexes adopt a high-spin configuration. A dinuclear three-coordinate complex bearing a nindigo ligand, $[\text{Co}^{\text{II}}(\text{N}(\text{SiMe}_3)_2(\text{dmp}_2\text{Nin}))_2]$ (**31**, Figure 5.20) similarly showed paramagnetically shifted resonances ranging from +81 to -27 ppm.³⁷ This complex showed a magnetic moment value typical of two non-interacting high-spin Co^{II}

centres.³⁷ These data suggest that **28**, which presents resonances in a similar range, might be a high-spin three coordinate Co^{II} complex. **28** showed to be much more unstable and susceptible to water traces than **19**. In fact water can reprotonate the ligand showing its characteristic resonances in the diamagnetic region of the spectrum (0-12 ppm). This contribution from restored ligand appears to be higher in the spectrum of **28** whereas is absent in the spectrum of **19**.

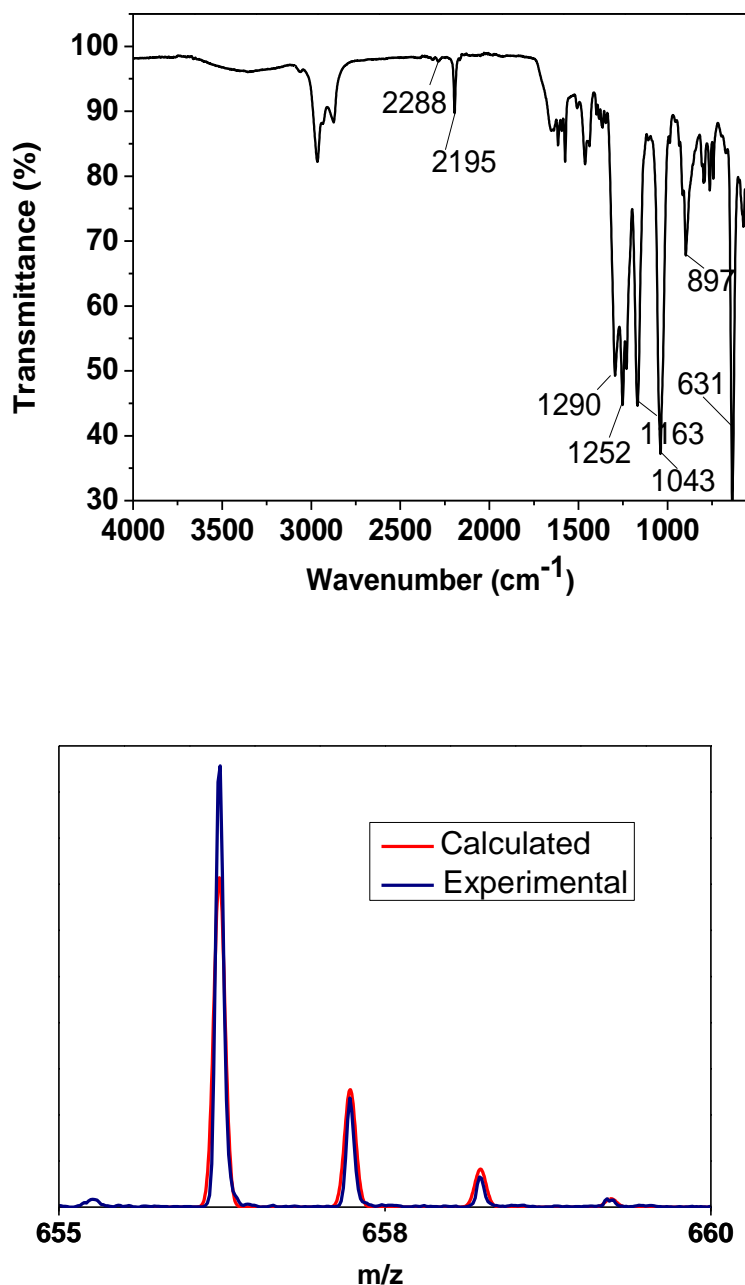


Figure 5.18. ATR/FTIR spectrum of complex **28** (top) and isotopic pattern of the ion $[\mathbf{28} + \text{H}^+]$ (blue) compared with the calculated isotopic pattern (red, bottom).

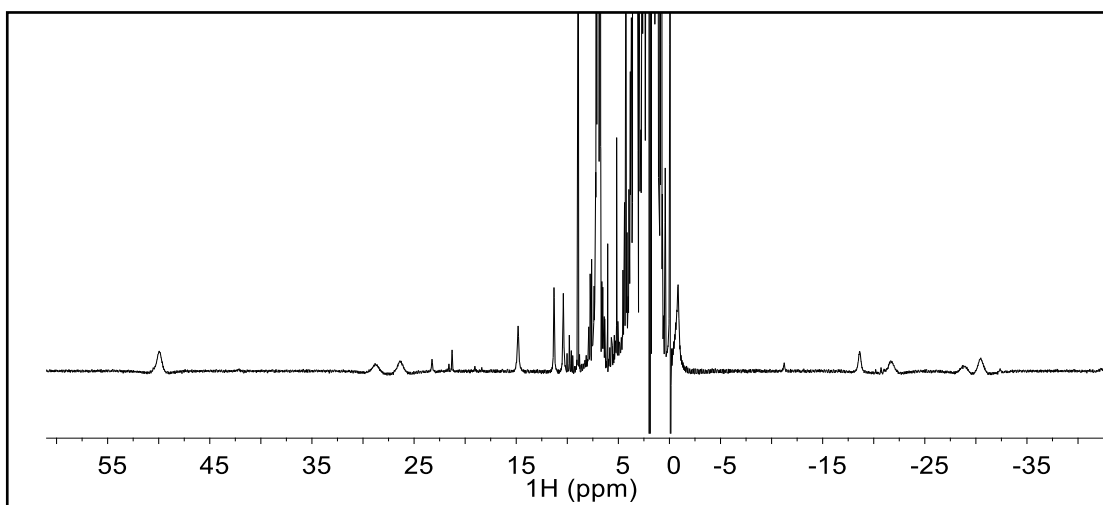


Figure 5.19. ^1H NMR (400 MHz, $\text{DMSO-}D_6$) of complex **28**.

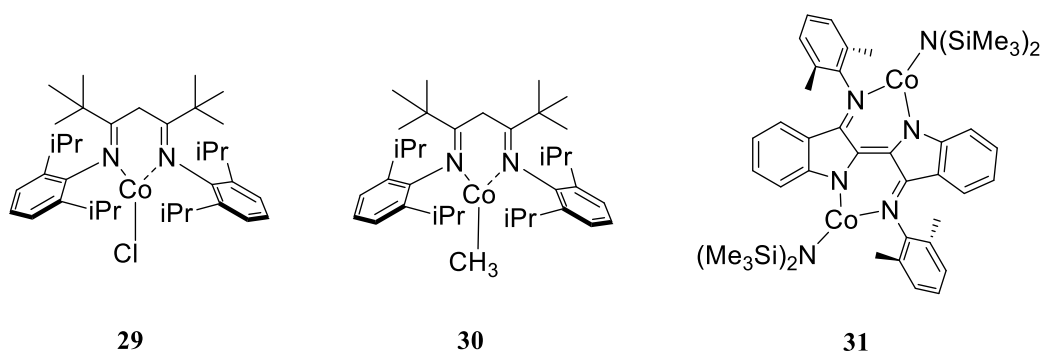
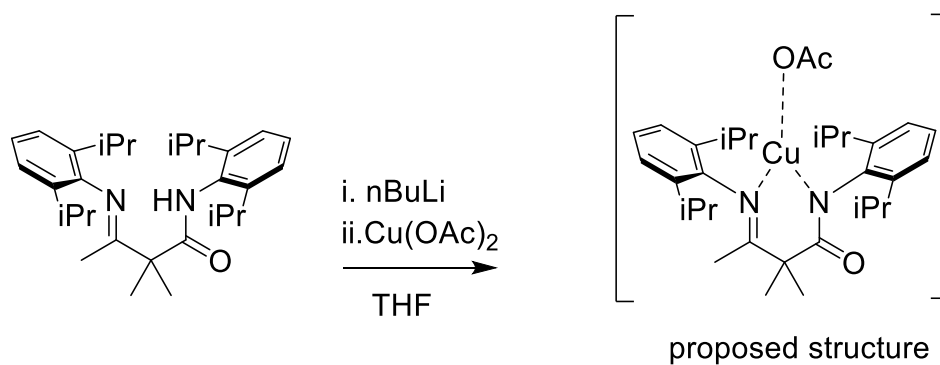


Figure 5.20. Selected spectroscopically characterized Co^{II} complexes.

5.2.3.3 Copper



Scheme 5.9. Complexation reactions of **15** with $\text{Cu}(\text{OAc})_2$ to yield **32**.

Upon addition of $\text{Cu}(\text{OAc})_2$ to a solution of lithium salt of **15** prepared *in situ*, the yellow solution turned an intense emerald green after 15 minutes of stirring at room temperature. $[(\text{MeIMAM}^{\text{iPr}_2})\text{Cu}^{\text{II}}(\text{OAc})]$ (**32**) (Figure 5.21, top) exhibited in the FTIR spectrum two intense bands at $\nu=1566$ and 1433 cm^{-1} which can be assigned respectively to the asymmetric stretching and to the symmetric stretching of the C=O of the metal-bound acetate.^{38,39,40,41} The band assigned to the asymmetric stretching appeared broad, showing another contribution at $\nu=1600\text{ cm}^{-1}$ which can be referred to the C=O stretching in the amide, being shifted due to the coordination of the amide to the metal ion. As observed for complexes **19** and **28**, the disappearance of the N–H stretching band at $\nu=3347\text{ cm}^{-1}$ suggested the deprotonation of the ligand occurred and was thus an indication that complexation was achieved.

An X-band EPR spectrum of complex **32** was recorded at 77 K from a frozen THF solution (Figure 5.21, bottom) showed clearly a pattern which could be ascribed to the presence of a $S = 1/2\ d^9\ \text{Cu}^{\text{II}}$ ion. The spectrum exhibited rhombic symmetry with $g_x > g_y > g_z$ ($g_x = 2.19$, $g_y = 2.05$ and $g_z = 1.98$, values calculated from spectral analysis) with $g_{\text{av}} = 2.07$ suggesting the localization of the unpaired spin on the metal centre (Table 5.4). The hyperfine coupling with the Cu ion ($I = 3/2$) giving rise to four lines was observable in the g_x component and the superhyperfine coupling with two non-equivalent N atoms of the ligand giving rise to two sets of three lines was evident in the g_y component of the spectrum. The presence of the observed superhyperfine patterns can be explained considering that the imine and the amide nitrogens in the ligand are non-equivalent. The hyperfine constants were preliminarily calculated from analysis of the spectrum and determined to be $A_x = 90 \times 10^{-4}\text{ cm}^{-1}$, $A_{y1} = 7.5 \times 10^{-4}\text{ cm}^{-1}$ and $A_{y2} = 9 \times 10^{-4}\text{ cm}^{-1}$ (Table 5.4). The simulation of the spectrum was not conclusive due to issues in simulating the superhyperfine coupling. Last, the extra feature at $g \approx 2.2$ could be ascribed to residual $\text{Cu}(\text{OAc})_2$ present in the reaction mixture.⁴²

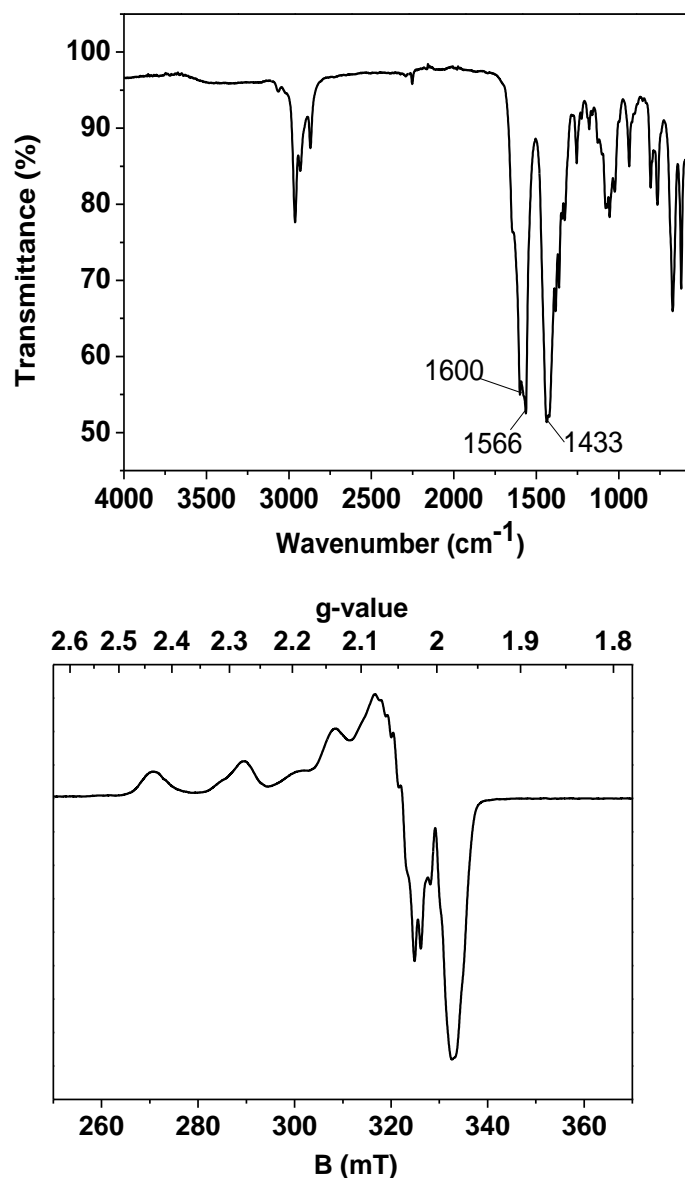


Figure 5.21 ATR/FTIR spectra of complex **32** (top) and X-band EPR spectrum (bottom) of **32** in frozen THF at 77 K, 0.0639 mW microwave power and 0.3 mT modulation amplitude. The spectrum has not been successfully simulated, preliminary g values are derived from spectral inspection.

Similar features were observed by X-band EPR in previously reported trigonal planar Cu complexes of β -diketiminate ligands. Holland and Tolman reported two complexes, $[\text{Cu}^{\text{II}}(\text{Cl})(\text{Me}^{\text{nacnac}^{\text{iPr}}})]$ (**33**) and $[\text{Cu}^{\text{II}}(\text{SCPh}_3)(\text{Me}^{\text{nacnac}^{\text{iPr}}})]$ (**34**, Figure 5.22).³ Both complexes presented an axial EPR spectrum showing hyperfine coupling with Cu in the g_{\parallel} component and superhyperfine coupling with 2 equivalent N atoms from the ligand in the g_{\perp} component. The spectrum of **33** presented a $g_{\parallel} = 2.20$ and $g_{\perp} = 2.05$ and $A_{\parallel} = 130 \times 10^{-4} \text{ cm}^{-1}$ and $A_{\perp} = 8 \times 10^{-4} \text{ cm}^{-1}$ (Table 6.4). It should be noted that this spectrum wasn't successfully simulated so the g values were derived from inspection of the spectrum. The spectrum of **34** showed g and A

values close to those observed for **33**, respectively $g_{\parallel} = 2.17$ and $g_{\perp} = 2.04$ and $A_{\parallel} = 111 \times 10^{-4} \text{ cm}^{-1}$ and $A_{\perp} = 13 \times 10^{-4} \text{ cm}^{-1}$ (Table 5.4). Both spectra were recorded at 20 K and the low temperature allowed a good resolution of the superhyperfine coupling. Another similar complex bearing a thiolate ligand was reported: $[\text{Cu}^{\text{II}}(\text{SPhMe}_2)(^{\text{Me}}\text{nacnac}^{\text{iPr}})]$ (**35**, Figure 5.22).⁴³ This complex presented an axial EPR spectrum very similar to the one of **34**, with five lines in the g_{\perp} component deriving from the coupling with the two equivalent nitrogen atoms of the β -diketiminato ligand. The parameters were simulated to be $g_{\parallel} = 2.18$ and $g_{\perp} = 2.04$ and $A_{\parallel} = 115 \times 10^{-4} \text{ cm}^{-1}$ and $A_{\perp} = 13 \times 10^{-4} \text{ cm}^{-1}$ (Table 6.4). The g and A values for **33-35** appear close to those observed for **32**, despite the different symmetry of the spectrum of the last (Table 5.4). The rhombic symmetry of the spectrum can be ascribed to the non-symmetric environment provided by **32** compared to β -diketiminato ligands. This is observed also in the non-equivalency of the nitrogen atoms in **32**.

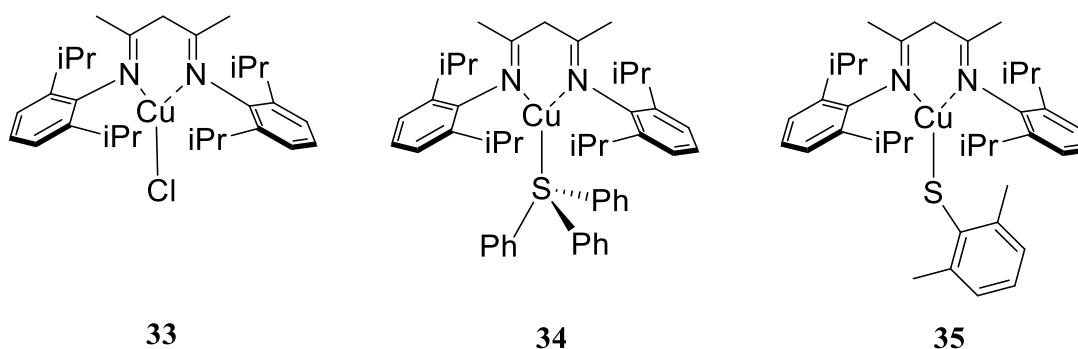


Figure 5.22. Selected three-coordinate Cu^{II} complexes characterized by EPR spectroscopy.

Table 5.4. X-band EPR parameters for selected three-coordinate Cu^{II} complexes.

Complex	g_x or g_{\parallel}	g_y or g_{\perp}	g_z	g_{av}	A_x or A_{\parallel} (10^{-4}cm^{-1})	A_y or A_{\perp} (10^{-4}cm^{-1})
32	2.19	2.05	1.98	2.07	90	7.5; 9
33	2.20	2.05	-	2.15	130	8
34	2.17	2.04	-	2.13	111	13
35	2.18	2.04	-	2.13	115	13

5.4 Conclusions

In summary, two variants of the desired IMAM ligand, **3** and **4**, were successfully obtained in reasonable yields and good purity with a two-step synthetic pathway. These new compounds were fully characterized and their existence as enamine tautomers both in solution and in the

solid state, was proved. The α -hydrogens demonstrated to be particularly sensitive to bases, being irreversibly deprotonated during complexation trials. The removal of this acidic site from the ligands was pursued through the 2,2-dimethylation of the α -carbon, providing ligands **15** and **16**. **15** was fully characterized with several spectroscopic techniques, establishing the absence of tautomerism. Characterization of **16** was hampered by the lower solubility of the precursor **4** in THF compared to **3**, giving crowded NMR spectra suggesting a mixture of products together with the desired one.

Complexation trials were performed, leading to the isolation of Cu^{II} complex **18** in base free conditions. The most encouraging results though were obtained by addition of alkyllithium and nickel, copper and cobalt salts to a THF solution of **15**. Notably by addition of Ni(OTf)₂, Co(OTf)₂ and Cu(OAc)₂, complexes **19**, **28** and **32** were respectively obtained. Even though their spectroscopic characterization is not complete, IR and NMR confirmed the complexation has occurred and ESI-MS suggested for **19** and **28** the formation of monomeric, low-coordinate species. These results confirmed the achievement of the desired novel ligands and their pivotal role in enforcing an unusual coordination number of 3 for d^7 , d^8 and d^9 metal ions.

5.5 Experimental section

Physical Methods

¹H, ¹³C-¹H and heteronuclear NMR analyses were performed either on an Agilent MR 400 MHz (400.13 MHz for ¹H NMR and 100.61 MHz for ¹³C-¹H NMR) or on a Bruker 600 MHz instrument. IR Spectra were recorded using a Perkin Elmer Spectrum 100 FT-IR/ATR. ESI Mass analyses were performed using a Micromass Time of Flight (ToF), interfaced with a Waters 2690 HPLC. X-Ray Diffraction Reflection Data were collected using a Bruker D8 Quest ECO diffractometer equipped with an Oxford Instrument Low Temperature Unit. EPR spectra of frozen solutions were acquired on a Bruker EMX X-band EPR, equipped with an Oxford Instruments CE 5396, ESR9 Continuous Flow Cryostat, a precision Temperature Controller and an Oxford Instruments TTL20.0/13 Transfer Tube.

Materials

All the reactions involving water-sensitive and/or air-sensitive compounds were performed under inert atmosphere using either Schlenk techniques or a nitrogen atmosphere glove box. All solvents and reagents were purchased from commercial suppliers and used as received, unless otherwise stated. Anhydrous THF and diethyl ether were distilled over

Na/benzophenone and stored in Schlenk bombs. Anhydrous DMF, DMA and methyl tert-butyl ether were purchased and used without further purification. Anhydrous acetonitrile was dispensed through an Innovative Technology PureSolv EN Solvent Purification System and deoxygenated by purging with Argon. Anhydrous dichloromethane was distilled over calcium hydride and stored in Schlenk bomb over 4 Å molecular sieves. M(OTf)₂ salts (M = Co, Cu) were prepared according to the same procedure reported for the manganese triflate⁴⁴ and stored in a nitrogen atmosphere glove box.

EPR analysis

A 1 mM EPR sample of **32** was prepared by transferring an aliquot of solution in THF in a EPR tube and by freezing it in liquid nitrogen. The EPR spectrum was recorded at 77 K, 9.222 GHz, 0.0639 mW microwave power, with a 120 mT field sweep in 84 s, and 0.3 mT modulation amplitude, with 100 kHz field modulation.

Synthesis of N-(2,6-diisopropylphenyl)-3-oxobutanamide (1)

The procedure was adapted from a reported procedure on a similar substrate.⁶ The same compound has been previously reported with a different procedure.⁴⁵ A mixture of acetylacetonate (20 mL, 158 mmol) and 2,6-diisopropylaniline (30 mL, 159 mmol, 1 eq.) were put in a Schlenk flask. A catalytic amount (0.15 eq.) of DMF was added and the flask was purged from air by applying vacuum and refilled with argon three times. The mixture was stirred overnight and heated at 145 °C. The product was extracted with EtOAc (3 x 50 mL), washed with brine and dried over magnesium sulfate. The solvent was removed *in vacuo* and the brown oil was frozen at -25 °C overnight. Hexane allowed to precipitate the final product as an off-white solid (21.08 g, 81 mmol, 51%).

δ^1_H (400 MHz, CDCl₃): 1.18 (12H, d, $J = 6.8$ Hz, -CH(CH₃)₂), 2.36 (3H, s, -CH₃), 3.02 (2H, sp, $J = 6.6$ Hz, -CH(CH₃)₂), 3.65 (2H, s, CH₂), 7.16 (2H, d, $J = 7.7$ Hz, 3,5-H on Ph), 7.27 (1H, t, $J = 7.6$ Hz, 4-H on Ph), 8.45 (1H, s, -NH).

ESI-MS: found: $m/z = 284.1611$ (M+Na)⁺, C₁₆H₂₃NNaO₂⁺ requires 284.1626

Synthesis of N-(2,6-dimethylphenyl)-3-oxobutanamide (2)

The procedure was adapted from a reported procedure on a similar substrate.⁶ The same compound has been previously reported with a different procedure.⁴⁵ A mixture of acetylacetonate (8.5 mL, 57.7 mmol) and 2,6-dimethylaniline (9 mL, 73.1 mmol, 1.1 eq.) were put in a Schlenk flask. A catalytic amount (0.15 eq.) of DMF was added and the flask was

purged from air by applying vacuum and refilled with argon three times. The mixture was stirred overnight and heated at 145 °C. The product was extracted with CH₂Cl₂ (3 x 50 mL), washed with brine and dried over magnesium sulfate. The solvent was removed *in vacuo* and the brown oil was frozen at -25 °C overnight. Hexane allowed to precipitate the final product as an off-white solid (5.73 g, 27.9 mmol, 42%).

δ_{H} (400 MHz, CDCl₃): 2.21 (6H, s, 2,6-CH₃ on Ph), 2.37 (3H, s, -CH₃), 3.65 (2H, s, CH₂), 7.08 (3H, m, 3,4,5-H on Ph), 8.43 (1H, s, -NH).

ESI-MS: found: $m/z = 228.0992$ (M+Na)⁺, C₁₂H₁₅NNaO₂⁺ requires 228.1000

Synthesis of N-(2,6-diisopropylphenyl)-3-((2,6-diisopropylphenyl)imino)butanamide – IMAM^{iPr}₂ (3)

N-(2,6-diisopropylphenyl)-3-oxobutanamide (7.29 g, 27.9 mmol) was dissolved in 30 mL of toluene. 2,6-diisopropylaniline (5.5 mL, 29.2 mmol, 1.1 eq.) was added to the solution and a catalytic amount (0.15 eq.) of *para*-toluenesulfonic acid was added. The mixture was heated at 165 °C and stirred under reflux overnight with a Dean-Stark apparatus to remove water. The solvent was removed *in vacuo*, the product was extracted with EtOAc (3 x 50 mL), washed with brine and dried over magnesium sulfate. The solvent was removed *in vacuo* and the brown oil was frozen at -25 °C overnight. Hexane allowed to precipitate the final product as an off-white solid (6.56 g, 15.6 mmol, 56%), which was then recrystallized from acetone and dried *in vacuo*. Crystals suitable for X-Ray diffraction were obtained by evaporation of a diethyl ether solution of the compound.

δ_{H} (400 MHz, DMSO-**D**₆): 1.03 (6H, d, $J = 6.8$ Hz, -CH(CH₃)₂), 1.14 (12H, d, $J = 6.8$ Hz, -CH(CH₃)₂), 1.20 (6H, d, $J = 6.8$ Hz, -CH(CH₃)₂), 1.54 (3H, s, -CH₃), 3.11 (4H, sp, $J = 6.8$ Hz, -CH(CH₃)₂ on Ph1), 3.15 (2H, sp, $J = 6.8$ Hz, -CH(CH₃)₂ on Ph2), 4.95 (1H, s, =CH), 7.12 (2H, d, $J = 7.7$ Hz, 3,5-H on Ph1), 7.17 (2H, d, $J = 7.7$ Hz, 3,5-H on Ph2), 7.21 (1H, t, $J = 7.6$ Hz, 4-H on Ph1), 7.25 (1H, t, $J = 7.6$ Hz, 4-H on Ph2), 8.62 (1H, s, O=C-NH), 10.48 (1H, s, HC=C(CH₃)-NH).

$\delta_{\text{C}}(101\text{H})$ (100 MHz, DMSO-**D**₆): 19.68 (CH₃), 22.62, 23.62, 24.16, 24.93 (-CH(CH₃)₂), 28.34, 28.49 (-CH(CH₃)₂), 87.48 (=CH), 123.03, 123.79 (3,5-C on Ph), 127.51, 128.30 (4-C on Ph), 133.60, 134.97, (2,6-C on Ph), 146.72, 147.12 (1-C on Ph), 157.90 (HC=C(CH₃)-NH), 170.78 (C=O).

ν_{max} (ATR-FTIR)/cm⁻¹: 3208 (N-H), 3127 (N-H), 2963 (C-H), 2925 (C-H), 2859 (C-H), 1624 (C=O), 1596 (C=N), 1582 (C=N), 1501 (C-H), 1461 (C-H), 1436 (C-H), 1329, 1304, 1260, 1221, 1188, 1096, 1052, 1028, 933, 801, 710, 694, 677, 657.

ESI-MS: found: $m/z = 421.3217$ ($M+H$)⁺, $C_{28}H_{41}N_2O^+$ requires 421.3213

X-Ray Diffraction was performed on this compound. The crystal data and the structure refinement are reported in **Table A.1**.

Synthesis of N-(2,6-dimethylphenyl)-3-((2,6-dimethylphenyl)imino)butanamide – IMAM^{Me}₂ (4)

The synthesis was performed analogous to what reported for compound **3** (see **5.2.3**). The final product was recovered as an off-white solid (5.27 g, 17 mmol, 55%), which was then recrystallized from acetone and dried *in vacuo*. Purification from residual 2,6-dimethylaniline was obtained by flash column chromatography over silica gel using a 90:10 mixture of Hexane:EtOAc as eluent. Crystals suitable for X-Ray diffraction were obtained by evaporation of a diethyl ether solution of the compound.

δ^1_H (400 MHz, DMSO- D_6): 1.53 (3H, s, -CH₃), 2.16 (12H, s, 2,6-CH₃ on Ph_{1,2}), 4.90 (1H, s, =CH), 7.02 (3H, broad s, 3,4,5-H on Ph₁), 7.09 (3H, broad s, 3,4,5-H on Ph₂), 8.63 (1H, s, O=C-NH), 10.31 (1H, s, HC=C(CH₃)-NH).

$\delta^{13}C$ -{1H} (100 MHz DMSO- D_6): 18.05 (CH₃ on Ph), 18.55 (CH₃ on Ph) 19.14 (CH₃), 87.16 (=CH), 125.88, 126.92 (3,5-C on Ph), 127.65, 128.06 (4-C on Ph), 136.61, 137.68, (2,6-C on Ph), 144.20 (1-C on Ph), 157.33 (HC=C(CH₃)-NH), 168.95 (C=O).

ν_{max} (ATR-FTIR)/ cm^{-1} : 3271 (N-H), 3126 (N-H), 2975 (C-H), 2922 (C-H), 2852 (C-H), 1622 (C=O), 1578 (C=N), 1511, 1473 (C-H), 1423 (C-H), 1379, 1329, 1272, 1216, 1165, 1093, 1037, 984, 908, 767, 713, 675, 631, 575

APCI-MS: found: $m/z = 309.1967$ ($M+H$)⁺, $C_{20}H_{25}N_2O^+$ requires 309.1961

XRD was performed for this compound. The crystal data and the structure refinement are reported in **Table A.2**.

Synthesis of [(DMA)₂(IMAM^{iPr})₂(OTf)Cu^{II}]OTf (5)

20 (0.124 g, 0.29 mmol, 1 eq) was dissolved into 3 mL of THF in a round bottom flask. Cu(OTf)₂(CH₃CN)₄ (0.167 g, 0.32 mmol, 1.1 eq) was added to the mixture which immediately turned green-brown. The solution was transferred into a Schlenk flask and the solvent was removed *in vacuo*. The solid was then redissolved in DMA and layered with toluene (1 mL) and excess diethyl ether to afford light green crystals suitable for X-Ray Diffraction.

XRD was performed for this compound. The crystal data and the structure refinement are reported in **Table A.3**.

Synthesis of [(IMAM^{Me}₂)₂(OTf)Cu^{II}]OTf (**6**)

21 (0.1125 g, 0.36 mmol, 1 eq) was dissolved into 3 mL of THF in a round bottom flask. Cu(OTf)₂(CH₃CN)₄ (0.194 g, mmol, 1.1 eq) was added to the mixture which immediately turned brown. The solution was filtered through a cannula, transferred into a Schlenk flask and concentrated. Then it was layered with pentane (1 mL) and excess diethyl ether to afford small green crystals suitable for X-Ray Diffraction.

Synthesis of N-(2,6-diisopropylphenyl)-3-((2,6-diisopropylphenyl)imino)-2,2-dimethylbutanamide – MeIMAM^{iPr}₂ (**15**)

The procedure was adapted on a reported procedure on β-enamineimines.²⁰ **3** (1.51 g, 3.59 mmol) was dissolved in 10 mL of dry THF into a Schlenk flask and stirred at -15 °C using a NaCl and ice cooling mixture. n-buthyllithium (1.43 mL of 2.5 M solution in hexane, 3.59 mmol, 1 eq.) was added slowly to the flask. The solution was left stirring for 15', then CH₃I (0.22 mL, 3.59 mmol, 1 eq.) was added dropwise to the cool solution which was left stirring for one hour while gradually warming up at room temperature. The same procedure was then repeated to add another equivalent of n-BuLi and of CH₃I. The solution was left to stir at rt overnight, then the solvent was removed *in vacuo*, the product extracted with CH₂Cl₂ (3 x 50 mL), filtered over celite and dried over magnesium sulfate. The solvent was then removed *in vacuo* to obtain a yellow sticky oil which was then washed with acetone, hexane and diethyl ether and dried for two hours *in vacuo* (1.12 g, 2.50 mmol, 70%).

δ_H (400 MHz, DMSO-D₆): 1.045 (6H, d, *J* = 6.8 Hz, -CH(CH₃)₂), 1.085 (12H, d, *J* = 6.8 Hz, -CH(CH₃)₂), 1.17 (6H, broad d, *J* = 6.8 Hz, -CH(CH₃)₂), 1.61 (6H, s, CH₃), 1.66 (3H, s, backbone CH₃), 2.77 (2H, sp, *J* = 6.8 Hz, -CH(CH₃)₂ on Ph1), 3.11 (2H, sp, *J* = 6.8 Hz, -CH(CH₃)₂ on Ph2), 6.97 (1H, t, *J* = 7.7 Hz, 4-H on Ph1), 7.07 (2H, d, *J* = 7.7 Hz, 3,5-H on Ph1), 7.17 (2H, d, *J* = 7.7 Hz, 3,5-H on Ph2), 7.27 (1H, t, *J* = 7.7 Hz, 4-H on Ph2), 9.08 (1H, s, O=C-NH)

δ_{3C} (100 MHz, DMSO-D₆): 17.22 (CH₃), 22.66, 23.09, 23.39, (-CH(CH₃)₂), 23.94 (α-CH₃), 27.10, 27.92 (-CH(CH₃)₂), 122.65, 122.87 (3,5-C on Ph), 127.54 (4-C on Ph), 132.70, 135.23 (2,6-C on Ph), 145.83, 146.14 (1-C on Ph), 171.63 (-C=N), 174.17 (O=C-NH).

v_{max} (ATR-FTIR)/cm⁻¹: 3347 (N-H), 2964 (C-H), 2933 (C-H), 2867 (C-H), 1653 (C=O), 1589 (C=N), 1463 (C-H), 1385, 1365, 1326, 1257, 1200, 1121, 1056, 1040, 932, 794, 778, 733

ESI-MS: found: *m/z* = 449.3534 (M+H)⁺, C₃₀H₄₅N₂O⁺ requires 449.3526

X-Ray Diffraction was performed on a potassium salt of this compound, **17**. The crystal data and the structure refinement are reported in **Table A.4**.

Synthesis of N-(2,6-dimethylphenyl)-3-((2,6-dimethylphenyl)imino)-2,2-dimethylbutanamide – MeIMAM^{Me}₂ (16)

The procedure was analogous to what reported for compound **15**.

ν_{max} (ATR-FTIR)/cm⁻¹: 3327 (N–H), 2975 (C–H), 2925 (C–H), 2920 (C–H), 2862 (C–H), 1648 (C=O), 1592 (C=N), 1469 (C–H), 1381, 1363, 1326, 1266, 1215, 1201, 1123, 1081, 1028, 920, 906, 765, 687, 623, 575

APCI-MS: found: $m/z = 337.2276$ (M+H)⁺, C₂₂H₂₉N₂O⁺ requires 337.2274

Synthesis of [(MeIMAM^{iPr}₂)(THF)(CH₃CN)(OTf)Cu^{II}]⁺OTf⁻ (18)

15 (0.52 mmol, 1 eq) was dissolved into 3 mL of THF in a round bottom flask. Cu(OTf)₂(CH₃CN)₄ (0.2972 g, 0.57 mmol, 1.1 eq) was added to the mixture which immediately turned intense green. The solution was filtered and concentrated. Crystals suitable for X-Ray diffraction were obtained by vapour diffusion of diethyl ether into the THF solution.

ν_{max} (ATR-FTIR)/cm⁻¹: 3295 (N–H), 3032 (C–H), 2967 (C–H), 2938 (C–H), 2876 (C–H), 2341, 2310, 2245 (C≡N), 1660 (C=O), 1517 (C=N), 1460, 1363, 1286, 1235, 1225, 1181, 1163, 1060, 1033 (S=O), 957, 924, 898, 809, 795, 753, 737, 636 (Cu–N), 574

X-Ray Diffraction was performed on this compound. The crystal data and the structure refinement are reported in **Table A5**.

Synthesis of [(MeIMAM^{iPr}₂)Ni^{II}(OTf)] (19)

15 was dissolved in 6 ml of dry THF into a Schlenk flask. While stirring, n-BuLi (2.5 M solution in hexane, 1.2 eq.) was added dropwise to the solution. Then Ni(OTf)₂(CH₃CN)₄ (1 eq.) was added, causing the yellow solution to turn emerald green within 10'. The solution was filtered over celite in a Schlenk-frit, then the solvent was removed in vacuo and the compound was taken up in pentane, the solvent was then removed to obtain a red-brown powder.

ν_{max} (ATR-FTIR)/cm⁻¹: 2969 (C–H), 2871 (C–H), 1655 (C=O), 1593, 1576 (C=N), 1464, 1289, 1251 (C–F), 1228 (C–F), 1164 (S–O), 1043 (S–O), 893, 800, 762, 735, 636, 576.

ESI-MS: found: $m/z = 655.2413$ (M+H)⁺, C₃₁H₄₄F₃N₂NiO₄S⁺ requires 655.2322

Synthesis of [(MeIMAM^{iPr}₂)Co^{II}(OTf)] (28)

15 was dissolved in 6 ml of dry THF into a Schlenk flask. While stirring, nBuLi (2.5 M solution in hexane, 1.2 eq.) was added dropwise to the solution. Then Co(OTf)₂(CH₃CN)₄ was added (1.05 eq.) causing the yellow solution to immediately turn dark blue. The solution was filtered over celite in a Schlenk-frit, then the solvent was removed in vacuo and the compound was taken up in pentane, the solvent was removed to obtain a blue powder.

ν_{\max} (ATR-FTIR)/ cm^{-1} : 2963 (C–H), 2875 (C–H), 2288 (C \equiv N), 2195 (C \equiv N), 1648 (C=O), 1613, 1576 (C=N), 1461, 1436, 1290, 1252 (C–F), 1229 (C–F), 1163 (S–O), 1043 (S–O), 897, 800, 762, 742, 631, 572.

ESI-MS: found: $m/z = 656.2334$ (M+H)⁺, C₃₁H₄₄CoF₃N₂O₄S⁺ requires 656.2300

Synthesis of [(MeIMAMⁱPr₂)Cu^{II}(OAc)] (32)

15 was dissolved in 6 ml of dry THF into a Schlenk flask. While stirring, n-BuLi (2.5 M solution in hexane, 1.2 eq.) was added dropwise to the solution. Then Cu(OAc)₂ (1 eq.) was added, causing the yellow solution to turn emerald green within 10'. The solution was filtered over celite in a Schlenk-frit, then the solvent was removed in vacuo and the compound was taken up in DCM, filtered again and layered with diethyl ether to obtain a green powder.

ν_{\max} (ATR-FTIR)/ cm^{-1} : 2959 (C–H), 2927 (C–H), 2866 (C–H), 1600 (CH₃–C=O), 1566, 1433 (CH₃–C=O), 1257, 1176, 1081, 1057, 1021, 935, 808, 765, 672, 602.

5.6 References

1. P. L. Holland, T. R. Cundari, L. L. Perez, N. A. Eckert and R. J. Lachicotte, *J. Am. Chem. Soc.*, 2002, **124**, 14416-14424.
2. N. A. Eckert, E. M. Bones, R. J. Lachicotte and P. L. Holland, *Inorg. Chem.*, 2003, **42**, 1720-1725.
3. P. L. Holland and W. B. Tolman, *J. Am. Chem. Soc.*, 1999, **121**, 7270-7271.
4. S. Yao, E. Bill, C. Milsmann, K. Wieghardt and M. Driess, *Angew. Chem. Int. Ed.*, 2008, **47**, 7110-7113.
5. D. J. E. Spencer, A. M. Reynolds, P. L. Holland, B. A. Jazdzewski, C. Duboc-Toia, L. Le Pape, S. Yokota, Y. Tachi, S. Itoh and W. B. Tolman, *Inorg. Chem.*, 2002, **41**, 6307-6321.
6. R. K. Yadlapalli, O. P. Chourasia, K. Vemuri, M. Sritharan and R. S. Perali, *Bioorg. Med. Chem. Lett.*, 2012, **22**, 2708-2711.
7. P. Holze, B. Horn, C. Limberg, C. Matlachowski and S. Mebs, *Angew. Chem. Int. Ed.*, 2014, **53**, 2750-2753.
8. P. Kiraly, R. W. Adams, L. Paudel, M. Foroozandeh, J. A. Aguilar, I. Timári, M. J. Cliff, M. Nilsson, P. Sándor, G. Batta, J. P. Waltho, K. E. Kövér and G. A. Morris, *J. Biomol. NMR*, 2015, **62**, 43-52.
9. M. Stender, R. J. Wright, B. E. Eichler, J. Prust, M. M. Olmstead, H. W. Roesky and P. P. Power, *J. Chem. Soc., Dalton Trans.*, 2001, 3465-3469.
10. P. O. Oguadinma and F. Schaper, *Organometallics*, 2009, **28**, 4089-4097.
11. N. W. Aboelella, B. F. Gherman, L. M. R. Hill, J. T. York, N. Holm, V. G. Young, C. J. Cramer and W. B. Tolman, *J. Am. Chem. Soc.*, 2006, **128**, 3445-3458.
12. H. Hamaki, N. Takeda, T. Yamasaki, T. Sasamori and N. Tokitoh, *J. Organomet. Chem.*, 2007, **692**, 44-54.

13. D. C. H. Do, A. Keyser, A. V. Protchenko, B. Maitland, I. Pernik, H. Niu, E. L. Kolychev, A. Rit, D. Vidovic, A. Stasch, C. Jones and S. Aldridge, *Chem. Eur. J.*, 2017, **23**, 5830-5841.
14. M. A. Land, B. Huo, K. N. Robertson, K. E. O. Ylijoki, P. T. K. Lee, J. Areephong, D. Vidović and J. A. C. Clyburne, *Dalton Trans.*, 2018, **47**, 10195-10205.
15. B. Ma, J. Arnold, *CSD Communication*, 2012, 906880.
16. A. W. Addison, T. N. Rao, J. Reedijk, J. van Rijn and G. C. Verschoor, *J. Chem. Soc., Dalton Trans.*, 1984, 1349-1356.
17. T. E. Patten, C. Troeltzsch and M. M. Olmstead, *Inorg. Chem.*, 2005, **44**, 9197-9206.
18. S. Benetti, R. Romagnoli, C. De Risi, G. Spalluto and V. Zanirato, *Chem. Rev.*, 1995, **95**, 1065-1114.
19. J. W. Bunting and J. P. Kanter, *J. Am. Chem. Soc.*, 1993, **115**, 11705-11715.
20. D. T. Carey, E. K. Cope-Eatough, E. Vilaplana-Mafe, F. S. Mair, R. G. Pritchard, J. E. Warren and R. J. Woods, *Dalton Trans.*, 2003, DOI: 10.1039/B212079H, 1083-1093.
21. I. Viera, E. Manta, L. González and G. Mahler, *Tetrahedron: Asymmetry*, 2010, **21**, 631-635.
22. N. O'Halloran, J. P. James and C. A. Downey, *Heterocycles*, 2008, **75**, 2681-2701.
23. S. L. Jain, P. Bhattacharyya, H. L. Milton, A. M. Z. Slawin, J. A. Crayston and J. D. Woollins, *Dalton Trans.*, 2004, , 862-871.
24. M. Ray, R. Mukherjee, J. F. Richardson, M. S. Mashuta and R. M. Buchanan, *J. Chem. Soc., Dalton Trans.*, 1994, 965-969.
25. R. Gopi, N. Ramanathan and K. Sundararajan, *J. Mol. Struct.*, 2015, **1083**, 364-373.
26. H.-C. Liang, E. Kim, C. D. Incarvito, A. L. Rheingold and K. D. Karlin, *Inorg. Chem.*, 2002, **41**, 2209-2212.
27. D. Jamróz, M. Wójcik and J. Lindgren, *Spectr. Acta Pt. A: Mol. Biomol. Spectrosc.*, 2000, **56**, 1939-1948.
28. X. Lu, H. Cheng, Y. Meng, X. Wang, L. Hou, Z. Wang, S. Chen, Y. Wang, G. Tan, A. Li and W. Wang, *Organometallics*, 2017, **36**, 2706-2709.
29. I. Koehne, N. Graw, T. Teuteberg, R. Herbst-Irmer and D. Stalke, *Inorg. Chem.*, 2017, **56**, 14968-14978.
30. D. H. Johnston and D. F. Shriver, *Inorg. Chem.*, 1993, **32**, 1045-1047.
31. G. A. van Albada, W. J. J. Smeets, A. L. Spek and J. Reedijk, *J. Chem. Crystallogr.*, 1998, **28**, 427-432.
32. C. Belle, C. Bougault, M.-T. Averbuch, A. Durif, J.-L. Pierre, J.-M. Latour and L. Le Pape, *J. Am. Chem. Soc.*, 2001, **123**, 8053-8066.
33. D. J. Mindiola and G. L. Hillhouse, *J. Am. Chem. Soc.*, 2001, **123**, 4623-4624.
34. D. J. Mindiola and G. L. Hillhouse, *J. Am. Chem. Soc.*, 2002, **124**, 9976-9977.
35. B. Horn, C. Limberg, C. Herwig and B. Braun, *Inorg. Chem.*, 2014, **53**, 6867-6874.
36. N. J. Hartmann, G. Wu and T. W. Hayton, *Angew. Chem. Int. Ed.*, 2015, **54**, 14956-14959.
37. S. Fortier, O. G.-d. Moral, C.-H. Chen, M. Pink, J. J. Le Roy, M. Murugesu, D. J. Mindiola and K. G. Caulton, *Chem. Commun.*, 2012, **48**, 11082-11084.
38. Y. Mathey, D. R. Greig and D. F. Shriver, *Inorg. Chem.*, 1982, **21**, 3409-3413.
39. D. A. Baldwin, A. B. Lever and R. V. Parish, *Inorg. Chem.*, 1969, **8**, 107-115.
40. D. A. Edwards and R. N. Hayward, *Can. J. Chem.*, 1968, **46**, 3443-3446.
41. G. B. Deacon and R. J. Phillips, *Coord. Chem. Rev.*, 1980, **33**, 227-250.

42. P. Sharrock and M. Melník, *Can. J. Chem.*, 1985, **63**, 52-56.
43. D. W. Randall, S. D. George, P. L. Holland, B. Hedman, K. O. Hodgson, W. B. Tolman and E. I. Solomon, *J. Am. Chem. Soc.*, 2000, **122**, 11632-11648.
44. P. J. Riedel, N. Arulsamy and M. P. Mehn, *Inorg. Chem. Commun.*, 2011, **14**, 734-737.
45. Q. Feng, D. Chen, D. Feng, L. Jiao, Z. Peng and L. Pei, *Appl. Organomet. Chem.*, 2014, **28**, 32-37.

Chapter 6

Conclusions and future work

6.1 Summary and conclusions

The main aim of this thesis, as outlined in Section 1.1.6, was to identify effective high-valent late-transition M–X (M = Ni, Cu, Au; X = O, OH, Cl) metal complexes for the oxidative activation of saturated C–H bonds. The final goal beyond the identification of these complexes was to study their mechanism of oxidation and elucidate potential differences linked to the role of the ancillary ligands. The focus was directed both towards first-row late transition metals, such as Ni and Cu, due to the overall dearth of high-valent oxidants containing these metals, and towards third-row transition metals, notably Au, due to the lack of mechanistic insights on Au^{III} oxidants, with the perspective to elucidate which active species are relevant to gold oxidation catalysis. In this regard, in Chapters 2 and 3 we identified discrete high-valent Au complexes, [Au(X)(terpy)](ClO₄)₂ (X = Cl, **1**; X = OH, **2**) which were capable of oxidising substrates bearing weak C–H bonds (DHA, CHD) and O–H bonds at room temperature in polar aprotic solvents (DMF, DMSO). The two complexes were characterized by ¹H NMR, XRD, CV and electronic absorption spectroscopy and modelled with DFT (Figure 6.1), highlighting their structural and spectroscopical similarity despite the different ancillary ligand.

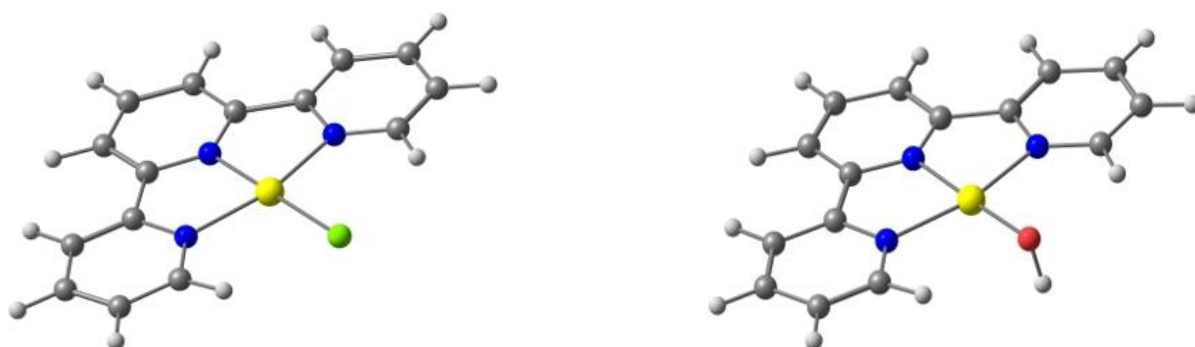
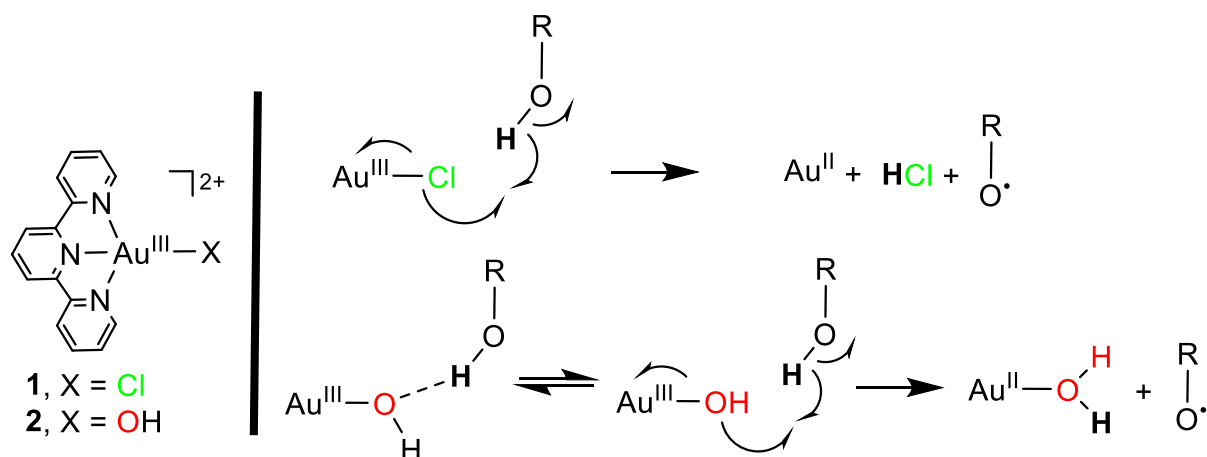


Figure 6.1. DFT optimized structures of complex **1** (left) and **2** (right).

Complexes **1** and **2** (Chapters 2 and 3) were reacted in the same conditions (25 °C, DMF) with 4-X-2,6-di-*tert*-butylphenols (X = CH₃O, ^tBu, H, CH₃) and 4-X-TEMPOH (X = O, H, CH₃O), showing the formation of stable radicals by electronic absorption spectroscopy and EPR, which were the result of a PCET oxidation of the substrates by the Au^{III} complexes. The same outcome was observed for **1** (Chapter 3), which reacted with the same substrate scope in the exact same conditions, although some differences in the mechanism of oxidation by these complexes were observed. Both **1** and **2** reacted with DHA and CHD and the almost quantitative formation of oxidation products, notably anthracene and benzene, was identified by ¹H NMR and GC-FID. Both

complexes demonstrated to follow a hydrogen atom transfer (HAT) mechanism of oxidation, which implies a concerted transfer of the proton and the electron from the substrate to the complex. Both **1** and **2** in fact showed a linear correlation between the BDFEs of the substrates and the free energy of activation (ΔG^\ddagger) in a Polanyi plot, with a slope of 0.39 for **1** and of 0.30 for **2**, which are both close to the ideal value of 0.5 for a HAT mechanism predicted by Marcus theory. Nevertheless, **1** showed linear kinetics of reaction with all the substrates explored, whereas **2** showed saturation kinetics, which suggested the presence of an equilibrium leading to an intermediate prior to the rate-determining step of the HAT oxidation (Scheme 6.1). We postulated the intermediate to be a H-bonded adduct between the complex and the substrate, a hypothesis which was corroborated by some literature examples of metal hydroxide complexes which showed similar kinetics,^{1,2} and by the value of *K*, the concentration of substrate at which half of the maximum rate is reached. In fact a four-fold difference in *K* was observed when deuterio-4-CH₃O-2,6-DTBP was used respect to proto-4-CH₃O-2,6-DTBP, suggesting the perturbation of the initial equilibrium by substituting a hydrogen with a deuterium atom. Furthermore, **1** was a more competent oxidant with respect to **2**, with faster reaction rates.



Scheme 6.1 Postulated mechanisms of oxidation of substrates by **1** and **2**.

An Eyring analysis showed a difference in the activation energy parameters between the two complexes, notably a less negative entropy (ΔS^\ddagger) and a lower free energy of activation (ΔG^\ddagger), a value obtained both from the Polanyi and the Eyring plot, for **1** with respect to **2**, which showed that a lower barrier for HAT occurs when the chloride is employed as ancillary ligand. Therefore **1** proved to be a more competent oxidant than **2** despite the structural similarity between the two complexes. We postulated that this difference could arise for two reasons. The first one is an electronic reason, which was supported by quantum chemical calculations showing a difference in the ligand field and the electron localised function between the two

complexes. The Au–Cl bond was more covalent than the Au–OH bond and the analysis of the electronic bond description of **1** showed a higher contribution of the Au^{II}–Cl[•] together with the dominant Au^{III}–Cl bond description. The partial radical character on the chlorine might explain the higher reactivity for **1** with respect to **2**. The other argument that would explain this reactivity difference is the thermodynamic driving force related to the bond strength of the products formed upon HAT. In fact, for oxidants following a HAT mechanism we can assess the relative strength of the oxidant based on the BDFE_{H-X} of the reduced and protonated species which is formed upon HAT. For **2**, the species formally obtained upon HAT is a [Au^{II}(H₂O)(terpy)]²⁺ complex, for which we have estimated a BDFE_{O-H} of 81±3 kcal/mol thanks to the Bordwell equation. For **1**, we were not able to trap the species formed after the HAT event, a putative [Au^{II}(••HCl)(terpy)]²⁺ adduct, due to its instability, therefore we assumed that HCl is probably readily released in solution. Thus we compared the reported value of BDE_{H-Cl} (103 kcal/mol) with the one for [Au^{II}(H₂O)(terpy)]²⁺, noticing a 22 kcal/mol difference. We believe that the main driving force for the higher reactivity of **1** compared to **2** can be ascribed to the higher strength of the HCl bond which is formed after the HAT event. To the best of our knowledge we can state that these results proved for the first time that Au^{III} complexes can be effective HAT oxidants and that Au^{III}–halide adducts can be more effective oxidants than the more widely invoked Au^{III}–oxygen ones.

In Chapter 4 we described the synthesis of three late-transition metal porphyrin complexes, [Cu(T(OMe)PP)] (**1**), [Ni(T(OMe)PP)] (**2**) and [Au(T(OMe)PP)]⁺ (**3**), taking inspiration from nature in an attempt to find effective high-valent late transition metal oxidants for hydrocarbon oxidation. In fact porphyrin-based oxidants are common in several enzymatic cycles and their oxidised form, notably as a metalloporphyrin π -cation radical, is present in highly oxidising compounds such as the P680 found in chlorophyll, the P865 found in bacteriochlorophyll and Compound I in Cytochrome P450 and heme peroxidases.³⁻⁵ After verifying by CV the presence of two reversible oxidation waves below 0.89V for **1** and **2**, both complexes were successfully oxidised to higher-valent species, **1OX** and **2OX**, by using phenoxythiinyll hexachloroantimonate as oxidant. The electronic nature of **1OX** and **2OX** was elucidated by electronic absorption spectroscopy, EPR and infra-red spectroscopy. Both species in fact showed broad absorption bands in the visible and near-IR region, for **1OX** at $\lambda = 506$, $\lambda = 614$ and $\lambda = 790$ nm and for **2OX** at $\lambda = 657$ and $\lambda = 900$ nm, which are typical of metalloporphyrin π -cation radicals (Figure 6.2). Furthermore, the EPR analysis showed the appearance of a signal at $g = 2.00$ for **2OX** which indicates an organic $S = \frac{1}{2}$ species, suggesting that the oxidation is

borne on the ligand rather than on the metal ion. Instead for **1OX** we observed the disappearance of the EPR signal typical of a Cu^{II} species (recorded for **1**) and the appearance of an isotropic signal at $g = 2.00$ that we ascribed to the conversion to a $\text{Cu}^{\text{II}\cdot+}$ cation radical together with some residual oxidant which was deemed responsible for the signal observed. We also recorded an infra-red spectrum of **2OX** which showed a new stretch at $\nu = 1263 \text{ cm}^{-1}$ which was assigned to a ring mode typical of metalloporphyrin π -radical cations. Therefore we concluded that **1OX** and **2OX** could be described as porphyrin π -cation radicals, respectively as a $\text{Cu}^{\text{II}\cdot+}$ and $\text{Ni}^{\text{II}\cdot+}$.

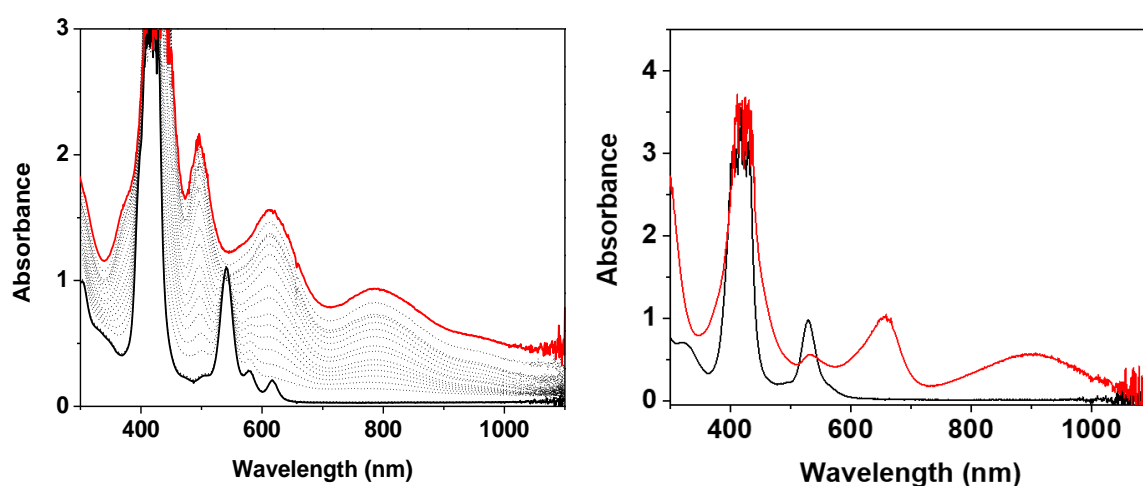
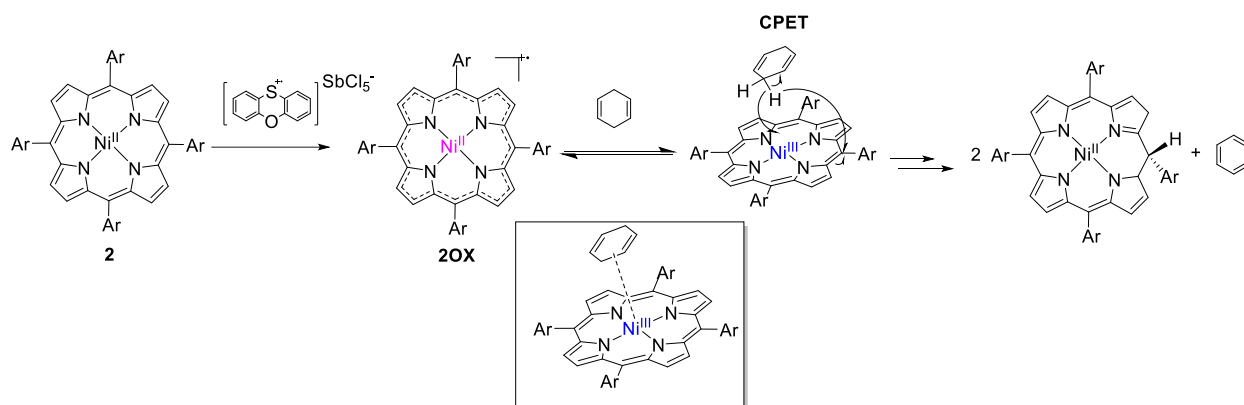


Figure 6.2. Left: Electronic absorption spectra (DCM, $-20 \text{ }^\circ\text{C}$) of **1** (black trace) and of **1OX** (red trace). Right: Electronic absorption spectra of **2** (black trace) and **2OX** (red trace).

After observing that **2OX** was potentially more reactive than **1OX**, we decided to investigate its reactivity towards saturated hydrocarbons. The $\text{Ni}^{\text{II}\cdot+}$ species showed to react with substrates with BDFEs ranging from 73 to 76 kcal/mol, notably xanthene, DHA, CHD, fluorene and triphenylmethane. The analysis of the post-reaction mixture by GC-FID or ^1H NMR showed the presence of oxidised organic products such as anthracene, benzene and 9-fluorenone in high yields, confirming the potential of **2OX** as a C–H bond oxidant. We observed a linear correlation between the BDFEs of the substrates and the free Gibbs energy of activation of the reactions with the substrates, derived from the values of k_2 , with a slope of 0.40 indicating a CPET mechanism. The Eyring analysis lead to a value of entropy of activation (ΔS^\ddagger) of $-37.5 \text{ cal mol}^{-1} \text{ K}^{-1}$, which would suggest an involvement of the metal centre in the oxidation step. This was in apparent contrast with the nature of **2OX** as a porphyrin π -radical cation, but the EPR analysis confirmed that a switch in the valence tautomerism of **2OX** occurs

upon addition of a substrate. For all but one reaction (with xanthene), we identified a new inorganic product by electronic absorption spectroscopy and ^1H NMR showing features typical of a Ni^{II} isoporphyrin.

We therefore postulated a mechanism of oxidation of hydrocarbon substrates by **2OX** (Scheme 6.2): the addition of the oxidant yields a Ni^{II} porphyrin π -cation radical (**2OX**), which upon addition of the substrate forms an adduct which shifts the equilibrium towards the Ni^{III} tautomer. Then the CPET oxidation occurs within this species, with the nickel ion accepting the electron and the ligand accepting the proton to yield a Ni^{II} isoporphyrin and the oxidised substrate. Our findings highlighted the potential of late transition metal porphyrin π -cation radicals as effective oxidants towards saturated hydrocarbons, mimicking the powerful Fe and Mg oxidant species present in biology. We also elucidated the mechanism of reaction of **2OX**, finding an analogy with the one observed for the Au^{III} complexes in Chapters 2 and 3, which also were proved to react via HAT, another form of concerted PCET. Therefore, these findings also highlighted the likelihood of concerted PCET oxidation mechanisms among high-valent late transition metal oxidants.



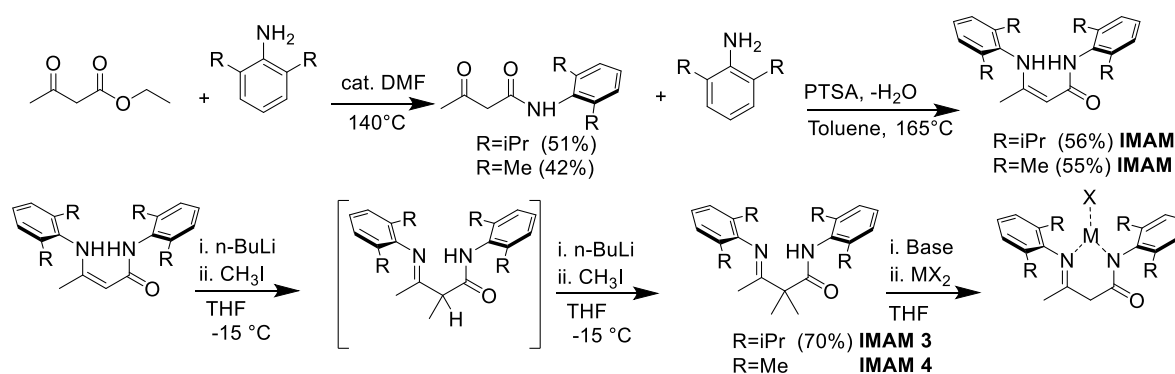
Scheme 6.2. Postulated mechanism of oxidation of hydrocarbon substrates by **2OX**.

In the last chapter of this thesis we described the synthesis of tailored ligands to synthesize the precursors of putative high-valent late transition metal oxidants in order to hurdle the “Oxo-wall”. In fact the geometry of the metal complex is crucial to allow the access to higher oxidation state for late transition metals with a high d electron count, such as Co, Ni and Cu, therefore we designed a class of tailored IMAM (Imino Amido) ligands to allow the isolation of complexes with trigonal planar geometry. These ligands bear a strong and localised σ -donor as a deprotonated amide which is supposed to coordinate to the metal cation and a neutral donor as an imine. The phenyl rings are supposed to bear bulky substituents in position 2 and 6 to favour the isolation of mononuclear complexes by shielding the coordination site. We were

able to achieve the desired ligands in a two-step synthesis, with different substituents on the aryl rings (isopropyl = IMAM 1, methyl = IMAM 2, Scheme 6.3) which we established to be present in solution only as the enaminic tautomer, as observed by ^1H NMR, ^{15}N - ^1H HSQC, ATR-FTIR and XRD. We then attempted to prepare complexes using these ligands. During the deprotonation step, we observed that the hydrogens in the α position between the amide and the imine functionality were affected by the addition of a base. We therefore decided to modify these ligands by alkylating the α -carbon in order to block the deprotonation in this position. We were thus able to synthesize the alkylated IMAM ligands (Scheme 6.3), but only the one bearing the isopropyl substituents (IMAM 3) was achieved in a pure form to allow its isolation and characterization by NMR, ATR-FTIR, MS and XRD.

We then attempted the complexation of Ni, Cu and Co with IMAM 3, reporting interesting preliminary results. In fact MS evidences showed the formation of mononuclear complexes with Ni^{II} and Co^{II} , whereas ^1H NMR showed paramagnetically shifted resonances typical of high spin d^8 and d^7 metal complexes, which would occur with a trigonal planar geometry. The EPR spectrum of the complex with Cu showed a signal typical of an $S = 1/2$ d^9 species with hyperfine coupling to a Cu ion and superhyperfine coupling to two non-equivalent N atoms. We therefore concluded that IMAM 3 is a robust ligand potentially capable to allow the isolation of mononuclear Ni^{II} , Co^{II} and Cu^{II} complexes with an unusual trigonal planar geometry. These result introduced a new class of ligands for coordination chemistry and notably opened new possibilities towards the isolation of late-transition metal oxo complexes by enforcing a low coordination number and a different geometry in order to hurdle the “Oxo-Wall”.

The results reported in this thesis represent therefore a further step in the identification, characterization and optimization of high-valent late transition metal oxidants for hydrocarbon activation from a synthetic, spectroscopic and mechanistic perspective.



Scheme 6.3. Synthetic pathway for the synthesis of IMAM ligands and their complexes.

6.2 Future work

The results reported in this thesis opened different pathways towards an expansion of the current knowledge of the field of high-valent late transition metal oxidants and their mechanisms of reaction.

1) A modification of the terpyridine ligand supporting the $[\text{Au}^{\text{III}}(\text{X})(\text{terpy})](\text{ClO}_4)_2$ complexes ($\text{X} = \text{Cl}$, **1**; $\text{X} = \text{OH}$, **2**) reported in Chapters 2 and 3 would be desirable to allow the isolation of the Au^{II} species obtained upon the HAT event, which are postulated to be respectively $[\text{Au}^{\text{II}}(\bullet\bullet\text{HCl})(\text{terpy})]^{2+}$ and $[\text{Au}^{\text{II}}(\text{H}_2\text{O})(\text{terpy})]^{2+}$. These entities lack of stability due to the unusual oxidation state of the metal and to the presence of neutral ancillary ligands, therefore a supporting ligand with stronger σ -donors such as amides or alkyl amines could enhance the stability of these species allowing their isolation and characterization. This would allow us to gain more insights on the BDFEs of these species, enabling a more reliable comparison of the strength of the two oxidants and a better elucidation of the products of the HAT step. This would also allow us to explore the catalytic reactivity of **1** and **2** towards both phenolic and hydrocarbon substrates, since the modified ligand platform would block the disproportionation and irreversible reduction of the gold cation, allowing the access to reversible reactions necessary for catalysis.

2) An extension of the hydrocarbon substrate scope for **1** and **2** would allow us to gain more mechanistic insights on the reaction with C–H bonds, in the same fashion applied to the substrates bearing O–H bonds. In fact the reactivity of both complexes with DHA and CHD appeared to be slow in the conditions used (DMF, 25 °C), preventing us to carry on an extensive kinetic study for this class of substrates. We believe that a change in the structure of the complex or in the conditions, such an increase of the working temperature or a modification of the ancillary ligand (as mentioned above) or of the counterion, in order to allow the solubility of **1** and **2** in different solvent mixtures, could enable an expansion of the substrate scope for saturated hydrocarbons.

3) For the work presented in Chapter 4, we reported the reactivity of a $[\text{Ni}^{\text{II}}(\text{T}(\text{OMe})\text{PP})]^{+\bullet}$ species (**20X**) towards hydrocarbons. We hypothesized the formation of a Ni^{II} isoporphyrin species but an expansion in the characterization of this species would allow us to confirm the postulated mechanism of reaction. Therefore more structural data obtained via ^{13}C -NMR, XRD and MS are required to prove the hypothesis of formation of this species after the HAT event.

4) The complex $[\text{Au}^{\text{III}}(\text{T}(\text{OMe})\text{PP})\text{Cl}]$ (**3**, Chapter 4) was synthesized and characterized but no reactivity studies were performed on it due to time constraints. Given the interesting results

obtained in Chapters 2 and 3 regarding the reactivity of Au^{III} oxidants, we think that an investigation and optimization of the conditions to explore the reactivity of **3** towards hydrocarbons might open new appealing avenues. In this case in fact the introduction of an external oxidant would not be necessary, given that the metal ion is already in a high oxidation state, potentially allowing milder reaction conditions. As seen for its Cu and Ni analogues, the addition of potential fifth or sixth ligands (such as Cl⁻, OH⁻, F⁻) could cause a change in the symmetry and electronic properties of these porphyrinic oxidants. Therefore the addition of salts such as Et₄NOH, Et₄NCl or ⁿBu₄NF could be explored for **3** in order to assess if coordination of these ligands could occur and potentially affect the reactivity of this gold complex.

5) In Chapter 5 we presented the synthesis of a new class of ligands called IMAM to enforce the isolation of low-coordinate late transition metal complexes, which would be precursors for powerful oxidants. We were able to obtain some preliminary results for the formation of mononuclear low-coordinate complexes with Co^{II}, Ni^{II} and Cu^{II} but more spectroscopic and structural data are necessary to confirm the effectiveness of these ligands, such as XAS, 2D-NMR and XRD. Furthermore, an expansion of the possible pool of substituents on the ligands, both on the phenyl rings and on the α -carbon, would allow us to produce a library of ligands with tunable steric and electronic properties, enhancing the chances of finding the optimal ones for the different transition metals explored.

Given the interesting results obtained, there are several longer-term objectives which are worth investigating for the topics developed in this thesis.

6) The results obtained in Chapters 2 and 3 suggest that a deeper exploration of gold oxidation catalysis is worth pursuing. Notably, the development of novel Au^{III} complexes bearing halides as ancillary ligands and their application to a variety of organic oxidation reaction could lead to a new whole field of catalysts. In particular Au^{III}-F complexes might be more effective oxidants, considering that they would lead to a higher thermodynamic driving force by releasing HF, which has a BDE = 136 kcal/mol, sensibly higher with respect to the one of HCl (103 kcal/mol). An extended comparative study of the mechanism of reaction of Au^{III}-F complexes versus Au^{III}-Cl complexes could give support to this postulate and could further clarify the nature of the active species of this type of oxidants. We believe that a new approach to gold catalysis could be possible with an expansion of the preparation and the application of Au-halide complexes.

7) The results obtained in Chapter 4 suggest that the preparation of a pool of Cu and Ni porphyrin π -cation radicals could be a breakthrough in biomimetic oxidation catalysis. In fact these compounds appear as powerful oxidants, therefore a tuning of the steric and electronics of the supporting porphyrin ligands could ensure their optimization, leading to longer-lived oxidants, to a broader substrate scope or to a higher reactivity. We believe that these species could be effective oxidants towards a wide variety of organic substrates therefore the development of a library of different complexes would allow us to expand the reaction scope. Furthermore, the possibility to oxidise again the low-valent complexes at the end of some reactions could open new avenues in catalysis for this class of compounds.

6.3 References

1. G. B. Wijeratne, B. Corzine, V. W. Day and T. A. Jackson, *Inorg. Chem.*, 2014, **53**, 7622-7634.
2. D. Dhar and W. B. Tolman, *J. Am. Chem. Soc.*, 2015, **137**, 1322-1329.
3. R. Silaghi-Dumitrescu, *J. Biol. Inorg. Chem.*, 2004, **9**, 471-476.
4. J. Barber, *Bioelectrochemistry*, 2002, **55**, 135-138.
5. B. Robotham and P. J. O'Malley, *Biochemistry*, 2008, **47**, 13261-13266.

Appendix A

A.1 Chapter 2

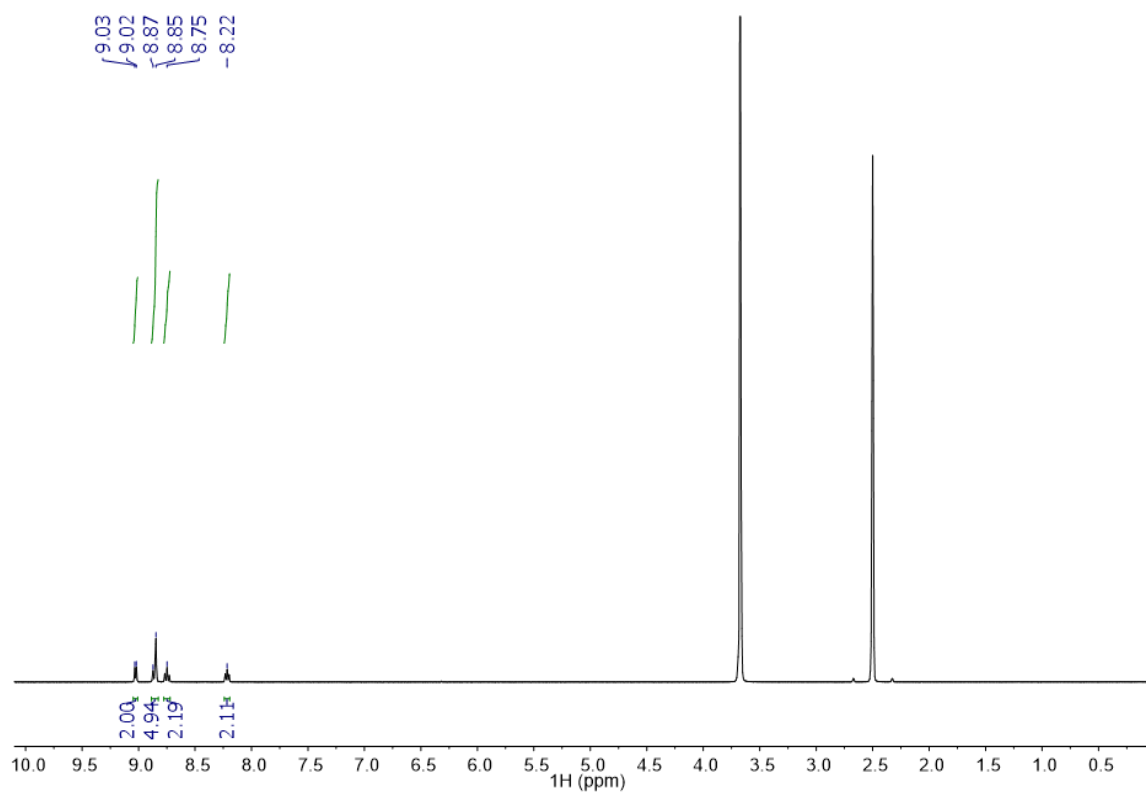


Figure A1. ^1H NMR spectrum (400 MHz, DMSO-D_6) of **1** in the presence of D_2O .

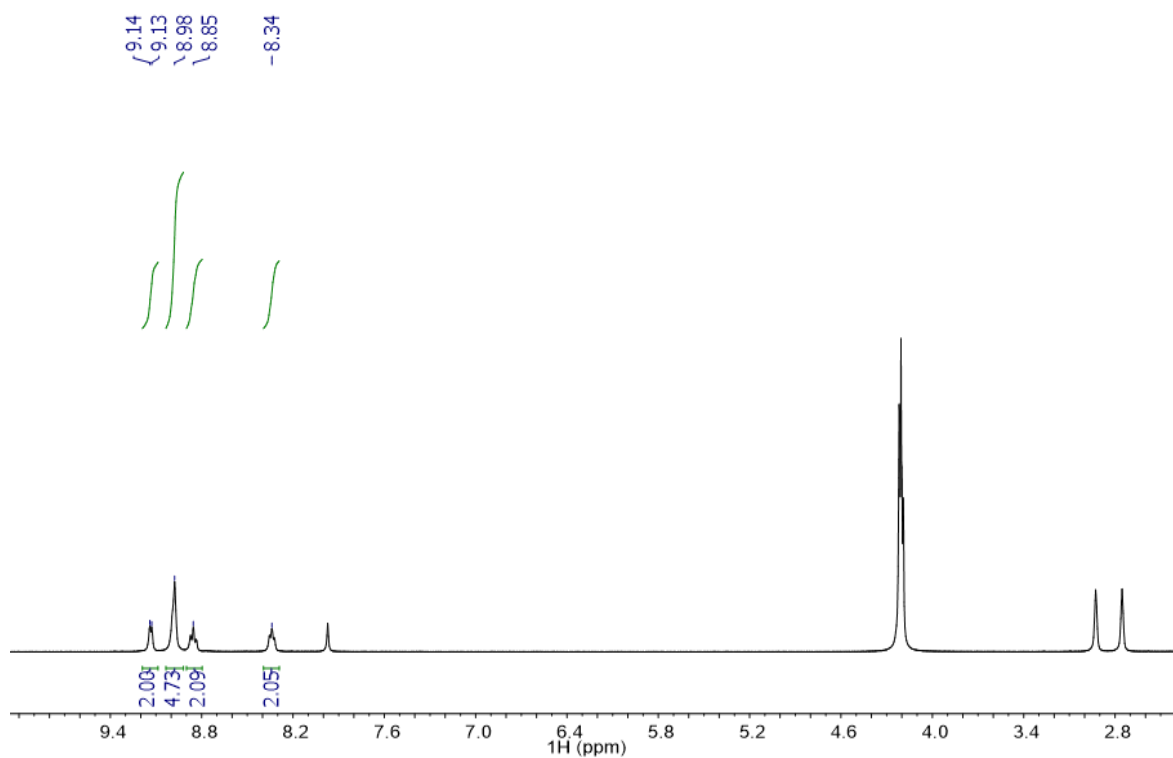


Figure A2. ^1H NMR spectrum (400 MHz, DMF-D_7) of **1** in the presence of D_2O .

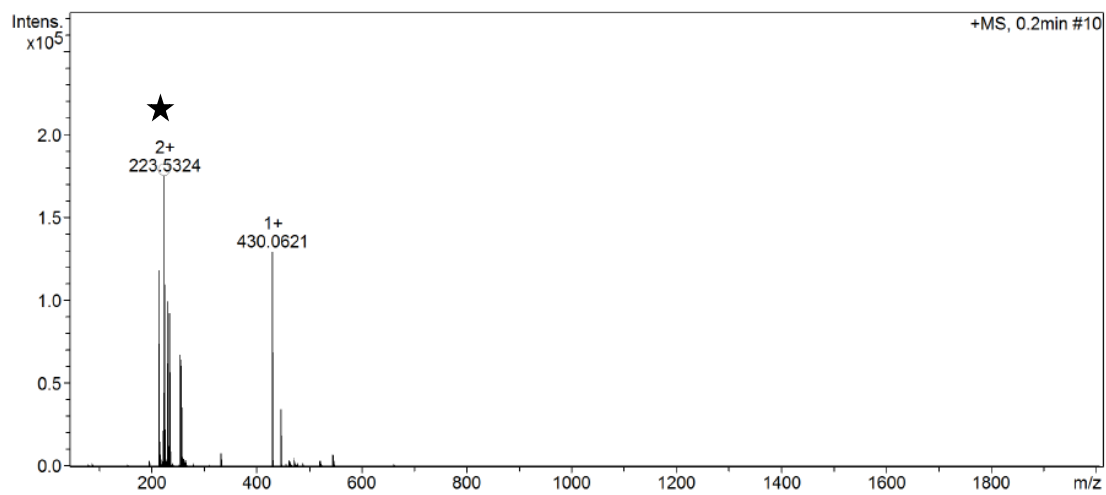


Figure A3. Positive mode ESI-MS spectrum of **1** (calculated m/z of $[\text{Au}(\text{OH})(\text{terpy})]^{2+} = 223.5317$).

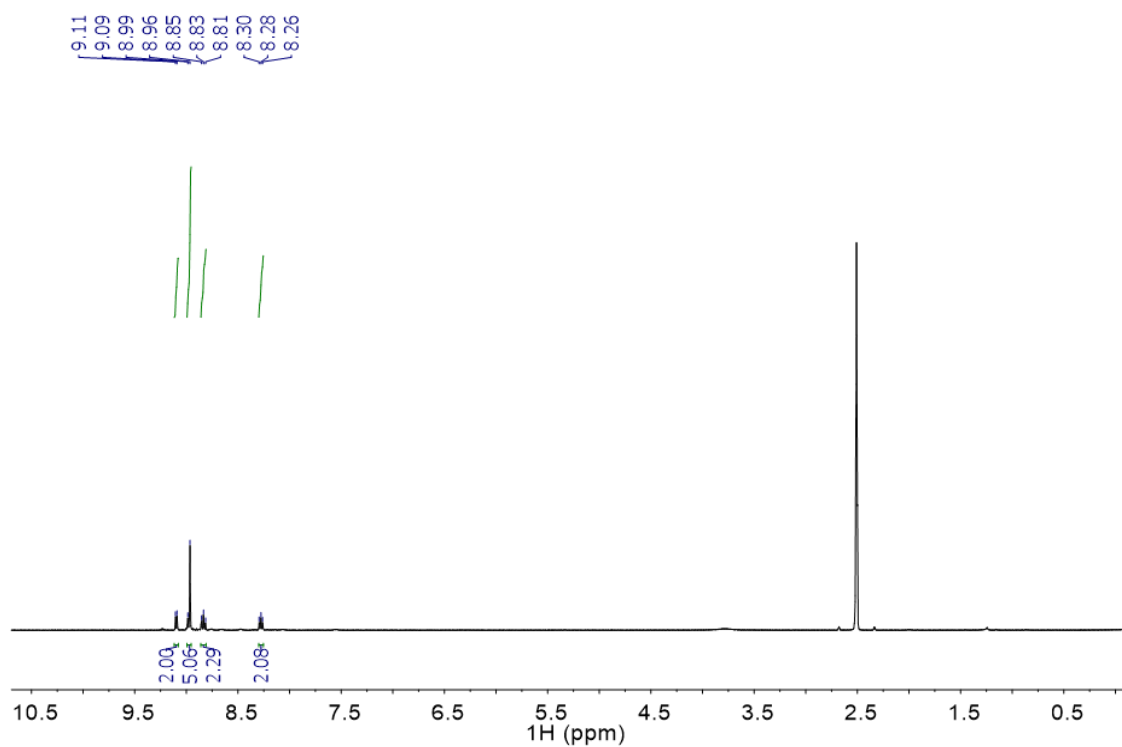


Figure A4. ^1H NMR spectrum (400 MHz, DMSO-D_6) of **2**.

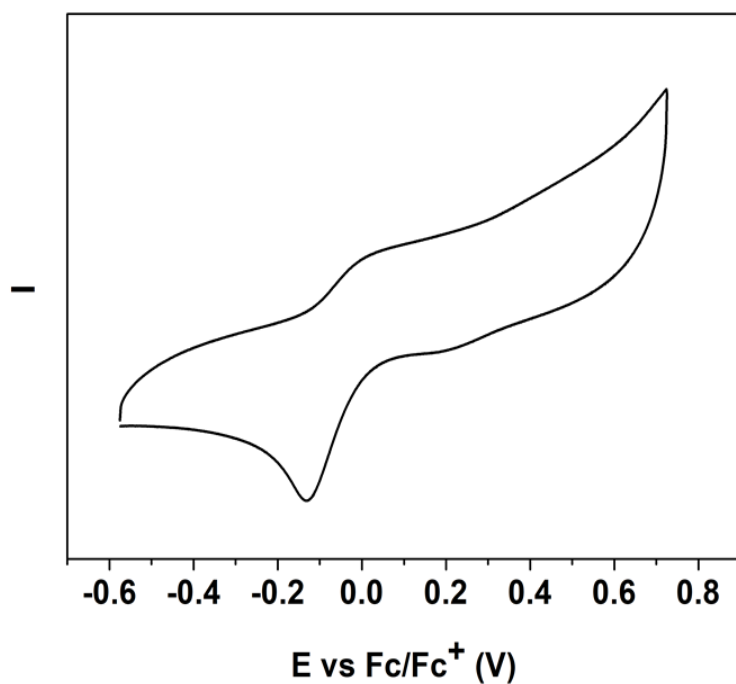


Figure A5. Cyclic voltammetry of **1** in DMF, supporting electrolyte: $^n\text{Bu}_4\text{NPF}_6$ 0.1 M, working electrode: carbon, counter electrode: Pt wire, reference electrode: Ag/AgNO_3 , scan rate: 0.1 V s^{-1} .

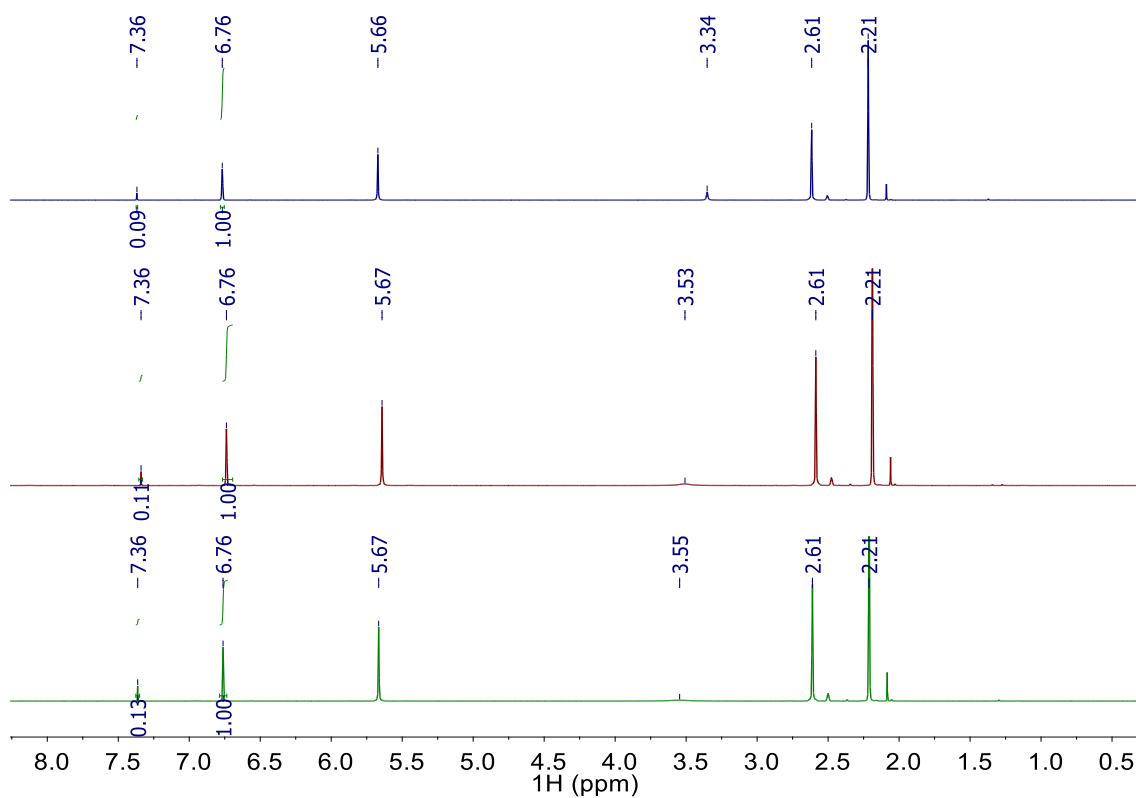


Figure A6. ^1H NMR spectra (400 MHz, DMSO-D_6) of the reaction between **1** and CHD (100 equiv.); blue = 0 s, red = 2 h, green = 5 h; benzene C–H: $\delta = 7.36$ ppm; H_2O : $\delta = 3.334$ -3.55 ppm; 1,3,5-trimethylbenzene (internal standard): $\delta = 2.21$ and 6.76 ppm.

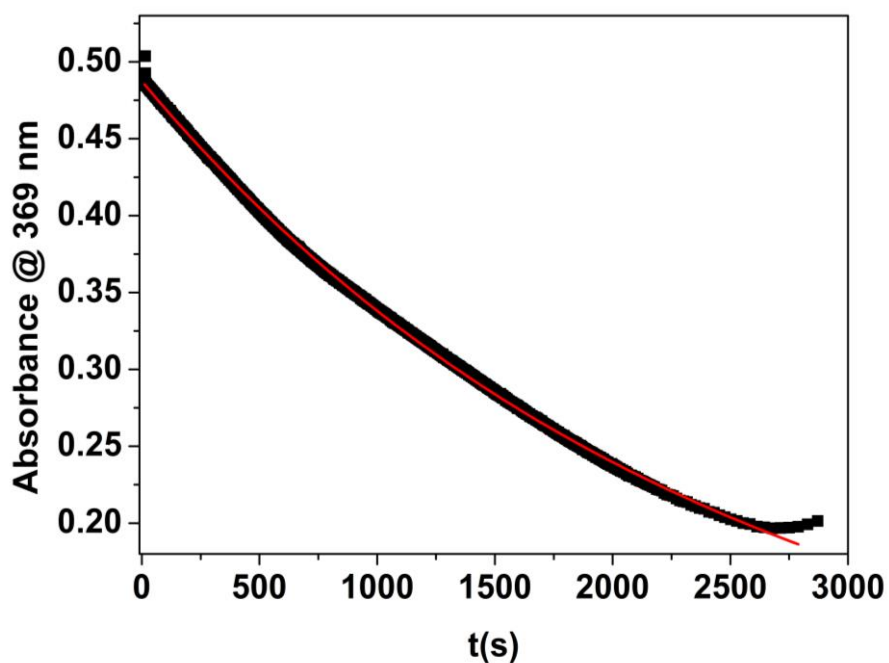


Figure A7. Plot of the absorbance at $\lambda = 369$ nm against time during the reaction between **1** (DMF, 25 °C, 0.15 mM) and DHA (500 equiv.).

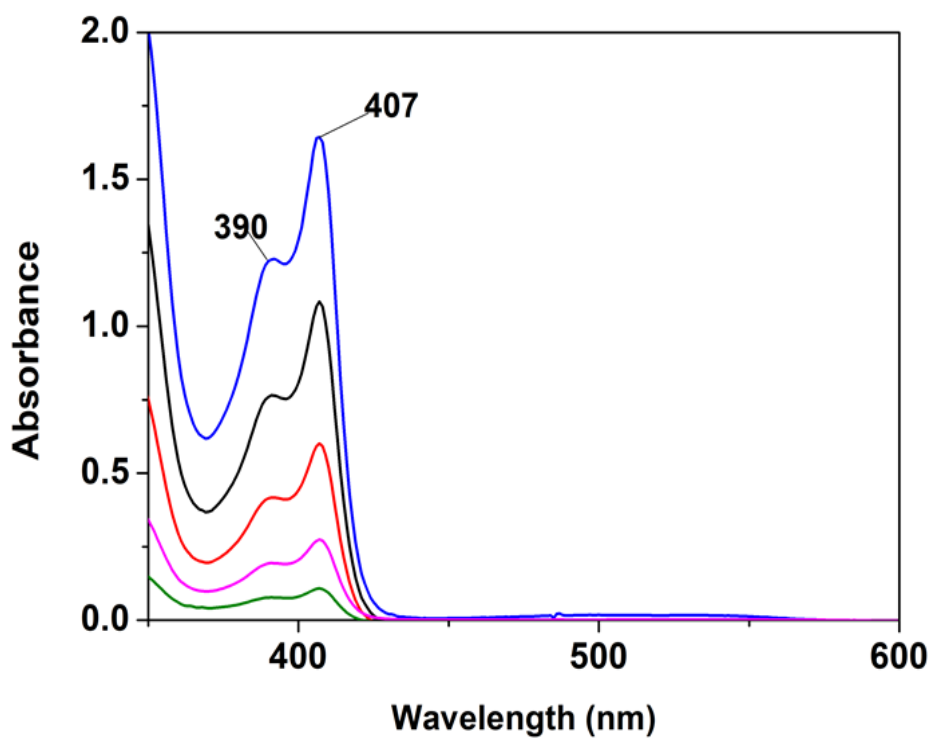


Figure A8. Electronic absorption spectra of 4-methoxy-2,6-di-*tert*-butylphenoxy radical in DMF at variable concentrations (0.052, 0.13, 0.26, 0.52, 0.78 mM).

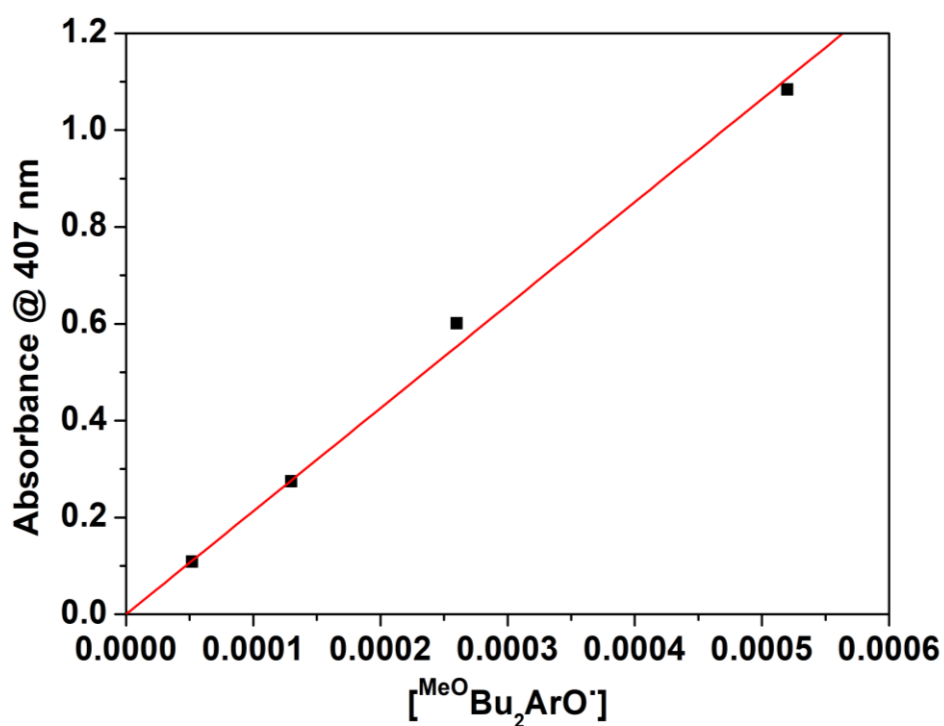


Figure A9. Plot of the absorbance vs concentration at $\lambda = 407$ nm of the 4-methoxy-2,6-di-*tert*-butylphenoxy radical in DMF.

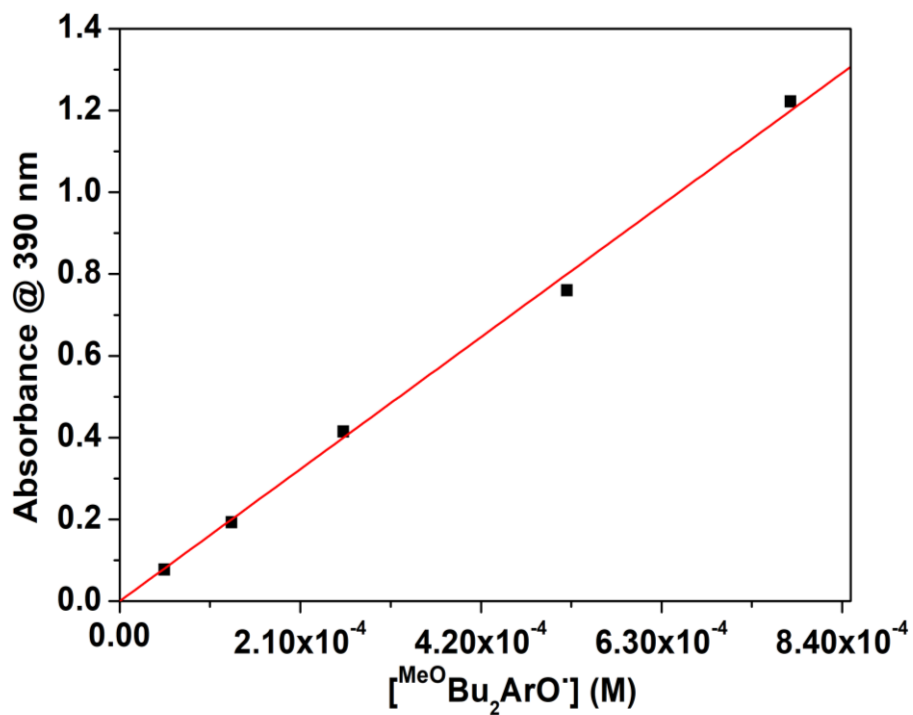


Figure A10. Plot of the absorbance vs concentration at $\lambda = 390$ nm of the 4-methoxy-2,6-di-*tert*-butylphenoxy] radical in DMF.

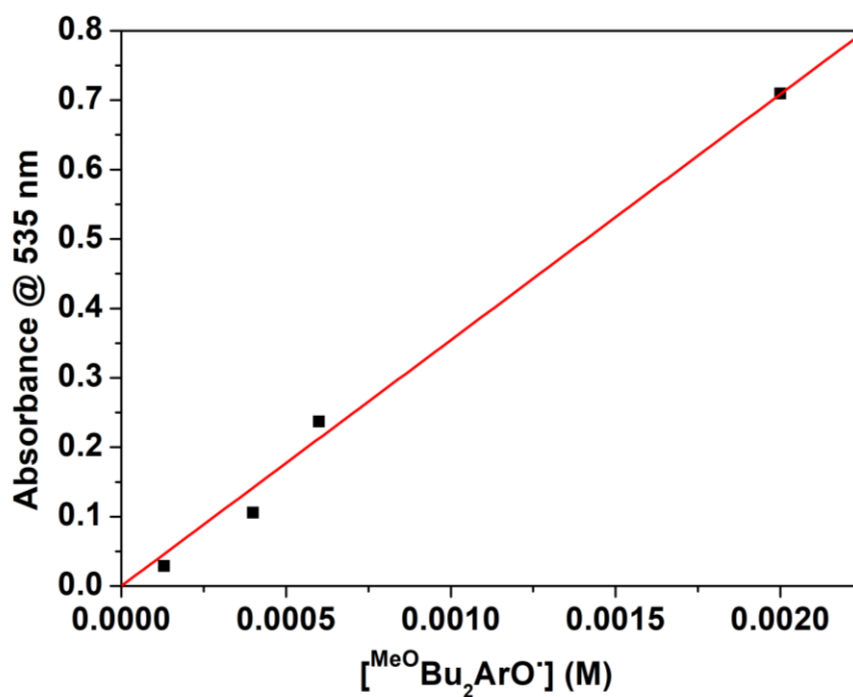


Figure A11. Plot of the absorbance vs concentration at $\lambda = 535$ nm of the 4-methoxy-2,6-di-*tert*-butylphenoxy] radical in DMF.

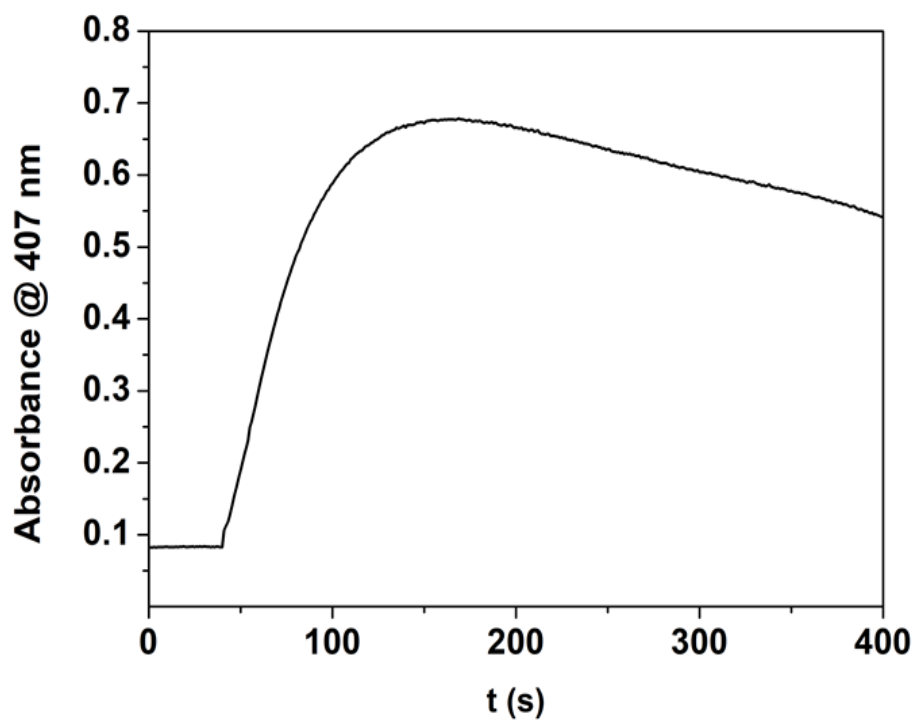


Figure A12. Plot of the absorbance at $\lambda = 407$ nm versus time during the reaction between **1** and 200 equiv. of 4-CH₃O-2,6-DTBP at 25 °C in DMF.

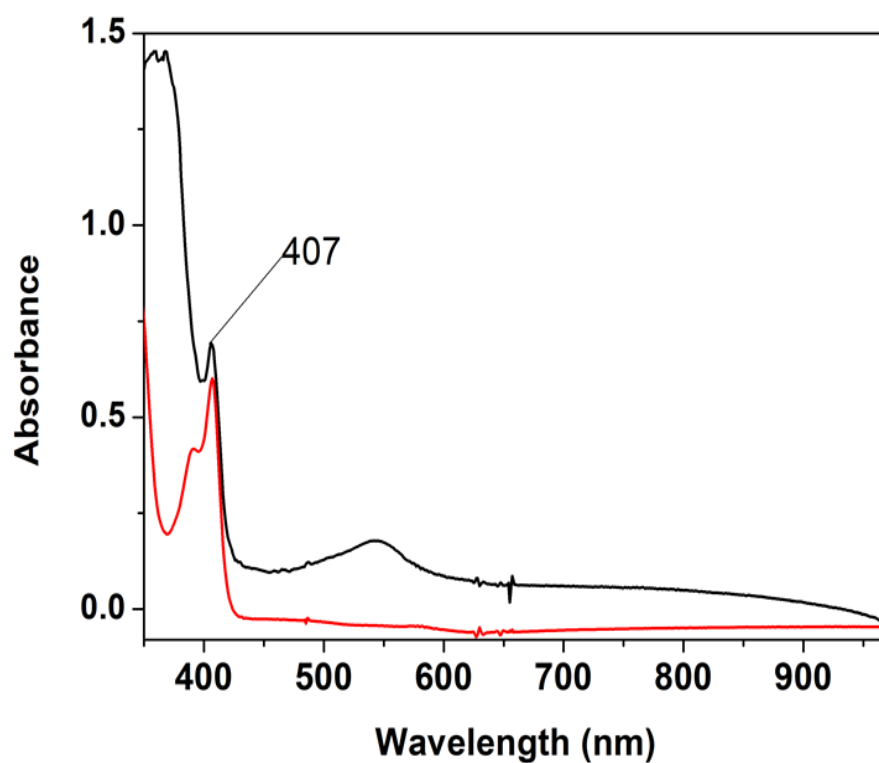


Figure A13. Electronic absorption spectra (DMF, 25 °C) of the independently synthesized 4-methoxy-2,6-di-*tert*-butylphenoxy radical (red trace) and of the reaction between **1** and an excess of 4-CH₃O-2,6-DTBP (black trace).

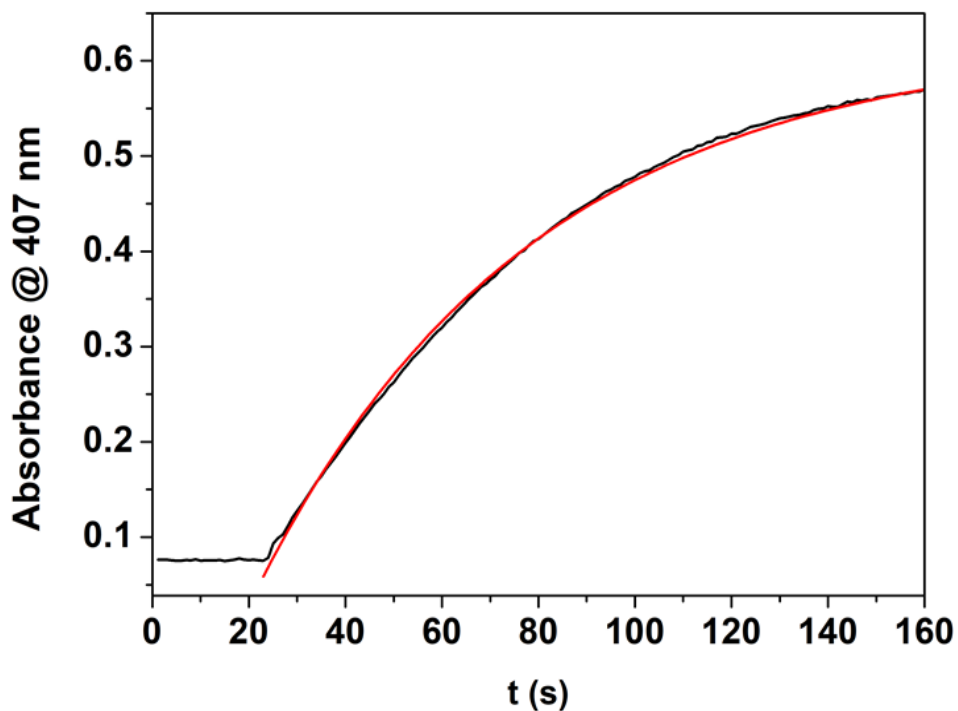


Figure A14. Fitting of the absorbance at $\lambda = 407$ nm vs. time during the reaction between **1** and 200 equiv. of 4-CH₃O-2,6-DTBP.

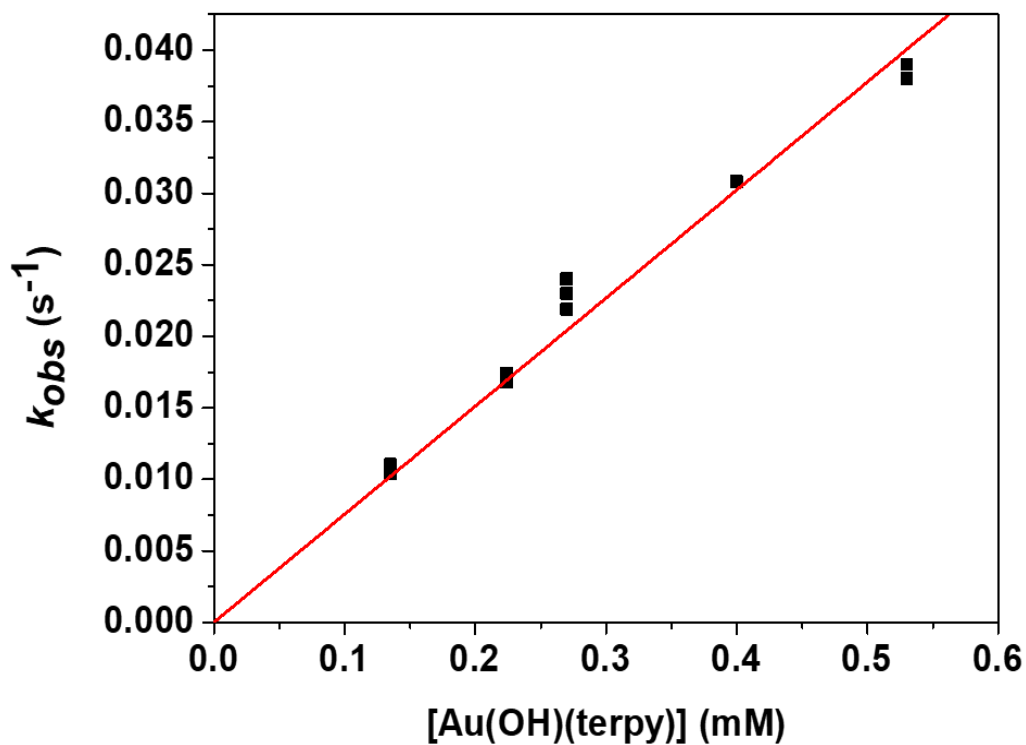


Figure A15. Plot of k_{obs} recorded in saturating conditions (350 equiv. of substrate) versus **1** in its reaction with 4-CH₃O-2,6-DTBP.

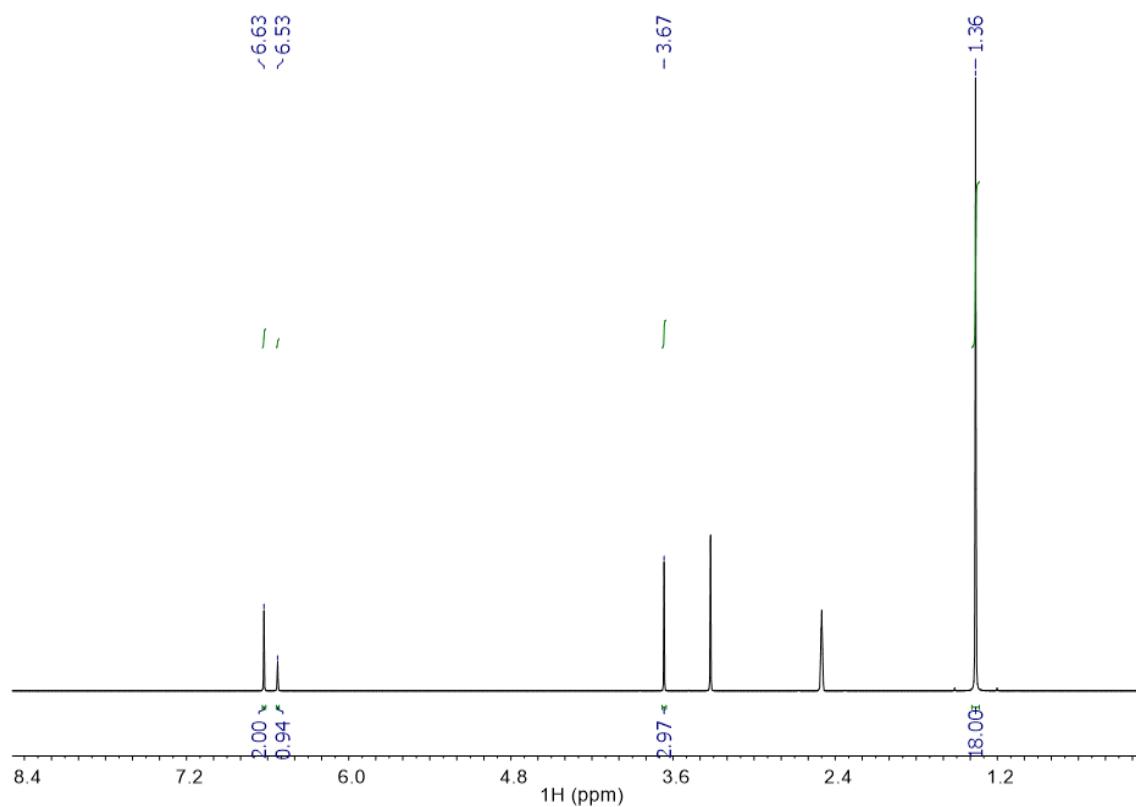


Figure A16. ^1H NMR spectrum (400 MHz, DMSO-D_6) of 4- CH_3O -2,6-DTBP.

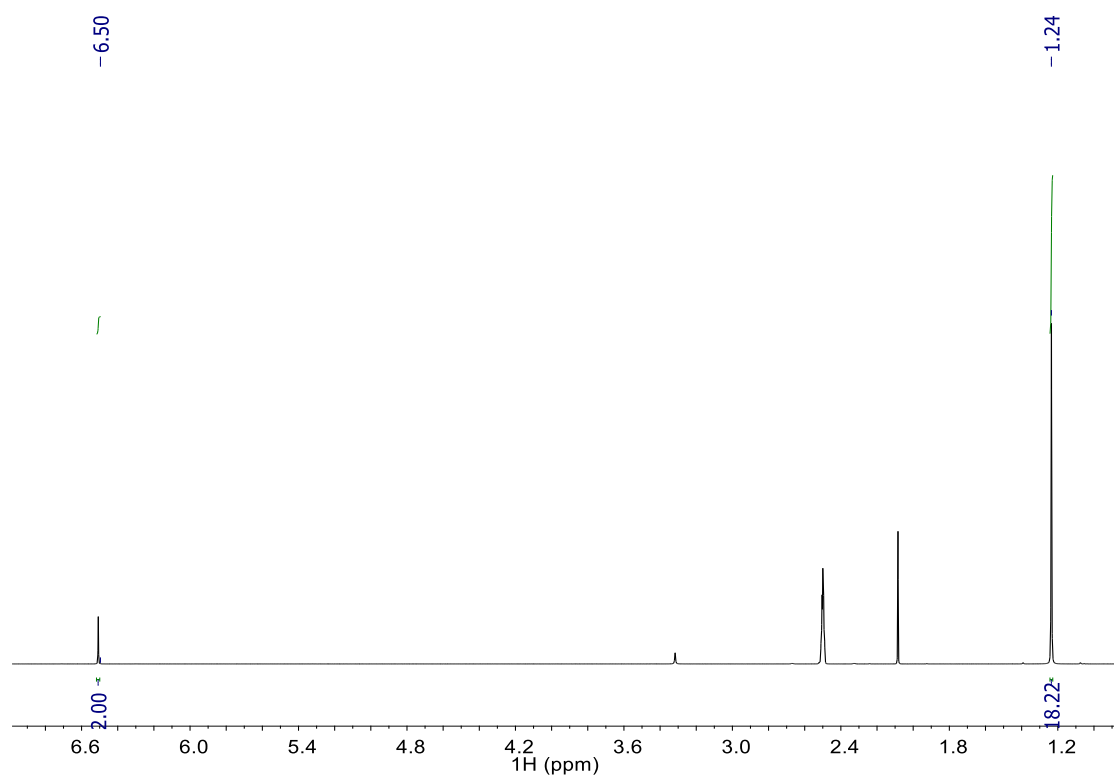


Figure A17. ^1H NMR spectrum (400 MHz, DMSO-D_6) of 2,6-di-*tert*-butylquinone (2,6-DTBQ).

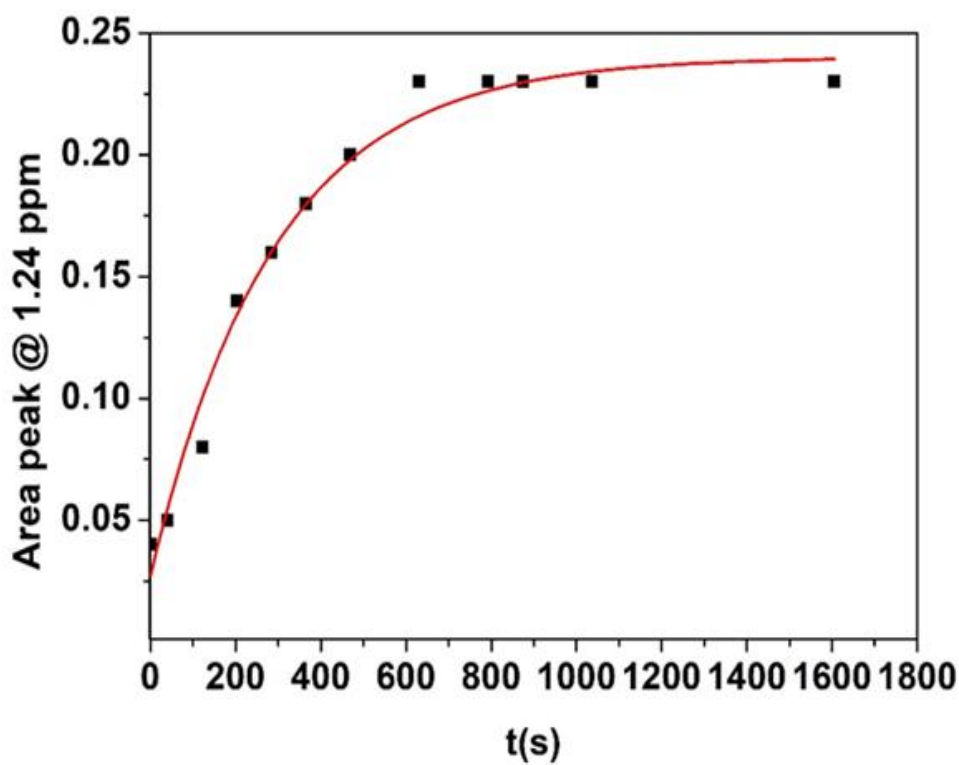


Figure A18. Plot of the area of the peak at $\delta = 1.24$ ppm in the ^1H NMR spectrum ($\text{C}(\text{CH}_3)_3$ in 2,6-DTBQ) versus time. The area has been calculated with respect to the DMSO solvent residual peak.

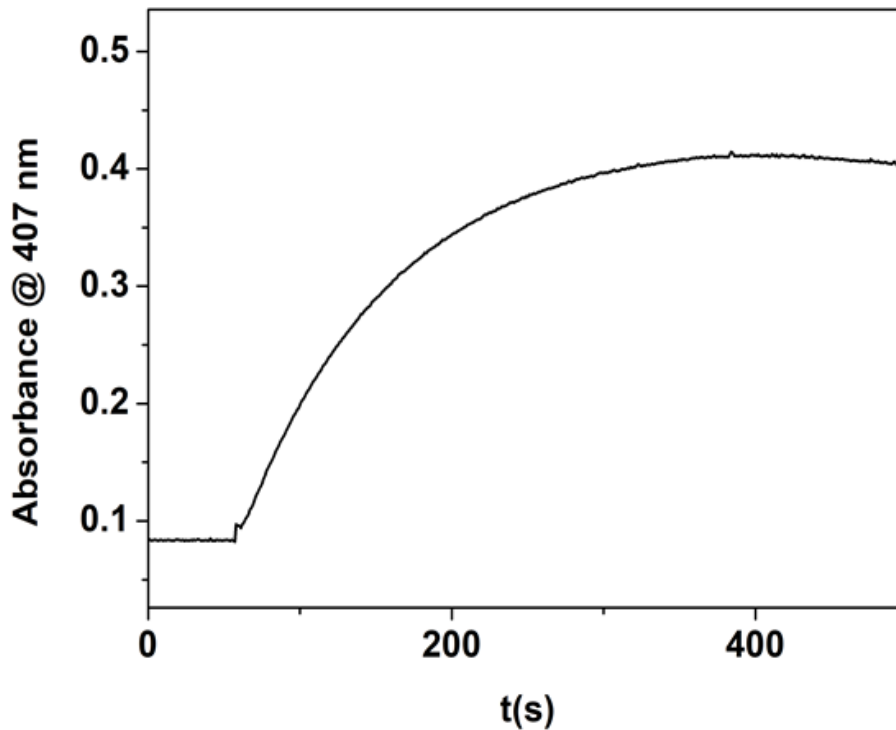


Figure A19. Plot of the absorbance at $\lambda = 407$ nm versus time during the reaction between **1** (DMF, 25°C) and 4- CH_3O -2,6-DTBP in absence of O_2 .

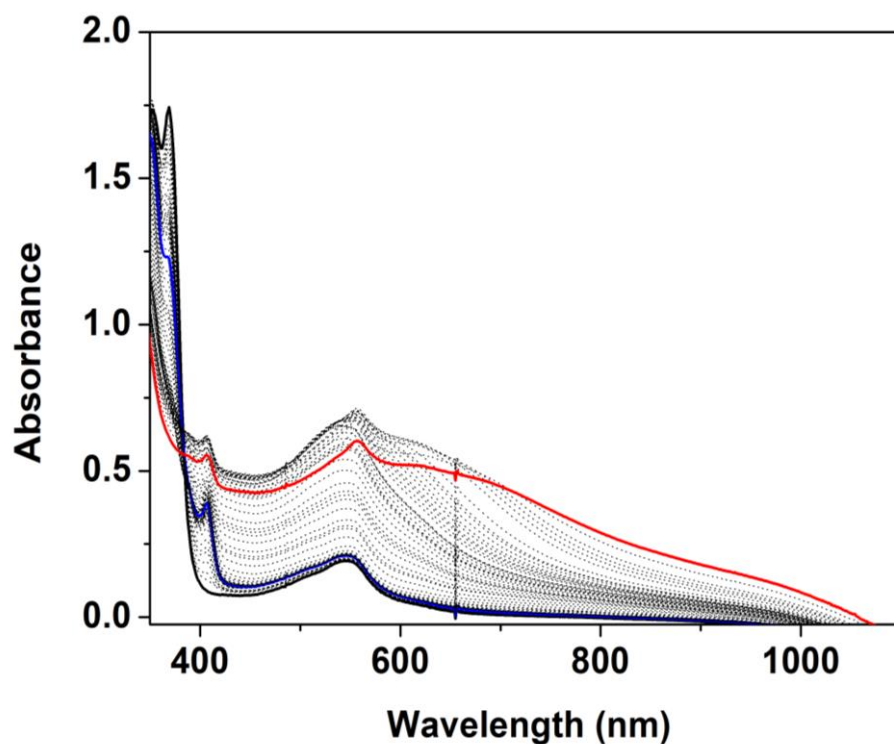


Figure A20. Electronic absorption spectra of the reaction of complex **1** (DMF, 25 °C, 0.45 mM) with 4-CH₃O-2,6-DTBP (100 equiv.) in the absence of O₂ monitored for 1000 s. Blue trace = 200 s, red trace = 1000 s.

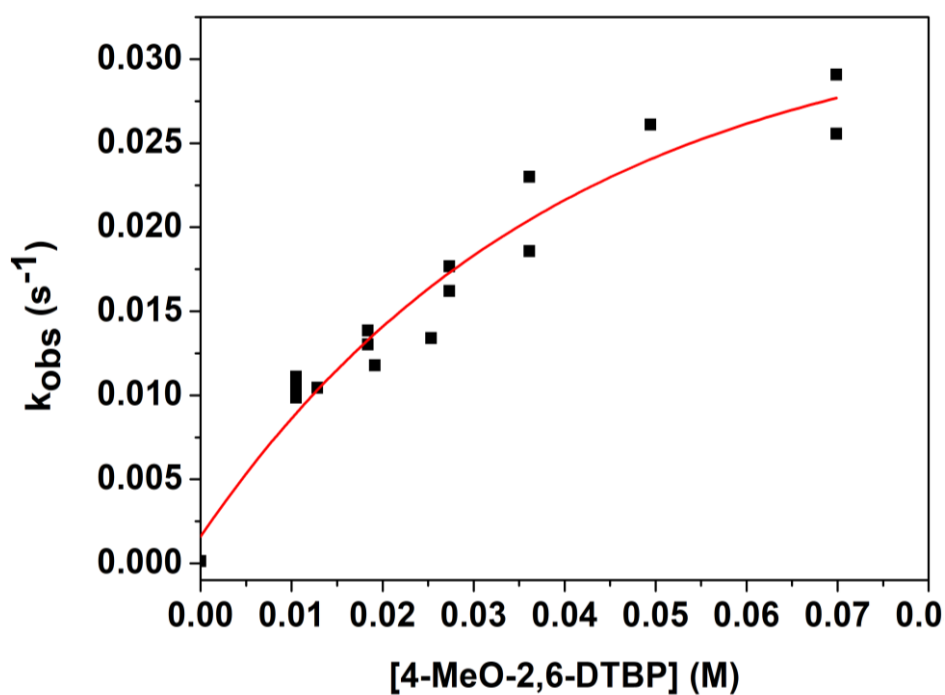


Figure A21. Plot of k_{obs} versus [4-CH₃O-2,6-DTBP] for the reaction between **1** and 4-CH₃O-2,6-DTBP in absence of O₂.

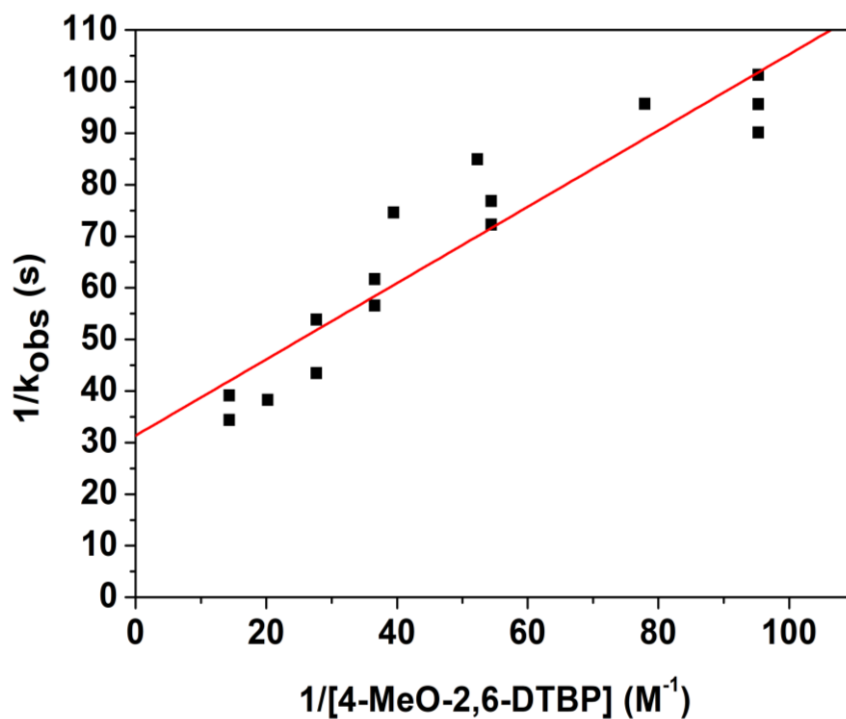


Figure A22. Plot of $1/k_{\text{obs}}$ against $1/[4\text{-CH}_3\text{O-}2,6\text{-DTBP}]$ in absence of O_2 .

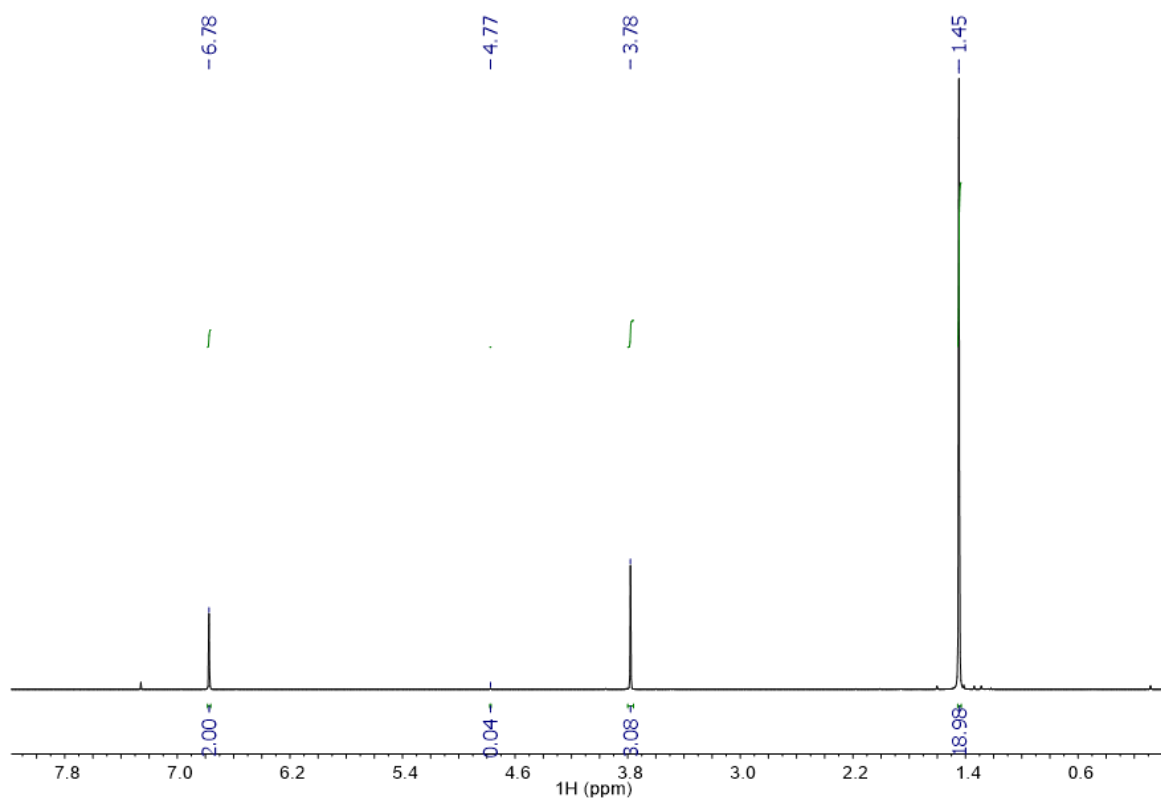


Figure A23. ^1H NMR (400 MHz, CDCl_3) of $4\text{-CH}_3\text{O-}[D]\text{-}2,6\text{-DTBP}$.

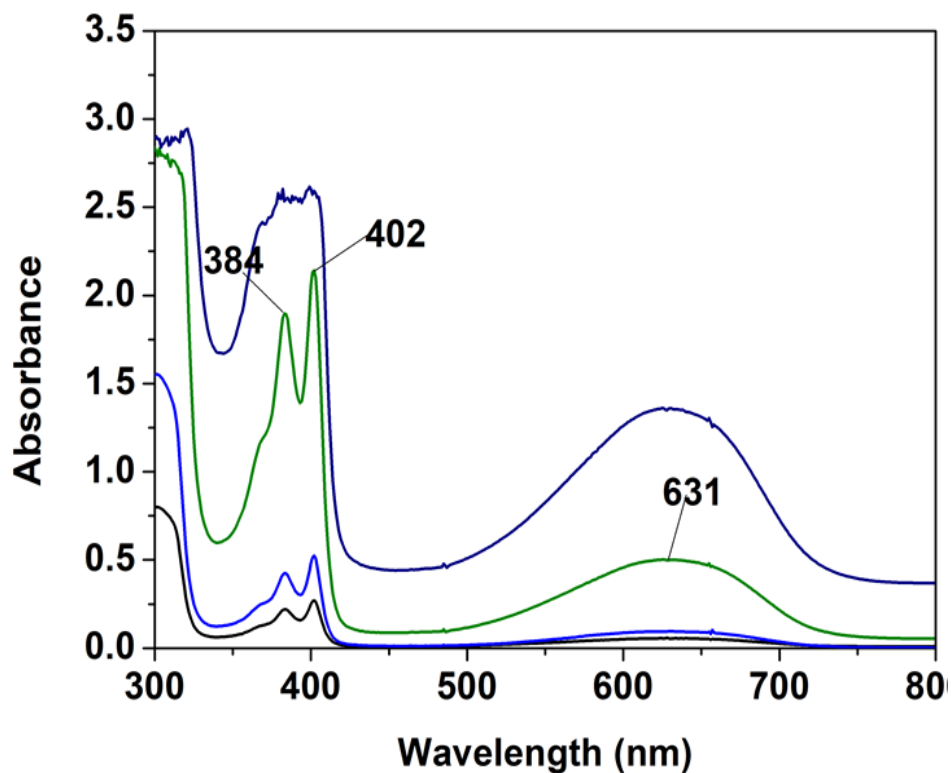


Figure A24. Electronic absorption spectra of 2,4,6-tri-*tert*-butylphenoxy radical in DMF at different concentrations (0.35, 0.75, 1.5 and 3.9 mM).

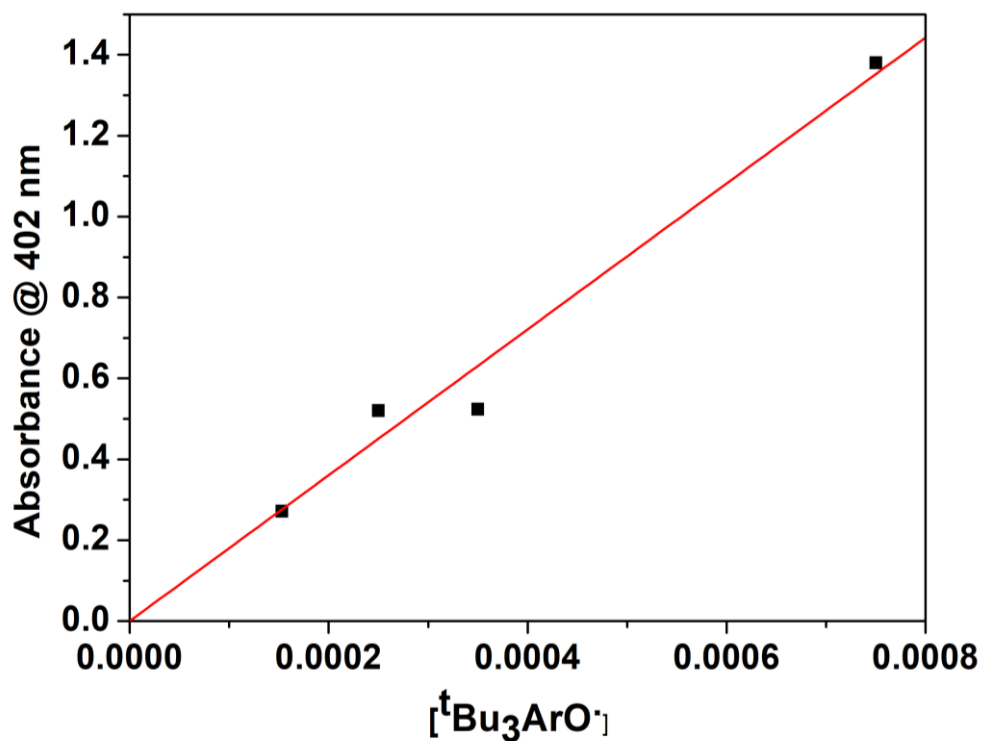


Figure A25. Plot of the absorbance vs. concentration at $\lambda = 402$ nm for the 2,4,6-tris-*tert*-butylphenoxy radical in DMF.

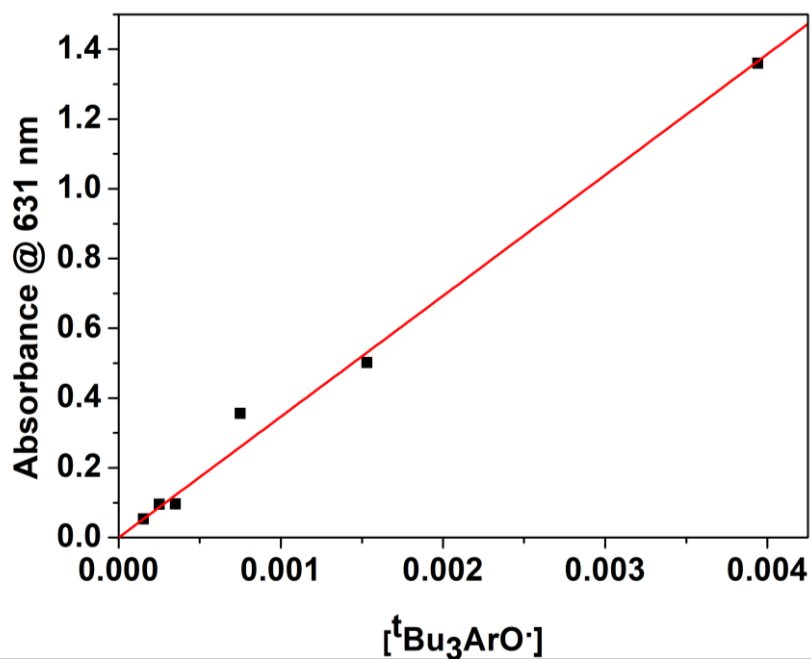


Figure A26. Plot of the absorbance vs. concentration at $\lambda = 631$ nm for the 2,4,6-tris-*tert*-butylphenoxy radical in DMF.

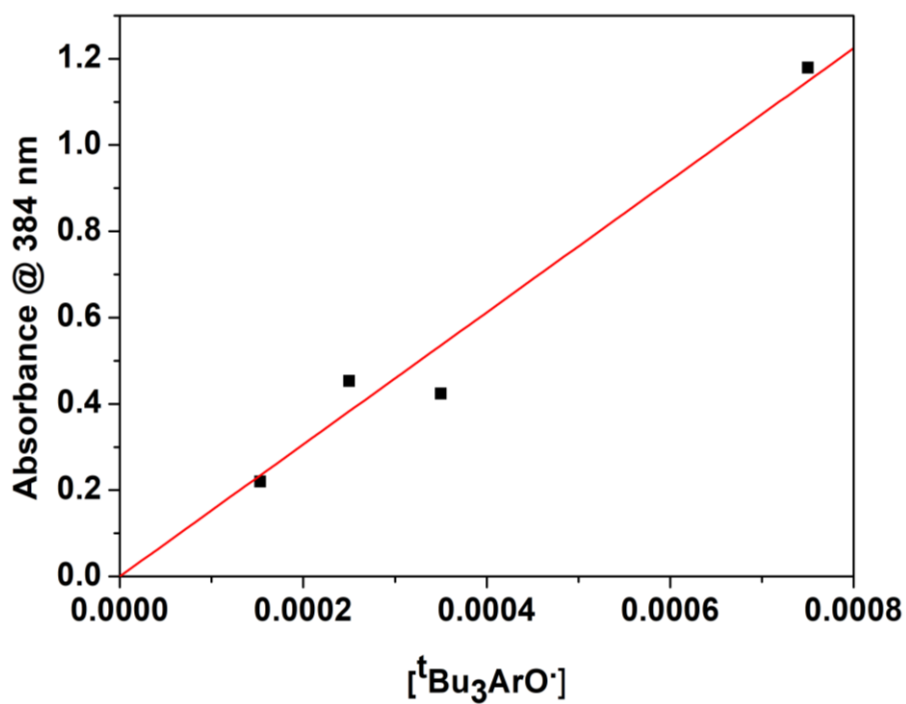


Figure A27. Plot of the absorbance vs. concentration at $\lambda = 384$ nm for the 2,4,6-tris-*tert*-butylphenoxy radical in DMF.

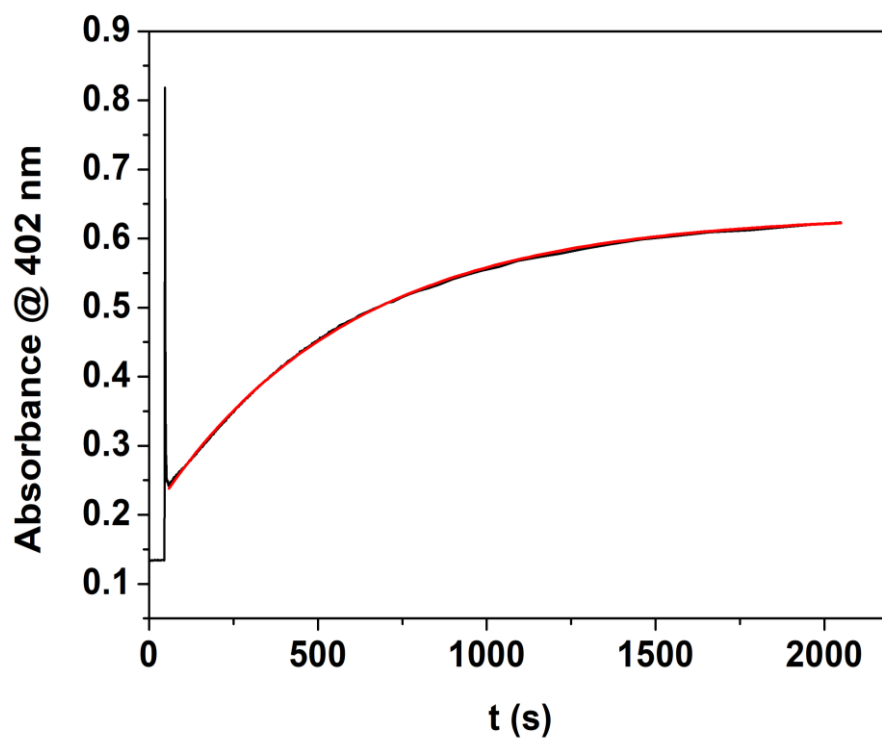


Figure A28. Plot of the absorbance at $\lambda = 402$ nm against time during the reaction between **1** (DMF, 25 °C) and 2,4,6-TTBP (1000 equiv.). Red line = fit.

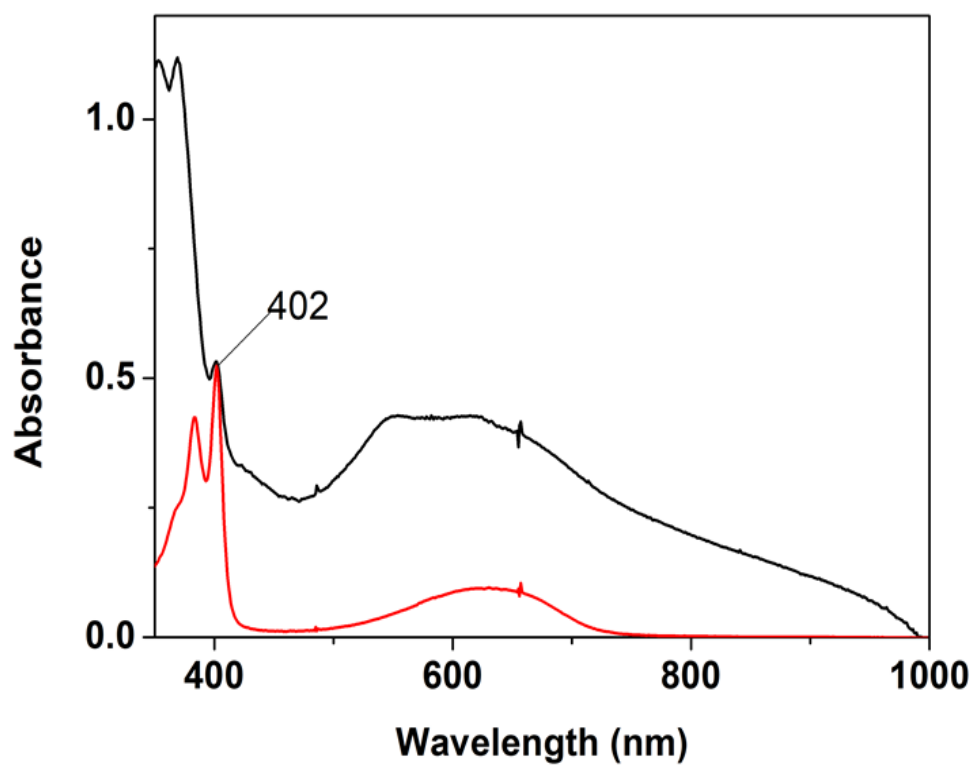


Figure A29. Electronic absorption spectra (DMF, 25 °C) of the independently synthesized 2,4,6-tris-*tert*-butylphenoxy radical (red trace) and of the reaction between **1** and an excess of 2,4,6-TTBP (black trace).

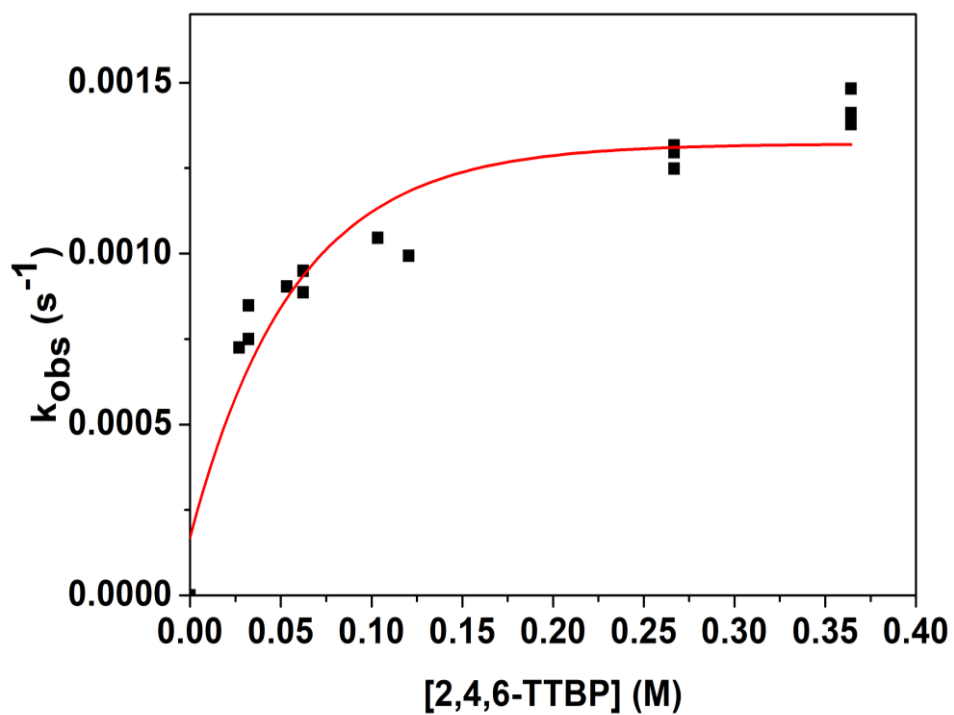


Figure A30. Plot of k_{obs} against [2,4,6-TTBP] for the reaction between complex **1** and 2,4,6-TTBP.

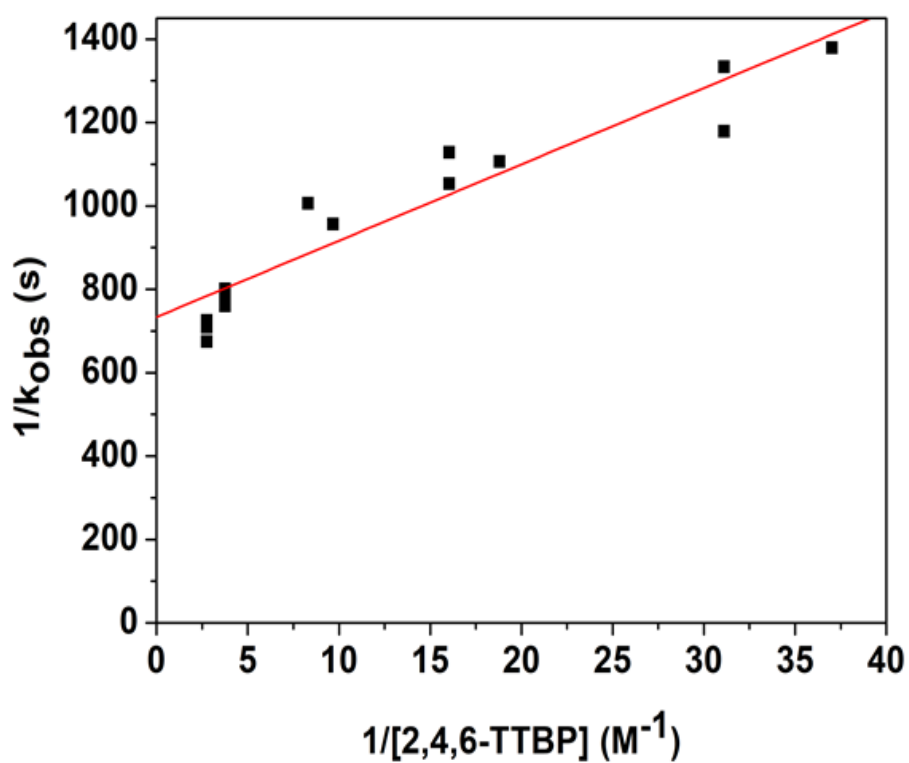
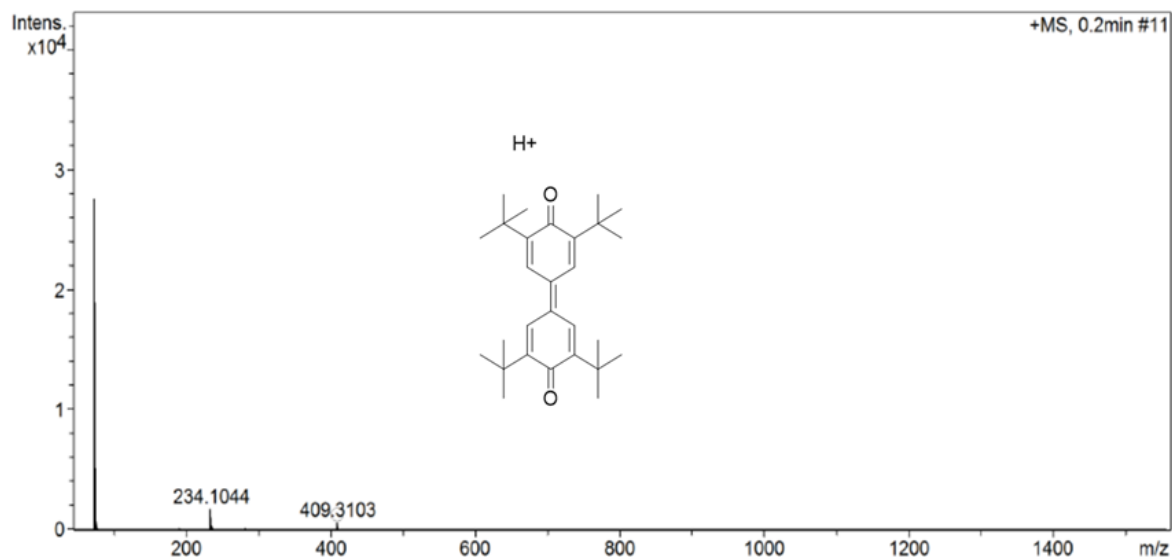


Figure A31. Plot of $1/k_{obs}$ against $1/[2,4,6-TTBP]$.



Meas. m/z	#	Ion Formula	m/z	err [mDa]	err [ppm]	rdb	N-Rule	e ⁻ Conf	mSigma
409.310274	1	C ₂₈ H ₄₁ O ₂	409.310107	-0.2	-0.4	8.5	ok	even	53.8

Figure A32. Positive mode ESI-MS spectrum of the reaction mixture of **1** and 2,6-DTBP showing the formation of 3,3',5,5'-tetra-tert-butyl-[1,1'-bis(cyclohexane)]-2,2',5,5'-tetraene-4,4'-dione (TTBTD).

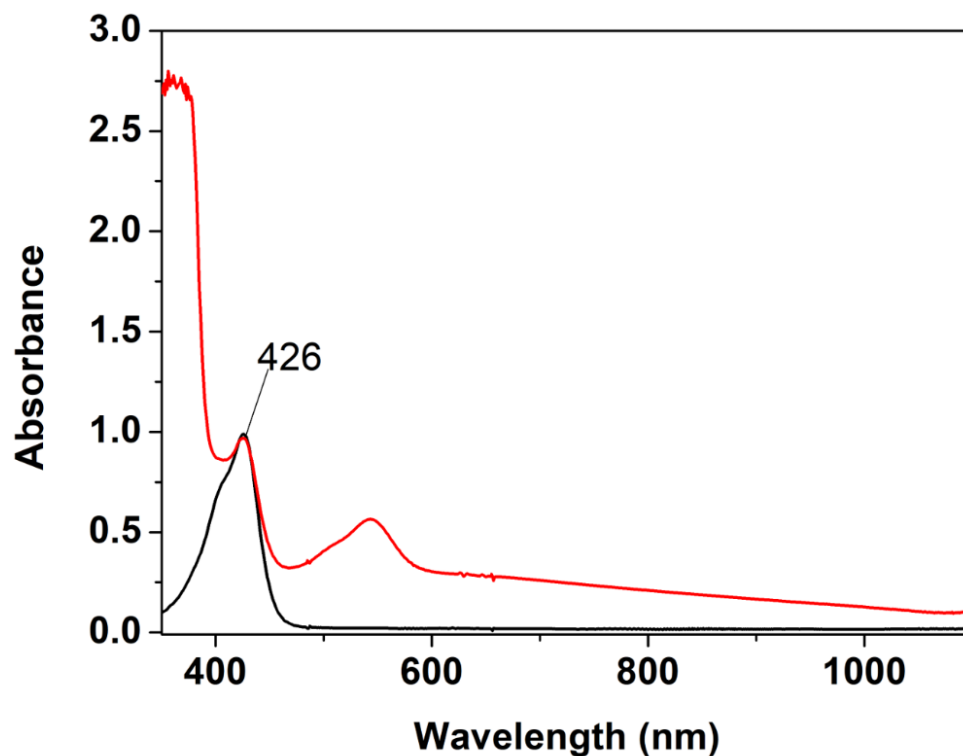


Figure A33. Electronic absorption spectra (DMF, 25 °C) of TTBTD (black trace) and of the reaction between **1** and an excess of 2,6-DTBP (red trace).

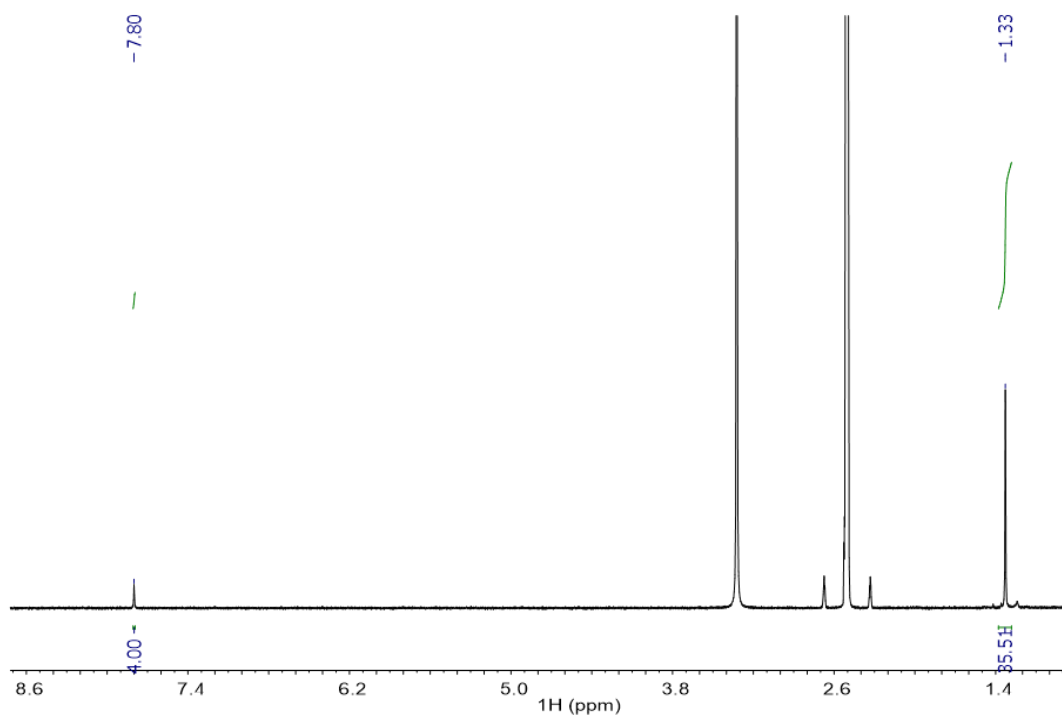


Figure A34. ^1H NMR spectrum (400 MHz, DMSO-D_6) of 3,3',5,5'-tetra-tert-butyl-[1,1'-bis(cyclohexane)]-2,2',5,5'-tetraene-4,4'-dione (TTBDT).

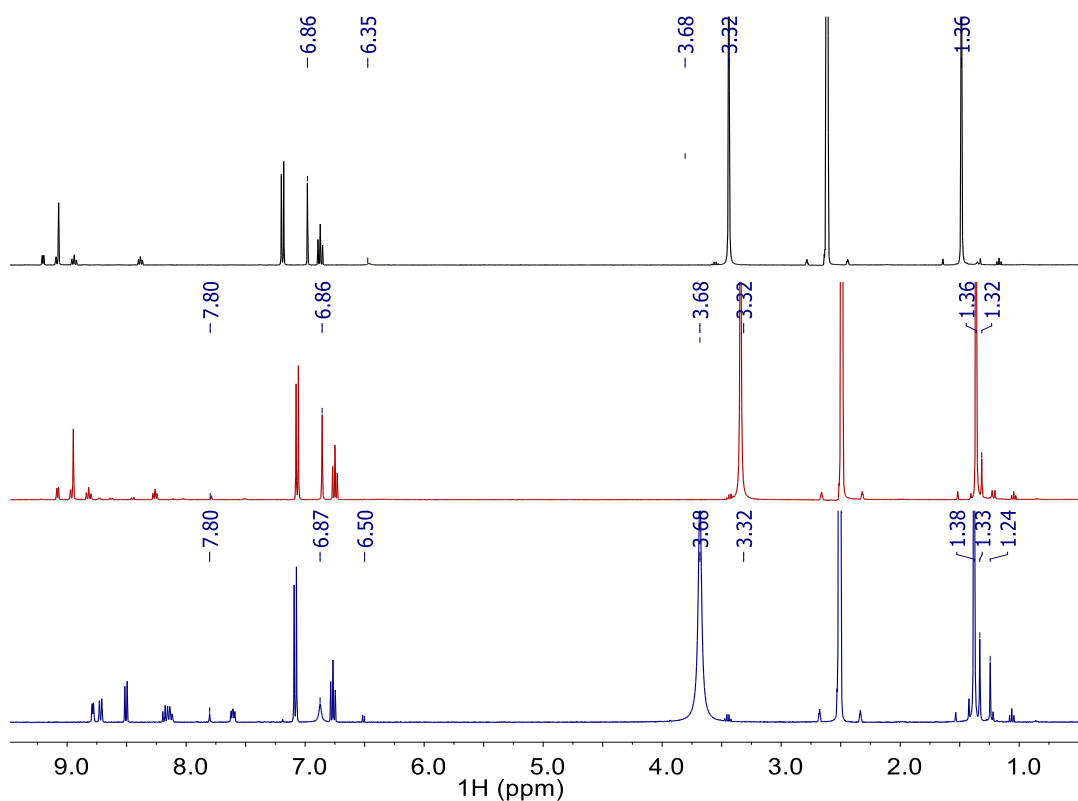


Figure A35. ^1H NMR spectra (400 MHz, DMSO-D_6) of the reaction between **1** and 2,6-DTBP (25 equiv.).

Black = 0 s, Red = 900 s, Blue = 4500 s. H_2O : $\delta = 3.32\text{-}3.68$ ppm.

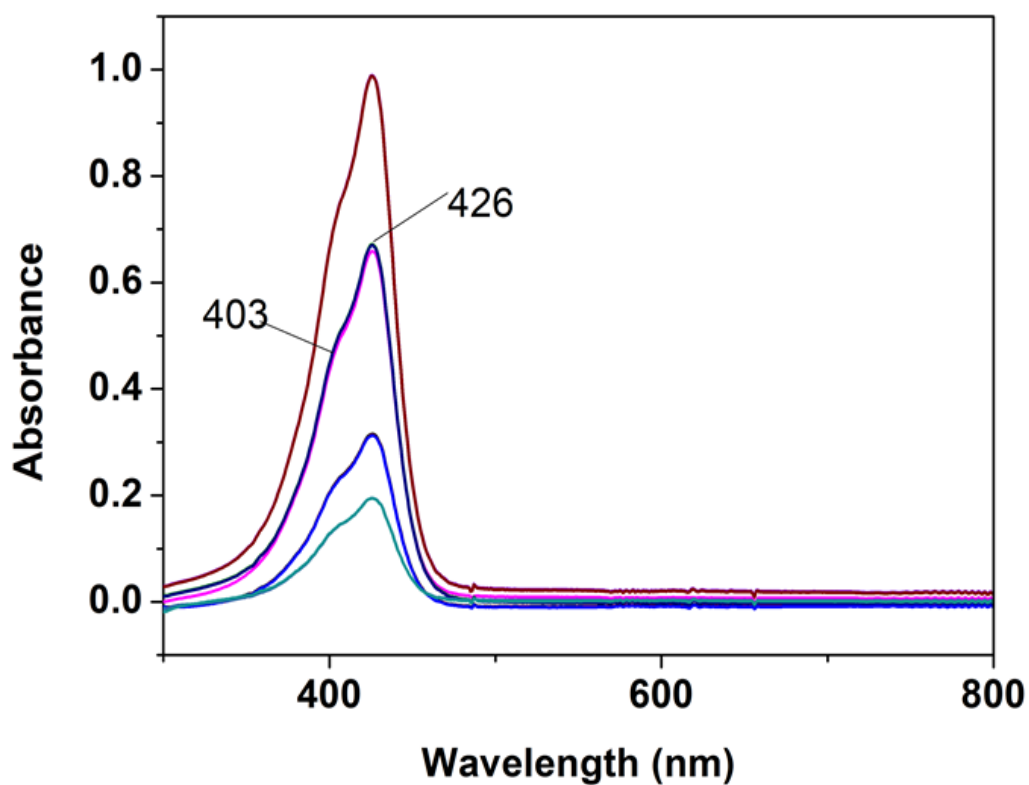


Figure A36. Electronic absorption spectra of TTBTd at 25 °C in DMF. $\epsilon_{426 \text{ nm}} = 32400 \pm 550 \text{ M}^{-1}\text{cm}^{-1}$, $\epsilon_{403 \text{ nm}} = 23400 \pm 420 \text{ M}^{-1}\text{cm}^{-1}$.

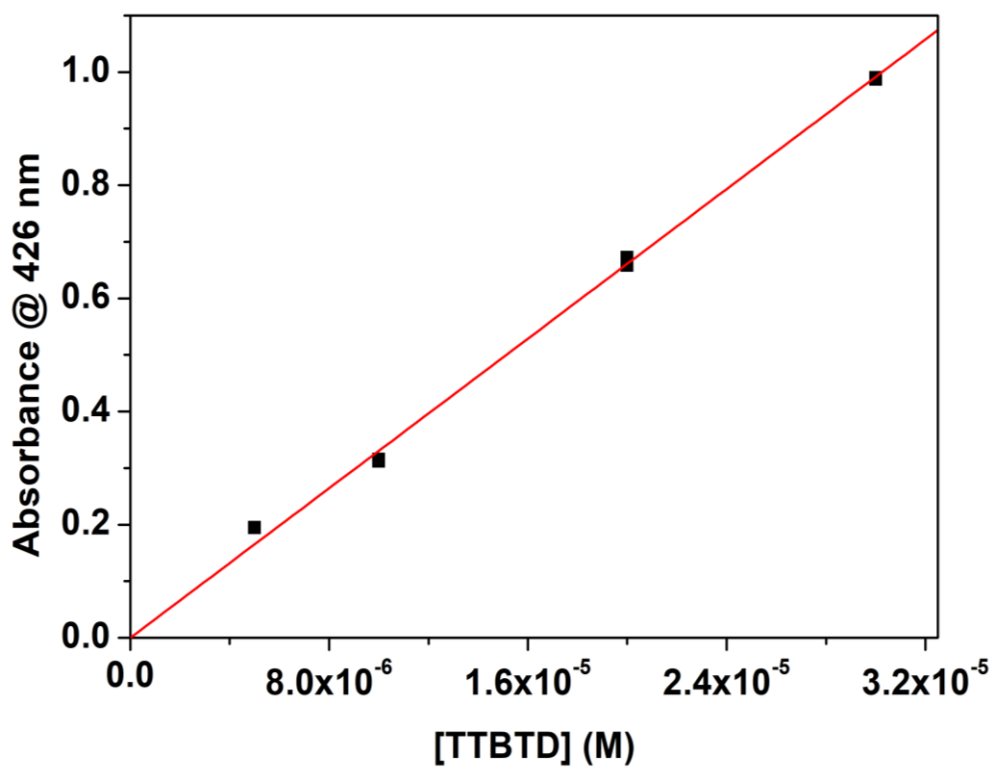


Figure A37. Plot of the absorbance vs. concentration at $\lambda = 426 \text{ nm}$ for TTBTd in DMF.

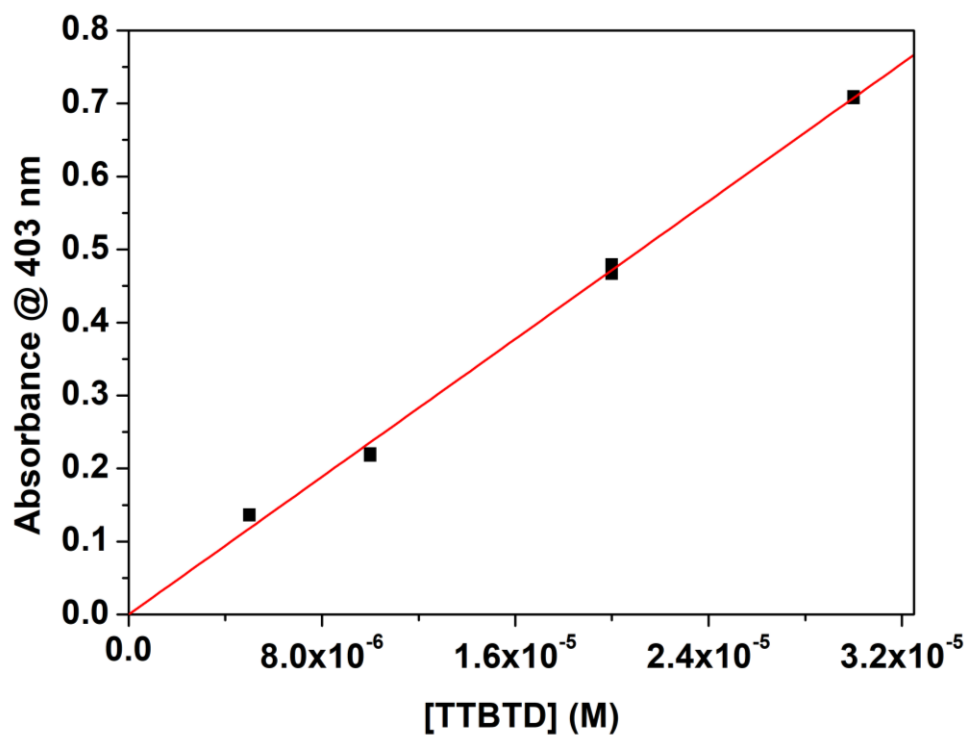


Figure A38. Plot of the absorbance vs. concentration at $\lambda = 403$ nm for TTBTD in DMF.

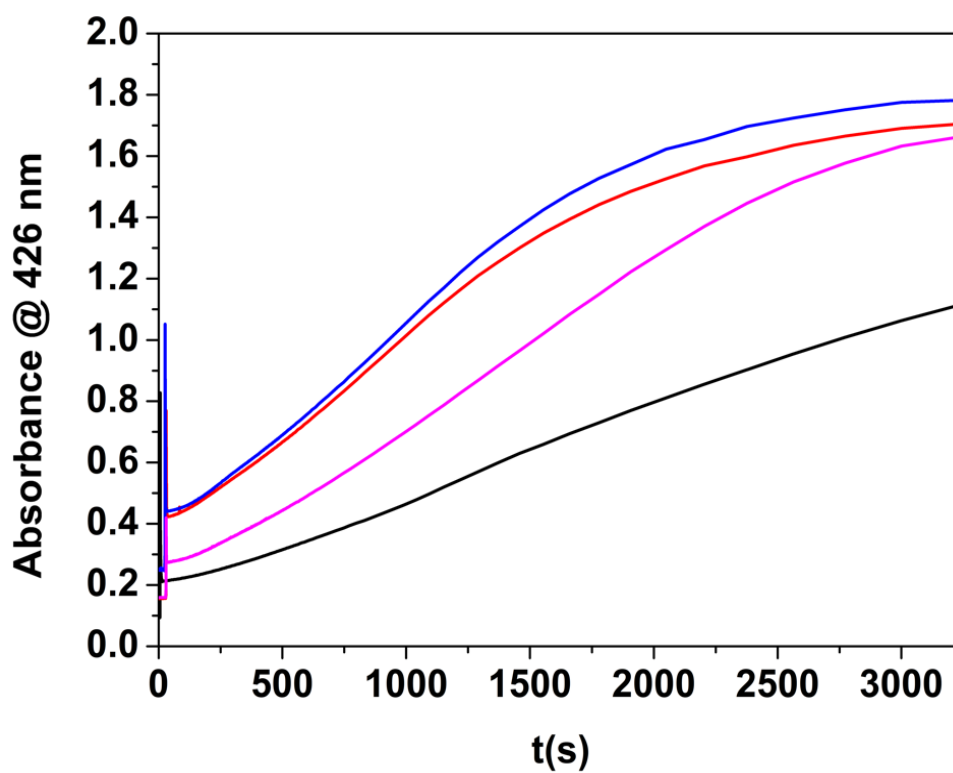


Figure A39. Plots of the absorbance at $\lambda = 426$ nm versus time for the reaction between **1** and 2,6-DTBP.

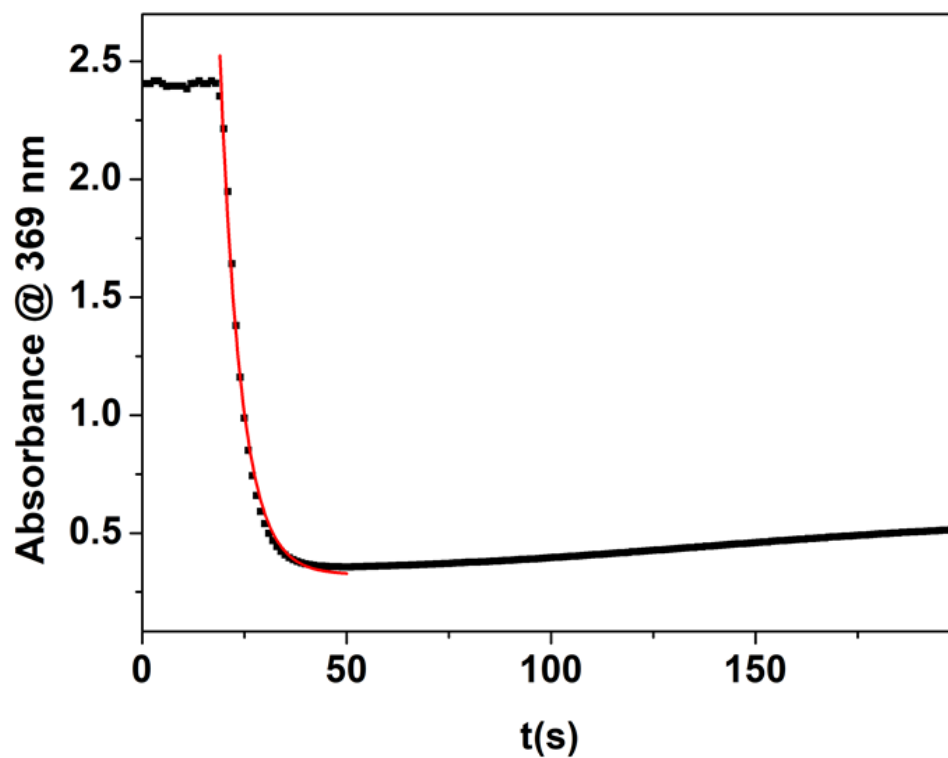


Figure A40. Plot of the absorbance at $\lambda = 369$ nm against time during the reaction between **1** and TEMPOH (50 equiv.) at 25 °C in DMF.

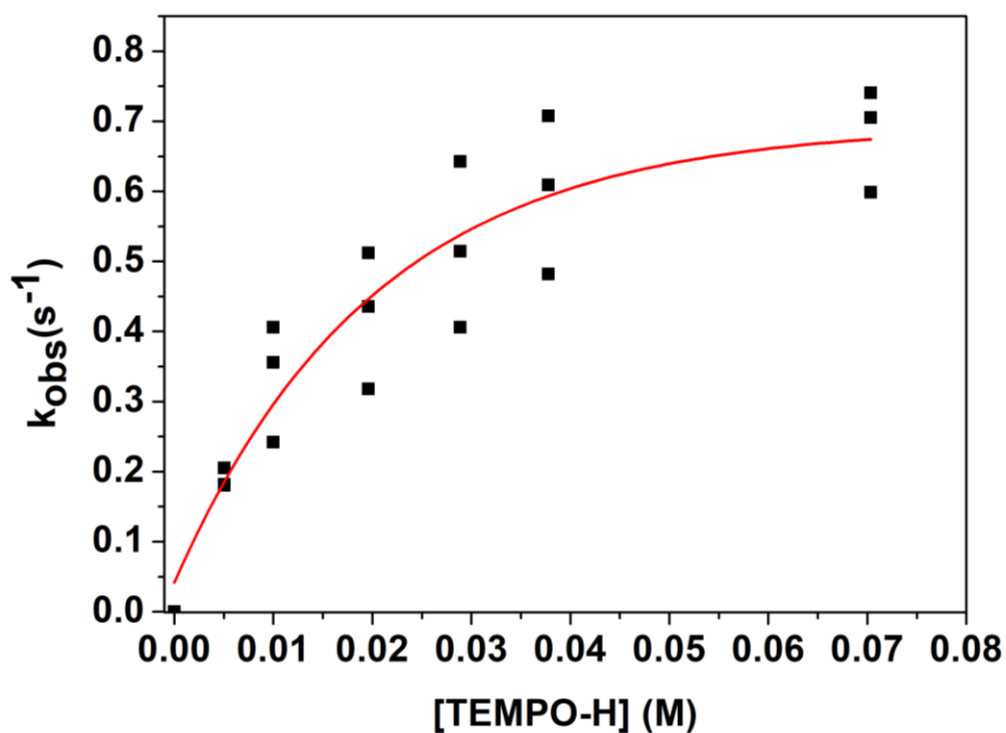


Figure A41. Plot of k_{obs} vs. [4-H-TEMPOH] determined for the reaction between **1** and 4-H-TEMPOH.

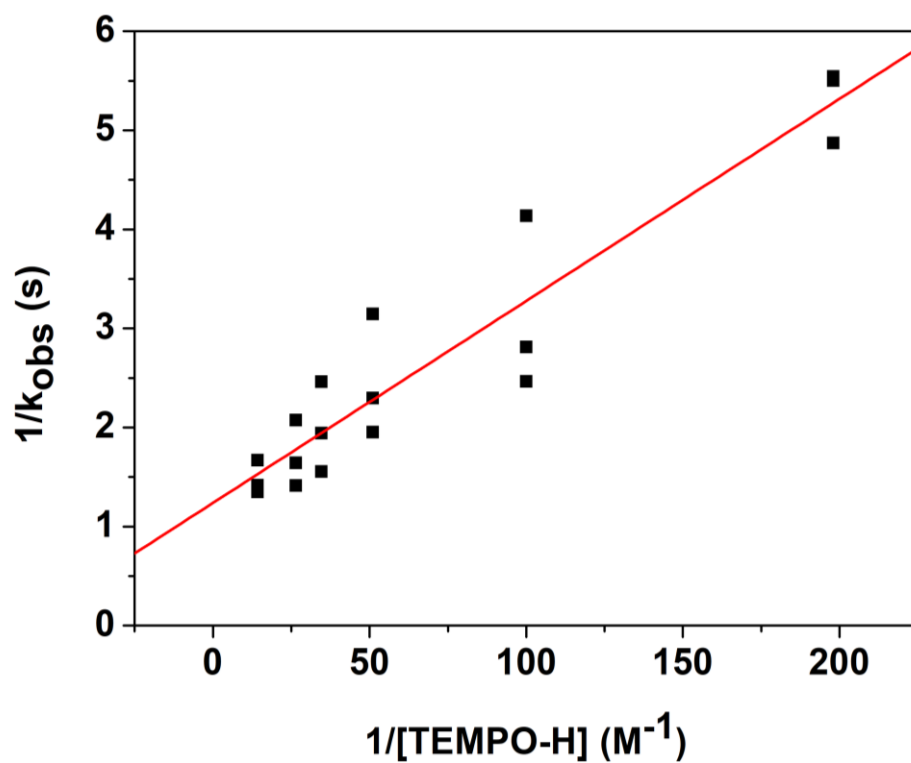


Figure A42. Plot of $1/k_{obs}$ versus $1/[4\text{-H-TEMPOH}]$.

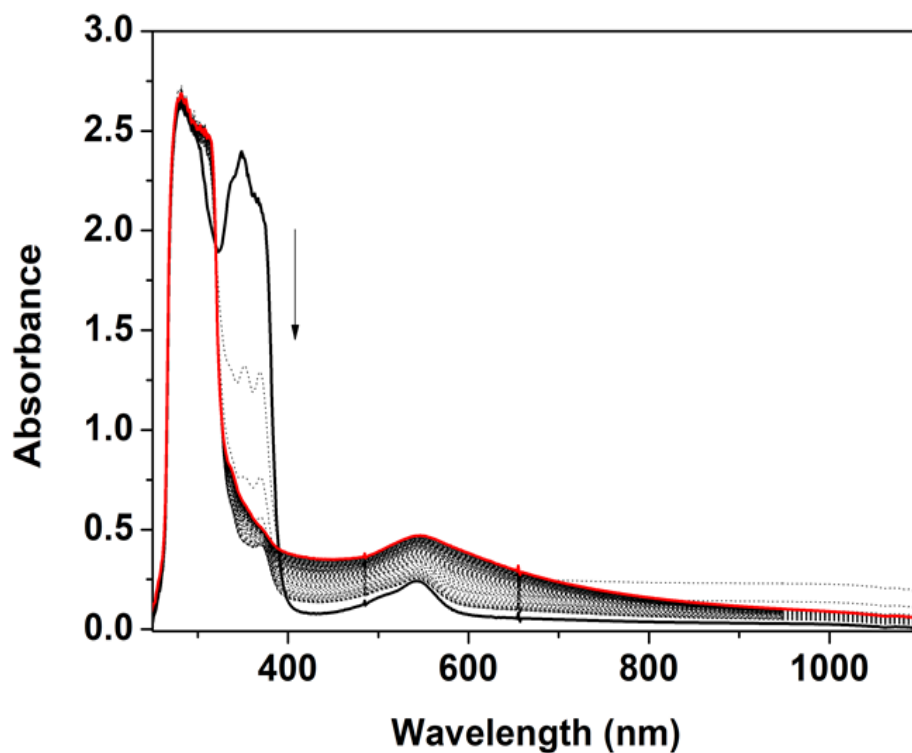


Figure A43. Electronic absorption spectra of the reaction between **1** (DMF, 25 °C, 0.75 mM) and 4-CH₃O-TEMPOH (50 equiv.), monitored for 600 s.

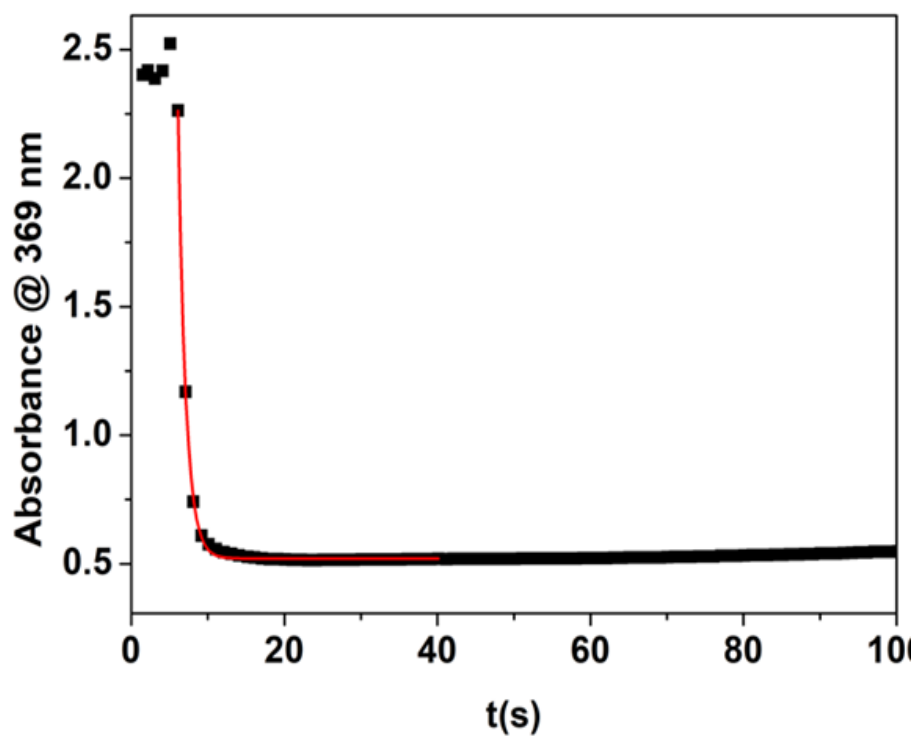


Figure A44. Plot of the absorbance at $\lambda = 369$ nm vs. time during the reaction between **1** (DMF, 25 °C) and 4-CH₃O-TEMPOH (100 equiv.).

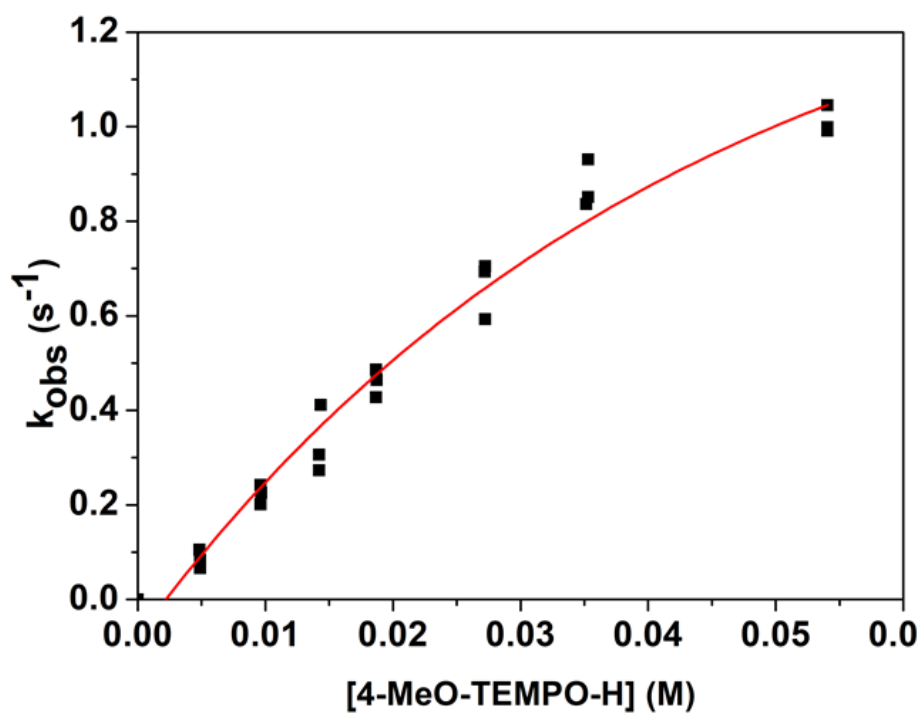


Figure A45. Plot of k_{obs} against [4-CH₃O-TEMPOH]. Due to our inability to fit accurately the decay of the band at $\lambda = 369$ nm with higher equivalents of substrate, k_1 was estimated to be 1.2 s⁻¹.

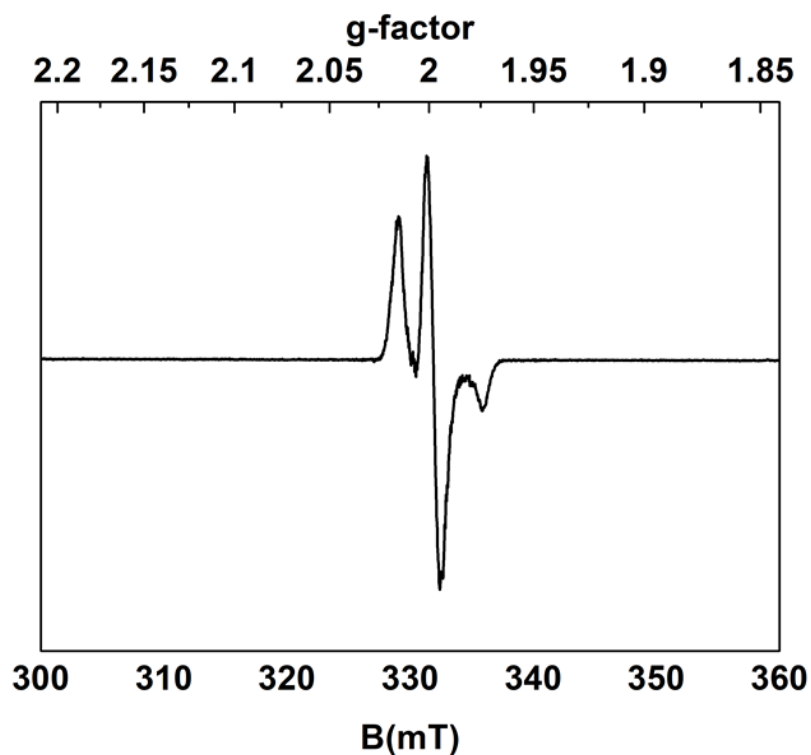


Figure A46. X-Band EPR spectrum of the reaction mixture of **1** with 4-CH₃O-TEMPOH (200 equiv.). The spectrum was acquired from a frozen DMF solution and measured at 77 K with a 2.02 mW microwave power and a 0.3 mT modulation amplitude

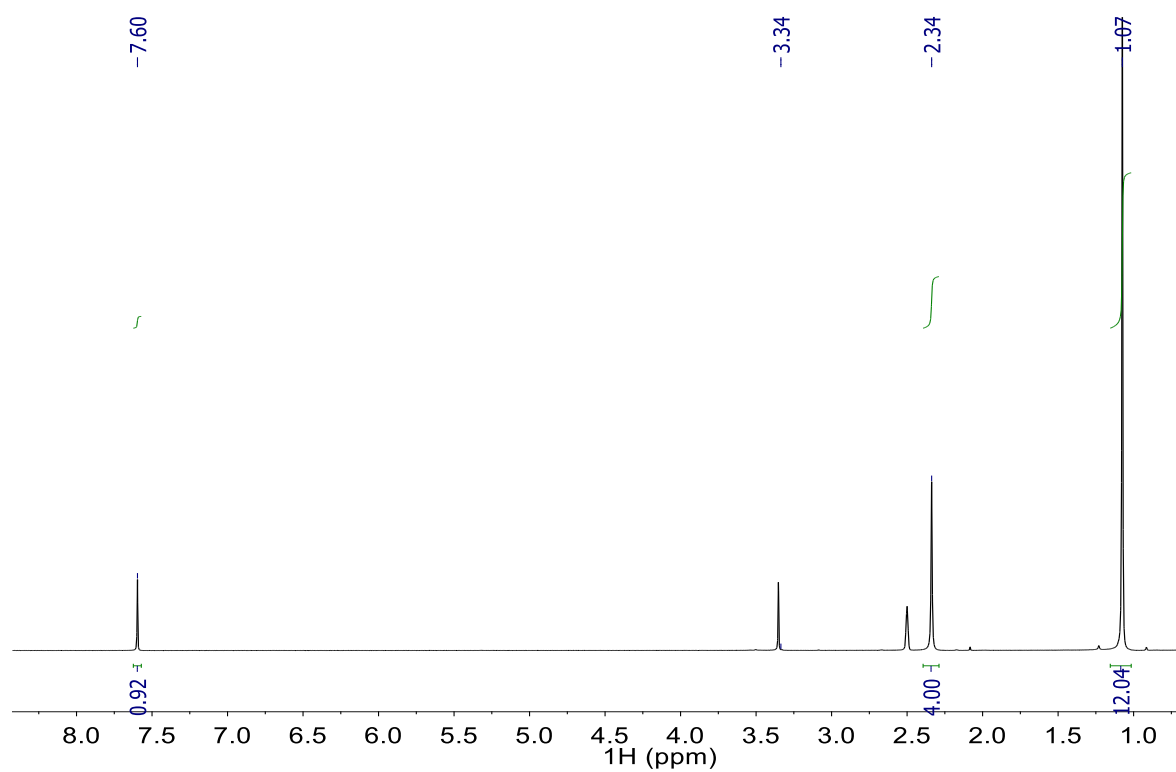


Figure A47. ¹H NMR (400 MHz, DMSO-D₆) of 4-oxo-TEMPOH.

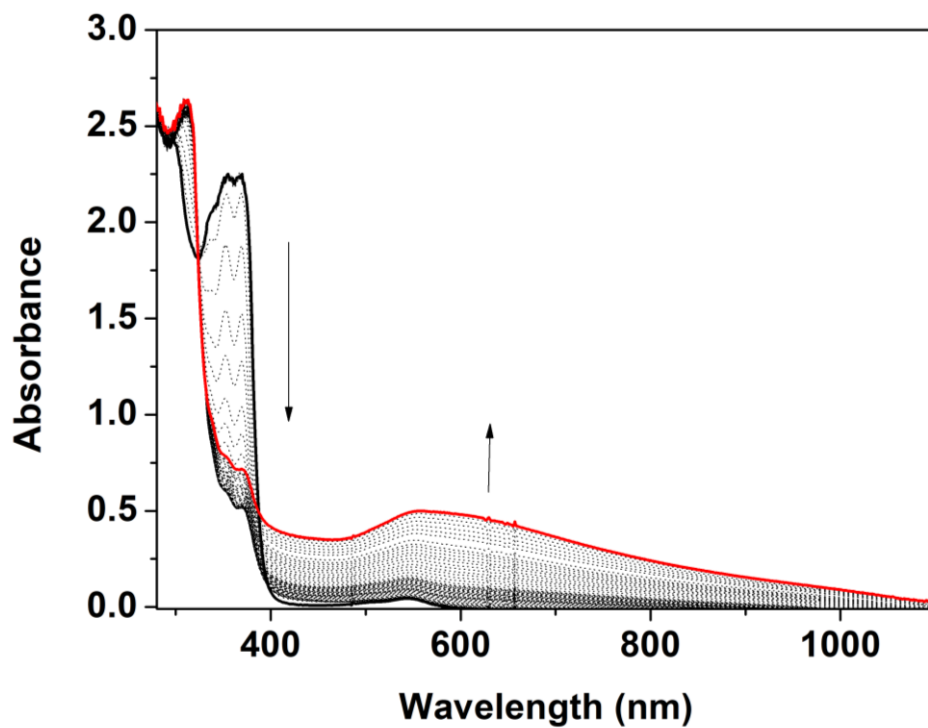


Figure A48. Electronic absorption spectra of the reaction between **1** (DMF, 25 °C, 0.6 mM) and 4-oxo-TEMPOH (25 equiv.), monitored for 600 s.

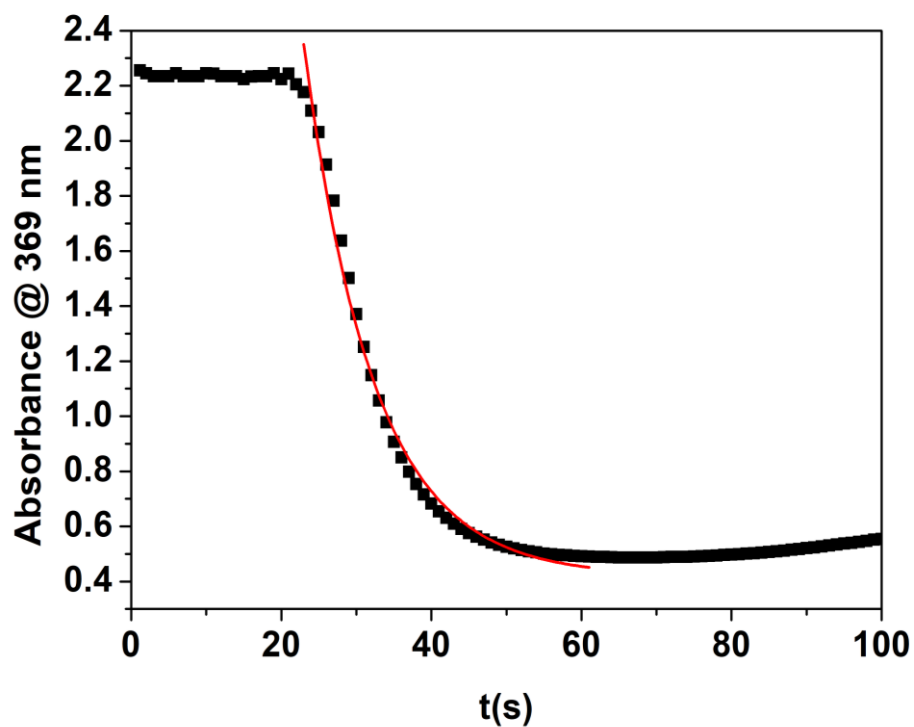


Figure A49. Plot of the absorbance at $\lambda = 369$ nm against time during the reaction between **1** (DMF, 25 °C, 0.6 mM) and 4-oxo-TEMPOH (25 equiv.).

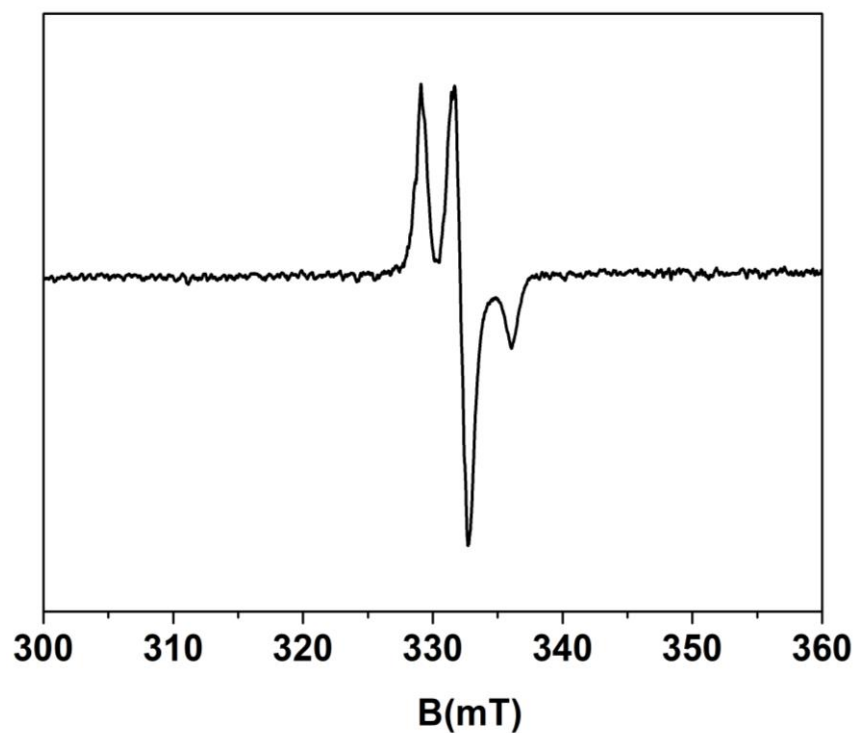


Figure A50. X-Band EPR spectrum of the reaction mixture of **1** with 4-oxo-TEMPOH (100 equiv.). The spectrum was acquired from a frozen DMF solution and measured at 77 K with a 2.02 mW microwave power and a 0.3 mT modulation amplitude.

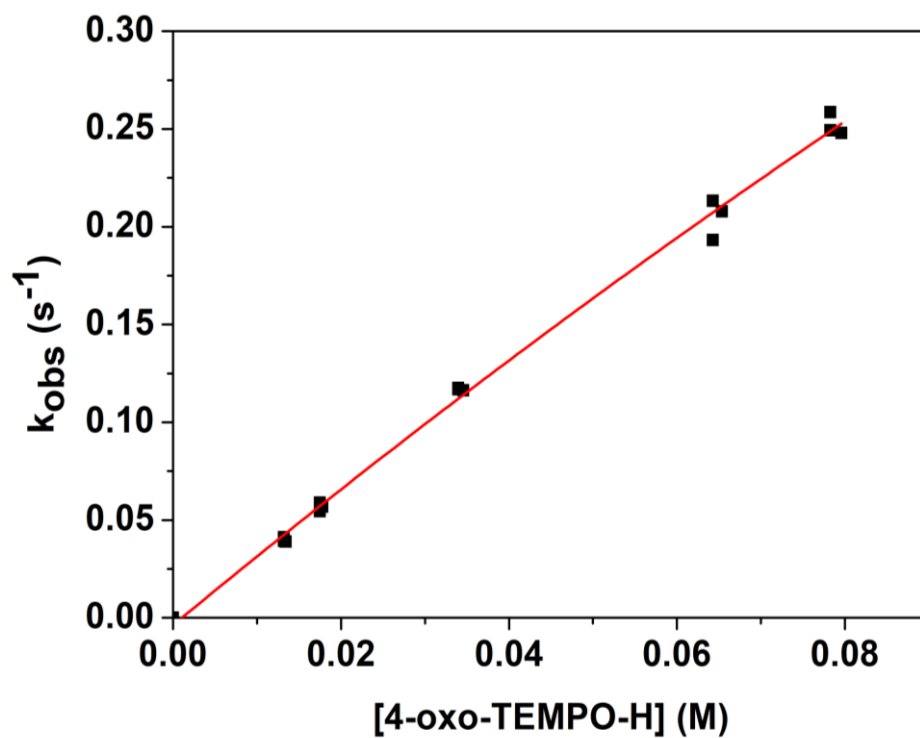


Figure A51. Plot of k_{obs} against [4-oxo-TEMPOH].

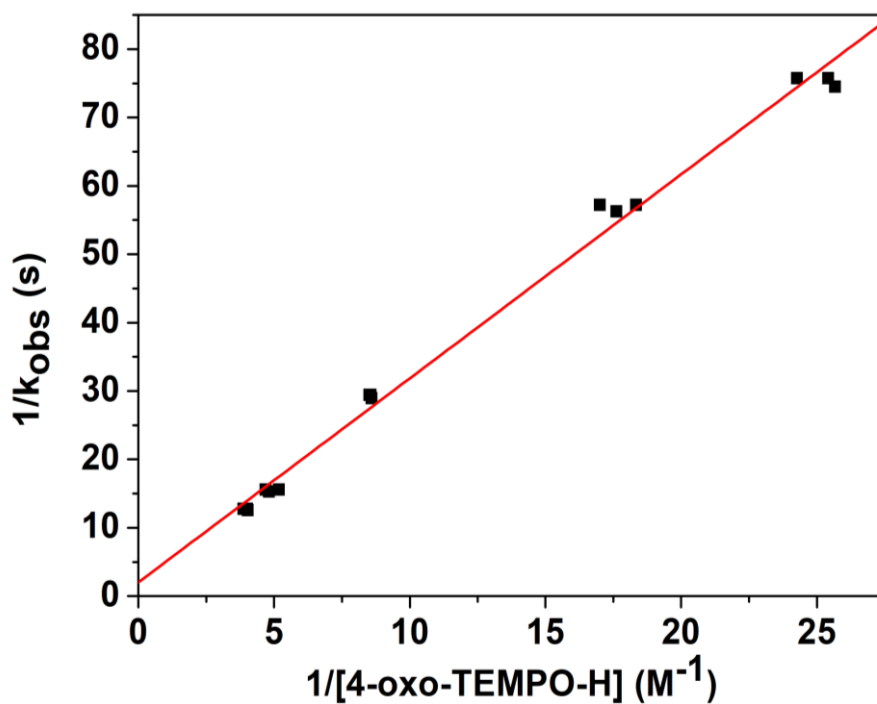


Figure A52. Plot of $1/k_{\text{obs}}$ versus $1/[4\text{-oxo-TEMPOH}]$.

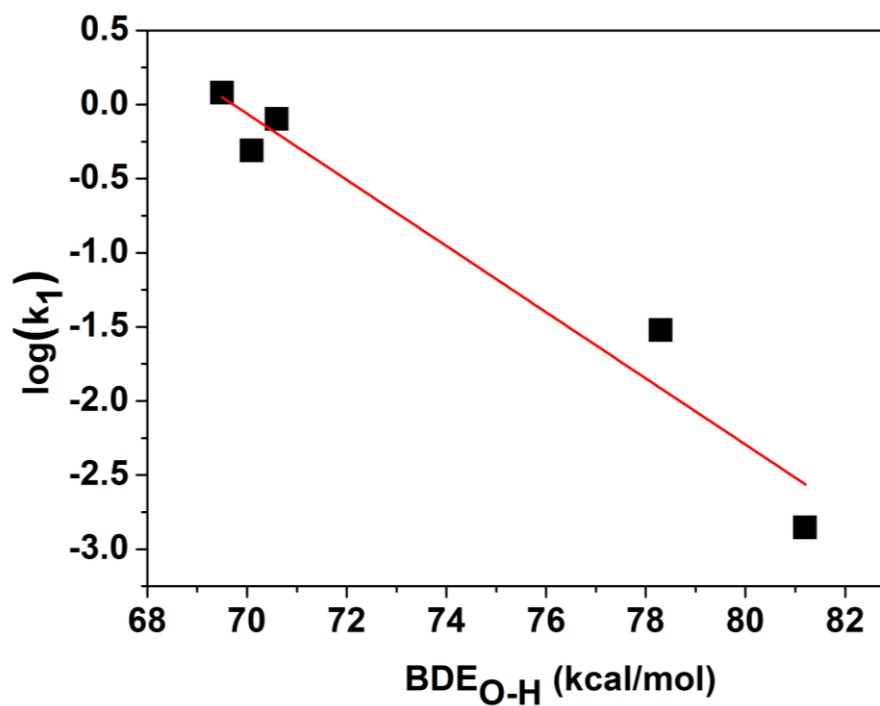


Figure A53. Plot of $\log(k_1)$ against the $\text{BDE}_{\text{O-H}}$ of the substrates. Slope = -0.21.

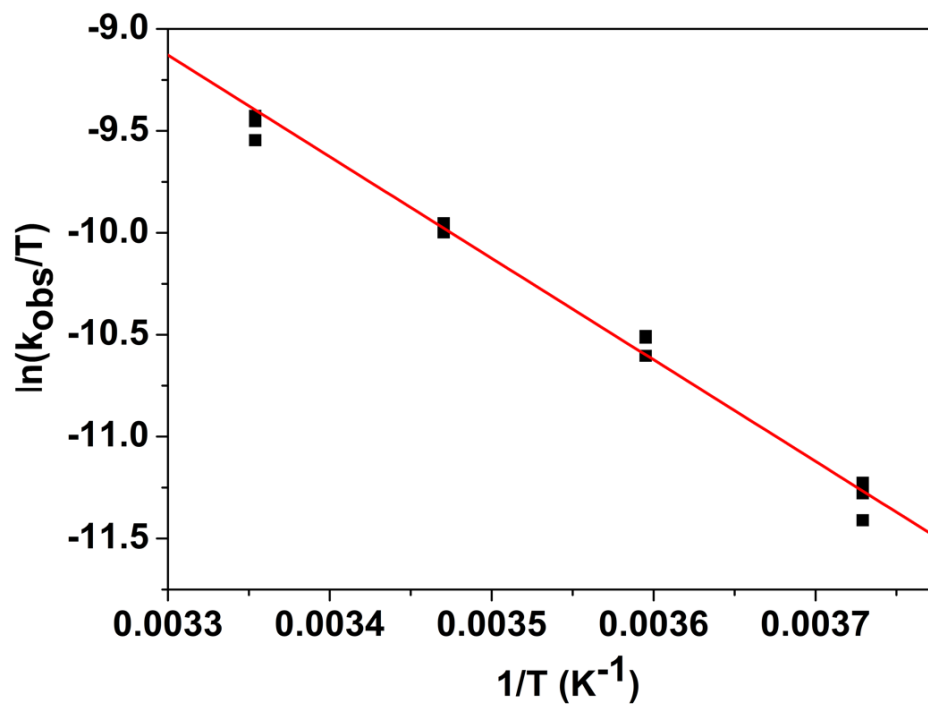


Figure A54. Plot of $\ln(k_{\text{obs}}/T)$ versus $1/T$ for **1** in its reaction with 4-CH₃O-2,6-DTBP. $\Delta H^\ddagger = 9.9(4)$ kcal/mol; $\Delta S^\ddagger = -33(3)$ cal mol⁻¹K⁻¹.

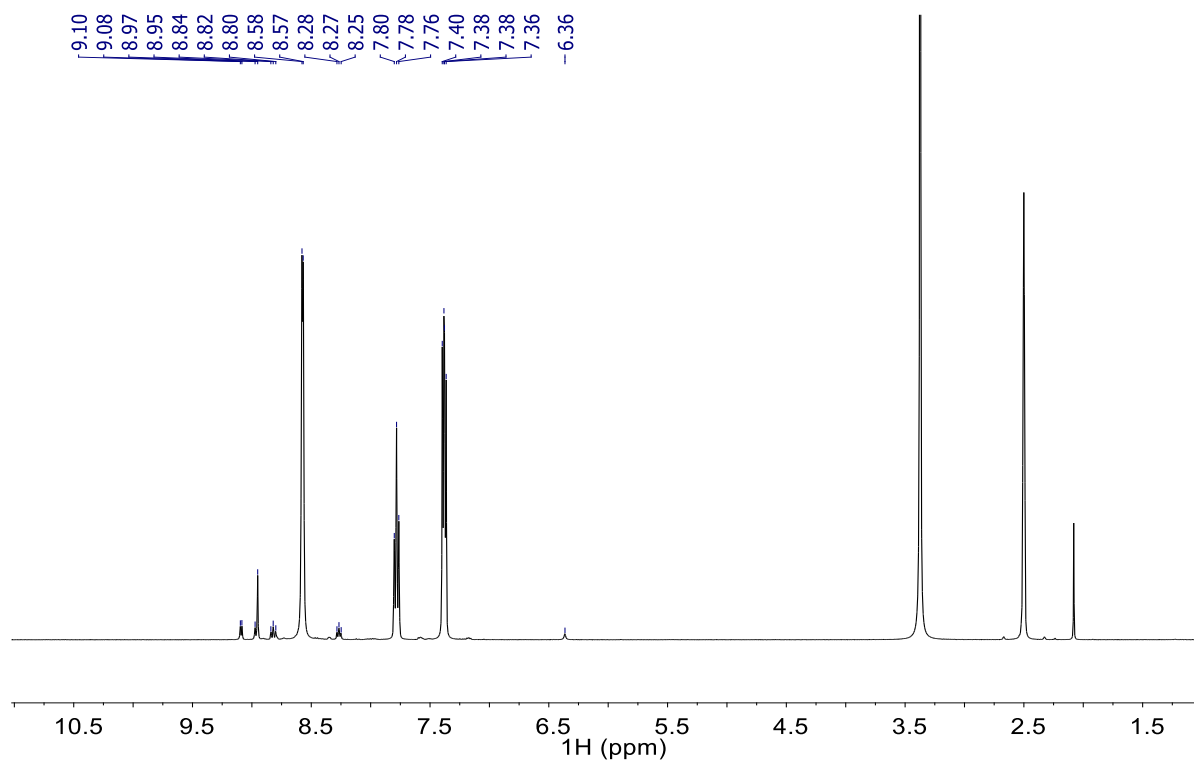


Figure A55. ¹H NMR (400 MHz, DMSO-D₆) of the reaction between **1** and excess pyridine.

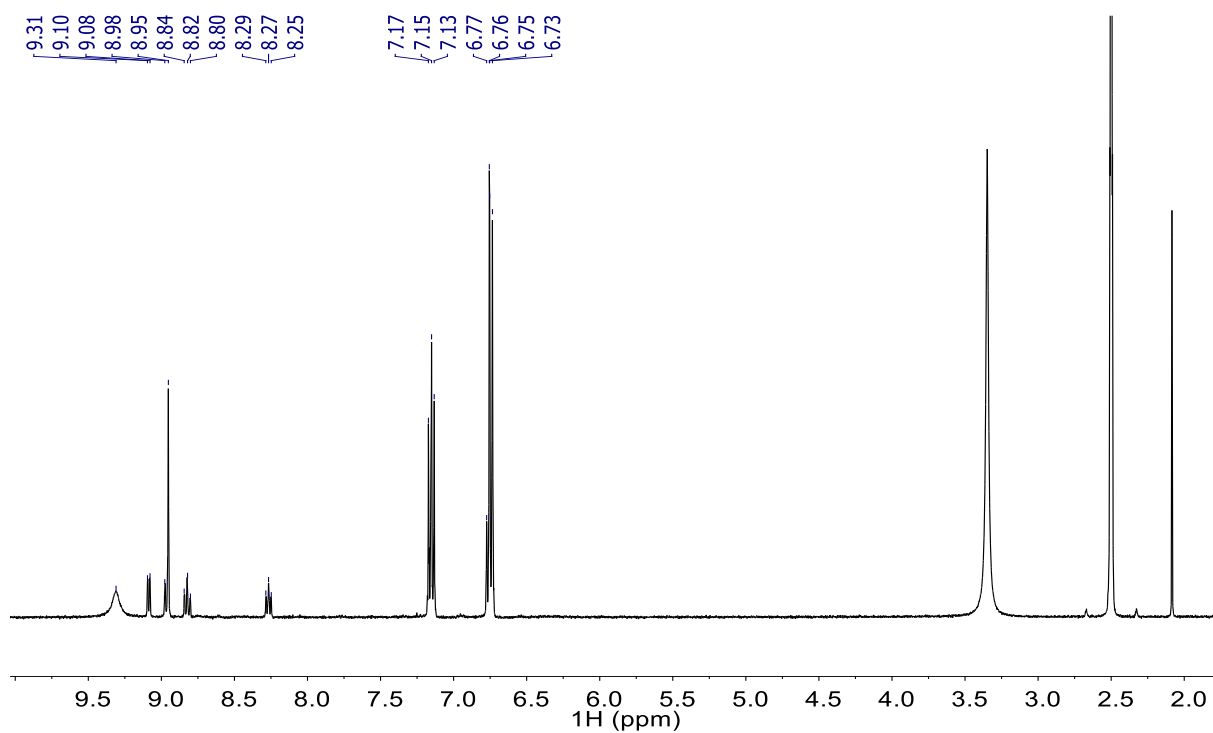


Figure A56. ¹H-NMR (400 MHz, DMSO-D₆) of the reaction between **1** and excess phenol.

A.2 Chapter 3

Table A1. Crystal structure data and refinement for **1**.

CCDC no.	2079645	ρ_{calc} (g/cm ³)	2.388
Empirical formula	C ₁₅ H ₁₁ AuCl ₃ N ₃ O ₈	μ (mm ⁻¹)	8.446
Formula weight	664.58	F(000)	632
Temperature (K)	100(2)	Crystal size (mm ³)	0.25 x 0.15 x 0.08
Crystal system	Monoclinic	Radiation	MoK α ($\lambda = 0.71073$ Å)
Space group	P2 ₁	2 θ range for data collection (°)	2.931 to 28.359
a (Å)	8.1167(4)	Index ranges	-10 $\leq h \leq$ 10, -18 $\leq k \leq$ 18, -11 $\leq l \leq$ 11
b (Å)	13.8166(6)	Reflections collected	17712
c (Å)	8.3177(4)	Independent reflections	4568 [R(int) = 0.0231]
α (°)	90	Data/restraints/parameters	4568 / 98 / 283
β (°)	97.7580(10)	Goodness-of-fit on F ²	0.917
γ (°)	90	Final R* indices [$I > 2\sigma(I)$]	R1 = 0.0141, wR2 = 0.0325
Volume (Å ³)	924.25(8)	R indices (all data)	R1 = 0.0156, wR2 = 0.0329
Z	2	Largest diff. peak and hole (e.Å ⁻³)	0.944 / -0.731

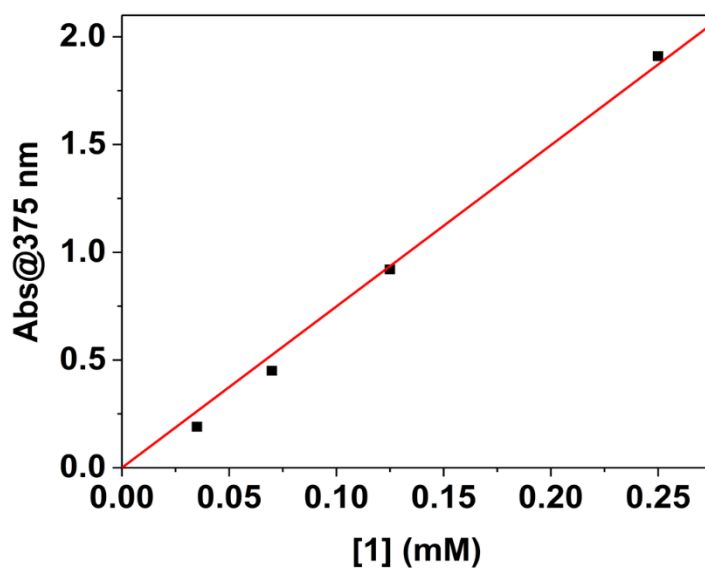


Figure A57. Plot of the absorbance vs. concentration for **1** at $\lambda = 375$ nm.

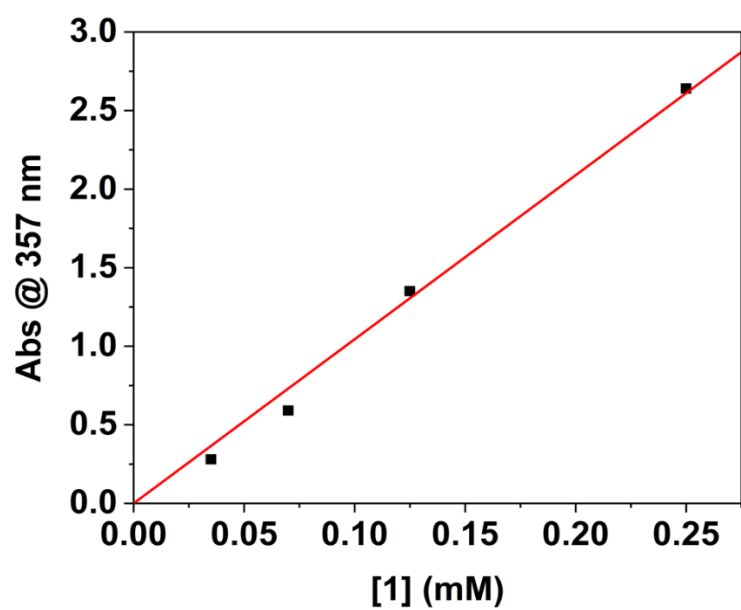


Figure A58. Plot of the absorbance vs. concentration for **1** at $\lambda = 357$ nm.

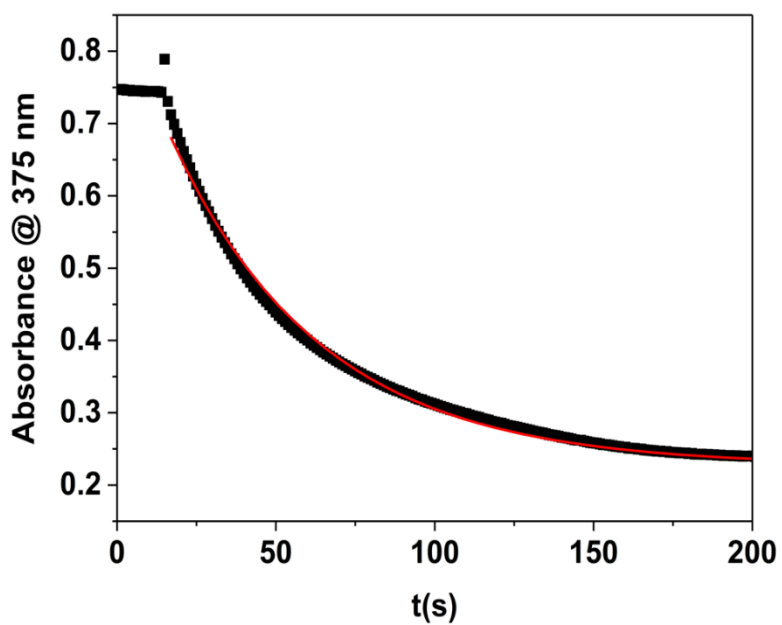


Figure A59. Plot of the absorbance at $\lambda = 375$ nm against time during the reaction between **1** and 4-CH₃O-2,6-DTBP (100 equiv.) at 25 °C in DMF.

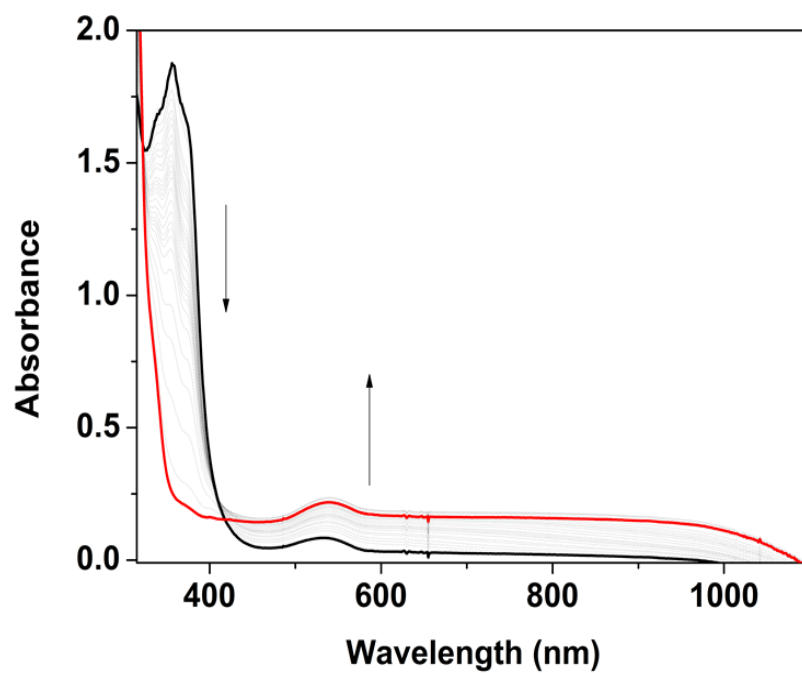


Figure A60. Electronic absorption spectra of the reaction of **1** (DMF, 25 °C, 0.17 mM) with 4-CH₃-2,6-DTBP (500 equiv.) monitored for 3000 s. black trace = 0 s, red trace = 3000 s.

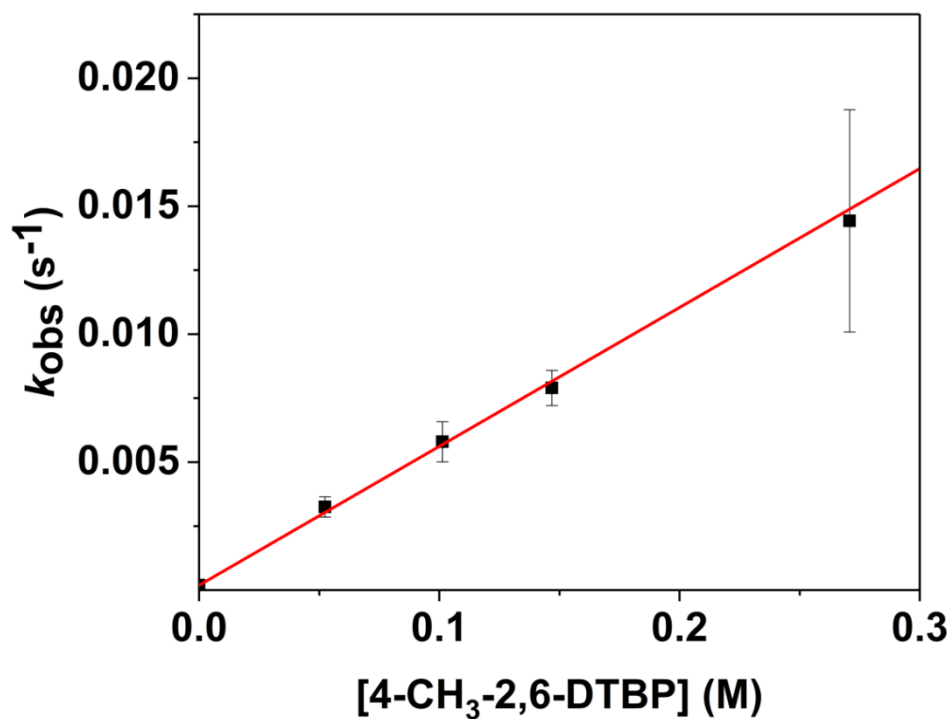


Figure A61. Plot of k_{obs} against [4-CH₃-2,6-DTBP] determined for the reaction between **1** and 4-CH₃-2,6-DTBP.

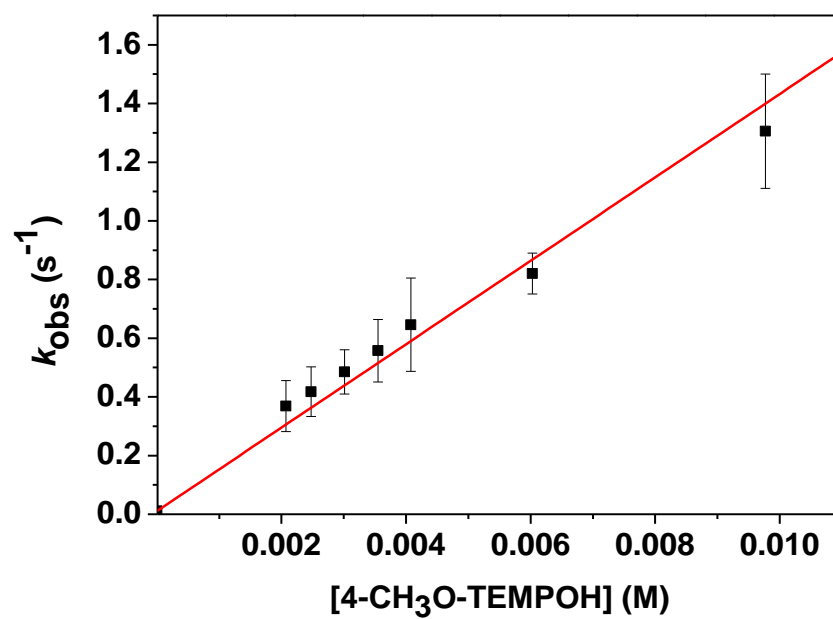


Figure A62. Plot of k_{obs} against [4-CH₃O-TEMPOH] determined for the reaction between **1** and 4-CH₃O-TEMPOH.

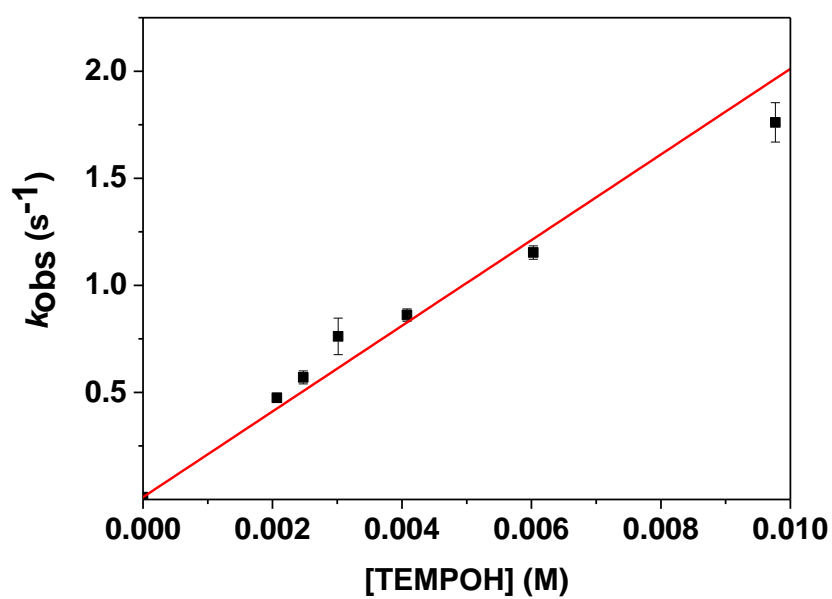


Figure A63. Plot of k_{obs} against [TEMPOH] determined for the reaction between **1** and TEMPOH.

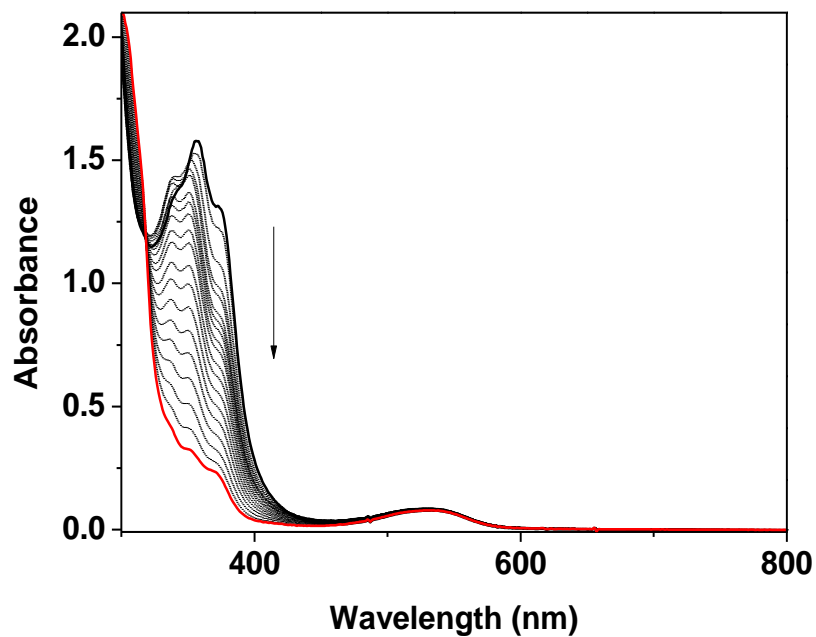


Figure A64. Electronic absorption spectra of the reaction of **1** (DMF, 25 °C, 0.15 mM) with 4-oxo-TEMPOH (20 equiv.) monitored for 100 s. black trace = 0 s, red trace = 100 s.

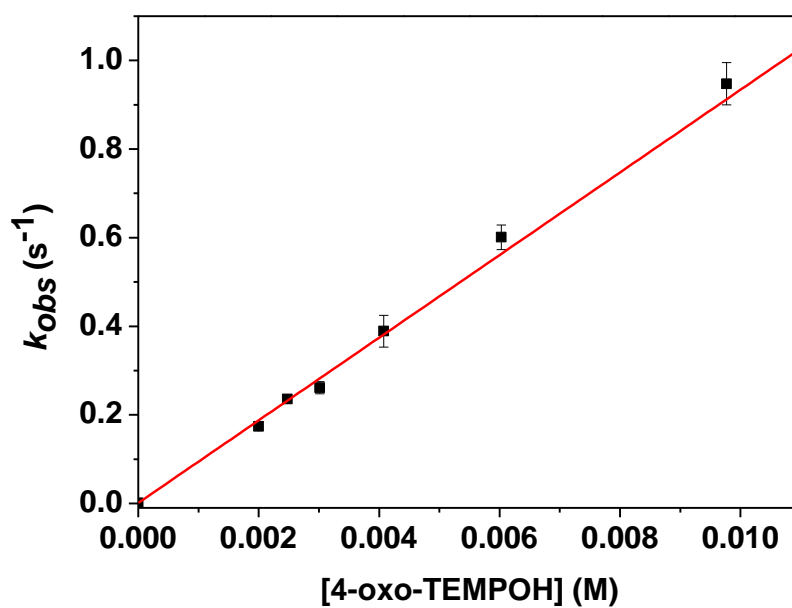


Figure A65. Plot of k_{obs} against $[4\text{-oxo-TEMPOH}]$ determined for the reaction between **1** and 4-oxo-TEMPOH.

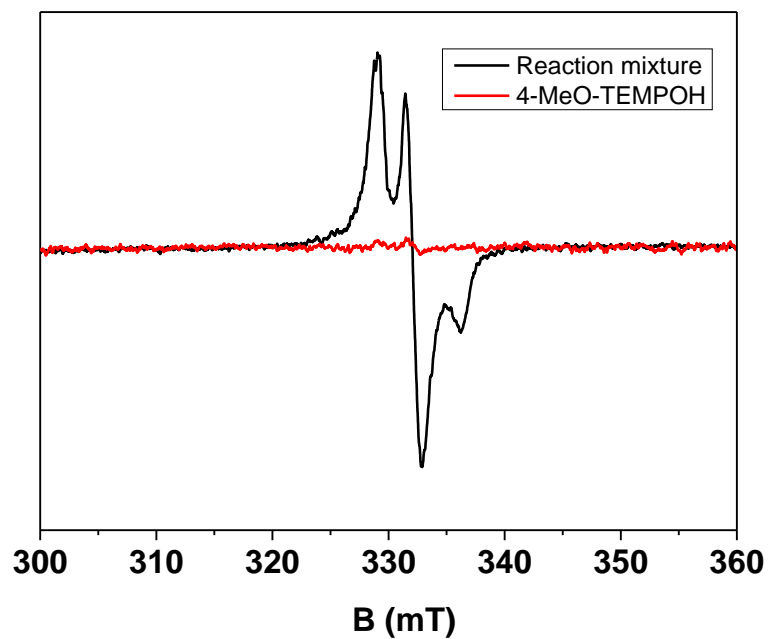


Figure A66. X-band EPR spectra of the reaction mixture of **1** with 4-CH₃O-TEMPOH (black trace) and of 4-CH₃O-TEMPOH alone (red trace) acquired from frozen DMF solutions at 77 K with a 2.01 mW microwave power and a 0.3 mT modulation amplitude.

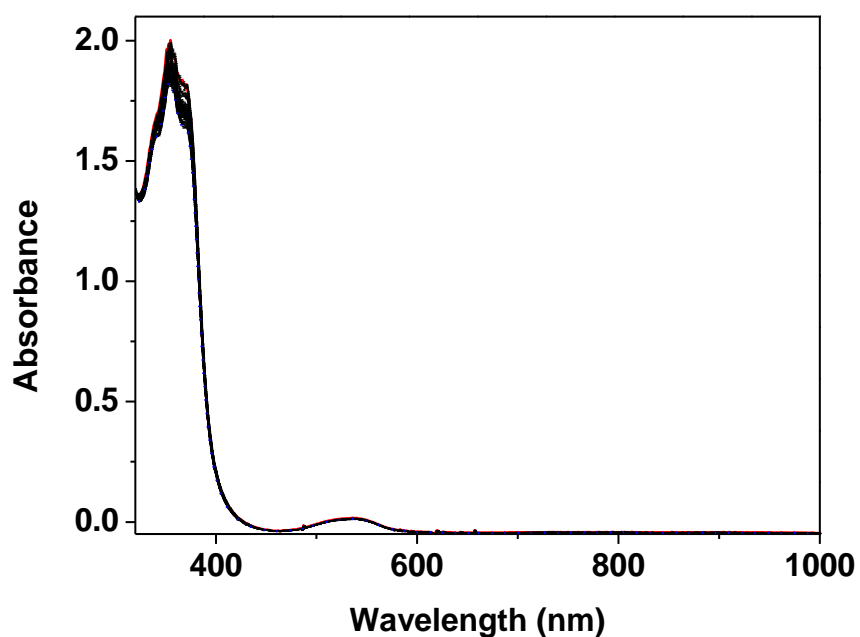


Figure A67. Change in the electronic absorption spectra of **1** upon addition of 20 equiv. benzoic acid (red trace, 20 equiv. benzoic acid).

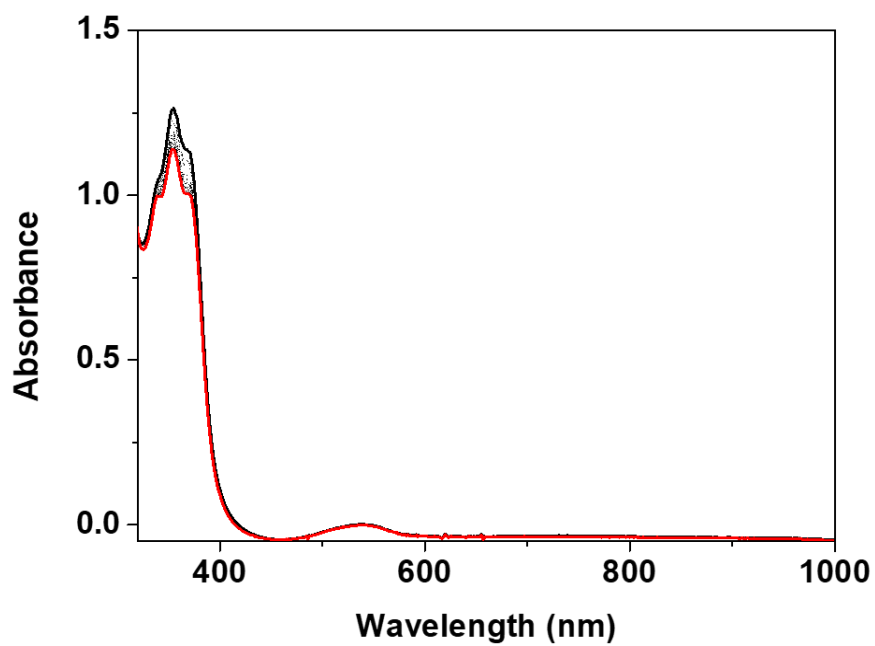


Figure A68. Change in the electronic absorption spectra of **1** upon addition of 20 equiv. acetic acid (red trace, 20 equiv. acetic acid).

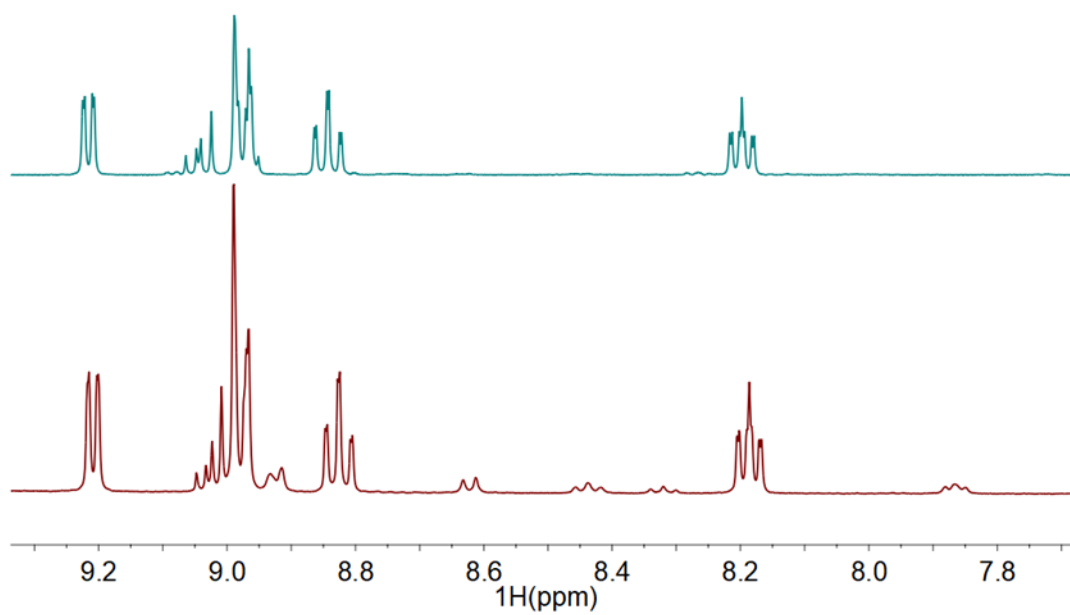


Figure A69. Selected region between 7.7 and 9.5 ppm of the ¹H NMR spectra (400 MHz, DMSO-D₆) of **1** before (green trace) and after (red trace) the addition of 20 equiv. of trifluoroacetic acid.

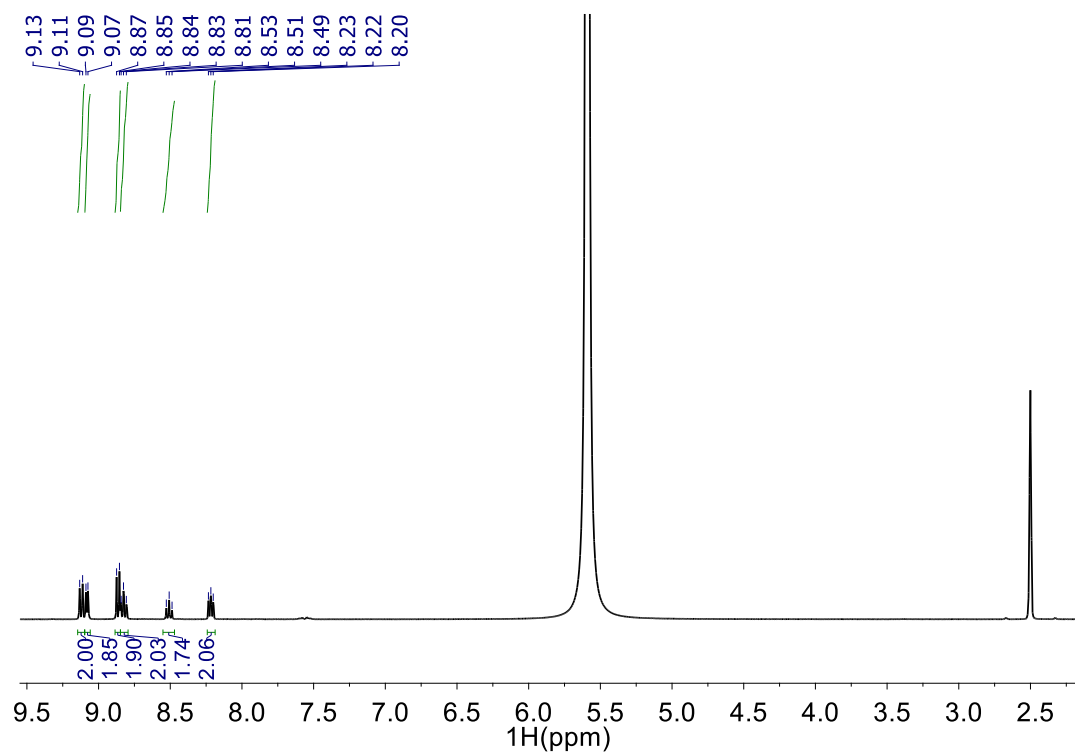


Figure A70. ^1H NMR spectra (400 MHz, DMSO-D_6) of free terpyridine after the addition of 2 equiv. of trifluoroacetic acid.

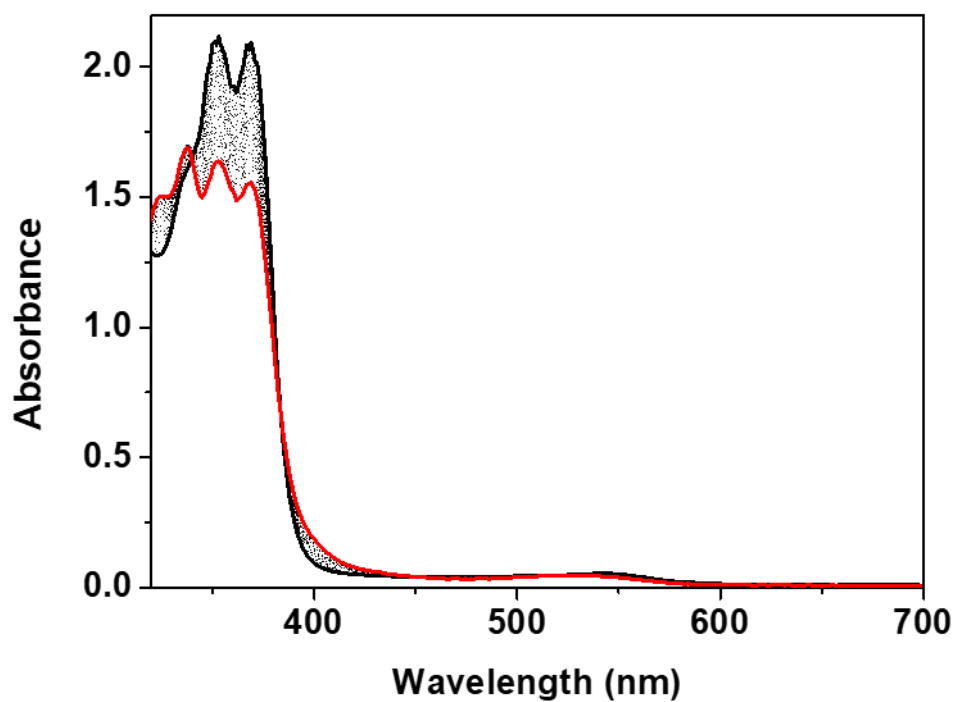


Figure A71. Change in the electronic absorption spectra of **2** upon the progressive addition of 1 equiv. of pyridinium triflate to yield 2H^+ (red trace, 15 equiv. pyridinium triflate).

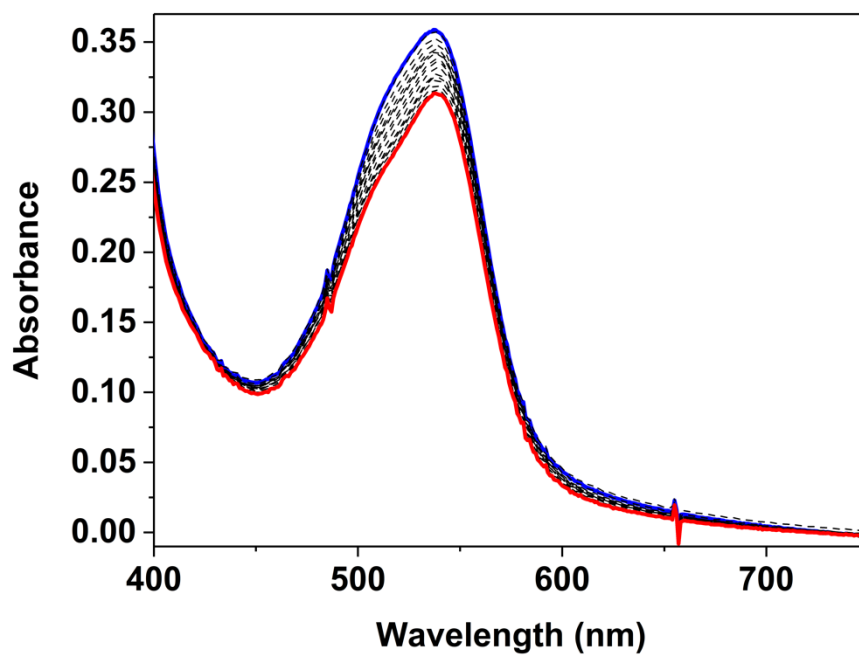


Figure A72. Change in the region between 400 and 700 nm of the electronic absorption spectra of 2H^+ (blue trace) upon the progressive addition of 1 equiv. of 2,6-lutidine up to 15 equiv. (red trace). A partial restoration of the feature typical of **2** is observed in the red trace.

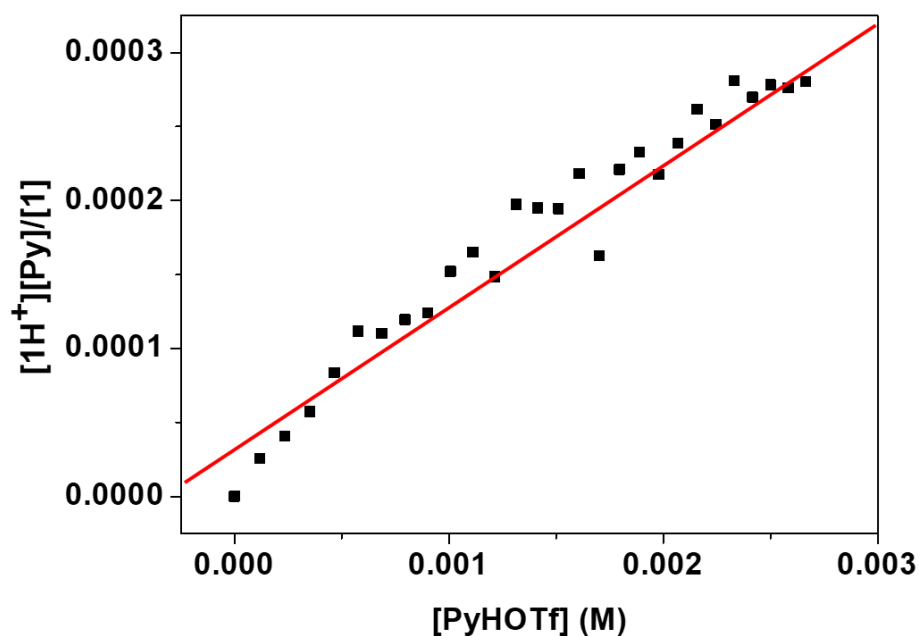


Figure A73. Plot of $[\text{PyHOTf}]$ vs $[\text{2H}^+][\text{Py}]/[\text{2}]$ considering the absorbance at $\lambda = 545$ nm. Slope = 0.10.

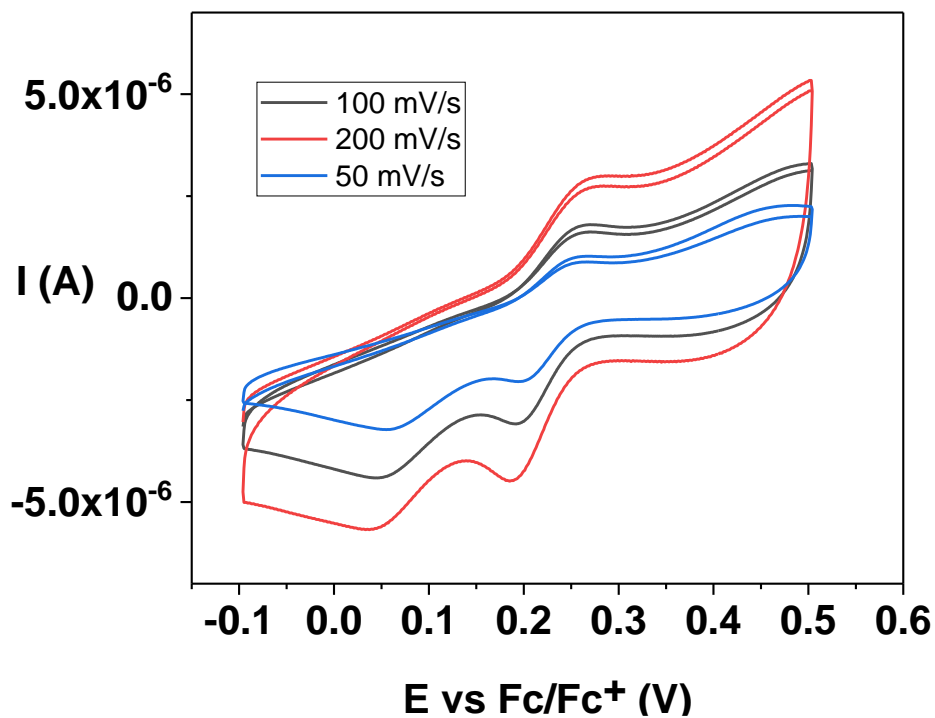


Figure A74. Cyclic voltammetry of 2H^+ obtained by adding 2 equiv. of PyHOTf to **2** (DMF, 1 mM), with a focus on the redox wave at $E_{1/2} = 0.22$ V. Blue trace : scan rate 0.05 V s^{-1} , black trace: scan rate 0.1 V s^{-1} , red trace: 0.2 V s^{-1} .

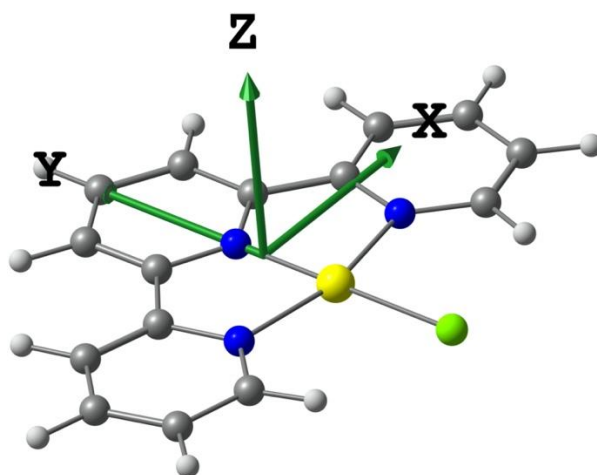


Figure A75. Optimized molecular structure of **1**.

Table A2. Atomic coordinates of optimized structure of **1**.

Au	0.000000000	0.000000000	0.000000000
Cl	0.000000000	-2.287016749	0.000000000
N	2.014413934	0.313342048	0.000000000
N	0.000059116	1.966910494	-0.000121867
N	-2.014360226	0.313346833	0.002918553
C	2.963719264	-0.632361113	0.000314639
H	2.621359501	-1.663434985	0.005904081

C	4.311739297	-0.284349468	-0.006967380
H	5.058928440	-1.073333423	-0.007150976
C	4.667370683	1.061160402	-0.013861409
H	5.714222094	1.356035059	-0.020121485
C	3.669665556	2.037016954	-0.012570356
H	3.920785270	3.094494821	-0.017576794
C	2.335957071	1.652692319	-0.005120240
C	1.201894111	2.580018732	-0.003766314
C	1.218373633	3.973951376	-0.002203227
H	2.162336559	4.511963192	-0.003153193
C	0.000075061	4.657861159	0.002330506
H	0.000087109	5.745347628	0.004181182
C	-1.218297211	3.973931738	0.004903264
H	-2.162255349	4.512008432	0.008955438
C	-1.201794091	2.580033731	0.003537988
C	-2.335889146	1.652717839	0.004356510
C	-3.669555247	2.037115349	0.006593810
H	-3.920457252	3.094691001	0.008801955
C	-4.667365487	1.061338273	0.006706519
H	-5.714178244	1.356297859	0.009104591
C	-4.311695070	-0.284170190	0.003599737
H	-5.058804357	-1.073168925	0.002314597
C	-2.963661785	-0.632329075	0.002027338
H	-2.621431546	-1.663510520	-0.001145959

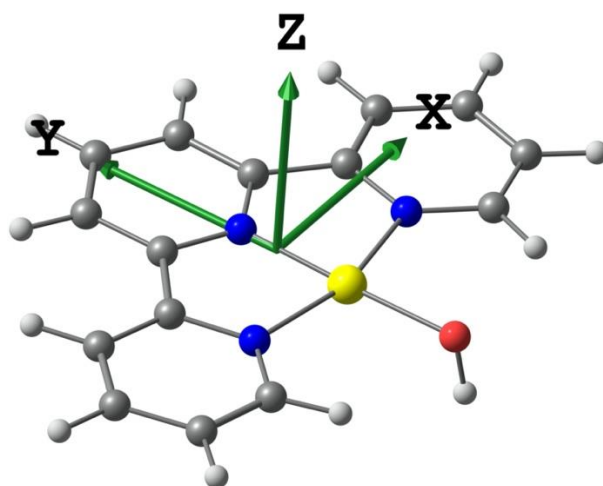


Figure A76. Optimized molecular structure of **2**.

Table A3. Atomic coordinates of optimized structure of **2**.

Au	0.000000000	0.000000000	0.000000000
O	0.000000000	-1.981090347	0.000000000
N	-2.006263957	0.307870068	0.023806548
N	0.003221354	1.962688896	0.072795245
N	2.007664126	0.302187567	0.000000000
C	-2.945292610	-0.646292743	0.011327596
C	-4.296097732	-0.308686422	0.037113276
C	-4.658769115	1.035027400	0.078052873
C	-3.668639784	2.019630095	0.095876225
C	-2.332393917	1.644701280	0.069085272
C	-1.197100153	2.577236402	0.090012757
C	-1.213296221	3.970886250	0.123757273
C	0.007536620	4.651818782	0.135419532
C	1.226152865	3.967295395	0.111096456
C	1.205449445	2.573723346	0.076819003

C	2.337765107	1.638124147	0.041175069
C	3.675135395	2.009777904	0.049519700
C	4.662421365	1.022723071	0.017230835
C	4.295794432	-0.320017968	-0.020319843
C	2.943920318	-0.654377453	-0.027548398
H	-2.584524731	-1.671857048	-0.015514246
H	-5.040103834	-1.100673472	0.025316350
H	-5.707704678	1.322150455	0.098917235
H	-3.928727510	3.074490170	0.131583973
H	-2.155388164	4.512016253	0.139179024
H	0.009252301	5.739073209	0.161177294
H	2.170068326	4.505467555	0.117786956
H	3.937900745	3.064045044	0.082691162
H	5.712263110	1.307085364	0.023866177
H	5.037718138	-1.113675100	-0.043600808
H	2.579786253	-1.678890182	-0.051649542
H	-0.032454772	-2.252823575	-0.935974169

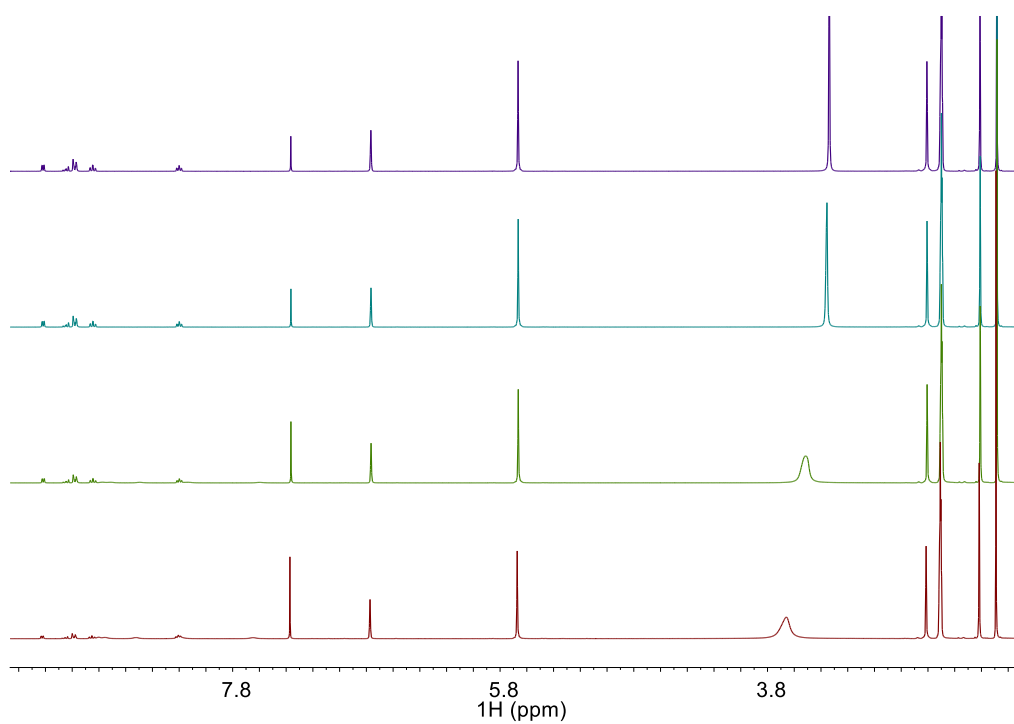


Figure A77. ^1H NMR spectra of the reaction between **1** and CHD (100 equiv.) in DMSO-D_6 ; purple = 0 s, blue = 2 h, green = 5 h, red = 24 h; benzene C–H: $\delta = 7.36$ ppm; H_2O : $\delta = 3.33\text{-}3.72$ ppm.

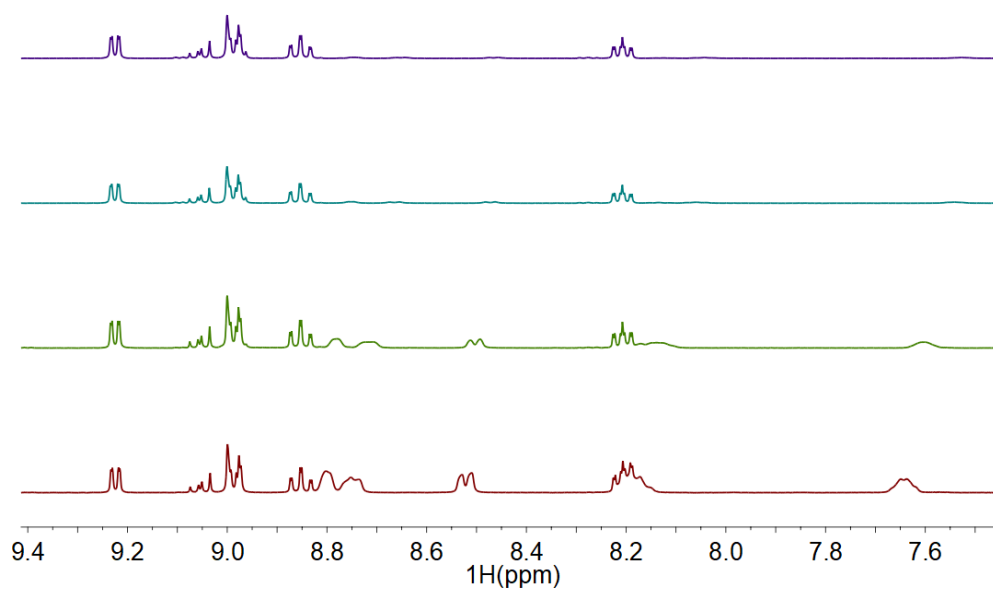


Figure A78. Zoom of the aromatic region (7.5-9.4 ppm) of the ^1H NMR spectra of the reaction between **1** and CHD (100 equiv.) in DMSO-D_6 .

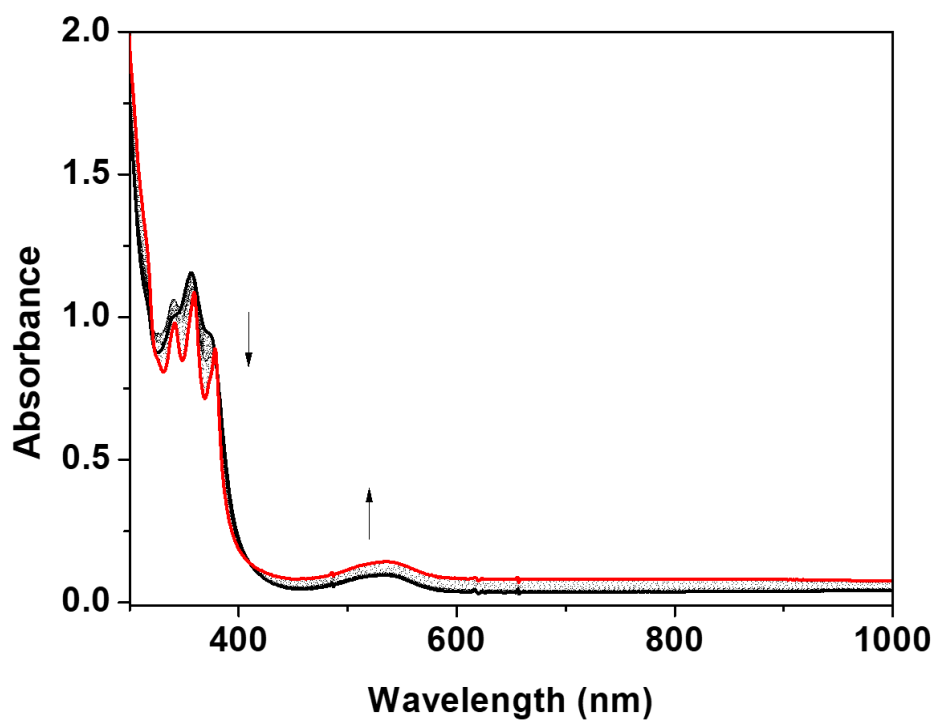


Figure A79. Electronic absorption spectra of the reaction between **1** (0.15 mM, DMF, 25 °C) and DHA (500 equiv.). Black trace = 0 s, red trace = 2500 s.

A.3 Chapter 4

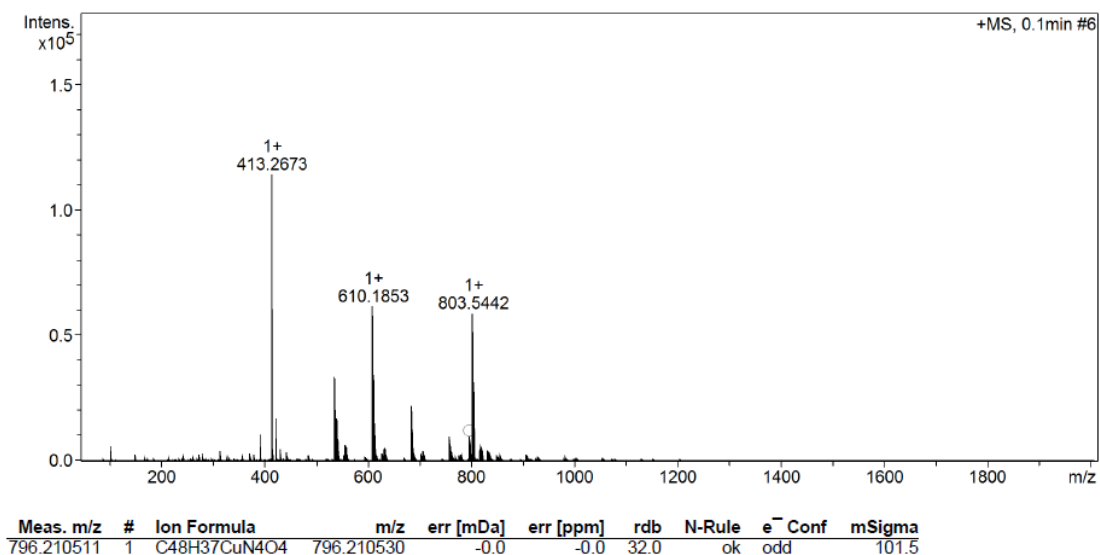


Figure A80. Positive mode ESI-MS spectrum of **1** (calculated m/z of [Cu(T(OMe)PP)]+H⁺ = 796.2105) .

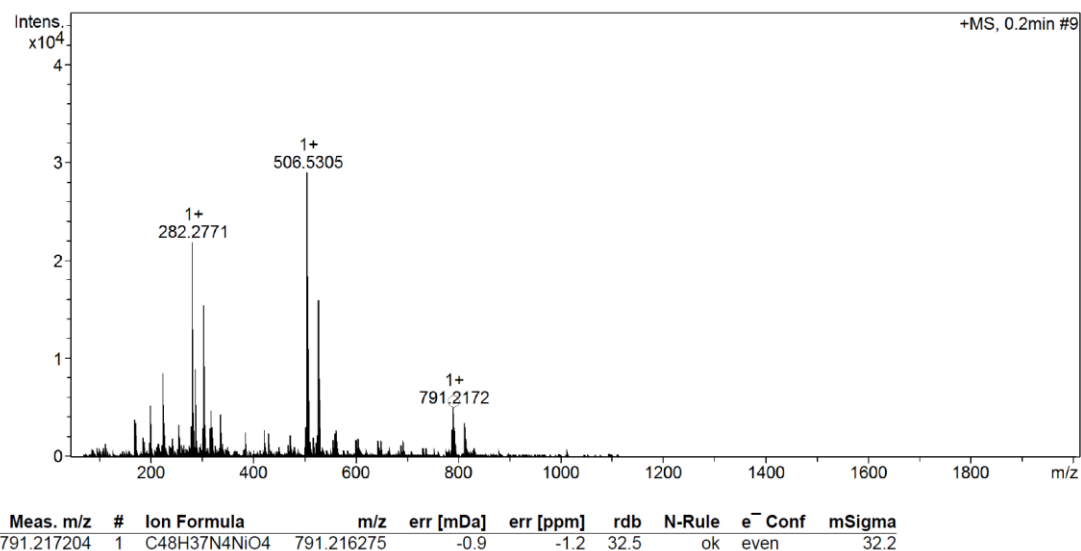


Figure A81. Positive mode ESI-MS spectrum of **2** (calculated m/z of [Ni(T(OMe)PP)]+H⁺ = 791.2163) .

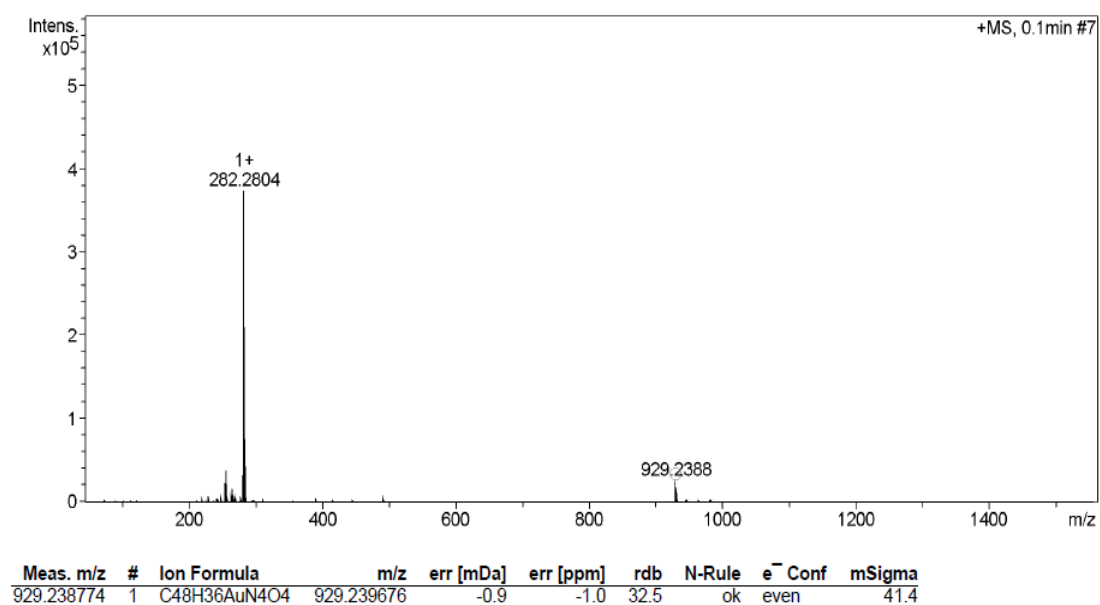


Figure A82. Positive mode ESI-MS spectrum of **3** (calculated m/z of [Au(T(OMe)PP)]⁺ = 929.2397) .

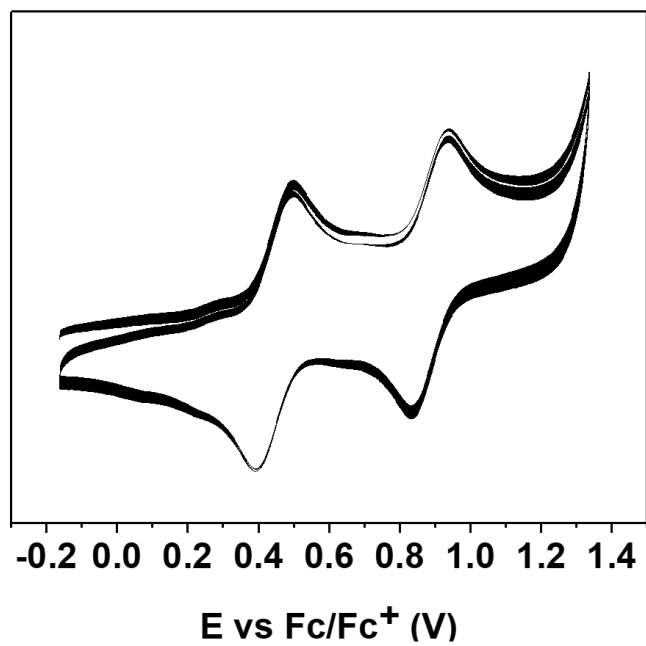


Figure A83. Cyclic voltammograms of **1** in DCM, 1mM, scan rate: 0.1 V/s.

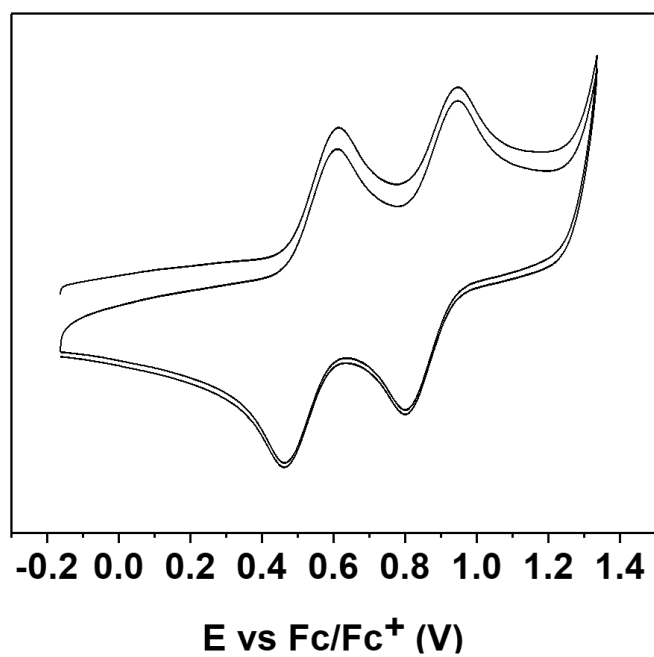


Figure A84. Cyclic voltammograms of **2** in DCM, 1mM, scan rate: 0.1 V/s.

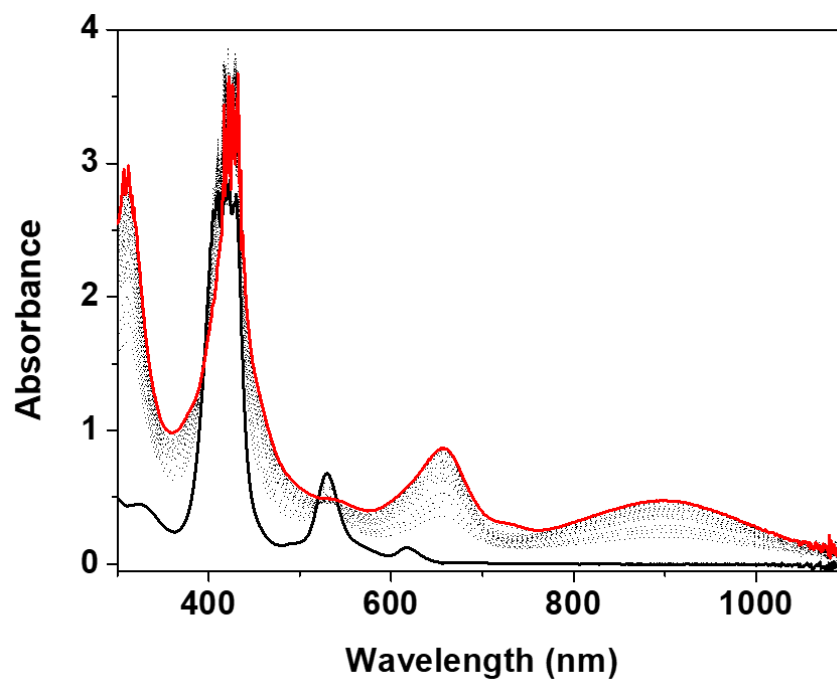


Figure A85. Electronic absorption spectra of **1** before (DCM, -20 °C, black trace) and after the addition of excess Magic Green to yield a new species (red trace).

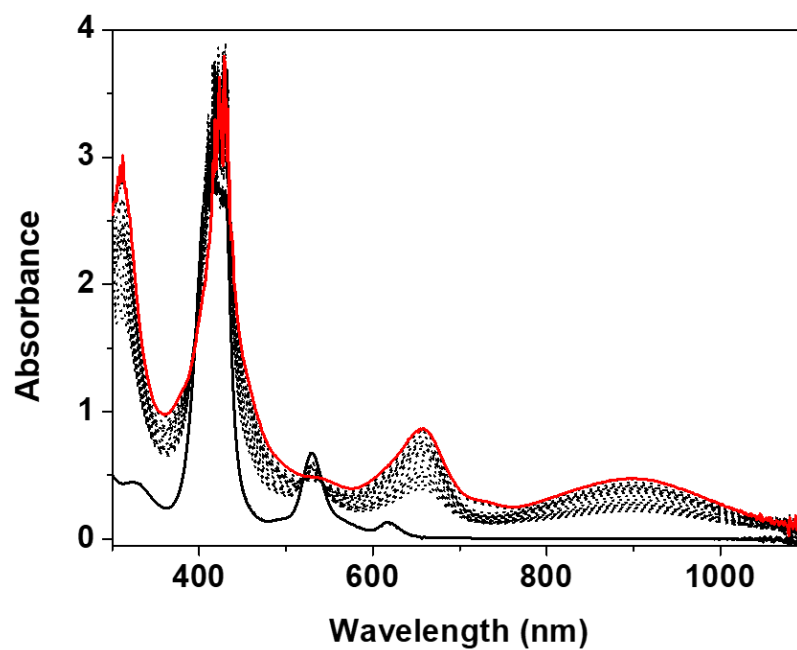


Figure A86. Electronic absorption spectra of **1** before (DCM, -20 °C, black trace) and after the addition of excess Magic Blue to yield a new species (red trace).

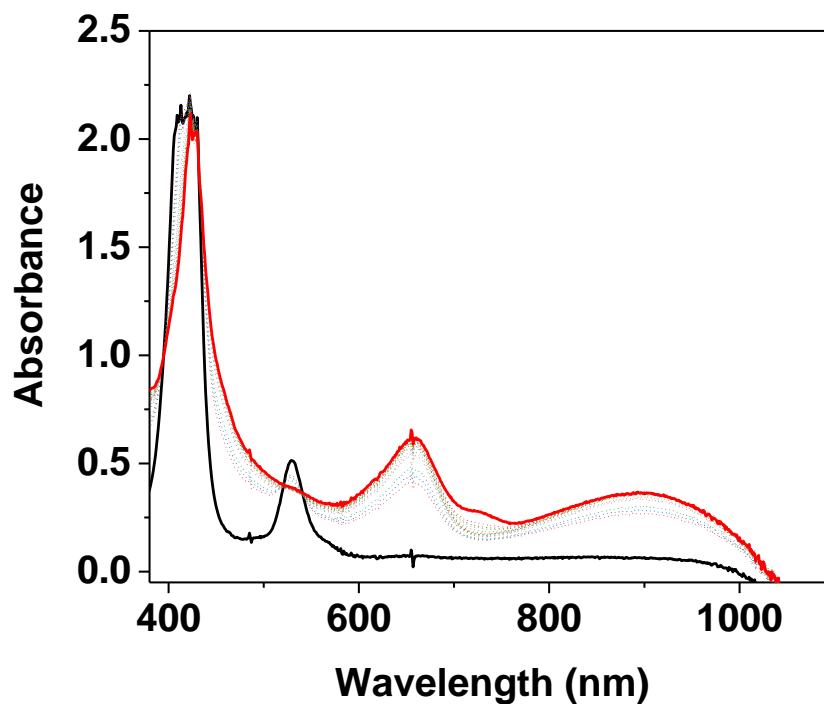


Figure A87. Electronic absorption spectra of **2** before (DCM, -20 °C, black trace) and after the addition of excess Magic Blue to yield a new species (red trace).

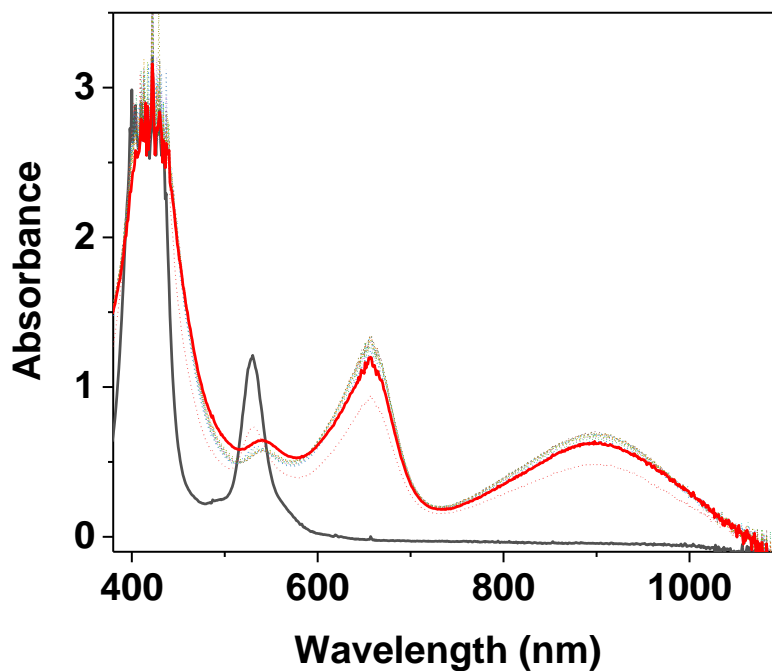


Figure A88. Electronic absorption spectra of **2** before (DCM, -20 °C, black trace) and after the addition of excess WCl_6 to yield a new species (red trace).

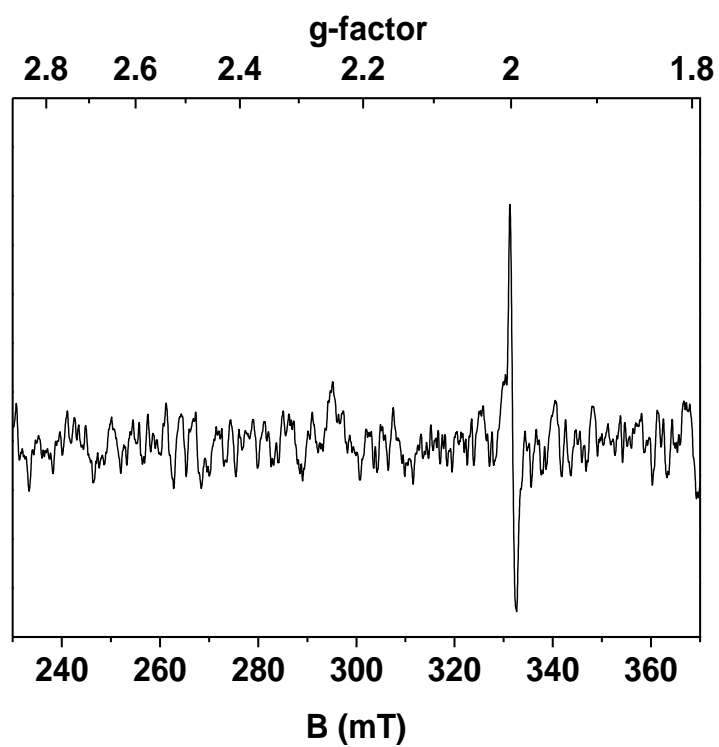


Figure A89. X-Band EPR spectrum of **2OX** obtained with 2 equiv. of WCl_6 , acquired from a frozen DCM solution, 77 K, 1.95 mW microwave power, 0.5 mT field modulation amplitude.

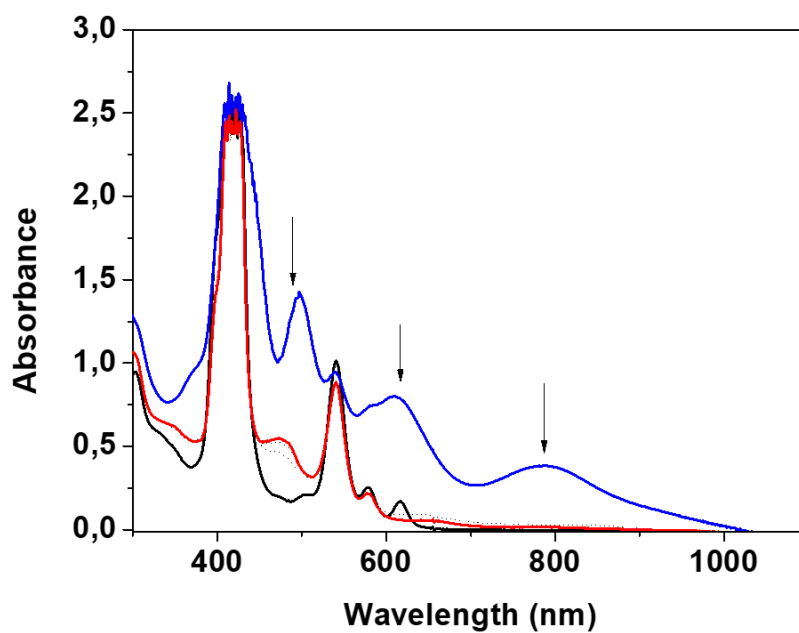


Figure A90. Electronic absorption spectra of **1** (0.08 mM, DCM, -20 °C, black trace), of **1OX** (blue trace) and after the addition of 1 equiv. Et_4NOH to **1OX** (red trace).

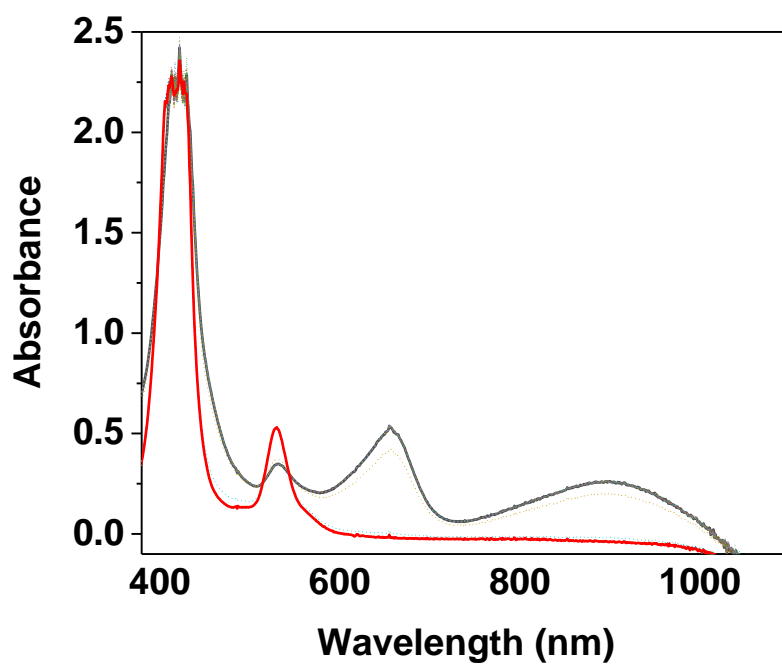


Figure A91. Electronic absorption spectra of **2OX** (black trace) and after the addition of 1 equiv. Et₄NOH to **2OX** (red trace).

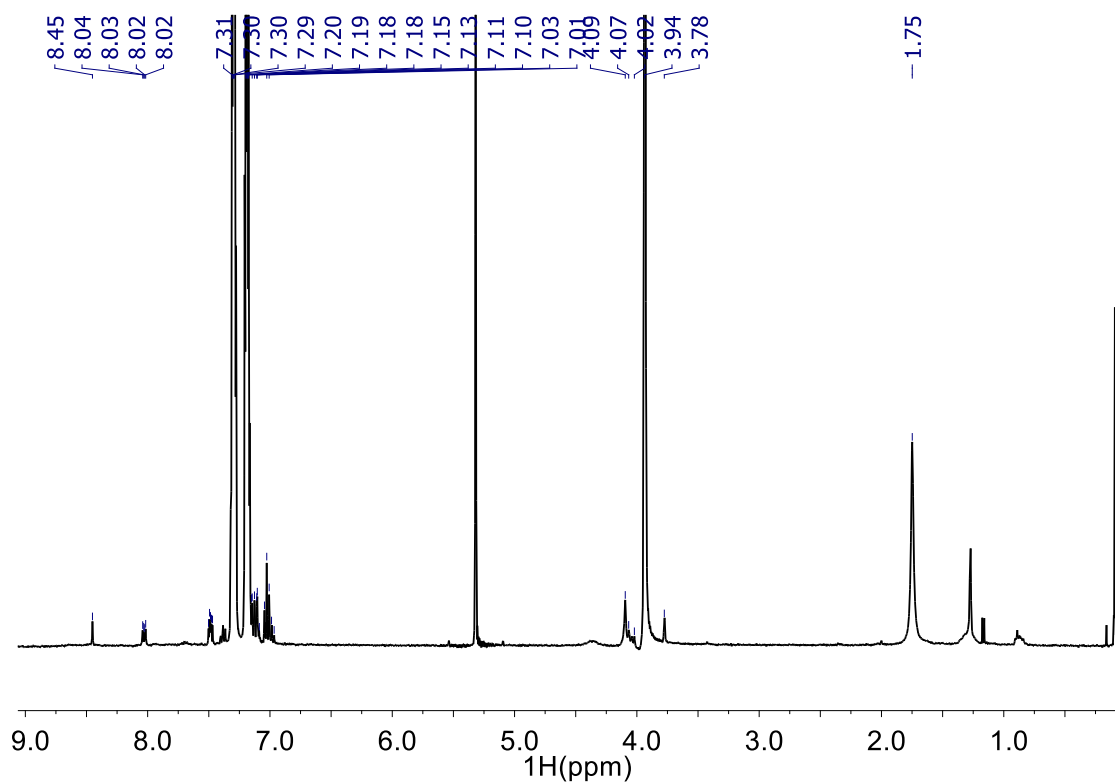


Figure A92. ¹H NMR (400 MHz, CD₂Cl₂) of the reaction between **2OX** and 25 equiv. DHA.

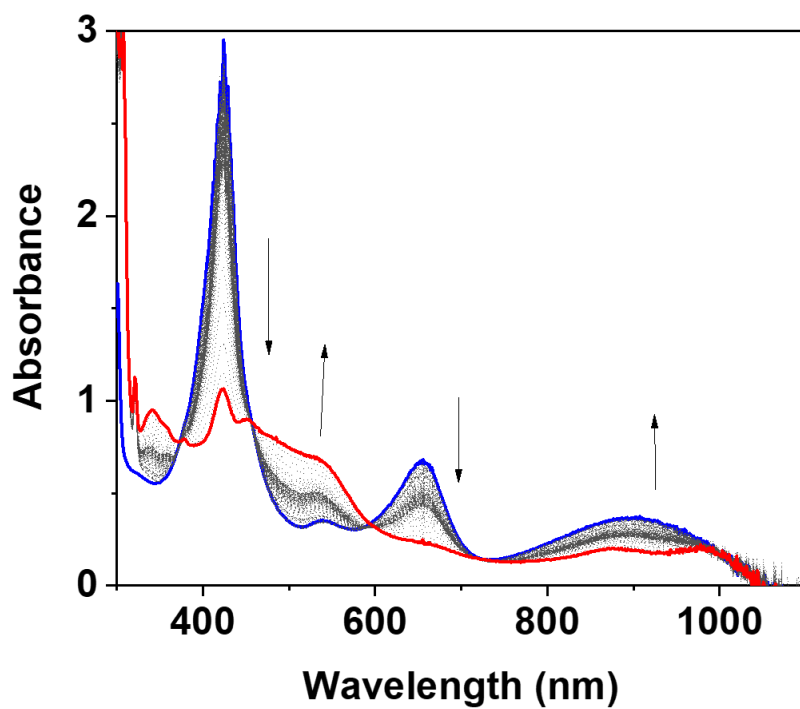


Figure A93. Electronic absorption spectra of the reaction between **2OX** (blue trace) and fluorene (500 equiv., 20 °C, DCM).

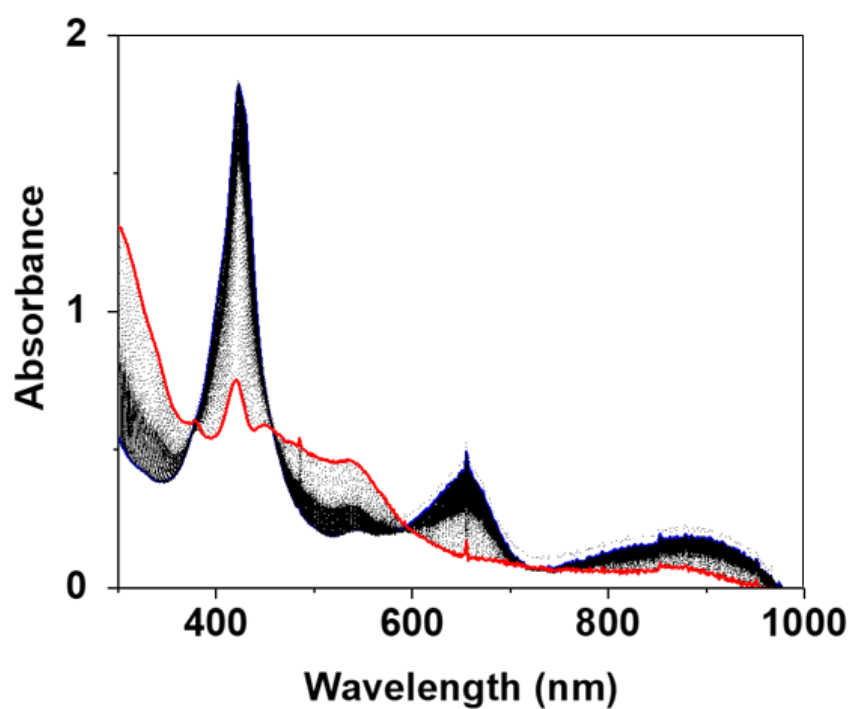


Figure A94. Electronic absorption spectra of the reaction between **2OX** (blue trace) and triphenylmethane (500 equiv., 20 °C, DCM).

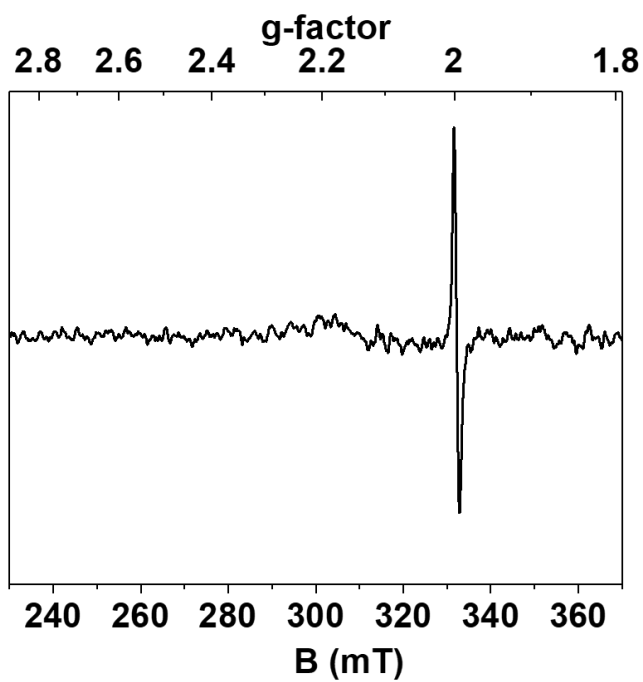


Figure A95. X-Band EPR spectrum of **2OX** in presence of excess anthracene, acquired from a frozen DCM solution, 77 K, 1.95 mW microwave power, 0.5 mT field modulation amplitude.

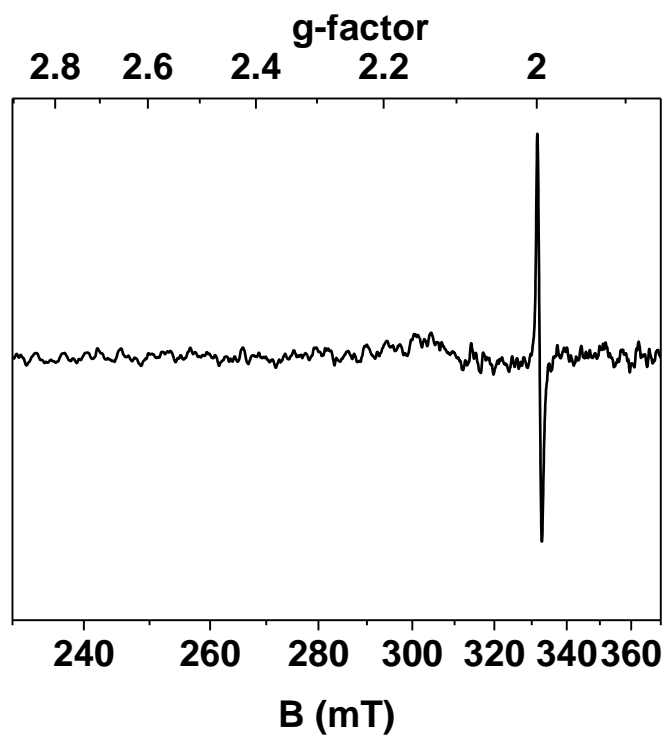


Figure A96. X-Band EPR spectrum of **2OX** in presence of excess **2**, acquired from a frozen DCM solution, 77 K, 1.95 mW microwave power, 0.5 mT field modulation amplitude.

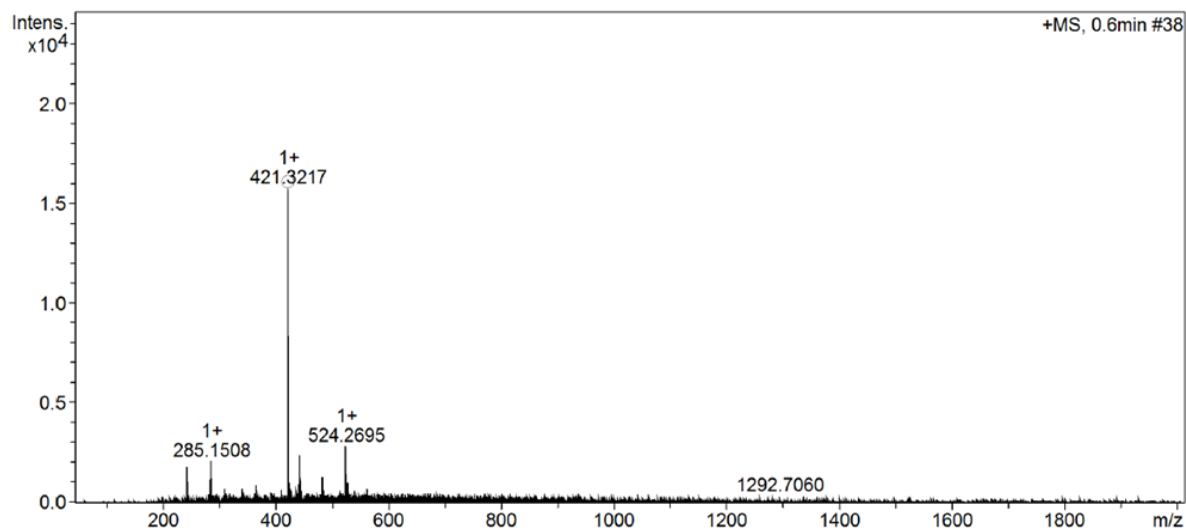
A.4 Chapter 5

Table A4. Crystal data and structure refinement for **3**.

Empirical formula	$C_{58}H_{85}N_4O_{2.50}$	μ	0.064 mm^{-1}
Formula weight	878.29	F(000)	962
Temperature	100(2) K	Crystal size	$0.23 \times 0.15 \times 0.08 \text{ mm}^3$
Crystal system	Triclinic	Radiation	MoK α ($\lambda = 0.71073 \text{ \AA}$)
Space group	$P\bar{1}$	2 θ range for data collection/ $^\circ$	1.594 to 26.500.
a/ \AA	11.8088(4)	Index ranges	$-11 \leq h \leq 14, -17 \leq k \leq 17, -$
b/ \AA	13.5755(5)		$23 \leq l \leq 23$
c/ \AA	18.5175(7)	Reflections collected	49399
$\alpha/^\circ$	108.2327(13)	Independent reflections	11338 [R(int) = 0.0542]
$\beta/^\circ$	100.3815(14)	Data/restraints/parameters	11338 / 1 / 615
$\gamma/^\circ$	94.1372(14)	Goodness-of-fit on F^2	1.016
Volume	$2746.98(17) \text{ \AA}^3$	Final R indices [$I > 2\sigma(I)$]	R1 = 0.0513, wR2 = 0.1151
Z	2	R indices (all data)	R1 = 0.1134, wR2 = 0.1359
$\rho_{\text{calc}}/ \text{g/cm}^3$	1.062	Largest diff. peak and hole/ e.\AA^{-3}	0.247 / -0.248

Table A5. Crystal data and structure refinement for **4**.

Empirical formula	C ₉₀ H ₁₁₂ N ₉ O _{4.50}	μ	0.069 mm ⁻¹
Formula weight	1391.88	F(000)	1502
Temperature	100(2) K	Crystal size	0.23 x 0.15 x 0.08 mm ³
Crystal system	Triclinic	Radiation	MoK α (λ = 0.71073 Å)
Space group	P $\bar{1}$	2 θ range for data collection/ ^o	1.594 to 26.500
a/ Å	10.9658(5)	Index ranges	-13 \leq h \leq 13, -20 \leq k \leq 20, -
b/ Å	16.1173(7)		30 \leq l \leq 30
c/ Å	23.9112(11)	Reflections collected	60315
α / ^o	91.976(2)	Independent reflections	17043 [R(int) = 0.0707]
β / ^o	98.732(2)	Data/restraints/parameters	17043 / 6 / 974
γ / ^o	98.590(2)	Goodness-of-fit on F ²	1.014
Volume	4123.1(3) Å ³	Final R indices [I > 2 σ (I)]	R1 = 0.0754, wR2 = 0.1889
Z	2	R indices (all data)	R1 = 0.1484, wR2 = 0.2277
ρ_{calc} / g/cm ³	1.121	Largest diff. peak and hole/ e.Å ⁻³	0.756/-0.512

**Figure A97.** Positive mode ESI-MS spectrum of **3** (calculated m/z of C₂₈H₄₁N₂O = 421.3213).

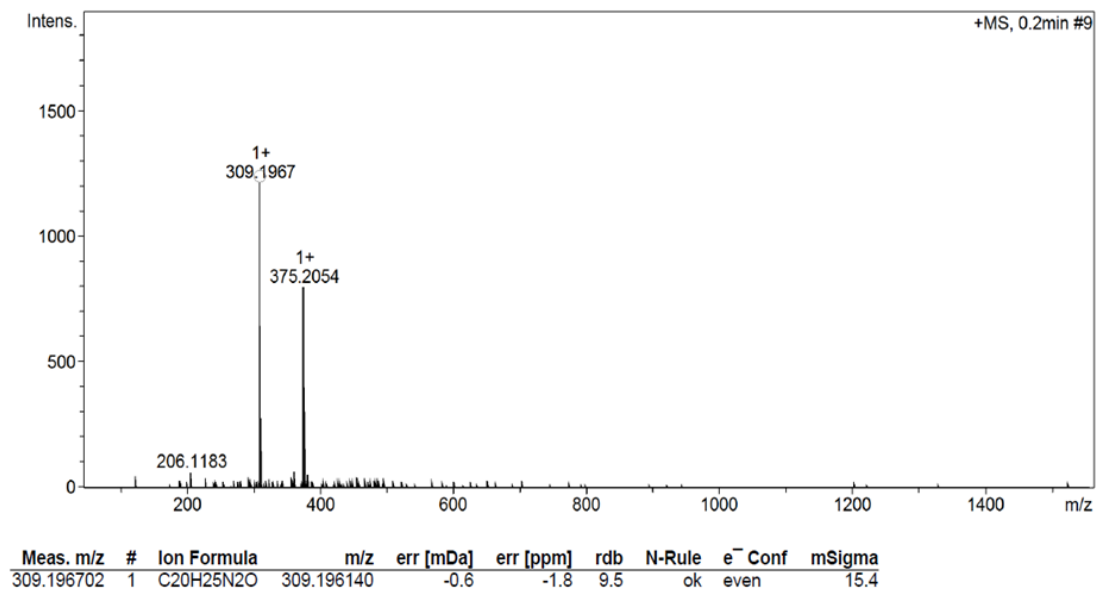


Figure A98. Positive mode ESI-MS spectrum of **4** (calculated m/z of C₂₀H₂₅N₂O = 309.1961) .

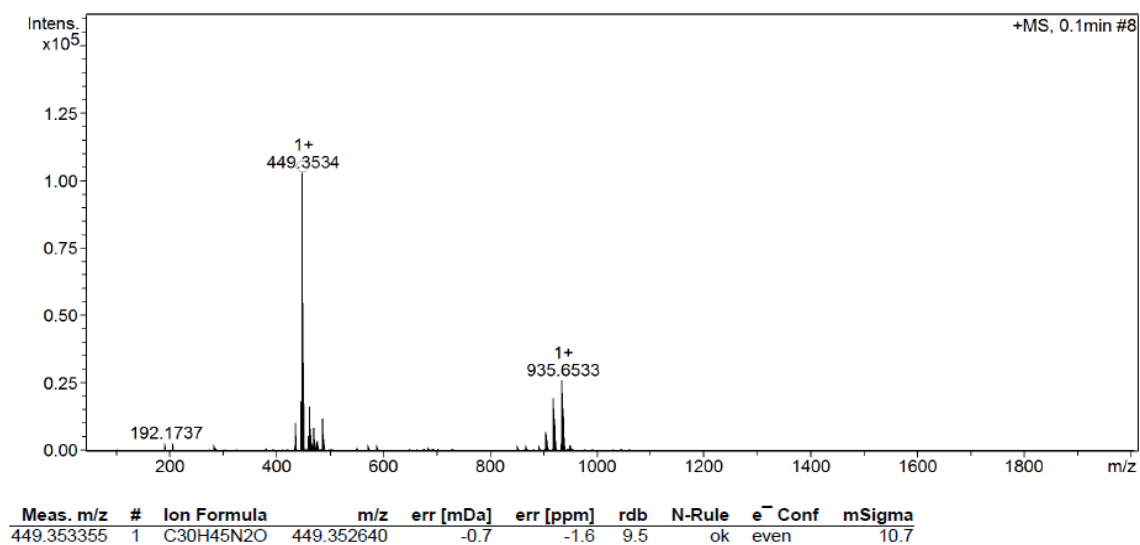


Figure A99. Positive mode ESI-MS spectrum of **15** (calculated m/z of C₃₀H₄₅N₂O = 449.3526) .

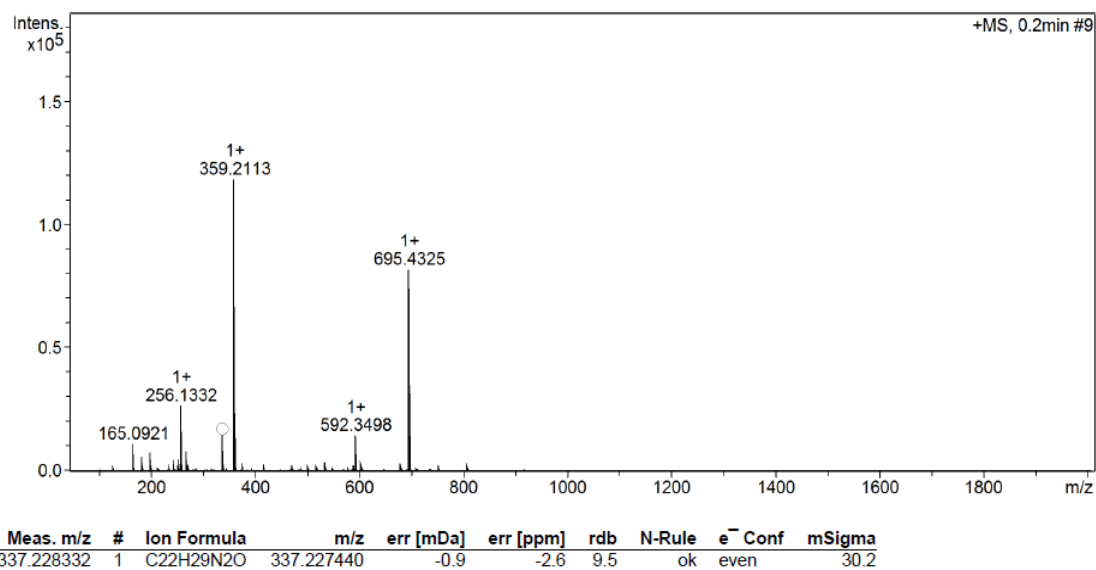


Figure A100. Positive mode ESI-MS spectrum of **16** (calculated m/z of C₂₂H₂₉N₂O = 337.2274).

Table A6. Crystal data and structure refinement for **13**.

Empirical formula	C ₃₈ H ₅₈ CuF ₆ N ₄ O ₉ S ₂	μ	0.610 mm ⁻¹
Formula weight	956.54	F(000)	2004
Temperature	100(2) K	Crystal size	0.39 x 0.37 x 0.21 mm ³
Crystal system	Monoclinic	Radiation	MoK α (λ = 0.71073 Å)
Space group	P2 ₁ /c	2 Θ range for data collection/°	2.624 to 26.491
a/ Å	20.6776(11)	Index ranges	-13 ≤ h ≤ 13, -20 ≤ k ≤ 20, -
b/ Å	11.2101(6)		30 ≤ l ≤ 30
c/ Å	21.0510(11)	Reflections collected	191529
α /°	90	Independent reflections	9950 [R(int) = 0.0456]
β /°	96.185(3)	Data / restraints / parameters	9950 / 131 / 706
γ /°	90	Goodness-of-fit on F ²	1.060
Volume	4851.2(4) Å ³	Final R indices [I > 2 σ (I)]	R1 = 0.0406, wR2 = 0.0921
Z	4	R indices (all data)	R1 = 0.0552, wR2 = 0.1034
ρ_{calc} / g/cm ³	1.310	Largest diff. peak and hole/ e.Å ⁻³	0.679 / 0.543

Table A7. Crystal data and structure refinement for **17**.

Empirical formula	C ₆₈ H ₁₀₂ K ₂ N ₄ O ₄	μ	0.190 mm ⁻¹
Formula weight	1117.73	F(000)	1216
Temperature	110(2) K	Crystal size	0.38 x 0.22 x 0.14 mm ³
Crystal system	Monoclinic	Radiation	MoK α (λ = 0.71073 Å)
Space group	P2 ₁ /n	2 Θ range for data collection/°	2.580 to 26.434
a/ Å	10.0947(7)	Index ranges	-12 \leq h \leq 12, -23 \leq k \leq 23, -
b/ Å	18.9113(12)		21 \leq l \leq 22
c/ Å	17.6985(12)	Reflections collected	32665
α /°	90	Independent reflections	6822 [R(int) = 0.0492]
β /°	100.957(2)	Data/restraints/parameters	6822 / 137 / 430
γ /°	90	Goodness-of-fit on F ²	1.192
Volume	3317.1(4) Å ³	Final R indices [I > 2 σ (I)]	R1 = 0.0841, wR2 = 0.1724
Z	2	R indices (all data)	R1 = 0.1005, wR2 = 0.1797
ρ_{calc} / g/cm ³	1.119	Largest diff. peak and hole/ e.Å ⁻³	0.537/-0.477

Table A8. Crystal data and structure refinement for **18**.

Empirical formula	$C_{38.50}H_{55.75}CuF_6N_{3.25}O_8S_2$	μ	0.656 mm^{-1}
Formula weight	933.77	F(000)	1954
Temperature	100(2) K	Crystal size	0.21 x 0.18 x 0.01 mm ³
Crystal system	Monoclinic	Radiation	MoK α ($\lambda =$ 0.71073 Å)
Space group	P2 ₁ /n	2 θ range for data collection/ $^\circ$	2.536 to 26.392
a/ Å	14.396(3)	Index ranges	-18 $\leq h \leq$ 18, -
b/ Å	17.124(3)		21 $\leq k \leq$ 21, -
c/ Å	18.311(4)		22 $\leq l \leq$ 22
$\alpha/^\circ$	90	Reflections collected	45945
$\beta/^\circ$	96.679(5) $^\circ$.	Independent reflections	9158 [R(int) = 0.0846]
$\gamma/^\circ$	90	Data / restraints / parameters	9158 / 334 / 703
Volume	4483.3(15) Å ³	Goodness-of-fit on F ²	1.030
Z	4	Final R indices [I > 2 σ (I)]	R1 = 0.0764, wR2 = 0.1909
$\rho_{\text{calc}}/ \text{g/cm}^3$	1.383	R indices (all data)	R1 = 0.1232, wR2 = 0.2246
		Largest diff. peak and hole/ e.Å ⁻³	1.529 / -0.968

